ASME
SETTING THE STANDARD

Journal of Engineering for Gas Turbines and Power

Published Bimonthly by ASME

VOLUME 131 • NUMBER 5 • SEPTEMBER 2009

Transactions of the ASME, Journal of Engineering for Gas Turbines and Power (ISSN 0742-4795) is published bimonthly (Jan., Mar., May, July, Sep, Nov.) by The American Society of Mechanical Engineers, Three Park Avenue, New York, NY 10016. Periodicals postage paid at New York, NY and additional mailing offices. POSTMASTER: Send address changes to Transactions of the ASME, Journal of Engineering for Gas Turbines and Power, c/o THE AMERICAN SOCIETY OF MECHANICAL ENGINEERS, 22 Law Drive, Box 2300, Fairfield, NJ 07007-2300.
CHANGES OF ADDRESS must be received at Society headquarters seven weeks before they are to be effective. Please send old label and new address.
STATEMENT from By-Laws. The Society shall not be responsible for statements or opinions advanced in papers or ... printed in its publications (B7.1, par. 3).

RESEARCH PAPERS

(Contents continued on inside back cover)

This journal is printed on acid-free paper, which exceeds the ANSI Z39.48-1992 specification for permanence of paper and library materials. ♾™
♻ 85% recycled content, including 10% post-consumer fibers.

Journal of Engineering for Gas Turbines and Power SEPTEMBER 2009

Volume 131, Number 5

TECHNICAL BRIEFS

The ASME Journal of Engineering for Gas Turbines and Power is abstracted and indexed in the following:

AESIS (Australia's Geoscience, Minerals, & Petroleum Database), Applied Science & Technology Index, Aquatic Sciences and Fisheries Abstracts, Civil Engineering Abstracts, Compendex (The electronic equivalent of Engineering Index), Computer & Information Systems Abstracts, Corrosion Abstracts, Current Contents, Engineered Materials Abstracts, Engineering Index, Enviroline (The electronic equivalent of Environment Abstracts), Environment Abstracts, Environmental Science and Pollution Management, Fluidex, INSPEC, Mechanical & Transportation Engineering Abstracts, Mechanical Engineering Abstracts, METADEX (The electronic equivalent of Metals Abstracts and Alloys Index), Pollution Abstracts, Referativnyi Zhurnal, Science Citation Index, SciSearch (The electronic equivalent of Science Citation Index), Shock and Vibration Digest

Characteristics of Flow and Flame Behavior Behind Rifled/Unrifled Nozzles

Kuo C. San[1]
Associate Professor
Department of Aviation and Communication Electronics,
Air Force Institute of Technology,
Kaohsiung, Taiwan 820, R.O.C.
e-mail: kcsan@mail.afats.khc.edu.tw

Hung J. Hsu
Department of Mechanical and Mechatronic Engineering,
National Taiwan Ocean University,
Keelung, Taiwan 202, R.O.C.

A novel rifled nozzle was installed behind a conventional combustion exhauster to improve combustion efficiency. The rifled nozzles improve the momentum transmission, turbulent strength, and mixing efficiency between the central jet and annular jet. The flow characteristics behind the nozzles (rifled and unrifled) were visualized and detected using the smoke-wire flow visualization, particle image velocimetry, and hot-wire anemometry. The cold flow structures were categorized into four modes—jet flow, single bubble, dual bubble, and turbulent flow. The topological scheme was adopted to analyze and verify these flow modes. The flame structures behind the nozzles (rifled and unrifled) are classified into three modes—jet flame, flickering flame, and turbulent flame—using the direct-photo visualization. The flame height of a 12-rifled nozzle is decreased by about 50% under that of an unrifled nozzle. The flame shedding frequency declines rapidly in the flickering flame mode and the relationship between the Strouhal number (Sr) and annular velocity (u_a) is $Sr=0.0238+0.13/u_a$. [DOI: 10.1115/1.3078388]

Keywords: rifled nozzles, flow characteristics, flame behavior

1 Introduction

Bluff bodies and swirling flow were utilized to increase the mixing between air and fuel flows and to improve the efficiency of combustion and heat transfer in industrial combustors, flow mixers, and other industrial equipments. The effects of swirling flow and bluff body form a low-pressure recirculation zone near the nozzle outlet and then increase the diffusion between the central jet-flow and recirculation zone. The increase in turbulent intensity and interaction time causes an intense mixing between the central jet and the recirculation zones. Accordingly, the mixing concentration and the combustion stability are increased. Gupta et al. [1], Rose [2], Chigier and Beer [3], and Davies and Beer [4] examined the typical flow properties in the recirculation zone such as the velocity profile and pressure distribution, and determined the relationship between the combustion efficiency and the bluff body/swirling jet.

Numerous recent studies have examined the flow around a bluff body flame stabilizer in both reacting and nonreacting environments. Carmody [5] used a pitot tube to delineate the mean flow field and pressure distribution when a free annular jet-flow moved around a circular bluff disk. Carmody found that 95% of energy in the mean flow was converted to an intensive turbulent disturbance within the range of $3r$, where r is the disk radius. Davies and Beer [4] utilized the hot-wire anemometry to investigate the mean flow structures, the effect of blockage ratio, and the turbulent properties when a free annular jet flew through a bluff body. They also defined three flow regions—recirculation region, transition region, and established region where the flow behavior in the established region is similar to that in the jet flow mode. Durao and Whitelaw [6] measured the mean velocity field, turbulent properties, probability density function (pdf) distributions, and energy spectra using a laser Doppler velocimeter (LDV) when a free annular jet flow passed a bluff body. Durao and Whitelaw indicated that the turbulent flow is not isotropic and that a larger blockage ratio of bluff body was associated with a shorter recirculation zone. Schefer et al. [7] examined the flow structures, velocity profiles, and the axial pdf-distribution between central-penetrating and unpenetrating flows using the two-dimensional LDV. Schefer et al. [7] found a dual-peak pdf-distribution near the rim of the central jet flow and a Gaussian pdf-distribution in the other regions.

Huang and Lin [8] investigated the flame temperature and the velocity distribution of a circular bluff disk (blockage ratio =0.44) by using the direct-photo and Schlieren flow visualization techniques. Huang and Lin classified the flame structures into seven modes—recirculated flame, transition flame, unsteady detached flame, laminar ring flame, developing flame, split flashing flame, and lift flame. They also found that a triple flame existed at the rim of the blue annular flame in the laminar ring-flame mode. Gu et al. [9] studied the unsteady aerodynamic structures and the stability limit of the turbulent nonpremixed flame using the humidity effect and the particle image velocimetry (PIV) scheme. Gu et al. [9] categorized the flame into four modes—recirculation zone flame, transition flame, central-jet dominated flame, and partially quenched flame—using different velocities of air and fuel. Gu et al. [9] determined that the increase in combustion reacting time significantly reduced the limit of the partially quenching flame when humid air joined the flow.

Many researchers have examined various mechanisms to produce swirling flow. Rose [2], Hartnett and Eckert [10], and Hübner et al. [11] mobilized axial swirling flow by rotating a cylinder. The cylinder was rotated from rest to 5000 rev/min (rpm) with an increment of 500 rpm, and the swirling flow was driven by the tangential linear momentum that was generated by the viscosity. However, the swirl intensity is weak because the viscosity of air is low. Chigier and Beer [3], Cheng [12], and Al-Abdeli and Masri [13] stirred the swirling flow by conducting a tangential flow into a swirl generator. Al-Abdeli and Masri [13] utilized a tangential inlet flow to control the swirling flow and increase the swirling number (S) as high as 1.59. Kerr and Fraser [14], Guttenfelder et al. [15], and Huang and Tsai [16] excited the swirling flow by changing the angle of a swirl vane pack. Huang and Tsai applied a swirl vane pack with an angle-tunable wing-airfoil to generate swirling flow. They found that the global unsteady flow field and the increase in turbulent intensity dominate the flow mixing.

Chervinsky [17] utilized the theoretical analysis and experimental results to examine the width, length, and temperature of

[1]Corresponding author.

Manuscript received June 15, 2008; final manuscript received November 30, 2008; published online May 22, 2009. Review conducted by Nader Rizk.

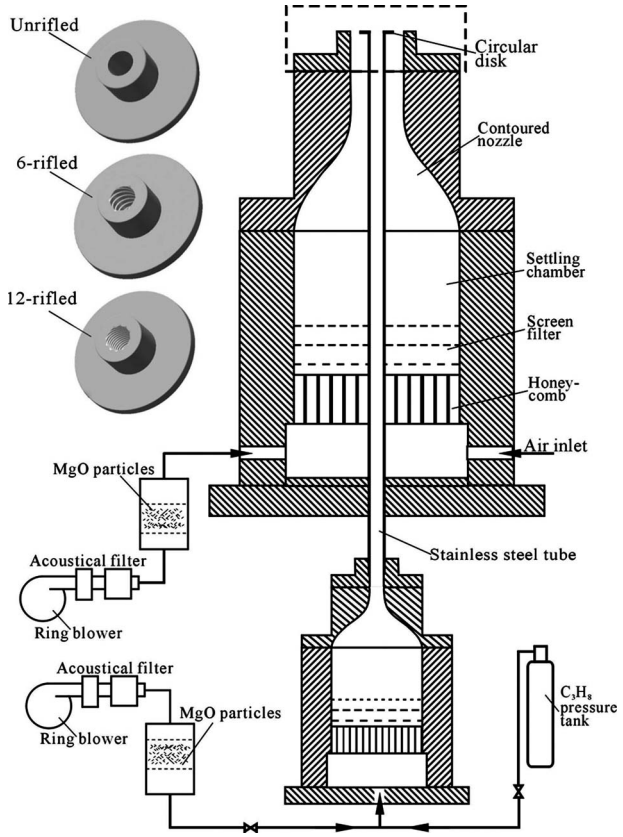

Fig. 1 Experimental setup

flames and the mass entrainment at a fixed flux of C_3H_8 with various swirling numbers. Chervinsky found that the increase in swirling number increases the flame width, the highest temperature, and the mass entrainment; however, it decreases the flame height. Chen and Driscoll [18] investigated the flame height of swirling flow and the velocity profile in the recirculation using the flow observation scheme. Chen and Driscoll [18] found that the recirculation increases the mixing efficiency of a large-scale flow structure. They also found that the increase in swirling number shortens the flame height and velocity in the recirculation zone, and that the flame height approaches a fixed value as $S>0.5$. Morcos and Abdel-Rahim [19] observed the flame length in both nonswirling and swirling flows. They found that the flame length generally decreased with increasing air-fuel mass flow rate ratio, burner tube diameter, axial distance between combustor exit and entrance of burner tube, fuel-air pressure ratio, and degree of swirling represented by air tangential angular speed. However, the flame length increased with increasing burner tube length. Morcos and Abdel-Rahim [19] also claimed that the flame length in a nonswirling flow is approximately 4% shorter than that in a swirling flow.

This investigation utilized the rifled nozzles with different swirling intensities to increase the interaction between the axial stress of central flow and the axial/tangential stress of swirled annular airflow, and therefore increase the turbulent intensity and the shedding efficiencies between the fuel and swirling jets. The smoke-wire flow visualization, PIV scheme, and topology analysis were applied to observe and analyze the flow structures behind the riffled nozzles. The flame modes, flame height, and flame shedding frequency were also probed.

2 Experiments

2.1 Experimental Setup. Figure 1 schematically depicts the experimental setup. The airflow was driven by a ring-blower at the outlet where an acoustical filter was installed to eliminate the ripples. The central jet comprised of air and C_3H_8 was for flow analysis and flame observations. A pressure regulator, a needle valve, and a rotameter were placed upstream to maintain the flow stability. The experimental apparatus utilized herein were separated into four sections—filter, settling chamber, rifled nozzle, and test sections. In the filter section, the honeycombs and meshes were applied to reduce the flow noise. The honeycombs were used to reduce the radial noise and the meshes installed in parallel were utilized to lower the axial noise. The settling chamber was used to reduce the turbulent intensity and the rifled nozzles were designed to generate swirling flow. In this investigation, three types of nozzles, as listed in Table 1, were adopted. In the test section, the exit diameter of swirling flow (D_o) was 30 mm and the diameter of central flow (d) was 5 mm. A bluff disk (diameter $D=20$ mm) was installed at the exit center. Consequently, the blockage ratio defined by $B=(D/D_o)^2$ was 0.444. The coordinate axes used herein are x and r, which represent the axial and radial axes, respectively. During flame observation, the nozzles burned commercial propane with composition of 95% C_3H_8, 3.5% C_2H_8, and 1.5% C_4H_{10}.

Table 1 Nozzle configurations

Nozzle	Rifles	Outer diameter (mm)	Inner diameter (mm)	Height (mm)	Length (mm)
6-rifled	6	40	30	52	107.6
12-rifled	12	40	30	52	107.6

2.2 Flow Visualization. The flow field was visualized using the smoke-wire visualization. The smoke-streak was produced by heating a zigzag tungsten wire placed close to the jet exit. The diameter of the tungsten wire was 0.2 mm and the zigzag structure was adopted to control the thickness and spacing of the smoke streaks. A thin coating of mineral oil was brushed on the wire surface and then electrically heated to create fine smoke streaks. The Reynolds numbers based on the tungsten-wire diameter were adjusted below 40 to prevent vortex shedding behind the wire [20]. The diameter of aerosol vapor was 1.7 ± 0.3 μm measured by a Malvern 1600C laser particle analyzer. The Stokes number [21] of oil aerosol was at the order of 10^{-3}, which is much lower than one, and therefore the smoke streaks were considered to follow the flow properly. The smoke streaks were illuminated by a 0.6 mm thick laser-light-sheet adjusted by a 20 deg laser-light-sheet expander. The laser wavelength is 540 nm supplied by a Spectra-Physics' Stabilite-2017 6 W argon-ion laser. Two-dimensional streak-images of flow patterns were retrieved using a charge-coupled device (CCD) camera and these images were recorded in a computer at a frame rate of 30 frames/s (fps). The CCD camera is JAI Model CV-A1 with a resolution of 1392 $\times$512 pixels. The pixels are 4.65 μm^2 and can be operated continuously or in an external trigger mode. The pixel array is zoomed and mapped to a physical region of approximately 13 $\times5$ cm^2 so that the spatial resolution is about 97 μm/pixel. The maximum framing rate of the CCD camera is 30 fps. The Data Translation Mateox Model Meteor-II frame grabber board is employed to digitize the analog voltage output from the CCD array of the camera. During the flame observations, a digital camera (SONY HDR-HC1) was utilized to capture the flame images, which were stored synchronously in a computer. The shutter of the digital camera was set in the range 1/4–1/10,000 s and the frame rate was set at 30 fps.

2.3 PIV Measurement. The PIV image acquisition system, comprised of an argon-ion laser, a high speed camera, and a data translation board, was utilized to measure the velocity contours. The laser light was transmitted by an optical fiber and the thickness of the laser was adjusted by a 20 deg laser-light-sheet ex-

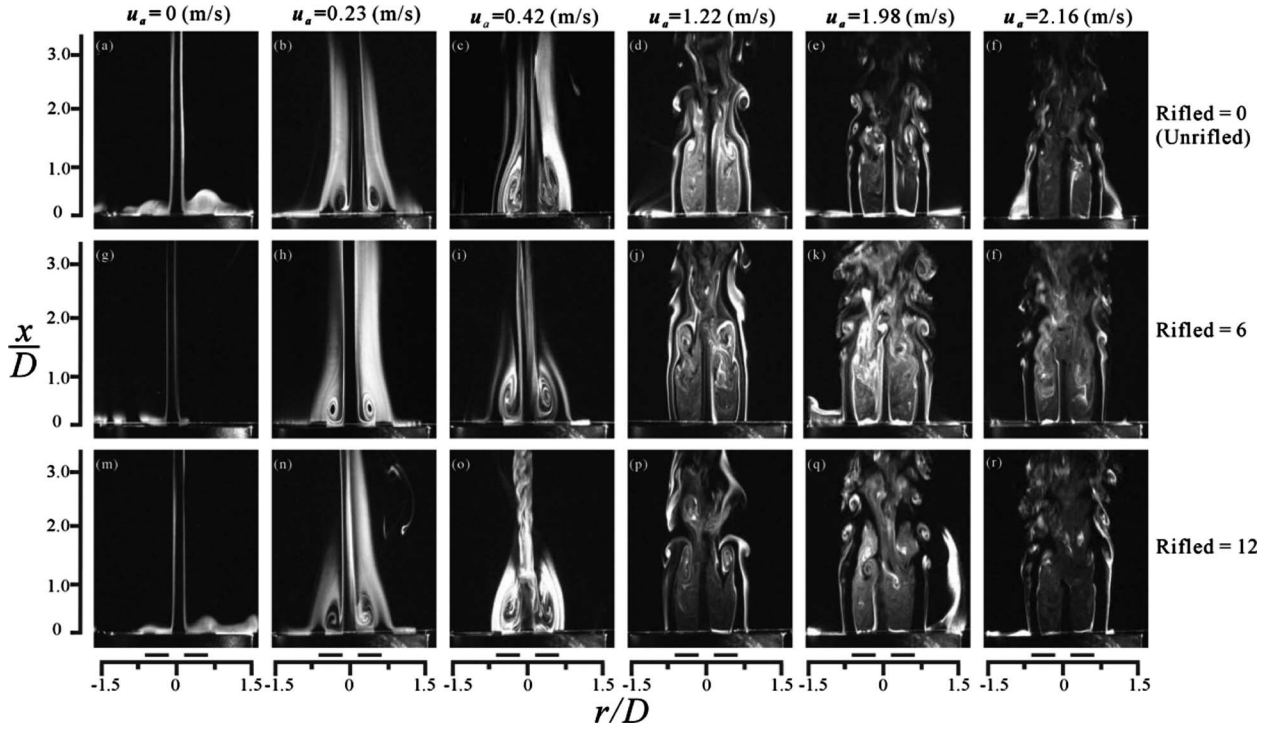

Fig. 2 Streak flow patterns at u_c=2.06 m/s: (*a*)–(*f*) for a unrifled nozzle, (*g*)–(*l*) for a 6-rifled nozzle, and (*m*)–(*r*) for a 12-rifled nozzle

pander. In this study, the thickness of laser was approximately 0.6 mm in the midplane. The wavelength of Ar-ion laser is 540 nm supplied by a Spectra-Physics' Stabilite-2017 6 W argon-ion laser. The particle images were recorded using a CCD camera with a resolution of 480×420 pixels (Redlake MASD, Inc., San Diego, CA, Model MotionScope PCI 2000S). The pixel array of the CCD was zoomed in and mapped onto a physical region of approximately 10×10 cm^2 to yield a spatial resolution of about 208 μm/pixel. The maximum frame rate was 2000 fps and the exposure time was adjustable in the range of 0.025–20 ms. The data translation board (MotionScope PCI controller) was employed to digitize the analog voltage output from the CCD camera. The magnesium oxide (MgO) particles were seeded in the flow field to scatter laser light. The diameter of MgO particles is 5 μm and the density is 3580 kg/m^3 at 25°C. The relaxation time constant is estimated to be less than 279 μs and the Stokes number is 0.007 within the range of experiment. Therefore, the slip between the flow and particles could be neglected.

Abernethy et al. [22] derived the uncertainty (U) in the PIV measurement. According to their results, the 95% confidence levels were formulated as follows:

$$U = [E^2 + (tS_{\bar{x}})^2]^{1/2} \tag{1}$$

where E is the bias error, $S_{\bar{x}}$ is the precision index of the average value, and the student's distribution t value equals 2 for a large sample. The bias error is estimated from the measured data or previous experimental judgments and the precision index of the mean is determined from the random error of the measured data [22]. Consequently, the uncertainty of the flow velocity was approximately 1.8% in this work.

2.4 Swirling Number. The swirling number is defined in Eq. (2) [1,16] and specifies the ratio of the axial component of angular momentum flux to the axial component of axial momentum flux.

$$S = \int_{D/2}^{D_o/2} uwr^2 dr / \frac{D_m}{2} \int_{D/2}^{D_o/2} u^2 r dr \tag{2}$$

where D_m is the mean diameter, that is, $(D+D_o)/2$, u represents the axial velocity and w denotes the tangential velocity near the nozzle exit.

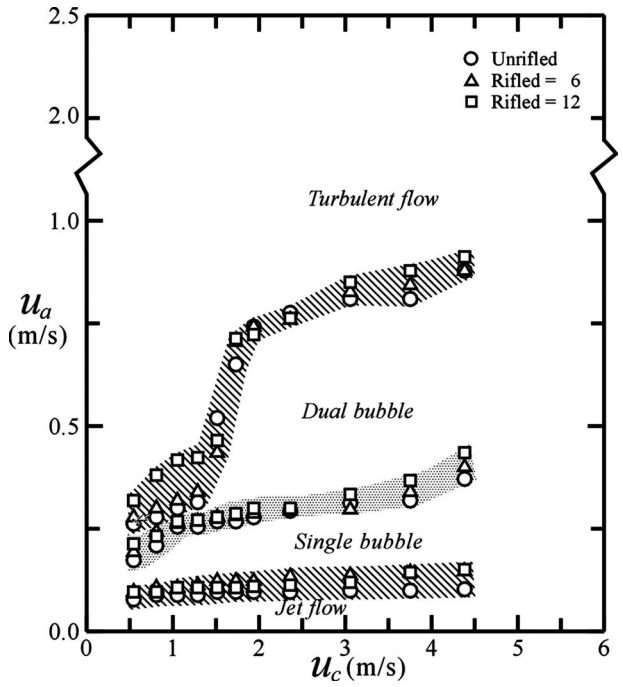

Fig. 3 Distribution of characteristic cold flow modes

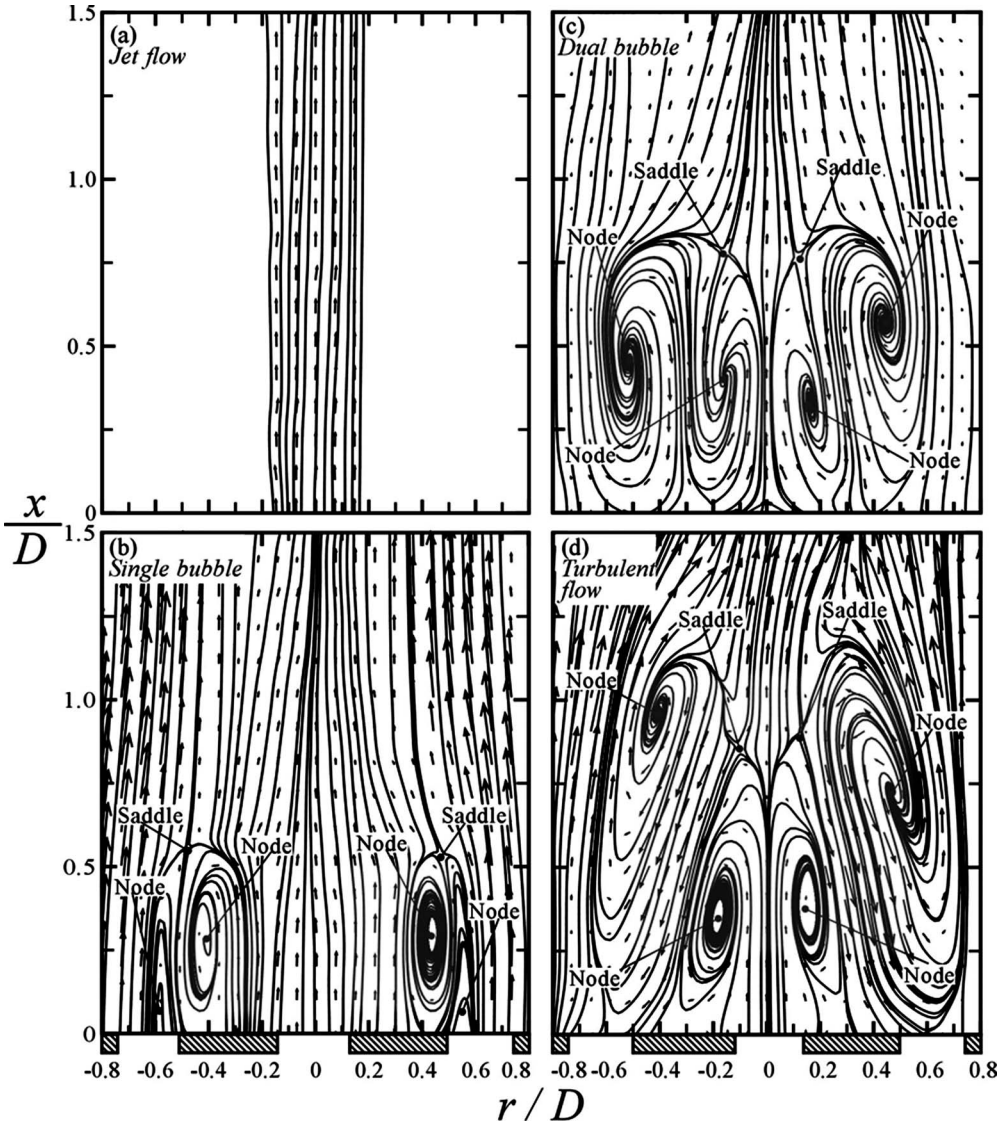

Fig. 4 Velocity vector fields and streamline patterns at u_c=2.06 m/s: (*a*) jet-flow mode (u_a=0), (*b*) single bubble mode (u_a=0.23 m/s), (*c*) dual bubble mode (u_a=0.42 m/s), and (*d*) turbulent flow mode (u_a=1.22 m/s)

2.5 Hot-Wire Anemometry. The vortex shedding behaviors were obtained using a hot-wire probe (TSI 1220-PI2.5) and a fast Fourier transform (FFT) analyzer (CF-920, ONO SOKKI Co., Yokohama, Japan). The highest temperature at which the hot-wire probe can operate was 300°C, and the diameter and length of hot-wire were 5 μm and 1.5 mm, respectively, yielding a dynamic response of 15–25 kHz. The accuracy of the frequency measurement depends both on the response of the hot-wire anemometer and on the record length and sampling rate of the FFT analyzer. The sampling frequency was set at 16 kHz and the uncertainty in the shedding frequency was estimated to be $<3\%$.

3 Results and Discussion

3.1 Smoke-Wire Visualization and Characteristic Flow Patterns. The smoke-wire visualization associated with the laser-light-sheet was employed to observe the recirculation structures of cold flow at different speed ratios of the central jet to the annular jet. Figure 2 shows the visualized smoke-wire patterns of the three nozzles when the central jet speed (u_c) was maintained constant at 2.06 m/s, whereas the annular jet speed (u_a) was varied from 0 m/s to 2.16 m/s.

Figures 2(*a*)–2(*f*) display the flow patterns at various annular jet speeds using a conventional unrifled nozzle. In Fig. 2(*a*), a straight flow that is symmetric about the *x*-axis moves downstream at u_a=0 (with no air annular jet) since the central momentum flux moves through the flow field without reverse flow. The flow pattern is defined as the *jet-flow mode*. Figure 2(*b*) shows a pair of stable recirculation bubbles that are produced by the entrainment effect at u_a=0.23 m/s. The flow pattern is dominated by the central jet, which can penetrate the recirculation zone due to the high axial momentum of central jet. The flow structure is called the *single bubble mode*. In Fig. 2(*c*), for u_a=0.42 m/s, two pairs of dual recirculation bubbles are observed. The inner bubbles drive the outer bubbles to move downstream since the central jet speed exceeds the annular jet speed. Additionally, the height of the recirculation bubble is increased to be higher than that in single bubble mode. The flow pattern is called the *dual bubble mode*. Figure 2(*d*) depicts a recirculation zone at u_a =1.22 m/s. The central jet collides with the annular flow at the top of the recirculation zone and an eddy-induced coherent structure moves downstream because of the shear stress effect in the

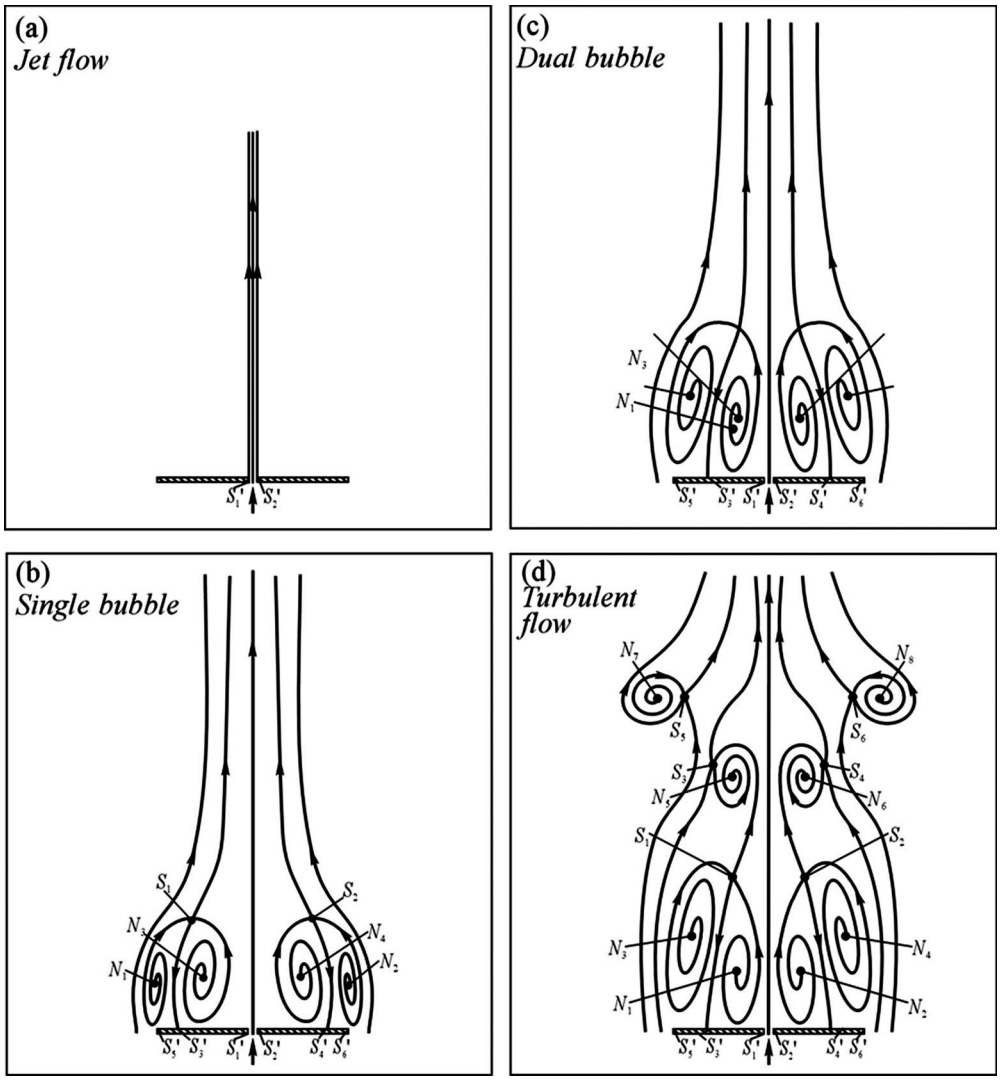

Fig. 5 Topological flow structures at u_c=2.06 m/s: (*a*) jet-flow mode (u_a=0), (*b*) single bubble mode (u_a=0.23 m/s), (*c*) dual bubble mode (u_a=0.42 m/s), and (*d*) turbulent flow mode (u_a =1.22 m/s)

annular flow. Furthermore, the increase in the annular flow velocity increases the bubble height. In Fig. 2(*e*), at u_a=1.98 m/s, the recirculation zone blocks the central momentum flux and a four-way saddle is formed lower than that in Fig. 2(*d*). In Fig. 2(*f*), at u_a=2.16 m/s, the position of the four-way saddle is lower than that in Fig. 2(*e*), and the turbulent intensity in the top region increases with the annular flow velocity. Accordingly, the flow patterns in Figs. 2(*d*)–2(*f*) are associated with the turbulent flow mode.

Figures 2(*g*)–2(*l*) present the flow structures as u_a changes from 0 m/s to 2.16 m/s for a 6-rifled nozzle. Figure 2(*i*) depicts a spiraled central airflow that moves downstream due to the angular acceleration of the rifled nozzle at u_a=0.42 m/s and S=0.15. The outer recirculation is entrained into the inner recirculation and then forms a swirling flow that moves forward along the central axis. In Fig. 2(*l*), when u_a=2.16 and S=0.45, the position of the four-way saddle is lower than that in Fig. 2(*f*) because of the momentum increase in the annular jet. Figures 2(*m*)–2(*r*) display the flow structures for a 12-rifled nozzle at various Reynolds numbers of the annular jet. In Fig. 2(*o*), when u_a=0.42 m/s and S =0.255, the four-way saddle is closer to the bluff disk than those in Figs. 2(*c*) and 2(*i*). Additionally, Fig. 2(*o*) shows a clear spiral jet adjacent to the central axis because of the high swirling strength. In Fig. 2(*r*), when u_a=2.16 m/s and S=0.512, the location of the four-way saddle is lower than those in Figs. 2(*f*) and 2(*l*) due to the increased intensity of the annular jet.

Figure 3 shows the mode regimes in the ranges of $0<u_a<2.5$ m/s and $0<u_c<6$ m/s according to the classification scheme utilized in Fig. 2. The four modes are distinguished clearly at $u_c>2$ m/s because the central airflow velocity is sufficiently high. The regime borders, which separate different characteristic modes are somewhat uncertain. The maximum uncertainty in both u_a and u_c at each mode border is about 0.01 m/s.

3.2 Streamline Vectors. Figure 4 plots the velocity vectors and instantaneous streamline patterns, which were visualized using the PIV scheme. Figure 4(*a*) shows the streamline pattern of the jet-flow mode. Without interference from the annular jet (u_a =0), the central jet streamlines move straight up from the disk center toward the downstream and no recirculation (no node or saddle) occurs in this mode. Figure 4(*b*) shows the streamline pattern of the single bubble mode in which two major recirculation bubbles are observed on both sides of the x-axis and two minor recirculation bubbles, which are absent when the streakflow pattern occurs adjacent to the disk surface. These two minor recirculation bubbles were formed due to the high intensity in the

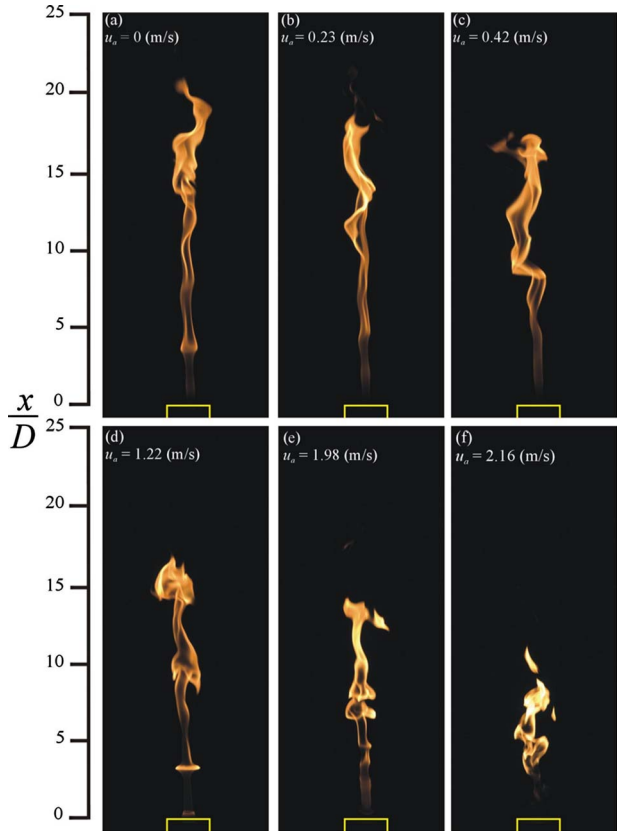

Fig. 6 Photographs of normalized flame height (x/D) for a unrifled nozzle at u_c=2.06 m/s: (*a*) u_a=0, (*b*) u_a=0.23, (*c*) u_a=0.42, (*d*) u_a=1.22, (*e*) u_a=1.98, and (*f*) u_a=2.16 m/s

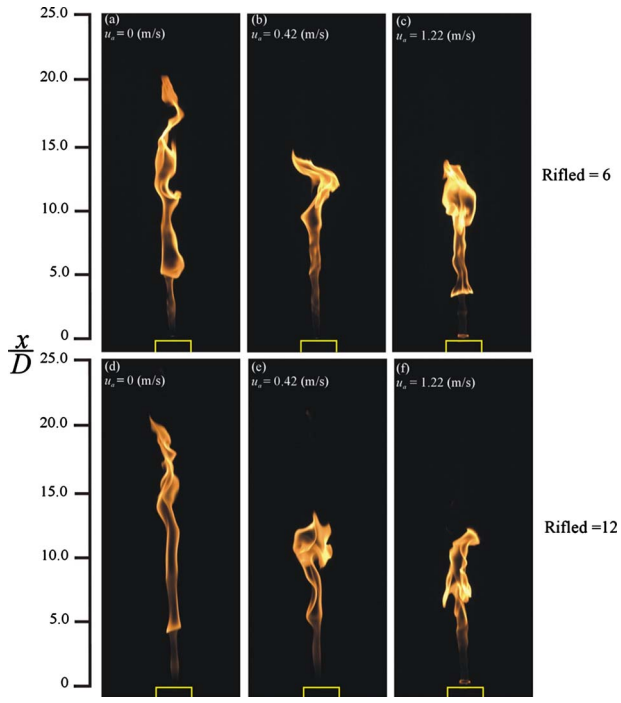

Fig. 7 Photographs of normalized flame height (x/D) at u_c=2.06 m/s: (*a*)–(*c*) for a 6-rifled nozzle and (*d*)–(*f*) for a 12-rifled nozzle

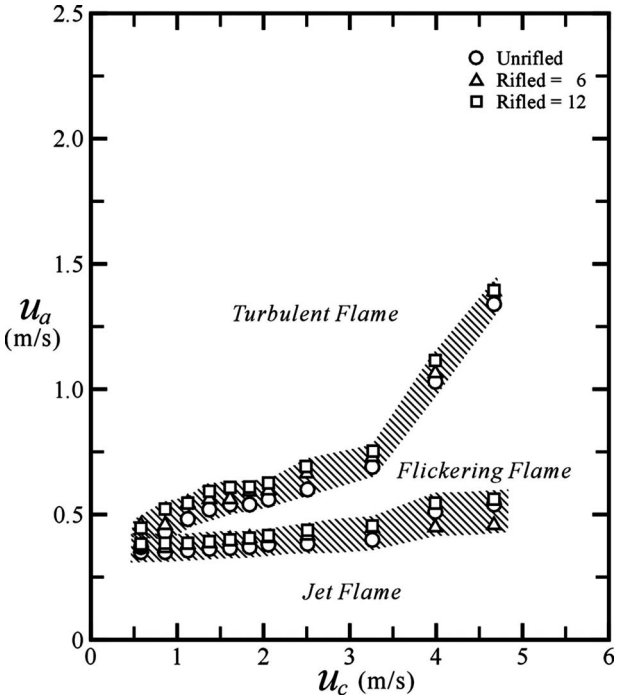

Fig. 8 Distribution of characteristic flame configurations

major bubbles, such that the annular jet separates and is reversed due to the entrainment effect. Moreover, the normalized height of recirculation zone (x/D) is about 0.55. Figure 4(*c*) shows the streamline pattern of dual bubble mode. Two pairs of dual bubbles were formed symmetrically about the x-axis. The normalized height of the outer bubbles (x/D) is about 0.80. Accordingly, the bubble scale in Fig. 4(*c*) is larger than that in Fig. 4(*b*). Figure 4(*d*) shows the streamline pattern of the turbulent flow mode where two pairs of dual bubbles are observed on each side of the x-axis. The normalized height (x/D) of the outer bubbles is $\approx$1.15. The height of the outer bubbles is extended because the momentum in annular airflow is sufficiently high.

3.3 Topological Analysis. Perry and Fairlie [23], Chong and Perry [24], and Lighthill [25] developed the topological sketch

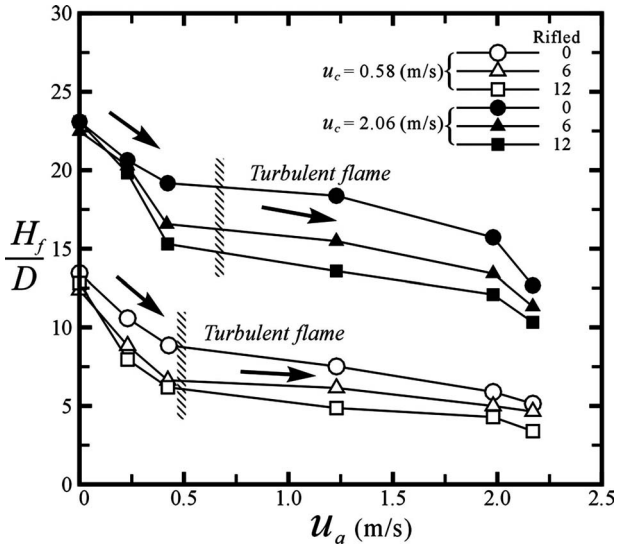

Fig. 9 Normalized flame height (H_f/D) against u_a at u_c=0.58 m/s (void symbols) and u_c=2.06 m/s (solid symbols)

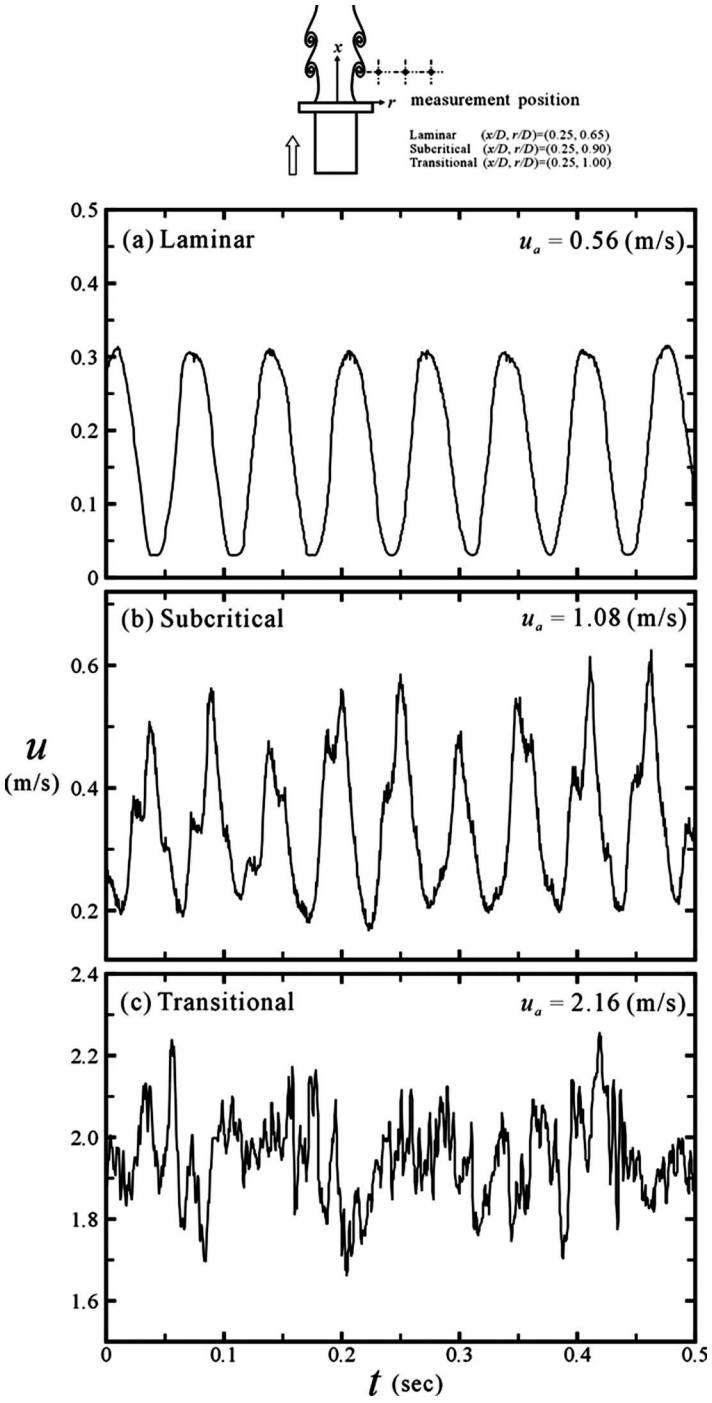

Fig. 10 Velocity profiles of flame shedding for (*a*) laminar, (*b*) subcritical, and (*c*) transitional modes

scheme to analyze the flow patterns. Perry and Steiner [26] adopted the critical point theory to determine the sectional streamline patterns and defined two main types of singular point—nodes and saddles. A node is associated with either attachment or separation. The topological lines are directed away from a nodal point of attachment but toward a nodal point of separation. Only two topological lines pass through a saddle point. One is inward and the other is outward [27]. For flow around a three-dimensional entity, some singular points in the flow pattern may be formed at particular positions where the velocities are zero and the streamline slope is indeterminate [28]. The topological scheme can reveal the steady flow structures and the evolution of the unsteady vortical structures. Finally, Hunt et al. [29] utilized the topological theory to formulate the relationship between nodes (including the four-way node N and the three-way node N'), saddles (including the four-way saddle S and the three-way saddle S') and obstacles in the flow field as follows:

$$\left(\sum N + \frac{1}{2}\sum N'\right) - \left(\sum S + \frac{1}{2}\sum S'\right) = 1 - n \tag{3}$$

where n is the connectivity of the flow section. For instance, $n=1$ for a single-connected region without obstacle, $n=2$ for one

entity, and $n=3$ for two entities present in the flow field.

Figure 5 plots the topological flow configurations of the four characteristic modes in the cold flow field. In Fig. 5(*a*), the topological configuration of the jet-flow mode reveals that the values of the critical points are $\Sigma N=0$, $\Sigma N'=0$, $\Sigma S=0$, and $\Sigma S'=2$, which fulfill the topological condition (Eq. (3)). Figure 5(*b*) depicts the topological flow configuration of the single bubble mode and four nodes (N_1-N_4): two four-way saddles (S_1 and S_2) and six three-way saddles ($S_1'-S_6'$). Accordingly, the values of critical points are $\Sigma N=4$, $\Sigma N'=0$, $\Sigma S=2$, and $\Sigma S'=6$, which satisfy Eq. (3). Figure 5(*c*) displays the topological flow configuration of the dual bubble mode. The values of critical points are the same as those determined in the single bubble mode. Accordingly, the topological condition is also satisfied in the dual bubble mode. Figure 5(*d*) presents the topological configuration in the turbulent flow mode where eight nodes (N_1-N_8), four four-way saddles (S_1-S_4), and six three-way saddles ($S_1'-S_6'$) are identified, and fulfill the topological condition.

3.4 Direct-Photo Visualization and Flame Modes. The fuel jet was discharged from the center of a bluff disk and was mixed with the annular air jet behind the unrifled, 6-rifled, and 12-rifled nozzles. The mixed flow was ignited behind the bluff disk, while the velocities of both the central fuel jet and the annular airflow were varied to observe directly the flame shapes. Figures 6 and 7 display the photographs of the flame configurations behind the nozzles.

For an unrifled nozzle, the central jet velocity is maintained at $u_c=2.06$ m/s and the annular airflow velocity is changed from 0 m/s to 2.16 m/s. Figure 6(*a*) shows the flame height without interference from annular airflow (i.e., $u_a=0$). Figure 6(*b*) shows the flame configuration at $u_a=0.23$ m/s. The flame structure is assembled as displayed in Fig. 6(*a*) because of the weak pressure gradient behind the bluff disk. The flow structures in Figs. 6(*a*) and 6(*b*) are those of the *jet flame mode*. Figure 6(*c*) shows an unstable flickering flame at $u_a=0.42$ m/s, and the flame structure is denoted as the *flickering flame mode*.

The flame height in Fig. 6(*d*) is shorter than that in Fig. 6(*a*) at $u_a=1.22$ m/s. The normalized flame height (x/D) of the recirculation bubble is approximately 0.8. Figure 6(*e*) shows a stable ring flame occurring at $x/D\approx 0.5$ at $u_a=1.98$ m/s. Figure 6(*f*) indicates that the flame is lifted at $x/D\approx 1.2$ when $u_a=2.16$ m/s. The flame structures in Figs. 6(*d*)–6(*f*) are called the *turbulent flame modes*.

3.4.1 Characteristic Flame Modes in Swirled Wake. Figure 7 depicts the characteristic flame configurations in the swirled wake behind the rifled nozzles. Figures 7(*a*)–7(*c*) present the modulated flame structures associated with a 6-rifled nozzle and Figs. 7(*d*)–7(*f*) present the flame configurations for a 12-rifled nozzle with a constant u_c of 2.06 m/s. Figures 7(*a*) and 7(*d*) show the modulated flame structures without interference from the annular swirled airflow ($u_a=0$). The flame structures are similar to those shown in Figs. 6(*a*) and 6(*b*), and therefore are called the jet flame modes. Figures 7(*b*) and 7(*e*) present an unstable flickering flame at $u_a=0.42$ m/s. Consequently, the flame structures are named the *flickering flame mode*. Figures 7(*c*) and 7(*f*) present the recirculation zones in the range of $x/D<0.8$ at $u_a=1.22$ m/s. The flame structures are then called the turbulent flame modes.

Figure 8 shows the distributions of the three flame modes as u_a and u_c varied from 0 m/s to 2.5 m/s and from 0 m/s to 6 m/s, respectively. The regime borders, which separate different characteristic flame modes, are associated with some uncertainties. The maximum uncertainty for u_a and u_c is 0.01 m/s.

3.4.2 Flame Height. Figure 9 shows the profiles of the normalized flame height (H_f/D) as u_a is varied from 0 m/s to 2.5 m/s at $u_c=0.58$ m/s and 2.06 m/s for the three nozzles utilized herein. The flame height in this manuscript was measured by the traditional photography scheme by using a Nikon Model D70s CCD with a resolution of 3008×2000 pixels and an exposure time of 30–1/8000 s. The flame height in this study was defined by averaging ten taken photos with an exposure time of 2 s for each photo. Figure 9 indicates that H_f/D declines as u_a increases. The flame height for $u_c=2.06$ m/s exceeds that for $u_c=0.58$ m/s at the same u_a because more propane is released. The flame heights behind the 12-rifled nozzle are lower than those of the unrifled and 6-rifled nozzles, since more swirling airflow is generated. Additionally, the flame height of a 12-rifled nozzle is approximately halved with comparing that for an unrifled nozzles. The swirling effect changes the axial jet flow to a radial one in the tangential direction. The swirling mechanism creates significant momentum, heat exchange, mass exchange, and drastic turbulence fluctuations. Consequently, the evident increases in the swirling intensity shorten the flame length and thus increase combustion efficiency.

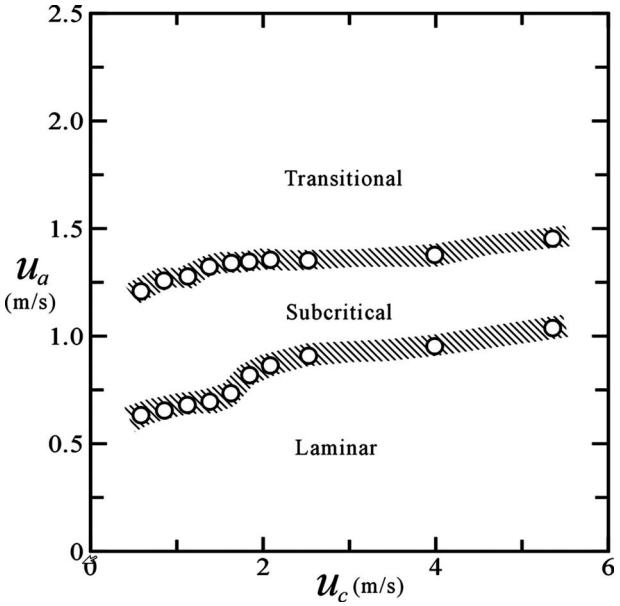

Fig. 11 Distribution of flame shedding modes

3.5 Vortex Shedding of Flame. The vortex shedding of the flame behind the nozzles was probed using a hot-wire anemometer. Figure 10 shows the velocity profiles (u) for various evolution times (t) at $u_a=0.56$ m/s, 1.08 m/s, and 2.15 m/s, while u_c is fixed at 2.06 m/s. To collect clear signals, a hot-wire probe was installed at $(x/D, r/D)=(0.25, 0.65)$, (0.25,0.90), and (0.25, 1.00) in the laminar, subcritical, and transitional modes, respectively. Figure 10(*a*) indicates that the time signals are periodic (sinusoidal wave) at $u_a=0.56$ m/s. Such vortex shedding is associated with the *laminar mode*. Figure 10(*b*) shows periodic signals at $u_a=1.08$ m/s, but some weak disturbances are multiplied in the sinusoidal waves. Such vortex shedding is named the *subcritical mode*. Figure 10(*c*) presents a random output at $u_a=2.16$ m/s, and therefore the vortex shedding profile is called the *transitional mode*. Figure 11 shows the distribution of vortex shedding modes as u_a and u_c vary in the ranges 0–2.5 m/s and 0–6 m/s, respectively.

Figure 12 displays the spectrum ($\log \Phi$) calculated using the FFT algorithm for the three vortex shedding modes, where Φ represents the power spectrum. Figure 12(*a*) shows a peak frequency of 11.90 Hz at $u_a=0.56$ m/s and $u_c=2.06$ m/s (i.e., in laminar vortex shedding mode). Figure 12(*b*) shows a peak frequency of 16.05 Hz at $u_a=1.08$ m/s (i.e., in subcritical vortex shedding mode). Figure 12(*c*) shows no peak frequency in the transitional vortex shedding mode at $u_a=2.16$ m/s. Consequently,

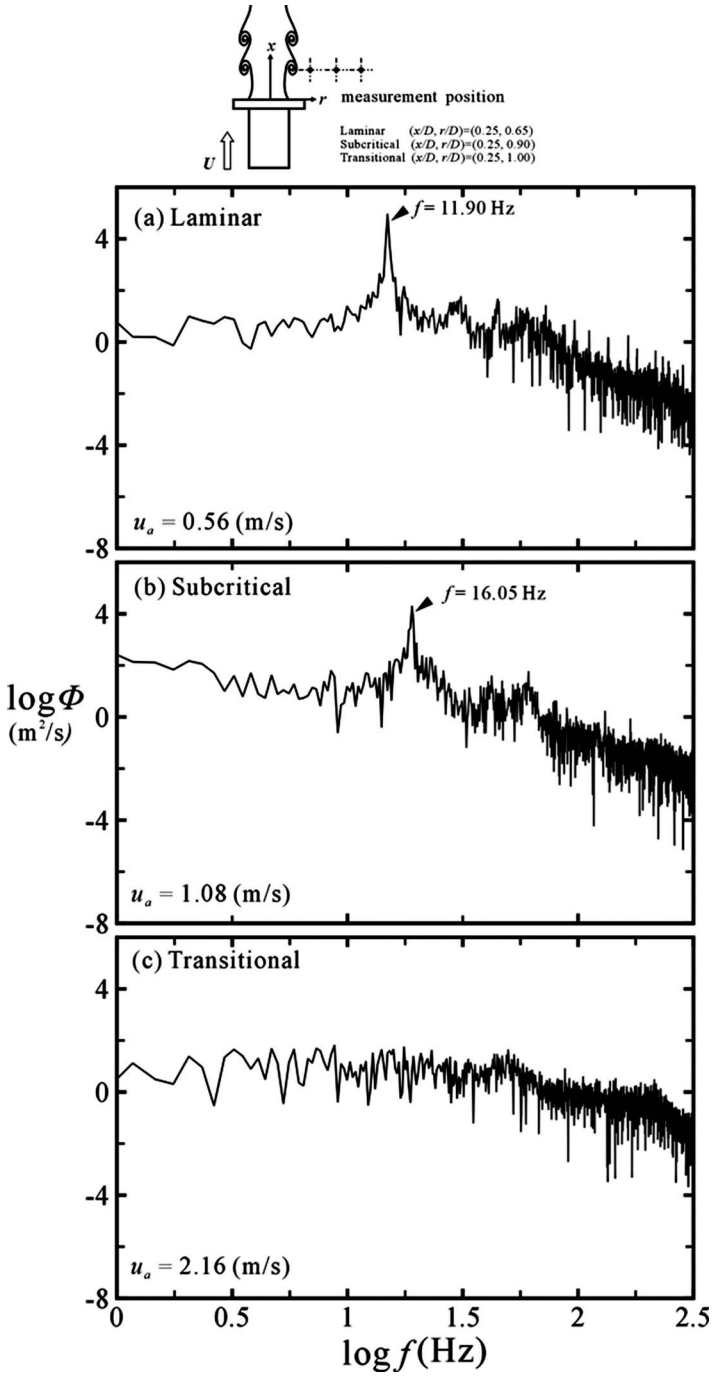

Fig. 12 Distributions of power spectrum (log Φ) versus logarithmic frequency (log *f*) for flame shedding in (*a*) laminar, (*b*) subcritical, and (c) transitional modes

no coherent flame structure is observed in the transitional mode.

Figure 13 shows the distributions of the pdf derived from the data given in Fig. 10. Figure 13(*a*) shows a dual-peak pdf in the laminar vortex shedding mode that is associated with the sinusoidal output plotted in Fig. 10(*a*). Figure 13(*b*) shows a Gaussian-like distribution in the subcritical vortex shedding mode associated with the multiplication of weak disturbance in the output signals. Figure 13(*c*) plots Gaussian distributions due to the random fluctuations of shedding velocities in the transitional vortex shedding mode.

The frequency of unsteady flow in the wake varying with free velocity is normalized and represented by the nondimensional groups: Strouhal number (Sr) is defined by $\mathrm{Sr}=fD/u_\infty$. Roshko [30] experimentally developed a well-known equation for the nondimensional frequency Sr of the Kármán vortex shedding in the wake behind a circular cylinder, as follows:

$$\mathrm{Sr} = 0.212 - \frac{4.5}{\mathrm{Re}} \quad \text{for } 300 < \mathrm{Re} < 2000 \tag{4}$$

Therefore, the limit of Strouhal number for a circular cylinder is 0.212. Figure 14 displays the distributions of the shedding frequency (f) and the Strouhal number with changing u_a in the range 0–1.6 m/s at two u_c of 0.58 m/s and 2.06 m/s. Figure 14(*a*) iden-

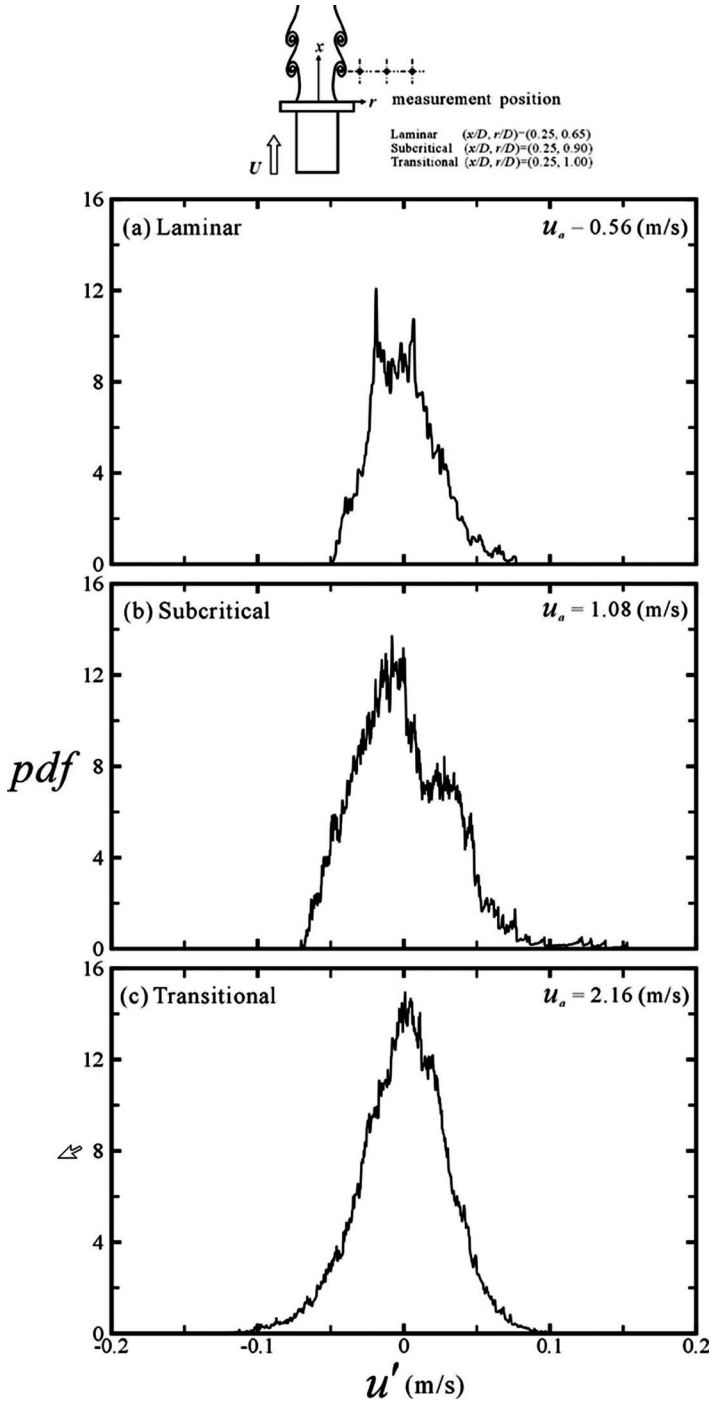

Fig. 13 Distributions of probability density function as a function of u' for flame shedding in (*a*) laminar, (*b*) subcritical, and (*c*) transitional modes

tifies three flame regimes—jet flame, flickering flame, and turbulent flame. In the jet flame regime, the shedding frequency increases with u_a at $u_a < 0.42$ m/s. In the flickering flame regime, the shedding frequency declines rapidly as u_a increases in the range of $0.42 < u_a < 0.5$ m/s. In the turbulent flame regime, the shedding frequency increases with u_a at $u_a > 0.5$ m/s. Figure 14(*b*) shows the profile of Sr against u_a, where Sr is defined as $\mathrm{Sr} = fd/u_a$. The Sr declines as u_a increases, and the relationship between Sr and u_a can be fitted using the following first-order correlation:

$$\mathrm{Sr} = 0.0238 + 0.13/u_a \tag{5}$$

4 Conclusion

This work adopted rifled nozzles with various swirl numbers to increase interaction between the axial stress of the central flow and the tangential stress of the swirled annular airflow. Additionally, the rifled nozzles are designed to increase the turbulent intensity and thereby increase the mixing and shedding efficiencies between the central flow and the swirled annular airflow. Smoke-wire flow visualization, the PIV scheme, topological analysis, and direct-photo visualization were adopted to observe and analyze the cold flow structures and flame configurations behind the riffled

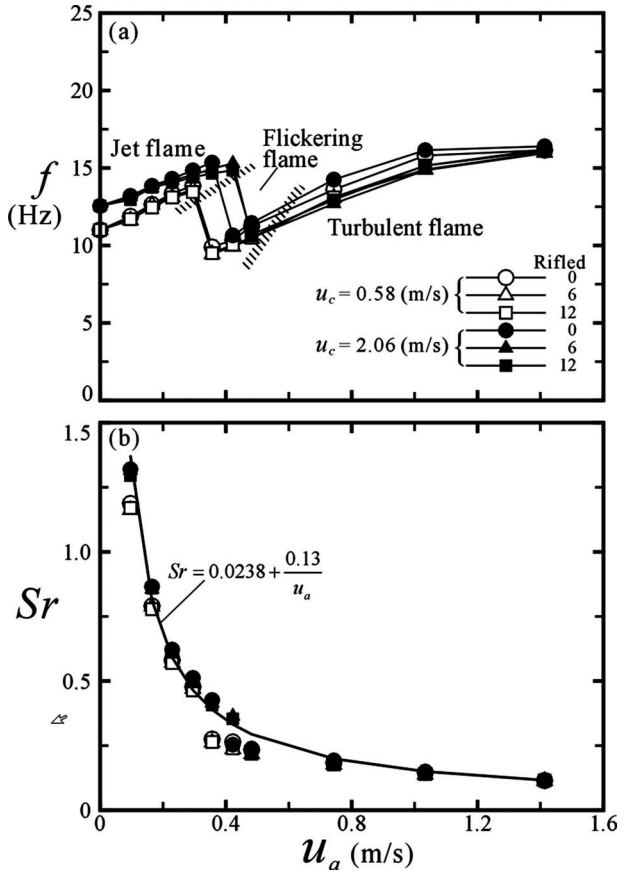

Fig. 14 Distributions of (*a*) *f* versus u_a and (*b*) Sr versus u_a

nozzles. The experimental data and discussion yield the following results.

(1) The cold flow structures behind the rifled/unrifled nozzles are classified into four modes—jet flow, single bubble, dual bubble, and turbulent flow—based on smoke-wire visualization.
(2) The flame configurations behind the rifled/unrifled nozzles are classified into three modes—jet flame, flickering flame, and turbulent flame—based on direct-photo visualization.
(3) The flame height declines as u_a increases, and the flame height behind a 12-rifled nozzle is decreased by about 50% under that of an unrifled nozzle because of the sufficiently high swirling intensity.
(4) The flame shedding frequency behind the nozzles declines rapidly in the flickering flame mode, and the relationship between Sr and u_a is regressed as $Sr=0.0238+0.13/u_a$.

Nomenclature

A_a = exit area of swirling jet: $\pi(D_o^2-D^2)/4$, 392.7 mm^2
A_c = exit area of central jet: $\pi d^2/4$, 19.6 mm^2
B = blockage ratio at jet exit: D^2/D_o^2, 0.444
D = diameter of blockage disk, 20 mm
d = exit diameter of central jet, 5 mm
D_c = diameter of control disk, 10 mm
D_h = hydraulic diameter of annular swirling jet at exit: D_o-D, 10 mm
D_m = mean diameter for calculation of swirl number: $(D+D_o)/2$, 25 mm
D_o = outer diameter of annular swirling jet at exit, 30 mm
f = frequency of instabilities in wake (Hz)
Q_a = volumetric flow rate of annular swirling flow
Q_c = volumetric flow rate of central jet
r = radial coordinate, originated at center of blockage disk
Ro = Roshko number of vortex shedding: fd^2/ν
Sr = Strouhal number of vortex shedding: fd/u
u = axial velocity
x = axial coordinate, originated at the center of the blockage disk
u_a = volumetric mean axial velocity of annular swirling jet at exit: Q_a/A_a
u_c = volumetric mean velocity of central jet at exit: Q_c/A_c
v = radial velocity
w = azimuthal velocity
Φ = power spectrum of fluctuating velocities
τ = time shift for calculating autocorrelation coefficient of fluctuation velocities

References

[1] Gupta, A. K., Lilley, D. G., and Syred, N., 1984, *Swirl Flow*, Abacus, Cambridge, UK, pp. 1–293.
[2] Rose, W. G., 1962, "A Swirling Round Turbulent Jet 1-Mean-Flow Measurements," ASME J. Appl. Mech., **29**, pp. 615–625.
[3] Chigier, N. A., and Beer, J. M., 1964, "Velocity and Static Pressure Distributions in Swirling Air Jets Issuing From Annular and Divergent Nozzles," ASME J. Fluids Eng., **86**, pp. 788–798.
[4] Davies, T. W., and Beer, J. M., 1971, "Flow in the Wake of Bluff-body Flame Stabilizers," Proceedings of the 13th Symposium (International) on Combustion, The Combustion Institute, Pittsburgh, PA, pp. 631–638.
[5] Carmody, T., 1964, "Establishment of the Wake Behind a Disk," ASME J. Basic Eng., **86**, pp. 869–882.
[6] Durao, D. F. G., and Whitelaw, J. H., 1978, "Velocity Characteristics of the Flow in the Near Wake of a Disk," J. Fluid Mech., **85**(2), pp. 369–385.
[7] Schefer, R. W., Namazian, M., and Kelly, J., 1994, "Velocity Measurement in Turbulent Bluff-Body Stabilized Flows," AIAA J., **32**, pp. 1844–1851.
[8] Huang, R. F., and Lin, C. L., 1994, "Characteristic Modes and Thermal Structure of Nonpremixed Circular-Disc Stabilized Flames," Combust. Sci. Technol., **100**, pp. 123–139.
[9] Gu, X., Zang, S. S., and Ge, B., 2006, "Effect on Flow Field Characteristics in Methane–Air Non-Premixed Flame With Steam Addition," Exp. Fluids, **41**(5), pp. 829–837.
[10] Hartnett, J. P., and Eckert, E. R. G., 1957, "Experiment Study of the Velocity and Temperature Distribution in a High Velocity Vortex Type Flow," ASME J. Fluids Eng., **79**, pp. 751–757.
[11] Hübner, A. W., Tummers, M. J., Hanjalić, K., and van der Meer, Th. H., 2003, "Experiments on a Rotating-Pipe Swirl Burner," Exp. Therm. Fluid Sci., **27**(4), pp. 481–489.
[12] Cheng, R. K., 1995, "Velocity and Scalar Characteristics of Premixed Turbulent Flames Stabilized by Weak Swirl," Combust. Flame, **101**(1–2), pp. 1–14.
[13] Al-Abdeli, Y. M., and Masri, A. R., 2003, "Recirculation and Flowfield Regimes of Unconfined Non-Reacting Swirling Flows," Exp. Therm. Fluid Sci., **27**(5), pp. 655–665.
[14] Kerr, N. M., and Fraser, D., 1965, "Swirl Part 1: Effect on Axisymmetrical Turbulent Jets," J. Inst. Fuel, **38**, pp. 519–526.
[15] Guttenfelder, W. A., Renfro, M. W., Laurendeau, N. M., Ji, J., King, G. B., and Gore, J. P., 2006, "Hydroxyl Time Series and Recirculation in Turbulent Nonpremixed Swirling Flames," Combust. Flame, **147**(1–2), pp. 11–21.
[16] Huang, R. F., and Tsai, F. C., 2001, "Observations of Swirling Flows Behind Circular Discs," AIAA J., **39**(6), pp. 1106–1112.
[17] Chervinsky, A., 1969, "Turbulent Swirling Jet Diffusion Flames," AIAA J., **7**(10), pp. 1877–1883.
[18] Chen, R. H., and Driscoll, J. F., 1988, "The Role of the Recirculation Vortex in Improving Fuel-Air Mixing Within Swirling Flames," 22 Symposium (International) on Combustion, The Combustion Institute, Pittsburgh, PA, pp. 531–540.
[19] Morcos, V. H., and Abdel-Rahim, Y. M., 1999, "Parametric Study of Flame Length Characteristics in Straight and Swirl Light-Fuel Oil Burners," Fuel, **78**(8), pp. 979–985.
[20] Mueller, T. J., 2000, "Flow Visualization by Direct Injection," *Fluid Mechanics Measurements*, 2nd ed., R. J. Goldstein, ed., Taylor & Francis, Washington, DC, pp. 367–450.
[21] Flagan, R. C., and Seinfeld, J. H., 1988, *Fundamentals of Air Pollution Engineering*, Prentice-Hall, Englewood Cliffs, NJ, pp. 295–307.
[22] Abernethy, R. B., Benedict, R. P., and Dowdell, R. B., 1985, "ASME Measurement Uncertainty," ASME J. Fluids Eng., **107**(2), pp. 161–164.
[23] Perry, A. E., and Fairlie, B. D., 1975, "Critical Points in Flow Patterns," Adv. Geophys., **18**, pp. 299–315.
[24] Chong, M. S., and Perry, A. E., 1990, "A General Classification of Three-

Dimensional Flow Fields," Phys. Fluids A, **2**(5), pp. 765–777.
[25] Lighthill, M. J., 1963, *Laminar Boundary Layers*, Oxford University Press, Oxford, pp. 48–88.
[26] Perry, A. E., and Steiner, T. R., 1987, "Large-Scale Vortex Structures in Turbulent Wakes Behind Bluff Bodies. Part 1. Vortex Formation," J. Fluid Mech., **174**, pp. 233–270.
[27] Madeleine, C., and Gerard, P., 1997, "Some Type Mechanisms in the Early Phase of the Vortex-Shedding Process From Particle-Streak Visualization," *Atlas of Visualization*, Vol. 3, Y. Nakagama, and Y. Tanida, eds., CRC, Boca Raton, FL, pp. 43–68.
[28] Josef, R., 1992, "The Topology of Separating and Reattaching Vortical Flows," *High Angle of Attack Aerodynamics: Subsonic, Transonic, and Supersonic Flows*, Springer-Verlag, New York, pp. 62–77.
[29] Hunt, J. C. R., Abell, C. J., Peterka, J. A., and Woo, H., 1978, "Kinematical Studies of the Flows Around Free or Surface-Mounted Obstacles; Applying Topology to Flow Visualization," J. Fluid Mech., **86**, pp. 179–200.
[30] Roshko, A., 1954, "On the Development of Turbulent Wakes from Vortex Streets," NACA Report 1191.

Passive Control of the Inlet Acoustic Boundary of a Swirled Burner at High Amplitude Combustion Instabilities

Nicolas Tran

Sebastien Ducruix

Thierry Schuller[1]
e-mail: thierry.schuller@em2c.ecp.fr

Laboratoire EM2C,
CNRS-Ecole Centrale Paris,
Châtenay-Malabry 92295, France

Perforated panels placed upstream of the premixing tube of a turbulent swirled burner are investigated as a passive control solution for combustion instabilities. Perforated panels backed by a cavity are widely used as acoustic liners, mostly in the hot gas region of combustion chambers to reduce pure tone noises. This paper focuses on the use of this technology in the fresh reactants zone to control the inlet acoustic reflection coefficient of the burner and to stabilize the combustion. This method is shown to be particularly efficient because high acoustic fluxes issued from the combustion region are concentrated on a small surface area inside the premixer. Theoretical results are used to design two types of perforated plates featuring similar acoustic damping properties when submitted to low amplitude pressure fluctuations (linear regime). Their behaviors nonetheless largely differ when facing large pressure fluctuation levels (nonlinear regime) typical of those encountered during self-sustained combustion oscillations. Conjectures are given to explain these differences. These two plates are then used to clamp thermoacoustic oscillations. Significant damping is only observed for the plate featuring a robust response to increasing sound levels. While developed on a laboratory scale swirled combustor, this method is more general and may be adapted to more practical configurations.
[DOI: 10.1115/1.3078206]

Keywords: perforated plate impedance, passive control, flame-acoustic interaction, combustion instabilities, nonlinear acoustics

1 Introduction

At the design stage of a gas turbine or jet engine, it is still nowadays very difficult to predict the potential occurrence of combustion instabilities, which may reduce performance and eventually cause damage to the installation. Many efforts have been devoted to the understanding and modeling of both combustion dynamics and occurrence of self-sustained combustion oscillations [1–3]. Yet, as thermoacoustic instabilities result from resonant coupling between flame dynamics and acoustics of a full system, detailed unsteady phenomena at the chamber boundaries must also be accounted for in order to yield correct predictions of unstable modes in practical combustors. Furthermore, this implies that combustion instabilities cannot be eliminated solely by design of the combustion chamber. The environment at the termination boundaries of the chamber, where acoustic fluxes can be exchanged, should also be carefully taken into account during the design process.

Numerous solutions have been developed to limit the consequences of such instabilities. While active control solutions aim at modifying the feedback loop to hinder the resonannt coupling between unsteady combustion dynamics and system acoustics, passive control methods are usually used to damp the resonant acoustic modes.

Active control methods have been developed using various strategies, ranging from the control of various flow input parameters (fuel flow, air flow, secondary jets, etc., see among others, Refs. [4–7]) to the active modulation of acoustic boundary conditions up- and downstream of the combustion chamber [8]. However, these solutions are often complex and fragile, making them difficult to adapt to large industrial applications. Passive methods are more robust and some have already proven their efficiency in real configurations. These methods consist mainly in the optimal positioning of damping devices such as quarter-wave or Helmholtz resonators [9] or perforated panels [10].

Perforated plates backed by cavities are widely used in industrial configurations to damp acoustic resonances induced by unsteady combustion oscillations. An important literature on various models is available, describing the perforated plate performance under acoustic excitation. These models are based on either theoretical considerations [11,12] or empirical results [13]. Each is adapted to a given configuration of perforated panels. While the model of Melling [11] considers the effect of the dissipative acoustic layer in each perforation, the model obtained by Narayana Rao and Munjal [13] is limited to the case of a grazing flow. The theory developed by Howe [12] considers the vortex-shedding, which occurs at the edges of an aperture, as the source of acoustic damping (see also Ref. [14]). It was shown in further works that the efficiency of this mechanism is increased in the presence of a resonant back-cavity. This was used by Hughes and Dowling [10] to design efficient screech noise absorbers. This work was continued by Eldredge and Dowling [15] to optimize absorption of axial acoustic waves by perforated liners. Extensive literature can be found on the experimental investigation of the properties of such systems [15,16]. The influence of the plate thickness [17–19] is also at stake, as the original theory considers only infinitely thin panels. However, less attention has been paid to the interaction with high intensity incident sound waves [20,21]. Yet in modern gas turbines undergoing thermoacoustic

[1]Corresponding author.

Contributed by the International Gas Turbine Institute of ASME for publication in the JOURNAL OF ENGINEERING FOR GAS TURBINES AND POWER. Manuscript received July 24, 2008; final manuscript received September 6, 2008; published online June 5, 2009. Review conducted by Dilip R. Ballal. Paper presented at the ASME Turbo Expo 2008: Land, Sea and Air (GT2008), Berlin, Germany, June 9–13, 2008 with the title "Passive Control of the Inlet Acoustic Boundary of a Swirled Turbulent Burner".

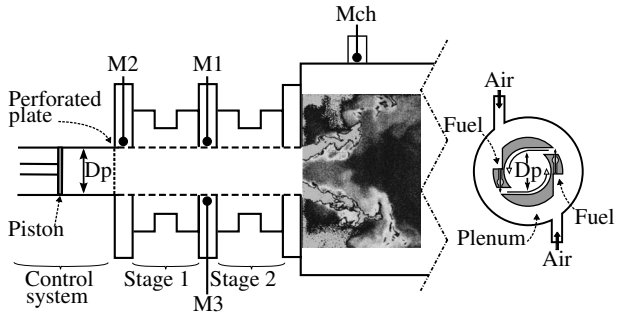

Fig. 1 Implementation of the passive control device at the inlet boundary condition of the burner. Microphone locations are indicated in the setup and a typical flame snapshot obtained from OH-LIF is shown to locate the flame.

instabilities, the level of pressure fluctuations can easily reach several hundred pascals [22], resulting in noise levels greater than 150 dB inside the combustion chamber. Application of perforated panels backed by cavities inside modern combustion chambers thus requires the investigation of their interaction with high levels of pressure fluctuation.

The current work presents an original use of perforated panels to control the inlet acoustic boundary condition of a lean turbulent combustor at frequencies typical of combustion instabilities associated with longitudinal modes. Instead of damping a specific mode of the chamber, the aim is to control the acoustic reflection coefficient from the fresh reactant zone, which acts on the turbulent reactive region. This is achieved by using a perforated plate inserted at the inlet of an inner tube, in which air and fuel are premixed before entering the combustion chamber. Adaptation of a perforated panel with a back cavity in this zone, as sketched in Fig. 1, is selected over any other region of the combustor because flame dynamics is known to be very sensitive to perturbations in the fresh reactants. It is also a region where intense acoustic fluxes are concentrated on small surface areas [23].

Using classical theoretical results, two perforated plates, both featuring the same reflection coefficient to small amplitude incident waves, are designed and then tested in an impedance tube (Fig. 2). Next, interactions of these perforated panels with pressure oscillations of large amplitudes are investigated. Finally, the proposed system, composed of a tunable cavity backing a perforated panel with bias flow, was implemented on an existing combustion facility, which exhibits strong thermoacoustic instabilities (Fig. 1). For both plates, the effect of the inlet acoustic boundary condition on self-sustained oscillations is studied.

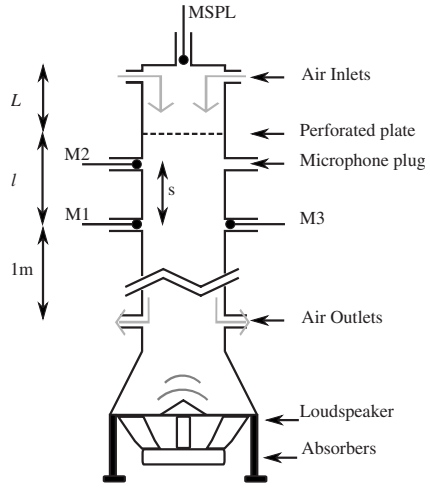

Fig. 2 Schematic of the impedance tube. The passive control system is located at the top of the impedance tube, above microphone M_2.

2 Acoustic Control by Perforated Plates With Bias Flow

The model of Howe [12] considers a single hole in a plate, through which a bias flow U generates trains of vortices. Using this model, it was later demonstrated that a resonant cavity, of depth L backing perforated plates of low porosity, enhances their acoustic damping properties [10]. However, the effect of aperture spacing is not considered either in the theory of Howe or in later improvements. The focus of this study is to use perforated panels for the control of the inlet acoustic boundary condition of a turbulent burner, where acoustic fluxes can be intense. It is therefore legitimate to base the associated design on this theory and its subsequent enhancements.

2.1 Theoretical Elements. Analytical expressions for acoustic dissipation by vortex-shedding were derived in the absence of interactions between neighboring jets flowing through the apertures. This is valid if the aperture spacing d is much larger than the aperture radius a. It is also assumed that incident acoustic waves are compact, requiring the aperture spacing to be much smaller than the wavelengths envisaged. In this case, the pressure gradient through the perforated plate can be linked to the pressure jump via the Rayleigh conductivity K_R of the apertures. This conductivity is a function of the Strouhal number $\mathrm{St}=\omega a/U$ based on the bias flow velocity U and the aperture radius a, as shown by Howe [12,24], $K_R=2a(\gamma-i\delta)$ where the real and imaginary parts γ and δ are fully determined by Bessel functions of the Strouhal number St.

Finally, the complex reflection coefficient at the front face of the perforated plate is a function of the geometrical parameters a and d, the cavity depth L, the bias flow velocity U, and the frequency via the wave number $k=2\pi f/c_0$:

$$R=\frac{(ikd^2/K_R)+1-(i/\tan(kL))}{(ikd^2/K_R)-1-(i/\tan(kL))} \tag{1}$$

In the absence of bias flow, $K_R=1$, there should be no absorption and the coefficient R should thus equal unity [16]. In the presence of a bias flow, R is a complex number, its modulus is lower than unity $|R|\leq 1$, and sound is absorbed due to sound-vortex interactions [10]. To control the reflection coefficient, five parameters must be fully determined. The number of parameters can be, however, easily reduced by geometrical constraints and operating condition limits.

2.2 Perforated Plate Design. This study is limited to longitudinal thermoacoustic instabilities, occurring at low frequencies in practical burners. The unstable frequencies to be controlled are thus limited to the range of 100–1000 Hz. As the upper limit was arbitrarily chosen, this method can easily be extended to higher frequencies. The lower limit sets the maximal length of the back cavity. Plates' dimensions are imposed by the geometrical constraints of the premixing line where it should be adapted. In the turbulent burner considered here, the inner premixing channel has a diameter $D_p=30$ mm (Fig. 1). The theoretical elements previously presented are limited to perforated plates of small porosity (typically below 10%). They cannot be used to determine the aperture radius-to-spacing ratio a/d. This gives the designer a certain degree of freedom provided that $a/d\ll 1$. Two plates were designed with the same hole radius $a=0.5$ mm and the same thickness $t=1$ mm. Plate P_8 has a ratio $a/d=0.063$ and plate P_4 a ratio $a/d=0.125$. The subscript designates the aperture spacing d in millimeters. It will be shown that the aperture spacing has considerable effects on the system response in the nonlinear regime. Finally, cavity depth and bias flow velocity are used as

Table 1 Parameters of the control system of the inlet boundary condition

Plate	a (mm)	d (mm)	σ (%)	U_{opt} (ms^{-1})	L (cm)
P_8	0.5	8	1.2	2.3	0–50
P_4	0.5	4	5.0	9.0	0–50

control parameters to vary the modulus of the reflection coefficient $|R|$. The system design was the result of an optimization for the final application with two prerequisites.

1. A smooth evolution of the modulus of the reflection coefficient must be associated with significant variations of the control parameters, the back cavity length L, and the bias flow velocity U.
2. The system must be robust and compact in order for it to be implemented in existing combustion chambers. The maximal cavity depth L was limited to $L=50$ cm. This value can be decreased when the lowest frequencies to control are higher.

It can be easily shown that for fixed geometrical properties of the plate perforations a and d, a single bias flow velocity U can be used to optimize the damping properties of the system within the range 100–1000 Hz [25]. In the present study, these optimal velocities are equal to $U_{opt}=2.3$ ms^{-1} and 9.0 ms^{-1}, respectively, for plates P_8 and P_4. As a result, the cavity depth L remains the only parameter needed to control the reflection coefficient at the front face of the perforated plate. Characteristics of the designed systems are summarized in Table 1.

3 Performance Assessment

3.1 Impedance Tube Facility. Plates were first characterized in an impedance tube facility, which allows for large amplitude of pressure fluctuations, up to 150 dB, and flow velocities inside the main tube from 0 ms^{-1} to 20 ms^{-1} at room temperature. The setup, sketched in Fig. 2, is equipped at its base with a high-efficiency loudspeaker controlled by a signal generator. The loudspeaker is fixed to the main cylindrical test section by a conical adaptation piece. The main cylinder tube has a diameter $D=50$ mm and is equipped with regularly spaced plugs for 1/4 in. microphones that can be flush mounted on the tube wall. The distance between the loudspeaker and the sample is long enough to ensure plane wave propagation inside the setup. Air, controlled by a mass flow meter, is fed at the top of the facility, where a microphone M_{SPL} is used to monitor the sound pressure level (SPL) inside the setup. The cavity depth L can be adjusted, between the air inlets and the perforated plate to be tested, using a set of DN50-type tubes. A three microphone technique is used to measure the impedance at the front face of the perforated plate, submitted to incident harmonic excitations [26]. Four B&K 4938 microphones M_1, M_2, M_3, and M_{SPL} connected to 2670-type amplifiers and a Nexus conditioner were calibrated using a 4231-type sound calibrator. Remaining phase mismatches were also minimized by switching the microphones as recommended by Chung and Blaser [26]. The test facility was benchmarked using known impedance conditions (closed tube, open tube with and without mean flow).

3.2 Control of the Reflection Coefficient by Cavity Depth Adjustment. Primary tests were carried out to ensure that the optimal theoretical bias flow velocity was the one yielding the maximal amplitude of variation of the reflection coefficient. The reflection coefficient of each perforated plate was then measured as a function of cavity depth L, from 0 to 50 cm, and of frequency f, from 100 to 1000 Hz, at their optimal bias flow velocities U_{opt}.

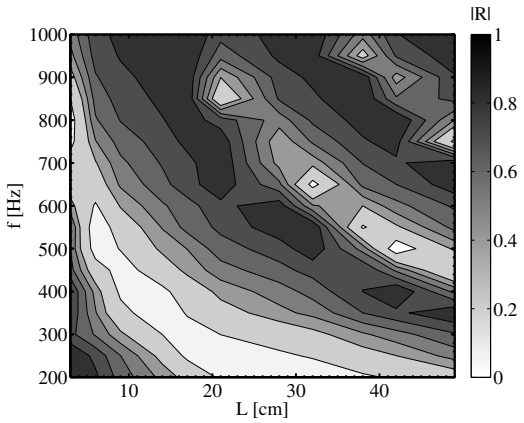

Fig. 3 Plate P_8, modulus of the reflection coefficient as a function of the depth and the frequency. SPL=110 dB.

Results for the modulus of the reflection coefficient $|R|$ are plotted in Fig. 3 for plate P_8 and in Fig. 4 for plate P_4, for a constant SPL of 110 dB controlled by the microphone M_{SPL} (Fig. 2). In these figures, maps of isolevels of the modulus $|R|$ are plotted as functions of cavity length L and modulation frequency f. Similar plots were obtained for the phase of the reflection coefficient. The evolution of the phase (not shown here) is barely affected by the chosen control parameters. The modulus features in both figures large clear bands corresponding to low modulus values separated from darker bands corresponding to higher moduli approaching unity. Isolated islands are also visible, which correspond to interpolation errors due to a coarse grid of measurement particularly in Fig. 3. This shows that a large amplitude of control over the modulus $|R|$ can be efficiently achieved by gradual modification of the cavity depth.

Experimental data gathered for each plate are compared in Fig. 5 with predictions for $f=300$ Hz, a frequency which is typical of combustion instabilities observed in the combustion test rig. Both plates feature the same trend. By augmenting the cavity depth L, the modulus $|R|$ of the reflection coefficient first decreases from values close to 0.8 at $L=5$ cm to a minimal value of 0.1 at $L=18$ cm for plate P_8 and 0.2 at $L=22$ cm for plate P_4, and then increases again for larger depths. Piloting the cavity depth L actually controls the value of the reflection coefficient. Theory matches data more closely for plate P_4. Results for the phase are well predicted except for low modulus values. In both cases, the reflection coefficient is reasonably well predicted. Other plates

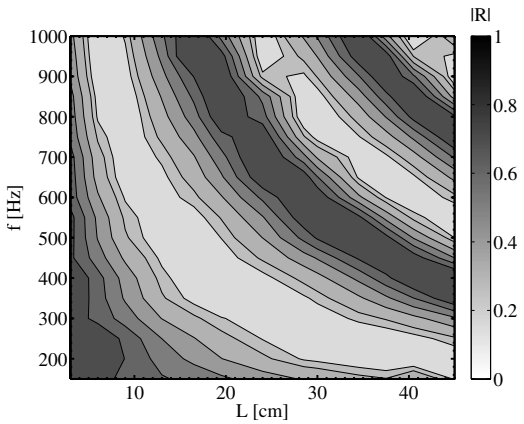

Fig. 4 Plate P_4, modulus of the reflection coefficient as a function of the depth and the frequency. SPL=110 dB.

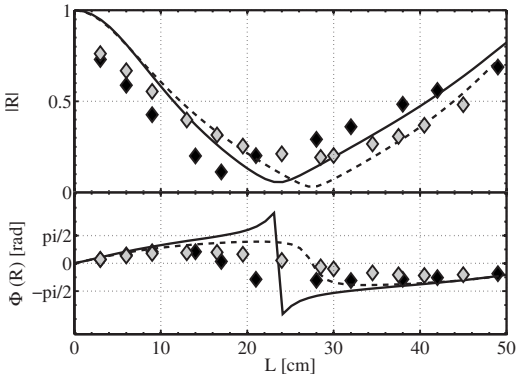

Fig. 5 Comparison between theoretical predictions (lines) and experimental data (symbols) for both plates at $f=300$ Hz. Black symbols and continuous line: P_8. Gray symbols and dashed line: P_4. SPL=110 dB.

were designed with different geometrical and flow operating characteristics. They feature the same damping properties for SPL lower than 110 dB.

3.3 Influence of High Amplitude Pressure Perturbations. The two designed systems produce satisfactory damping for moderate sound pressure levels. However, combustion chambers experience large levels of pressure fluctuations up to several hundreds of pascals during unstable operation [27]; at limit cycles, fluctuations can even reach a few percent of the operating pressure [28]. It is therefore interesting to test the plates' performance under strong acoustic forcing. Few works consider such high amplitude acoustic interactions with perforated panels (e.g., Refs. [19–21]). As the model of Howe is based on linear acoustics, nonlinear effects cannot be anticipated.

The response of the system to large pressure fluctuations was studied using the high-efficiency loudspeaker. Investigation on the influence of the SPL on the system response is led at two frequencies: one at which the modulus is the lowest and the other at which $|R|$ is maximized. The SPL is increased from 80 dB to 145 dB and the corresponding values of the modulus $|R|$ of the reflection coefficient are plotted in Fig. 6 for these two frequencies. Below 110 dB, the response is linear for both systems and the reflection coefficient is independent of the sound pressure level. Above 115 dB, the response of the cavity equipped with plate P_4 remains independent of the SPL for low and high modulus values. The behavior of the system equipped with plate P_8 exhibits, on the contrary, a strong dependence to the SPL. Low values of the modulus, obtained at $f=400$ Hz, quickly raise (+0.2/decade) when the SPL is increased, while high values, measured at $f=1000$ Hz, diminish. It is interesting to note that for a SPL of 140 dB, this system exhibits a nearly uniform reflection coefficient $|R|=0.7$ in the entire frequency range from 100 Hz to 1000 Hz.

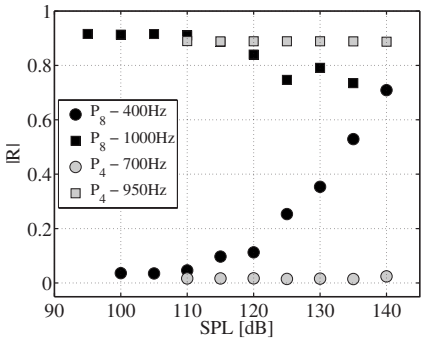

Fig. 6 Effect of the SPL on plates P_8 and P_4. Two frequencies were chosen for each plate, one yielding an almost perfect reflection (squares) and the other a nearly anechoic termination (circles).

While these two plates provide similar damping properties in the linear regime, their nonlinear response substantially differs. When considering practical applications, it is thus important to check the nonlinear response of such damping devices, which can lead to significantly distinct behaviors. Further investigation is under way to better understand this phenomenon.

Two reasons can be proposed to explain these differences. First, plate P_4 features more holes than plate P_8, which increases the vortex-sound interactions in the vicinity of the plate. This may favor sound damping. A second reason may be the difference in bias flow velocity. The larger jet velocity obtained within the apertures of plate P_4 is thus more robust to incident perturbations. However, these conjectures should be confirmed by further theoretical and experimental elements.

4 Application to the Acoustic Control of a Turbulent Swirled Combustor

The system tested in the impedance tube under controlled cold flow configurations is adapted here to a combustion facility delivering a thermal power of about 40 kW in order to control the reflection coefficient of the premixer inlet. Performances of the two plates are studied and their effects on self-sustained oscillations are investigated.

4.1 Combustion Test Rig. The combustion facility is an atmospheric swirl-stabilized, staged premixer operating in lean partially premixed conditions, connected to a rectangular combustion chamber, as sketched in Fig. 1. The chamber is composed of concrete walls and two lateral quartz windows. Its total length is 50 cm, with a square test section of 10×10 cm^2. The premixer is composed of two identical stages, in which tangential injections of air-propane mixture create a strong swirl (swirl number above 0.6) in an inner cylinder ($D_p=30$ mm, Fig. 1) [29]. The staging, which adds a degree of control on the combustion, concerns only the fuel repartition as air is fed equally in each stage. This configuration presents a strong precessing vortex core (PVC) due to the important swirl, which stabilizes the flame in an inverted conical shape and compact form [30–32]. The flame is typically 10–15 cm long. To prevent flashback inside the premixer, air is injected axially upstream of the premixing channel; this mass flow corresponds to a small fraction of the total tangential mass flow ($\approx$2.5%). Under normal operating conditions, flame visualizations locate the base of the flame just inside the burner outlet [29]. This burner exhibits strong unstable regimes, depending on the staging, characterized by intense acoustic fluxes inside the chamber and the premixer.

The combustion chamber and the premixer are equipped with B&K microphones identical to those that are used in the impedance tube. All are flush mounted on calibrated water-cooled waveguides. The premixer is equipped with three microphones, M1, M2, and M3, as sketched in Fig. 1. The chamber is also equipped with three microphones: the first one M_{ch} is just above the flame, the second one is located in the middle of the chamber, and the last one is placed just before the exhaust. A photomultiplier tube, equipped with a narrow band filter centered on the wavelength $\lambda=431$ nm and monitoring CH^* spontaneous emission from the flame, is used to measure fluctuations of the heat release rate in the flame region, where the microphone M_{ch} is located. Results presented in Figs. 7–10 are measured at the rear side of the premixer with the microphone M2 and inside the combustion chamber with the microphone M_{ch}. Signals were digitized using an 8192 Hz sampling frequency for a total acquisition time of 13 s. Power spectral densities (PSDs) are computed using a Welch periodogram method with a frequency resolution of 4 Hz.

The acoustic properties of the initial rear side piece of the premixer were characterized and serve as the reference case. This piece behaves almost as a perfectly reflecting acoustic boundary

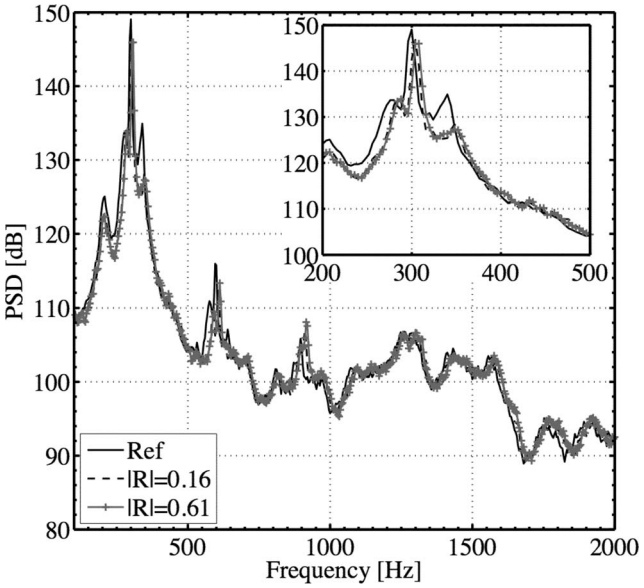

Fig. 7 PSD inside the premixer using the passive control solution with plate P_8. Microphone M2. Indicated moduli values correspond to predictions for a SPL of 110 dB.

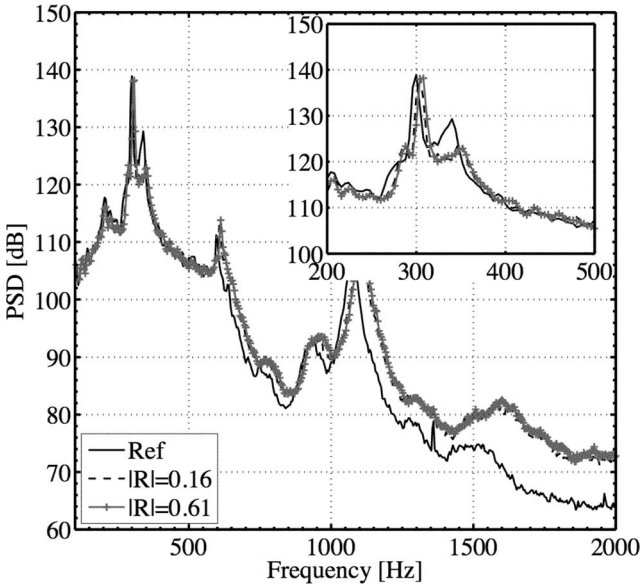

Fig. 8 PSD inside the chamber using the passive control solution with plate P_8. Microphone M_{ch}. Indicated moduli values correspond to predictions for a SPL of 110 dB.

condition, with $|R| \simeq 1$ for the frequency range of interest. The impedance control system is adapted at the inlet boundary of the burner, as sketched in Fig. 1. The rear side piece of the premixer is replaced by the perforated plate and a sliding piston is used to modify the back cavity depth L. The bias flow velocity U is adjusted to the optimal values found in Sec. 2. Perforated plates are positioned such that there is no change in the original geometry of the facility neither in cross section nor in length. Even though the premixer inner diameter is small, equal to 30 mm, the reduced available surface for acoustic damping directly faces the flame in a region of strong acoustic fluxes. Therefore it is expected that the system has important effects on the global acoustic energy balance. It should be noted that this impedance control system may be adapted to facilities presenting the same inlet characteristics as, for example, annular combustion chambers found in industrial gas turbines.

4.2 Influence of the Upstream Adaptive Impedance on Thermoacoustic Oscillations. Results inside the premixer (Fig. 7) and the chamber (Fig. 8) are first presented using the control system equipped with plate P_8. The reference case corresponding to the original premixer design shows a spectrum that features a large pressure peak of about 148 dB inside the premixer and about 138 dB inside the chamber at a frequency $f=290$ Hz. This frequency also corresponds to a strong organized motion of the flame, characterized by large fluctuations of the CH^* emission

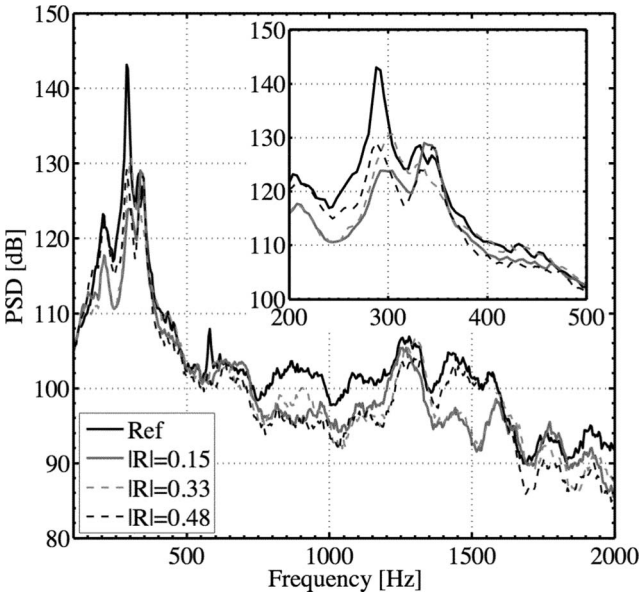

Fig. 9 PSD inside the premixer using the passive control solution with plate P_4. Microphone M_2. Indicated moduli values correspond to both prediction and measurements for a SPL of 140 dB.

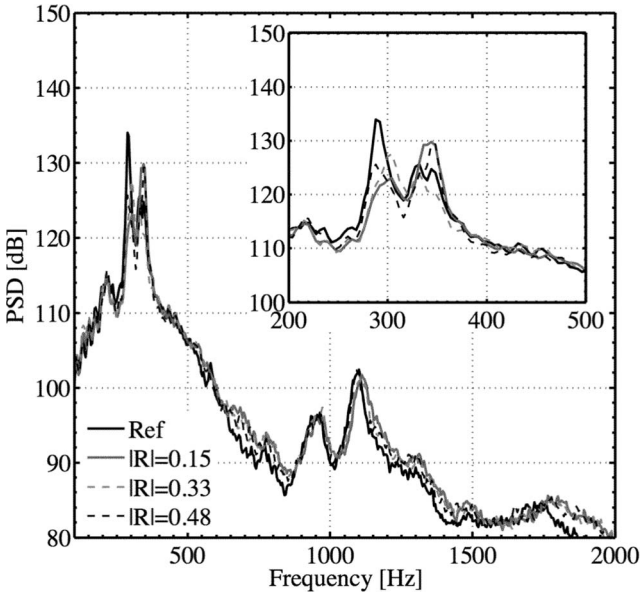

Fig. 10 PSD inside the chamber using the passive control solution with plate P_4. Microphone M_{ch}. Indicated moduli values correspond to both prediction and measurements for a SPL of 140 dB.

signal as measured by the photomultiplier tube. This self-sustained combustion oscillation is the signature of a strong unstable regime [23].

The passive control system developed was tested with plate P_8 in order to damp this oscillation by modifying the inlet boundary condition. To this purpose the back cavity depth L was modified to tune the modulus of the reflection coefficient at the rear side of the premixer, but this alteration did not seem to significantly attenuate pressure peaks inside the premixer or the chamber. Results are presented for two values of the cavity depth, which theoretically corresponds to two distinct values of the modulus, $|R|=0.16$ and $|R|=0.61$ for frequencies $f=290-300$ Hz in the case of a SPL of 110 dB. Yet, it was demonstrated in Sec. 3.3 that when the system is equipped with plate P_8, it loses its ability to efficiently control $|R|$ when the SPL increases. For levels equivalent to those found in the combustion facility during unstable regimes, this system features a nearly constant reflection coefficient $|R|\simeq 0.7$ in the entire frequency range 100–1000 Hz (Fig. 6). This is confirmed by the nonevolution of the PSD during the firing tests. It can be further noticed that when the passive control system is set up, pressure levels slightly diminish in comparison to the reference case (the bold black line). This is due to the fact that the value of the reflection coefficient is slightly lower than unity throughout the whole frequency range. However, spectra are only barely affected by cavity depth adjustment and the system remains globally inefficient. Peaks are only slightly shifted toward higher frequencies because of phase distortions induced by the passive control system.

Results are different once the system is equipped with plate P_4. It was used to impose three different values of $|R|$ at $f=290$ Hz, $|R|=0.15$, 0.33, and 0.48, by controlling the back-cavity depth as described in Sec. 3. These values are independent of the SPL up to 140 dB, as it was demonstrated in the impedance tube. This result is confirmed by the evolution of the PSD in the premixer (Fig. 9) and the chamber (Fig. 10) when the premixer rear side acoustic boundary condition is modeled by the proposed system. The reflection coefficient was measured in situ during the firing tests and the retrieved values correspond to the ones measured in the impedance tube with a SPL of 140 dB. The lower the modulus of the reflection coefficient, the lower the amplitude of the instability pressure peak at 290 Hz. In the most favorable case, when the cavity depth is adjusted to yield a reflection coefficient $|R|=0.15$, the amplitude of the peak diminishes by almost 20 dB inside the premixer and by more than 10 dB inside the chamber. The reduction is so significant that the second instability peak at $f=340$ Hz becomes dominant.

The amplitude of the peak at $f=290$ Hz follows the evolution of the modulus of the reflection coefficient $|R|$. When $|R|$ is decreased, the peak is attenuated. The passive control solution using a variable cavity depth backed with the plate P_4 is robust enough to damp high sound pressure levels reached during unstable operations and is an efficient way to control the inlet acoustic boundary of the combustion facility.

5 Conclusion

Available theoretical elements were used to design two perforated panels that are meant to provide control of the acoustic properties at their front face when backed by a cavity of tunable depth in the presence of a bias flow. It was demonstrated first in theory, and then checked in an impedance tube, that each system yields efficient control of the modulus of the reflection coefficient when submitted to small pressure fluctuations, up to 110 dB. Submitting the system to higher sound pressure levels, equivalent to those classically measured in combustion facilities during unstable regimes, highlighted very distinct behaviors between the two perforated plates. While plate P_8 enters its nonlinear regime for moderate sound pressure levels (at 115 dB), plate P_4 keeps a linear acoustic behavior in the whole range investigated (up to 145 dB). In terms of control of the reflection coefficient by the cavity depth, large pressure oscillation levels render the control system with plate P_8 totally inefficient, whereas the system with plate P_4 retains its damping properties. Conjectures for these differences were made but should be confirmed by further investigations.

The implementation of the proposed system as a passive control solution for the inlet acoustic boundary condition of a turbulent burner confirms this result. The system equipped with plate P_8 is ineffective, while, with plate P_4, the system is robust and produces large reduction in levels of pressure oscillations during typical self-sustained oscillations (up to -20 dB in the premixer and -10 dB in the chamber). Although it has been applied to a specific configuration, it aims to be more general and applicable to any type of combustor in which the upstream boundary condition is accessible.

Acknowledgment

This work is supported by EADS Corporate Research Foundation.

References

[1] Candel, S., 2002, "Combustion Dynamics and Control: Progress and Challenges," Proc. Combust. Inst., **29**(1), pp. 1–28.
[2] Ducruix, S., Schuller, T., Durox, D., and Candel, S., 2003, "Combustion Dynamics and Instabilities: Elementary Coupling and Driving Mechanisms," J. Propul. Power, **19**, pp. 722–734.
[3] Lieuwen, T., and Yang, V., 2006, *Combustion Instabilities in Gas Turbine Engines: Operational Experience, Fundamental Mechanisms, and Modeling*, (Progress in Astronautics and Aeronautics, Vol. 210).
[4] Bloxsidge, G. J., Dowling, A., Hooper, N., and Langhorne, P., 1988, "Active Control of Reheat Buzz," AIAA J., **26**(7), pp. 783–790.
[5] Lang, W., Poinsot, T., and Candel, S., 1987, "Active Control of Combustion Instability," Combust. Flame, **70**(3), pp. 281–289.
[6] Billoud, G., Galland, M., Huynh Huu, C., and Candel, S., 1992, "Adaptive Active Control of Combustion Instabilities," Combust. Sci. Technol., **81**, pp. 257–283.
[7] Bernier, D., Ducruix, S., Lacas, F., Candel, S., Robart, N., and Poinsot, T., 2003, "Transfer Function Measurements in a Model Combustor: Application to Adaptive Instability Control," Combust. Sci. Technol., **175**, pp. 993–1013.
[8] Bothien, M., Moeck, J., and Paschereit, C., 2007, "Impedance Tuning of a Premixed Combustor Using Active Control," ASME Paper No. GT2007-27796.
[9] Bellucci, V., Flohr, P., Paschereit, C., and Magni, F., 2004, "On the Use of Helmholtz Resonators for Damping Acoustic Pulsations in Industrial Gas Turbines," ASME J. Eng. Gas Turbines Power, **126**, pp. 271–275.
[10] Hughes, I. J., and Dowling, A. P., 1990, "The Absorption of Sound by Perforated Linings," J. Fluid Mech., **218**, pp. 299–335.
[11] Melling, T., 1973, "The Acoustic Impedance of Perforates at Medium and High Sound Pressure Levels," J. Sound Vib., **29**, pp. 1–65.
[12] Howe, M. S., 1979, "On the Theory of Unsteady High Reynolds Number Flow Through a Circular Aperture," Proc. R. Soc. London, Ser. A, **366**(1725), pp. 205–223.
[13] Narayana Rao, K., and Munjal, M. L., 1986, "Experimental Evaluation of Impedance of Perforates With Grazing Flow," J. Sound Vib., **108**(2), pp. 283–295.
[14] Bechert, D. W., 1980, "Sound-Absorption Caused by Vorticity Shedding, Demonstrated With a Jet Flow," J. Sound Vib., **70**(3), pp. 389–405.
[15] Eldredge, J. D., and Dowling, A. P., 2003, "The Absorption of Axial Acoustic Waves by a Perforated Liner With Bias Flow," J. Fluid Mech., **485**, pp. 307–335.
[16] Leppington, F. G., and Levine, H., 1973, "Reflection and Transmission at a Plane Screen With Periodically Arranged Circular or Elliptical Apertures," J. Fluid Mech., **61**, pp. 109–127.
[17] Peat, K. S., Sugimoto, R., and Horner, J. L., 2006, "The Effects of Thickness on the Impedance of a Rectangular Aperture in the Presence of a Grazing Flow," J. Sound Vib., **292**(3–5), pp. 610–625.
[18] Celik, E., Sever, A. C., and Rockwell, D., 2005, "Self-Sustained Oscillations Past Perforated and Slotted Plates: Effect of Plate Thickness," AIAA J., **43**(8), pp. 1850–1853.
[19] Luong, T., Howe, M. S., and McGowan, R. S., 2005, "On the Rayleigh Conductivity of a Bias-Flow Aperture," J. Fluids Struct., **21**(8), pp. 769–778.
[20] Dragan, S. P., and Lebedeva, I. V., 1998, "Absorption of High-Intensity Sound by a Perforated Panel," Acoust. Phys., **44**, pp. 167–172.
[21] Jing, X., and Sun, X., 2002, "Sound-Excited Flow and Acoustic Nonlinearity at an Orifice," Phys. Fluids, **14**(1), pp. 268–276.
[22] Dowling, A. P., and Stow, S. R., 2003, "Acoustic Analysis of Gas Turbine Combustors," J. Propul. Power, **19**(5), pp. 751–764.
[23] Tran, N., Ducruix, S., and Schuller, T., 2009, "Damping Combustion Instabilities With Perforates at the Premier Inlet of a Swirled Burner," Proc. Combust. Inst., **32**, pp. 2917–2924.

[24] Howe, M. S., 1998, *Acoustics of Fluid-Structure Interaction*, Cambridge University Press, Cambridge.
[25] Tran, N., Schuller, T., and Ducruix, S., 2007, "Analysis and Control of Combustion Instabilities by Adaptive Reflection Coefficients," 13th AIAA/CEAS Aeroacoustics Conference, Paper No. AIAA-2007-3716.
[26] Chung, J. Y., and Blaser, D. A., 1980, "Transfer Function Method of Measuring In-Duct Acoustic Properties. I. Theory," J. Acoust. Soc. Am., **68**, pp. 907–913.
[27] Uhm, J. H., and Acharya, S., 2005, "Low-Bandwidth Open-Loop Control of Combustion Instability," Combust. Flame, **142**(4), pp. 348–363.
[28] Eckstein, J., Freitag, E., Hirsch, C., and Sattelmayer, T., 2006, "Experimental Study on the Role of Entropy Waves in Low-Frequency Oscillations in a rql Combustor," ASME J. Eng. Gas Turbines Power, **128**(2), pp. 264–270.
[29] Dioc, N., 2005, "Etude expérimentale des mécanismes d'instabilités dans un brûleur à injection étagée. application aux turbines à gaz," Ph.D. thesis, Ecole Centrale Paris, Châtenay-Malabry.
[30] Huang, Y., Sung, H.-G., Hsieh, S.-Y., and Yang, V., 2003, "Large-Eddy Simulation of Combustion Dynamics of Lean-Premixed Swirl-Stabilized Combustor," J. Propul. Power, **19**(5), pp. 782–794.
[31] Roux, S., Lartigue, G., Poinsot, T., Meier, U., and Berat, C., 2005, "Studies of Mean and Unsteady Flow in a Swirled Combustor Using Experiments, Acoustic Analysis, and Large Eddy Simulations," Combust. Flame, **141**(1-2), pp. 40–54.
[32] Syred, N., 2006, "A Review of Oscillation Mechanisms and the Role of the Precessing Vortex Core (PVC) in Swirl Combustion Systems," Prog. Energy Combust. Sci., **32**(2), pp. 93–161.

Enhanced Fault Localization Using Probabilistic Fusion With Gas Path Analysis Algorithms

A. Kyriazis
Research Assistant
e-mail: ankyr@ltt.ntua.gr

K. Mathioudakis
Professor
e-mail: kmathiou@central.ntua.gr

Laboratory of Thermal Turbomachines,
National Technical University of Athens,
P.O. Box 64069,
Athens 15773, Greece

A method for gas turbine fault identification from gas path data, in situations with a limited number of measurements, is presented. The method consists of a two stage process: (a) localization of the component or group of components with a fault and (b) fault identification by determining the precise location and magnitude of component performance deviations. The paper focuses on methods that allow improved localization of the faulty components. Gas path analysis (GPA) algorithms are applied to diagnostic sets comprising different combinations of engine components. The results are used to derive fault probabilities, which are then fused to derive a conclusion as to the location of a fault. Once the set of possible faulty components is determined, a well defined diagnostic problem is formulated and the faulty parameters are determined by means of a suitable algorithm. It is demonstrated that the method has an improved effectiveness when compared with previous GPA based methods. [DOI: 10.1115/1.3078793]

1 Introduction

Engine health monitoring is of great importance for gas turbines today, since it is related to safety, aircraft availability, fleet management, etc. In recent years, a lot of effort has been made in the domain of engine diagnostics and the results can be found in many published works.

Undoubtedly, the most popular approach is the gas path analysis (GPA), with which the discipline of gas turbine diagnostics has been initiated. Its first approach was linear GPA. The fundamentals of linear gas path analysis were laid by Urban [1]. Least-squares techniques coupled to gas path analysis have been presented by Doel [2,3]. These methods utilize a linear system of equations, which interrelates measurable thermodynamic quantities along the engine (temperatures, pressures, etc.) with flow capacity and efficiency factors of engine components, representing their state of health. Linear GPA is the diagnostic approach mostly used in engines in service today applied under different formulations by the major engine manufacturers [3–6]. Nonlinear GPA approaches have been developed later and constitute more sophisticated approaches. Early studies of nonlinear GPA were introduced by the group of the authors, through the adaptive modeling technique [7,8], which was later applied to different engine types by Tsalavoutas et al. [9]. Nonlinear GPA studies have been performed by several more authors [10,11].

The application of GPA methods for the estimation of the health parameters in practical cases encounters a number of difficulties. The most important obstacle is the lack of measurements, which lead to underdetermined systems of equations. In order to overcome this problem, many approaches have been proposed among which are Kalman filtering [12,13], optimization techniques [14–16], and combinatorial approach [17]. The basic idea of all these methods is that when individual component faults exist, they can be detected by some first decision criteria. This allows a reduction in the number of unknown health parameters, which can then be evaluated more accurately, provided of course that the faulty component has been identified correctly at the first step.

Another problem is the inaccuracy of measurements due to the presence of noise. The effect of noise can be reduced if a series of measurements is available instead of a single measurement set. Noise reduction can be achieved in many ways varying from a simple averaging to the application of more sophisticated methods such as Kalman filtering [13], nonlinear filters [18], and median filters [19–21].

The method proposed in the present paper constitutes an advancement of techniques previously introduced by Mathioudakis et al. [14] and Aretakis et al. [17]. It enhances these techniques by first handling the obstacle of underdetermination with the concept of engine partition and second by introducing a statistical processing of the diagnostic results of the first stage. The proposed procedure aims to derive fault probabilities about the state of each health parameter and use them to proceed with identification of faulty component and improved estimation of fault magnitude. Finally, a probabilistic fusion task is presented in order to further enhance the diagnostic effectiveness of the proposed methodology.

2 Basics of GPA Fault Diagnosis

In performance diagnostics, the engine is considered as a system, whose operating point is defined by means of a set of variables, denoted as $\boldsymbol{u}$. The health condition of its components is represented through the values of a set of appropriate *health parameters*, contained in a vector $\boldsymbol{f}$. The system is monitored through measured variables (speeds, pressures, temperatures, etc), contained in a vector $\boldsymbol{Y}$. The operating engine establishes a relationship between these quantities, that is, the health parameters and the measurements, which can be expressed through a functional relation:

$$\boldsymbol{Y} = \boldsymbol{F}(\boldsymbol{u}, \boldsymbol{f}) \tag{1}$$

This function can be realized by a computer model capable of handling the numerical interrelations among the quantities of interest and thus allowing the simulation for healthy or faulty operation of the engine. The purpose of a diagnostic procedure is to obtain a solution to the inverse problem of Eq. (1), that is, to determine the values of component health parameters, $\boldsymbol{f}$, when a set of measured quantities $\boldsymbol{Y}$ is available, for given operating conditions $\boldsymbol{u}$. In cases usually encountered in practice, the available measurements are fewer than the health parameters, leading to an underdetermined system of equations. Determination of a unique

Contributed by the International Gas Turbine Institute of ASME publication in the JOURNAL OF ENGINEERING FOR GAS TURBINES AND POWER. Manuscript received September 17, 2008; final manuscript received September 30, 2008; published online June 9, 2009. Review conducted by Allan Volponi. Paper presented at the ASME Turbo Expo 2008: Land, Sea and Air (GT2008), Berlin, Germany June 9–13, 2008.

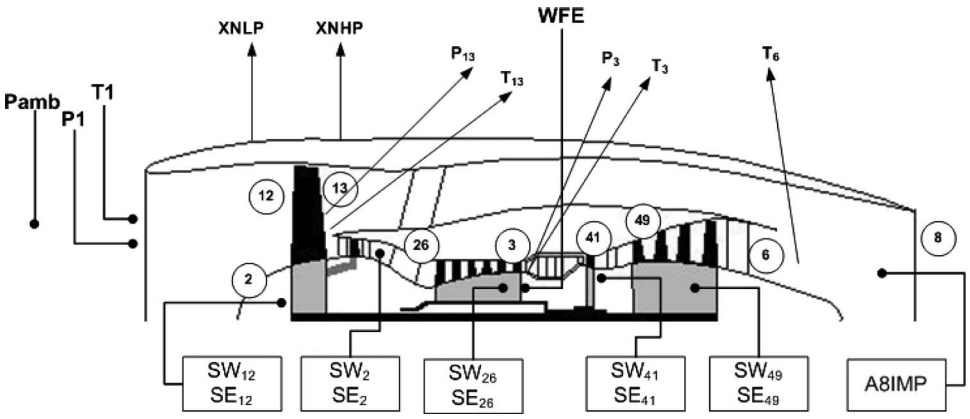

Fig. 1 Layout and station numbering of the considered engine

solution for $\boldsymbol{f}$ is only possible by using information in addition to the measurements, as, for example, discussed in Ref. [14].

3 Engine Partitioning for Fault Localization

The first stage of the proposed method is to reduce the number of unknowns by selecting the most probable candidates among a large set of unknown health parameters. This is achieved by considering groups of components, which are candidates to contain the faulty components. The engine is divided to partitions, taking into account its layout and physics of operation. For each partition, the nonlinear optimization GPA method proposed by Mathioudakis et al. [14] is used to estimate the deviations of health parameters. An objective function (OF) is minimized, the form of which is given in Appendix A. A first pass of calculations is thus performed, as many times as the different parts of each partition, estimating each time the corresponding health parameters.

In order to demonstrate the concept, an example case is presented. The utilized engine is a partially mixed high bypass ratio turbofan, typical in civil aviation today, presented in Fig. 1. It has been used as a test case in numerous diagnostic studies and therefore constitutes a benchmark case. For monitoring purposes, seven quantities are measured and 11 health parameters are used to represent components' condition, all shown in Fig. 1. For the definition of the employed quantities, the reader is referred to Refs. [14,17].

Two different modes of partitioning were implemented, namely, the cold-hot-nozzle (CHN) partition and the LP-HP-nozzle (LHN) partition, shown in Fig. 2. Since the number of health parameters for each part of the partition is smaller than the number of the measurements, a unique solution can be derived for the relevant health parameters.

The cold-hot-nozzle partition consists of three parts; therefore, the GPA method will be applied three times, once per part. For the cold part, the health parameters of the fan component and the two compressors are estimated, namely, SW_{12}, SE_{12}, SW_2, SE_2, SW_{26},

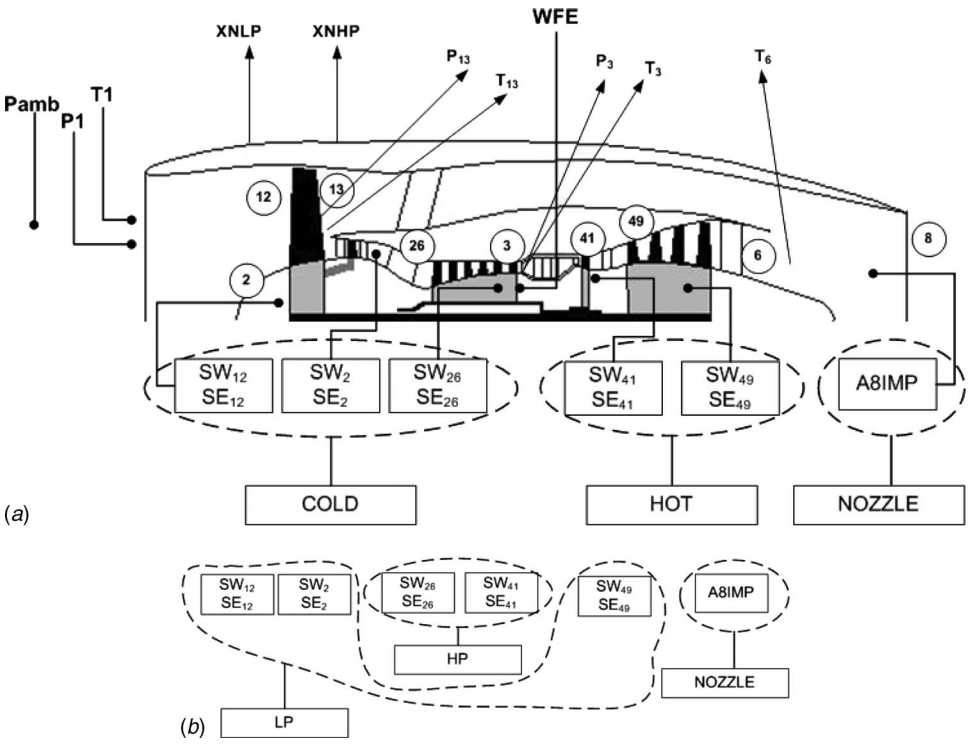

Fig. 2 Two modes of partitioning an engine: (*a*) Cold-hot-nozzle, (*b*) LP-HP-nozzle

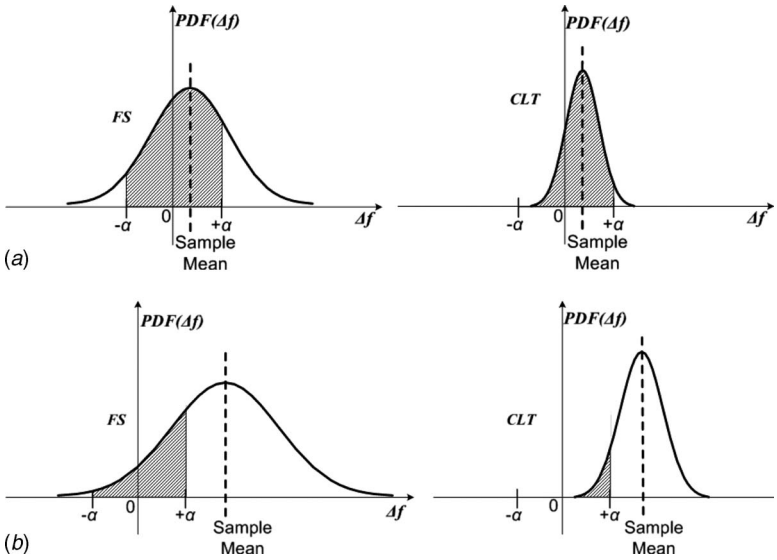

Fig. 3 Derivation of fault probabilities by integration: (*a*) Nonfaulty health parameter, (*b*) faulty health parameter

and SE_{26}. Likewise for the hot part, the health parameters SW_{41}, SE_{41}, SW_{49}, and SE_{49} are estimated. For the nozzle, the A8IMP alone is estimated.

The other mode of partition (LP-HP-nozzle) consists of three parts with the last one being the same as for the other mode, namely, the nozzle part. For this mode, the health parameters are chosen considering as diagnostic sets (groups of engine components) the different spools, the high pressure (HP) and the low pressure (LP). For the LP part, six health parameters, SW_{12}, SE_{12}, SW_2, SE_2, SW_{49}, and SE_{49}, are estimated. For the HP part, the corresponding parameters are SW_{26}, SE_{26}, SW_{41}, and SE_{41}.

4 Statistical Processing and Derivation of Fault Probabilities

Given a sequence of N measurement sets, the nonlinear optimization procedure applied to a partition mode provides a series of N estimations concerning the whole set of health parameters. The estimations are in terms of percentage deviations from nominal value ("deltas"). From the N estimated values, the sample mean and the sample standard deviation, for the statistical sample population of each health parameter are derived:

$$\overline{X_j} = \overline{\Delta f_j} = \frac{1}{N}\sum_{n=1}^{N} \Delta f_j^n \tag{2}$$

$$s_j = \sqrt{\frac{1}{N-1}\sum_{n=1}^{N} (\Delta f_j^n - \overline{\Delta f_j})^2} \tag{3}$$

The linearity assumption of the diagnostic problem applies if the deviations of the health parameters are small in magnitude; see Ref. [22], a situation that is common in practice. The measurements $\mathbf{Y}$ of the engine are assumed to have normal distributions and therefore, due to linearity assumption, the health parameters also have normal distributions (see, for example, Ref. [23]). Based on that, it also applies that the Δf_j follow normal distribution. For the purpose of the proposed statistical processing, two different variants have been developed. A user may select between them. These are as follows.

(i) The first variant considers each Δf_j as a random variable with normal distribution as mentioned earlier. The mean and standard deviation of this distribution are estimated directly by Eqs. (2) and (3). The entire available sample population is utilized in this variant; therefore, it will be referred as full_sample (FS) from now on.

(ii) The second variant considers the sample mean $\overline{X_j}$ as a random variable. From central limit theorem (CLT), see Ref. [23], it is known that the distribution of sample mean is normal when the considered population has normal or even unknown distribution. The mean of the distribution of $\overline{X_j}$ approximates its value as the sample size becomes larger. The standard deviation is equal to

$$\sigma_{\overline{X_j}} = \frac{s_j}{\sqrt{N}} \tag{4}$$

For this variant, the Student t distribution can also be utilized but as the number of degrees of freedom (dfs) becomes larger the t distribution approximates the normal distribution. It is noted that $df = N-1$ and since the common situation is N to be usually large, therefore, the normal distribution has been adopted without great loss of generality. This variant will be referred as CLT from now on.

Small deviations of a health parameter may occur due to the measurement or setpoint inaccuracies or even small drifts on the engine performance with operating time, occasions that are not considered as faulty. Consequently, we consider a threshold a, such that only deviations of the health parameters (Δf_j) larger than a are categorized as faults. This threshold, for each health parameter f_j, depends on the engine and the nature of the parameters.

In order to derive a probability that a health parameter f_j is not faulty, an integration of the normal distributions is performed in the interval $[-a, a]$ for both variants. Example cases of four estimation situations are shown in Fig. 3.

The probability for healthy (nonfaulty) condition is very large in case (a) were two different distributions by both statistical variants are presented. The value of sample mean is the same for both cases but the value of standard deviation differs. In case (b), the probability for healthy condition is small (and thus high for faulty). Again in this case two different distributions are presented with same sample mean and different standard deviations.

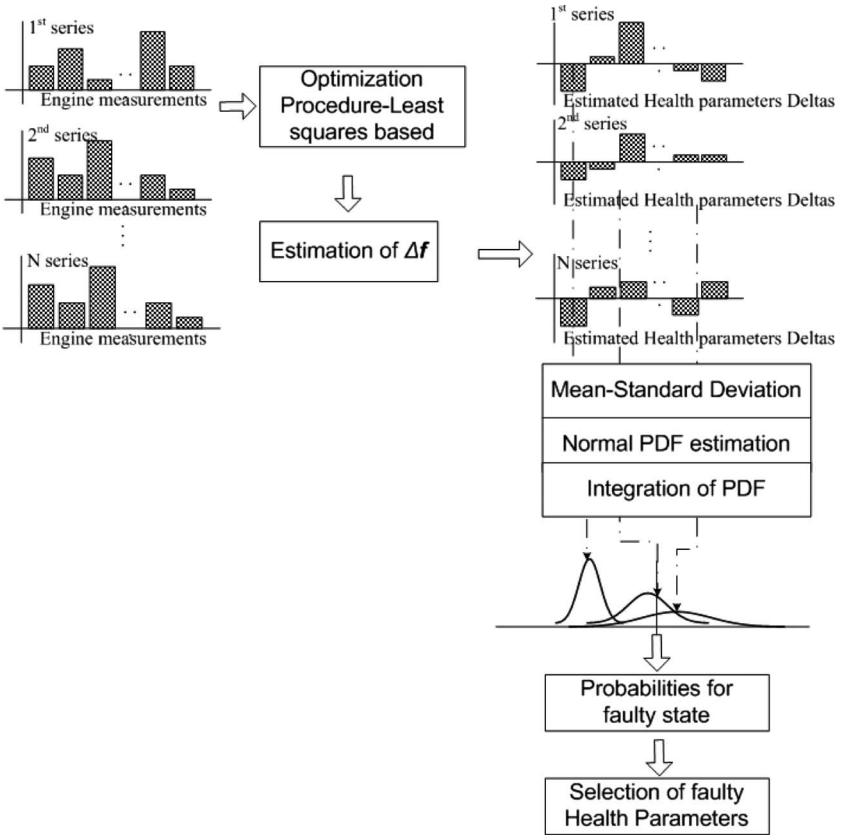

Fig. 4 Flowchart of the procedure for faulty components selection

$$P_{\mathrm{FS}}(f_j \in \text{nonfaulty}) = \int_{-a}^{a} \text{normpdf}(\Delta f_j)\, d\Delta f_j \tag{5}$$

$$P_{\mathrm{FS}}(f_j \in \text{faulty}) = 1 - P_{\mathrm{FS}}(f_j \in \text{nonfaulty}) \tag{6}$$

$$P_{\mathrm{CLT}}(f_j \in \text{nonfaulty}) = \int_{-a}^{a} \text{normpdf}(\overline{\Delta f_j})\, d\overline{\Delta f_j} \tag{7}$$

$$P_{\mathrm{CLT}}(f_j \in \text{faulty}) = 1 - P_{\mathrm{CLT}}(f_j \in \text{nonfaulty}) \tag{8}$$

The P_{FS} probability is obtained when the full_sample variant is adopted while the P_{CLT} probability is obtained by utilizing the CLT variant.

4.1 Fault Isolation Criteria. The localization and isolation of the fault are done by first examining the fault probabilities (of either two variants) for all health parameters f_j from a considered engine partition and then setting an appropriate criterion as follows: A health parameter f_j is considered to be faulty when

$$P(f_j \in \text{faulty}) \geq P_{\mathrm{thr}}$$

In the applications that follow, the threshold probability P_{thr} is taken to be 50%. A component is chosen to be faulty when at least one of the health parameters that describe its health condition is found faulty. It is noted that for the correct application of the proposed method, the considered combinations of engine components must cover the whole set of the health parameters of the engine, condition that is fulfilled in the partition cases presented here. The procedure so far is presented in Fig. 4.

After this localization the least-squares optimization is performed again, but this time only to the health parameters found faulty. This is the second pass.

For example, let us consider the cold-hot-nozzle partition. After the completion of first pass, estimations for all 11 health parameters have been derived. The PDF integration is performed upon these estimations, by adopting one of the two variants, deriving fault probabilities for the 11 health parameters. An implementation example is given later in the paper.

The estimated values resulting from the second pass derive again a new sample mean value and standard deviation according to Eqs. (2) and (3). These values are used to derive the diagnostic index (DI):

$$\mathrm{DI}_j = \frac{\overline{X_j}}{s_j} \tag{9}$$

Such a parameter has been introduced by the group of authors in previous publications, e.g., Refs. [14,24]. It is noted that in Ref. [24] the DI is presented with a slightly different definition.

A faulty component is chosen to be the one that comprises the health parameter with the maximum DI. The flowchart of the entire procedure is shown in Fig. 5.

4.2 Fusion Mechanism. Improvement to the diagnostic result can be achieved by performing a probabilistic fusion task upon the proposed statistical method. This probabilistic fusion technique utilizes the concept of aggregation theory and pooling extraction [25].

For the purposes of the current work, the *linear opinion pool* is used for probabilities aggregation. This scheme is also known as weighted average. The probability consensus for health parameter f_j is derived by the equation

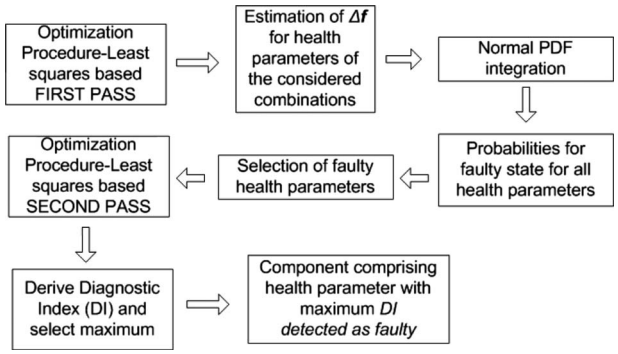

Fig. 5 Schematic representation of the whole procedure

$$G(j) = \frac{\sum_{h=1}^{z} w_{hj} \bullet p_h(f_j)}{\sum_{h=1}^{z} w_{hj}} \tag{10}$$

where $G(j)$ is the probability consensus value, w_{hj} are the corresponding weights, and $p_h(f_j)$ is the probability of health parameter f_j to be faulty by either of the two variants.

This fusion methodology is applied after the completion of the PDF integration to the outputs of the first pass, if more than one partition is considered. The probabilities derived by probability consensus are then utilized to proceed to the second pass. The procedure is presented in Fig. 6.

5 Implementation for Component Faults in a Turbofan Engine

In order to evaluate the effectiveness of the proposed method, an application to the turbofan test case is presented. This test case presents a situation of practical interest in today's jet engine applications since it involves a type of engine and faults that occur in practice.

The available fault scenario consists of 15 fault cases, which are described in Appendix B. For each fault case, a series of $N=50$ measurement sets has been exploited. Noisy data were produced by simulation, with the aid of an engine model, from the cruise section of a flight. These data are contaminated with noise of realistic magnitude as explained in Appendix B.

5.1 Individual Procedures. The results of the proposed diagnostic method, concerning the two engine partitions and the application of both statistical variants, are presented in Table 1. In Table 2, the results of GPA based methods, developed by the group of authors in the past, are given for comparison. These methods are the basic nonlinear least-squares (NLLS) optimization procedure presented by Mathioudakis et al. [14], combinatorial (CMBN) approach by Aretakis et al. [17], and probabilistic reasoning (Parzen index (PI)) by Romessis et al. [24].

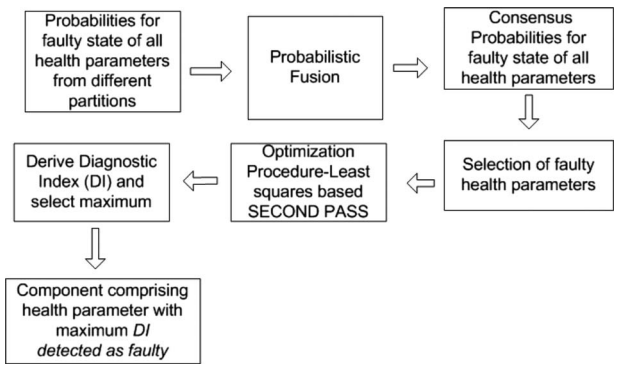

Fig. 6 Probabilistic fusion for enhancement

Table 1 Results of fault localization, derived by engine partition methods

Fault case	Affected component	FS		CLT	
		CHN	LHN	CHN	LHN
A	FAN, LPC	HPT	LPC	FAN	FAN
B	FAN	FAN	FAN	FAN	FAN
C	HPC	HPC	HPC	LPC	HPC
D	HPC	HPC	HPC	HPC	HPC
E	HPC	HPC	LPC	HPC	LPC
F	HPT	HPT	HPT	HPT	HPT
G	HPT	HPT	HPT	HPT	HPT
H	HPT	HPT	HPT	HPT	HPT
I	LPT	LPT	LPT	LPT	LPT
J	LPT	HPT	LPT	LPC	LPT
K	LPT	LPT	LPC	LPT	LPT
L	LPT	LPT	LPT	LPT	LPT
M	NZLE	NZLE	HPC	NZLE	NZLE
N	NZLE	NZLE	LPC	NZLE	FAN
O	NZLE	NZLE	NZLE	NZLE	NZLE

CHN: cold-hot-nozzle; LHN: LP-HP-nozzle

A misdiagnosis is noted by underline. From this table, we can conclude that the first partition CHN for both statistical variants presents a better performance for locating the faulty component than all the other previous GPA methods. The second partition has a better performance with CLT variant but the same effectiveness with the other GPA methods for FS variant. It is noted that fault case **j**, which is misdiagnosed by almost all methods, presented observability problems, as discussed by Mathioudakis et al. [14] and Aretakis et al. [17]. This was not the case, however, for the LHN partition concerning both statistical variants. Likewise fault case **c** with same observability problems was detected correctly by both partitions except for CHN partition adopting CLT variant.

In order to demonstrate the mechanism of the method, it is useful to show examples of intermediate results. A case with nozzle fault, case **m**, is considered, since for this case one of the partition modes succeeds while the other one fails (for FS variant). In Fig. 7, the values of fault probabilities for the 11 health parameters, derived by PDF integration on the estimations of the first pass, are shown. They concern both engine partitions using the FS processing variant. Parameters SW_{12}, SE_{12}, SE_2, SW_{26},

Table 2 Results of fault localization, derived by previous GPA methods

Fault case	Affected component	NLLS	CMBN	PI
A	FAN, LPC	FAN	FAN	FAN
B	FAN	FAN	FAN	FAN
C	HPC	LPC	LPC	LPC
D	HPC	HPC	HPC	HPC
E	HPC	HPC	HPC	HPC
F	HPT	HPT	HPT	HPT
G	HPT	HPT	HPT	HPT
H	HPT	HPT	HPT	LPT
I	LPT	LPT	LPT	LPT
J	LPT	HPT	LPC	HPT
K	LPT	HPT	LPC	HPT
L	LPT	HPT	LPT	LPT
M	NZLE	NZLE	LPC	NZLE
N	NZLE	NZLE	NZLE	NZLE
O	NZLE	NZLE	NZLE	NZLE

NLLS: nonlinear least-squares; CMBN: combinatorial approach; PI: Parzen index

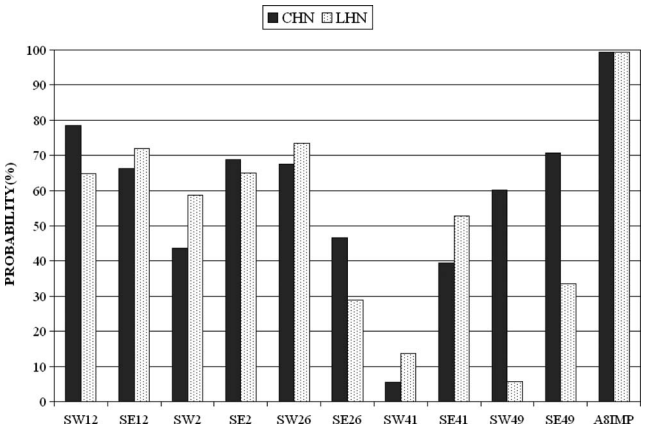

Fig. 7 Probabilities after first pass from CHN and LHN partitions (FS)

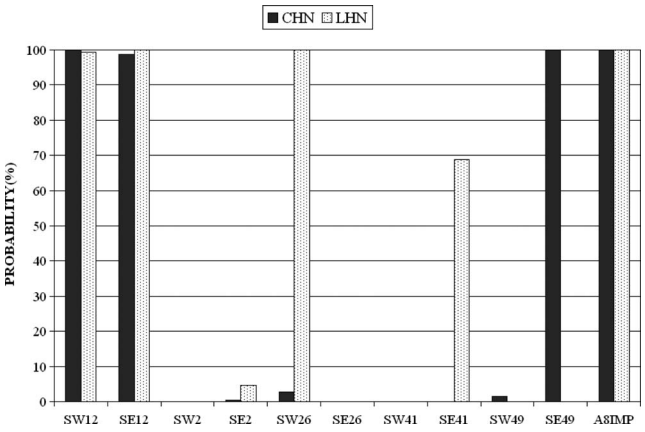

Fig. 9 Probabilities after first pass from CHN and LHN partitions (CLT)

SW_{49}, SE_{49}, and A8IMP are found to be faulty for CHN partition, as the corresponding probabilities are more than 50%. For the LHN partition, the candidate faulty parameters are SW_{12}, SE_{12}, SW_2, SE_2, SW_{26}, SE_{41}, and A8IMP. The second pass is then performed, by estimating these parameters only. The DI values for the above parameters are shown in Fig. 8. The A8IMP is finally selected as the faulty parameter, as it has the greatest value of DI for CHN partition while for LHN the SE_2 is finally chosen as the faulty parameter.

In Figs. 9 and 10, the corresponding results for the two partitions are presented but now the CLT statistical processing variant has been employed. It is seen that in this case health parameter A8IMP is (correctly) selected as the faulty parameter

5.2 Fusion Procedure. The improvement that can be achieved by application of probabilistic fusion will now be demonstrated. The fusion task is performed after the completion of first pass of both partitioning modes cold-hot-nozzle and LP-HP-nozzle, upon the probability values of health parameters to be (or not) faulty, as derived with the PDF integration. The final selection in order to proceed with the second pass is done upon the values of the derived consensus after the application of the aggregation function. For each statistical processing variant, a different consensus is derived since the probabilities are different.

The consensus values derived from fusion of the probabilities of Figs. 7 and 9 are shown in Fig. 11. In Fig. 12, the diagnostic indices after the completion of second pass (selected health parameters from the consensus probabilities) are shown, again for the same fault case **m** as before and for both variants. We see that the fusion procedure selects the correct faulty health parameter (A8IMP) improving thus the final diagnostic decision.

For the application of the aggregation probabilistic fusion, besides the available probability values derived by the PDF integration method for each partition, the weights W_i had to be also defined. The selection of the weights, in general cases of aggregation concept, is performed in such a way to combine both experience and efficiency. For the purposes of the current work, the

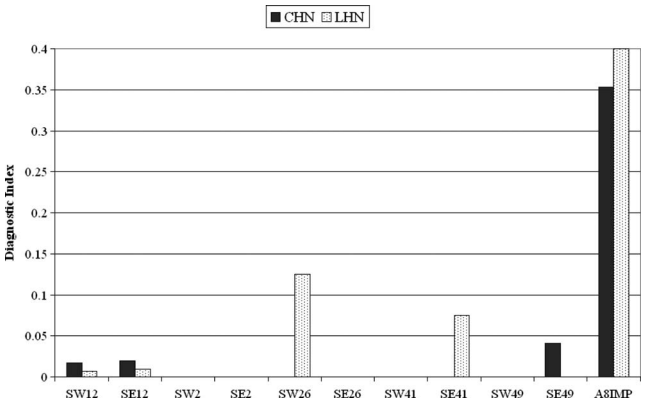

Fig. 10 Diagnostic Index after second pass, CHN, and LHN partitions (CLT). NZLE component found faulty by both CHN and LHN.

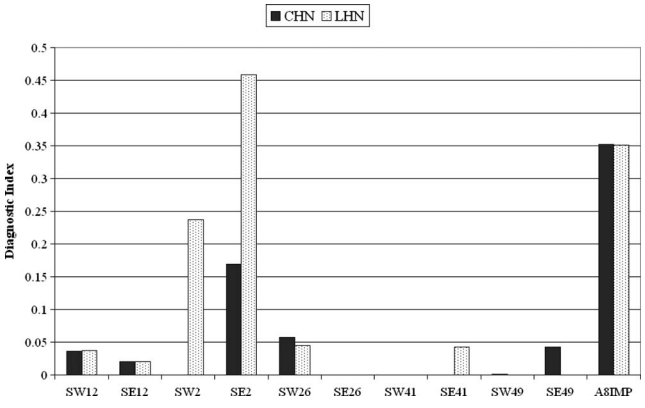

Fig. 8 Diagnostic index after second pass, CHN, and LHN partitions (FS). (A8IMP parameter found faulty-NZLE component for CHN, SE2 parameter found faulty-high pressure compressor (HPC) component for LHN.)

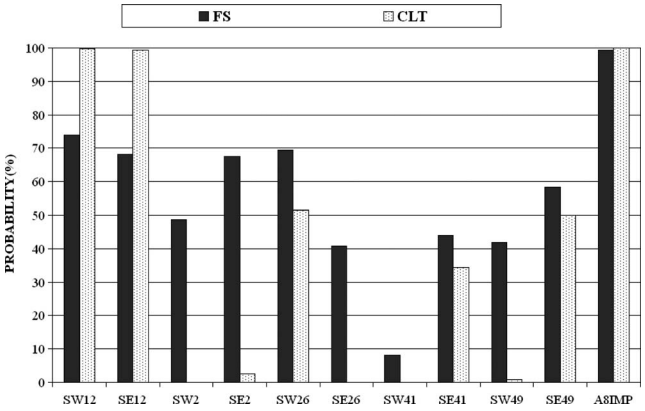

Fig. 11 Consensus probabilities after first passes of the utilized partitions (for FS and CLT)

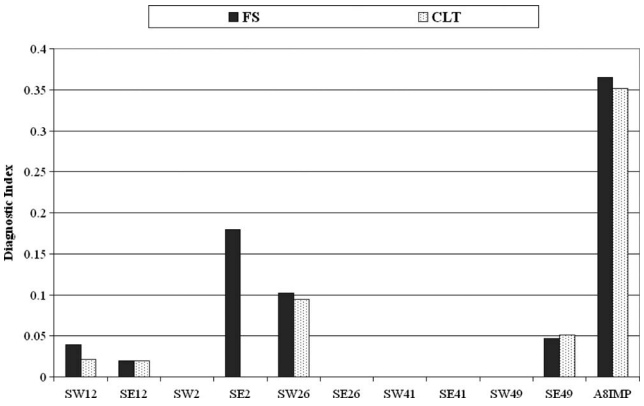

Fig. 12 Diagnostic index after second pass from the utilized partitions. (A8IMP parameter found faulty-NZLE component.)

efficiency of each partition, as presented in Table 1, is defined indirectly through the number of misdiagnoses. If a partition mode has lesser misdiagnoses than other, then it is more effective. From Table 1, it is clear that the CHN partition has twice the effectiveness of the LHN partition for FS variant. Therefore, for the derivation of the final consensus, the weight $W_{\text{cold-hot-nozzle}}$ had the double value from the corresponding weight for the other considered partition. In the case of CLT variant, the weights W_i were equal since both partitions had equal number of misdiagnoses.

In Tables 3 and 4, the results of the probabilistic fusion on the two considered partitions are given. It is evident that the probabilistic fusion methodology led to an improvement of the diagnostic effectiveness since only 1 fault case out of 15 was misdiagnosed for both variants.

6 Concluding Remarks

An approach for enhancement of the effectiveness of previous GPA methods has been presented. This proposed method is used together with a least-squares optimization diagnostic method, in order to solve the diagnostic problem. The problem of underdetermined diagnostic systems is handled and well defined systems are constructed through the notion of engine partitioning.

Effectiveness of the method has been demonstrated by application to simulated noisy data sets of a turbofan engine. Its performance was compared with the performance of previous GPA methods on the same data set. It was verified that the proposed method constitutes a reliable tool for the improvement of the final diagnostic decision.

Table 3 Results upon application of the probabilistic fusion method for FS variant

Fault case	Affected component	CHN	LHN	Fusion
A	FAN, LPC	HPT	LPC	FAN
B	FAN	FAN	FAN	FAN
C	HPC	HPC	HPC	HPC
D	HPC	HPC	HPC	HPC
E	HPC	HPC	LPC	HPC
F	HPT	HPT	HPT	HPT
G	HPT	HPT	HPT	HPT
H	HPT	HPT	HPT	HPT
I	LPT	LPT	LPT	LPT
J	LPT	HPT	LPT	HPT
K	LPT	LPT	LPC	LPT
L	LPT	LPT	LPT	LPT
M	NZLE	NZLE	HPC	NZLE
N	NZLE	NZLE	LPC	NZLE
O	NZLE	NZLE	NZLE	NZLE

Table 4 Results upon application of the probabilistic fusion method for CLT variant

Fault case	Affected component	CHN	LHN	Fusion
A	FAN, LPC	FAN	FAN	FAN
B	FAN	FAN	FAN	FAN
C	HPC	LPC	HPC	HPC
D	HPC	HPC	HPC	HPC
E	HPC	HPC	LPC	LPC
F	HPT	HPT	HPT	HPT
G	HPT	HPT	HPT	HPT
H	HPT	HPT	HPT	HPT
I	LPT	LPT	LPT	LPT
J	LPT	LPC	LPT	LPT
K	LPT	LPT	LPT	LPT
L	LPT	LPT	LPT	LPT
M	NZLE	NZLE	NZLE	NZLE
N	NZLE	NZLE	FAN	NZLE
O	NZLE	NZLE	NZLE	NZLE

It is noted here that the fusion procedure can be applied to any set of probabilities for the condition of the various factors being faulty. Any other method that produces such probabilities (e.g., Bayesian belief networks, probabilistic neural networks, and pattern recognition methods) could be used as an input to the fusion procedure, which drives the subsequent second pass. On the other hand, the PDF integration procedure, as a last step of the first pass, allows the derivation of probabilities that can be fed to any fusion method (not only the fusion with probability aggregation presented here). It has the particular feature that it converts values calculated by an estimation procedure to probability values. In this respect, the approach proposed here is of more general usefulness, as it can be coupled to other diagnostic methods.

Upon application of the PDF integration, the second stage of the method is performed by selecting the final faulty component of the engine. It is noted that this stage can be appropriately modified in order to permit selection of more than one faulty component at the end, enabling thus a multifault scenario.

Acknowledgment

The work for this paper has been carried out in the frame of project TATEM (Technologies and Techniques for New Maintenance Concepts) and financial support of the Commission of the European Union Contract No. AIP3-CT-2004-502909 is gratefully acknowledged.

Nomenclature

- A8IMP = nozzle exhaust area
- C_i = weight factor of OF (Appendix A) (Eq. (A1))
- cold = cold part of the engine
- $\boldsymbol{F}(\,)$ = function representing engine's behavior (Eq. (1))
- $\boldsymbol{f}$ = vector of health parameters
- $\boldsymbol{f}^r$ = reference values of vector $\boldsymbol{f}$
- HPC = high pressure compressor
- HPT = high pressure turbine
- hot = hot part of the engine
- LPC = low pressure compressor
- LPT = low pressure turbine
- NZLE = nozzle
- P_{amb} = ambient pressure
- PDF = probability density function
- P_i = total pressure at engine station i
- SE_i = efficiency factor at engine station i
- SW_i = flow factor at engine station i
- s_j = sample standard deviation of health parameter f_j (Eq. (3))

T_i = total temperature at the station i of the engine
$\boldsymbol{u}$ = vector of quantities defining operating point
WFE = fuel flow rate
W_i = vector of weights for probabilistic fusion
G = probability consensus of probabilistic fusion for vector $\boldsymbol{f}$ (Eq. (6))
XNHP = high pressure shaft, rpm
XNLP = low pressure shaft, rpm
Y = vector of measured quantities
Y_i = measured quantity
Δf_j = percentage deviation of health parameter f_j
$\bar{X}_j$ = sample mean of health parameter f_j (Eq. (2))
σ_{f_j} = standard deviation of health parameter f_j
σ_{Y_i} = standard deviation of measured quantity Y_i

Subscripts and Superscripts

g = measured or simulated value of a Y_i (Eq. (A1))
h = identification number of a partition
i = station along the engine
j = identification number of the estimated health parameter
m = value of a Y_i derived by the engine model (Eq. (A1))
$\boldsymbol{r}$ = reference value ("healthy" engine)
z = total number of utilized partitions in probabilistic fusion

Appendix A: Objective Function of the Nonlinear Optimization GPA Method

The diagnostic problem is solved by minimization of an objective function of the following form:

$$\mathrm{OF} = C_1 \sum_{i=1}^{K} \left[\frac{Y_i^m(f) - Y_i^g}{Y_i^g \sigma_{Y_i}} \right]^2 + C_2 \sum_{i=1}^{K} \left| \frac{Y_i^m(f) - Y_i^g}{Y_i^g \sigma_{Y_i}} \right| + C_3 \sum_{j=1}^{L} \left| \frac{f_j - f_j^r}{f_j^r \sigma_{f_j}} \right| + C_4 \sum_{j=1}^{L} \left[\frac{f_j - f_j^r}{f_j^r \sigma_{f_j}} \right]^2 \quad \text{(A1)}$$

Each of the first two sums expresses the measurement compatibility condition: The health parameters under estimation must be such that the vector of measurements $\boldsymbol{Y}$ is reproduced as accurately as possible. The last two terms ensure that the values of health parameters cannot be significantly different from their reference, a fact resulting from experience. It is the addition of these terms that allows the estimation for $\boldsymbol{f}$ when a smaller number of measurements is available. All deltas are weighted by the inverse of the standard deviation of the corresponding quantity. Weight factors C_i are included for the possibility of changing the relative importance of the different terms. The reference values $\boldsymbol{f^r}$ of the health parameters can be chosen to represent a "best" guess of the values to be determined.

The formulation of this function encompasses different methods of solving the diagnostic problem including linear and nonlinear approaches, as reported by Mathioudakis et al. [14]. This is done primarily by examining the relation between the number K of available measurements and the number L of health parameters to be estimated. For $K \geq L$ by choosing nonzero C_1 or C_2 and $C_3 = C_4 = 0$, an exact solution for $\boldsymbol{f}$ can be derived. For $K < L$ either C_3 and/or C_4 would have to be nonzero and the derived solution for $\boldsymbol{f}$ would be as close as possible to the actual values.

Table 5 The considered fault cases

Fault Case	Affected component	Actual deviated health parameters
		ΔSW2=−0.7%, ΔSE2=−0.4%, ΔSW12=−1%,
A	FAN, LPC	ΔSE12=−0.5%
B	FAN	ΔSE12=−1%
C	HPC	ΔSW26=−1%, ΔSE26=−0.7%
D	HPC	ΔSE26=−1%
E	HPC	ΔSW26=−1%
F	HPT	ΔSW41=+1%
G	HPT	ΔSW41=−1%, ΔSE41=−1%
H	HPT	ΔSE41=−1%
I	LPT	ΔSE49=−1%
J	LPT	ΔSW49=−1%, ΔSE49=−0.4%
K	LPT	ΔSW49=−1%
L	LPT	ΔSW49=+1%, ΔSE49=−0.6%
M	NOZZLE	ΔA8IMP=+1%
N	NOZZLE	ΔA8IMP=−1%
O	NOZZLE	ΔA8IMP=+2%

Appendix B: Fault Cases and Noise Magnitude

A fault scenario comprised of 15 fault cases has been examined, covering possible faults in all individual components of the engine. This set of cases has been evaluated by several researches and diagnostic methods [13,14,17].

The considered fault cases are representative of those usually encountered in practice and are given in Table 5. The magnitude of the noise for operating point quantities and measurements is given in Refs. [14,17]. The noise levels were considered, according to the engine manufacturers, in terms of three times the standard deviation (3σ) of each measured quantity.

References

[1] Urban, L. A., 1972, "Gas Path Analysis Applied to Turbine Engine Condition Monitoring," AIAA/SAE Eighth Joint Propulsion Specialist Conference, AIAA Paper No. 72-1082.
[2] Doel, D., 1994, "An Assessment of Weighted-Least-Squares Based Gas Path Analysis," ASME J. Eng. Gas Turbines Power, **116**(2), pp. 366–373.
[3] Doel, D., 1994, "TEMPER—A Gas-Path Analysis Tool for Commercial Jet Engines," ASME J. Eng. Gas Turbines Power, **116**(1), pp. 82–89.
[4] Urban, L. A., and Volponi, A. J., 1992, "Mathematical Methods of Relative Engine Performance Diagnostics," SAE Technical Paper No. 922048.
[5] Doel, D., 2003, "Interpretation of Weighted Least Squares Gas Path Analysis Results," ASME J. Eng. Gas Turbines Power, **125**(3), pp. 624–633.
[6] Barwell, M. J., 1987, "COMPASS—Ground Based Engine Monitoring Program for General Applications," SAE Technical Paper No. 871734.
[7] Stamatis, A., Mathioudakis, K., and Papailiou, K. D., 1990, "Adaptive Simulation of Gas Turbine Performance," ASME J. Eng. Gas Turbines Power, **112**(2), pp. 168–175.
[8] Stamatis A., Mathioudakis K., M. Smith, and Papailiou K. D., 1990, "Gas Turbine Component Fault Identification by Means of Adaptive Performance Modelling," ASME Paper No. 90-GT-376.
[9] Tsalavoutas, A., Pothos, S., Mathioudakis, K., and Stamatis, A., 1999, "Monitoring of the Performance of a Twin Spool Ship Propulsion Turbine by Means of Adaptive Modelling," RTO Symposium on Gas Turbine Operation and Technology for Land, Sea and Air Propulsion and Power Systems, Ottawa, Canada, Oct. 18–21, Paper No. RTO-MP-34.
[10] Lee Y., and Singh R., 1996, "Health Monitoring of Turbine Engine Gas Path Components and Measurement Instruments," ASME Paper No. 96-GT-242.
[11] Groenstedt, T. V., 2001, "A Multi Point Gas Path Analysis Tool for Gas Turbine Engines With a Moderate Level of Instrumentation," XV ISABE, Bangalore, India, Sept. 3–7, Paper No. ISABE-2001-1139.
[12] Volponi A., 1994, "Sensor Error Compensation in Engine Performance Diagnostics," ASME Paper No. 94-GT-58.
[13] Dewallef P., Leonard O., and Mathioudakis K., 2004, "On-Line Aircraft Engine Diagnostic Using a Soft-Constrained Kalman Filter," ASME Paper No. GT2004-53539.
[14] Mathioudakis, K., Kamboukos, Ph., and Stamatis, A., 2004, "Gas Turbine Component Fault Detection From a Limited Number of Measurements," Proc. Inst. Mech. Eng., Part A, **218**, pp. 609–618.
[15] Zedda M., Singh R., 1999, "Gas Turbine Engine and Sensor Diagnostics," Paper No. ISABE 99-7238.
[16] Gulati, A., Taylor, D., and Singh, R., 2001, "Multiple Operating Point Analysis Using Genetic Algorithm Optimization for Gas Turbine Diagnostics," XV ISABE, Bangalore, India, Sept. 3–7, Paper No. ISABE 2001-1139.
[17] Aretakis, N., Mathioudakis, K., and Stamatis, A., 2003, "'Non-Linear Engine Component Fault Diagnosis From a Limited Number of Measurements Using a Combinatorial Approach," ASME J. Eng. Gas Turbines Power, **125**(3), pp. 642–650.
[18] Verma, R., and Ganguli, R., 2005, "Denoising Jet Engine Gas Path Measurements Using Nonlinear Filters," IEEE/ASME Trans. Mechatron., **10**(4), pp. 461–464.

[19] Ganguli, R., and Dan, B., 2004, "Trend Shift Detection in Jet Engine Gas Path Measurements Using Cascaded Recursive Median Filter With Gradient and Laplacian Edge Detector," ASME J. Eng. Gas Turbines Power, **126**(1), pp. 55–61.
[20] Ganguli, R., 2003, "Jet Engine Gas-Path Measurement Filtering Using Center Weighted Idempotent Median Filters," J. Propul. Power, **19**(5), pp. 930–937.
[21] Ganguli, R., 2002, "Data Rectification and Detection of Trend Shifts in Jet Engine Gas Path Measurements Using Median Filters and Fuzzy Logic," ASME J. Eng. Gas Turbines Power, **124**(4), pp. 809–816.
[22] Kamboukos, Ph., and Mathioudakis, K., 2005, "Comparison of Linear and Non-Linear Gas Turbine Performance Diagnostics," ASME J. Eng. Gas Turbines Power, **127**(1), pp. 49–56.
[23] Lapin, L., 1990, *Probability and Statistics for Modern Engineering*, 2nd ed., Duxbury, Belmont, CA, Chaps. 5 and 7.
[24] Romessis, C., Kamboukos, Ph., and Mathioudakis, K., 2007, "The Use of Probabilistic Reasoning to Improve Least Squares Based Gas Path Diagnostics," ASME J. Eng. Gas Turbines Power, **129**(4), pp. 970–976.
[25] Kyriazis A., Mathioudakis K., "Gas Turbine Fault Diagnosis Using Fuzzy-Based Decision Fusion," 18th ISABE, Beijing, China, Sept. 2–7, Paper No. ISABE 2007-1274.

Real-Time Transient Three Spool Turbofan Engine Simulation: A Hybrid Approach

Naveed U. Rahman
Research Student
e-mail: n.ur-rahman@cranfield.ac.uk

James F. Whidborne
CEng
MIET
e-mail: j.f.whidborne@cranfield.ac.uk

Dynamics, Simulation and Controls Group,
Cranfield University,
Bedfordshire, MK43 OAL, UK

This paper presents a transient three-spool turbofan engine simulation model that uses a combination of intercomponent volume and iterative techniques. The engine model runs in real time and has been implemented in MATLAB/SIMULINK environment. The main advantage of this hybrid approach is that it preserves the accuracy of the iterative method while maintaining the simplicity of the intercomponent volume method. The iterative approach is applied at each engine subsystem to solve algebraic thermodynamic equations for exit enthalpy, entropy, and temperature, whereas the intercomponent volume method is used to calculate pressures derivatives and hence pressures at corresponding engine stations. This allows the engine state vector to be updated at each pass through the engine calculations. This technique was applied as a test case on the Rolls Royce Trent 500 three-spool turbofan engine, and the results were compared with an iterative method. As the engine state vector is updated during each cycle, the model lends itself for easy integration into nonlinear aircraft simulations, real-time engine diagnostics/prognostics, and jet engine control applications. [DOI: 10.1115/1.3079611]

1 Introduction

Transient engine models that are fast and accurate are required in a variety of engineering applications. These include prediction of stall margins during engine acceleration, real-time fault diagnosis, or engine control system design. In addition, transient engine models may be used to study integrated aircraft/engine control concepts [1], in which the engine transients are directly linked with the performance of the flight control system.

Traditionally two methods have been used for simulation of engine transients, namely, (i) the constraint satisfying iterative method [2,3] and (ii) the intercomponent volume (ICV) method [4,5]. The later approach is less accurate but faster and can be conveniently used for applications such as nonlinear aircraft flight simulations, where advantages gained in speed may be traded off with accuracy. Zhou et al. [4] used the intercomponent volume approach to simulate the startup characteristics for a turbofan engine, whereas Rahman and Whidborne [5] used this approach to investigate the effect of engine bleed on its performance. However for a more accurate prediction of engine behavior, the iterative approach is generally preferred. In the iterative method an initial guess is made for certain engine parameters such as the compressor pressure ratios, nondimensional turbine flows, nozzle pressures, etc. and a single run through the engine calculations is made. The resulting errors in continuity of mass flow and energy balance are noted. The initial guess is then improved by use of numerical procedures such as the Newton–Raphson method [6]. This process is repeated until a certain minimum error condition is met. Both design and off-design operating conditions can be simulated in this way. The transient part may be modeled by associating a component volume with each of the compressor, turbine, or nozzle and calculating the mass and energy storage in these volumes. The difference between the compressor and turbine work done at any given time instant gives an estimate of rotor acceleration and hence rotor speed. The iterative approach toward engine modeling is adequately described by Sellers and Daniele [2] and Parker and Guo [3].

Following this introduction, Sec. 2 presents a basic layout of the three-spool turbofan used in this work and also details the engine model using the hybrid approach. Section 3 presents the results of design point (DP), off-design, and engine transients for the Rolls Royce Trent 500 turbofan engine and a comparison with an iterative technique such as that used by Sellers and Daniele [2]. Finally, Sec. 4 concludes the paper.

2 The Hybrid Engine Model

This work presents a hybrid approach toward engine modeling, in which the intercomponent volume method is used to calculate the mass flow accumulation inside each volume and the iterative approach is used to solve the thermodynamic algebraic equations associated with each engine component. The rate of change in mass flow in the volume is used to calculate pressure derivatives which are integrated to get pressures. With knowledge of instantaneous spool speeds in addition to these pressures, the compressor/turbine mass flows and efficiencies are calculated using static component maps. An iterative approach is then followed to calculate the exit enthalpy, entropy and temperatures at each engine station. A schematic for a three-spool turbofan engine is shown in Fig. 1 and following Ref. [7], various engine stations have been designated as follows:

(a) 1: inlet (entry)
(b) 2: inlet (exit)
(c) 2.1: low pressure compressor (LPC) outlet
(d) 2.2: intermediate pressure compressor (IPC) outlet
(e) 3: high pressure compressor (HPC) outlet
(f) 4: combustor outlet (CMB)
(g) 4.1: high pressure turbine (HPT) outlet
(h) 4.2: intermediate pressure turbine (IPT) outlet
(i) 5: low pressure turbine (LPT) outlet
(j) 9: nozzle (main outlet)
(k) 19: nozzle (bypass outlet)

The Rolls Royce Trent 500 engine generates approximately 275 kN of thrust under sea level static (SLS) conditions. With reference to Fig. 1, the entry point of the mass flow into the system is from the fan or low pressure (LP) compressor stage, w_{LP}, and the main burner fuel flow input, w_f. The mass flow exits from the three exhaust nozzles, these are the core exhaust nozzle mass flow, w_{core}, the bypass nozzle mass flow, w_{bypass}, and the bleed mass flow from the intermediate compressor to the wing

Manuscript received October 3, 2008; final manuscript received November 26, 2008; published online June 9, 2009. Review conducted by Allan Volponi.

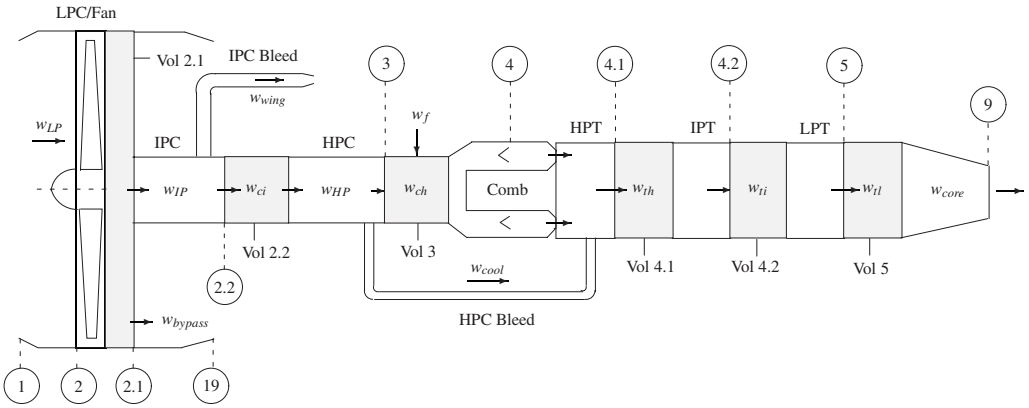

Fig. 1 Three-spool turbofan schematic

duct, w_{wing}. To simulate the three-spool turbofan, the following choice of state vector, X, and control vector, u, was made:

$$X = [P_{2.1}, P_{2.2}, P_3, P_{4.1}, P_{4.2}, P_5, N_L, N_I, N_H]$$

$$u = [w_f]$$

where P_i are the total pressures at the ith station, N_L, N_I, and N_H are the physical shaft speeds of the low pressure, intermediate pressure (IP), and high pressure (HP) rotors, respectively, and w_f is the main burner fuel flow rate. The three-spool engine was simulated by calculation of the state derivatives, $\dot{X}$. The state derivatives for pressures and the three-spool speeds will therefore be discussed next.

2.1 Calculation of Pressure Derivatives: $\dot{P}_i$. When the engine is running in a steady state condition, the net mass flow into the system equals the net mass flow out of the system. However, as the engine accelerates or decelerates, a transient state occurs and there will be accumulation or depletion of mass at various stages inside the engine. From the gas law, the rate of change of mass is proportional to rate of change of pressure and temperature

$$\dot{P} = \frac{R}{V}(T\dot{m} + m\dot{T}) \tag{1}$$

The above equation has two derivatives, the terms $\dot{m}T$ and $m\dot{T}$. Fawke [8] showed that the temperature derivative can be neglected in comparison to the mass derivative term. To calculate the pressure derivatives, the mass flow errors inside the control volumes are required. These have been obtained as follows.

2.1.1 Mass Flow Error at LPC/Fan Exit: $\dot{m}_{2.1}$. With reference to Fig. 2, an intercomponent volume, $V_{2.1}$, is placed at the fan exit and the entry of the intermediate compressor and the bypass duct. The mass flow, w_{cl}, entering into this volume is from the low pressure compressor, which is a function of LP corrected shaft speed, $N_L{}^*$, and fan pressure ratio, $(P_{2.1}/P_2)$. With the assumption of zero bleed from the LP stage we have

$$w_{\text{LP}} = w_{cl} = f\left(\frac{P_{2.1}}{P_2}, N_L{}^*\right) \tag{2}$$

The mass flow exiting from the control volume, $V_{2.1}$, goes into the intermediate pressure compressor and the bypass nozzle. The mass flow ingested by the intermediate compressor is a function of the intermediate compressor pressure ratio $(P_{2.2}/P_{2.1})$ and the IP corrected shaft speed $N_I{}^*$. A certain percentage of IP compressor mass flow, ϕ_{IP}, may be drawn for flow control or turbine cooling purposes and the reduced mass flow exiting the IP compressor is termed w_{ci}. The mass flow ingested by the IP compressor in terms of percentage bleed and exiting mass flow is given as

$$w_{\text{IP}} = \frac{w_{ci}}{1 - \phi_{\text{IP}}} = f\left(\frac{P_{2.2}}{P_{2.1}}, N_I^*\right) \tag{3}$$

The bypass nozzle mass flow is a function of the bypass nozzle pressure ratio, $(P_{2.1}/P_a)$, and the bypass nozzle area, A_{19}, besides some other gas parameters

$$w_{\text{bypass}} = \frac{A_{19}P_{2.1}}{R}\left(\frac{P_{2.1}}{P_a}\right)^{-1/\gamma}\sqrt{\frac{2g_c c_p}{T_{2.1}}\left(1 - \left(\frac{P_{2.1}}{P_a}\right)^{-R/c_p}\right)} \tag{4}$$

The mass flow error inside the control volume is therefore

$$\dot{m}_{2.1} = w_{cl} - w_{\text{IP}} - w_{\text{bypass}} \tag{5}$$

In the current analysis, it is assumed that there is no bleed taken from the LP compressor stage. In practice however, there might be some bleed off-take from this stage to maintain cabin pressure and the supply of fresh air for the crew and passengers.

2.1.2 Mass Flow Error at IPC Exit: $\dot{m}_{2.2}$. With reference to Fig. 3, an intercomponent volume, $V_{2.2}$, was placed between IP compressor exit and the high pressure compressor entry. The mass flow entering this volume is the reduced mass flow after bleed extraction from the IP stage and is referenced as w_{ci}. The mass flow, w_{HP}, exiting from this volume is that ingested by the HP compressor. A certain percentage, ϕ_{HP}, of this HP mass flow is bled for turbine cooling purposes, and the net mass flow exiting from the HP stage is w_{ch}. Thus

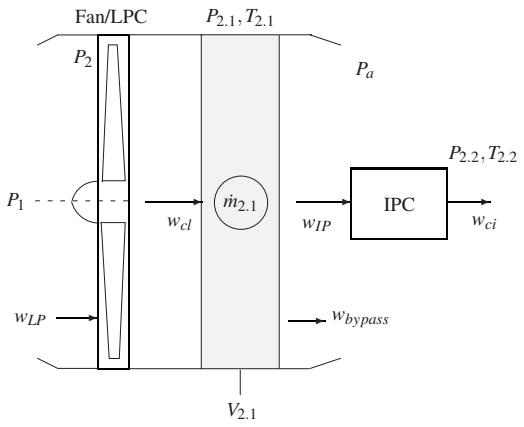

Fig. 2 Intercomponent volume ($V_{2.1}$) between fan and IPC/bypass nozzle

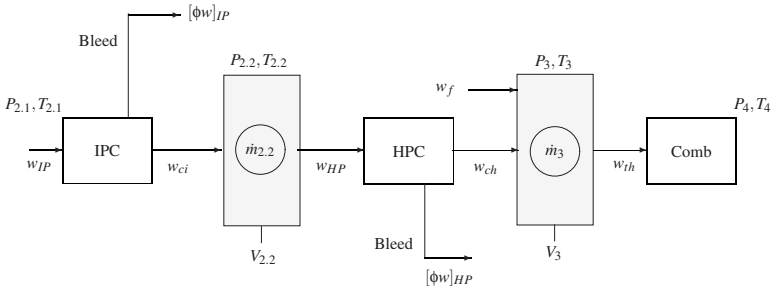

Fig. 3 Intercomponent volumes, $V_{2.2}$ and V_3

$$w_{\mathrm{HP}} = \frac{w_{ch}}{1-\phi_{\mathrm{HP}}} = f\left(\frac{P_3}{P_{2.2}}, N_H^*\right) \tag{6}$$

where the HP mass flow itself is a function of HP pressure ratio, $(P_3/P_{2.2})$, and HP corrected shaft speed, N_H^*. The mass flow accumulating inside the control volume is therefore

$$\dot{m}_{2.2} = w_{ci} - w_{\mathrm{HP}} \tag{7}$$

2.1.3 Mass Flow Error at HPC Exit: $\dot{m}_3$. The intercomponent volume, V_3, was placed at the HP compressor exit and combustor entry. The mass flows entering this volume are the main burner fuel flow, w_f, and the mass flow exiting from the HP stage, w_{ch}. The mass flow, w_{th}, exiting from this volume is that extracted by the HP turbine. Thus the mass flow accumulated inside this volume is

$$\dot{m}_3 = w_{ch} + w_f - w_{th} \tag{8}$$

The HP turbine mass flow, w_{th} is a function of HP turbine pressure ratio, $(P_4/P_{4.1})$, and HP corrected shaft speed, N_H^* and is obtained from a turbine map. Thus

$$w_{th} = f\left(\frac{P_4}{P_{4.1}}, N_H^*\right) \tag{9}$$

It should be noted that since a fixed percentage of total pressure loss is assumed inside the combustor, therefore the pressure derivative at HP turbine entry, $\dot{P}_4$, is the same as combustor entry, $\dot{P}_3$, and no intercomponent volume is required to calculate P_4.

2.1.4 Mass Flow Errors at HPT, IPT, and LPT Exit: $\dot{m}_{4.1}$, $\dot{m}_{4.2}$, and $\dot{m}_5$. As in Fig. 4, the intercomponent volume, $V_{4.1}$, accepts mass flows from the HP turbine and also the cooling mass flow, $[\phi w]_{\mathrm{HP}}$, from the HP compressor stage. The mass flow, w_{ti}, exiting from volume $V_{4.1}$ is that ingested by the IP turbine stage and is a function of IP turbine pressure ratio $(P_{4.1}/P_{4.2})$ and the IP corrected shaft speed, N_I^*.

$$w_{ti} = f\left(\frac{P_{4.1}}{P_{4.2}}, N_I^*\right) \tag{10}$$

With reference to Fig. 4, the accumulated mass at the HP, IP, and LP turbine exits are

$$\dot{m}_{4.1} = w_{th} + [\phi w]_{\mathrm{HP}} - w_{ti} \tag{11}$$

$$\dot{m}_{4.2} = w_{ti} - w_{tl} \tag{12}$$

$$\dot{m}_5 = w_{tl} - w_{\mathrm{core}} \tag{13}$$

The mass flow, w_{tl}, ingested by the LP turbine stage is a function of LP turbine pressure ratio, $(P_{4.1}/P_{4.2})$, and LP corrected shaft speed, N_L^*, and is obtained from the LP turbine map

$$w_{tl} = f\left(\frac{P_{4.2}}{P_5}, N_L^*\right) \tag{14}$$

and the mass flow through the convergent core nozzle is

$$w_{\mathrm{core}} = \frac{A_9 P_5}{R}\left(\frac{P_5}{P_a}\right)^{-1/\gamma}\sqrt{\frac{2g_c c_p}{T_5}\left(1-\left(\frac{P_5}{P_a}\right)^{-R/c_p}\right)} \tag{15}$$

This completes the calculation of the mass flow errors inside the control volumes. The pressure derivatives can now conveniently be obtained using Eq. (1). As an example, for the intercomponent

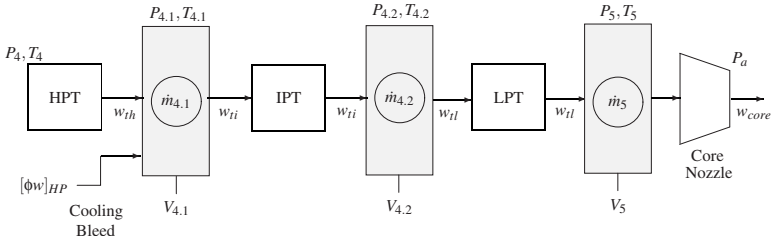

Fig. 4 Intercomponent turbine volumes ($V_{4.1}$, $V_{4.2}$, V_5)

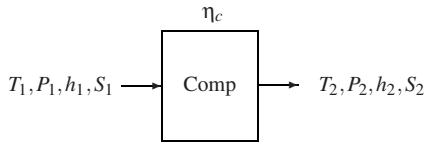

Fig. 5 Thermodynamic conditions for the compressor

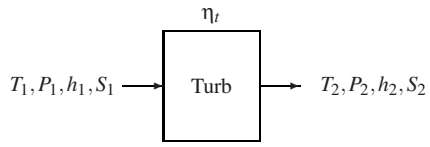

Fig. 7 Thermodynamic conditions for the turbine

volume, V_5, associated with LP turbine and the convergent nozzle, the pressure derivative is

$$\frac{dP_5}{dt} = \frac{RT_5}{V_5}\dot{m}_5 = \frac{RT_5}{V_5}(w_{tl} - w_{\text{core}}) \tag{16}$$

Similarly pressure derivatives related to the remaining intercomponent volumes can be obtained. If the initial pressures are known, then from the knowledge of the initial state vector, X_0, the subsequent time history of P_i can be obtained by convenient numerical integration methods.

2.2 Calculation of Speed Derivatives: $\dot{N}$. The remaining derivatives of the state vector, i.e., the rotational acceleration derivatives $\dot{N}_L$, $\dot{N}_I$, and $\dot{N}_H$ can be calculated by estimating the difference in torque generated by the turbine and that required by the compressor

$$\dot{N} = \frac{dN}{dt} = \frac{(\eta_m \tau_{\text{turb}} - \tau_{\text{comp}})}{I_s} \tag{17}$$

The turbine torque, τ_{turb}, or the compressor torque, τ_{comp}, can be expressed in terms of turbine and compressor work and physical spool speeds. The work term can be further expressed as a function of enthalpy change and mass flow rate through a particular engine component. For example, across the LP compressor, the torque was calculated as

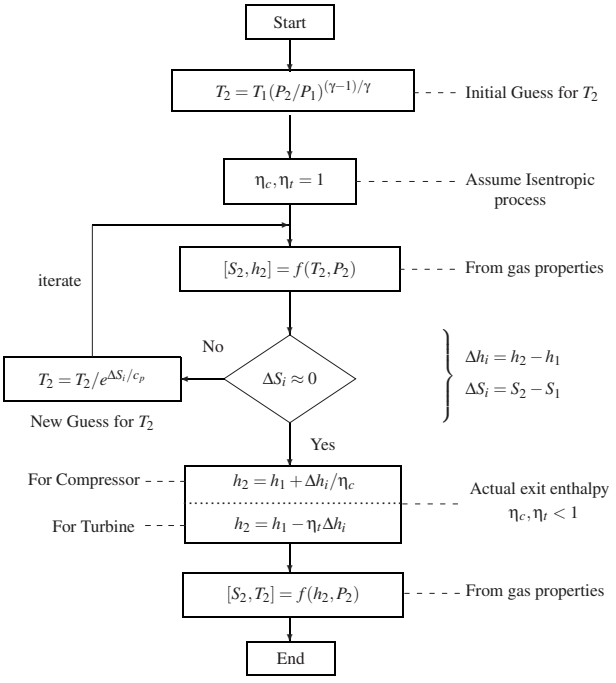

Fig. 6 Iterative solution for compressor/turbine thermodynamics

$$\tau_{\text{LPC}} = \frac{60}{2\pi N_L} w_{\text{LP}}(h_{2.1} - h_2) \tag{18}$$

The torques for the other stages were calculated in a similar fashion. For the calculation of speed derivatives it now remains to calculate the enthalpy change across each of the compressor or the turbine stages. This requires an iterative solution of algebraic thermodynamic equations and will be briefly discussed next.

2.3 Iterative Solution of Compressor Thermodynamics. Figure 5, shows a compressor stage with input conditions $[T_1, P_1, h_1, S_1]$ and exit conditions $[T_2, P_2, h_2, S_2]$. The intercomponent volume approach provides the pressure derivative and hence pressure at the compressor exit stage, therefore the exit pressure P_2 is known. From a knowledge of current spool speed, N, and the compressor pressure ratio, compressor efficiency, η_c, and mass flow, w_c, can be calculated from component maps. It is now desired to calculate exit temperature, T_2, specific enthalpy, h_2, and entropy, S_2, for the compressor stage. Figure 6 shows the iterative process that was used to solve the thermodynamic algebraic loop. The steps involved are as follows.

1. An initial guess for the exit temperature, T_2, is made using an estimate for compressor exit temperature from Cohen et al. [9].
2. Assuming the process to be isentropic ($\eta_c = 1$), the isentropic exit enthalpy, h_2, and entropy, S_2, are calculated using thermodynamic properties of air.
3. The difference in entropy, ΔS_i, is noted and a new guess for T_2 is made using the Gibbs equation [10] for a calorically perfect gas.
4. The process is repeated until an exit temperature, T_2, is found for which the process is isentropic, i.e., $\Delta S_i \approx 0$.
5. The isentropic rise in enthalpy, Δh_i is divided by the compressor efficiency to get the actual change in enthalpy across the compressor stage.
6. Once the exit enthalpy is known, the corresponding exit temperature, T_2, is obtained iteratively by solving the equation $h = c_p(T)T$. Exit entropy, S_2, is then obtained as function of temperature from gas tables.

2.4 Iterative Solution of Turbine Thermodynamics. Figure 7 outlines a corresponding turbine stage. The turbine exit pressure, P_2, and therefore pressure ratio is known from the mass flow accumulation in the component volumes, hence the turbine efficiency, η_t, and mass flow, w_t, can be calculated from turbine maps. Since the turbine extracts energy from the flow, there is a drop in pressure and temperature across the turbine stage. The turbine exit parameters, T_2, h_2, and S_2, can be calculated using a similar approach, as described for the compressor in Fig. 6, except in this case the turbine pressure ratio, (P_2/P_1), is less than 1.0, whereas for the compressor stage the converse is true. With the assumption that the turbine process is isentropic, the turbine exit enthalpy, h_2, is calculated iteratively. The isentropic process assumption implies that the drop in enthalpy would be higher, i.e., the turbine would be able to extract more work from the flow. This isentropic drop in enthalpy, Δh_i, is multiplied by the turbine efficiency to get the actual drop in enthalpy across the turbine stage. Once the exit enthalpy is known, the corresponding exit temperature, T_2, is obtained by iteratively solving the equation h

Table 1 Rolls Trent 500 design point parameter validation

Station	ID	Mass flow (kg/s)	Pressures (atm)			% error	Temperatures (K)			% error
		DYNGEN	DYNGEN	Hybrid	ICV	ICV	DYNGEN	Hybrid	ICV	ICV
1	Entry	902.55	1.000	1.000	1.000	0.00	288.15	288.15	288.15	0.00
2	Inlet	902.55	0.990	0.990	0.990	0.00	288.15	288.15	288.15	0.00
2.1	LPC	902.55	1.504	1.504	1.482	−1.46	330.55	330.49	328.75	−0.05
2.2	IPC	120.65	8.730	8.692	8.591	−1.59	580.67	579.78	578.09	−0.04
3	HPC	120.29	39.02	38.96	38.18	−2.15	913.63	913.14	909.30	−0.04
4	Comb.	123.29	36.68	36.62	35.89	−2.15	1632.5	1632.3	1642.9	+0.06
4.1	HPT	123.29	14.23	14.15	13.74	−3.44	1352.0	1351.5	1337.2	−0.11
4.2	IPT	123.29	6.560	6.531	6.253	−4.67	1148.3	1148.5	1114.4	−2.95
5	LPT	123.29	2.005	1.992	1.895	−5.80	885.75	885.96	838.94	−5.20

$=c_p(T)T$ for the current value of the fuel to air ratio. The exit entropy, S_2, is then obtained as for the compressor.

3 Simulation Results

The hybrid approach presented above was validated on the three-spool Rolls Royce Trent 500 turbofan engine using MATLAB/SIMULINK. Engine manufacturers usually keep the engine parameters proprietary, and it is difficult to obtain real engine data. However, given the design point or nominal operating conditions, the DYNGEN program by Sellers and Daniele [2] was used to automatically generate representative compressor and turbine maps for the Trent 500.

3.1 Design Point Validation. The engine model was initialized from X_0 and was allowed to reach a steady state with the fuel set to a design point value of 2.6399 kg/s. Table 1 presents the resulting design point engine parameters at different engine stations. Three sets of data are presented for comparison purposes. These are the following.

1. The design point iterative solution from DYNGEN, which will be taken as reference.
2. The hybrid solution using intercomponent volume method for pressures and the iterative method for subsystem thermodynamic parameters.
3. The third approach also uses the ICV method for pressures, but the temperature increase across the compressor and the temperature decrease across the turbine are calculated using the following standard relationships from Walsh and Fletcher [11], (SLS conditions are assumed):

$$\Delta T_c = \frac{1}{\eta_c} T_1 \left(\left(\frac{P_2}{P_1} \right)^{(\gamma-1)/\gamma} - 1 \right) \tag{19}$$

$$\Delta T_t = \eta_t T_1 \left(1 - \left(\frac{P_2}{P_1} \right)^{(\gamma-1)/\gamma} \right) \tag{20}$$

Table 1 shows that there is a good match between the iterative and hybrid approach, whereas the pure ICV approach, which uses Eqs. (19) and (20), shows significant errors in the pressure and temperatures. Figure 8 illustrates these errors as a percentage of the reference iterative method values. Most of the errors in the hybrid approach are less than 0.5% and can be attributed to the fact that the component maps are represented by only ten discrete points per line, and linear interpolation is used for curves that are adequately represented by second or higher order polynomials.

Besides temperatures and pressures, the net thrust generated by the hybrid method at the design point fuel setting is 278.2 kN in contrast to 264.6 kN from the ICV method. The reference thrust from the iterative code (DYNGEN) was 278.6 kN.

3.2 Transient Simulation. The transient on the three-spool turbofan was simulated by a sudden reduction in fuel flow from 2.6399 kg/s (design point) to a fuel flow value of 2.0 kg/s. A fuel flow rate of −5.0 kg/s was assumed, so that it takes approximately 0.2 s to reach the new fuel setting. The response of the hybrid approach was compared with that of the iterative method. Figures 9–11 show the transient response on the compressor maps.

3.2.1 Transients on the Compressor Maps. Figure 9 shows the LP compressor or fan map with corrected mass flow on the x-axis and fan pressure ratio on the y-axis. The design point is indicated by DP. When the fuel flow is suddenly reduced to 2.0 kg/s from its initial design point value, the LP compressor slows down to its new steady state value on the running line. Two transient response plots are shown, Path DP to A is the response obtained with the hybrid approach and the Path DP to B with the iterative approach

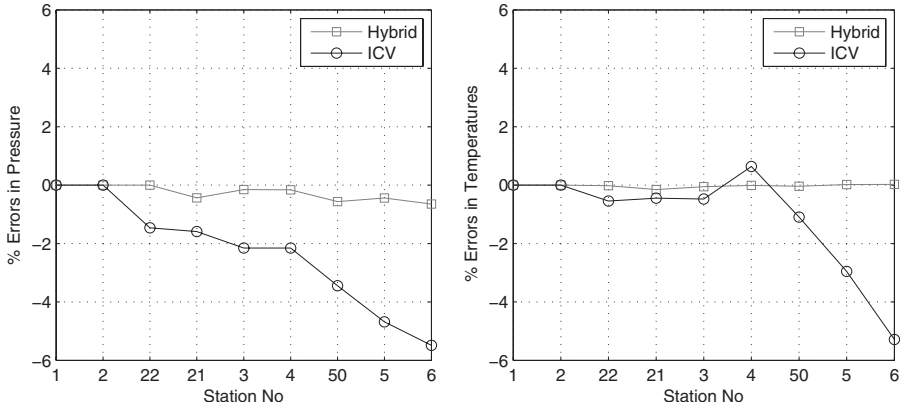

Fig. 8 Percentage errors in pressures and temperatures at design point

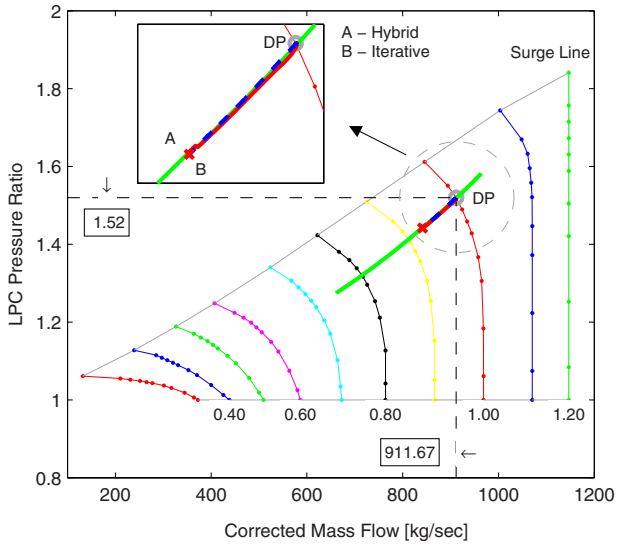

Fig. 9 Transient on LPC/fan map—step reduction in fuel

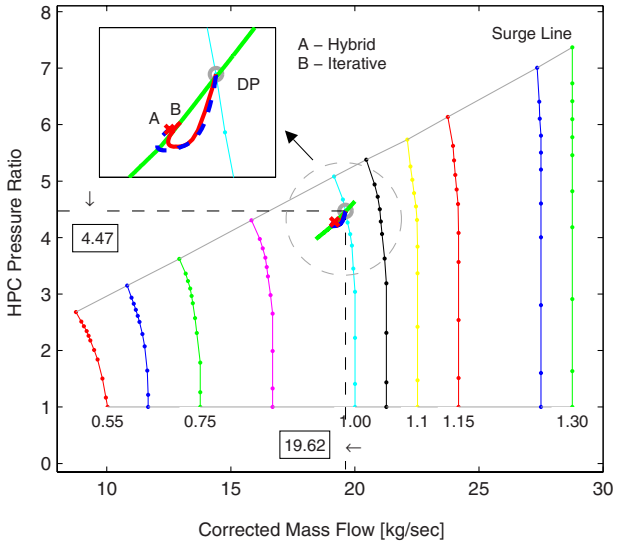

Fig. 11 Transient on HPC map—step reduction in fuel

(DYNGEN). Both paths are almost identical indicating a good transient and steady state match between the two approaches. It may be noted that although a substantial step in fuel flow was initiated, the transient response of the LP compressor remains almost entirely on the steady running line.

Figure 10 shows the locus of the transient on the IP compressor map. During the transient the operating point moves up toward the surge line and then settles down on the running line corresponding to the new fuel setting. The hybrid and the iterative methods give consistent behavior during the transient and on the new steady state point.

Figure 11 shows the HP compressor map. As the fuel flow is reduced, the operating point on the HP compressor moves away from the surge line and takes a curved path before settling down on the steady running line of the HP compressor. Here again, the transient response is quite consistent between the two methods, however the steady state operating point of the hybrid method (point *A*) is marginally offset from that of iterative method (point *B*). The reason for this offset is attributed to the fact that the turbine maps of the iterative method use enthalpy work function

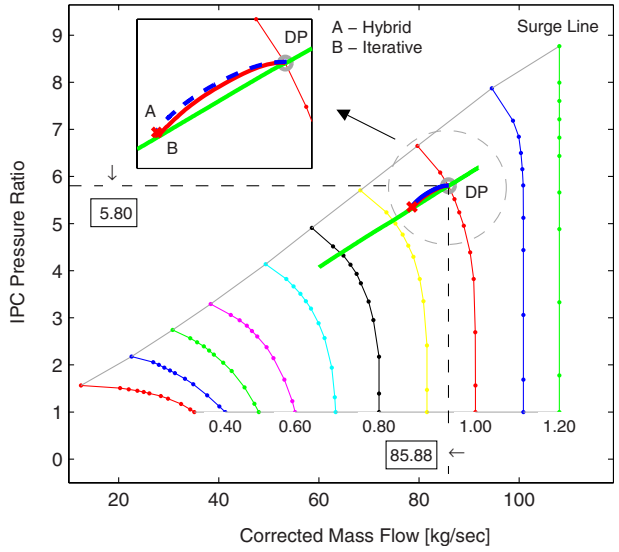

Fig. 10 Transient on IPC map—step reduction in fuel

$(\Delta h/T)$ as function of turbine corrected speed and turbine flow.

The hybrid method however uses turbine pressure ratio as function corrected speed and turbine flow. The enthalpy work function turbine maps were converted to turbine pressure ratio maps using this relationship from Seldner and Mihaloew [12]

$$\frac{P_2}{P_1} = \left(1 - \frac{1}{\eta_t c_p}\left(\frac{\Delta h}{T_1}\right)\right) \tag{21}$$

For the map conversion process, the design point turbine entry temperatures were used. The matching of design point or the starting point of the transient is therefore very accurate, however for off-design conditions the operating point on the corresponding compressor maps settles down at a slightly offset location from that of the iterative method. This effect is pronounced for the high temperature stages and is almost negligible for the LP stages.

3.2.2 Pressure Derivatives. Figure 12 shows the transient response of the pressure derivatives evaluated in Sec. 2. The plot shows six pressure derivatives from the compressor to the turbine stages. Larger pressure changes are observed in the HP stages and vice versa. The transient response of the pressure derivatives from the hybrid and the iterative techniques show a good match. It may be mentioned here that the simulation step size chosen for the hybrid approach was 5 ms, whereas that of the iterative approach was set at 25 ms. The iterative method showed convergence problems below this time step and hence is limited in capturing very fast changes in pressure. All the pressure derivatives show consistent results with both approaches.

3.2.3 Pressures, Temperatures, and Thrust. The integration of the pressure derivatives in Fig. 12 yields the pressure at each engine station. An iterative technique was then applied to solve the thermodynamic algebraic equations and to find out, respectively, the temperatures and enthalpies for each of the compressor and turbine exits. Figure 13 shows the temperature and pressure plots during the transients. Results from both the hybrid and iterative approaches are plotted and are in good agreement. The thrust plots are also shown in Fig. 13. Both the bypass and the core thrust from the hybrid and iterative approaches are consistent at the design point, during the transient and at the off-design point.

4 Conclusions

A three-spool turbofan engine was simulated by use of a hybrid approach, that uses a combination of intercomponent volumes and iterative techniques to represent steady state and transient engine

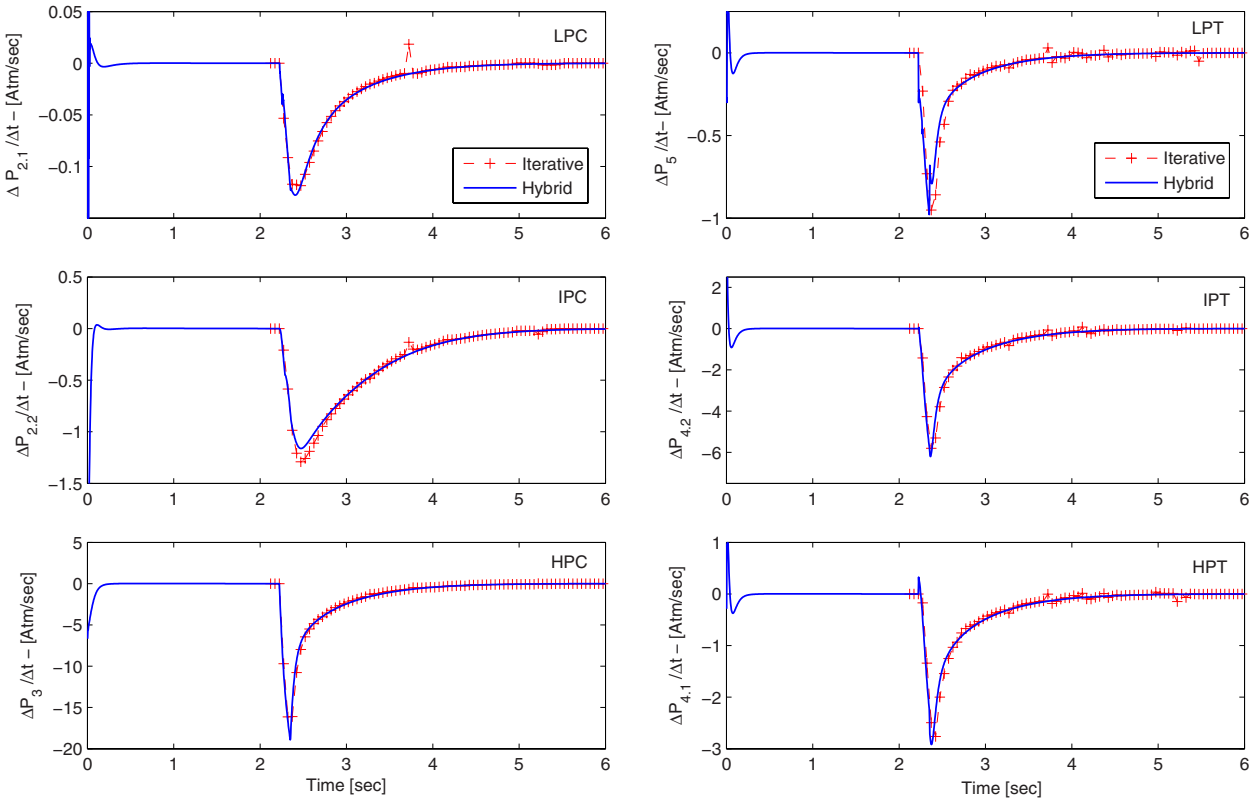

Fig. 12 Pressure derivatives—step reduction in fuel

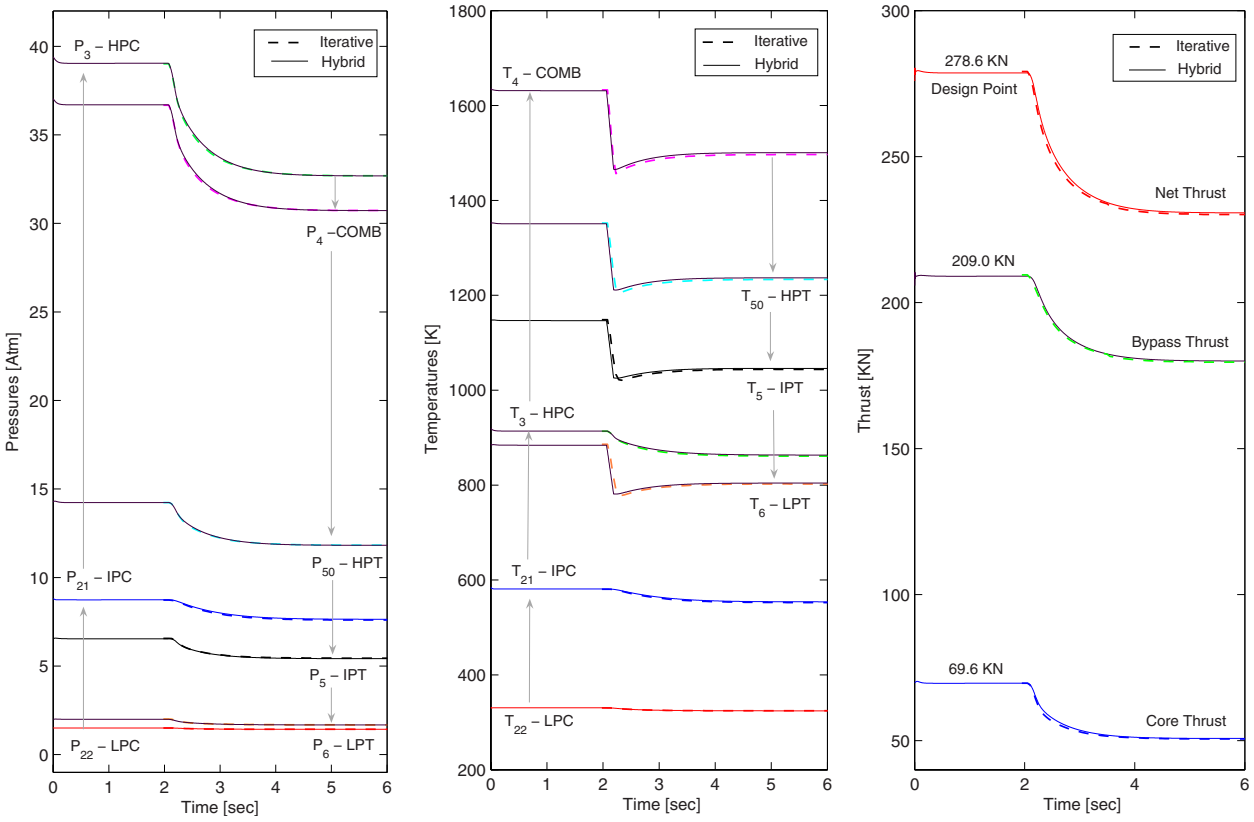

Fig. 13 Pressures, temperatures, and thrust—step reduction in fuel

thermodynamics. After an initial theoretical framework for the hybrid engine model, design point and transient simulations were performed. The design point calculations were compared using three approaches: (i) a purely iterative technique such as DYNGEN, (ii) a hybrid technique, which uses the ICV technique for pressures and an iterative process for enthalpies and temperature, and (iii) an ICV technique with an assumption of fixed values of gas constants and simplified expressions for temperature change across the component stage. The design point calculations revealed the results of the hybrid approach following closely that of the iterative method. The noniterative technique showed increasing errors across the HP stages. The transient results of the hybrid method were also in close agreement with those of the hybrid method. Limitations of the intercomponent volume method imposes careful selection of component volumes and simulation step times. Larger component volumes than actual will allow larger simulation time step with a corresponding reduction in peak value of pressure derivatives. The steady state however will not be affected. To summarize, the method presented in this work runs faster when compared with a purely iterative approach, has comparable accuracy and is convenient to implement and integrate with other programs such as nonlinear aircraft flight simulations and real-time engine diagnostics/prognostics applications.

Nomenclature

A_9 = main nozzle exit area
A_{19} = bypass nozzle exit area
c_p = specific heat at constant pressure
g_c = prop. constant, $g_c=1$ in SI units
h_i = specific enthalpy at ith station
I_s = spool inertia
Δh = specific enthalpy change
$\dot{m}_i$ = mass storage rate at ith volume
N = shaft rotational speed in rpm
N_L^* = corrected LP compressor speed
N_I^* = corrected IP compressor speed
N_H^* = corrected HP compressor speed
N_t^* = corrected turbine speed
P_a = ambient pressure
P_i = total pressure at ith station
R = gas constant
S_i = entropy at ith station
T_i = total temperature at ith station
ΔT = temperature change
w_f = mass flow of fuel
w_{cl} = LP compressor exit mass flow
w_{ci} = IP compressor exit mass flow
w_{ch} = HP compressor exit mass flow
w_{tl} = LP turbine entry mass flow
w_{ti} = IP turbine entry mass flow
w_{th} = HP turbine entry mass flow
w_{core} = main nozzle exit mass flow
w_{wing} = wing nozzle exit mass flow
w_{bypass} = bypass nozzle exit mass flow
u = control vector
V = intercomponent volume
X = state vector
η_c = compressor isentropic efficiency
η_m = mechanical transmission efficiency
η_t = turbine isentropic efficiency
ϕ = bleed fraction from compressor mass flow
γ = ratio of specific heats
τ_{turb} = torque generated by the turbine
τ_{comp} = torque required by the compressor

References

[1] Gill, K., Wilde, P., Gueroult, R., and Crowther, W. J., 2007, "Development of an Integrated Propulsion and Pneumatic Power Supply System for Flapless UAVs," AIAA Aviation Technology, Integration and Operations Conference, Belfast, UK, Sept. 18–20, Paper No. AIAA 2007-7726.
[2] Sellers, J. F., and Daniele, C. J., 1975, "DYNGEN—A Program for Calculating Steady State and Transient Performance of Turbojet and Turbofan Engines," NASA Technical Report No. NASA TN D-7901.
[3] Parker, K., and Guo, T. H., 2003, "Development of Turbofan Engine Simulation in a Graphical Simulation Environment," NASA Technical Report No. NASA TM 2003-212543.
[4] Zhou, W. X., Huang, J. Q., and Duo, J. P., 2006, "Development of Component Level Model for a Turbofan Engine," Journal of Aerospace Power, **21**(2), pp. 248–253.
[5] Rahman, N.U., and Whidborne, J. F., 2008, "A Numerical Investigation Into the Effect of Engine Bleed on Performance of a Single-Spool Turbojet Engine," J. Aerosp. Eng., Part G, **222**, pp. 939–949.
[6] Whittaker, E. T., and Robinson, G., 1967, *The Calculus of Observations: A Treatise on Numerical Mathematics*, 4th ed., Dover, New York, pp. 84–87.
[7] SAE, 2004, "Aircraft Propulsion System Performance Station Designation and Nomenclature," SAE Paper No. AS755D.
[8] Fawke, A. J., 1970, "Digital Computer Simulation of Gas Turbine Dynamic Behavior," Ph.D. thesis, University of Bristol, Bristol.
[9] Cohen, H., Rogers, G. F. C., and Saravanamuttoo, H. I. H., 1996, *Gas Turbine Theory*, Addison-Wesley Longman, Harlow, Essex, UK.
[10] Mattingly, J. D., 1996, *Elements of Gas Turbine Propulsion*, McGraw-Hill, New York.
[11] Walsh, P. P., and Fletcher, P., 1999, *Gas Turbine Performance*, Blackwell Science, Oxford.
[12] Seldner, K., and Mihaloew, R. J., 1972, "Generalized Simulation Technique for Turbojet Engine System Analysis," NASA Technical Report No. NASA TN-D 6610.

Maria Cristina Cameretti
Renzo Piazzesi
Fabrizio Reale
Raffaele Tuccillo

Dipartimento di Ingegneria Meccanica per l'Energetica (D.I.M.E.),
Università di Napoli Federico II,
Via Claudio 21,
Napoli 80125, Italy

Combustion Simulation of an Exhaust Gas Recirculation Operated Micro-gas Turbine

Following their recent experiences in the search of methods for reducing the nitric oxide emissions from a micro-gas turbine, the authors discuss in this paper the results of the combustion simulation under different conditions induced by the activation of an exhaust recirculation system. The theoretical approach starts with a matching analysis of the exhaust gas recirculation equipped microturbine, and then proceeds with the computational fluid dynamics analysis of the combustor. Different combustion models are compared in order to validate the method for NO_x reduction by the point of view of a correct development of the chemically reacting process. [DOI: 10.1115/1.3078193]

1 Introduction

In recent papers [1,2], the authors have presented a refined methodology aiming to find the best compromise between the need to reduce the NO_x emission from a micro-gas turbine (MGT) and the preservation of satisfactory efficiency and energy saving levels. The method is found on an integrated approach consisting of both the component matching analysis and the computational fluid dynamics (CFD) based validation of the most interesting cases. The latter refers to the activation of the exhaust recirculation at the compressor inlet (exhaust gas recirculation (EGR)), in order to generate conditions close to those characterized by a Moderate and Intense Low oxygen Dilution (MILD) or "flameless" combustion [3–7] because of the addition of inert species to the oxidant and of the increased fuel/oxygen equivalence ratio.

The current technical literature suggests that this combustion regime is able to produce an effective control of the thermal mechanism of the nitric monoxide formation because of the simultaneous occurrence of a temperature peak cutoff and of an oxygen defect in the oxidizing species. The achievement of such conditions can be obtained either by an internal flue gas recirculation within the combustor [4,6–10], or by an external EGR system [1–3], like the one recalled in this paper.

The requirement of a high reactant temperature is met by a recuperated microturbine. The need to comply with the conflicting goals of reduced environmental impact and high energetic performance is fulfilled through the optimal choice of the EGR ratio and recuperator by-pass ratio [1,11]. Both parameters have been determined within an extended range of electrical and thermal demands of a cogenerating micro-gas turbine.

This paper deals with the main problems that have been left open by the previous authors' works, such as the following.

- Special care must be paid to the identification of the mechanisms of self-ignition and pollutant formation at different load levels.
- A more accurate description of the combustion development is needed when the combustor operates under conditions close to the flameless regime with a reduced oxygen/fuel ratio.
- The carbon monoxide control, since the *EGR* induced conditions enhance the typical trade-off between the increase of this pollutant and the thermal nitric oxide (NO) reduction.

Based on the above items, the authors' work is therefore specifically addressed to a refined CFD based simulation of the combustion process under both conventional and modified conditions for the reactant quality. To this purpose, the combustion development is approached by both classical methods, such as the finite rate-eddy dissipation (FRED) model, and the more updated mechanisms based on the "flamelet" hypothesis [12,13]. The latter approach also incorporates refined oxidation mechanisms, so leading to a more detailed description of the early phases of the fuel ignition.

In this way the most interesting cases suggested by the cycle analysis for an efficient NO_x reduction can receive a definite answer about the actual possibility of producing a reliable combustion process within the existing lean-premixed combustion chamber of the microturbine.

2 The EGR Operated Micro-gas Turbine

2.1 Operating Characteristics of the Micro-gas Turbine. The previously referenced authors' papers [1,2] provide an exhaustive discussion of the performance and emission levels of the micro-gas turbine, whose main specifications are given in Table 1.

The related plant layout in Fig. 1 includes the recuperator by-pass system, which was introduced in order to allow the cogenerating system to meet variable thermal and mechanical requirements [11,14]. In this sense, the system response is governed by the by-pass ratio

$$X_b = 1 - \frac{\dot{m}_{g,R}}{\dot{m}_g} \tag{1}$$

where $X_b=0$ corresponds to a fully recuperated cycle, while $X_b > 0$ increases the amount of recoverable thermal output.

On the other hand both the part-load operation and the activation of the recuperator by-pass induce unfavorable conditions for the combustion, since an increased fuel flow rate through the pilot diffusive line of the lean-premixed combustor is needed [15–17]. This results in increased temperature peaks and, consequently, in an acceleration of the nitric oxide formation mechanisms. The plant simulation under variable mechanical load or by-pass ratio, clearly indicate the possible increase in thermal NO concentration in the exhaust (Figs. 2 and 3), here and after estimated as mole fraction on a dry basis.

In particular, Fig. 2 highlights that a variable speed operation, although ensure higher efficiencies at reduced mechanical outputs,

Contributed by the International Gas Turbine Institute of ASME for publication in the JOURNAL OF ENGINEERING FOR GAS TURBINES AND POWER. Manuscript received July 27, 2008; final manuscript received September 10, 2008; published online May 26, 2009. Review conducted by Dilip R. Ballal. Paper presented at the ASME Turbo Expo 2008: Land, Sea and Air (GT2008), Berlin, Germany, June 9–13, 2008.

Table 1 Base features of the MGT

MGT specifications	
Mech. arrangement	Single shaft
Pressure ratio	3.9
Compressor exit temp.	468 K
Combustor inlet temp. (fully regenerative cycle)	905 K
Turbine inlet temp.	1223 K
Turbine exit temp.	951 K
Recuperator exit temp. (fully regenerative cycle)	530 K
Rated mechanical output	110 kW
Nominal speed	64,000 rpm
Compressor, turbine	Radial flow

would lead to higher NO production. Actually, a reduction in the shaft speed also decreases the pressure ratio and, therefore the combustor inlet temperature. As stated before, such a situation implies an enhanced intensity of the pilot flame in the combustor. Similarly, the recuperator by-pass technique also affects the temperature level of the air entering the combustion chamber. A same mechanical output as the one with a fully recuperated cycle can be therefore reached by increasing the overall fuel-air equivalence ratio.

The EGR system attempts to overcome the above problems by allowing the system to approach the "MILD-combustion" concept because of the addition of inert species to the oxidant and of the increased fuel/oxygen equivalence ratio. The self-ignition is however preserved by the high temperature of the reactants produced by the internal heat recovery. The recirculated gases are addressed to the compressor inlet, and the plant layout (Fig. 1) must therefore include a cooling heat exchanger after the air mixing with the exhaust fraction. The latter is defined through the X_{EGR} parameter, whose definition can be derived from Eq. (2).

For EGR mass flow rate,

$$\dot{m}_{EGR} = (1 - X_b)X_{EGR}\dot{m}_g \tag{2}$$

For oxidant mass flow rate,

$$\dot{m}_{ox} = \dot{m}_a + \dot{m}_{EGR} \tag{3}$$

For actual exhaust/air ratio,

$$\frac{\dot{m}_{EGR}}{\dot{m}_a} = (1 - X_b)X_{EGR}\left(1 + \frac{\dot{m}_f}{\dot{m}_a}\right) \tag{4}$$

The last relationship puts into evidence that the by-pass activation would require higher EGR ratios for achieving the same air dilution with inert species (Fig. 4).

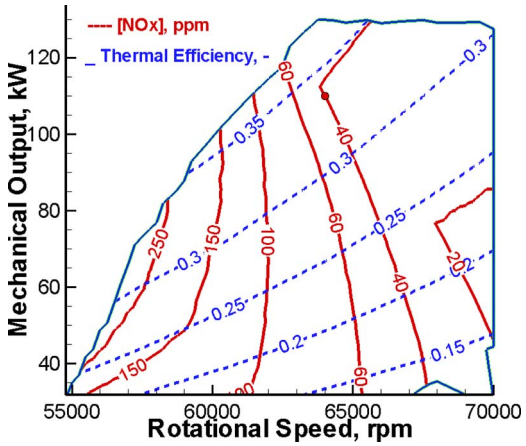

Fig. 2 Operating map of the MGT with efficiency and NO_x levels

2.2 Cycle Analysis With the Component Matching Approach. Before proceeding with the CFD based analysis of the combustion process induced by the EGR solution, an accurate cycle analysis has been carried out. The thermodynamic approach is fully described in previous authors' papers, and here it is simply recalled that each gas state is estimated by accessing the JANAF tables, [18] and a thermokinetic model [11,16] provides a provisional estimate of the thermal NO formation. The recuperator efficiency and the related pressure losses are computed as functions of the actual gas flow rate through this device [11,19], while a fixed value of 0.85 is established for the cooling effectiveness of the oxidant after cooler.

In addition to the above features the component matching approach includes the limits in turbine and compressor flow capacities [1,2]. Besides the general validity of this approach, this particular case takes advantage of a correct estimation of the actual operating conditions of the rotating devices because of the increasing temperature at the compressor inlet with the EGR ratio. The model also accounts for the slight decrease in the turbine pressure ratio that results from the increased back pressure induced by losses through the recirculation valve.

The general problem is usually solved with two independent variables (e.g., the load level and the turbine shaft speed) but the presence of the recuperator by-pass and EGR options adds two degrees of freedom (DOFs) and consequently, the full solution could only be examined in a multidimensional space. More af-

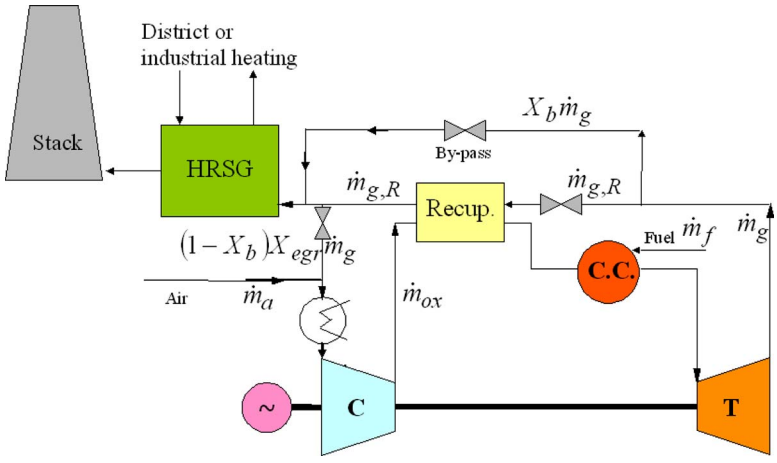

Fig. 1 Plant layout of the micro-gas turbine with internal and external heat recovery and with the exhaust recirculation option

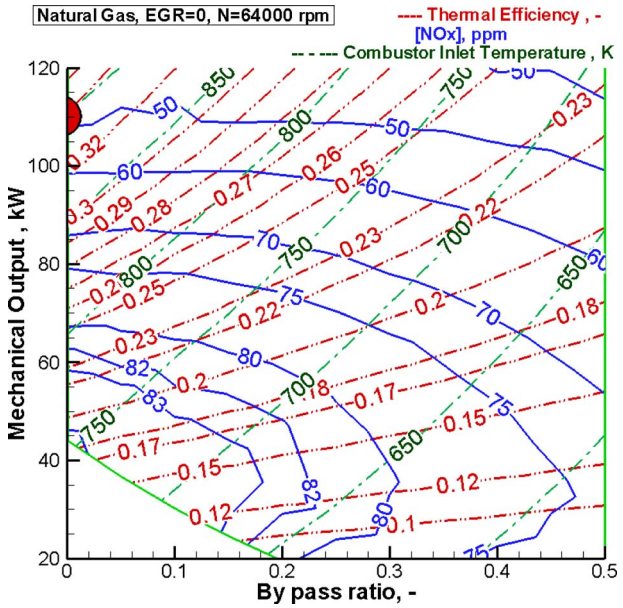

Fig. 3 Operating map of the MGT with variably recuperated cycles

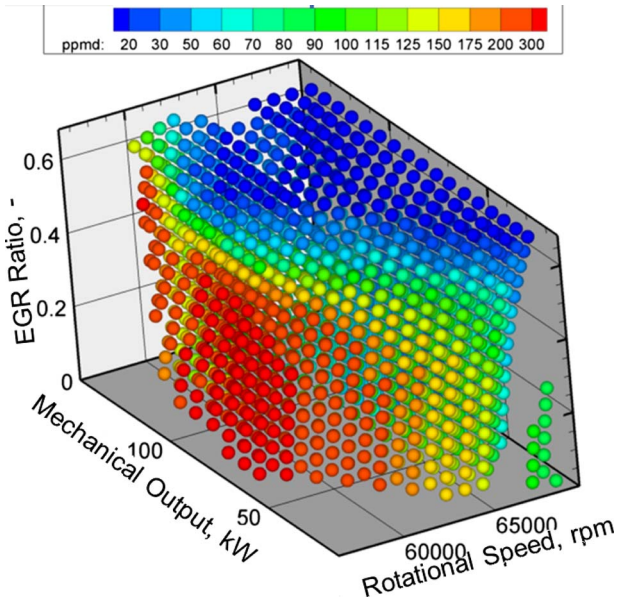

Fig. 5 Thermal NO emission map for variable speed EGR operated micro-gas turbine

fordable insights are provided in Figs. 5 and 6 that display the results of two different DOF solutions, say, for $X_b=0$ and constant shaft speed, respectively. In both cases, the figures give an immediate sketch of the EGR levels that are needed for reducing the thermal NO emissions.

The fully recuperated cycle, variable speed case in Fig. 5, confirms that for both low loads and reduced shaft speeds higher EGR ratios are required. Figure 6, which refers to the variably recuperated cycles—constant speed cases, confirms the comments on Fig. 4: real benefits in terms of nitric oxide control can be obtained for even higher EGR levels when the recuperator by-pass is activated.

If returning to the original problem in the 2D space (Fig. 7), the benefits from the EGR option are more clearly evidenced: a X_{EGR} value of 0.6–0.65 would really lead to a significant reduction in NO emission both at full load and all over the part-load range of the micro-gas turbine.

For given values of the mechanical output (i.e., 100% and 60% load), Figs. 8 and 9 display the trend of NO concentration and thermal efficiency as functions of the EGR ratio. The curves in Fig. 8 are helpful for establishing feasible compromises between the efficiency decrease (mainly induced by the temperature increase at the compressor inlet) and the pollutant reduction. The same diagram confirms that the part-load operation requires a more relevant air dilution with inert species for achieving the objective of NO_x control. In this case, a less dramatic penalty in thermal efficiency is observed.

Finally, Fig. 9 shows an example of the oxidant composition at the combustor inlet for different load levels, when varying the EGR ratio. These trends, together with those of the mass flow rate and temperature of the air entering the combustion chamber, represent the main set of variable inlet boundary conditions for the CFD based simulation of the combustion process.

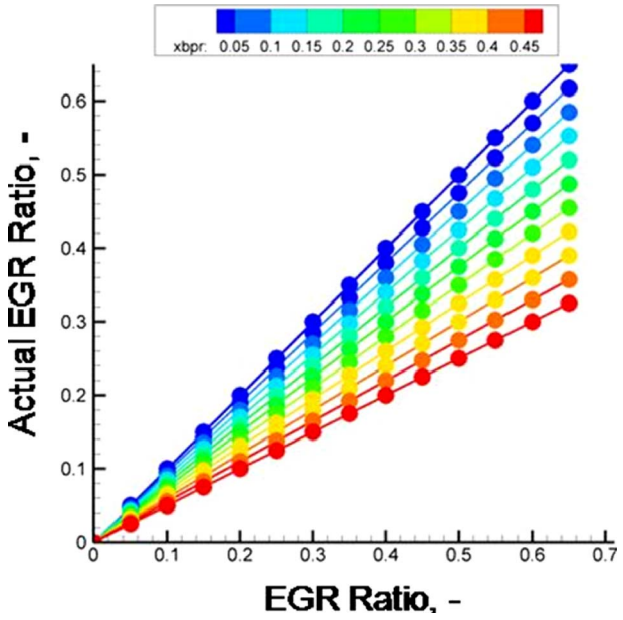

Fig. 4 The effect of the recuperator by-pass on the actual exhaust recirculation fractions

3 CFD Simulation of the Combustion Process

The encouraging results suggested by the cycle analysis in terms of the possible nitric oxide reduction resulting from the EGR activation are worthy of an accurate validation through the CFD analysis of the combustion process. Actually, the previous authors' papers [1,2] have evidenced that the NO reduction could also be counterbalanced by an increase in unburned species and in carbon monoxide production. On the other hand the CFD results were also affected by uncertainties due to the simplified models adopted for the combustion simulation.

This section aims therefore to overcome such limits thanks to an improved accuracy of the reaction models. To this purpose, the authors focused their attention on a limited number of cases to be investigated by different numerical approaches.

First, the simple 100% methane oxidation considered in the previous works was replaced by a complete set of kinetic equations for describing the combustion of a variable-composition natural gas

$$CH_4 + \tfrac{3}{2}O_2 \rightarrow CO + 2H_2O$$

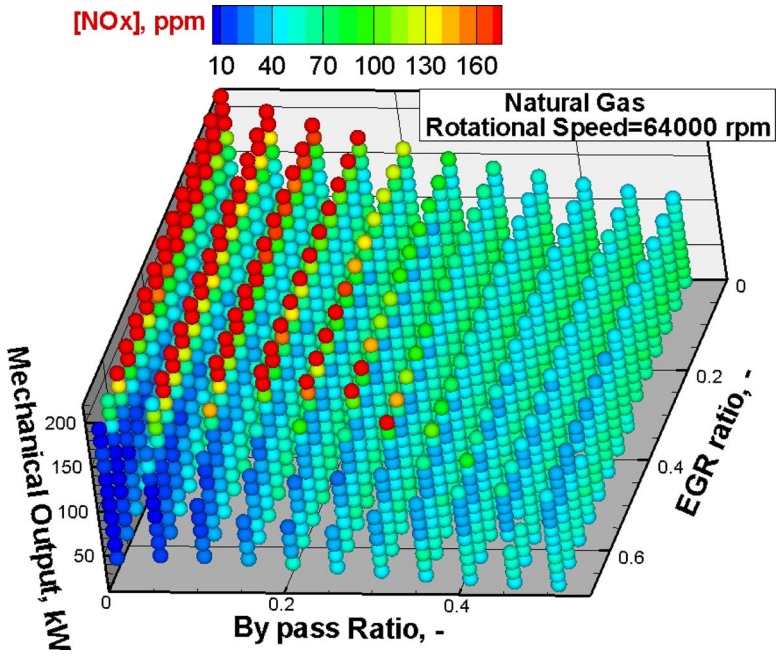

Fig. 6 Thermal NO emission map for constant speed EGR operated micro-gas turbine with variably recuperated cycles

$$R_f = 5.012 \times 10^{+11} \exp\left(-\frac{2 \times 10^{+8}}{RT}\right)[CH_4]^{0,7}[O_2]^{0,8}$$

$$CO + \tfrac{1}{2}O_2 \rightarrow CO_2$$

$$R_f = 2.239 \times 10^{+12} \exp\left(-\frac{2 \times 10^{+8}}{RT}\right)[CO]^{1}[O_2]^{0,25}$$

$$C_2H_6 + \tfrac{7}{2}O_2 \rightarrow 2CO_2 + 3H_2O$$

$$R_f = 6.186 \times 10^{+09} \exp\left(-\frac{1.256 \times 10^{+8}}{RT}\right)[C_2H_6]^{0,1}[O_2]^{1,65}$$

$$C_3H_8 + \tfrac{7}{2}O_2 \rightarrow 3CO + 4H_2O$$

$$R_f = 5.62 \times 10^{+09} \exp\left(-\frac{1.256 \times 10^{+8}}{RT}\right)[C_3H_8]^{0,1}[O_2]^{1,65}$$

$$C_4H_{10} + \tfrac{13}{2}O_2 \rightarrow 4CO_2 + 5H_2O$$

$$R_f = 4.161 \times 10^{+09} \exp\left(-\frac{1.256 \times 10^{+8}}{RT}\right)[C_4H_{10}]^{0,15}[O_2]^{1,6} \quad (5)$$

In addition, the chemical kinetics scheme was introduced both in a finite rate-eddy dissipation model [20–22] and in the computation of the Probability Density Function (PDF) tables for employing the flamelet based combustion model [12,13]. In particular, the flamelet tables were generated by considering variable oxygen and inert contents in the oxidant, in accordance with the

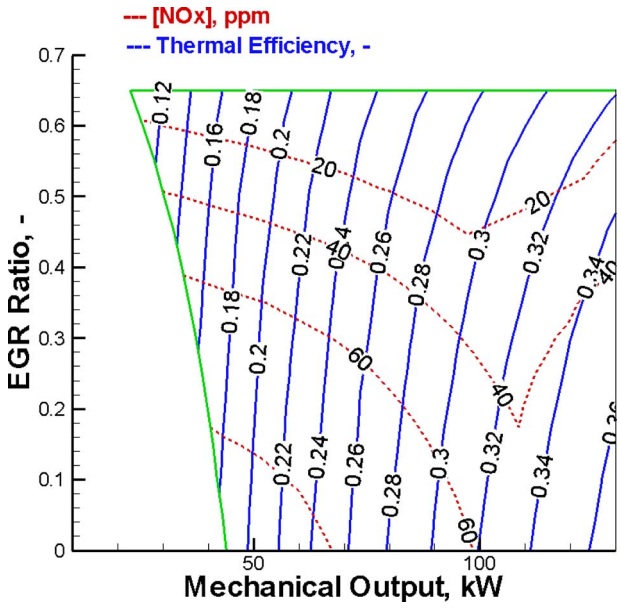

Fig. 7 Operating map of the MGT with efficiency and NO levels, for constant speed and variable EGR ratios

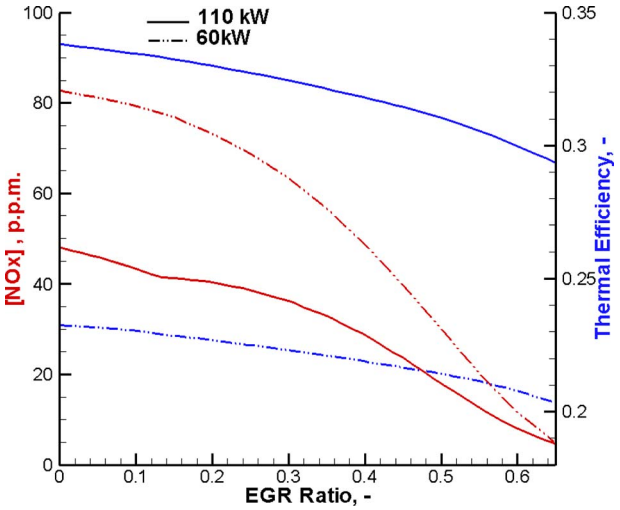

Fig. 8 The EGR effect on MGT efficiency and emissions

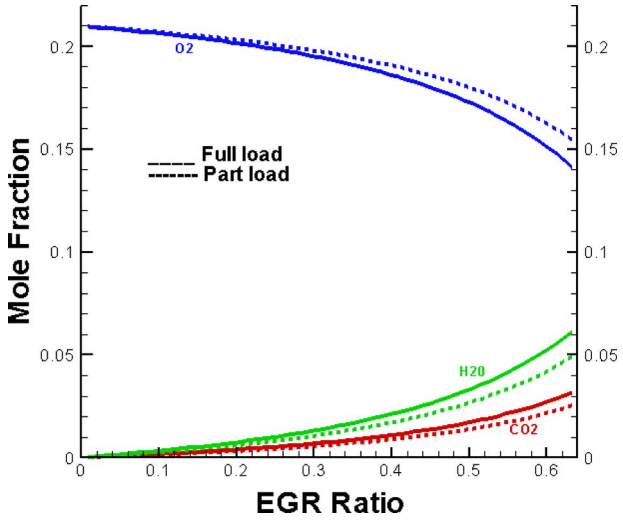

Fig. 9 The EGR effect on the oxidant composition

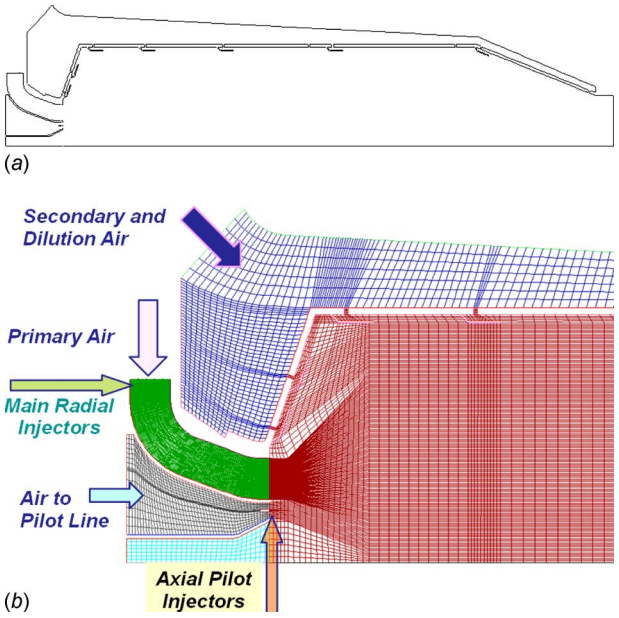

Fig. 11 2D computational domain and details of the block-structured mesh

EGR ratio considered. In both reaction models the computation of both thermal [23,25] and prompt nitric oxide formation is also activated, according to the standard schemes implemented in the FLUENT® solver.

A further relevant difference is represented by the assumption of the Reynolds stress five-equation turbulence model that replaced the k-ε scheme adopted in the previous computations. This allowed removal of the isotropy hypothesis so leading to a more accurate estimate of both the turbulent mixing rate in the eddy dissipation model and the turbulent flame speed in the flamelet model (FLAM).

The lean-premixed combustor of the tubular type, expressly conceived by the Ansaldo Research Center [17,24] for the MGT application, was exhaustively described in previous authors' papers [1,2,15,16], and Figs. 10 and 11 display the 3D view of the combustion chamber and the 2D axisymmetric domain assumed for the reacting-flow solution.

With regard to the numerical grid generation, a block-structured variably spaced mesh was chosen instead of the unstructured one employed in the previous referenced works. The preliminary numerical experiments led to a grid spacing convergence with 38,000 cells. Details of the mesh refinement within the premixed channel and the primary combustor region are evidenced in Fig. 11.

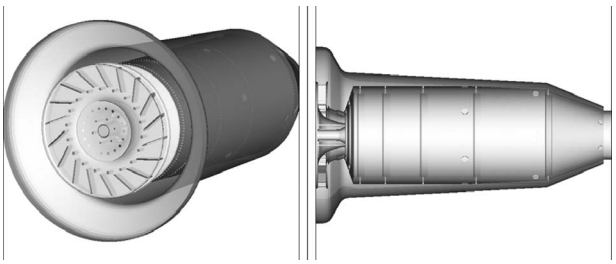

Fig. 10 The lean-premixed combustor

As stated, the cycle analysis provides the boundary conditions in terms of oxidant flow rate and composition together with the thermodynamic properties at combustor inlet. Additional conditions were derived from preliminary fully 3D computations [16] with the FLUENT® flow solver, so allowing the assignment of the mass flow rate splitting between the primary and the secondary and dilution air inlets. The same calculations also provided the average flow angle of the swirled intake into the premixed line, and the inlet turbulence parameters as well.

3.1 Results With the Finite Rate-Eddy Dissipation Model. The attention was focused on a limited number of examples, say, the base rating condition and the one at 60% load at the same rotational speed, both examined by the point of view of the effect of the EGR activation. Table 2 compares the most significant input parameters at combustor inlet and some space-averaged properties at combustor outflow, for normal operation and for a 65% EGR rate. At full-load condition, a 10% fraction of the fuel flow rate is addressed to the pilot stoichiometric line, the latter requiring a 36.5% of the total fuel at 60% load. As expected, a relevant increase in the overall fuel/oxygen equivalence ratio is observed when the EGR option is activated because of the air dilution with inert species and of the increased mass flow rate of fuel that is necessary for reaching the same mechanical output.

Table 2 Input data and average properties at combustor exit from computations with the finite rate-eddy dissipation reaction model

		Inlet data			Outlet			
Operating condition	X_{EGR}	F/O equiv. ratio	T_{in} (K)	$[O_2]$ % (mol)	$\bar{T}_{ex}$ (K)	[NO] (ppm)	[CO] (ppm)	$[CH_4]$ (ppm)
X_b=0	0.0	0.140	907.0	21	1181	69.5	121	417
Full load	0.65	0.231	903.7	14.4	1203	3.99	182	646
X_b=0.0	0.0	0.114	800.5	21	997	52.9	208	1632
60% load	0.65	0.173	808.8	15.6	1032	7.90	264	1822

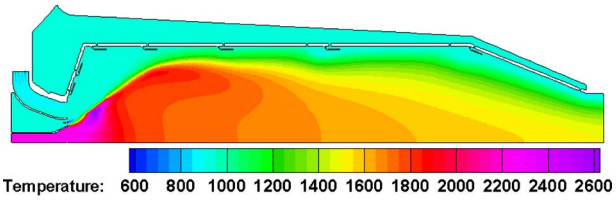

(*a*)

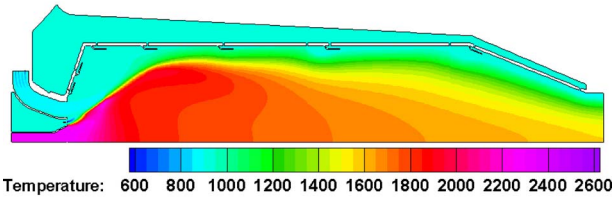

(*b*)

Fig. 12 Temperature distributions for different combustion regimes

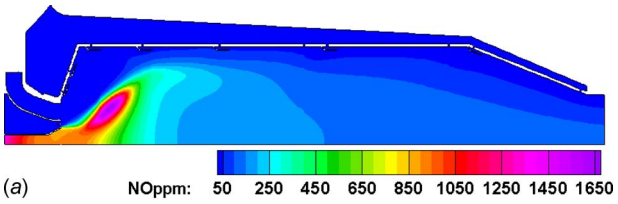

(*a*)

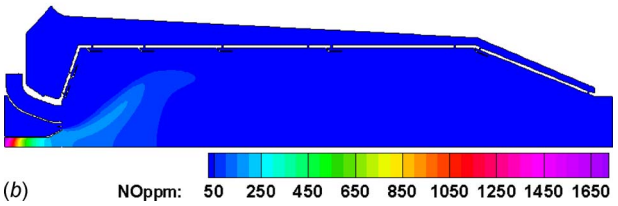

(*b*)

Fig. 14 Nitric oxide distributions for different combustion regimes

Both operating conditions seem to take advantage of the exhaust recirculation, as confirmed by the noticeable reduction in nitric oxide emission. According to the purpose of the CFD based analysis, the results in Table 2 also put into evidence that increases in both carbon monoxide and unburned hydrocarbons result from the oxygen defect in the reactants.

The contours in Figs. 12 and 13 confirm that smoother temperature profiles are attainable with the EGR activation, while a regular combustion development seems however to be ensured. Regarding to the nitric oxide formation mechanisms, a relevant reduction in the local formation rates is shown in Fig. 14 because of the temperature peak abatement. As a further proof of the benefits arising from the exhaust recirculation, Table 3 reports the values of the nitric oxide formation rates for normal and EGR based operations. The latter condition actually reduces the average values of all the formation rates, but the most significant results are represented by the maximum value of the thermal NO rate, whose value is decreased by two orders of magnitude.

3.2 The Flamelet Based Approach. As anticipated, the results of the CFD simulations employing the classical finite rate-eddy dissipation model are worthy of an accurate validation. Actually, such results suggest a fairly correct combustion development even in the presence of an inert-diluted oxidant flow. Therefore, the adoption of a different combustion model, such as a flamelet based scheme, appears to be appropriate for a definite check of the computational cases.

As well known, the flamelet model [12] approaches the more general problem of a nonpremixed turbulent combustion through the transport equation of a single scalar quantity

$$\frac{\partial}{\partial t}(\rho\bar{f}) + \nabla \cdot (\rho \boldsymbol{v}\bar{f}) = \nabla \cdot \left(\frac{\mu_t}{\sigma_t} \nabla \bar{f}\right) \tag{6}$$

where f is the mixture fraction defined as a function of the atomic mass fraction of each ith elementary species participating in the process

$$f = \frac{Z_i - Z_{i,\text{ox}}}{Z_{i,\text{fuel}} - Z_{i,\text{ox}}} \tag{7}$$

The conservation equation (6) holds under the hypothesis of uniform diffusion coefficients for all the chemical species, like what usually occurs in turbulent flows. In this case, the transport of all species may be represented by a single equation (6). Consequently, each thermochemical property, ϕ_i, can be expressed as a function of the mixture fraction

$$\phi_i = \phi_i(f) \tag{8}$$

The chemistry-turbulence interaction is approximated by PDF functions. The introduction of a detailed chemistry into the CFD computations is operated by considering each turbulent flame as composed of locally one-dimensional laminar flamelets, whose properties are described by the mixture fraction and by an additional variable, say, the scalar dissipation rate, χ. The latter is strictly dependent on the local turbulence parameters. The tables of flamelet properties can be derived either from experiments or from calculations. This second option was accessed in the present work, and this required building of flamelet libraries in accordance with the oxidant and the fuel characteristics. A preliminary sensitivity analysis was also needed for a proper estimate of both the initial values of the scalar dissipation rate and of the scalar

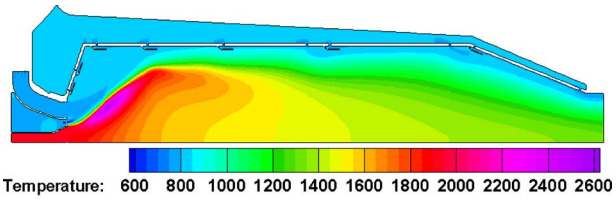

(*a*)

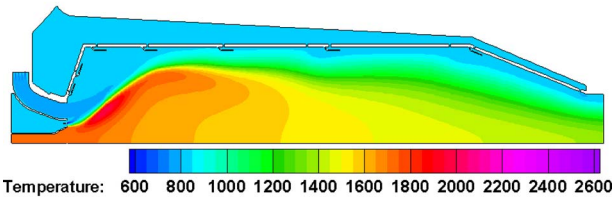

(*b*)

Fig. 13 Temperature distributions for different combustion regimes

Table 3 Volume-averaged and maximum formation rates of nitric oxides (full-load)

X_{EGR}	Value	Thermal NO rate (kmol/(m^3 s))	Prompt NO rate (kmol/(m^3 s))	N_2O rate (kmol/(m^3 s))
0.0	Average	3.25×10^{-4}	2.93×10^{-6}	3.43×10^{-5}
	Maximum	1.60×10^{-1}	2.52×10^{-3}	1.60×10^{-3}
0.65	Average	1.62×10^{-5}	1.02×10^{-6}	8.82×10^{-7}
	Maximum	3.64×10^{-3}	4.67×10^{-4}	3.25×10^{-4}

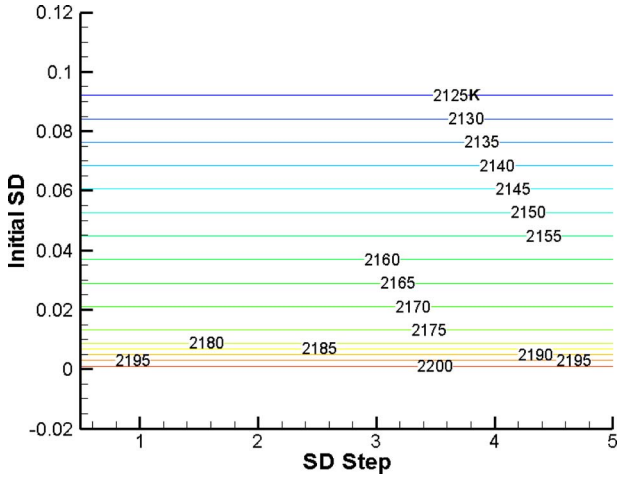

Fig. 15 Contours of maximum temperature estimated in the flamelet tables

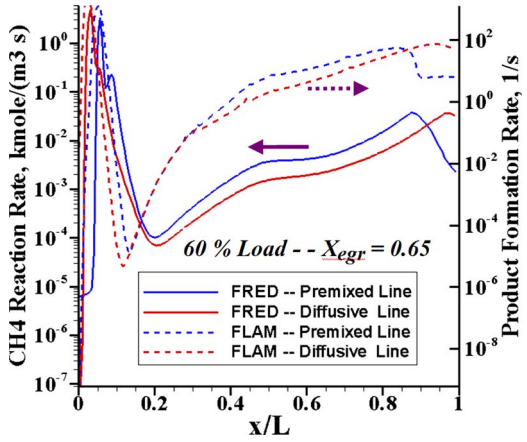

Fig. 17 Comparison of reaction rates with the different combustion models

dissipation step. Figure 15 displays an example of this analysis in terms of contours of the maximum combustion temperature estimated by varying the above parameters in the flamelet table generation.

Figure 16 shows the influence of the oxidant composition on the laminar flame speed profiles as functions of the mean mixture fraction. The trends appear to be in accordance with the oxygen defect related to high EGR rates.

In the following, the results of the application of the flamelet based approach to the part-load combustion cases are discussed. An initial comparison of the results obtainable with either the FRED or the FLAM model was needed, in order to verify the consistency of the temperature and NO distribution predicted by the first one and displayed in the previously discussed figures (Figs. 12–14). So, Figs. 17–19 allow such comparison in terms of axial profiles of turbulence intensity, chemistry rates, and temperatures. The profiles were derived by axial cuts of the computational domains along straight lines starting from the premixed channel and the pilot fuel injector, respectively.

It is of interest to observe that the turbulence governed processes are affected by the turbulence level distribution (Fig. 20) characterized by an initial peak, close to the primary region, and a successive increase that is related to the dilution air mixing with the main gas stream. Such distributions, which do not present substantial differences if looking at the two models adopted, clearly affect the combustion development. Actually, both the reaction rate predicted by the FRED model and the overall product formation rate by the FLAM (Fig. 17) are strictly in accordance with the turbulence level trend. It is also worth noting to appreciate the satisfactory agreement with the chemistry rates resulting

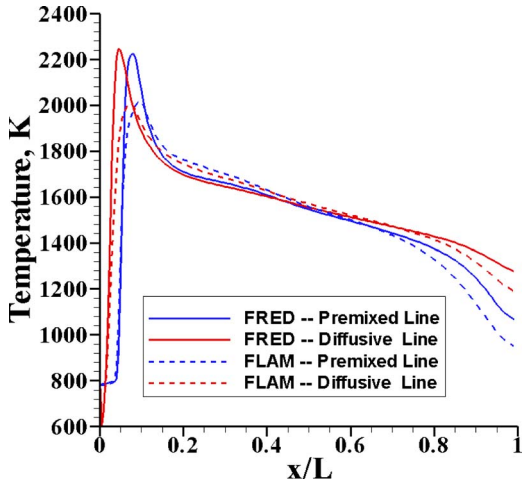

Fig. 18 Comparison of temperature profiles with the different combustion models

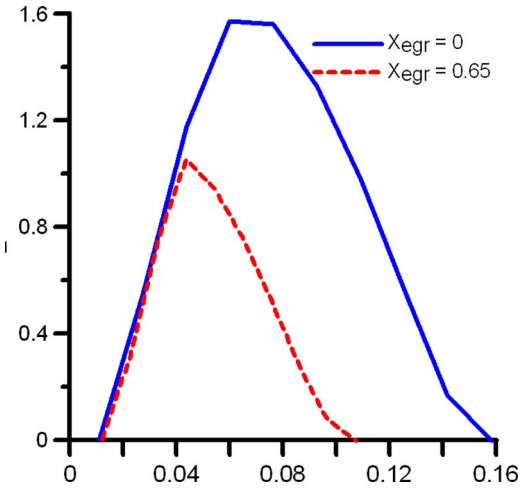

Fig. 16 Laminar flame speed profiles for different oxidant compositions

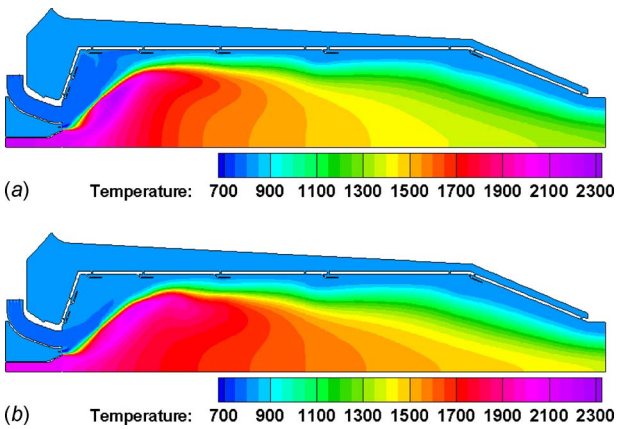

Fig. 19 Temperature distributions for different combustion regimes

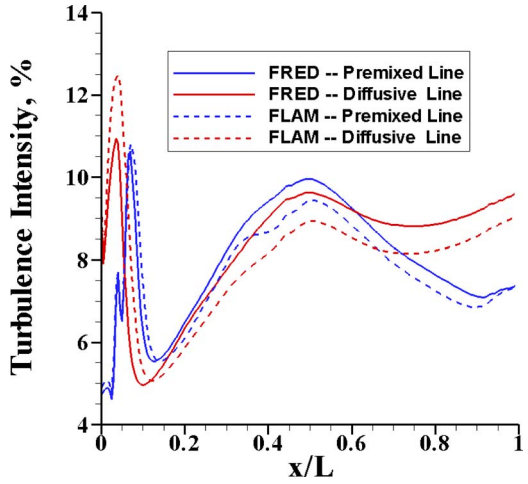

Fig. 20 Comparison of turbulence level profiles with the different combustion models

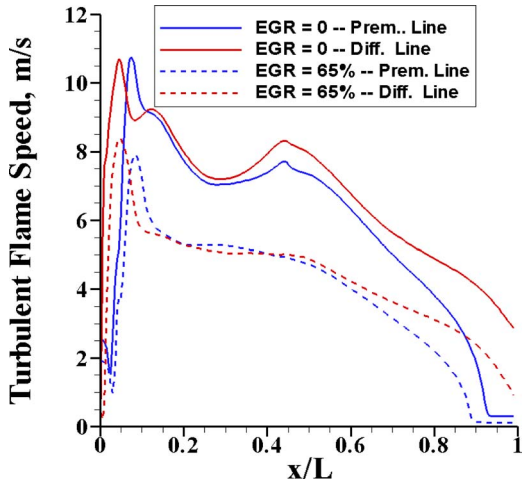

Fig. 22 EGR effect on the axial profiles of the turbulent flame speed

from the two models. This represents an encouraging confirmation about the possibility of a correct combustion development, even in the presence of the relevant oxygen defect that occurs for the 65% EGR cases discussed in these figures. Such a qualitative accordance can be also detected in the temperature profiles in Fig. 18, even if a systematic attenuation in temperature peaks can be observed.

Basing on the satisfactory indications from Figs. 17, 18, and 20, the results of the CFD simulations with the flamelet model for part-load combustor operation can be discussed in the Figs. 19 and 21–24, by analyzing the effect of the exhaust recirculation option [25].

The temperature distributions within the computational domain (Fig. 19) confirm the good accordance with the results of the FRED model in Fig. 13. In addition, the peak reduction can be appreciated together with a smoother variation in the temperature levels toward the combustor outflow. This demonstrates that the *EGR* based solution allows a fair approach to the MILD regime.

Figure 21 shows the actual axial profiles of the laminar flame speed, whose dependence on both the mean mixture fraction and the oxidant composition was already evidenced in Fig. 16. This figure emphasizes the effect of the local composition of the reactants: therefore, the low oxygen concentration in the 65% EGR case induces a drastic reduction in the baseline flame speed starting from the primary combustor region.

The actual values of the flame speed are those corrected by the turbulence effects (Fig. 22). The turbulent flame speed pattern is affected by both the laminar speed profiles and the local turbulence levels (Fig. 20). This explains the permanence of significant levels of the flame speed along most of the axial flow path. The effect of both the oxygen defect and the increased inert species' contents is clearly detectable in terms of control of the turbulent combustion.

The direct comparison of the temperature axial distributions (Fig. 23) with no EGR activation and with the 65% EGR option highlights that the method proposed is really helpful to produce flatter profiles, so is closer to the MILD regime concept [26]. Consequently, in the 65% EGR case the thermal NO formation rate (Fig. 24) is significantly reduced in the most critical region, say, the one of the primary combustion, while the higher rates in the secondary and dilution regions attain however negligible values, so that no practical effect is exerted on possible increases in the nitric oxide formation.

As a general final comment to the above discussed result, it could be concluded that the application of the flamelet based model has provided a significant validation of the results suggested by other models, in terms of achievement of smoother

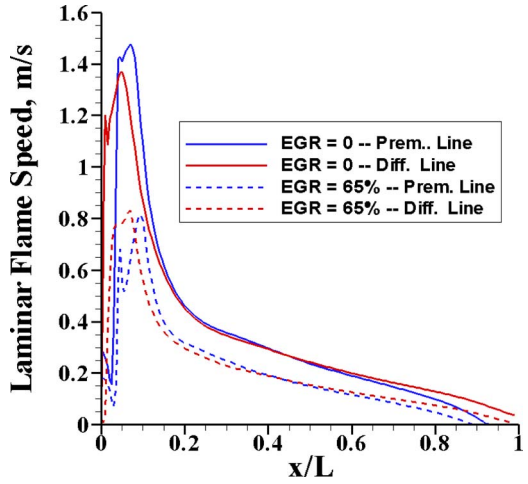

Fig. 21 EGR effect on the axial profiles of the laminar flame speed

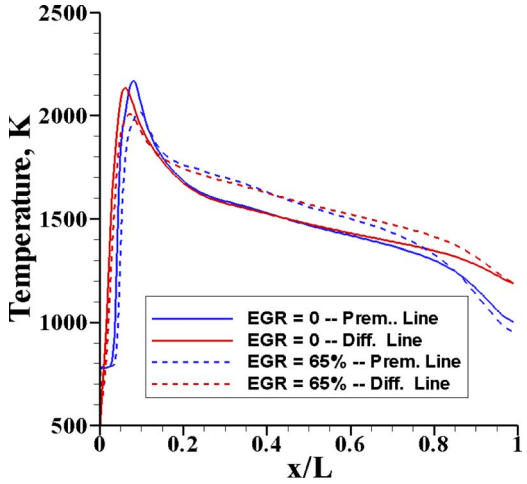

Fig. 23 EGR effect on the axial profiles of gas temperature

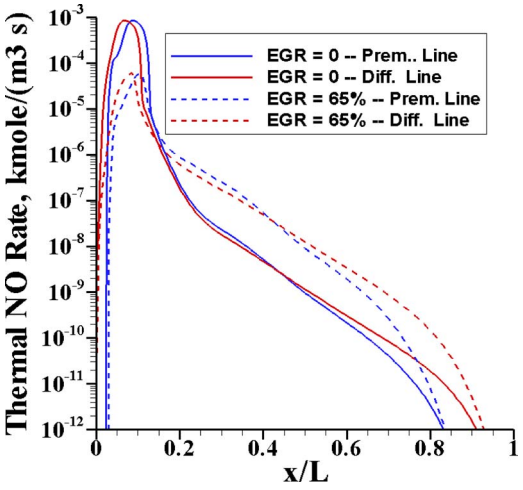

Fig. 24 EGR effect on the axial profiles of the NO formation rate

combustions with the exhaust recirculation method. At the same time, it is confirmed that the EGR cases can also lead to a fairly efficient combustion development.

4 Conclusion

Starting from the results of a matching analysis of an EGR operated micro-gas turbine, the authors have selected some cases of interest to prove the effectiveness of this method for the thermal NO_x control.

The validation of the cycle analysis prediction has been obtained by a CFD based simulation employing two different reacting-flow models, so as to achieve a definite confirmation of the combustion process effectiveness under conditions characterized by strongly modified reactant compositions. An innovative aspect has been represented by the introduction of a flamelet based approach for a rather different approximation of the turbulent combustion with respect to the classical finite rate-eddy dissipation schemes.

The good agreement exhibited by the CFD indications, which result from the adoption of both combustion models, can be intended as numerical evidence of the satisfactory combustion effectiveness and of the nitric oxide control induced by the exhaust recirculation system.

More accurate numerical approaches (e.g., combustion simulation in 3D domains with Large Eddy Simulation (LES) turbulence schemes), together with experimental indications, will provide in the future ultimate answers about the practical possibility of employing the method proposed in this paper. Basing on the current state of the art, the authors' proposal of an external EGR system may be considered as an alternate solution to the modifications to the combustor configuration and fluid dynamics, which seem to be a challenging solution for a down-sized combustor that equips the micro-gas turbine.

Acknowledgment

The Ansaldo Ricerche S.p.A. is acknowledged for suggesting provisional data of the MGT cycle parameters and combustor configuration.

The research is carried out with the financial support of Italian Department for University and Research (PRIN 2005).

The reference CFD calculations are licensed by Fluent Inc.

Nomenclature

f = mean mixture fraction
$\dot{m}$ = mass flow rate
N = shaft rotational speed
R_f = forward reaction rate
T = temperature
v = velocity
X_b = recuperator by-pass ratio
X_{EGR} = EGR ratio
Z_i = elementary chemical species

Greek

μ = dynamic viscosity
ρ = density
ρ_t = turbulent Prandtl number
χ = scalar dissipation

Subscripts

a = air
ex = combustion chamber outlet
f = fuel
in = combustion chamber inlet
g = exhaust gas
cc = mixing conditions
ox = oxidant
R = recuperator
st = stoichiometric
t = turbulent

References

[1] Cameretti, M. C., Reale, F., and Tuccillo, R., 2006, "Cycle Optimization and Combustion Analysis in A Low-NOx Micro-Gas Turbine," ASME J. Eng. Gas Turbines Power, **129**, pp. 994–1003.
[2] Cameretti, M. C., Reale, F., and Tuccillo, R., 2007, "NO_x Suppression From a Micro-Gas Turbine Approaching the Mild-Combustion Regime," ASME Paper No. GT2007-27091.
[3] Camporeale, S. M., and Fortunato, B., 2007, "Thermodynamic Analysis of Semi-Closed Gas Turbine Combined Cycles With High Temperature Diluted Air Combustion," ASME Paper No. GT2007-28330.
[4] Levy, Y., Sherbaum, V., and Erenburg, V., 2007, "The Role of the Recirculating Gases at the Mild Combustion Regime Formation," ASME Paper No. GT2007-27369.
[5] Duwig, C., Szasz, R. Z., and Fuchs, L., 2006, "Modelling of Flameless Combustion Using Large Eddy Simulation," ASME Paper No. GT2006-90063.
[6] Levy, Y., Sherbaum, V., and Rao, G. A., 2007, "Preliminary Analysis of a New Methodology for Flameless Combustion in Gas Turbine Combustors," ASME Paper No. GT2007-27766.
[7] Li, G., Gutmark, E. J., Overman, N., and Cornwell, M., 2006, "Experimental Study of a Flameless Gas Turbine Combustor," ASME Paper No. GT2006-91051.
[8] Dagaut, P., and Cong, T. L., 2007, "Kinetics of Natural Gas, Natural Gas/Syngas Mixtures Oxidation and Effect of Burnt Gas Recirculation: Experimental and Detailed Modeling," ASME Paper No. GT2007-27146.
[9] Schütz, H., Lückerath, R., Kretschmer, T., Noll, B., and Aigner, M., 2006, "Analysis of the Pollutant Formation in the FLOX® Combustion," ASME Paper No. GT2006-91041.
[10] Brueckner-Kalb, J. R., Napravnik, C., Hirsch, C., and Sattelmayer, T., 2007, "Development of a Fuel-Air Premixer for a Sub-ppm Nox Burner," ASME Paper No. GT2007-27779.
[11] Bozza, F., Cameretti, M. C., and Tuccillo, R., 2005, "Adapting the Micro-Gas Turbine Operation to Variable Thermal and Electrical Requirements," ASME J. Eng. Gas Turbines Power, **127**, pp. 514–524.
[12] Peters, N., 2000, *Turbulent Combustion*, Cambridge University Press, Cambridge, England.
[13] Tuncer, O., Acharya, S., and Uhm, J., 2007, "Dynamics, NO_x and Flashback Characteristics of Confined Pre-Mixed Hydrogen Enriched Methane Flames," ASME Paper No. GT2007-28158.
[14] Ibrahim, O., Zimmermann, P., Hirsch, C., Sattelmayer, T., Gerhard, B., and Steinbach, C., 2004, "A Microturbine Operating With Variable Heat Output," ASME Paper No. GT-2004-53011.
[15] Cameretti, M. C., and Tuccillo, R., 2005. "A CFD Based Off-Design Study of Micro-Gas Turbines Combustors," ASME Paper No. GT-2005-68924.
[16] Tuccillo, R., and Cameretti, M. C., 2005, "Combustion and Combustors for MGT Applications," Paper No. RTO-MP-AVT-131.
[17] Parente, J., Mori, G., Anisimov, V., and Croce, G., 2004, "Micro Gas Turbine Combustion Chamber Design and CFD Analysis," ASME Paper No. GT2004-54247.
[18] McBride, B. J., and Gordon, S., 1994, "Computer Program for Calculation of Complex Equilibrium Composition and Applications," NASA Technical Report No. RP 1311.
[19] Lagerström, G., and Xie, M., 2002, "High Performance & Cost Effective Recuperator for Micro-Gas Turbines," ASME Paper No. GT-2002-30402.
[20] Magnussen, B. F., and Hjertager, B. H., 1977, "On Mathematical Modeling of

Turbulent Combustion With Special Emphasis on Soot Formation," 16th Symposium on Combustion, The Combustion Institute, Pittsburgh.
[21] Nicol, G. D., Malte, P. C., Hamer, A. J., Roby, R. J., and Steele, R. C., 1998,"A Five-Step Global Methane Oxidation—NO Formation Mechanism for Lean Premixed Gas Turbine Combustion," ASME Paper No. 98-GT-185.
[22] Novosselov, I. V., and Malte, P. C., 2007, "Development and Application of an Eight-Step Global Mechanism for CFD and CRN Simulations of Lean-Premixed Combustors," ASME Paper No. GT2007-27990.
[23] Zeldovich, Y. B., Sadovnikov, P. Y., and Frank-Kamenetskik, D. A., 1947, *Oxidation of Nitrogen in Combustion*, Academy of Science of SR, Institute of Chemical Physics, Moscow, Leningrad.
[24] Russo, C., Parente, J., Mori, G., and Anissimov, V. V., 2007, "Micro Gas Turbine Combustor Emissions Evaluation Using the Chemical Reactor Modelling Approach," ASME Paper No. GT2007-27687.
[25] Miller, J. A., and Bowman, C. T., 1989, "Mechanism and Modelling of Nitrogen Chemistry in Combustion," Prog. Energy Combust. Sci., **15**, pp. 287–338.
[26] Cavaliere, A., and de Joannon, M., 2004, "Mild Combustion," Prog. Energy Combust. Sci., **30**(4), pp. 329–366.

Proposal of a Novel Multifunctional Energy System for Cogeneration of Coke, Hydrogen, and Power

Hongguang Jin
Institute of Engineering Thermophysics,
Chinese Academy of Sciences,
Beijing 100190, P.R.C.
e-mail: hgjin@mail.etp.ac.cn

Shien Sun
Institute of Engineering Thermophysics,
Chinese Academy of Sciences,
Beijing 100190, P.R.C.;
Graduate University of Chinese Academy of Sciences,
Beijing 100190, P.R.C.
e-mail: sunshien@gmail.com

Wei Han

Lin Gao

Institute of Engineering Thermophysics,
Chinese Academy of Sciences,
Beijing 100190, P.R.C.

This paper proposes a novel multifunctional energy system (MES), which cogenerates coke, hydrogen, and power, through the use of coal and coke oven gas (COG). In this system, a new type of coke oven, firing coal instead of COG as heating resource for coking, is adopted. The COG rich in H_2 is sent to a pressure swing adsorption (PSA) unit to separate about 80% of hydrogen first, and then the PSA purge gas is fed to a combined cycle as fuel. The new system combines the chemical processes and power generation system, along with the integration of chemical conversion and thermal energy utilization. In this manner, both the chemical energy of fuel and thermal energy can be used more effectively. With the same inputs of fuel and the same output of coking heat, the new system can product about 65% more hydrogen than that of individual systems. As a result, the thermal efficiency of the new system is about 70%, and the exergy efficiency is about 66%. Compared with individual systems, the primary energy saving ratio can reach as high as 12.5%. Based on the graphical exergy analyses, we disclose that the integration of synthetic utilization of COG and coal plays a significant role in decreasing the exergy destruction of the MES system. The promising results obtained may lead to a clean coal technology that will utilize COG and coal more efficiently and economically.
[DOI: 10.1115/1.3078791]

1 Introduction

Hydrogen is a very promising energy carrier for the long term. It usually can be produced from methane and naphtha through several processes, including steam reforming and hydrogen separation. On one hand, coke oven gas (a by-product in the coking process), contains about 50–60% hydrogen. However, at present, almost half of coke oven gas (COG) was burned directly in coking process, and most of the rest were discharged into the atmosphere [1]. In some iron works, hydrogen is separated from clean COG by means of pressure swing adsorption (PSA). It would be highly desirable to recover more hydrogen from COG at a lower cost in the future [2–5]. Hence, more attention should be focused on the effective utilization of COG.

On the other hand, a coal-based hydrogen plant or integrated gasification combined cycle (IGCC) plant requires a gasification subsystem that includes a gasifier, an air separation unit, and a cleanup unit, thereby making its configuration more complex and its capital cost more expensive. For example, the investment cost ($/kW) for an IGCC plant is about double that of a natural gas combined cycle plant, which limits the large-scale application of IGCC. And the thermal efficiency of coal-fired steam power plant is not high, which is 35–43%. Based on these facts, it is necessary to create a new method that can synthetically utilize both COG and coal in order to improve the efficiency of fuel utilization and decrease capital cost at the same time.

The polygeneration system, as one of the promising technologies, has been attracting increased attention. For chemical processes, the composition adjustment and poor utilization of thermal energy result in high energy cost for the production of chemicals. For power plants, the high exergy destruction in combustion process, which accounts for about 30% of the total fuel exergy input, limits the increase of thermal efficiency. However, the polygeneration system has the potential to overcome the shortcomings of single systems (chemical product processes and power generation systems) by system integration for producing chemicals and electricity simultaneously. To date, some polygeneration systems with different configurations have been proposed [6–11], and several projects have also been funded with the goal of verifying the feasibility of polygeneration plants in the United States and China [2–4]. Most researchers presented economic analyses and energy analyses of the polygeneration systems [7,9,10]. Meanwhile, some of the researchers presented the exergy analyses of the polygeneration systems [12,13]. Less attention has been paid on the internal effect of the chemical product processes and the power generation subsystem. In fact, we should focus on the synergetic consideration of polygeneration system integration based on both chemical conversion and thermal energy utilization simultaneously.

The aims of this paper are to identify a new approach to utilize COG and coal synthetically and efficiently, to disclose the internal phenomena of the indirect gasification of coal through exergy analysis using energy utilization diagram (EUD) methods, and to synthesize a new system integrating chemical product processes and a power generation system.

2 Novel MES System

2.1 Conceptual Design of the Synthetic Utilization of COG and Coal. The scheme of the conventional coking plant is shown in Fig. 1(*a*). In the coking chamber, the coking coal is heated up to 950–1050°C in the absence of air to drive off the volatile compounds and finally turn it into coke. In this process, the feeding coking coal is partially converted into coke, and at the same time, it is partially converted into coke oven gas. To maintain the temperature of the coking process, about 45% of the coke oven gas is cycled back into the coke oven to be burned as heating source.

Contributed by the International Gas Turbine Institute of ASME for publication in the JOURNAL OF ENGINEERING FOR GAS TURBINES AND POWER. Manuscript received September 8, 2008; final manuscript received September 23, 2008; published online May 26, 2009. Review conducted by Dilip R. Ballal. Paper presented at the ASME Turbo Expo 2008: Land, Sea and Air (GT2008), Berlin, Germany, June 9–13, 2008.

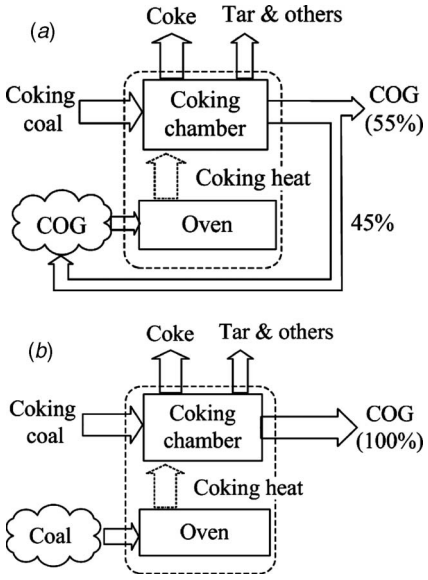

Fig. 1 (*a*) Conventional coking process and (*b*) novel coking process

The heat would be transferred to the coking chamber through the coke oven wall. However, in the coking process of the new system, the coal rather than COG is burned to supply thermal energy, which is shown in Fig. 1(*b*) [14]. Hence, more COG can be substituted and used for other purpose. Besides, when the quantity of coking coal in the coke chamber and the conditions of reaction, such as temperature and pressure, are the same as those of the conventional method, the new coke oven and the conventional coke oven will generate the same quality of coke.

Compared with the conventional coke oven, the new method substituted the low-quality coal for the COG with a high H_2 content. In other words, more COG can be saved to export by this method, and this part of COG can be considered as generating from coal. Therefore, it is equivalent that the coal is gasified indirectly through the new method. Since a gasifier, a cleanup unit and an air separation unit (ASU) are not required in the indirect gasification of coal, comparing with coal gasification method, the system will become simpler and the investment might be reduced.

Since the COG is rich in H_2 (about 50–60%), it can be used to produce H_2 by the PSA unit. Compared with a coal-based hydrogen plant, the gasification and shift reaction ($CO+H_2O=CO_2+H_2$) is eliminated. And the PSA purge gas, whose lower heating value is about 20 MJ/N m^3, can be sent to a combined cycle as fuel. Since the turbine inlet temperature (TIT) of gas turbine can reach up to 1430°C, which is much higher than that of the coking process (950–1050°C), the exergy destruction of combustion of COG in the combustor of gas turbine can be decreased, obviously comparing with that in the coke oven. That is to say, the gas turbine can utilize the COG more efficiently than the coke oven.

2.2 Configuration of New MES System. Figure 2 shows a flowchart of coking chamber and a flowchart of the new multifunctional energy system (MES) system, which includes three subsystems: a coking subsystem (oven and f2), a PSA subsystem (a1, a2, f1, and PSA), and a power generation subsystem (a3, b, c, d, HRSG, e1, e2, and g). In the coking chamber, the coking coal is converted into coke, COG, tar, and others. One ton of coking coal (about 25 GJ) can be converted into about 0.706 tons of coke (about 17.7 GJ), 337 N m^3 of COG (about 6.0 GJ), 0.064 tons of tar, and others (about 1.3 GJ) [15]. The COG generated in the coking chamber was cleaned up first to remove sulfur and other harmful components, and then sent to the MES system. In the coking subsystem, the coal is burned with preheated air to provide the high-temperature thermal energy for coking. After supplying the high-temperature thermal energy in the oven, the flue gas preheats (in f2 unit) the air, which will be fed to the oven for the burning of coal, and the water, which will be sent to the heat recovery steam generator (HRSG) to generate steam. In the PSA unit, the clean COG is initially compressed (a1), and then cooled (f1) down to near ambient temperature. The compressed COG is sent to the absorption unit where the impurity is separated, after the heavy hydrocarbon in the COG was absorbed by the preabsorption unit. In the absorption unit, hydrogen passes through; the other contents are absorbed at high pressure. And then, by decreasing the pressure of the absorption unit, the other contents are released from the absorption unit. The hydrogen from the absorption unit will be compressed to 60 bar through the hydrogen compressor (a2), after being cleaned up further through deoxygenizing and drying. The purity of hydrogen production can reach an even higher value than 99.99%. The purge gas from the PSA subsystem will be fed to the power subsystem (combined cycle). The power subsystem is composed of a gas turbine, a heat recovery steam generator, and steam turbines. And it supplies the power and steam that are required in the former processes.

3 Evaluation of MES System

3.1 Reference Systems. With the multi-input of COG and coal and the multi-output of coke (coking heat), hydrogen, and power, the evaluation of the new MES system will be based on the comparison with single systems. The method of utilizing the COG

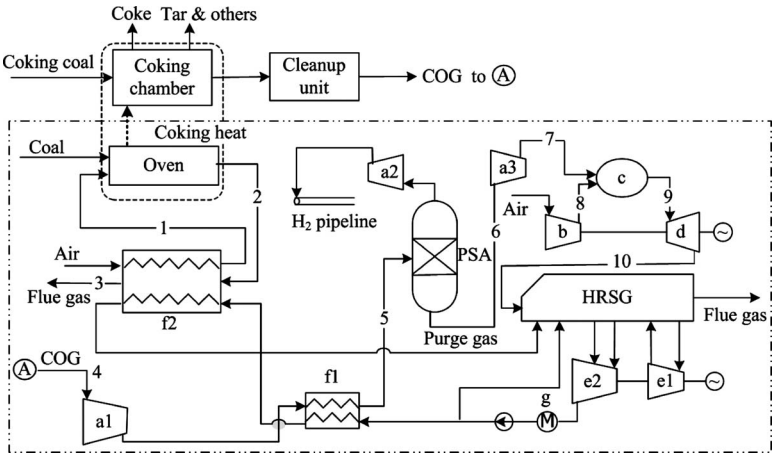

Fig. 2 Flow diagram of the new MES system

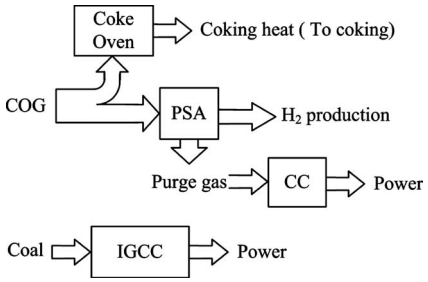

Fig. 3 Utilization of COG and coal in reference systems

and coal in reference systems is shown in Fig. 3. In the COG-based plant (COGP), the model of the JN60-82 coke plant (CP) is selected as one of the reference systems. The thermal energy consumption of coke is about 3240 MJ per ton, and the quantity of heat absorbed by coking coal is about 2570 MJ/tons of coke [15]. About 45 percent of the COG generated in the coking process is burned directly to provide the thermal energy required by coking process. The rest of the COG will be used to produce hydrogen through PSA technology. About 85% of hydrogen in the COG is separated through the PSA process. The purge gas from the PSA process will be fed to a combined cycle (GE model MS 206B, which is decided by the scale of the system) as fuel. In the combined cycle (CC) plant, the turbine inlet temperature and the pressure ratio are 1140°C and 11.8, respectively, and the thermal efficiency is 49.8%, which is based on the composition of the purge gas and the GE model. It is assumed that the power required by the PSA process is supplied by the combined cycle. Coal is used to generate power through an integrated gasification combined cycle power plant. The IGCC plant is composed of a Texaco gasifier, a cleanup unit, an air separation unit, and a combined cycle (GE model MS 9FA). For the gasifier, the oxygen consumption is about 0.86 kg of oxygen per kilogram of coal, and the cold gas efficiency (ratio of the energy of cold produced gas to that of coal input based lower heating value) is about 76.8%. The steam condition in HRSG is the same as that in the MES system. Based on the simulation result, the thermal efficiency of the IGCC is 43.9%.

3.2 Evaluation of New MES System. In the MES system, the coking subsystem is based on the coke-making plant, which produces 2×10^6 tons of coke per year. The power subsystem is based on a heavy-duty gas turbine (GE model MS 206FA, which is selected by the scale of the system) of current technology with a turbine inlet temperature of 1288°C and a pressure ratio of 15. The steam, which is saturated at the pressure of 12 MPa and is reheated at the pressure of 3.9 MPa, is generated in a HRSG. The temperatures of both the superheated and reheated steams are 538°C. The main assumptions here, which are based on industrial datum, are shown in Table 1.

The MES system was studied through the use of the commercial software ASPEN PLUS. During the evaluation, the elemental chemical composition of coal (wt %) is as follows: 68.54% C, 3.97% H, 6.85% O, 0.74% N, 1.08% S, 9.98% Ash, and 8.84% W, and its lower heating value (LHV) is 26,710 kJ/kg. The pressure, temperature, mass flow, and composition of the main points in Fig. 2 are listed in Table 2.

The performance comparisons of the MES system to that of the reference systems (COGP and IGCC) are shown in Table 3. With the same quantity of COG and coal inputs and the same quantity of coking heat output, the MES system produces hydrogen of 197.2 MW, which is 65.3% higher than that of the reference systems (119.3 MW). It also produces power output of 233.9 MW, which is a little higher than that of the reference systems (230.5 MW). The thermal efficiency of the reference systems is about 61.9%, and their exergy efficiency (the ratio of exergy inputs to exergy outputs) is about 57.1%. However, the thermal efficiency of the MES system can reach to 70.8%, and its exergy efficiency is as high as 66.0%. Both thermal efficiency and exergy efficiency are much higher than those of the reference systems. Assuming that the reference systems produce the same quantities of power and hydrogen as the proposed system, the energy saving ratio (ESR) of the new system is about 12.5%, which is shown in Table 3.

Table 1 Main assumption for evaluation

Chemical process	
PSA inlet pressure (MPa)	1.0
Hydrogen separation ratio (%)	80
Isentropic syngas compressor	0.80
Pressure loss of heat exchangers (%)	3
Surplus air ratio of coal combustion	1.3
Power plant	
Isentropic efficiency of air compressor	0.88
Isentropic efficiency of gas turbine	0.9
Isentropic efficiency of pump	0.8
Pinch point in HRSG (°C)	15
Pressure loss of HRSG (gas-side) (%)	3
Pressure loss of HRSG (steam, water) (%)	10
Condensation pressure (MPa)	0.007

In order to reveal the internal phenomena of the MES system and to locate the key processes for the high performance, exergy analyses were studied for both the MES system and the reference systems. The results are listed in Table 4. The exergy analyses are also based on the MES system and the reference systems have the same assumption of COG and coal, and the same output of quantity of coking heat.

Comparing the exergy distributions of the MES system with those of the reference systems in Table 4, the production outputs of hydrogen and power are increased by 79.1 MW and 3.4 MW. The exergy destruction of gasification (including ASU, gasifier, and cleanup unit) and heat exchanges is decreased obviously, as compared with the reference systems. The exergy destruction for gasification is avoided in the MES system, which is about 56.8 MW (about 6.1 percentage points of input exergy) in the reference systems. Also, the exergy destruction for heat exchangers is decreased from 53.8 MW to 37.4 MW. These give rise to an increased output of MES as compared with single systems.

4 Discussions

The proposed system integrates the thermal cycle, the coking process, and the PSA process. Since the material (COG and coal) and thermal energies can be interchanged in the two sides, there is a big potential to utilize the material and thermal energies more efficiently. In order to reveal the internal phenomena of the key process in the MES system, the graphical exergy analysis with energy utilization diagram (EUD methodology) was adopted [16,17]. The EUD methodology considers that an energy transformation takes place between an energy donating process and an energy-accepting process. It focuses graphically on the energy level difference in a pair of energy donor and energy acceptor, and presents the internal phenomena for exergy destruction graphically. The variations in both the energy level and the energy quantity are graphically shown with A-ΔH coordinates. Here energy level A is a dimensionless criterion ($A=\Delta\varepsilon/\Delta H=1-T_0\times\Delta S/\Delta H$, a ratio of exergy change to energy change), and the energy quantity change ΔH refers to any kind of energy such as thermal energy, power consumption or generation, energy change in chemical reactions, etc. The exergy destruction is equivalent to the shaded area between the energy donor and the energy acceptor.

Table 2 Parameters of the main points of the MES system

Point	G (kg/s)	p (bar)	T (°C)	CH_4	C_2H_6	CO	CO_2	H_2	H_2O	O_2	N_2
				Percent molar composition (%)							
1	144.7	1.03	1030							21	79
2	153.8	1.00	1150				11.6		4.6	7.1	77.6
3	153.8	0.97	120				11.6		4.6	7.1	77.6
4	20.0	1.01	25	20.5	2.4	8.7	2.8	57.3		1.7	6.7
5	20.0	10	38	20.5	2.4	8.7	2.8	57.3		1.7	6.7
6	18.4	1	38	37.7	4.4	16.1	5.2	21.1		3.1	12.3
7	18.4	15.5	366	37.7	4.4	16.1	5.2	21.1		3.1	12.3
8	414.3	15.8	426							21	79
9	432.7	15.0	1288				4.3		7.0	13.1	75.6
10	432.7	15.0	590				4.3		7.0	13.1	75.6

4.1 Significant Role of the Coal-Fired Coke Oven in the MES System. To disclose the role of a coal-fired coke oven in the MES system, we assume that both conventional method and coal-fired coke oven produce coal gas and the same quantity of coking heat. In the MES system, the coal was burned in coal-fired coke oven rather than COG. Therefore, we can gain coking heat and coal gas (COG) without gasification in the new method. In the conventional method, a part of the COG generated by cooking is burned to generate coking heat in the coke oven. And in order to gain that part of the coal gas, the coal burned in the coke oven of the MES system has to be gasified by gasification processes.

Figure 4(*a*) shows the exergy destruction distribution of the combustion of coal in the coal-fired coke oven. In the coking subsystem, the combustion of coal acts as the energy donating reaction (curve A_{ed1}), and the three streams (curve A_{ea1}, A_{ea2}, and A_{ea3}). which act as energy acceptors are the preheating of coal, the preheating of air, and the heating of the coking. The exergy destruction for the combustion of coal in the oven was equivalent to the area between the curves of the energy donor (A_{ed1}) and the energy acceptors ($A_{ea1}-A_{ea3}$), which is 69.2 MW.

Figure 4(*b*) shows the combustion of COG in a conventional coke oven and the exergy destruction distribution of the gasification of coal in the gasifier. Curve A_{ed1} represents the combustion of COG, which acts as an energy donating reaction in the CP system, and three streams (curve A_{ea1}, A_{ea2}, and A_{ea3}) acted as energy acceptors: the preheating of COG and air and the heating of coking chamber. The exergy destruction for the combustion of

Table 3 Results for the new MES system and reference systems

	MES	Reference systems		
		COGP	IGCC	Total of ref.
	Inputs			
COG (MW)	643.1	643.1		643.1
Coal (MW)	276.3		276.3	276.3
	Outputs			
Coking heat (MW)	219.8	219.8		219.8
Hydrogen (MW)	197.2	119.3		119.3
Power (MW)	233.9	109.3	121.2	230.5
Overall efficiency (%)	70.8	69.7	43.9	61.9
Exergy efficiency (%)	66.0	63.3	42.9	57.1
Energy saving ratio[a]	12.5			

[a]The definition of energy saving ratio is $(Q_{ref}-Q_{MES})/Q_{ref}$. The hydrogen production difference between the MES system and the reference systems is supplied by the coal-based hydrogen plant, whose thermal efficiency (LHV base) is about 63%.

Table 4 Exergy balance of the new MES system and reference systems

	MES		Reference systems		
			COGP	IGCC	Total of ref.
		Inputs (MW)			
COG	645.2	69.6%	645.2		645.2
Coal	282.3	30.4%		282.3	282.3
		Exergy destructions (MW)			
Gasification				56.8	56.8
Combustion in oven	69.2	7.5%	65.0		65.0
Combustion in GT	126.8	13.7%	76.5	49.8	126.3
Heat exchangers	37.4	4.0%	36.9	16.9	53.8
PSA unit	12.2	1.3%	8.0		8.0
GT Compressors	11.9	1.3%	6.7	6.0	12.7
Gas turbine	15.2	1.6%	8.1	7.7	15.8
Steam turbine	19.5	2.1%	9.1	14.4	23.5
Exhaust emission	22.5	2.4%	25.6	9.5	35.1
Auxiliaries	0.5	0.1%	0.8		0.8
		Outputs (MW)			
Thermal exergy	178.1	19.2%	178.1		178.1
Power	233.9	25.2%	109.3	121.2	230.5
Hydrogen	200.2	21.6%	121.1		121.1
Total (MW)	927.5	100.0%	645.2	282.3	927.5

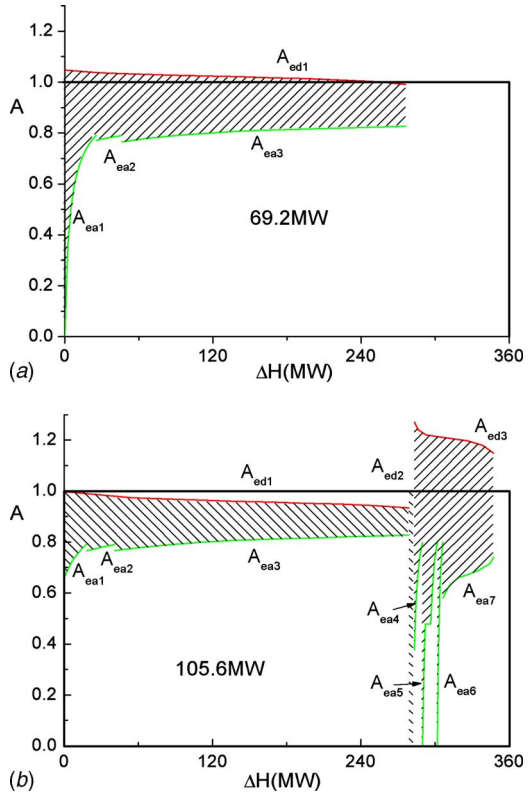

Fig. 4 (*a*) EUD for combustion of coal in coal-fired coke oven and (*b*) EUD for combustion of COG and gasification of coal in reference systems

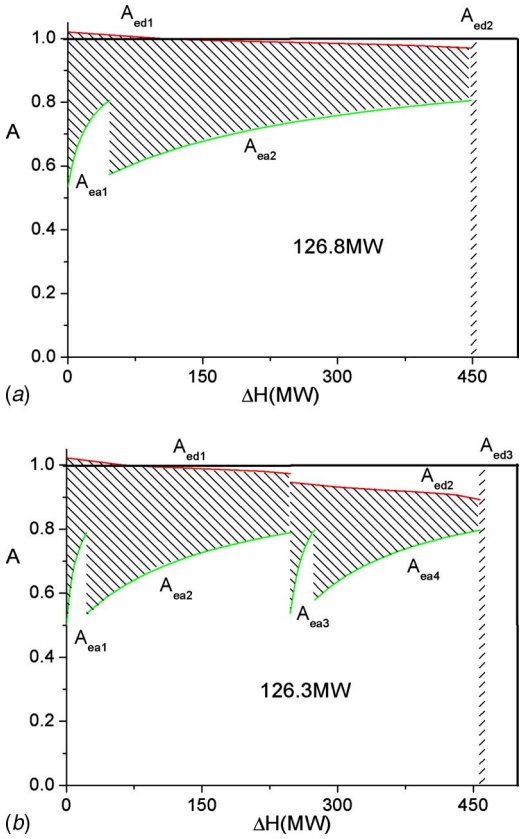

Fig. 5 (*a*) EUD for the combustion of purge gas in MES system and (*b*) EUD for combustion of purge gas and syngas in reference systems

COG is 65.0 MW (the shaded area below the curve of A_{ed1}). The area below the curve of A_{ed2} represents the exergy destruction in the mixing process of air and COG. The curve of A_{ed3} represents the partial combustion in the gasifier, which acts as the energy donating reaction. The energy accepters included chemical reaction (A_{ea7}) and the preheating of three streams of oxygen (A_{ea4}), coal (A_{ea5}), and water (A_{ea6}), which were preheated to the specific gasification temperature of 1346°C. The exergy destruction in the gasifier is 40.6 MW (the shaded area below the curve of A_{ed3}).

Comparing Fig. 4(*a*) with Fig. 4(*b*), notice that the utilization of coal and COG is obviously different. As the partial combustion in the IGCC system needs pure oxygen as an oxidant, the energy level of the partial combustion of coal (A_{ed3} in Fig. 4(*b*)) is higher than that of the burning of coal with air (A_{ed1} in Fig. 4(*a*)) in the coke oven process. Moreover, the thermal energy quantity (ΔH) between the energy donor and the energy acceptor in coal-fired coke oven (279 MW) is also lower than that of the reference methods (348 MW). Affected by these two factors, the exergy destruction of the coal-fired coke oven (the shaded area in Fig. 4(*a*) and 4(*b*)) is decreased from 105.6 MW to 69.2 MW (34.5%). Since both coal and COG are utilized in an efficient way, the performance of the coal-fired coke oven is superior to that of the conventional methods.

In Table 4, notice that the exergy destruction for combustion in both the MES system and the reference systems is the main source of exergy destruction. Figures 5(*a*) and 5(*b*) show the combustion in the combustors of the gas turbines in the MES system and the reference systems, respectively.

Figure 5(*a*) is the EUD for the combustion of PSA purge gas in the MES system. In the CC subsystem, the combustion of PSA purge gas acts as the energy donating reaction (curve A_{ed1}) and the two streams (curve A_{ea1} and A_{ea2}) act as energy acceptors, which are the preheating of fuel gas and air to the specific combustion temperature of 1288°C. The exergy destruction for the combustion of PSA purge gas is equivalent to the area between the curves of the energy donor (A_{ed1}) and the energy acceptors (A_{ea1} and A_{ea2}), which is 126.8 MW. The area below the curve of A_{ed2} represents the exergy destruction in the mixing process of air and PSA purge gas.

Figure 5(*b*) gives the EUD for the combustion of PSA purge gas and syngas (gasified from coal) in the reference systems. Curve A_{ed1} represents the combustion of PSA purge gas in the CC system, and the two streams (curve A_{ea1}, and A_{ea2}) acts as energy acceptors, which are the preheating of fuel gas and air. The exergy destruction for the combustion of PSA purge gas is 76.5 MW (the shaded area below the curve of A_{ed1}). Curves A_{ed2}, A_{ea3}, and A_{ea4} present the burning of syngas in the IGCC system. The exergy destruction for the combustion of coal is 49.8 MW (the shaded area below the curve of A_{ed2}). The area below the curve of A_{ed3} represents the exergy destruction in the mixing processes.

Comparing Fig. 5(*a*) with Fig. 5(*b*), notice that the exergy destruction for the combustion of purge gas in the MES system, which is 126.8 MW, is almost the same as that of the combustion of purge gas and syngas in the reference systems, which is 126.3 MW. According to the former analyses, we can find that the gasification process results in large exergy destruction, which is 56.8 MW. And the exergy destruction of the combustion of the syngas gasified from the coal is 49.8 MW (the shaded area below the curve of A_{ed2} in Fig. 5(*b*)). Therefore, the exergy destruction in the utilization of coal (gasification and combustion) is 106.6 MW in the IGCC system. However, the exergy destruction of the utilization (combustion) of coal in the MES system is only 69.2 MW. Consequently, the coal is used more efficiently in the MES system than that in the IGCC system. Besides, the exergy destruction for the combustion of COG in the MES system is 126.8 MW, which is lower than that in the reference systems, which is 141.5 MW

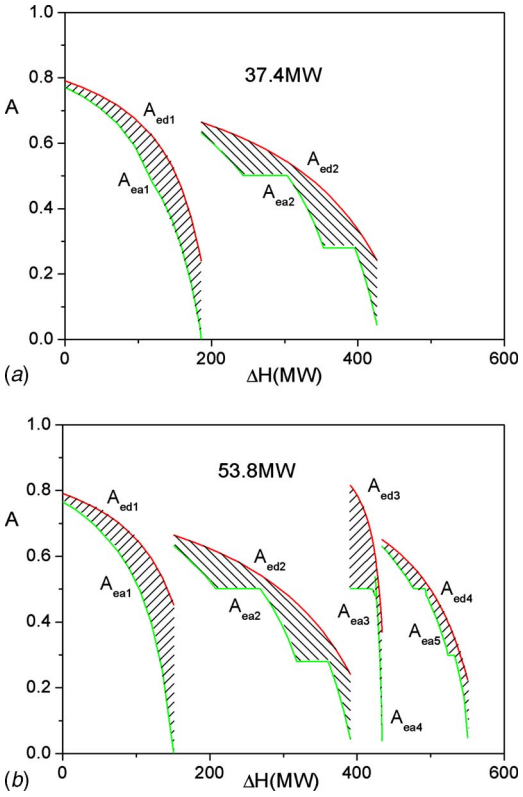

Fig. 6 (*a*) EUD for heat exchanges in MES system and (*b*) EUD for exchanges in reference systems

(the total exergy destruction of the combustion in the COGP system), as shown in Table 3. In a word, both the COG and coal are utilized more efficiently in the new system.

4.2 Thermal Integration of the Chemical Process and the Power Generation System. Figures 6(*a*) and 6(*b*) show the exergy destruction for heat exchanges in the MES system and the reference systems, respectively. In the MES system, the thermal energy released from the coking or the PSA subsystem is recovered by the power subsystem, which means that the thermal energy can be used more efficiently. For example, the surplus quantity of heat of exhausted gas in the oven was used to preheat the water from the steam turbine. The heat exchanges in the MES system are shown in Fig. 6(*a*). The exhausted gas from the oven was used to preheat the air and water in the MES system (curves A_{ed1} and A_{ea1} in Fig. 6(*a*)). The exergy destruction of heat exchange in this process is 14.6 MW, which is equivalent to the area between curve A_{ed1} and curve A_{ea1}. The heat exchanges in the HRSG unit of the MES system were represented by the curves A_{ed2} and A_{ea2}, and the exergy destruction is about 22.8 MW (the shaded area between the curves of A_{ed2} and A_{ea2}).

The heat exchanges in reference systems (COGP and IGCC) are shown in Fig. 6(*b*). In the COGP system, the heat exchanges between the exhausted gas from the oven and the gases (the air and COG) fed to the oven in the reference system (CP) are represented by curves A_{ed1} and A_{ea1}, and the exergy destruction in this process is 18.9MW (the shaded area between the curves of A_{ed1} and A_{ea1}). The heat exchanges of the HRSG unit in the COGP system (CC) are represented by curves A_{ed2} and A_{ea2} in Fig. 6(*b*), and the exergy destruction of this was 18.0 MW (the shaded area between the curves of A_{ed2} and A_{ea2}). In the IGCC system, the heat exchanges are represented by curves A_{ed3}, A_{ed4}, A_{ea3}, A_{ea4}, A_{ea5}, and A_{ea3}. Curves of A_{ed3}, A_{ea3}, and A_{ea4} show the exergy destruction in the raw syngas cooling processes, which is 9.7 MW (the shaded area between the curves of A_{ed3}, A_{ea3}, and A_{ea4}). Curves of A_{ed4} and A_{ea5} represent the heat exchanges of the HRSG unit, and the exergy destruction in this process is 7.2 MW (the shaded area between the curves of A_{ed2} and A_{ea2}).

Table 5 Initial cost of the MES and reference systems

	CP	PSA	CC	IGCC	Total
Ref. systems ($ million)	42.9	10.8	89.6	200.0	343.3
MES ($ million)	55.8	17.8	146.6	-	220.2

In Table 4, notice that the exergy destruction for the heat exchanges in the MES system is decreased by 16.4 MW (about 1.8 percentage points of input exergy) as compared with the reference systems. Comparing Fig. 6(*a*) with Fig. 6(*b*), the average energy level difference between the energy donor and the energy acceptor was decreased from 0.10 in heat exchanges of the reference systems to 0.09 in those of the MES system. Because the coking process and the power plant are integrated into the MES system, the IGCC system is not required, and the exergy destruction in heat exchange processes of the IGCC system is eliminated. So the energy quantities changes ΔH for heat exchanges are decreased from 550 MW to 426 MW. Consequently, the total exergy destruction for heat exchanges is decreased.

4.3 Economic Benefit and CO_2 Reduction. The MES system proposed here is intended for a more effective utilization of COG and coal. In the power subsystem, the conventional steam turbine can be adopted without modification. The gas turbine needs only a little modification in order to adapt to the purge gas, and it is not a technology obstacle [9,18]. For the PSA subsystem, the small and middle scales of the PSA unit are commonly used, but there is still a need to develop a large-scale PSA unit.

For the whole system, the coal-fired coke oven is the key equipment. The structure of the coal-fired coke oven is similar to that of a conventional coke oven except that the fuel burned in the oven is not COG but coal. We can change the structure of the conventional oven to fit the variation in the fuel, or we only need to burn the coal outside the oven, and then send the high-temperature gas to the oven, which will transfer heat to the coking chamber, as cited in Ref. [14]. Since the condition of the coking chamber (the surface temperature of the oven walls) is the same as that in a conventional coke oven, the coking process has no change, but the high-temperature fouling on the wall should be taken into account. Such techniques as the treatment of coal to remove most of the components of sulfur and ash and the proper combustion needed to minimize the fouling should be adopted.

The investment of the conventional coke oven with the output of 2×10^6 tons of coke per year is about $42.9 million. The coal-fired coke oven can be manufactured from the conventional coke oven with little modification. Because of the differences between conventional and coal-fired oven, such as the difference in high-temperature fouling on wall, we assume that the coal-fired oven costs approximately $55.8 million, which is higher by about 30% than that of the conventional coke oven. In Table 5, the investment of PSA, CC, and IGCC is $10.8 million, $89.6 million, and $200.0 million, respectively [19]. Supposing that the scale factor is 0.67 [19] and the cost to treat coal to remove sulfur and ash in the MES system is the same as that in the IGCC, the investment of the PSA subsystem and the CC subsystem in the MES is about $17.8 million and $146.6 million, respectively. Since the investment of gasifier, cleanup unit, and air separation unit, which is about $68 million, is avoided, the total investment of the MES system will be decreased by about 35%, as compared with the reference systems. Even compared with the coal-fired steam power plant, which has lower investment and lower thermal efficiency than the IGCC system, the total investment of the MES system could also be decreased by nearly 14%. It must be noted that the cost estimation is valid only for preliminary analyses.

Table 6 CO_2 emission reduction in the MES system

	CO_2 emission (10^4 tons)
MES system	116
Conventional systems	439 (272[a])
Coke oven	29
COG discharge	231 (35[a])
Power generation	136
Hydrogen product	72
CO_2 emission reduction	323 (156[a])

[a]The COG is discharged after combustion.

Aside from this, with the same input the MES system can produce more hydrogen and power compared with the conventional systems. Therefore, the MES system may gain high economic benefit.

At present, about 300×10^6 tons of coke per year is produced in China, which is more than half of the amount of coke produced in the world. At the same time, about 140×10^9 m^3 of COG per year is produced. Almost half of it is burned through the coking process, and most of the rest passes out to atmosphere directly, or is discharged into air after combusting. Take a coke plant producing 2×10^6 tons of coke per year, for example. It generates 932×10^6 m^3 of COG per year, including 21% CH_4. About 45% of the COG is recycled back to the oven, and about 282,000 tons of CO_2 are generated in this process. If the rest of it passes out to the atmosphere, about 91,500 tons of CH_4 (the greenhouse effect of CH_4 is 21 times higher than that of CO_2), and 101,000 tons of CO_2 and CO are discharge into atmosphere, which are equivalent to 2.02×10^6 tons of CO_2. Therefore, about 2.31×10^6 tons of CO_2 are emitted into atmosphere in the utilization and discharge of the COG.

In order to gain the same quantity of coke, hydrogen, and power as the proposed system, the conventional methods discharge about 4.39×10^6 tons of CO_2 equivalents. However, the proposed MES system only discharges about 1.16×10^6 tons of CO_2. Therefore, the CO_2 emission in the proposed system will be reduced by 3.23×10^6 tons per year as compared with that in the conventional methods with the same outputs, which is shown in Table 6. Besides, the cost of CO_2 avoided is about \$16–28/ton CO_2 in the IGCC systems, and the cost of CO_2 avoided is about \$4–6/tons CO_2 in coal-based hydrogen plants [19]. In order to avoid that part of CO_2, which is avoided without cost in the MES system, some equipment for capture with high investment have to be adopted, and the total cost of CO_2 avoided in the conventional systems is about \$15.6–24.5 million per year.

If half of the coke plants in China are integrated with the proposed system, the CO_2 emission of them will be reduced by 243×10^6 tons per year as compared with the conventional methods. In order to avoid this part of CO_2 emission, the total cost of CO_2 avoided of the conventional methods is about \$1.5 billion per year. In other words, the strong reduction (about \$1.5 billion per year, which is the cost for CO_2) could be achieved only by replacement of half of the existing plants for coke and the relative systems, which are hydrogen production and combined cycle. The reason for the reduction in CO_2 emission is mainly due to energy saving with the effective utilization of COG.

Furthermore, based on the new method (coal-fired coke oven), some different multifunctional energy systems, such as the c-generation of coke, power, and other chemical products (methanol or dimethyl ether), can be synthesized. This kind of coking process can be used as a new method for the utilization of coal. According to cascade conversion of the composition of coal, it gasifies coal partially. And then the COG produced by this process is sent to a new type of MES system, and the coke can be fed to a conventional boiler or burned by pure oxygen with CO_2 capture. This method can produce hydrogen from coal without conventional gasification equipments and utilize coal more efficiently. This will provide a new option for clean coal technology.

5 Conclusions

This paper proposes a new kind of multifunctional energy system, which can utilize COG and coal more effectively through the synthetic utilization of COG and coal by the coal-fired coke oven. With the same inputs of COG and coal, the new system provided about 65% hydrogen more than that of the reference systems, when almost the same quantity of coking heat and power was generated. Based on the integration of chemical processes and the power generation system, the fuel and thermal energy were utilized efficiently from the viewpoint of the whole system. The graphical exergy analyses (EUD methodology) revealed that the COG and coal were utilized synthetically through the coal-fired coke oven. The new method allows for the elimination of gasification processes. Compared with the conventional methods, the exergy destruction of gasification, which accounts for 6.1% corresponding to the input exergy of the system, is avoided. The exergy destructions for heat exchangers were decreased by 30%, which accounts for 1.8% corresponding to the input exergy of the system. The proposed MES system provides a new method to utilize coal and COG synthetically, which does not only simplify the system and decrease the investment, but also improves the thermal efficiency and reduces CO_2 emission. Furthermore, it will provide a promising option for sustainable energy systems.

Acknowledgment

This study is supported by the NSFC Project No. 50836005 and the China National Key Projects (Project No. 2005CB221207).

Nomenclature

A = energy level
G = mass flow rate
H = enthalpy
P = pressure
Ref. = reference systems
S = entropy
T = temperature
ε = exergy

References

[1] Xie, K., 2005, *Focus on Coal Chemical Engineering*, Chemical Industry, Beijing.
[2] BP Group, 2005, "BP Statistical Review of World Energy."
[3] Nexant, Inc., 2006, "Multi-Client Study Prospectus: Polygeneration From Coal Integrated Power, Chemicals and Liquid Fuels," Nexant Report.
[4] U.S. DOE, 2003, "Early Entrance Co-Production Plant," U.S. DOE Technical Report No. DE-FC26-00NT40693.
[5] Onozaki, M., Watanabe, K., Hashimoto, T., Saegusa, H., and Katayama, Y., 2006, "Hydrogen Production by the Partial Oxidation and Steam Reforming of Tar From Hot Coke Oven Gas," Fuel, **85**, pp. 143–149.
[6] Jin, H., Han, W., and Gao, L., 2007, "Multi-Functional Energy System (MES) With Multi Fossil Fuels and Multi Products," ASME J. Eng. Gas Turbines Power, **129**(2), pp. 331–337.
[7] Gray D., and Tomlinson G., 2002, "Hydrogen From Coal," Mitretek Technical Paper No. MTR 2002-31.
[8] Sun, S., Gao, L., Jin, H., and Lin, R., 2007, "System Study on Polygeneration System for Methanol and Power Production Based on Coke Oven Gas and Coal Gas," Proceedings of the ECOS2007, Padova, Italy, Jun., pp. 1009–1016.
[9] Lozza, G., and Chiesa, P., 2002, "Natural Gas Decarbonization to Reduce CO_2 Emission From Combined Cycles—Part II: Steam-Methane Reforming," ASME J. Eng. Gas Turbines Power, **124**, pp. 89–95.
[10] Hemmes, K., Zachariah-Wolff, J. L., Geidl, M., and Andersson, G., 2007, "Towards Multi-Source Multi-Product Energy Systems," Int. J. Hydrogen Energy, **32**, pp. 1332–1338.
[11] Cai, R., Lin, R., Xiao, Y., and Xu, D., 1993, "Coal-Fired Combined Cycle Power Generation Technology With High Efficiency, Low Pollution, and Low Water Consumption," UNESCO, Senior Conference of Cleaning Coal-Fired Technology in China, Beijing, China.
[12] Ni, W., Li, Z., and Xue, Y., 2000, "Polygeneration Energy Systems Based on Coal Gasification, Energy and Environment," Eng. Sci., **2**(8), pp. 59–68.
[13] Gao, L., Jin, H., and Liu, Z., 2004, "Exergy Analysis of Coal-Based Polygen-

eration System for Power and Chemical Production," Energy, **29**, pp. 2359–2371.
[14] Jin, H., Sun, S., and Gao, L., 2006, "The Technology of a Novel Coal-fired Coke Oven," China Patent No. 200610089586.9.
[15] Yan, X., 1997, "Test and Measurement of the Model JN60-82 Coke Oven," Gas & Heat, **17**(4), pp. 10–16.
[16] Ishida, M., and Kawamura, K., 1982, "Energy and Exergy Analysis of a Chemical Process System With Distributed Parameters Based on the Energy-Direction Factor Diagram," Ind. Eng. Chem. Process Des. Dev., **21**, pp. 690–702.
[17] Jin, H., and Ishida, M., 1993, "Graphical Exergy Analysis of Complex Cycles," Energy, **18**(6), pp. 615–625.
[18] Chiesa, P., Lozza, G., and Mazzocchi, L., 2005, "Using Hydrogen as Gas Turbine Fuel," ASME J. Eng. Gas Turbines Power, **127**, pp. 73–80.
[19] Metz, B., Davidson, O., Coninck, H., Loos, L., and Meyer, M., 2005, "IPCC Special Report on Carbon Dioxide Capture and Storage."

Implications of Turbine Erosion for an Aero-Engine's High-Pressure-Turbine Blade's Low-Cycle-Fatigue Life-Consumption

Muhammad Naeem
Institute of Space Technology (IST),
P.O. Box 2750,
Islamabad 44000, Pakistan

Some in-service deterioration in any mechanical device, such as a military aero-engine, is inevitable. As a result of experiencing any deterioration, an aero-engine will seek a different steady operating point thereby resulting in a variation in the high-pressure spool speeds in order to provide the same thrust to keep aircraft's performance invariant. Any increase in the high-pressure spool speed results in greater low-cycle fatigue damage for the hot-end components and thereby higher engine's life-cycle costs. Possessing better knowledge (of the impacts of high-pressure turbine's erosion upon the low-cycle fatigue life-consumption of aero-engine's hot-end components) helps the users to take wiser management decisions. For a military aircraft's mission profile, using bespoke computer simulations, the impacts of turbine erosion for high-pressure turbine-blade's low-cycle fatigue life-consumption have been predicted. [DOI: 10.1115/1.3078383]

1 Introduction and Background

High-performance aircraft, as used in modern aviation, especially for military purposes, are complex in design and are required to operate under severe stresses and temperatures [1]. Thus designer and users of these aircraft continually seek greater reliability, increased availability, enhanced performance, and improved safety as well as low life-cycle costs. In-service costs consist mainly of those associated with [2] (i) the fuel consumed during the operation, and (ii) the replacement of the system's components. Therefore any extensions of life expectations or reductions in fuel-usage of aero-engines directly lower the life-cycle costs and depend on the types of operation or mission undertaken, operating conditions experienced, and rate of in-service aero-engine deterioration.

Some in-service deterioration in any mechanical device, such as a military aero-engine, is inevitable. Several publications describe engine-performance deterioration. A preliminary investigation regarding the impacts of aero-engine's deteriorations on military aircraft mission's effectiveness established that there is a significant adverse impact of aero-engine deteriorations. It also indicated that the extent of adverse impacts varies with the type of aero-engine's component. Among the major aero-engine's components, low-pressure compressor (LPC) being the overall severest followed by high-pressure turbine (HPT) [3]. This necessitated the need for a comprehensive investigation for the impacts of LPC's fouling as well as of HPT's erosion. Hence this investigation was undertaken. The impacts of LPC's fouling have already been investigated [4–6].

There are many components in a gas-turbine engine, but its performance is highly sensitive to changes in only a few. The majority of these potentially sensitive parts are the rotating components. Among these the HPT blades are the most sensitive components, because they are subjected to both the highest rotating speeds and gas temperatures [3] and so have been selected for present investigation.

Manuscript received May 6, 2008; final manuscript received December 1, 2008; published online May 22, 2009. Review conducted by David Walls.

2 Performance Deterioration of Gas Turbines

In an ideal world, an engine would operate with the same performance from the time it enters service until it is removed. This of course does not happen in reality as the engine will deteriorate. There is very little reliable quantitative data on the magnitudes of performance deterioration of engine components as their service lives are extended, except for that in the papers written by Grewal [7], Sallee and co-workers [8,9], and Saravanmutto and co-workers [10,11]. Sallee's [8] paper pertains to studies conducted on the "Pratt and Whitney JT9D family of engines." Sallee [8] produced several performance deterioration mathematical models for the JT9D engine's behavior. These models show that the performance-loss mechanisms are associated with the following.

(a) The compressors cause reductions in both flow capacity and efficiency.
(b) The turbines result in a flow capacity increase and an efficiency fall.

3 Erosion

This, in the present context, is the abrasive removal of material from the flow-path components by hard particles suspended in the gas stream. As a result, the gas-turbine's aerofoil blades become eroded, some of the leading edges blunted, the trailing edges thinned and the surface roughness increased. It also causes losses of the blades' camber and length, as well as of the seal material. Erosion of the aerofoil also occurs as a result of the engine's ingestion of foreign particles. The rate of foreign particle entry will be greatly influenced by the engine-intake design. This is particularly evident with aircrafts such as the General Dynamics F-16 whose intake acts as a large air scoop and is located below the belly of the aircraft in contrast to the Russian MIG 29. When the MIG 29 is on the ground, the main intakes are blocked off and flow is directed to the engines through open doors located on top of the aircraft [12]; these doors are shut after take-off.

The erosion of aerofoil's profile leads to changes in the aerofoil's inlet angle and throat opening. The consequent widening of the tip and seal clearances results in increased air-leakage losses [2].

4 High-Pressure Turbine Performance-Deterioration

The performance-loss mechanisms, which cause the majority of HPT deteriorations, are (i) blade-tip clearance increases and (ii) vane twisting and bowing. Increased clearances between the rotor blades and the casing are caused predominately by centrifugal and thermal loads imposed during engine transients and by distortions of the engine casing as a result of changing flight loads [12]. Vane distortion ensues as a result of both aerodynamic loads and from stresses due to thermal gradients. As the vanes distort, coolant air is allowed into the main gas stream resulting in a reduction in the turbine's efficiency [2]. Bowing of the HPT's vanes causes the flow area to increase and hence an increase in the flow capacity [13].

5 Potential-Failure Modes

The major ones for turbine components are creep, mechanical fatigue, i.e., low-cycle fatigue (LCF) and vibration induced high-cycle fatigue (HCF), thermal fatigue, oxidation, and sulphidation. At temperatures below approximately 800°C, mechanical fatigue is usually the dominant failure mode. At higher temperatures, i.e., above about 1000°C, creep, oxidation, and thermal fatigue (acting alone or together) usually cause failure. In the intermediate temperature range, any of the several failure modes described can be dominant, depending on the structure, the material, and the engine cycle employed. Despite possible interactions of the major failure modes, a region of available life of the component does exit [14].

6 Low-Cycle Fatigue

This is caused by the imposition of varying loads (and hence stresses) on a component of an aero-engine. LCF occurs after relatively low numbers (typically $<50{,}000$) of cycles of high-stress amplitude. Due to the high-stress levels implicit in LCF, it is normally accompanied by plastic deformation and is often termed "high-strain fatigue," as plastic strain is the primary parameter governing life. For a military-fighter aircraft's engine, LCF is probably the most significant life-reducing failure-mechanism and is the direct result of the many throttle changes experienced during this application. In general, the engine components that are subject to LCF are also those that are unlikely to be contained (because of the normally very high rotational speeds and thereby damage occurring to components down stream) in the event of a fatigue failure. It is these that are critical to flight safety and should be monitored.

In the 1960s, most critical components were limited by creep and stress rupture properties. Less than 1% of all rotating components were life limited by LCF. However, today's designs find well over 75% of these components limited in life by LCF [15].

7 Factors Affecting LCF Life Usage in Military Aviation

There is a wider spectrum of usage for military aero-engines because military aircrafts fly a greater variety of mission profiles than civil airliners. It is rare for a modern military plane to be restricted to a single role. This, together with the need to maintain crew proficiency in various aspects of their roles, means that many different mission profiles are flown regularly.

The large throttle movements necessary to exploit fully the performance of military aircraft also have a dramatic impact on LCF life consumption. It should be remembered that the relationship between applied stress and remaining life is logarithmic, and that mechanical stress imposed on the engine varies as the square of its rotational speed. Therefore, a modest increase in the range of throttle movement can have a drastic impact on the fatigue-life consumed.

There can also be huge variations in the engine usage on what are nominally-identical missions. In formation flying, the throttle usages for the lead aircraft and the one at the rear of the formation and also the LCF life usage between the engines of these two aircrafts differ by an order of magnitude [16]. In addition, there is evidence of large variations in throttle handling that may occur between different pilots flying the same mission even using the same aircraft type. May et al. [17], after studying several United States Air Force missions flown in F15, F5, and A10 aircrafts, concluded that different pilots made significantly different usages of the throttle while flying the same mission. This led to a variation by a factor of as much as 5 in the number of idle-maximum power-idle throttle-excursions per sortie. Consequently, efforts to develop LCF life-usage monitoring have primarily been focused on military operations in order to achieve economic lives in this highly-demanding environment without compromising safety.

8 Aircraft Gas-Turbine Engine LCF Life-Consumption

It is necessary to carry out two steps to ensure that the useful lives of critical components are not exceeded. The first is the setting of an accurate life expectancy. The second is a means for determining and controlling the rate of life consumption in actual service.

The fatigue-damage calculation algorithm can be analyzed in the following three discrete steps [2].

(1) Determine the number of load cycles already completed from the measured values of the pertinent engine parameters.
(2) Calculate the fatigue damage incurred during each individual load-cycle.
(3) Estimate the total life consumed by summing up the damage incurred during each individual load-cycle.

9 Cycle Counting Methods

LCF damage of an aero-engine results from the application of varying loads. In order to determine these loads, it is necessary to relate them to measurable engine parameters. For example, the centrifugal stresses in a place can be determined [18] via

$$S_i = S_{\text{ref}} \left[\frac{\Phi_i}{\Phi_{\text{ref}}} \right]^2 \tag{1}$$

An essential step in the prediction of fatigue life is the reduction of service strain or stress history to a series of cycles and half-cycles. This process is known as the cycle-counting method. Various methods have been developed to identify the individual cycles from a complex loading-history. One of the early cycle-extraction methods was the Range–Mean method. In an attempt to overcome the problems inherent in the Range–Mean and similar counting methods, as discussed in more detail by Dowling [19], various alternative methods have been proposed, which share the following two characteristics.

(1) Each part of the overall history is counted only once.
(2) Smaller ranges are counted down to a predetermined threshold.

Probably the most widely-used method is the rain-flow, or the Pagoda-roof, method first developed by Matsuishi and Endo [20] and then subsequently by others [19,21,22]. For a more complete description of the rain flow method, the reader is referred to Refs. [19,21]. The same method was used for the present investigation.

10 Low-Cycle Fatigue-Damage Calculation

The chosen cycle-counting technique will transform the complex load history into a succession of stress ranges about a mean stress. The next stage in the algorithm process is to calculate the actual fatigue damage caused by each individual cycle.

Two important methods for calculation of LCF damage are the stress-life and strain-life methods [2]. However, due to the concept of LCF as high-strain fatigue, the strain-life method is generally considered to be more appropriate. First, the nominal cen-

trifugal stress is calculated at each measured value of spool speed using Eq. (1). Then the local stress and strain at the notch for the first applied nominal stress is calculated using Neuber's rule (Eq. (2)) and the cyclic stress-strain curve (Eq. (3)), which may be combined to give Eq. (4) [23], as follows:

$$K_t^2 = \frac{\sigma}{S}\frac{\varepsilon}{e'} \tag{2}$$

$$\varepsilon = \frac{\sigma}{E} + \left[\frac{\sigma}{K'}\right]^{1/n'} \tag{3}$$

$$\left[\frac{\sigma^2}{E}\right] + \sigma\left[\frac{\sigma}{K'}\right]^{1/n'} = \frac{(K_t S)^2}{E} \tag{4}$$

For subsequent load-applications, the local delta stress is calculated by combining Eq. (2) with the hysteris stress-strain rule of Eq. (5) to give Eq. (6) [23].

$$\frac{\Delta\varepsilon}{2} = \frac{\Delta\sigma}{2E} + \left[\frac{\Delta\sigma}{2K'}\right]^{1/n'} \tag{5}$$

$$\frac{(\Delta\sigma)^2}{2E} + \Delta\sigma\left[\frac{\Delta\sigma}{2K'}\right]^{1/n'} = \frac{(K_t\Delta S)^2}{2E} \tag{6}$$

The local notch stress can be deduced by adding $\Delta\sigma$ to the value of σ at the origin of the hysteris loop, and the local strain range $\Delta\varepsilon$ can be determined from

$$\Delta\varepsilon = \frac{(K_t\Delta S)^2}{\Delta\sigma E} \tag{7}$$

This value of local strain range is then inserted into the strain-life Eq. (8) to determine the cyclic life N_f, as follows:

$$\frac{\Delta\varepsilon}{2} = \frac{\Delta\varepsilon_e}{2} + \frac{\Delta\varepsilon_p}{2} = \frac{\sigma_f}{E}(2N_f)^b + \varepsilon_f(2N_f)^c \tag{8}$$

Equation (8) can be modified to account for the mean stress effects by including the mean stress σ_0 in the elastic strain term as proposed by Morrow [24]. This leads to

$$\frac{\Delta\varepsilon}{2} = \frac{(\sigma_f - \sigma_0)}{E}(2N_f)^b + \varepsilon_f(2N_f)^c \tag{9}$$

The final step is to sum up the damage arising during each individual cycle. Several researchers have presented theoretical syntheses for predicting the cumulative damage. The most common and well known is the Palmgren–Minor cumulative damage law [25] expressed as

$$\frac{n_f}{N_f} = \frac{n_1}{N_1} + \frac{n_2}{N_2} + \frac{n_3}{N_3} + \cdots \tag{10}$$

When the value n_f/N_f, becomes unity, the component is considered to have failed. In reality, component failure occurs at ratios of between 0.61 and 1.49 [26]. As pointed out in the ESDU paper on fatigue-life estimation [23], although the Palmgren–Minor law may be considered inaccurate in some respects, it is simple and has been widely applied, and the reasons for its inadequacies are recognized and can be compensated for in the design process.

11 Computer Modeling and Simulations

Because of the enormous cost reductions and rapid results achieved relative to experimental/trial techniques, the use of validated computer-simulation techniques has attained recently the status of an advanced engineering procedure. Many scenarios can be simulated without incurring the major difficulties and expenses of preparing and testing engines. Hence the implications of various factors such as variations in deteriorations for engine as a whole or either of its major components, changes in operating environment, etc., on engine performance can be studied and appreciated before they are encountered in service. The more accurate the simulation, i.e., preferably being based on actual measured data, the more realistic will be the predictions achieved.

For the purpose of the present investigation the "Engine's Performance-Simulation Program (NAEEMPAK)," "Aircraft's Flight-Path and Performance-Simulation Program," "Aircraft and Engine's Performance-Simulation Program (NAEEMPAKA)," and "Low-Cycle Fatigue Life-Usage Prediction Program (NAEEMPAKB)" have been used. These programs were developed by the author while completing his Ph.D. at the Cranfield Unversity, UK, and are proprietary to the author. The programs were further enhanced and tailored to accomplish the present task.

NAEEMPAK is basically an updated version of the engine-performance simulation program TURBOMATCH. TURBOMATCH has been used widely at the Cranfield University for many years. It facilitates design point and off-design performance calculations and has the ability to simulate the behavior of an engine and the effects of implanted faults in its components, for instance, a reduction in component efficiency or mass flow capacity. It is based on the aero- and thermodynamic balancing of the gas turbines, using the method of component matching in which the compatibilities of the flow between the various compressors and turbines are determined.

The Aircraft's Flight-Path and Performance-Simulation Program integrates the simulation of each flight stage to give a complete mission profile for the military aircraft. Details regarding aircraft's performance throughout the mission profile, as described in referred publications [2,27,28], formed the basis for development of this program.

NAEEMPAKA is basically a combination of NAEEMPAK and the aircraft's flight path and performance-simulation program. This program simulates the flight path of the military aircraft. The NAEEMPAK supplies the engine's net thrust and specific fuel-consumption values to the aircraft's flight path and performance-simulation program, so enabling the pertinent flight parameters to be evaluated for each flight-stage. It requires data for (i) the engines, (ii) the geometric and aerodynamic characteristics of the aircraft, and (iii) the mission profile. These inputs are defined by the user through separate input files.

NAEEMPAKB has been used for the purpose of LCF life evaluation [2]. The strain-life technique (as described (very briefly) earlier) has formed the basis for the development of this computer program. Program requires data for (i) the engine's design and blade material (defined by the user through a separate file) and (ii) high-pressure spool speed (HPSS) history (obtained from the NAEEMPAKA).

12 HPT Blade's Material

Despite a wide literature review the author was unable to determine the exact type and specification of the material used for HPT's blades of the F404 engine. Therefore, it was decided to assume any of the typical materials (such as MAR M002, INCO 792, INCO 713, INCO 718, NIMONIC 75, NIMONIC 80A, NIMONIC 115, etc.) used for manufacturing of turbine's blade. During literature review to determine the material properties required for predicting the LCF life (for the method chosen), the author could only find the relevant data for INCO 718, hence this material was used for the present investigation. The relevant LCF properties for INCO 718 are shown in Table 1.

13 Aircraft and Engines Chosen

For this investigation, the performance of a McDonnell Douglas F-18 aircraft, powered by two nominally-identical F404-GE-400 aero-engines, has been assessed. The reason for selecting the F404 was twofold. First, the F404 engine is a typical new-technology engine, and, as such, the results of the investigation will be applicable to other similar new-generation engines. Second, sufficient relevant data were available.

Table 1 Fatigue properties for the INCO 718

Fatigue property	Numerical value
Young's modulus	158×10^9
Cyclic strength coefficient	1433×10^6
Cyclic strain coefficient	0.0945
Fatigue strength coefficient	1311×10^6
Fatigue strength exponent	−0.0596
Fatigue ductility coefficient	0.389
Fatigue ductility exponent	−0.631
Endurance strain	0.001

14 Assumed Mission-Profile

In general, unlike those for civil aircraft, the mission profiles for military aircrafts can be relatively complex. However, for the purpose of the present analysis, the following (a relatively simple) aircraft mission profile has been assumed:

(1) short take-off (TO) with reheat (RH) on, followed by climbing after TO, from sea level to 6000 m (m), while accelerating to Mach number (M) 0.6 within 420 s (s)
(2) climbing from 6000 m to 8000 m while accelerating from M 0.6 to 0.7 in 250 s
(3) climbing at a constant M 0.7, from 8000 m to 10,500 m in 100 s, followed by acceleration (ACC) from M 0.7 to 1.0 within 100 s
(4) cruising at 10,500 m and M 1.0 until a preset time (1800 s from take-off) followed by deceleration to M 0.95 within 60 s
(5) enhancement of engines' power to 80%, attaining and then cruising at maximum M (for total time duration of 900 s) followed by acceleration/deceleration to M 0.85 within 60 s
(6) cruising at 10,500 m and M 0.85 for a set time period of 900 s followed by cruising to cover a distance of 500 km (km)
(7) accelerating as a result of RH for 60 s, followed by decelerating by switching off the RH, to M 0.85 within 200 s
(8) descending at a constant M 0.85, from 10,500 m to 8000 m within 300 s, followed by cruising toward a set target at 3000 km from home base
(9) descending from 8000 m to 4500 m while decelerating to M 0.5 within 250 s, followed by loitering for 100 s
(10) descending to land within 350 s, followed by landing approach, flare, touch down, ground roll, and finally switch-off

15 Undertaking the Computer Simulation

The basic methodology is to fly the aircraft through a complete mission-profile with (i) both engines functioning properly and (ii) with both engines suffering identical prescribed degrees of HPT's erosion. Subsequently the NAEEMPAKB is run using the results of the NAEEMPAKA along with relevant material data as inputs. Thus the LCF life usage is predicted for each flight, so determining the impacts of the HPT's erosion on the LCF life usage as a function of the aircraft's flight path.

The relationship between physical degradation and simulated degradation is realized by choosing certain ratios between component efficiency and mass flow capacity degradations. Sallee and co-workers [8,9] described how the efficiency and mass flow capacity are affected by the engine configuration and degradation. Although several publications have described different HPT's efficiencies to mass flow capacity deteriorations ratios, as yet, precise performance-parameters change due to typical faults in the engine's components and their inter-relationships are not known accurately [29]. The exact ratios chosen can be open to some individual subjectivity and so it was worthwhile establishing the values of their ratios commonly concluded from the previous research [2]. Hence, for this assessment, a single-term empirical "erosion index (EI)" was defined to describe the effect of the reduction in efficiency as well as the increase in mass flow capacity of HPT. For example, for an erosion model (EM) 1:0.5 (i.e., HPT's efficiency to mass flow capacity deteriorations' ratio), an efficiency of 96% and a flow capacity of 102% of those for a clean engine may be described as 4% EI. As the erosion usually starts from irregular pits and crevices randomly distributed on the blade contour, its effects on the turbine performance are insignificant initially. Therefore more severe erosion damages, which noticeably influence enough the turbine performance, have been considered. As such, for the purpose of the present analysis, the effects of EM 1:0.5 for the following set of engine conditions have been assessed:

- clean engines (i.e., a HPT's EI of zero for the both engines)
- HPT's EI of 1%, 2%, 3%, … or 6% for the both engines

The effects of varying proportions of HPT's mass flow capacity deterioration for a given HPT's efficiency deterioration level have been also assessed by considering EMs 1:0.25, 1:0.5, 1:0.75, 1:1, 1:1.5, 1:2, 1:3, and 1:4.

For the purpose of the present analysis, HPT's EI of 6% is considered an outage for military operations, i.e., the breaking down of a component and thereby stopping the further use of machine (aero-engine in this case) until an appropriate replacement or repair is undertaken [2].

16 Discussions and Analysis of Results

The aim of the present investigation is to quantify the impacts of a military aircraft's turbofan HPT's erosion on the blade's LCF life-consumption for a specified mission profile. An important factor, which needs to be realized when examining the results, is that the numerical values for the effects of HPT's erosion are not definitive but nevertheless are considered good "ball park" figures. In addition, the trends of the effects are important as they provide insight into how the engine behaves.

The prime factor responsible for any change in the HPT blade's LCF life-consumption is the variation in the HPSS. A higher HPSS results in greater LCF damage and thereby higher blade's LCF life-consumption. The variations in HPT's erosion levels would require the engine(s) to run at different HPSS and/or turbine entry-temperatures (TETs) in order to meet the thrust requirement for achieving the same aircraft's performance.

17 Aero-Engine's Behavior

Any mission profile would always be a combination of altitude, M, and engine power setting. Therefore, prior to an overall analysis of HPT blade's LCF life-consumption, it was considered appropriate to first see how the concerned engine parameter is affected by any variation in altitude/M/day temperature/engine power setting or any combination of these. For the purpose of the present investigation, day temperature variations have been expressed in terms of the international standard atmosphere deviation (ISAD) (i.e., an ISAD of 0 K for a standard day temperature of 15°C and ISAD of −15 K and 35 K for day temperatures of 0°C and 50°C, respectively). All HPSS and maximum high-pressure spool speed (MHPSS) values have been expressed as percentage of its design point value. The results are analyzed in subsequent paragraphs.

Figures 1–7 illustrate the variation in HPSS with increasing altitude/M/ISAD/TET/HPT's erosion, and at constant LPSS/NT conditions (with increasing HPT's erosion) for stipulated HPT's EMs, and with increasing HPT's flow capacities for a given HPT's efficiency level, respectively. A critical analysis establishes the significant and clear variation trends of HPSS for different sets of stipulated conditions.

With increasing altitude, for the same levels of M, TET, and ISAD, the HPSS increases very slightly but linearly within the

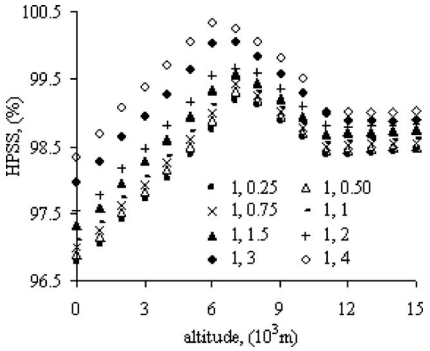

Fig. 1 HPSS at M 0.95, TET 1555 K, and ISAD 0 K for stipulated HPT EMs with increasing altitude

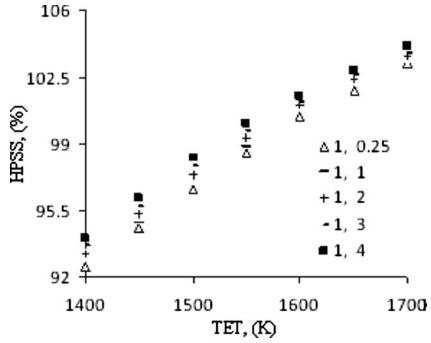

Fig. 4 HPSS at an altitude 10,000 m, M 0.95, and ISAD 0 K for stipulated HPT EMs with increasing TET

stratosphere. However, within the troposphere it varies significantly following a clear variation trend (i.e., an almost linear increase until reaching its peak at about 6000 m altitude and subsequently an almost linear reduction until the end of the troposphere) (see Fig. 1). With an increase in M/ISAD, the trend in variations within the troposphere remains almost the same but the whole pattern drifts toward the right, i.e., in the direction of increasing altitude, whereas with an increase in TET, it drifts toward left. At a given altitude, HPSS is significantly less at lower TET levels [30].

With increasing M, for the same levels of altitude, TET and ISAD, the HPSS initially increases with slightly increasing rate, then linearly followed by a decreasing rate reaching its peak at about M 1.3 and subsequently reduces almost linearly (see Fig. 2). With an increase in altitude/TET, the whole pattern drifts toward the right (i.e., in the direction of increasing M), whereas with an increase in ISAD, it drifts toward left [30].

With increasing ISAD, for the same levels of altitude, M, and TET, the HPSS initially increases almost linearly followed by a decreasing rate until reaching its peak value and subsequently reduces with slightly increasing rate (see Fig. 3). With an increase in altitude/TET, the trends of variation remain almost the same but whole pattern drifts toward the right (i.e., in the direction of increasing ISAD), whereas with an increase in M, it drifts toward left [30].

With increasing TET, for the same levels of altitude, M, and ISAD, the HPSS increases significantly and with slightly decreasing rate (see Fig. 4). At lower TET levels, the HPSS at lower ISAD/M, at higher altitude, and for engines without RH are higher, whereas at higher TET levels, the HPSS at higher ISAD/M, at lower altitude, and for engines with RH are higher. HPSS is higher for engines without RH at TET levels lower than the design point, whereas it is lower for engines without RH at TET levels higher than the design point [30].

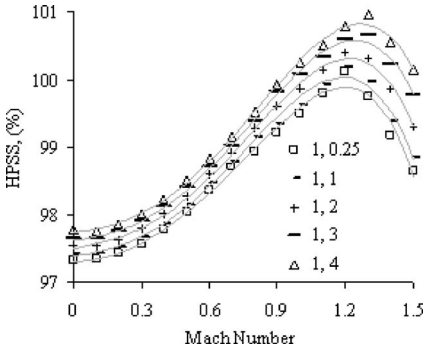

Fig. 2 HPSS at an altitude 10,000 m, TET 1555 K, and ISAD 0 K for stipulated HPT EMs with increasing M

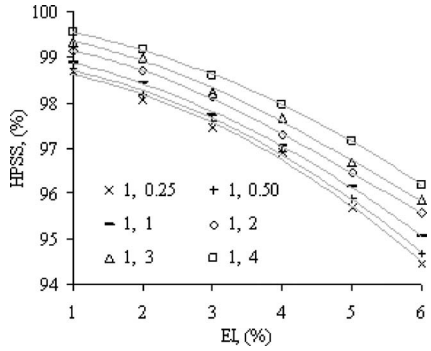

Fig. 5 HPSS at an altitude 10,000 m, M 0.95, TET 1555 K, and ISAD 0 K for stipulated HPT EMs with increasing HPT's erosion

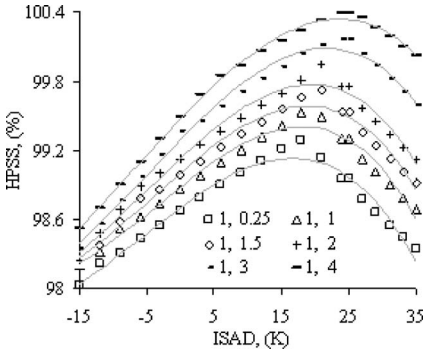

Fig. 3 HPSS at an altitude 10,000 m, M 0.95, and TET 1555 K for stipulated HPT EMs with increasing ISAD

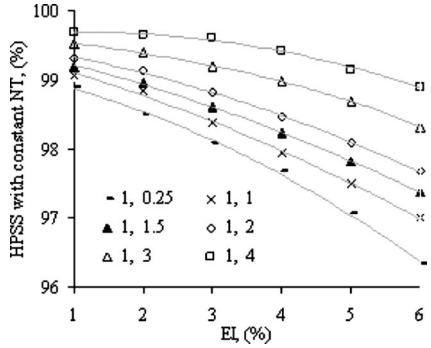

Fig. 6 HPSS at an altitude 10,000 m, M 0.95, ISAD 0 K, and constant NT for stipulated HPT EMs with increasing HPT's erosion

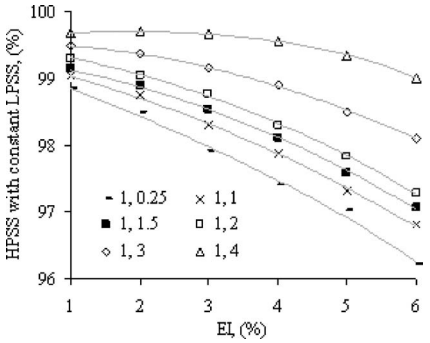

Fig. 7 HPSS at an altitude 10,000 m, M 0.95, ISAD 0 K, and a constant LPSS for stipulated HPT EMs with increasing HPT's erosion

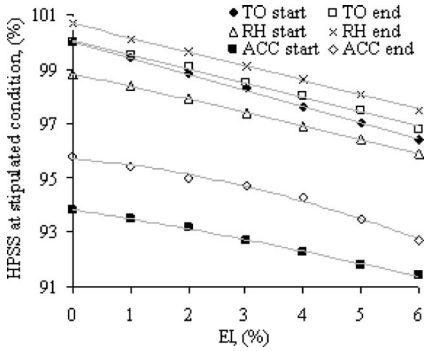

Fig. 9 HPSS at stipulated conditions with increasing HPT's erosion

With increasing HPT's erosion, for the same levels of altitude, M, TET, and ISAD, the HPSS decreases significantly and with slightly increasing rate (see Fig. 5).

With increasing HPT's erosion, for the same levels of altitude, M, and ISAD, the HPSS decreases with slightly increasing rate for constant net thrust (NT) and low-pressure spool speed (LPSS) conditions considered separately (see Figs. 6 and 7). However, this is accompanied with significant variations in TET.

At the same conditions, HPSS is significantly higher for higher HPT's flow capacities for a given HPT's efficiency level (see Figs. 1–7). However, with increasing flow capacity levels, its peak value slightly drifts toward the left with increasing altitude, whereas it slightly drifts toward the right with increasing M/ISAD (see Figs. 1–3).

18 Aero-Engine: Aircraft Combination's Behavior

For the purpose of subject investigation, while the aircraft flies through the assumed mission profile, in addition to the behavior of fitted aero-engines in isolation, the behavior of aero-engines' and aircraft's aerodynamic structure combination as a whole is of greater importance. During flight segments such as TO and combat/RH phases, the aero-engines' peak performance plays the dominant role and the aircraft performs according to the maximum available NT from the engines. Whereas during some other flight segments, e.g., cruising at a specified altitude and M, the aircraft's aerodynamic characteristics play the dominant role and aero-engines are run at a power setting such that the NT available from the engines balances the aircraft's drag. Therefore, the engine parameter of concern, i.e., HPSS/MHPSS, has been also observed during some important flight segments and results analyzed in subsequent paragraphs. Finally the aero-engine's HPT blade's LCF life-consumption has been predicted for the complete mission profile.

Figures 8–13 illustrate (i) HPSS during TO, RH, and ACC phases for a given EM and HPT's erosion; (ii) HPSS at the start and end of TO, RH, and ACC phases for a given EM but with increasing HPT's erosion; and (iii) MHPSS during TO, ACC, RH, and enhancement of power to 80% followed by cruising at constant power setting flight phases for the stipulated EM but with increasing HPT's erosion, respectively. A critical analysis establishes a significant variation (with differing variation trends) in HPSS/MHPSS during different flight phases as well as for different points on the mission profile with varying EMs and HPT's erosion levels.

For the conditions assumed for the present investigation, for a given HPT's EM and with the same HPT's erosion levels, HPSS (i) increases initially with a decreasing rate, however, subsequently remains almost invariant during TO; (ii) increases with slightly increasing rate during RH; and (iii) reduces initially with a slightly decreasing rate, reaches minimum value, and then starts increasing with slightly increasing rate (i.e., there is a dip) during ACC (see Fig. 8).

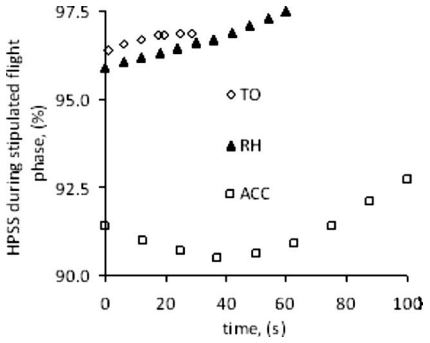

Fig. 8 HPSS during stipulated flight phase

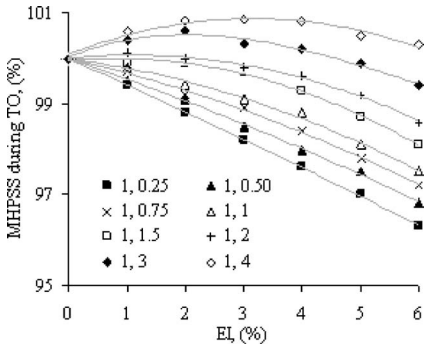

Fig. 10 MHPSS during TO for stipulated EMs with increasing HPT's erosion

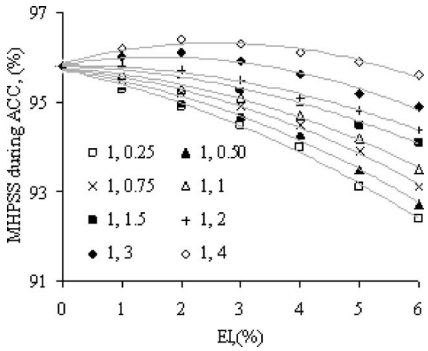

Fig. 11 MHPSS during ACC for stipulated EMs with increasing HPT's erosion

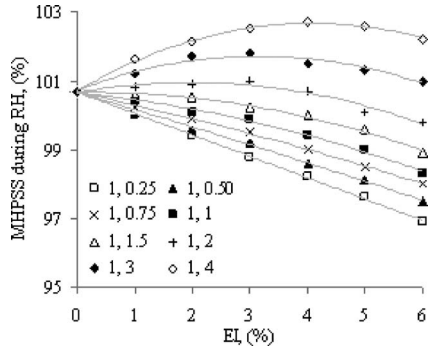

Fig. 12 MHPSS during RH for stipulated EMs with increasing HPT's erosion

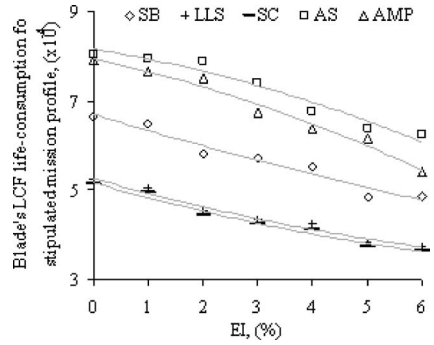

Fig. 14 HPT blade's LCF life-consumption (for stipulated mission profiles) with increasing HPT's erosion

At any given point, with increasing HPT's erosion, HPSS (i) reduces almost linearly during RH; (ii) reduces almost linearly (and with a slightly decreasing rate from start to end of TO) during TO; and (iii) reduces almost linearly and with slightly increasing rate in earlier and later parts of acceleration, respectively (see Fig. 9). For example at the start of TO, it is 100%, 98.8%, 97.6%, and 96.4% with HPT's EM (1, 0.50) and EI of 0%, 2%, 4%. and 6%, respectively, i.e., a reduction of 3.6% as a result of an increase in HPT's EI from 0% to 6%. Whereas at the end of TO, it is 100%, 99.1%, 98%, and 96.8%, i.e., a reduction of 3.2%, respectively.

With increasing HPT's erosion, for various EMs, a clear variation trend is observed for MHPSS during TO. At lower flow capacity levels for a given efficiency level, e.g., EM (1, 0.25), the MHPSS reduces almost linearly with increasing HPT's EI. Whereas with increased flow capacities, the reduction in MHPSS no more remains linear, rather it reduces with slightly increasing rate. However, at any given EI, it is significantly higher for higher flow capacities for a given HPT's efficiency level. Also with increasing flow capacities, the extent of reduction in MHPSS reduces with increasing EI. As a result, for an EM (1, 1.5), the MHPSS remains almost invariant from an EI of 0% to 2% whereas for an EM (1, 4), MHPSS even increases from 100% to 100.85% for an increase in EI from 0% to 3% and subsequently MHPSS starts decreasing with slightly increasing rate (see Fig. 10).

An almost similar variation trend is observed for MHPSS during TO, ACC, and RH phases with only one exception. Unlike TO and RH phases where at lower flow capacity level for a given efficiency level, e.g., EM (1, 0.25), the MHPSS reduces almost linearly; during ACC phase, it reduces with slightly increasing rate (see Figs. 10–12). Like TO, ACC, and RH phases, a clear and distinct variation trend of MHPSS is also observed for "enhancement of engines' power to 80%, followed by cruising at constant power setting" flight phase (see Fig. 13).

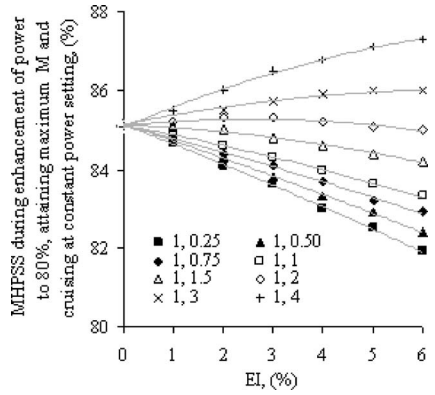

Fig. 13 MHPSS during enhancement of power to 80%, attaining maximum M and cruising at constant power setting for stipulated EMs with increasing HPT's erosion

19 Representative Peacetime Training Mission Profiles for a Military Aircraft

The details covered so far establish the significance of variations in altitude, M, engine power settings, etc., for HPSS of aeroengine of a military aircraft. Also typical mission profiles for a military aircraft vary significantly (dependent on their role) in terms of altitude, M, and required engine power settings. Therefore, instead of restricting the present investigation to the assumed mission profile, it was considered appropriate to extend the analyses by considering representative peacetime training mission profiles such as air superiority, simple cruise, low-level strike, and strategic bombing for a military aircraft [5].

20 HPT Blade's LCF Life Consumption

For a given mission profile, an overall increase in HPSS as a result of HPT's erosion leads to higher LCF damage and thereby affects the blade's LCF life-consumption adversely, i.e., LCF life-consumption increases. For the conditions assumed for the present investigation (i.e., for a LPSS limiting of 100% of its design point value and no TET limiting) and for the same EMs, blades' LCF life-consumption reduces significantly and with slightly decreasing rate with increasing HPT's erosion levels. For example for the assumed mission profile (AMP), for HPT's EM (1, 0.50), the blade's LCF life consumption with HPT's EI of 2%, 4%, and 6% is 7.59×10^{-4}, 6.38×10^{-4}, and 5.38×10^{-4}, respectively, as compared with 7.92×10^{-4} for clean engines (i.e., a reduction of 4.17%, 19.44%, and 32.07%, respectively). With increasing HPT's erosion level, the rate of reduction in blades' LCF life-consumption is almost the same for all mission profiles except AMP where it is significantly higher (see Fig. 14).

Among the four representative mission profiles of a military aircraft, air superiority is the severest in terms of blade's LCF life consumption whereas the simple cruise is the least severe. At HPT's EI of 6%, blade's LCF life consumption for air superiority mission profile is 28.78%, 67.02%, and 71.61% higher as compared with strategic bombing, low-level strike, and simple cruise mission profiles, respectively. The significant variation in the levels of blades' LCF life-consumption for different mission profiles is due to the reason that it varies with any change in nature/extent of flight segment(s) as well as their interarrangement in any given mission profile.

As a result of the reduced blade's LCF life consumption, before the HPT blades' are considered unsafe for further use, for HPT's EI of 6%, the aircraft can fly through air superiority, strategic bombing, low-level strike, and simple cruise mission profiles 1600, 2061, 2568, and 2603 times as compared with 1242, 1505,

1909, and 1928 for HPT's EI of 0%, respectively (i.e., an increase of 28.82%, 36.94%, 34.52%, and 35.01%, respectively, as a result of an increase in HPT's EI from 0% to 6%).

For different conditions and flight segments discussed earlier, the variation in HPSS/MHPSS for various EMs with increasing HPT's erosion levels is accompanied with significant variation in TETs. For example at constant NT condition, and with EM (1, 0.50), TET for HPT's EI of 6% increases to 1628 K as compared with that of 1555 K for clean engines. An increase in TET leads to greater creep and thermal fatigue damages of HPT's blades (areas of future investigations).

21 Conclusions

Bespoke computer simulations have been used to explore the relative implications of turbine erosion for an aero-engine's HPT-blade's LCF life-consumption. The turbine erosion has a significant and favorable effect on the blade's LCF life-consumption. However, this is on the cost of a significant increase in TETs, thereby an expected significant increase in levels of creep and thermal fatigue damages of HPT's blades. The blade's LCF life-consumption varies significantly with the type of mission flown and is the severest for air superiority mission profile.

The results of such an investigation as the present for a variety of mission profiles under various operating conditions/engine's deterioration levels will provide a wide database and can lead to managers taking wiser decisions. Hence the engines' utilization and operational-effectiveness of the mission can usually be improved. However, greater benefits will be achieved if the present analysis is considered as an integral part of a more comprehensive analysis including the aero-engine's creep and thermal fatigue life usages, fuel-usage/weapon carrying capability, aircraft's mission operational-effectiveness, and life cycle costs aspects. The detailed investigations regarding the impacts of turbine erosion on aero-engine's HPT blades' creep as well as thermal fatigue lives are underway. The results of analyses and predictions would be presented in the form of separate papers in near future.

Nomenclature

b, c = fatigue-strength and ductility exponent, respectively
e' = nominal strain
E = elastic modulus
K' = cyclic strength coefficient
K_t = theoretical elastic-stress concentration factor
M = free stream Mach number
N_f = number of cycles to failure (i.e., to the onset of crack-initiation life)
N_i = number of stress cycles to failure under condition i
n_i = number of cycles applied at condition i
n' = cyclic strain hardening coefficient
S = stress imposed
ε, ε_f = local notch root strain and fatigue-ductility coefficient, respectively
Φ_i, Φ_{ref} = spool-speed at ith and reference condition, respectively
σ, σ_f = local notch root stress and fatigue-strength coefficient, respectively
σ_0 = mean stress
ΔS = blade stress range for cycle from blade speed $\Phi_L \rightarrow \Phi_H \rightarrow \Phi_L$
$\Delta\varepsilon$, $\Delta\varepsilon_e$, and $\Delta\varepsilon_p$ = strain range, elastic strain range, and plastic strain range, respectively
$\Delta\sigma$ = local stress range

References

[1] Devereux, B., and Singh, R., 1994, "Use of Computer Simulation Techniques to Assess Thrust Rating as a Means of Reducing Turbo-Jet Life Cycle Costs," International Gas-Turbine and Aero Engine Congress and Exposition, The Hague, The Netherlands, Jun. 13–16.
[2] Naeem, M., 1999, "Implications of Aero-Engine Deterioration for a Military Aircraft's Performance," Ph.D. thesis, Cranfield University, UK.
[3] Naeem, M., Singh, R., and Probert, D., 2001, "Impacts of Aero-Engine Deterioration on Military Aircraft Mission's Effectiveness," Aeronaut. J., **105**(1054), pp. 685–695.
[4] Naeem, M., 2006, "Impacts of Low-Pressure (LP) Compressor's Deterioration Upon an Aero-Engine's High-Pressure (HP) Turbine Blade's Life Consumption," Aeronaut. J., **110**(1106), pp. 227–238.
[5] Naeem, M., 2008, "Impacts of Low-Pressure (LP) Compressor's Deterioration of a Turbofan Engine Upon Fuel Usage of a Military Aircraft," Aeronaut. J., **112**(1127), pp. 33–45.
[6] Naeem, M., 2008, "Impacts of Low-Pressure (LP) Compressor's Fouling of a Turbofan Upon Operational-Effectiveness of a Military Aircraft," Appl. Energy, **85**(4), pp. 243–270.
[7] Grewal, M. S., 1988, "Gas-Turbine Engine Performance Deterioration Modelling and Analysis," Ph.D. thesis, Cranfield University, UK.
[8] Sallee, G. P., 1980, "Performance Deterioration Based on Existing (Historical) Data," Report No. NASA-CR-135448.
[9] Sallee, G. P., Kruckenberg, H. D., Toomy, E. H., 1986, "Analysis of Turbofan-Engine Performance Deterioration and Proposed Follow-On Test," Report No. NASA-CR-134769.
[10] Saravanamuttoo, H. I. H., and Lakshminarasimha, A. N., 1985, "A Preliminary Assessment of Compressor Fouling," Paper No. ASME 85-GT-153.
[11] Zhu, P., and Saravanamuttoo, H. I. H., 1991, "Simulation of Advanced Twin-Spool Industrial Gas Turbine," ASME Paper No. 91-GT-34.
[12] Little, P. D., 1994, "The Effects of Gas Turbine Engine Degradation on Life Usage," MS thesis, Cranfield University, UK.
[13] MacDonald, S., 1993, "A Dynamic Simulation of the GE F404 Engine for the Purpose of Engine Health Monitoring," MS thesis, Cranfield University, UK.
[14] Haub, G. L., and Hauhe, W. E., 1990, "Field Evaluation of On-Line Compressor Cleaning in Heavy-Duty Industrial Gas-Turbines," ASME Paper No. 90-GT-107.
[15] Nicholas, T., Haritos, G. K., and Christoff, J. R., 1985, "Evaluation of Cumulative Damage Models for Fatigue Crack Growth in an Aircraft Engine Alloy," Jet Propuls., **1**(2), pp. 131–136.
[16] O'Connor, C. M., 1988, "Military Engine Condition Monitoring Systems: The UK experience," Proceedings of the Advisory Group for Aerospace Research and Development, Neuilly Sur Seine, France, Paper No. AGARD-CP-448.
[17] May, R. J., Jr., Chaffee, D. R., Stumbo, P. B., and Reitz, M. D., 1981, "Tactical Aircraft Engine Usage: A Statistical Study," American Institute of Aeronautics and Astronautics, Report No. AIAA-81-1652.
[18] Balderstone, A. W., 1996, "A Generic Computer Model to Predict an Aero-Engine's Low-Cycle Fatigue," MS thesis, Cranfield University, UK.
[19] Dowling, N. E., 1972, "Fatigue Failure Predictions for Complicated Stress-Strain Histories," J. Mater., **7**(1), pp. 71–87.
[20] Matsuishi, M., and Endo, T., 1968, "Fatigue of Metals Subjected to Varying Stress," Japan Society of Mechanical Engineers Conference, Fukuoka, Japan.
[21] Downing, S. D., and Socie, D. F., 1982, "Simple Rainflow Counting Algorithms," Int. J. Fatigue, **4**(1), pp. 31–40.
[22] Rychlik, I., 1987, "A New Definition of the Rainflow Cycle Counting Method," Int. J. Fatigue, **9**(2), pp. 119–121.
[23] ESDU, 1995, "Fatigue-life Estimation Under Variable-Amplitude Loading Using Cumulative Damage Calculations," *Fatigue-Endurance Data Contents*, Vol. 2, ESDU International, London.
[24] Morrow, J., 1968, *Fatigue-Design Hand Book: A Guide for Product Design and Development Engineers*, Vol. 4, Society of Automotive Engineers, Warrendale, PA.
[25] Palmgren, A., 1924, "Die lebensdauer von Kugellagern," VDI Z. (1857-1968), **68**, pp. 339–341.
[26] Miner, M. A., 1945, "Cumulative Damage in Fatigue," ASME J. Appl. Mech., **12**, pp. A159–A164.
[27] Eshelby, M., 1996, "Propulsion System Performance and Integration" *Lecture Notes*, Department of Propulsion, Power, Energy and Automotive Engineering, School of Mechanical Engineering, Cranfield University, UK.
[28] Raymer, D. P., 1992, *Aircraft Design: A Conceptual Approach* (AIAA Education Series)," American Institute of Aeronautics and Astronautics, Inc., Washington, DC..
[29] Stevenson, J. D., and Saravanamuttoo, H. I. H., 1995, "Effects of Cycle Choice and Deterioration on Thrust Indicators for Civil Engine," 12th International Symposium on Air-Breathing Engines, Melbourne, Australia, Sept. 10–15, Paper No. ISABE 95-7077.
[30] Naeem, M., 2008, "Implications of Day Temperature for A High-Pressure-Turbine Blade's Low-Cycle-Fatigue Life Consumption," J. Propul. Power, **24**(3), pp. 624–628.

R. Castilla
LABSON,
Department of Fluid Mechanics,
U.P.C.,
Colom, 7-11,
Terrassa E-08222, Spain

M. Gutes
ArvinMeritor GmbH,
Albert Einstein Str., 14-20,
Dietzenbach D-63128, Germany

P. J. Gamez-Montero

E. Codina

LABSON,
Department of Fluid Mechanics,
U.P.C.,
Colom, 7-11,
Terrassa E-08222, Spain

Experimental Study of the Shaft Motion in the Journal Bearing of a Gear Pump

The movement of the shaft of a driven gear in a gear pump is experimentally studied. Three different methods are considered, and the use of a laser micrometer measurement method is validated. In order to use the laser micrometer, some modifications are made to the gear pump. Experimental results for different working pressures and rotational velocities are shown. For a low nondimensional working pressure, defined in a similar way as the Sommerfeld load, experimental and numerical results agree very well for relative eccentricity. Nevertheless, experimental results made clear that the role of the lateral plate of the pump is very important for high nondimensional working pressure. A value of 100 is given for the critical nondimensional working pressure in order to avoid wear and slant in the lateral plate. Frequency analysis of the outlet pressure, as well as the precise measurement of the wear in the pump case, support experimental observation of the inability of the journal to retain the shaft for high nondimensional pressure.
[DOI: 10.1115/1.3078202]

1 Introduction

Simple and inexpensive journal bearings are extensively used in small gear pumps. Gear pumps are used to drive a liquid (usually oil) against a rather large pressure, about 100–300 bars. Due to the internal operation of the pump and this large pressure in the outlet, the load on the shafts of the journal bearings in the pump undergoes large variations and a rapid rate of change. In the present work, the motion of the shaft in a gear pump is experimentally studied. The objective is to establish, using also analysis via theoretical and numerical results, the correct parameter design in order to obtain a simple and reliable journal bearing with hydrodynamic lubrication. The method used for this purpose is a pair of laser micrometers acting in a real gear pump.

The first measurement of the motion of a journal using a laser device was probably made by Ji-Bin et al. [1], who observed that other methods available were not suitable due to low acquisition frequency and problems with calibration. However, their measurements were performed on an experimental model.

In the work by Jaloszynski and Evers [2], an optical sensor was specially manufactured for measurement of the movement of the crankshaft of a car. They were able to make this measurement with a gap of 64 μm and a range of angular velocities from 350 rpm to 1100 rpm, under a maximum pressure of 55 bars. The sensor was installed flush to the bearing surface in a model, and it was found that the measured displacements were two and even three times greater than that of the considered mathematic models.

Much more recently, Lu and Khonsari [3] published an experimental study of journal bearings under oscillatory motion, but this work was mainly concerned with friction hysteresis and did not measure the position of the shaft with respect to the journal.

Measurement of the motion of the shaft in a gear pump is complex, since the system consists of seven rigid solids, four of them (gears and lateral plates) having six degrees of freedom. The gear pump and its parts are shown in Fig. 1. Furthermore, the pressure inside the case can reach a pressure of 200 bars, and the case is hermetically sealed.

In order to register the position of the shaft inside the pump, three types of measurement systems have been initially considered: an eddy current sensor, a noncontact inductive transducer, and a laser micrometer.

The TR-102 inductive transducer, made by HBM (Darmstadt, Germany), was recently used by Cereska and Vekteris [4] for measurement of the movement of the rotor in a hydrodynamic bearing. Additionally, an inductive transducer was also previously used by E. Christensen et al. [5], showing that a hole up to three times bigger than the radial gap does not have an important influence on the experimental results. However, the tests performed by the authors on the TR-102 inductive transducer show that it is not suitable for the purpose of this work, since it is very sensitive to vibrations and, furthermore, can only properly work at pressures of up to 25 bars.

The U105-12 eddy current sensor, made by Micro-Epsilon (Dorfbach, Germany), requires such a fine pump machining precision for installation that it has been removed from consideration. Finally, it was decided that a Keyence LS-5041 laser micrometer should be used, in spite of its higher cost. The main advantage of

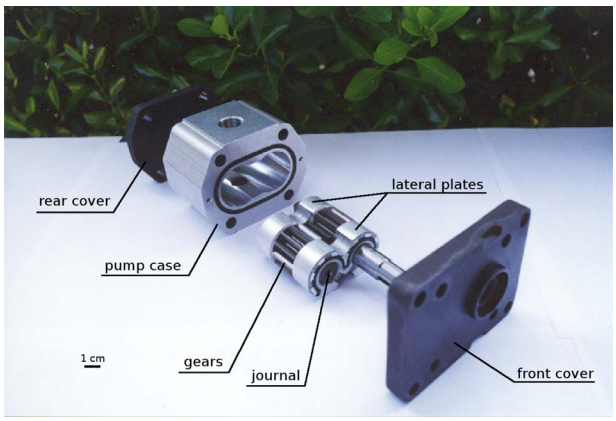

Fig. 1 Parts of the gear pump used in the experimental study

Manuscript received July 15, 2008; final manuscript received October 23, 2008; published online May 26, 2009. Review conducted by Patrick S. Keogh.

Table 1 Specifications of the Keyence LS-5041 laser micrometer

Laser type	Visible red semiconductor, 670 nm, class II
Laser scan rate	1200 Hz
Laser scan velocity	121 m/s
measuring range	Up to 40 mm
Repeatability	± 0.3 μm max
Resolution	± 0.05 μm
Minimum target width	0.2 mm

using a laser micrometer is that the measurement is external, and, hence, the equipment is not exposed to contact with oil at high pressures.

2 Experimental Setup

The Keyence LS-5041 laser micrometer consists of a transmitter and receiver head. The main characteristics of this equipment are summarized in Table 1.

In order to make the required measurements, some modifications are required. First, because the more loaded shaft is that of the driven gear, as pointed out in Appendix B, and because it is usually completely confined inside the body, it had to be taken out. This was done by replacing the driven gear, which has a short shaft, by a driving gear (but functionally still driven), which has a long shaft. The back cover was also replaced by a front cover, in order to have an exit for the shaft to the outside. Also, a 3 mm bar stick was installed in this cover in order to measure its position. This stick will be referred to hereinafter as *fixed stick* (fs), since it will act as a reference for the rest of the positions.

After some preliminary tests, it was made clear that the lateral plate moves as well, which was not initially expected. In order to measure this movement, two more 3 mm bar sticks were added to the lateral plate. These bars were installed in the suction zone, as shown in Fig. 2, in order to avoid leakage by pressure difference with the atmosphere. These sticks will be referred to as *upper stick* (us) and *lower stick* (ls). Two holes had to be made in the back cover in order to measure the position of the upper and the lower sticks from the outside using the laser micrometer. The modified test pump is shown in Fig. 3.

Two pairs of transmitting-receiving heads were placed on a disk able to rotate 360 deg for measurement of the position in the *x-y* plane. The test rig with the two laser micrometers is shown in Fig. 4.

It will be assumed that the position of the fixed stick is invariable with time. The absolute position of the shaft and lateral plate will be measured in reference to this stick. The position of the lateral plate is measured with two sticks in order to calculate not only the position, but also the rotation and the instantaneous center of rotation.

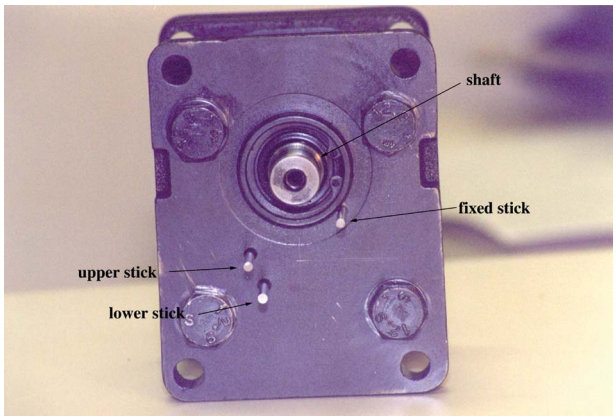

Fig. 3 Pump with two driver shafts and two front covers. The driven sticks in the lateral plate come out the front cover through two preformed holes. The bar stick driven in the front cover is also shown.

The laser sensors are installed in a rotating disk with several slots. With the slots and the rotational positions of the disk, all ranges of measurement can be covered. The sensors are then put into "segment mode" and the distances between shaft and sticks are measured. In Table 1, some of the variables and the corresponding segments are presented. A scheme of the segments is shown in Fig. 5. (Also see Table 2.)

3 Experimental Results

All tests were performed with a real pump, with the modifications described in Sec. 2. The tests were performed with 5 bars, 50 bars, 100 bars, 150 bars, and 200 bars of working pressure. A value of 5 bars is the lowest pressure allowable with the present experimental rig due to the pressure drop in the components. The pump velocities used in the test were 537 rpm, 1078 rpm, 1241 rpm, 1608 rpm, 1808 rpm, 2012 rpm, and 2417 rpm. Round numbers in rotational velocity have been avoided in order to minimize possible interferences with electrical noise.

Figure 6 shows the eccentricity of the relative motion of the shaft, or the motion of the shaft as seen by the bearing. Appendix A briefly describes how these results were calculated from the micrometer records. The eccentricity is larger than the clearance stated by the manufacturer. It should be kept below 90 μm, but reaches values close to 200 μm. The clearance between shaft and

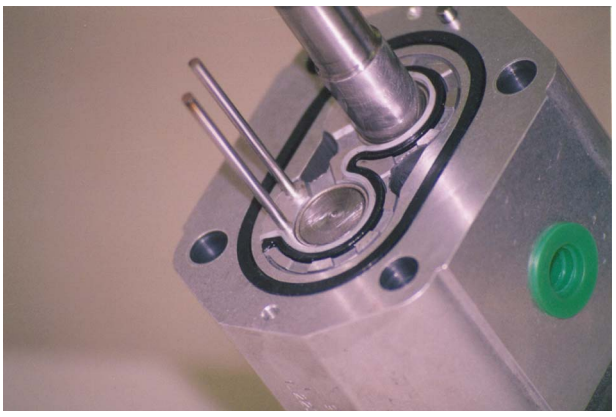

Fig. 2 Lateral plate with the two 3 mm bar sticks driven in

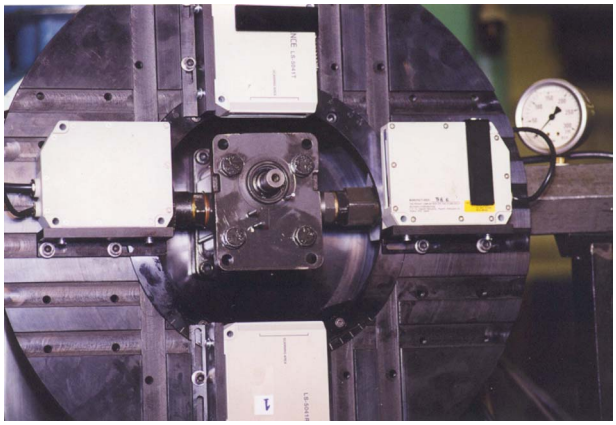

Fig. 4 Test rig with the rotating disk, the two transmitter-receiving pairs, and the test pump

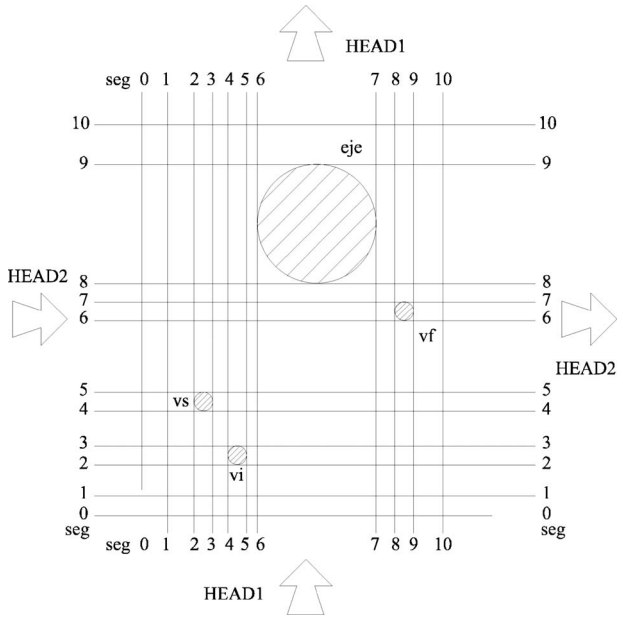

Fig. 5 Segments in the Keyence Sensor

journal was measured before the test, giving a correct value around 50 μm. After some operation time at high pressure, the clearance was measured at 210 μm. It can be suggested that lubrication at the beginning of the journal operation may be insufficient for high pressure, and thus wear occurs. We consider that the clearance of the journal in all presented tests is the measured value of 210 μm.

Contrary to what is stated by the hydrodynamic theory or the numerical simulations, eccentricity decreases when the pressure is sufficiently high. Furthermore, the equilibrium angle is smaller than such suggested by numerical results. Figure 7 shows the equilibrium angle as a function of pressure. Its variation from 5 bars to 200 bars is four times smaller than the results obtained with numerical simulations. This is also displayed in Fig. 10, where the angle is plotted versus the rotational velocity for different pressures. The theoretical prediction is only satisfied for low pressure, below 50 bars. In Figs. 6, 8, and 9, the eccentricity grows only from 5 bars to 50 bars, and in Figs. 10 and 11, the angle also increases with velocity only for low pressures.

The reason for this disagreement among the experimental, theoretical, and numerical results is the motion of the lateral plate (see Appendix A). The slant of the lateral plate is shown in Fig. 12. The lateral plate usually acts to slightly reduce the slant angle (i.e., rotates clockwise) when the pressure grows from 5 bars to 50 bars. Nevertheless, this rotation is inside the range of measurement error and, hence, it is difficult to state that it actually exists, or that the lateral plate maintains its position for so low a pressure. For higher pressure, the slant angle increases. This implies a counterclockwise rotation and, hence, a translation of the journal toward the inlet zone. The shaft is also pushed toward this direction,

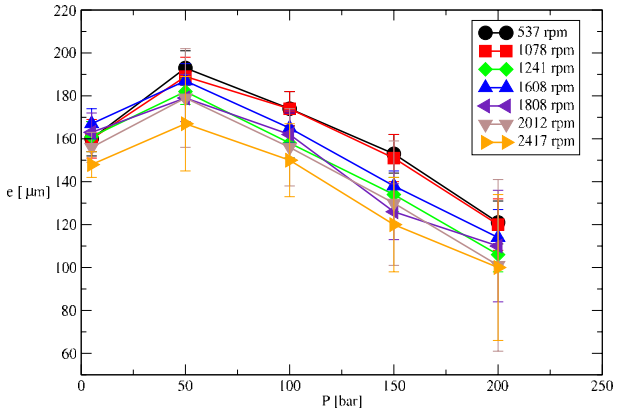

Fig. 6 Eccentricity of relative motion of the shaft as a function of pressure, for different angular velocities

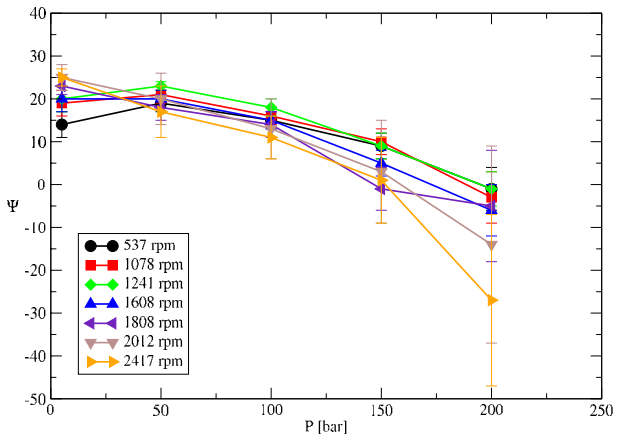

Fig. 7 Equilibrium angle of relative motion of the shaft as a function of pressure for different angular velocities

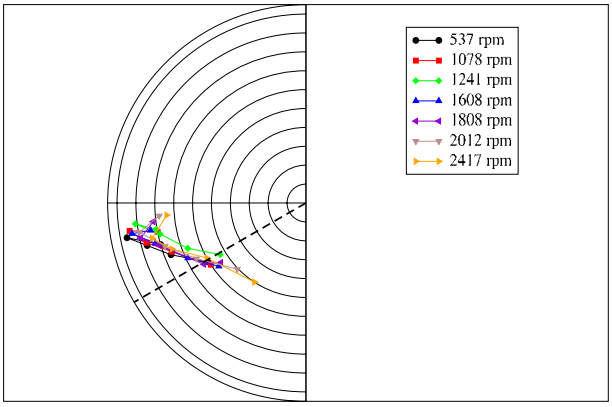

Fig. 8 Polar graph with position of the journal for constant angular velocity and operating pressure variables. Load mean direction is indicated with a dashed line.

Table 2 Definition of segments in the laser micrometer. The segments are displayed in Fig. 5.

Variable	Segment	Description
X_{rel}	HEAD 1 seg (3,6)	x position of shaft referred to as the upper stick
X_{abs}	HEAD 1 seg (7,8)	x position of shaft referred to as the fixed stick
X_{ul}	HEAD 1 seg (3,4)	x distance between upper and lower sticks
Y_{rel}	HEAD 2 seg (5,8)	y position of shaft referred to as the upper stick
Y_{abs}	HEAD 2 seg (7,8)	y position of shaft referred to as the fixed stick
Y_{ul}	HEAD 2 seg (3,4)	y distance between upper and lower sticks

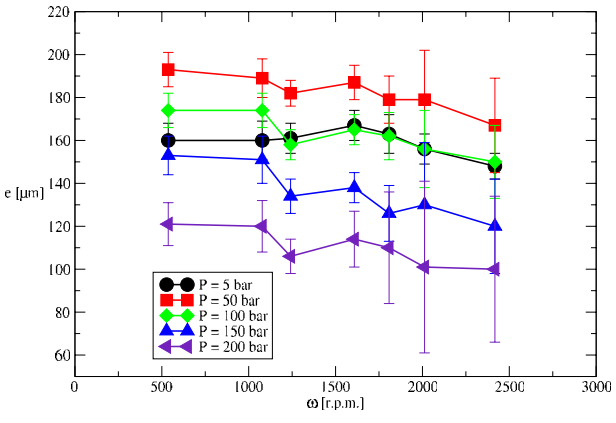

Fig. 9 Eccentricity of the shaft in the bearing as a function of rotational velocity for different pressures

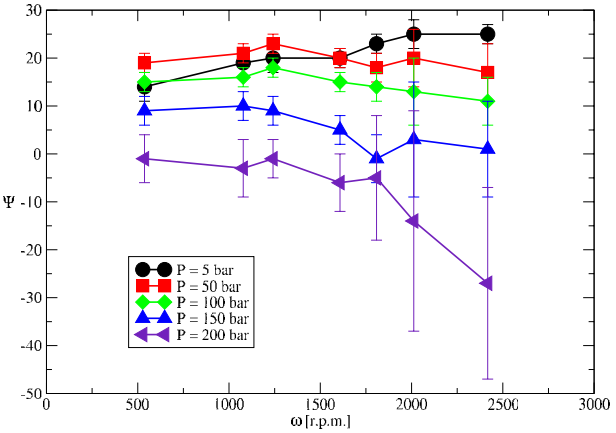

Fig. 10 Equilibrium angle of relative motion of the shaft as a function of rotational velocity for different pressures

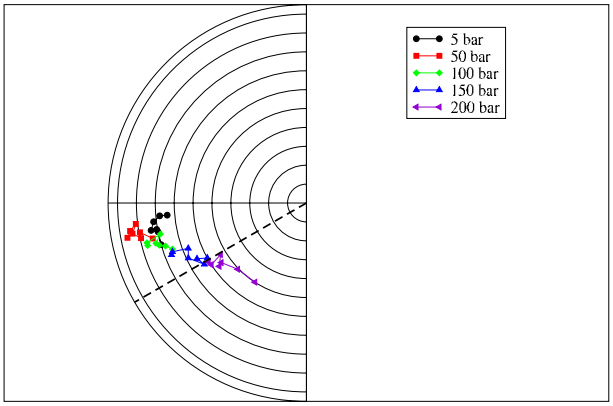

Fig. 11 Polar graph with position of journal for different pressure. Load mean direction is indicated with a dashed line.

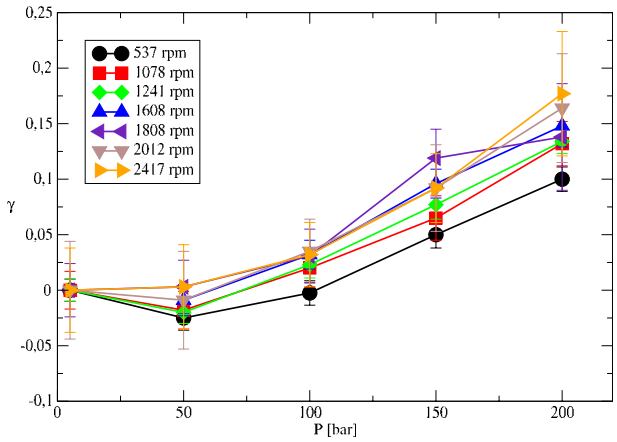

Fig. 12 Variation in slant of lateral plate with working pressure

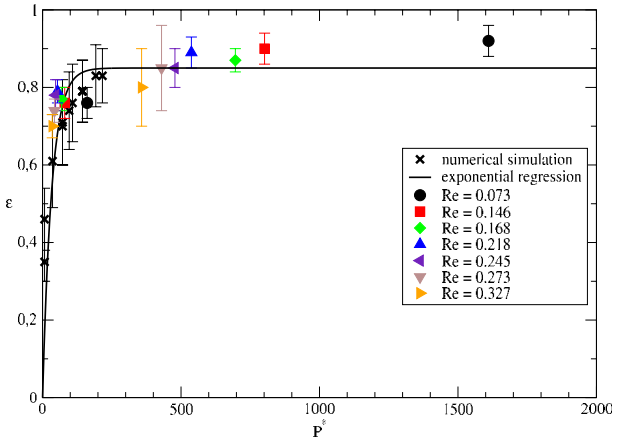

Fig. 13 Relative eccentricity versus nondimensional pressure for numerical simulation and presented experiments

but the effect is a reduction in the eccentricity if the shaft is not allowed to follow the journal via the restraint of the pump case. Movement of the shaft is denied by the contact of gears and case. These two pieces are manufactured with a very low tolerance, often even negative, in order to reduce the leakage between teeth and case. The gap is obtained by working wear. The results presented show that the movement of the lateral plate can be so large that the bearing is not able to lift the journal until the wear of the case is very strong. This must be avoided because leakage can be greatly increased when the pump works at lower pressure, due to excessive wear of the case.

For the purpose of comparison with numerical results (see Appendix B or Ref. [6] for a description of the numerical simulation), the data have been nondimensionalized. Similar to the Sommerfeld load [7], the nondimensional pressure is defined as

$$P^* = \frac{P}{\omega\eta}\left(\frac{c}{R_b}\right)^2 \tag{1}$$

and, as usual, the eccentricity is normalized with the clearance

$$\varepsilon = \frac{e}{c} \tag{2}$$

Also, following El-Shafei [8], the Reynolds number is defined as

$$\mathrm{Re} = \frac{\rho\omega c^2}{\eta} \tag{3}$$

The Reynolds numbers obtained in the present work are much lower than those in the El-Shafei paper (less than 0.5 in front of up to 50), most likely due to the difference of clearances in the journal. This means that that the laminar regime is completely dominated by viscosity. Because of this, the results presented in this paper are not comparable with the results of El-Shafei.

Figure 13 shows the relative eccentricity versus the nondimensional pressure, both for numerical simulations and for experimental data. In Fig. 13, the error bars show the size of the orbits from which it can be observed that these values are similar for

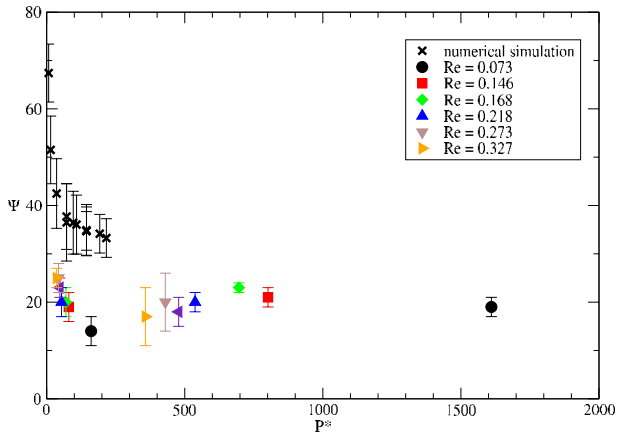

Fig. 14 Attitude angle versus nondimensional pressure for numerical simulation and presented experiments

both numerical and experimental results. Due to the different values of the clearance, the nondimensional pressures are normally larger for experiments than for numerical simulation. For low P^*, the agreement between numerical and experimental results is very good. The numerical results of eccentricity can be approximated by an exponential function, which is supported also by experimental results. The optimal exponential function for the limit eccentricity of 0.85 is

$$\varepsilon = 0.85[1 - \exp(-0.03P^*)] \tag{4}$$

which is also plotted in Fig. 13. This allows for the definition of a characteristic nondimensional working pressure equal to the inverse of the coefficient of P^* in the exponential function $P^*_{ch} \approx 33$ and a critical nondimensional working pressure

$$P^*_{cr} = 3P^*_{ch} \tag{5}$$

For this P^*_{cr}, the relative eccentricity will reach 95% of its limit value. In conclusion, $P^*_{cr} = 100$ should serve as a limit for the working pressure for a gear pump in order to avoid wear in the journal bearing. This value should be taken as an indicative estimate; although it has been obtained with nondimensional results, the experimental and numerical tests have been performed with only one model of pump.

In the case of the attitude angle, displayed in Fig. 14, the values obtained by numerical simulations are overestimated, principally for low P^*. Nevertheless, it seems that there is a tendency toward a limit value of 20–25 deg for numerical results that is also supported by experimental data.

Due to the high value of c in the experimental tests, the values of P^* are much larger than in the numerical simulation. For these high values of P^* (not simulated) the unexpected displacement of the lateral plate described above is found. The translation and rotation of the lateral plate, measured from the position of the upper and the lower sticks, are responsible for the eccentricity reduction. The scenario is then as follows. For low P^*, the journal bearing behaves more or less as described by numerical simulation, with a similar relative eccentricity and size of orbit. When P^* increases, although the eccentricity tends to increase as stated by numerical simulations, the lateral plate is also pushed toward the suction side. If the tolerance between the lateral plate and the pump case is large enough, the journal may be unable to follow the bearing and is sustained by the contact between gears and pump case. The behavior of the lateral plate depends not only on the tolerance, but also (and maybe more importantly) by the film fluid between it and the case, which has a strong pressure distribution. Thus, effects of the squeeze film are probably involved. This scenario is supported by precise measurement of the case in the gear zone after operation, which shows important wear due to the incapability of the bearing to properly lift the journal.

This behavior of the journal bearing, gears, and lateral plates is also experimentally supported by the frequency analysis. Experimental reported works [9] and the numerical results (see Appendix B), as well as pressure measurements in the outlet made for this purpose, show that the main frequency of the behavior of the gear pump is the gearing frequency. Figure 15 displays the power spectrum obtained from the pressure measurements in the outlet for an experiment at 1500 rpm and 100 bars of working pressure, with a similar pump with 12 teeth. The first peak (A) is placed at 300 Hz, which is the gearing frequency for 12 teeth and this velocity. The second (B) and next peaks are the harmonics of the gearing frequency. The first harmonic (B) is bigger than the gearing frequency peak due to the configuration of gap, decompression slot, and total contact ratio in the contact path of the gears. For some values of these parameters, two high pressure chambers can be created for an interval of time in the contact path.

Figure 16 shows the spectrum of the horizontal movement of the shaft from numerical simulation for 150 bars and 1500 rpm

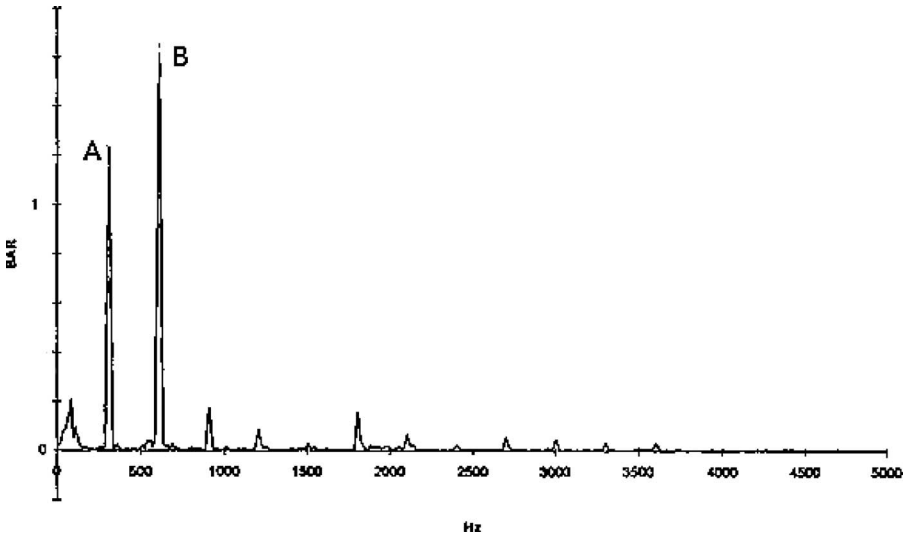

Fig. 15 Spectrum of the pressure outlet for 100 bars of working pressure and 1500 rpm. The first peak is related to the gearing frequency.

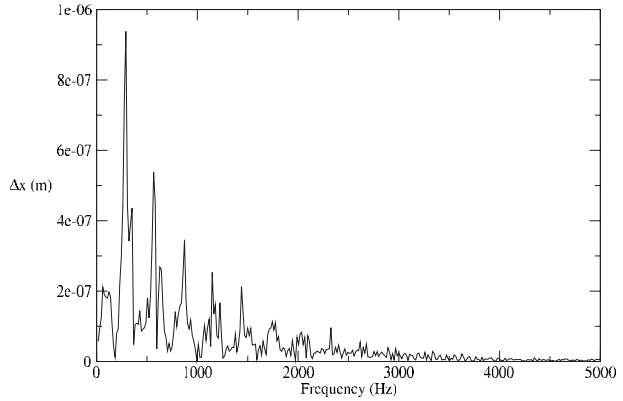

Fig. 16 Spectrum of the *x* movement obtained from numerical simulations (see Appendix B) for an experiment with conditions of 150 bars and 1500 rpm. The first main peak is at 300 Hz, the gearing frequency. The rotation frequency is not visible.

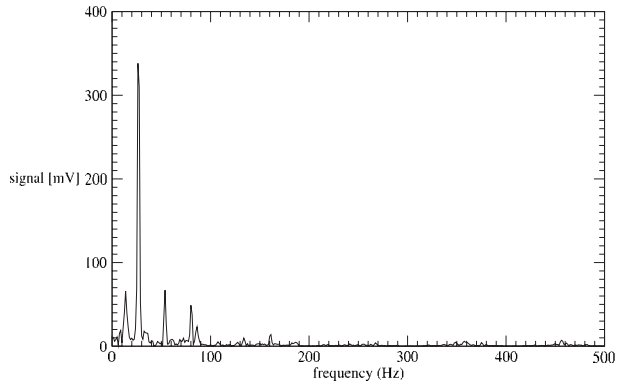

Fig. 17 Spectrum of the relative *x* movement of the shaft for an experiment at 100 bars and 1608 rpm. The main peak is in the rotational frequency around 27 Hz.

(see Appendix B). The first main peak is also located at 300 Hz. The peak for the rotational frequency (25 Hz) is rather weak.

Figure 17 shows the spectrum of the horizontal relative movement of the shaft for a pump with working conditions of 100 bars and 1608 rpm, obtained by discrete Fourier transform of the x coordinate of the relative orbit. The main peaks are related to the rotational velocity of the shaft and the two first harmonics, but the gearing frequency is not seen. It can be suggested that the movement of the shaft is not greatly influenced by the gearing. It should be explained by means of other phenomena, such as contact of gears and case, or squeeze film, or other sources of unbalance that always occur at the rotational speed [10].

4 Conclusions

The movement of the shaft in a gear pump is investigated by varying the working pressure and the rotational velocity. The measurement of this movement is extremely complex, since the shaft moves inside a journal bearing, which is not constrained in the pump case. Hence, not only does the motion of the shaft need to be measured, but also the motion of the lateral plate. These measurements have been made outside the pump with two micrometer lasers. This has been considered the best experimental method for this study, due to the required features and the high pressure inside the pump.

The tests have been performed with a commercial pump, duly modified in order to take the journal and lateral plate out of position for the purpose of measurement. For the sake of comparison with previous numerical simulations described in the Appendix B, pressure and eccentricity have been nondimensionalized and a proper Reynolds number has been defined as well. For low nondimensional working pressure, the numerical relative eccentricity values agree very well with numerical results. However, numerical simulations overestimate attitude angle even for low P^*. For large values of P^*, an unanticipated phenomenon occurs; the lateral plate moves appreciably. This forces the behavior of the journal bearing to change completely. If the movement of the lateral plate is large enough (allowed by manufacturing tolerances), it is observed that the journal cannot be properly operated with the current bearings. This is supported by precise measurement of wear on the case done by the teeth, and frequency analysis, which shows no influence of gearing.

Summarizing, the main conclusions of the present work are the following:

- The use of a pair of laser micrometers is a suitable method for measurement of motion of the shaft of a journal bearing in a gear pump, providing that some modifications are made to the pump.
- The lateral plate has a more important role in the hydrodynamic behavior of the journal than expected. It is then important to measure not only the movement of the shaft but also the movement of the lateral plate, in order to obtain the relative motion.
- The spectrum of the relative motion of the shaft does not show the gearing frequency and is dominated by the rotational frequency. This suggests that, contrary to the numerical results, the journal dynamics are more greatly influenced by phenomena other than gearing. A peak in the rotational frequency is usually related to some kind of unbalance and, in the present case, it seems plausible to attribute that to contact, either of the journal and bearing or of the gears and case.
- An estimated critical value of $P^*=100$ has been found in order to avoid reaching the limit value of eccentricity. This value must be taken with caution, since although it has been obtained in nondimensional form, the tests have been performed only with one pump model.
- For high P^*, the experimental and numerical results are not comparable due to the lateral plate movement. This should be considered in the numerical model in order to make it suitable for use in the correct design of the journal bearing.

Nomenclature

c = clearance of the bearing (m)
b_{ij} = damping coefficients (N s/m)
d_j = diameter of the journal (m)
d_s = diameter of the stick (m)
e = eccentricity (m)
k_{ij} = stiffness coefficients (N/m)
m_b = mass of journal-gear set (kg)
p = pressure around the journal (Pa)
w = load of pressure distribution around the journal (N)
(x,y) = reference system of upper stick (m)
F_T = total load over the shaft (N)
P = working pressure (bar)
P^* = nondimensional working pressure
P^*_{ch} = characteristic nondimensional working pressure
P^*_{cr} = critical nondimensional working pressure
R_b = radius of the bearing (m)
Re = Reynolds number
(X,Y) = reference system of laser micrometer (m)
ε = relative eccentricity
γ = slant of lateral plate
φ = angle of line lower-upper sticks in the (x,y) system

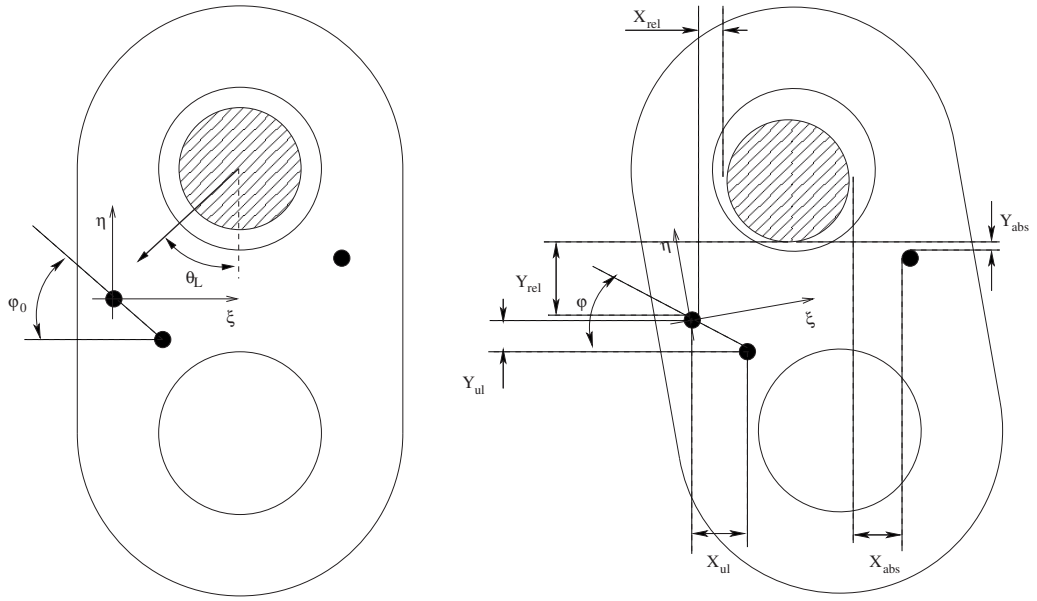

Fig. 18 Scheme of lateral plate with sticks

φ_0 = angle of line lower-upper sticks in the (ξ, η) system
ψ = attitude angle of the journal
θ = angular coordinate around the shaft
θ_L = angle of load over shaft
η = viscosity of the fluid (Pa s)
ρ = density (kg/m^3)
ω, Ω = rotational velocity (1/s)
(ξ, η) = reference system of lateral plate (m)

Appendix A: Calculation of Eccentricity and Attitude Angle From Raw Data

As noted in the paper, it is assumed that the stick installed in the front cover is stationary. It will be referred to as fs, and will be linked to the reference system (X,Y), where X and Y are the directions determined by the laser micrometers. The sticks in the lateral plate are named us and ls. Two more reference systems, centered in the upper stick, are also adopted. The system (x,y) is parallel to the stationary system (X,Y), and the system (ξ, η) is rotated by an angle γ and is, therefore, fixed to the lateral plate, both in position and in rotation, as displayed in Fig. 18.

In this system (ξ, η), the position of the bearing center is invariable:

$$\xi_b = 15.500 \text{ mm}$$

$$\eta_b = 26.500 \text{ mm} \tag{A1}$$

The rotation of the lateral plate (slant angle) is calculated as

$$\gamma = \varphi_0 - \varphi \tag{A2}$$

where

$$\varphi_0 = \arctan\frac{|\xi_{ls}|}{|\eta_{ls}|} \tag{A3}$$

with $|\xi_{ls}|=4$ mm and $|\eta_{ls}|=10$ mm, and

$$\varphi = \arctan\frac{|Y_{ul}|}{|X_{ul}|} = \arctan\frac{|Y_{us} - Y_{ls}|}{|X_{us} - X_{ls}|} \tag{A4}$$

The X and Y coordinates of ls and us are read from the segments (3,8) and (5,8) in HEAD 1, and segments (5,6) and (3,6) in HEAD 2 (see Table 2 and Fig. 5).

With the slant of the lateral plate γ, the center of the journal can be obtained with

$$x_j = \frac{d_s}{2} + X_{rel} + \frac{d_j}{2}$$

$$y_j = \frac{d_s}{2} + Y_{rel} + \frac{d_j}{2} \tag{A5}$$

where $d_j=7.994$ mm is the diameter of the journal and $d_s=1.500$ mm is the diameter of the stick. The position of the bearing in the (ξ, η) system is then

$$\xi_j = x_j \cos\gamma + y_j \sin\gamma$$

$$\eta_j = -x_j \sin\gamma + y_j \cos\gamma \tag{A6}$$

and the eccentricity and attitude angle are calculated with

$$e = \sqrt{(\xi_j - \xi_b)^2 + (\eta_j - \eta_b)^2} \tag{A7}$$

$$\psi = \arctan\frac{|\xi_j - \xi_b|}{|\eta_j - \eta_b|} - \theta_L \tag{A8}$$

where θ_L is the load angle. In the present case of a gear pump, it is difficult to define θ_L, since the load is not only variable in modulus, but also in direction. Based on the computational calculation of the load in the driven gearwheel of the gear pump (see Appendix B), an approximate mean value $\theta_L=60$ deg has been considered.

The measurements consist of 1024 samples acquired at a frequency of 1200 Hz. The value considered for the calculations is the mean value of the 1024 samples with the standard deviation as an error estimation that can be taken as an estimation of the orbit size.

Table 3 Example of measurements for the experiment with conditions of 150 bars and 1808 rpm

X_{us}	-15.755 ± 0.002
Y_{us}	-11.301 ± 0.002
X_{ls}	-11.620 ± 0.003
Y_{ls}	-21.201 ± 0.004
X_{rel}	5.494 ± 0.003
Y_{rel}	17.171 ± 0.003

By way of example, let us consider the experiment for $P = 150$ bars and 1808 rpm. The measurements are displayed in Table 3.

From these values,

$$\varphi = \arctan\frac{|Y_{us} - Y_{ls}|}{|X_{us} - X_{ls}|} = 67.328 \pm 0.017 \text{ deg} \tag{A9}$$

and

$$\gamma = \varphi_0 - \varphi = 0.870 \pm 0.017 \tag{A10}$$

The coordinates of the journal in the (x, y), calculated from the (A5) system are

$$x_j = 14.989 \pm 0.003 \text{ mm} \tag{A11}$$

$$y_j = 26.666 \pm 0.003 \text{ mm} \tag{A12}$$

and, in the (ξ, η) system, Eq. (A6) yields

$$\xi_j = 15.392 \pm 0.011 \text{ mm} \tag{A13}$$

$$\eta_j = 26.435 \pm 0.007 \text{ mm} \tag{A14}$$

and, hence, the eccentricity and the attitude angle are

$$e = 0.126 \pm 0.013 \text{ mm} \tag{A15}$$

$$\psi = (59 \pm 5) - 60 \text{ deg} = -1 \pm 5 \tag{A16}$$

The error due to the flexibility of the bars has been estimated by means of the usual formulas for a cantilever beam [11]. It has been estimated that the force at the end of the bars is the product of mass and acceleration, calculated as the second order finite difference of the absolute position. The maximum acceleration calculated is of the order 500 mm/s^2, and the mass of the bar is 2 g. This gives an inertial force of 10^{-3} N and a deflection at the end of 0.05 μm, which is negligible compared with the size of the orbits, even more so when the measurements have not been taken at the end of the bar, but rather at the first quarter.

Appendix B: Brief Description of the Numerical Simulations

Experimental data reported in the present work have been compared with numerical results. These numerical results have been computed by using Lund's method [6,12] combined with the resolution of two-dimensional generalized Reynolds equations with the finite element method.

The first step is to calculate the load on the journal. A specific code has been developed to make this calculation. This program calculates the load on each gearwheel from the geometrical parameters (number of teeth, modulus of gears, diameter, and width of gears, etc.) and working conditions (pressure and rotational velocity). Figure 19 shows the instantaneous load as the sum of the pressure contribution and the contact force. It can be observed that the load is larger on the driven gear.

With the load, the equation of motion of the journal,

$$\begin{bmatrix} m_b & 0 \\ 0 & m_b \end{bmatrix}\begin{bmatrix} \Delta\ddot{x} \\ \Delta\ddot{z} \end{bmatrix} = \begin{bmatrix} F_T \cos\phi \\ F_T \sin\phi \end{bmatrix} - \begin{bmatrix} w_x \\ w_z \end{bmatrix} \tag{B1}$$

is solved. In Eq. (B1), m_b is the mass of the journal-gear set, F_T is the load on the gear, and w_i is the load due to the pressure distribution on the bearing.

The force w on the journal due to the fluid film is linearized with Lund's method [6,12].

$$\begin{bmatrix} w_x \\ w_z \end{bmatrix} = \begin{bmatrix} (w_x)_0 \\ (w_z)_0 \end{bmatrix} + \begin{bmatrix} k_{xx} & k_{xz} \\ k_{zx} & k_{zz} \end{bmatrix}\begin{bmatrix} \Delta x \\ \Delta z \end{bmatrix} + \begin{bmatrix} b_{xx} & b_{xz} \\ b_{zx} & b_{zz} \end{bmatrix}\begin{bmatrix} \Delta\dot{x} \\ \Delta\dot{z} \end{bmatrix} \tag{B2}$$

where $(w_x)_0$ and $(w_z)_0$ are the forces in the initial position, k_{ij} are the stiffness coefficients, and b_{ij} are the damping coefficients.

The values of these coefficients are calculated with

$$\begin{bmatrix} (w_x)_0 \\ (w_z)_0 \end{bmatrix} = \begin{bmatrix} \int_y\int_\theta p_0 \cos\theta R_b d\theta dy \\ \int_y\int_\theta p_0 \sin\theta R_b d\theta dy \end{bmatrix} \tag{B3}$$

$$\begin{bmatrix} k_{xx} & k_{xz} \\ k_{zx} & k_{zz} \end{bmatrix} = \begin{bmatrix} \int_y\int_\theta p_x \cos\theta R_b d\theta dy & \int_y\int_\theta p_z \cos\theta R_b d\theta dy \\ \int_y\int_\theta p_x \sin\theta R_b d\theta dy & \int_y\int_\theta p_z \sin\theta R_b d\theta dy \end{bmatrix} \tag{B4}$$

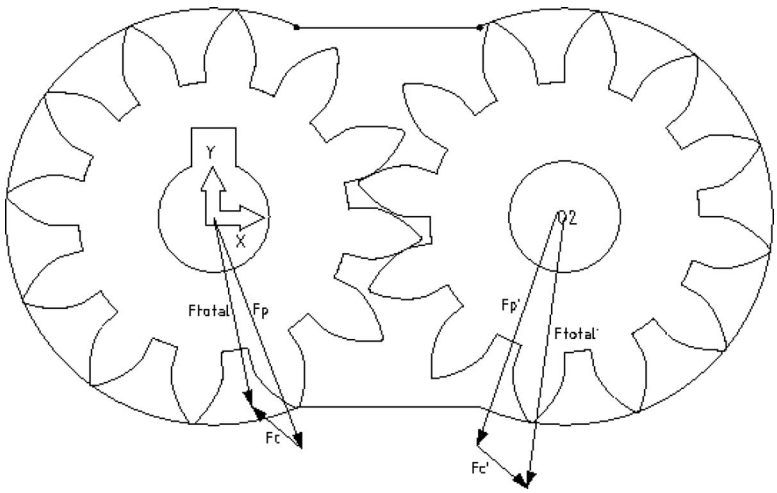

Fig. 19 Calculated load on the driving gear (left) and the driven gear (right). F_p and $F_{p'}$ are the loads due to the pressure distribution, considering that suction is located below. The total load is the sum of the load due to pressure and contact force.

$$\begin{bmatrix} b_{xx} & b_{xz} \\ b_{zx} & b_{zz} \end{bmatrix} = \begin{bmatrix} \int_y \int_\theta p_{\dot{x}} \cos\theta R_b d\theta dy & \int_y \int_\theta p_{\dot{z}} \cos\theta R_b d\theta dy \\ \int_y \int_\theta p_{\dot{x}} \sin\theta R_b d\theta dy & \int_y \int_\theta p_{\dot{z}} \sin\theta R_b d\theta dy \end{bmatrix} \tag{B5}$$

where

$$p_0 = (p)_0, \quad p_x = \left(\frac{\partial p}{\partial x}\right)_0, \quad p_z = \left(\frac{\partial p}{\partial z}\right)_0, \quad p_{\dot{x}} = \left(\frac{\partial p}{\partial \dot{x}}\right)_0, \quad p_{\dot{z}} = \left(\frac{\partial p}{\partial \dot{z}}\right)_0 \tag{B6}$$

are the solutions of the Reynolds equations,

$$\left[\frac{1}{R_b^2}\frac{\partial}{\partial\theta}\left(\frac{h^3}{12\eta}\frac{\partial}{\partial\theta}\right) + h^3\frac{\partial}{\partial y}\left(\frac{1}{12\eta}\frac{\partial}{\partial y}\right)\right]\begin{pmatrix} p_0 \\ p_x \\ p_z \\ p_{\dot{x}} \\ p_{\dot{z}} \end{pmatrix} = \begin{pmatrix} \frac{\Omega}{2}\frac{\partial h}{\partial\theta} \\ -\frac{\Omega}{2}\left(\sin\theta\frac{3\cos\theta}{h}\frac{\partial h}{\partial\theta}\right) - \frac{h^3}{4\eta R_b^2}\frac{\partial p_0}{\partial\theta}\frac{\partial}{\partial\theta}\left(\frac{\cos\theta}{h}\right) \\ \frac{\Omega}{2}\left(\cos\theta\frac{3\sin\theta}{h}\frac{\partial h}{\partial\theta}\right) - \frac{h^3}{4\eta R_b^2}\frac{\partial p_0}{\partial\theta}\frac{\partial}{\partial\theta}\left(\frac{\sin\theta}{h}\right) \\ \cos\theta \\ \sin\theta \end{pmatrix} \tag{B7}$$

where Ω is the angular velocity, η is the viscosity of the fluid, and h is the fluid film height. A complete deduction in these equations can be found in Ref. [12].

With finite element software developed in-house, the two-dimensional equations (B7) are solved for each timestep. Then, the pressure and derivative distributions are integrated in order to obtain the equilibrium load, the stiffness coefficients, and the damping coefficients (Eqs. (B3) and (B4)), and, finally, the equation of motion (B2) is solved with a fifth-order Runge–Kutta method.

References

[1] Ji-Bin, Y., Yu-Lin, Q., and Chen-Wen, C., 1990, "Measurement of Oil Film Thickness Between W-N Helical Gear Tooth Profiles Using Laser Transmission Method," ASME J. Tribol., **112**(4), pp. 708–711.

[2] Jaloszynski, T. M., and Evers, L. W., 1997, "Dynamic Film Measurements in Journal Bearings Using an Optical Sensor," SAE Technical Papers Series No. 970846.

[3] Lu, X., and Khonsari, M. M., 2008, "An Experimental Study of Oil-Lubricated Journal Bearings Undergoing Oscillatory Motion," ASME J. Tribol., **130**(2), p. 021702.

[4] Cereska, C., and Vekteris, V., 2006, "Diagnostic of Temperature of System of Rotor With Bearings of Sliding." Diffus. Defect Data, Pt. B, **113**, pp. 379–392.

[5] Christensen, E., Tonnesen, J., and Lund, J. W., 1976, "Dynamic Film Pressure Measurements in Journal Bearings for Use in Rotor Balancing," ASME J. Eng. Ind., **98**(1), pp. 92–100.

[6] Gutes, M., 2008, "Estudio de un cojinete hidrodinámico y movimiento del eje conducido en una bomba de engranajes externos," Ph.D. thesis, Technical University of Catalonia, Terrassa, Barcelona.

[7] Cameron, A., 1983, *Basic Lubrication Theory*, 3rd ed., Ellis Horwood Ltd., Chichester, UK.

[8] El-Shafei, A., 1995, "Modeling Fluid Inertia Forces of Short Journal Bearings for Rotordynamic Applications," J. Vibr. Acoust., **117**, pp. 462–469.

[9] Castilla, R., Wojciechowski, J., Gamez-Montero, P. J., Vernet, A., and Codina, E., 2008, "Analysis of the Turbulence in the Suction Chamber of an External Gear Pump Using Time Resolved Particle Image Velocimetry," Flow Meas. Instrum., **19**(6), pp. 377–384.

[10] Rao, J. S., 1996, *Rotor Dynamics*, New Age International, New Delhi, India.

[11] Fogiel, M., 1980, *Handbook of Mathematical, Scientific and Engineering Formulas, Tables, Functions, Graphs, Transforms*, Research and Education Association, New Jersey.

[12] Hamrock, B. J., 1994, *Fundamentals of Fluid Film Lubrication*, McGraw-Hill, New York.

Controlling *n*-Heptane HCCI Combustion With Partial Reforming: Experimental Results and Modeling Analysis

Vahid Hosseini

W. Stuart Neill

Institute for Chemical Process and Environmental Technology, National Research Council, Ottawa, ON, K1A 0R6, Canada

M. David Checkel

University of Alberta, Edmonton, AB, T6G 2G8, Canada

One potential method for controlling the combustion phasing of a homogeneous charge compression ignition (HCCI) engine is to vary the fuel chemistry using two fuels with different auto-ignition characteristics. Although a dual-fuel engine concept is technically feasible with current engine management and fuel delivery system technologies, this is not generally seen as a practical solution due to the necessity of supplying and storing two fuels. Onboard partial reforming of a hydrocarbon fuel is seen to be a more attractive way of realizing a dual-fuel concept, while relying on only one fuel supply infrastructure. Reformer gas (RG) is a mixture of light gases dominated by hydrogen and carbon monoxide that can be produced from any hydrocarbon fuel using an onboard fuel processor. RG has a high resistance to auto-ignition and wide flammability limits. The ratio of H_2 to CO produced depends on the reforming method and conditions, as well as the hydrocarbon fuel. In this study, a cooperative fuel research engine was operated in HCCI mode at elevated intake air temperatures and pressures. n-heptane was used as the hydrocarbon blending component because of its high cetane number and well-known fuel chemistry. RG was used as the low cetane blending component to retard the combustion phasing. Other influential parameters, such as air/fuel ratio, EGR, and intake temperature, were maintained constant. The experimental results show that increasing the RG fraction retards the combustion phasing to a more optimized value causing indicated power and fuel conversion efficiency to increase. RG reduced the first stage of heat release, extended the negative temperature coefficient delay period, and retarded the main stage of combustion. Two extreme cases of RG composition with H_2/CO ratios of 3/1 and 1/1 were investigated. The results show that both RG compositions retard the combustion phasing, but that the higher hydrogen fraction RG is more effective. A single-zone model with detailed chemical kinetics was used to interpret the experimental results. The effect of RG on combustion phasing retardation was confirmed. It was found that the low temperature heat release was inhibited by a reduction in intermediate radical mole fractions during low temperature reactions and during the early stages of the negative temperature coefficient delay period. [DOI: 10.1115/1.3078189]

1 Introduction

Diesel engine manufacturers are pursuing a variety of combustion strategies for simultaneously achieving high fuel conversion efficiency while producing near-zero engine-out NO_x and particulate matter (PM) emissions, which is commonly referred to as high efficiency clean combustion (HECC). The mixing-controlled HECC strategy involves the use of higher levels of exhaust gas recirculation (EGR) than current diesel technology to reduce the combustion temperatures. This technology appears to require very high fuel injection pressures with small injector nozzle holes and benefits from the use of an oxygenated diesel fuel (see Ref. [1]). The premixed HECC or HCCI strategy involves the uncontrolled auto-ignition of a homogeneous air/fuel mixture under highly diluted conditions with excess air and/or EGR. It has been shown to produce very low NO_x and PM emissions and has the potential to have a high fuel conversion efficiency due to the short duration of heat release. On the other hand, HCCI combustion suffers from the lack of a direct method to control combustion phasing, as well as high HC and CO emissions [2].

Manuscript received June 26, 2008; final manuscript received July 21, 2008; published online May 22, 2009. Review conducted by Dilip R. Ballal. Paper presented at the 2008 Spring Conference of the ASME Internal Combustion Engine Division (ICES2008), Chicago, IL, April 27–30, 2008.

HCCI combustion phasing may be controlled indirectly by varying the in-cylinder temperature history or by altering the auto-ignition properties of the fuel chemistry. Parameters that affect the in-cylinder temperatures include the intake temperature, intake pressure, compression ratio, engine speed, and coolant temperature. The fuel composition directly affects the auto-ignition process, which is commonly specified in terms of cetane number for diesel fuel or octane number (resistance to auto-ignition) for gasoline. Other parameters, such as relative air/fuel ratio (λ), residuals, and EGR affect both the in-cylinder temperatures and chemical composition.

The dual-fuel approach to altering diesel fuel chemistry by blending an appropriate quantity of a secondary fuel with a higher resistance to auto-ignition is one way to control the combustion phasing over a wide operating range independent of engine load. Several previous studies have examined dual-fueled HCCI combustion. Christensen et al. [3] examined a single-cylinder engine in HCCI mode with various blends of *n*-heptane/iso-octane and regular gasoline/diesel blends. In an experimental study by Stanglmaier et al. [4], fuel blending of additized F-T naphtha and natural gas was effectively used to control the phasing of HCCI combustion. Zheng et al. [5] examined dual-fuel HCCI combustion using dimethyl ether (DME)/methanol blends to expand the operating range.

Dual-fuel engines are not desirable due to the necessity of car-

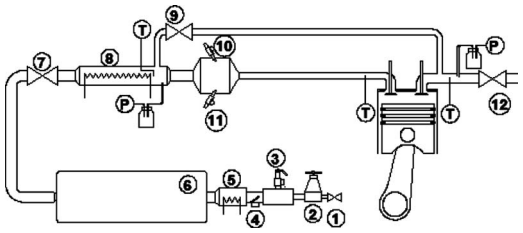

Fig. 1 Schematic of the CFR engine experimental setup, described in Table 1

rying two fuels onboard. Instead, partial reforming of diesel fuel with an onboard fuel reformer, which produces hydrogen rich gases, as the secondary fuel seems to be an attractive solution. This paper explores the possibility of HCCI combustion phasing control of a diesel-type fuel using reformer gas (RG).

RG or synthetic gas (syngas) is a mixture of light gases dominated by H_2 and CO. Steam reforming of natural gas is the main industrial method to produce H_2 in large quantities. Fuel reforming can be done by partial oxidation, steam reforming, or autothermal conversion. Details of reforming principles and techniques may be found in previous literature such as Ref. [6] or Ref. [7].

Shudo [8] altered the HCCI combustion of DME by adding H_2 and CO. The effect of RG on HCCI combustion of natural gas was investigated by Tsolakis and Megaritis [9]. It was found that the combustion phasing and duration were significantly changed by RG addition, leading to reductions in NO_x and PM emissions using diesel and biodiesel fuels. Eng et al. [10] studied the effects of partial oxidation RG on HCCI combustion of iso-octane and *n*-heptane. The authors also investigated the detailed chemical kinetics of H_2 enrichment on iso-octane and *n*-heptane autoignition. Hosseini and Checkel [11–13] investigated the effects of RG addition on HCCI combustion of a series of low octane primary reference fuels (PRFs), high octane PRFs, and natural gas.

2 Experimental Setup

A single-cylinder cooperative fuel research (CFR) engine manufactured by Waukesha Engine was used for the experiments. The engine has a variable compression ratio, a pancake combustion chamber with flat-top piston, and a bore $\times$ stroke of 82.6 $\times$ 114.3 mm^2. Compressed air was used to supply air to the engine. An electrical heater (8) was installed inside the intake to control the air temperature. Recirculated exhaust gas (EGR) was controlled manually by adjusting a manual EGR gate valve (9) as well as a butterfly valve (12) to set the exhaust back pressure. Liquid (10) and gaseous (11) injectors were installed in the intake plenum to fuel the engine. Figure 1 shows the main experimental hardware. The component description is provided in Table 1.

Table 1 List of the main components of the experimental setup in Fig. 1

Item No.	Description
1	Air supply main valve
2	Intake pressure regulator
3	High pressure relief valve
4	Low pressure relief valve
5	Hot wire anemometer
6	Intake pulsation damping barrel
7	Throttle valve
8	Intake heater
9	EGR valve
10	*n*-heptane injector
11	RG injector
12	Exhaust back-pressure valve

3 Operating Conditions

The engine was operated under steady state conditions with a constant speed of 800 rpm. The compression ratio was fixed at 11.8. The intake temperature of the air, fuel, RG, and EGR mixture just prior to entering the engine, $T_{\text{intake,mix}}$, was maintained at 110°C. Intake absolute pressure was kept constant at 140 kPa. The *n*-heptane mass flow rate was decreased as the RG blend fraction increased to maintain a constant air/fuel ratio. For example, if the engine was operated at 800 rpm, wide open throttle, atmospheric intake pressure, and $\lambda = 2.0$, increasing RG blend fraction from 0% to 30% corresponded to a 23% decrease in the *n*-heptane mass flow rate. Since liquid fuel was being replaced with gaseous fuel, the air mass flow rate to the engine was reduced by 3%, and the total energy flow rate to the engine was reduced by 1%. Hence, RG was introduced to the intake mixture as "RG blending" and not "RG enriching."

4 Definitions

EGR was defined as the ratio of CO_2 concentration in the intake to CO_2 concentration in the exhaust. RG blending as defined on a mass basis as RG blend fraction $= 100 \times \dot{m}_{\text{RG}} / (\dot{m}_{\text{RG}} + \dot{m}_{n\text{-heptane}})$, where $\dot{m}$ is the mass flow rate of *n*-heptane or RG.

Relative air/fuel ratio was calculated using the chemical valence method as described in [14] due to the presence of oxygen (CO) in the reformer gas. A more comprehensive method for calculating the air/fuel ratio of oxygenated fuels (or when oxidizer contains fuel) was described by Mueller [15].

Heat release calculations were performed using a single-zone well-stirred model using air as the working fluid, as described in Ref. [16]. The Woscnhi heat transfer correlation for HCCI engines [17] was used to calculate gross heat release (GHR) from net heat release. Referring to the net rate of heat release (NRHR) graph in Fig. 2(*a*), the maximum low temperature net rate of heat release (LTHR_{max}), maximum high temperature net rate of heat release (HTHR_{max}), and negative temperature coefficient (NTC) duration are defined. Using the cumulative gross heat release graph in Fig. 2(*b*), the start of combustion (SOC) is defined as the crank angle degree (CAD), where 10% of GHR_{max} occurs and combustion duration (CD) was defined as the time it requires to go from SOC to 90% of GHR_{max} on a CAD basis.

An uncertainty analysis was performed to quantify the cyclic variations of key combustion parameters. The key combustion parameters (SOC, CD, LTHR_{max}, HTHR_{max}, NTC, and indicated mean effective pressure (IMEP)) were calculated for 100 individual engine cycles and were averaged. In this paper, the error bars that appear in the graphs represent $\pm 2\sigma$.

5 Fuels

n-heptane was selected for this study because it is a volatile diesel fuel component with a high cetane number (54). It was injected into the intake plenum at a low pressure (413 kPa). The high volatility of *n*-heptane and the elevated intake temperature ensured that complete fuel vaporization occurred even at low port fuel injection pressures.

Simulated RG was provided from a high pressure tank. A natural gas injector supplied by alternative fuel systems was used. The injection pressure was held constant at 689 kPa. Two simulated RG compositions were examined. RG 75/25 was a mixture of 75% H_2–25% CO, and RG 50/50 was a mixture of 50% H_2–50% CO by volume. RG 75/25 was representative of a high H_2 content RG (to intensify H_2 effects) that is produced by steam reforming of natural gas. Onboard reforming of gasoline or diesel fuels produces RG similar to RG 50/50 through partial oxidation or autothermal reforming. The two RG cases of 75/25 and RG 50/50 represent the high and low limits for H_2 content, respectively. A comparison of the characteristics of RG 75/25 and RG 50/50 may be found in Ref. [18]. In practice, RG contains inert gases such as

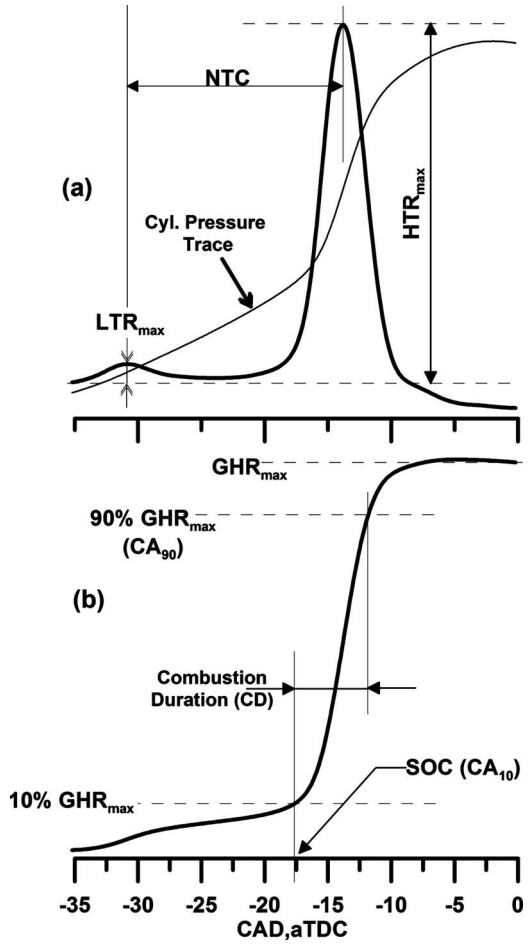

Fig. 2 Combustion characteristic definitions using (*a*) net rate of heat release and (*b*) gross cumulative heat release curves

N_2, CO_2, and H_2O. A portion of the EGR may be considered to be the inert component of RG. For example, at $RG_{mass,frac}=10\%$ and a stoichiometric mixture for *n*-heptane HCCI combustion, 10% of fuel mass and less than 0.7% of intake mixture is occupied by RG. If it is assumed that RG is a product of partial oxidation with air, and 75% of RG mixture is made up of inert gases, the total amount of EGR that should be considered to be the inert gas part of RG is 0.5% of intake mixture. Hence, in this case 0.5% of EGR (as EGR is also quantified by percent intake mixture) is considered to be the inert gas fraction of RG.

6 Experimental Results

Operating points. A series of experiments were performed at constant λ and EGR conditions, as indicated in Fig. 3. Each group is labeled with capital letters A–F, and the symbols used in Fig. 3 remain unchanged throughout the paper. The majority of constant λ cases had high EGR rates, as the operating region was large enough to group a series of constant λ data. The variation between λ and EGR within each group is shown by an uncertainty value indicated by a ± sign. In each group, the RG blend fraction was progressively increased from 0% to 30%.

Heat release characteristics. Figure 4 shows the NRHR and gross cumulative heat release for data set B shown in Fig. 3.

Figure 5 shows that increasing the RG blend fraction effectively retarded *n*-heptane HCCI combustion timing, while keeping all other influential parameters constant. On average; a 10% increase in the RG blend fraction retarded the combustion phasing by 4.4 CAD for the cases considered. It would require an increase in λ of 0.88 to achieve a similar delay in the combustion phasing using λ

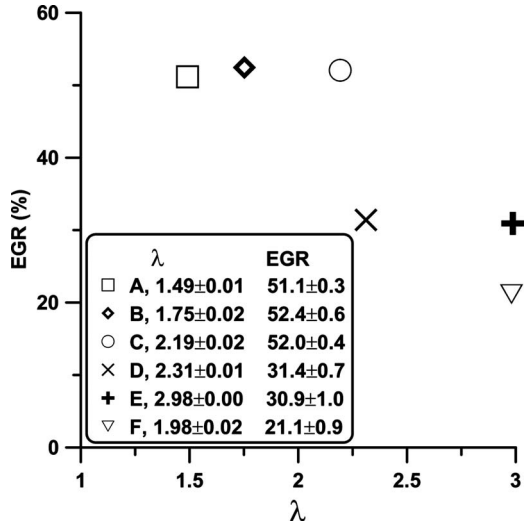

Fig. 3 Selected λ-EGR constant cases, *n*-heptane HCCI combustion, $N=800$ rpm, CR=11.8, and $T_{intake,mix}=110°C$

control for the same operating region, which corresponds to an IMEP reduction of 1.8 bar (see Ref. [19] for baseline experiments).

Figure 6 shows that increasing the RG blend fraction did not significantly affect the combustion duration, which for the purposes of this study was defined as the number of crank angle degrees between 10% and 90% heat release. Since the RG blend fraction affects low temperature heat release (LTHR), which was

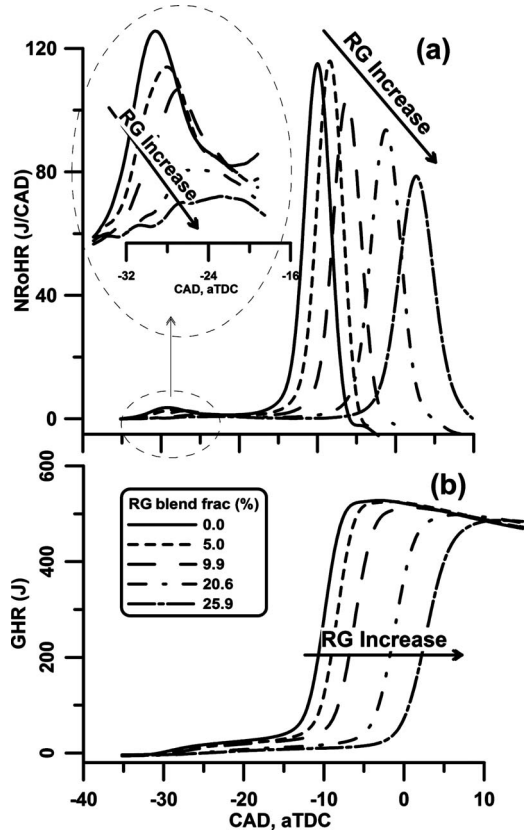

Fig. 4 Effect of RG on (*a*) net rate of heat release and (*b*) gross cumulative heat release for data set B in Fig. 3

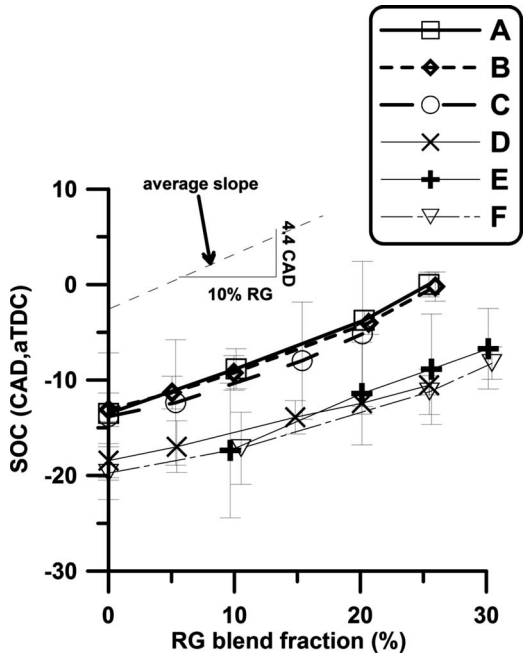

Fig. 5 Effect of RG on start of combustion for operating points in Fig. 3, error bars indicate ±2σ

typically less than 5% of the heat release, the RG did not change the duration of the high temperature heat release (HTHR) stage according to our definition.

Figure 7 shows the effect of RG on maximum low temperature rate of heat release ($LTHR_{max}$). Increasing the RG blend fraction by 10% decreased $LTHR_{max}$ by about 15%. The start of the LTHR stage remained relatively constant. The gross heat release was constant for all cases due to the constant energy flow to the engine (see Fig. 4(*b*)), while $HTHR_{max}$ was reduced due to the retardation of $HTHR_{max,time}$ (see Figs. 4(*a*) and 8).

Replacing *n*-heptane with RG was expected to reduce the heat capacity of the intake mixture and to increase the ratio of specific heats resulting in higher compression temperatures. As the start of the LTHR stage is highly temperature dependent, it was expected that the LTHR timing might be advanced due to higher compression temperatures. However, the start of LTHR was not significantly affected by RG addition. LTHR heat release was relatively small compared with the HTHR heat release and it was difficult to detect the start of LTHR.

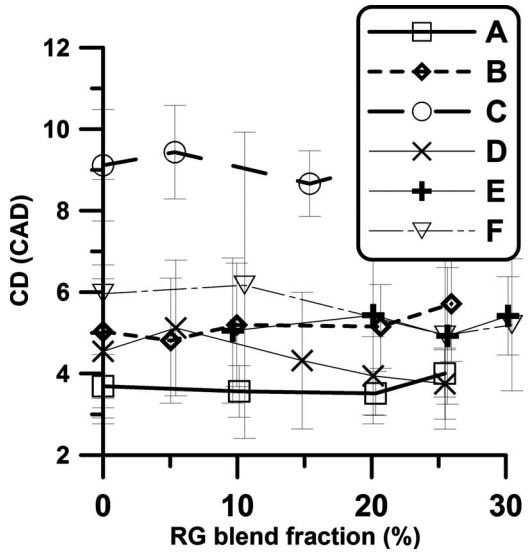

Fig. 6 Effect of RG on combustion duration for operating points in Fig. 3, error bars indicate ±2σ

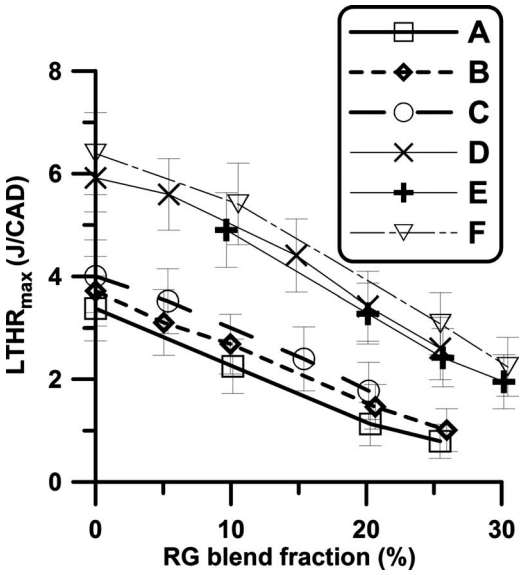

Fig. 7 Effect of RG on maximum low temperature heat release for operating points indicated in Fig. 3, error bars indicate ±2σ

Thus, the timing of the LTHR stage was characterized by the location of peak heat release ($LTHR_{max}$). Increasing the RG blend fraction reduced $LTHR_{max}$ by suppressing the low temperature combustion reactions and consequently retarding $LTHR_{max,time}$. The gross cumulative heat release (Fig. 4(*b*)) remained constant, as energy flow to the engine was held constant. However, the $HTHR_{max,time}$ was retarded considerably by increasing the RG blend fraction. Figure 8 shows that $HTHR_{max,time}$ was retarded by approximately 5.1 CAD when the RG blend fraction was increased by 10%. This was slightly more than the 4.4 CAD delay in the SOC for 10% RG blending, which may be related to the

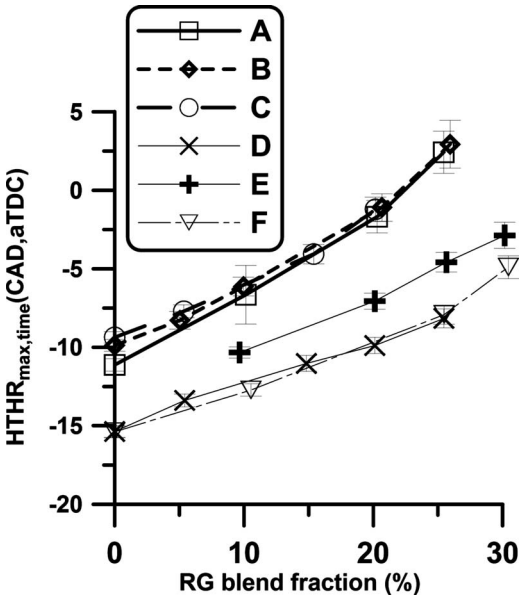

Fig. 8 Effect of RG on maximum high temperature heat release timing for operating points indicated in Fig. 3, error bars indicate ±2σ

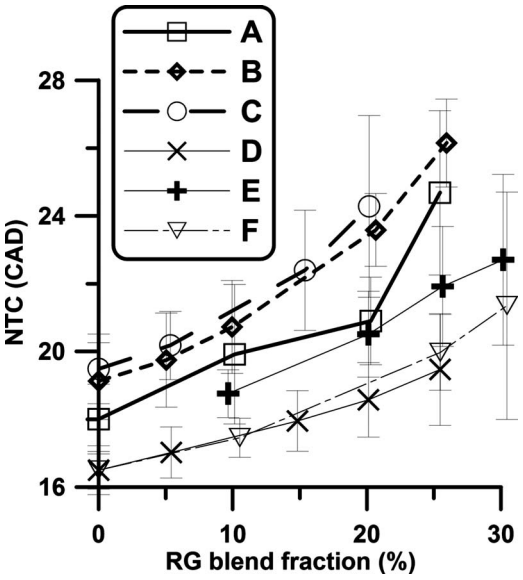

Fig. 9 Effect of RG on negative temperature coefficient duration for operating points indicated in Fig. 3, error bars indicate ±2σ

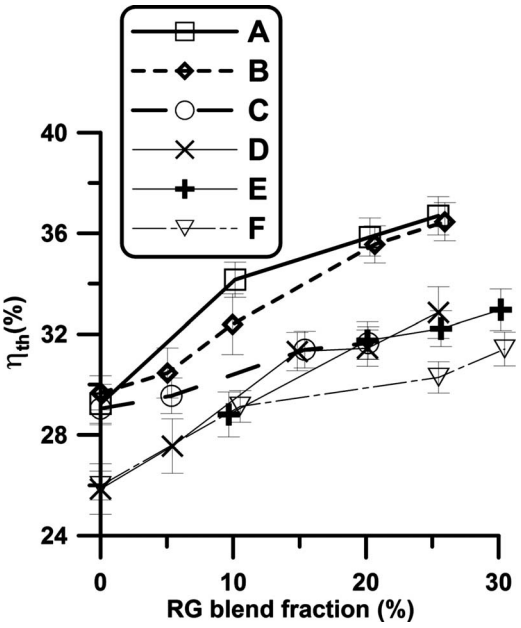

Fig. 11 Effect of RG on indicated thermal efficiency (η_{th}) for operating points in Fig. 3, error bars indicate ±2σ

slight retardation in $LTHR_{max,time}$. Increasing the RG blend fraction reduced $LTHR_{max}$, hence the required energy to initiate the main combustion stage had to be supplied by the compression process. Figure 9 shows that the NTC duration increases with increasing RG blend fraction due to a relatively constant $LTHR_{max,time}$ and a delayed $HTHR_{max,time}$.

Power and efficiency. Stable HCCI combustion was achieved as indicated by a coefficient of variation in IMEP of less than 3% for all operating points investigated. As the RG fraction was increased, IMEP increased due to the retardation of the combustion phasing toward an optimal combustion phasing. Figure 10 shows that a 10% increase in RG blend fraction led to an average IMEP increase of 0.25 bar due to the more optimized combustion phasing. This caused a 2.8% increase in thermal efficiency (η_{th}) on average for each 10% RG blend fraction increase, as indicated in Fig. 11.

The combustion timings for all cases examined in this study were advanced. The retardation of combustion timing by higher EGR, lower intake temperature, lower compression ratio, or higher λ was not possible.

The peak cylinder pressure was close to top dead center (TDC) for most of the baseline experiments (without RG blending). RG blending retarded the combustion timing toward a more optimized value, which led to higher indicated thermal efficiencies.

RG composition effects. Two similar cases of RG 75/25 and RG 50/50 were chosen for comparison. The EGR rates for the two cases were $(52.3 \pm 1.8)\%$ and $(51.7 \pm 1.0)\%$, respectively. Figure 12 shows pairs of constant λ and RG blend fraction for two cases of RG 75/25 and RG 50/50. While λ was identical in each pair, differences in the initial conditions and EGR rates led to small differences in the IMEP.

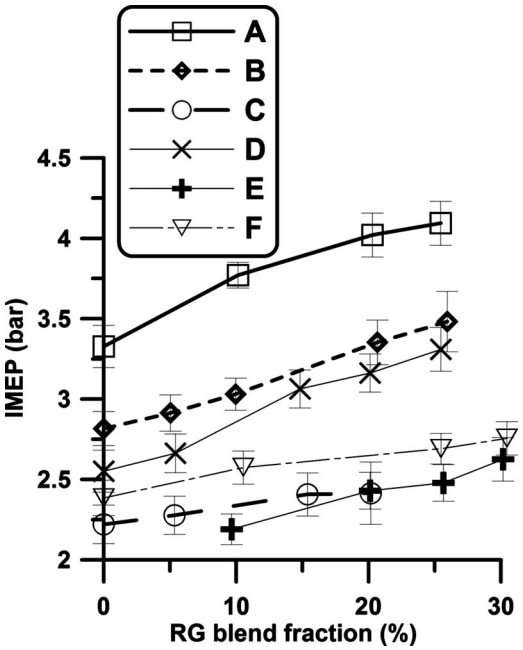

Fig. 10 Effect of RG on indicated mean effective pressure for operating points indicated in Fig. 3, error bars indicate ±2σ

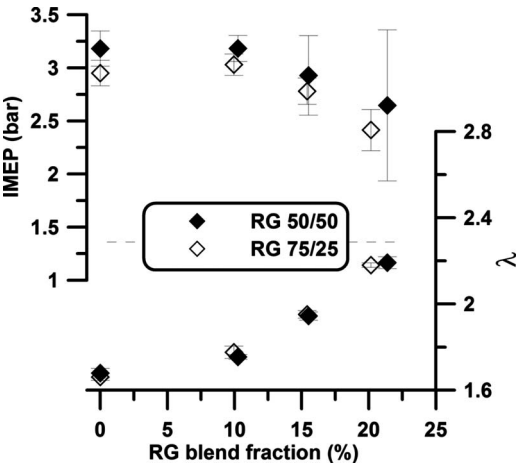

Fig. 12 Selected pairs of constant λ, similar EGRs, and identical RG blending fractions

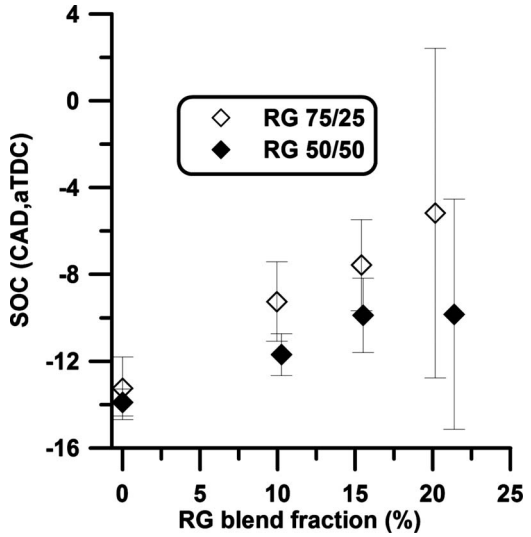

Fig. 13 Effect of RG composition on *n*-heptane HCCI combustion timing retardation, error bars indicate ±2σ

Note that by increasing RG blend fraction, λ is also increased due to difficulties in finding constant λ cases within the operating range.

Figure 13 shows the effect of RG composition on retardation of *n*-heptane HCCI combustion phasing. Despite identical λ values, Fig. 13 shows that RG 75/25 was more effective in retarding the SOC than RG 50/50. At RG blend fraction=0%, the two operating points were virtually the same and the starts of combustion were identical. At RG blend fraction=10%, the difference between SOCs were 2.4 CAD. At RG blend fraction=15%, the difference between SOCs was 2.6 CAD, and at RG blend fraction=20% the difference in SOCs increased to 4.8 CAD.

Figure 14 shows the effect of RG composition on net rate of heat release for two cases of RG 75/25 (top) and RG 50/50 (bottom). As indicated, RG 75/25 was more effective at reducing low temperature heat release than RG 50/50 and the retardation of the high temperature heat release (HTHR) stage was larger in the RG 75/25 case.

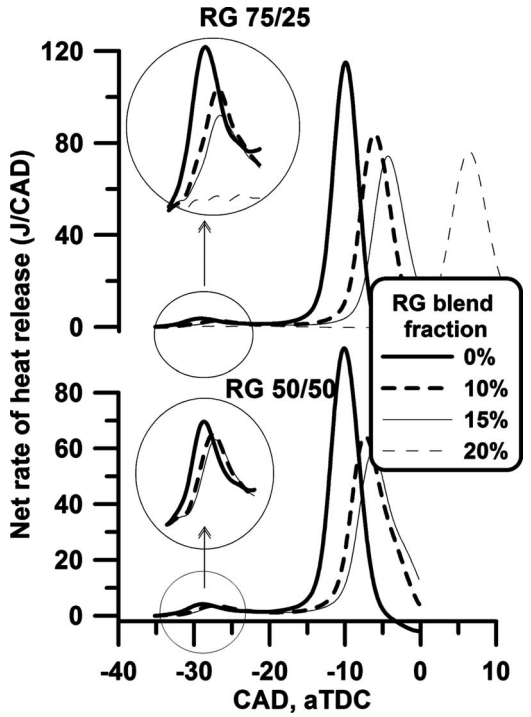

Fig. 14 Effect of RG composition on net rate of heat release

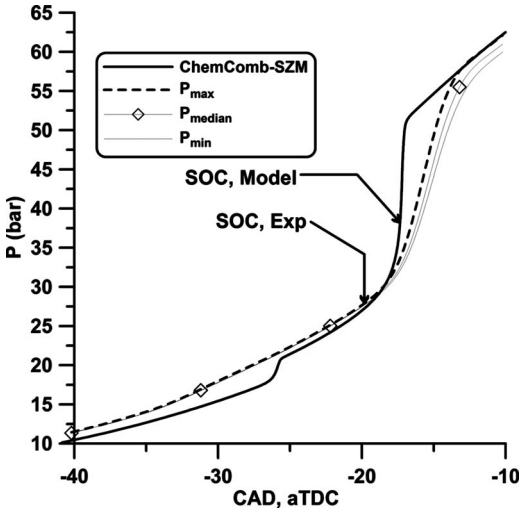

Fig. 15 Comparison of experimental pressure traces of point 1, data set F with ChemComb-SZM, experiment: supercharged *n*-heptane HCCI combustion, N=800 rpm, CR=11.8, $T_{intake,mix}$ =110°C, intake pressure=143 kPa, λ=2.94, EGR=19.9%, and RG blend fraction=0.0%

7 Numerical Simulation

Model description. A MATLAB®-based stand alone thermodynamic model with detailed chemical kinetics was developed to investigate RG effects on HCCI combustion of *n*-heptane. The model, described previously by Kongsereeparp and Checkel [20–23], simulates the closed portion of an HCCI combustion cycle using a single-zone model (SZM) or multizone model (MZM) configuration. The initial conditions are prescribed pressure, temperature, and equivalence ratio (φ) at intake valve closure, or mass flow rates of the intake mixture components.

ChemComb-SZM was used in this study to simulate the thermodynamics and detailed chemical kinetics of the combustion process up until the point of ignition. This model was found to predict the SOC to within the range of the measured engine cyclic variations. Since ChemComb-SZM assumes homogeneity of temperature, residuals, and φ, it overpredicts P_{max}, $(dP/d\theta)_{max}$, IMEP, and other engine parameters. However, ChemComb-SZM proved to be computationally efficient and reasonably accurate for predicting the early stages of combustion. The *n*-heptane chemical kinetic mechanism used for this study was adopted from a semireduced chemical kinetic mechanism developed by Golovichev [24] with 57 species and 290 reactions.

Chemical kinetic model validation. Experimental data set F was chosen for the purposes of validating the numerical simulation. Cylinder pressure traces predicted by ChemComb-SZM were compared with the corresponding experimental data at the start of HTHR, which occurs just prior to the 10% cumulative heat release location (SOC). For each operating point, 100 consecutive cycles of cylinder pressure data were processed, and the cycles with maximum P_{max}, minimum P_{max}, and median P_{max} were plotted. For simplicity, these cycles were named P_{max} (maximum P_{max}), P_{min} (minimum P_{max}), and P_{median} (median P_{max}).

Figures 15 and 16 compare ChemComb-SZM predictions with experimental data for RG fractions of 0% and 30.4%, respectively. The complete validation results can be found in Ref. [25]. Figure 17 shows that the numerical simulation correctly predicts the trend of increasingly retarded SOC as the RG fraction increases.

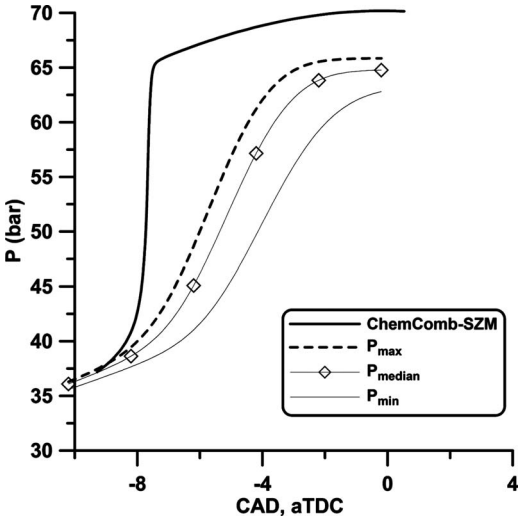

Fig. 16 Comparison of experimental pressure traces of point 1, data set F with ChemComb-SZM, experiment: supercharged *n*-heptane HCCI combustion, N=800 rpm, CR=11.8, $T_{intake,mix}$ =110°C, intake pressure=143 kPa, λ=3.00, EGR=21.7%, and RG blend fraction=30.4%

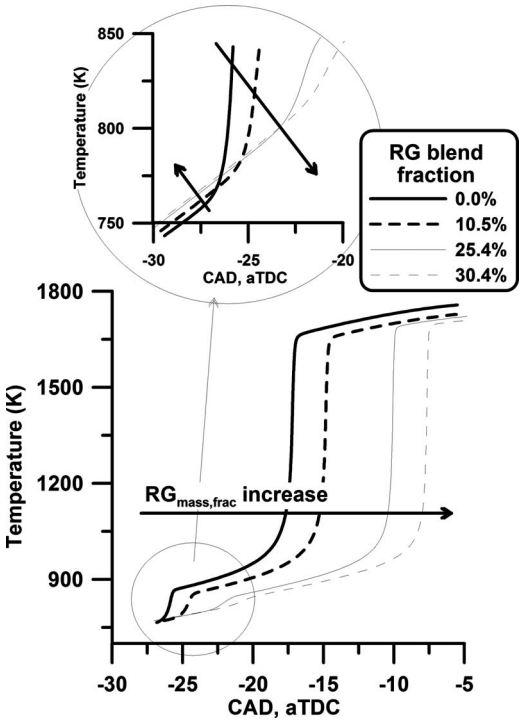

Fig. 18 ChemComb-SZM simulation results for in-cylinder temperature during and after compression for data set F in Fig. 3

The experimental results showed that 10% RG blend fraction increased retarded SOC by 4.4 CAD, whereas ChemComb-SZM predicted 3.1 CAD of SOC retardation for 10% RG blending.

The differences between the numerical simulation and experimental data were reasonable given the assumptions inherent in the single-zone model and the experimentally observed cyclic variability in the SOC.

Detailed analysis using ChemComb-SZM. Figure 18 shows the cylinder temperature traces predicted by ChemComb-SZM for the experimental data set F in Fig. 3.

The cylinder temperature history during the early stages of low temperature heat release (−30 to −20 CAD) has been magnified in the figure. The compression temperatures of the high RG blend fraction blends were higher than those of the low RG blend fraction blends before low temperature heat release is initiated. After low temperature combustion starts, however, the trend reverses with lower temperatures predicted as the RG blend fraction increases.

The low temperature heat release behavior may be further investigated by looking at key species concentrations during the LTHR and NTC combustion stages. Figure 19 shows the mole fraction evolution of key intermediate radicals formed during the combustion process: hydrogen peroxide (H_2O_2), formaldehyde (CH_2O), and hydroxyl (OH). Both formaldehyde and hydrogen peroxide are key radicals that accompany two-stage auto-ignition behavior.

The radical pool formation is initiated during the LTHR stage and continues during the NTC delay period. Before the main combustion stage (HTHR), all intermediate species are converted to hydroxyl radicals.

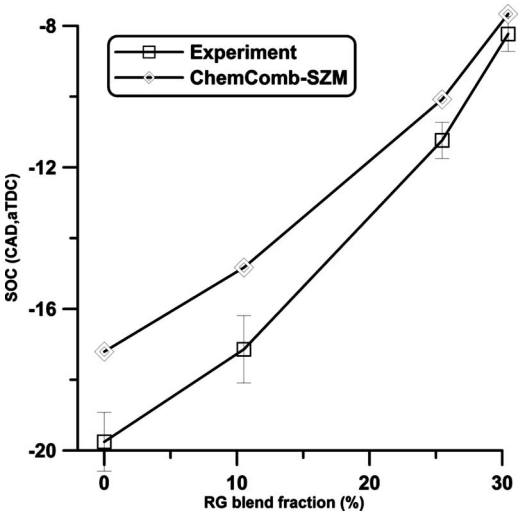

Fig. 17 A comparison of combustion timing (SOC) prediction by ChemComb-SZM with actual experimental combustion timing for data set F in Fig. 3, error bars on experimental SOC show the cyclic variation indicating ±2σ

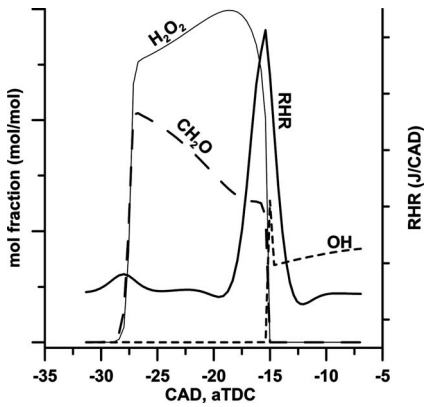

Fig. 19 Typical mole fraction traces of key species of OH, H_2O_2, and CH_2O compared with net rate of heat release in *n*-heptane HCCI combustion

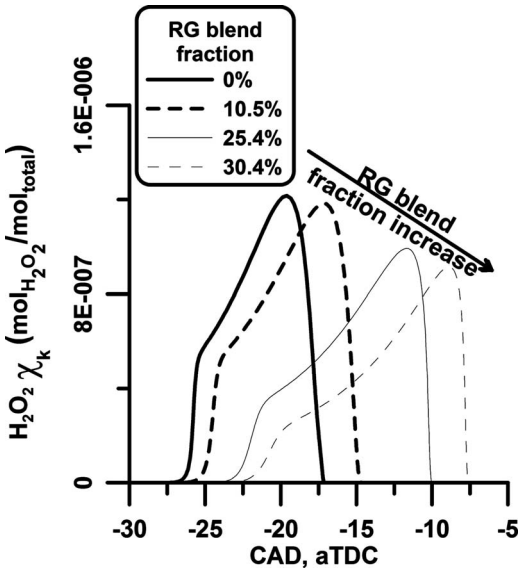

Fig. 20 Effect of RG on mole fraction of hydrogen peroxide (H_2O_2), *n*-heptane HCCI combustion simulated by ChemComb-SZM for data set F in Fig. 3

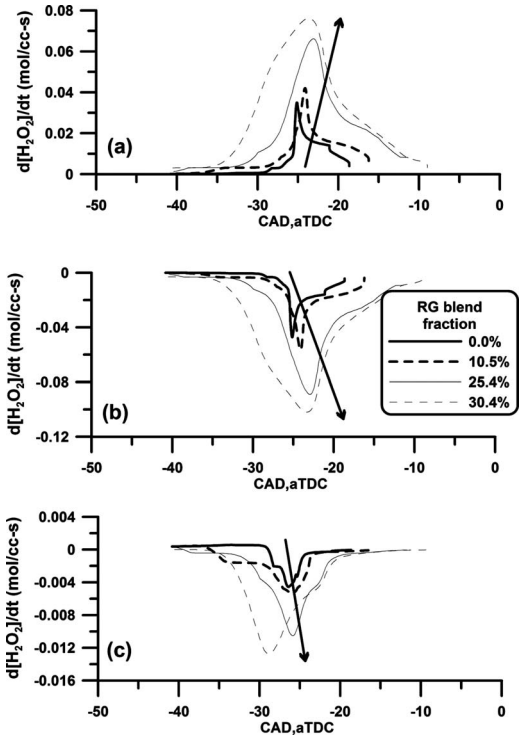

Fig. 21 Effect of RG on the reaction rates of H_2O_2, (*a*) production rate for Reaction 122, (*b*) production rate for Reaction 123, and (*c*) total production rate (from all 19 reactions)

The last stage is decomposition of the fuel molecules by OH radicals, which is associated with nonreversible reactions and abrupt heat release of the HTHR stage. Figure 20 shows the effect of RG on the H_2O_2 mole fraction. Increasing RG blend fraction decreased the molar fraction of H_2O_2 and retarded the timing of radical production.

Analysis of reaction rates in the main mechanisms used in ChemComb-SZM [24] indicates that Reaction 122 is the main source of H_2O_2 production during NTC

$$\text{Reaction 122:} \quad 2HO_2 \leftrightarrow O_2 + H_2O_2$$

Reaction 123 is the key reaction responsible for H_2O_2 destruction

$$\text{Reaction 123:} \quad OH + OH(+M) \leftrightarrow H_2O_2(+M)$$

Figure 21 shows that increasing the RG blend fraction increased both the production and destruction rates of the H_2O_2 radical during LTHR.

Figure 21(*c*) shows that increasing the RG blend fraction caused an overall net destruction of H_2O_2 radicals. The alteration of the key reaction rates happened during LTHR. Looking at the LTHR stage, the concentration of H_2O_2 radicals was decreased, as shown in Fig. 20. The mole fraction ratio of maximum OH to maximum H_2O_2 was decreased considerably. This ratio shifted progressively from $[OH]=0.94[H_2O_2]$ to $[OH]=0.08[H_2O_2]$, as the RG blend fraction increased from 0% to 30%, as shown in Fig. 22.

During LTHR, RG replaced most of the OH with H_2O_2 radicals through the following series of reactions:

$$\text{Reaction 101:} \quad H_2 + OH \leftrightarrow H_2O + H$$

$$\text{Reaction 97:} \quad CO + OH \leftrightarrow CO_2 + H$$

The H radical produced combines quickly with O_2 to form HO_2, and then with another H atom to form H_2O_2. OH is a highly active radical at low temperatures, while both HO_2 and H_2O_2 are almost inert during LTHR. Converting highly reactive OH radicals to less reactive HO_2 and H_2O_2 resulted in less chain branching reactions during LTHR, thus leading to less heat release during NTC and retardation of HTHR. These results are in agreement with findings of previous modeling and chemical kinetic studies such as Refs. [26,27].

Figure 23 compares the SOC prediction of the numerical simulation to the experimental data for the two cases of RG 75/25 and RG 50/50.

ChemComb-SZM was able to predict the SOC to within the cyclic variability of the observed SOC for both cases. For the case of RG 50/50, the experimental results showed 2.4 CAD retardation in combustion timing with 10% RG compared with a prediction of 1.7 CAD in SOC retardation by ChemComb-SZM. For the case of RG 75/25, the experimental results showed 5.5 CAD in SOC retardation for a 10% RG blend fraction increase, while the numerical simulation predicted 5.1 CAD in combustion timing retardation.

Figure 24 shows the mole fraction of hydrogen peroxide as a function of crank angle for different RG blend fractions and RG

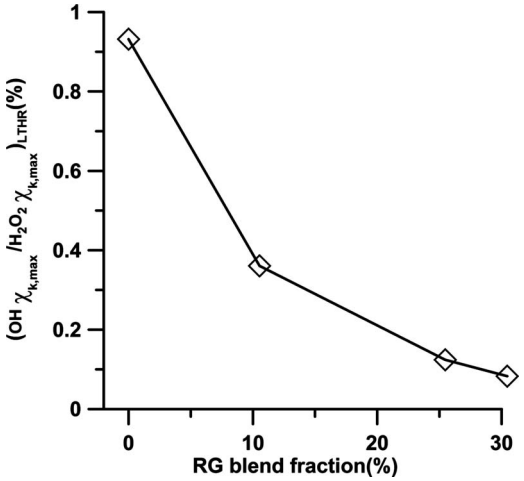

Fig. 22 Effect of RG on the ratio of maximum mole fraction during LTHR for OH/H_2O_2 ratio

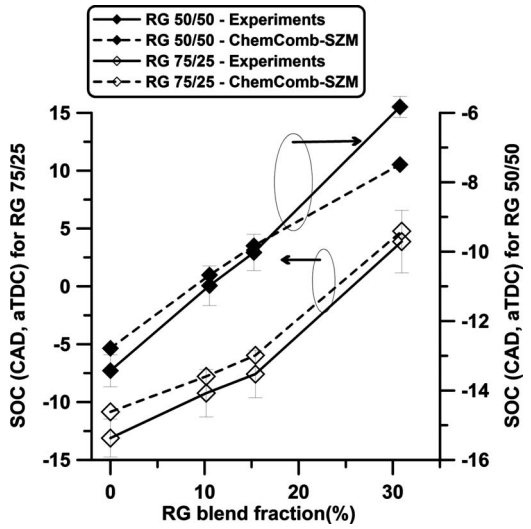

Fig. 23 A comparison of SOC prediction by ChemComb-SZM and experimental results for two cases of RG 75/25 (left *Y*-axis) and RG 50/50 (right *Y*-axis), error bars indicate ±2σ

compositions of 75/25 and 50/50. The graphs show that increasing RG blend fraction for both RG compositions reduces the mole fraction of intermediate radicals such as H_2O_2.

There was less delay in the formation of the H_2O_2 intermediate radical for the case of RG 50/50. Based on H_2O_2 radical concentrations shown in Fig. 24, the timing of maximum H_2O_2 molar concentration was retarded by 5 CAD for RG 75/25 and less than 3 CAD for RG 50/50. Thus, the RG 75/25 composition that contains a higher concentration of hydrogen gas is more effective in retarding the combustion timing.

8 Discussion

HCCI combustion timing is a complex function of several engine operating parameters such as compression ratio, intake temperature, EGR, air/fuel ratio, speed, and intake pressure. In this study, the effect of RG blending fraction and composition on *n*-heptane HCCI combustion timing was investigated, keeping other influential parameters constant. It was found that RG blending was effective in retarding *n*-heptane HCCI combustion over a wide range of conditions.

In the *n*-heptane experiments presented in this paper, λ did not have a large influence on HCCI combustion timing. In Fig. 5, λ variation between selected groups of operating points (Fig. 3) did not significantly change the SOC. EGR altered *n*-heptane HCCI combustion timing in distinct steps, as indicated in Fig. 5. On the other hand, an increase in EGR from 30% to 50% retarded combustion timing by an average of 5 CAD independent of λ. These results are comparable to those obtained by Peng et al. [28], in which a high compression ratio (CR=18.0) was used to operate a HCCI combustion engine with *n*-heptane. The engine was operated with an extremely lean ($6.0<\lambda<14.0$ at 0% EGR) and highly diluted mixture (up to 70% EGR) with intake temperature=30°C. The timings of the LTHR and HTHR combustion phases were strong functions of EGR and independent of λ. λ only affected HTHR timing when $\lambda>9.0$. In the current study, λ reduced $LTHR_{max}$, prolonged NTC, and delayed $HTHR_{max,time}$ (see Fig. 7–9).

Whereas λ did not have a strong influence on *n*-heptane HCCI combustion timing and EGR effects came with an IMEP penalty, RG was shown to be capable of combustion timing control with power and fuel conversion efficiency gains. For the selected cases, the indicated power (IMEP) was increased by an average of 0.25 bar for each 10% RG blend fraction increase (see Fig. 10), and indicated that thermal efficiency was increased by an average of 2.8% for a 10% RG blend fraction increase (see Fig. 11). Note that the efficiency penalty of fuel reforming was not considered in the indicated thermal efficiency calculation. If a 78% reforming efficiency is assumed for partial oxidation reforming of a hydrocarbon fuel (see Ref. [29]), and replacing 10% of *n*-heptane with RG, a total cycle efficiency decrease of less than 1% is expected for RG blend fraction=10%, which would be compensated by a 2.8% increase in indicated thermal efficiency due to RG blending. Increasing indicated power and indicated thermal efficiency was the result of more optimized combustion timing by RG blending.

A single-zone thermodynamic model with detailed chemical kinetics was used to interpret the experimental data. The numerical simulation SOC predictions showed good agreement with the experimental data, and qualitatively predicted the SOC retardation due to RG blending (see Fig. 17). During the compression stroke, the numerical simulation predicted higher temperatures as the RG

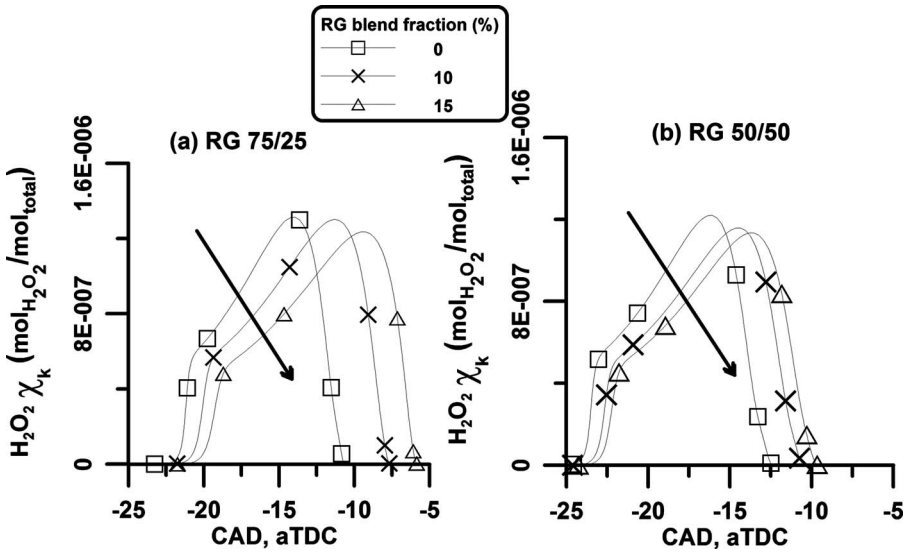

Fig. 24 Effect of RG composition on H_2O_2 mole fraction for (*a*) RG 75/25 and (*b*) RG 50/50

blend fraction increased (see Fig. 18). Replacing *n*-heptane (specific heat of C_p=224.9 J/mol K [30]) with RG (specific heats of C_{p,H_2}=28.84 J/mol K and $C_{p,CO}$=29.14 J/mol K [30]) led to higher compression temperatures. When the low temperature reactions were initiated around 760 K, the higher RG blending fractions produced lower temperatures after LTHR and during the NTC delay period. This is an indication of lower heat release during LTHR by the higher RG blend fractions that confirmed the experimental observations.

Lower heat release during LTHR was associated with a lower molar concentration of intermediate radicals as the RG blend fraction increased. For example, increasing the RG blend fraction decreased the molar concentration of H_2O_2 during NTC (see Fig. 20). However, lower H_2O_2 molar concentrations during the NTC delay period were not a result of low reaction rates. In the chemical kinetics mechanism that was used in this study, 19 reactions contributed to the production and destruction of H_2O_2. Among them, Reactions 122 and 123 were the main H_2O_2 production and destruction reactions, respectively. Increasing the RG blend fraction increased the rates for Reactions 122 and 123 (see Figs. 21(*a*) and 21(*b*)). However, the summation of all 19 reaction rates showed a relative increase in the H_2O_2 radical destruction rate. Increasing the RG blend fraction increased both the production and destruction of H_2O_2 radicals, but the net effect was in favor of lowering the H_2O_2 molar concentration (see Fig. 21(*c*)). The effect of RG blending was to progressively convert highly reactive hydroxyl radicals formed during LTHR to less reactive H_2O_2 radicals (see Fig. 22).

In practice, the H_2 to CO ratio in RG varies depending on the hydrocarbon fuel, the reforming technique, and the fuel reforming conditions. To investigate effects of RG composition on SOC retardation of *n*-heptane HCCI combustion, two extreme cases of RG were used. It was found that both RG compositions of RG 75/25 and RG 50/50 were effective in retarding *n*-heptane HCCI combustion timing, but RG 75/25 was more effective (see Fig. 13). The experimental results showed that $LTHR_{max}$ reduction with RG 75/25 was stronger than with RG 50/50 (see Fig. 14). Numerical simulations were performed to confirm the RG composition effects, which were in agreement with the findings of Shudo and Yamada [27] and Shudo and Takahashi [31] for RG addition on HCCI combustion of DME. Increasing the H_2 fraction in RG also increased the combustion retardation in their study. The current results are also in agreement with the results of numerical simulations performed by Subramanian et al. [26]. Using both detailed and reduced chemical kinetic mechanisms, the authors concluded that at temperatures around 600 K, the presence of CO lengthens *n*-heptane HCCI ignition delay by 5–10%, while H_2 addition lengthens the ignition delay by 10–15%.

Both H_2 and CO suppress the formation of radical pools. In the chemical kinetic mechanism used, Reactions 97 and 101 are responsible for OH radical consumption by CO and H_2, respectively. Similar to the discussion in Ref. [27], Reaction 101 is 3–6 times faster than Reaction 97 in the temperature range of 700–1000 K, where low temperature oxidation occurs. Migrating from RG 75/25 to RG 50/50 favors Reaction 97, and radical consumption by RG was reduced. The similarity of combustion suppression by H_2 and CO makes the application of fuel reforming attractive as a mean of combustion timing control for fuels with two-stage combustion. Practically, it means that small variations in onboard fuel reformer output during its operation will not have a large effect on combustion timing control.

9 Conclusions

The effects of reformer gas blends (RG, binary mixture of H_2, and CO) on homogenous charge compression ignition combustion of *n*-heptane were examined. It was found that RG blending was effective in retarding the combustion phasing. The mechanisms were reduction in the low temperature heat release followed by prolongation of the negative temperature coefficient delay period and a delay in the high temperature heat release. On average, increasing RG blend fraction by 10% retarded combustion timing by 4.4 crank angle deg.

Shifting *n*-heptane HCCI combustion timing toward a more optimized value increased indicated power at constant energy flow rate, as well as indicated thermal efficiency. On average, increasing the RG blend fraction by 10%, increased IMEP by 0.25 bar and indicated thermal efficiency by 2.8%.

A single-zone chemical kinetics model confirmed the experimental observations. It was found that RG initially increased compression temperatures, but after the low temperature heat release stage it reduced in-cylinder temperatures by lowering the energy released during the low temperature reactions. The model also showed that RG blending enhanced both the production and destruction of intermediate radicals during low temperature reactions. The overall effect was to decrease the total concentration of intermediate radicals.

Two extreme cases of RG compositions with 75% H_2–25% CO (RG 75/25) and 50% H_2–50% CO (RG 50/50) were examined. It was found that both RG compositions retarded *n*-heptane HCCI combustion phasing, but the higher H_2 content RG was more effective in retarding the combustion phasing.

Acknowledgment

The authors gratefully acknowledge the contributions of the Auto21 National Center of Excellence and the Government of Canada's PERD AFTER program that supported this work.

Nomenclature

ChemComb	=	thermodynamic model of HCCI combustion with detailed chemical kinetics
GHR	=	gross accumulative heat release (J)
HTHR	=	high temperature heat release (J)
LTHR	=	low temperature heat release (J)
NRHR	=	net rate of heat release (J/CAD)
RG	=	reformer gas (H_2/CO) mixture
SOC	=	start of combustion (CA10)
P_{max}	=	maximum cylinder pressure (bar)
$(dP/d\theta)_{max}$	=	maximum rate of pressure rise (bar/CAD)
$T_{intake,mix}$	=	intake mixture (air, fuel, RG, and EGR) temperature
σ	=	standard deviation of cyclic variation

References

[1] Upatniek, A., Mueller, C. J., and Martin, G. C., 2005, "The Influence of Charge-Gas Dilution and Temperature on DI Diesel Combustion Processes Using a Short-Ignition-Delay, Oxygenated Fuel," SAE Paper No. 2005-01-2088.

[2] Sjöberg, M., and Dec, J. E., 2003, "Combined Effects of Fuel-Type and Engine Speed on Intake Temperature Requirements and Completeness of Bulk-Gas Reactions for HCCI Combustion," SAE Paper No. 2003-01-3173.

[3] Christensen, M., Hultqvist, A., and Johansson, B., 1999, "Demonstrating the Multi-Fuel Capability of a Homogeneous Charge Compression Ignition Engine With Variable Compression Ratio," SAE Paper, 1999-01-3679.

[4] Stanglmaier, R. H., Ryan, T. W., and Souder, J. S., 2001, "HCCI Operation of a Dual-Fuel Natural Gas Engine for Improved Fuel Efficiency and Ultra-Low NOx Emissions at Low-to-Moderate Engine Loads," SAE Paper No. 2001-01-1897.

[5] Zheng, Z., Yao, M., Chen, Z., and Zhang, B., 2004, "Experimental Study on HCCI Combustion of Dimethyl Ether (DME)/Methanol Dual Fuel," SAE Paper No. 2004-01-2993.

[6] Jamal, Y., and Wyszynski, M. L., 1994, "On-Board Generation of Hydrogen-Rich Gaseous Fuels—A Review," Int. J. Hydrogen Energy, **19**(7), pp. 557–572.

[7] Dicks, A. L., 1996, "Hydrogen Generation From Natural Gas for the Fuel Cell Systems of Tomorrow," J. Power Sources, **61**, pp. 113–124.

[8] Shudo, T., 2006, "An HCCI Combustion Engine System Using On-Board Reformed Gases of Methanol With Waste Heat Recovery: Ignition Control by Hydrogen," Int. J. Veh. Des., **41**, pp. 206–225.

[9] Tsolakis, A., and Megaritis, A., 2005, "Partially Premixed Charge Compression Ignition Engine With On-Board H_2 Production by Exhaust Gas Fuel Reforming of Diesel and Biodiesel," Int. J. Hydrogen Energy, **30**, pp. 731–745.

[10] Eng, J. A., Leppard, W. R., and Sloane, T. M., 2002, "The Effect of POx on the Autoignition Chemistry of n-Heptane and Iso-Octane in an HCCI Engine," SAE Paper No. 2002-01-2861.
[11] Hosseini, V., and Checkel, M. D., 2006, "Using Reformer Gas to Enhance HCCI Combustion of CNG in a CFR Engine," SAE Paper No. 2006-01-3247.
[12] Hosseini, V., and Checkel, M. D., 2007, "Effect of Reformer Gas on HCCI Combustion—Part I: High Octane Fuels," SAE Paper No. 2007-01-0208.
[13] Hosseini, V., and Checkel, M. D., 2007, "Effect of Reformer Gas on HCCI Combustion—Part II: Low Octane Fuels," SAE Paper No. 2007-01-0206.
[14] Hosseini, V., and Checkel, M. D., 2005, "Alternative Mode Combustion Study: HCCI Fueled With Heptane and Spark Ignition Fueled With Reformer Gas," ASME Internal Combustion Engine Fall Technical Conference, Ottawa, Canada, Paper No. ICEF2005-1240.
[15] Mueller, C. J., 2005, "The Quantification of Mixture Stoichiometry When Fuel Molecules Contain Oxidizer Elements or Oxidizer Molecules Contain Fuel Elements," SAE Paper No. 2005-01-3705.
[16] Heywood, J. B., 1988, *Internal Combustion Engine Fundamentals*, McGraw-Hill, New York.
[17] Chang, J., Güralp, O., Filipi, Z., Assanis, D., Kuo, T.-W., Najt, P., and Rask, R., 2004, "New Heat Transfer Correlation for an HCCI Engine Derived From Measurements of Instantaneous Surface Heat Flux," SAE Paper No. 2004-01-2996.
[18] Hosseini, V., and Checkel, M. D., 2008, "Reformer Gas Composition Effect on HCCI Combustion of N-Heptane, Iso-Octane, and Natural Gas," SAE Paper No. 2008-01-0049.
[19] Hosseini, V., 2008, "Reformer Gas Application in HCCI Combustion Engine," Ph.D. thesis, University of Alberta, Edmonton, AB, Canada.
[20] Kongsereeparp, P., Kashani, B., and Checkel, M. D., 2005, "A Stand-Alone Multi-Zone Model for Combustion in HCCI Engines," ASME Internal Combustion Engine Fall Technical Conference, Ottawa, Canada, Paper No. ICEF2005-1241.
[21] Kongsereeparp, P., and Checkel, M. D., 2007, "Investigating the Effects of Reformed Fuel Blending in a Natural Gas- and N-Heptane-HCCI Engine Using a Multi-Zone Model," SAE Paper No. 2007-01-0205.
[22] Kongsereeparp, P., and Checkel, M. D., 2007, "Novel Method of Setting Initial Conditions for Multi-Zone HCCI Combustion Modeling," SAE Paper No. 2007-01-0674.
[23] Kongsereeparp, P., and Checkel, M. D., 2007, "Investigating the Effects of Reformed Fuel Blending in a Methane- or N-Heptane-HCCI Engine Using a Multi-Zone Model," SAE Paper No. 2007-01-0205.
[24] Golovichev, V., 2007, http://www.tfd.chalmers.se/~valeri/MECH.html.
[25] Hosseini, V., Neill, W. S., and Checkel, M. D., 2008, "Controlling N-Heptane HCCI Combustion With Partial Reforming: Experimental Results and Modeling Analysis," ASME Internal Combustion Engine Spring Technical Conference, Chicago, IL, Paper No. ICEF200-1618.
[26] Subramanian, G., Da Cruz, A. P., Bounaceur, R., and Vervisch, L., 2007, "Chemical Impact of CO and H2 Addition on the Auto-Ignition Delay of Homogenous N-Heptane/Air Mixtures," Combust. Sci. Technol., **179**(9), pp. 1937–1962.
[27] Shudo, T., and Yamada, H., 2007, "Hydrogen as an Ignition-Controlling Agent for HCCI Combustion Engine by Suppressing the Low-Temperature Oxidation," Int. J. Hydrogen Energy, **32**(14), pp. 3066–3072.
[28] Peng, Z., Zhao, H., and Ladommatos, N., 2003, "Effects of Air/Fuel Ratios and EGR Rates on HCCI Combustion of N-Heptane, a Diesel Type Fuel," SAE Paper No. 2003-01-0747.
[29] Docter, A., and Lamm, A., 1999, "Gasoline Fuel Cell Systems," J. Power Sources, **84**, pp. 194–200.
[30] Dean, J. A., 1999, *Lange's Handbook of Chemistry*, 15th ed., McGraw-Hill, New York.
[31] Shudo, T., and Takahashi, T., 2004, "Influence of Reformed Gas Composition on HCCI Combustion of Onboard Methanol-Reformed Gases," SAE Paper No. 2004-01-1908.

Xiaoyong Wang

Tsu-Chin Tsao[1]
e-mail: ttsao@seas.ucla.edu

Department of Mechanical and Aerospace Engineering,
University of California, Los Angeles,
Los Angeles, CA 90095

Chun Tai

Hyungsuk Kang

Volvo Powertrain North America,
Hagerstown, MD 21742

Paul N. Blumberg
Consultant,
Southfield, MI 48034

Modeling of Compressed Air Hybrid Operation for a Heavy Duty Diesel Engine

This paper presents the analysis and modeling of a 10.8 l heavy-duty diesel engine modified for operating compressed air hybrid engine cycles. A lumped parameter model is developed to first investigate the engine cylinder-air tank mass and energy interaction. The efficiency of compressed air energy transfer is defined based on the second law of thermodynamics. A high fidelity model is developed using commercially available software (GT-POWER) to capture the effects of engine friction, heat transfer, gas dynamics, etc. Engine valve timing for optimal efficiency in air regeneration and the corresponding engine speed-torque maps are established using the detailed engine model. The compressed air hybrid engine maps are then incorporated into vehicle simulation (ADVISOR) to evaluate the potential fuel economy improvement for a refuse truck under a variety of driving cycles. Depending on the particular driving cycle, the simulation has shown a potential 4–18% fuel economy improvement over the truck equipped with the conventional baseline diesel engine. [DOI: 10.1115/1.3078788]

Keywords: air hybrid, regenerative braking, air compressing, air motoring, availability

1 Introduction

In 1999, Schechter proposed new engine cycles that lead to the concept of "air hybrid" engines [1]. Three new engine cycles were introduced: air compressor (AC), air motor (AM), and air power-assist (APA). In regenerative braking, the engine is configured to run the AC cycle. In this mode, the vehicle kinetic energy drives the engine to produce compressed air while the vehicle is slowing down. The AC cycle works the same way as the engine brake does, but the compressed air is collected and stored in an on-board air tank instead of being discharged into the ambient. To recover the energy subsequently during vehicle acceleration or launch, the engine runs in either the AM or APA cycle. AM is a pure air power cycle, while APA is a combination of air work and fuel work.

In his second paper [2], Schechter further discussed the energy absorption and recovery process, supporting with preliminary thermodynamic analysis of ideal cycles. Tai et al. [3] worked on the modeling of an air hybrid gasoline engine using the commercial software application GT-POWER. This was the first time that the air hybrid concept was considered from a practical point of view to evaluate its potential for fuel economy improvement. Andersson et al. [4] proposed a dual storage tank air hybrid configuration for trucks and buses. The purpose is to increase AC mode brake mean effective pressure (BMEP), i.e., to absorb energy at a higher rate, while still operating in thermodynamically efficient type I compression braking as described by Schechter [1]. Trajkovic et al. [5] conducted a demonstrative experimental study of air hybrid operations on a Scania D12 single cylinder diesel engine equipped with a prototype pneumatic valvetrain capable of variable valve timing.

In this paper, we analyze the air cycles in a systematic way to understand the physics of the air hybrid operations. Based on the analysis, optimal system operating strategies are proposed. In the application to heavy-duty diesel engine hybridization, the system is modeled using GT-POWER in a more practical manner. In principle, the model simulation results agree with the theoretical analysis. The model is then used to generate optimal operating maps for vehicle simulation.

2 AC and AM Cycles

In this study, we only consider the basic energy regenerative cycles—the air compressing and air motoring cycles. The AC cycle is the energy regeneration cycle and the AM cycle is the energy reuse cycle. In this section, cylinder *P-V* diagrams are utilized to develop conceptual understanding of the cycles.

Figure 1 shows the *P-V* diagram of the AC cycle. This is a two-stroke cycle, consisting of intake ($1 \rightarrow 2$), compression ($2 \rightarrow 3$), discharge ($3 \rightarrow 4$), and expansion ($4 \rightarrow 1$) processes. Ideally, these processes are considered as adiabatic (compression and expansion) or isobaric (discharge and intake). Under these assumptions, the cycle work can be analytically calculated by

$$W = \int P dv \tag{1}$$

The engine torque is then determined accordingly. It can be seen that the cycle work is related to engine valve events. Intuitively, by retarding or advancing intake valve close (IVC), the amount of air trapped in the cylinder varies and the compression line moves horizontally. This provides a mechanism to change the cycle work and, thus, engine torque by controlling IVC. Setting IVC at bottom dead center (BDC) or slightly after BDC, the cycle work is maximized. If exhaust valve open (EVO) is set when the cylinder pressure is equal to the tank pressure P_t, the cycle is referred as AC type I. To achieve more work or higher torque, EVO can be advanced. Dashed line $2' \rightarrow 3'$ in Fig. 1 shows a case in which the exhaust valve is opened much earlier than the equilibrium pressure at 3 such that the enclosed cycle area is increased. Such a cycle is called AC type II. However, the extra work comes with a cost. Process $2' \rightarrow 3'$ involves air blowdown from the air tank back into the cylinder and this process is highly irreversible. In other perspective, work consumed increases while the amount of high pressure air delivered does not. AC type II thus has lower cycle efficiency.

[1]Corresponding author.

Manuscript received August 17, 2008; final manuscript received August 27, 2008; published online May 26, 2009. Review conducted by Dilip R. Ballal. Paper presented at the 2008 Spring Conference of the ASME Internal Combustion Engine Division (ICES2008), Chicago, IL, April 27–30, 2008.

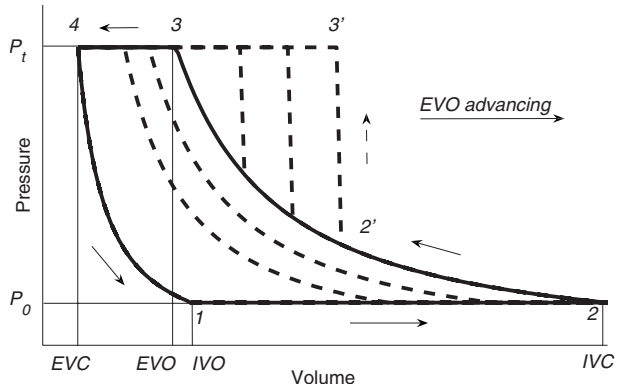

Fig. 1 AC *P-V* diagram

The AM cycle is shown in Fig. 2. AM is the reverse cycle of AC. The compressed air from the air tank is introduced to the cylinder through the exhaust valves or intake valves, in this study, the exhaust valves. The high pressure air expands in the cylinder as the piston moves toward BDC to perform work. The air expands to the ambient pressure before or at BDC. Such cycles are referred as AM type I. In situations when more work/torque is needed, exhaust valve close (EVC) is retarded and the expansion line $(2 \rightarrow 3)$ moves outward, as shown by the dashed lines $(2 \rightarrow 2' \rightarrow 3')$. The air does not fully expand when the exhaust valves are opened to discharge. The cycle is called AM type II. The residual energy of the compressed air is wasted and the cycle is less efficient.

The cycle descriptions from the *P-V* diagrams give us an idea how the cycles should be operated. In AC, IVC is used to control the torque and is called the primary independent variable. In AC type II, EVO becomes independent instead. In AM type I or type II, EVC is the independent variable for torque control. In both AC and AM modes, the torque control mechanism is regulating the amount of air admitted during the intake phase through appropriate valve timing. The torque is proportional to the cycle work, thus is directly governed by the first law of thermodynamics.

3 Cycle Efficiency

In the work of Tai et al. [3], air mass flow was used as an indication of the cycle performance. In Sec. 4, an energy based efficiency definition will be developed. The cycle efficiency indicates the energy conversion performance of the air hybrid engine. The energy consumed by an AC cycle or recovered by an AM cycle is calculated directly from the *P-V* diagram as stated in Sec. 2. The compressed air energy in the storage tank can be quantified by its availability. Here the internal energy is not a good measure, since not all of the energy may be available to do the useful work later on.

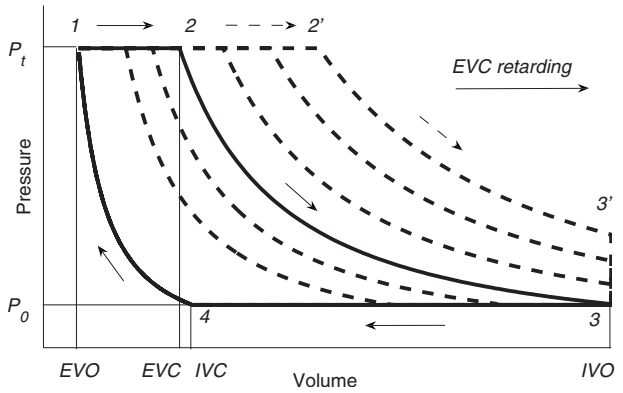

Fig. 2 AM *P-V* diagram

In thermodynamics, the availability of the system is defined as the maximum useful work that can be obtained from the system. In other words, a system's total energy (or internal energy if kinetic and potential energy are negligible) may not be fully available to perform useful work. For thermal energy systems, it is true that only a portion of the total energy can be extracted for useful work, and the rest of the energy has to be wasted and rejected to its environment. Using availability, the efficiencies of AC and AM can be defined as

$$\eta \triangleq -\frac{\Delta B}{W} \quad \text{for AC}$$
$$\eta \triangleq -\frac{W}{\Delta B} \quad \text{for AM} \tag{2}$$

Because of the sign convention of W and B, negative signs are added to define the efficiency as positive numbers. As AC and AM cycle efficiencies are defined separately, they can be multiplied together to get the so-called round-trip efficiency:

$$\eta \triangleq -\frac{W_{\text{AM}}}{W_{\text{AC}}} \tag{3}$$

By definition, the round-trip efficiency directly tells the percentage of the vehicle kinetic energy during braking that is recovered for vehicle acceleration.

The efficiency definitions, Eq. (2), are very straightforward and clear except that the availability B is a little involved. Given the air states (P, V, or T) and the ambient states (P_0, V_0, or T_0), the availability B is defined as [6,7]

$$B \triangleq (U - U_0) + P_0(V - V_0) - T_0(S - S_0) \tag{4}$$

According to this definition, the availability of a system at a specified state depends on the environment state. It is obvious that at the environment state, the availability of air is 0 ("the dead state"). In our context, the environment state is the ambient atmosphere state, usually taken as 1.013 bars and 300 K. The first term in the definition is the internal energy change to bring the air to the dead state. The second term is the environmental work, which cannot be usefully extracted. The third term incorporates the entropy change and represents the heat transfer in the process.

For a system to achieve its maximum useful work potential, i.e., availability, the system has to undergo a reversible process from its initial state to its environment state. If the process is not reversible, there is another term that reduces useful work, i.e., the $T_0 S_{\text{gen}}$ term in Eq. (5), which is called irreversibility. As stated by the second law of thermodynamics, any practical process is irreversible and the generated entropy S_{gen} during a process is always positive. Thus, the useful work is always less than the availability. The associated irreversibility of a process reduces the process efficiency.

$$W_u = (U - U_0) + P_0(V - V_0) - T_0(S - S_0) - T_0 S_{\text{gen}} \tag{5}$$

In AC, the air availability during 1 cycle is the minimal piston work required to bring air from the state of the ambient to the state of the tank. In AM, the air availability during one cycle is the maximal piston work that can be extracted to bring air from the state of the tank to the state of the ambient.

The definitions in Eq. (2) give us a dimensionless quantity that is convenient to compare with other cycles. It also indicates how well the cycle compares with a perfect cycle. Because cycle irreversibilities reduce useful work, this definition encourages controlling the cycles to be as close to reversible as possible. The irreversibility increases if there is a significant pressure difference

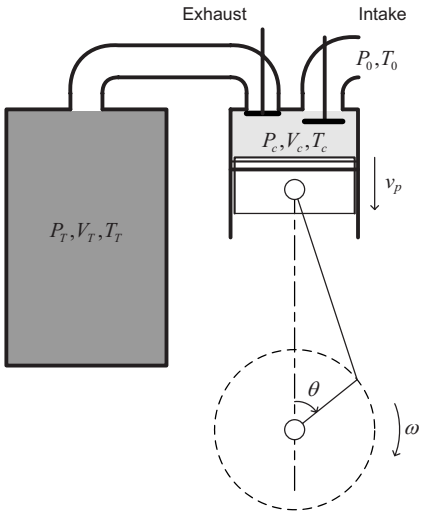

Fig. 3 Cylinder-tank model

between the upstream and downstream pressures, such as air blowdown when the engine valves are opened in type II cycles (Figs. 1 and 2).

In the ideal case, the valves are opened when upstream and downstream pressures are equal; thus there is no blowdown. This timing strategy is implemented in Ref. [5]. In practice, opening at equal pressure is not the best choice for the following reasons: (i) the valve opening process takes time, usually 2–6 ms; (ii) a pressure differential is needed to generate flow. Thus, valve opening timings should be optimized including these dynamic effects and the cycle efficiency serves as the optimization index.

4 Cylinder-Tank Interaction

To help understand the AC and AM cycles, we need to look at the in-cylinder processes, including the flow of air between the tank and the cylinder while the tank is being charged or discharged. The cylinder-tank system is illustrated in Fig. 3. The air tank is connected to the cylinder through the exhaust valve. There are three important components: the cylinder, the valves, and the tank. In the following, the air within these major components are modeled based on thermodynamics and piston kinematics.

4.1 In-Cylinder Process. The cylinder is modeled as an open system that exchanges mass at any given instantaneous thermodynamic state with the ambient or the air storage tank. Through piston motion, its volume changes with respect to the crankshaft position as a function engine speed. The quantities we are looking for are the cylinder pressure versus time (or crank angle) and the mass at its instantaneous thermodynamic state, which is delivered or received from the tank or the ambient. The following equations describe the mass, energy and states of the air in the cylinder:

$$\frac{dE}{dt} = h_i \dot{m}_i - h_o \dot{m}_o - P\frac{dV}{dt}$$

$$PV = mRT$$

$$\frac{dm}{dt} = \dot{m}_i - \dot{m}_o$$

$$\frac{dV}{dt} = \tfrac{1}{4}\pi D^2 v_p = f(\omega, \theta)$$

$$E = mc_v T$$

$$h = c_p T \tag{6}$$

The energy change is caused by mass flow (enthalpy H), mechanical work, and heat transfer. The air is considered as an ideal gas and the ideal gas equation is used to relate pressure, temperature, volume, and mass. The mass flow takes place only when the intake or exhaust valve is open. When all the valves are closed, as the piston moves, the air inside the cylinder undergoes polytropic processes. If heat transfer is neglected, the process follows the adiabatic compression and expansion lines as shown in Figs. 1 and 2.

4.2 Valve Flow. Valve flow is critical in AC or AM operations because most of the losses and irreversibilities are associated with air entering or exiting the cylinder through the engine valves. Modeling of the gas dynamics is complicated and beyond the scope of this work. We follow most of the approaches in the literature, such as in Refs. [6,8,9], to model it as one-dimensional isentropic flow in a converging nozzle emptying into a large volume. Define the critical pressure

$$P_c = \left(\frac{2}{\gamma+1}\right)^{\gamma/(\gamma-1)} P_1 \tag{7}$$

If $P_2 > P_c$, the mass flow rate is given by

$$\dot{m}_{\text{is}} = \rho_0 A_v c \left[\frac{2}{\gamma-1}\left(\left(\frac{P_2}{P_1}\right)^{2/\gamma} - \left(\frac{P_2}{P_1}\right)^{(\gamma+1)/\gamma}\right)\right]^{1/2} \tag{8}$$

If $P_2 \le P_c$, the flow is choked, and the mass flow rate is given by

$$\dot{m}_{\text{is}} = \rho_0 A_v c \left(\frac{2}{\gamma+1}\right)^{(\gamma+1)/2(\gamma-1)} \tag{9}$$

where P_1 is the upstream pressure and P_2 is downstream pressure. $c = (\gamma R T_1)^{1/2}$ is the upstream stagnation sound speed.

The valve discharge coefficient, C_d, is introduced to account for the irreversibilities in the port flow. Since the valve flow area is represented by A_v, the cross area of the port, C_d also accounts for the valve lift in calculating the effective flow area. C_d is experimentally determined on a flow bench and the effective flow area is given by

$$A_{\text{eff}} = C_d A_v \tag{10}$$

And the actual flow rate is

$$\dot{m}_a = C_d A \dot{m}_{\text{is}} \tag{11}$$

C_d is tabulated as a function of valve lift or L/D. C_d represents the deterioration of actual mass flow rate from isentropic case under the same upstream states and the same downstream pressure.

4.3 Air Tank. The air tank is modeled as a control volume, which exchanges mass only with the cylinder. The tank has a fixed volume V_T. The tank is assumed to be well insulated so that the heat transfer between the tank and the ambient can be considered negligible. The mean-value model of its state is given by

$$\frac{dE}{dt} = h_o \dot{m}_o$$

$$PV_T = mRT \tag{12}$$

$$E = mc_v T$$

where h_0 and $\dot{m}_0$ are the enthalpy and mass flow through the exhaust valves as in Eq. (6). The pressure and temperature determined by Eq. (12) are used to calculate the tank air entropy S.

5 MD11 Air Hybrid Engine Model

MD11 is one of the current production engines of Volvo Powertrain NA. A simplified MD11 model is developed based on the analysis in Sec. 4 using MATLAB Simulink. In this section, we establish the air hybrid model of this engine using the GT-POWER

Table 1 MD11 Specification

Engine type	10.8 l in-line 6
Horsepower (hp at rpm)	300 at 2100
Torque (N m at rpm)	1672 at 1200
Bore × stroke (mm)	123 × 152
Compression ratio	16:1

engine simulation software from Gamma Technologies. GT-POWER provides an excellent intuitive graphic user interface and facilitates a fast beginning in the construction of sophisticated engine models. On the other hand, the governing physics of the phenomena are embedded in the code and are not evident to the user. In Sec. 4, the major physical relationships were revealed. GT-POWER allows modeling the air hybrid engine in greater detail and in an accurate way. The major specifications of the baseline MD11 engine are listed in Table 1.

The air hybrid lends itself to many different configurations. Our design is illustrated in Fig. 4. The air handling system of the engine is modified to accommodate air flow in different directions under different running modes. There are three air switching valves: compressor bypass valve; intake three-way valve, and exhaust three-way valve. These components have to handle the pressure and temperature range of the intended design. The air flow direction is summarized as follows:

(a) AC mode: intake pipe → compressor by-pass → intake three-way → intake manifold → intake valves → cylinder → exhaust valves → exhaust manifold → exhaust three-way → air tank

(b) AM mode: air tank → exhaust three-way → exhaust manifold → exhaust valves → cylinder → intake valves → intake manifold → intake three-way → exhaust pipe

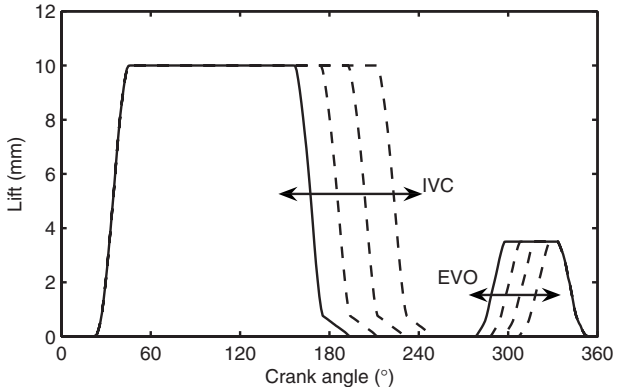

Fig. 5 Camless intake and exhaust valve profiles

The tank has a volume of 280 l, comparable to a truck onboard fuel tank (75 gal). As future work, the typical driving cycle of the targeted vehicle application can be used to optimize the tank size.

Another important change to the baseline engine is the replacement of the conventional mechanical valvetrain with a hydraulic actuated camless valvetrain. The opening and closing timings of each valve are specifiable. The intake valve takes about 5 ms to open from 0 mm to 10 mm, and 5 ms to close. The exhaust valve takes about 2.87 ms to open from 0 mm to 3.5 mm, and 2.76 ms to close. The profiles are shown in Fig. 5 in the crank angle domain. The valve traces are from the valvetrain design phase of the program. Because of generally higher density of the exhaust air in air cycle modes, the exhaust valve lift can be reduced without restricting the flow. This was studied systematically using the GT-POWER model, and the results indicated that with 3.5 mm lift

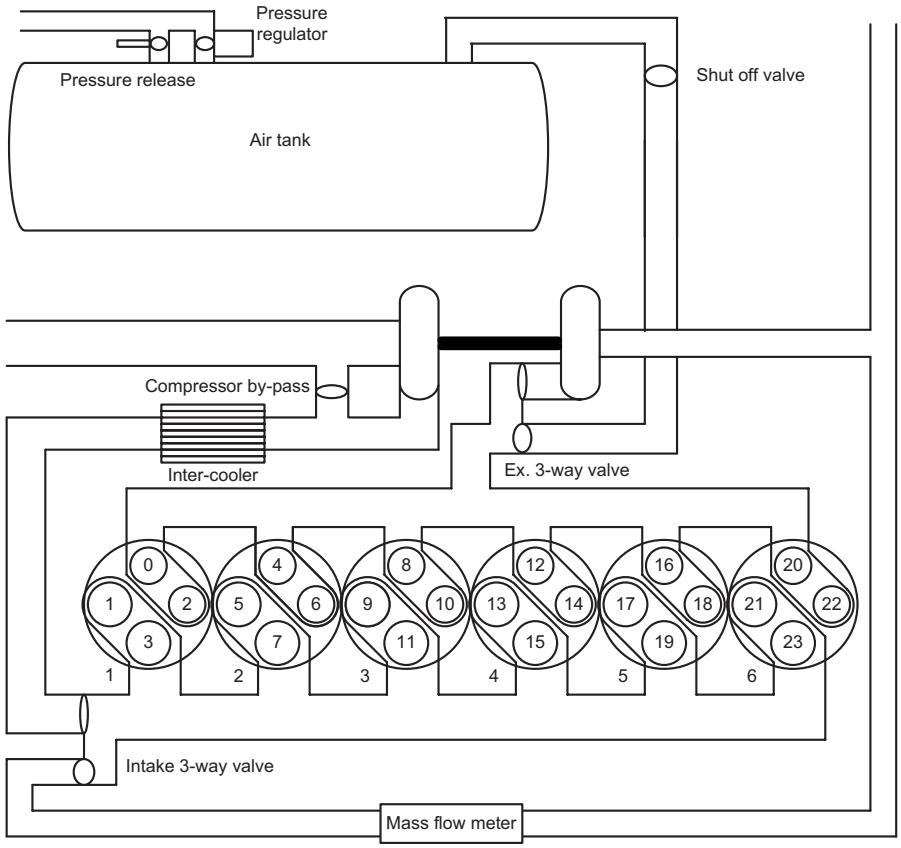

Fig. 4 MD11 air hybrid configuration

Table 2 Running conditions: AC example

Speed	IVO	IVC	EVO	EVC	Tank pressure
800 rpm	45°	180°	320°	355°	3–15 bar

the exhaust flow restriction imposed by the reduced lift was negligible. Note that in internal combustion (IC) engine mode the full 10 mm lift is used for the exhaust valves.

6 Highlights of the Model

The air hybrid engine has special components and runs atypical operating modes that are not usually seen in conventional engine modeling. GT-Power itself is not designed to easily accommodate these special requirements. Therefore, in the modeling there are some novel treatments.

Valve actuation and fuel delivery. In the model, the valve can be actuated once or twice per cycle to achieve either two-stroke AC/AM modes or four-stroke IC mode. The valve timings can be specified a priori or can be adapted cycle by cycle by a controller. The fuel delivery and the engine valves can be deactivated for each single cylinder independently. In AC or AM modes, the fuel is deactivated for all the cylinders.

Air handling system. The air handling system ensures air flow switching, air delivery, and storage. The compressed air it handles has high pressure and high temperature. In steady-state simulation, used primarily to obtain optimal timings for efficiency maps, the storage tank has a semi-infinite volume tank so that the pressure and temperature can be maintained at virtually constant values. In transient simulation, the storage tank has a realistic finite volume of 280 l.

Efficiency optimization. The code was developed to include calculation of AC or AM efficiency cycle by cycle according to Eq. (2). An optimization algorithm was also developed and implemented as a user defined function to automatically search for the optimal timings according to the timing strategies described earlier.

7 Transient Simulation

As an example, for the conditions in Table 2, the GT-Power model simulation results are compared with the Simulink model and are plotted in Figs. 6–8. The simplified Simulink model is able to capture the major characteristics of the air compression and delivery process. The simplified model has slightly faster charging rate and it needs less cycles (168 versus 180) for the tank pressure to reach 15 bars. This is consistent with the fact that the GT-Power model indicates a lower efficiency during the entire process (Fig. 7). Although the two models show the same trends for the AC process, the differences in the results should be noticed. The GT-Power model tries to represent the complete engine system and, thus, has far more components, such as valve ports, runners, manifolds, bends, flow splits, switching valves, etc. The GT-Power model takes into account other factors, such as heat transfer, flow friction, and flow momentum, which are not considered in the Simulink model. The simulation results verify the analytical modeling of the process, while the GT-Power model is more inclusive and accurate.

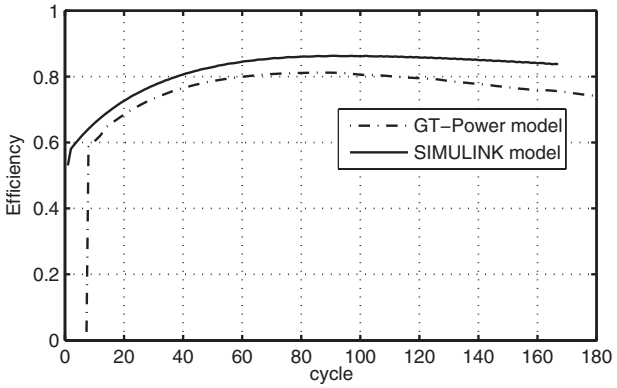

Fig. 7 AC efficiency versus engine cycles

Shown in Fig. 8, the cylinder compression and expansion curves are very close from both models when all the valves are closed, but the simplified model is not able to capture the cylinder pressure pulsation during valve openings. This is because the wave dynamics and pressure propagation are ignored in the simplified model. In the GT-Power model, a 1D momentum equation is used to capture the wave dynamics [10]. The pressure pulsation causes the air flow direction to change during the exhaust valve opening. The Simulink model only captures the average mass flow. During intake valve opening, the air momentum helps to trap more air. This is shown in the GT-Power model *P-V* curve that the cylinder starts compression with a higher pressure. This explains the slight difference between the two compression lines in Fig. 8.

8 Steady State Simulation

The GT-Power air hybrid engine model is used to optimize the AC and AM operations. In order to achieve steady-state simulation for a given external condition, the air tank assumes a sufficiently large volume so that the pressure change due to air addition in AC or air usage in AM is extremely small. The optimization problem is summarized in Table 3. The objective of optimization is the cycle efficiency. There is only one independent variable in each mode, which is used for engine torque regulation. Note that the independent variable is interchangeable with depen-

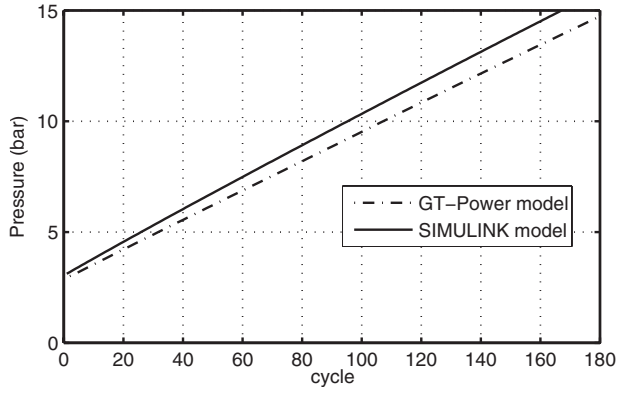

Fig. 6 Tank pressure versus engine cycles

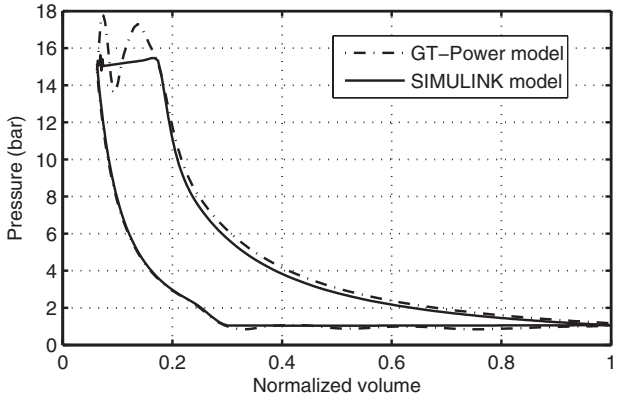

Fig. 8 *P-V* diagrams of last cycle

Table 3 Valve timing strategy

Timing variables	AC type I	AM type I
IVO	To be optimized	To be optimized
IVC	Torque regulation	To be optimized
EVO	To be optimized	Fixed at approximately TDC
EVC	Fixed at approximately TDC	Torque regulation
Timing variables	AC type II	AM type II
IVO	To be optimized	Fixed at approximately BDC
IVC	Fixed at approximately BDC	To be optimized
EVO	Torque regulation	Fixed at approximately TDC
EVC	Fixed at approximately TDC	Torque regulation

dent variables. For example, one can use EVO in AC type I for torque regulation and set IVC to be optimized. The fixed angle around top dead center (TDC) should avoid valve-piston collision.

In type I AC and AM, the optimization involves two variables. From a physical point of view, valve timing affects the efficiency only because of the pressure imbalance across that valve at the valve event. In our setup, one timing would not significantly affect the pressure imbalance at the second valve event. Thus the two variables to be optimized can be assumed to be weakly coupled. The two-variable optimization is then reduced to two one-variable optimizations that proceed sequentially. We implemented the so-called Brent method [11] for the one-variable search problem.

The steady-state simulation with valve timing optimization is used to establish the AC and AM operation maps. The engine hybrid operation space is defined by speed (600–2100 rpm), load (0–15 bar BMEP), and tank pressure (3–15 bars). The space is discretized to form a grid of operation points. At each point, the timings are searched for the best efficiency. As an example of the map, the 900 rpm maps are shown in Figs. 9 and 10.

From the plots, it can be seen that the maps do not span to the entire design space. Some points in the maps are not achievable under this speed, such as points with high load and low tank pressure. Some points result in high tank temperature that exceeds design limits and are not allowed. Those are generally high load and high pressure points. Under different speeds, the realizable space is different. Shown in Fig. 9, EVO is advanced as load increases under the same pressure. When the load exceeds the maximum load that AC type I can provide, the engine enters AC type II. The extra load is contributed by the back flow of the air from the tank not by the fresh air charge and thus has lower efficiency, as shown in Fig. 10. The efficiency shown is the brake efficiency, which includes the engine friction.

In controlling the hybrid operation, the requirements are as follows: (1) meet driver's torque command and (2) ensure optimal operation under that torque/load condition. Figure 10 tells that under the same tank pressure, there is a load range in which the process is more efficient. In general, the engine load can be brought as close to the range as possible by the transmission while the vehicle braking torque requirement is still met.

In the AM mode, the compressed air enters into the cylinder through the exhaust valves and exits through the intake valves after expansion. 900 rpm AM maps are shown in Figs. 11 and 12. As in AC, the AM maps only partially occupy the design space.

Figure 11 shows that under light loads, intake valve open (IVO) is early and before BDC. When the tank pressure is higher, IVO is earlier for the same load. This agrees with the analysis from the *P-V* diagram. As load goes up and exceeds the maximum torque that AM type I can provide, the cylinder will enter into AM type

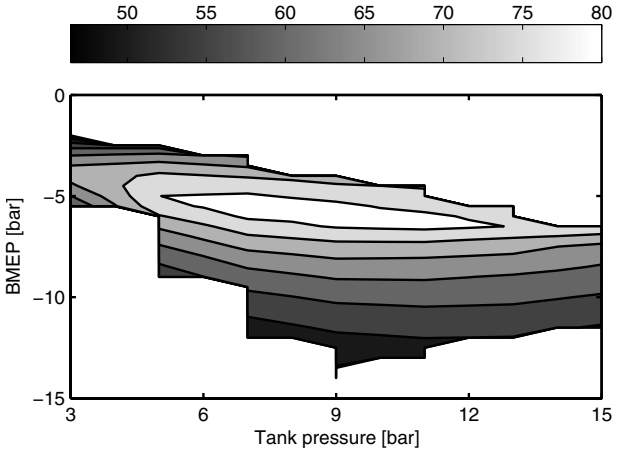

Fig. 10 Efficiency map (unit: %) for AC 900 rpm

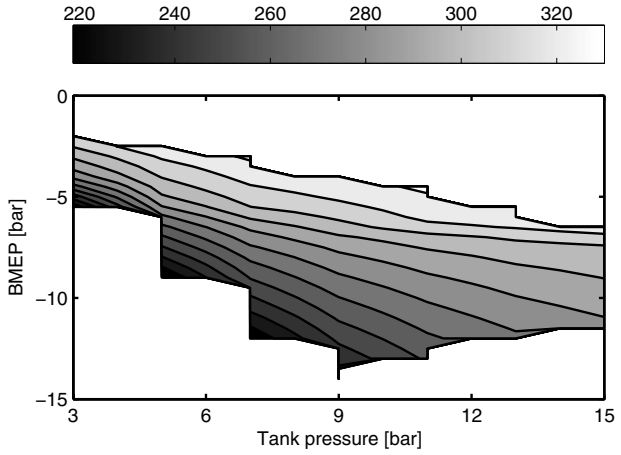

Fig. 9 EVO (unit: deg) map for AC 900 rpm

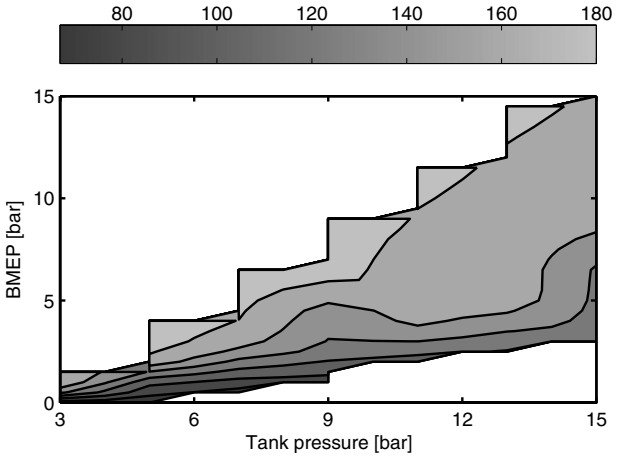

Fig. 11 IVO (unit: deg) map for AM 900 rpm

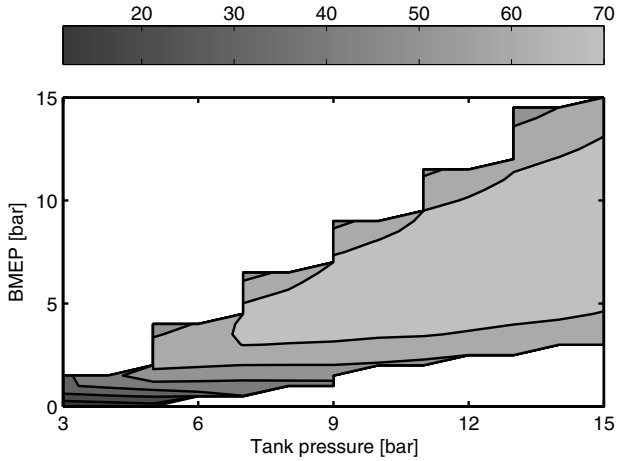

Fig. 12 Efficiency (unit: %) map for AM 900 rpm

II. In that case, IVO will be fixed at BDC. In AM type II, the efficiency decreases, as shown in Fig. 12. This is because more air is used to boost the torque but is not fully expanded in the cylinder before being discharged.

Both Figs. 10 and 12 show that the efficiency is low under light engine loads. The main reason is due to the engine friction. In AC mode, a portion of the vehicle kinetic energy is spent to overcome the friction. In AM mode, a portion of the compressed air work is used to overcome the friction. Thus, friction hurts the efficiency in both modes. Under light loads, the friction portion becomes dominant and thus reduces the brake efficiency. This is not significantly different in concept from operation in normal IC engine mode. The lighter the desired useful output load, the larger fraction of indicated work is consumed by mechanical friction losses.

9 Vehicle Simulation

The vehicle simulation model is based on ADVISOR[2] Simulink package. The package is a complete backward vehicle model. The package is modified to incorporate the air hybrid engine model and its control. The target baseline vehicle is a garbage refuse truck.

10 Model Modifications

The air hybrid engine model is represented by three engine maps for its IC, AC, and AM operation modes. AC and AM maps are obtained from the steady-state simulations. The IC mode map is supplied by the manufacturer. The air tank model is the same as described by Eq. (12). The air tank is assumed to be perfectly insulated. It tracks two states—pressure and temperature. The temperature is fed back to correct air flow rate from the map.

11 Engine Mode Scheduling

The mode scheduling strategy is aimed at minimizing fuel consumption. Air compression and storage are allowed whenever possible in vehicle braking. The stored air energy is used as much as possible during acceleration and cruising.

Launching/accelerating/cruising. The engine is scheduled to run AM if the energy level, as indicated by tank pressure, is sufficient. When the tank pressure drops below a minimum pressure (3 bars in this study), the engine switches to IC mode. Maintaining a minimum pressure in the tank ensures an efficient air compression and storage process when AC starts.

Idling. It is more fuel efficient if the engine is shut down during idling. However, it is very challenging to start the engine with a camless valvetrain. The difficulties include valve phase initialization and actuator power supply, if not electrically powered. In addition, sometimes auxiliary equipment such as the hydraulic pump or the air conditioner needs to be running during idling. Considering these constraints, the engine is scheduled to run during idling periods.

Braking. The engine runs in AC mode and if the command for braking force exceeds the AC capacity, the service brake is applied. Through a regulator, the air tank discharges excessive air for safety when its upper pressure limit (15 bars in this study) is reached.

[2]Developed by National Renewable Energy Laboratory, U.S. DOE.

Table 4 Driving cycle simulation results

Driving cycles	Base (miles/gal)	APA (miles/gal)	Efficiency (%)
WVU city	3.51	3.87	10
WVU suburban	4.48	4.87	9
WVU interstate	6.62	6.98	5
CBD truck	3.37	3.8	13
City suburban	3.91	4.34	11
NY composite	2.96	3.48	18
NY bus	2.18	2.57	18
Manhattan bus	3.04	3.56	17
BAC coach	4.04	4.21	4
Simple refuse	1.09	1.23	13
30 days	3.04	3.31	9

12 Driving Cycle Simulation Results

Various driving cycles are used to evaluate the fuel economy improvement of the garbage refuse truck equipped with the air hybrid engine. The fuel economy simulation results are summarized in Table 4. The improvement ranges from 4% to 18% and is strongly dependent on the driving cycle. Since the fuel economy improvement simply comes from the regenerative braking, it is generally true that city driving patterns, which have a great deal of stop-and-go operation, benefit most from the hybrid operation. City buses and refuse trucks are good potential applications. It is worthy to point out that the 30 day cycle is recorded from a real garbage truck during a month's operation and 9% represents a very good approximation of the real fuel savings that the driver would get had the truck been equipped with the air hybrid engine.

13 Conclusions and Future Work

In this work, we present the framework to analyze and understand the air hybrid cycles. Intake and exhaust valve timings are identified as the major variables to operate the cycles and the timing strategies are proposed for the AC and AM modes. The independent valve timing is used to regulate the engine brake torque to meet the driver's demand, while the dependent timings are optimized for cycle efficiency.

The strategies are applied to the modeling of a particular air hybrid configuration of the MD11 engine using GT-POWER. The simulation results agree with the analysis of the cylinder-tank interaction and the differences are highlighted. For the refuse truck application, the driving cycle simulation shows 4–18% fuel economy improvement. Another advantageous consequence of AC is the saving of the friction brake usage. When operating in AM mode, the engine can output high torque at very low engine speed, thus improve vehicle launching performance. High braking or launching torque can be achieved by type II operations.

While current work focuses primarily on the understanding of the cycles and fuel economy evaluation, the technology has the potential to reduce emissions. This is an important area to be addressed in future work.

Significant technical challenges are obvious in implementing this technology. The major hurdles among them include the following: reliable and flexible valvetrain, switching and sealing of high pressure and temperature air, etc. Starting of the engine is

also challenging as in all camless applications. The authors have started the experimental work on the MD11 air hybrid engine and the initial results were presented by Kang et al. [12]

Acknowledgment

This work was sponsored by the U.S. Department of Energy under Contract No. DE-FC26-05NT42417 and Mack Trucks, Inc.

Nomenclature

W = cylinder work
B = availability
V = volume
S = entropy
$\dot{m}$ = mass flow rate
θ = crank angle
R = gas constant
γ = specific hear ratio
C_d = discharge coefficient
L = valve lift
D_v = valve diameter
v_p = piston speed
c_p = constant pressure specific heat
c_v = constant volume specific heat
A_{eff} = valve effective flow area
P = cylinder pressure
η = efficiency
U = internal energy
T = temperature
m = mass
V_T = tank volume
h = specific enthalpy
D = bore
E = total energy
ρ = density
A_v = valve area
c = sound speed
ω = engine speed

References

[1] Schechter, M. M., 1999, "New Cycles for Automobile Engines," SAE Paper No. 1999-01-0623.
[2] Schechter, M. M., 2000, "Regenerative Compression Braking—A Low Cost Alternative to Electric Hybrids," SAE Paper No. 2000-01-1025.
[3] Tai, C., Tsao, T. C., Levin, M. B., Barta, G., and Schecther, M. M., 2000, "Using Camless Valvetrain for Air Hybrid Optimization," SAE Paper No. 2003-01-0038.
[4] Andersson, M., Johansson, J., and Hultqvist, A., 2000, "An Air Hybrid for High Power Absorption and Discharge," SAE Paper No. 2005-01-2137.
[5] Trajkovic, S., Tunestal, P., Johansson, B., Carlson, U., and Hoglund, A., 2007, "Introductory Study of Variable Valve Actuation for Pneumatic Hybridization," SAE Paper No. 2007-01-0288.
[6] Çengel, Y. A., and Boles, M. A., 1994, *Thermodynamics: An Engineering Approach*, 2nd ed., McGraw-Hill, New York.
[7] Hsieh, J. S., 1993, *Engineering Thermodynamics*, Prentice-Hall, Englewood Cliffs, NJ.
[8] Ferguson, C. R., and Kirkpatrick, A. T., 2001, *Internal Combustion Engines: Applied Thermosciences*, 2nd ed., Wiley, New York.
[9] Heywood, J. B., 1988, *Internal Combustion Engine Fundamentals*, McGraw-Hill, New York.
[10] Gamma Technologies, 2004, *GT-POWER User's Manual, Version 6.1*, Westmont, IL.
[11] Sprott, J. C., 1991, *Numerical Recipes*, Cambridge University Press, Cambridge.
[12] Kang, H., Tai, C., Smith, E., Wang, X., Tsao, T.-C., Blumberg, P. N., and Stewart, J., 2008, "Demonstration of Air-Power-Assist (APA) Engine Technology for Clean Combustion and Direct Energy Recovery in Heavy Duty Application," SAE World Congress, Detroit, Paper No. 08PFL-298.

X.-X. Yuan
Department of Civil Engineering,
Ryerson University,
350 Victoria Street,
Toronto, ON, M5B 2K3, Canada

M. D. Pandey
Department of Civil and Environmental Engineering,
University of Waterloo,
200 University Avenue,
West Waterloo, ON, N2L 3G1, Canada

J. Riznic
Canadian Nuclear Safety Commission,
P. O. Box 1046,
Station B,
Ottawa, ON, K1P 5S9, Canada

A Stochastic Model for Piping Failure Frequency Analysis Using OPDE Data

The accurate estimation of piping failure frequency is an important task to support the probabilistic risk assessment and risk-informed in-service inspection of nuclear power plants. Although probabilistic models have been reported in the literature to analyze the piping failure frequency, this paper proposes a stochastic point process model that incorporates both a time dependent trend and plant-specific (or cohort) effects on the failure rate. A likelihood based statistical method is proposed for estimating the model parameters. A case study is presented to analyze the Class 1 pipe failure data given in the OPDE Database. [DOI: 10.1115/1.3094027]

1 Introduction

The degradation and failure of piping systems can have adverse effect on the safety and reliability of a nuclear power plant. Piping failure frequency in a particular system or of a particular class is an important input parameter to probabilistic safety assessment (PSA) and risk-informed in-service inspection (RI-ISI) of systems important to safety. Reliability and safety analyses conducted during the design stage are generally based on generic failure rates [1]. In the case of an operating plant, it is of interest to evaluate plant-specific failure rates and investigate their departure from generic reference values. For this purpose, the nuclear industry collects and compiles pipe failure events in a database such as OPDE Project Database.

In general, the piping failure frequency is defined as [2]

$$\lambda = \frac{1}{N}\left(\frac{n}{T}\right) \tag{1}$$

where n is the number of pipe failure events, T is the total exposure time, and N is the total population of pipes (length or number of segments) vulnerable to failure. The typical unit of failure frequency is number of failures per reactor year per meter length of pipe.

The statistical estimation of pipe failure frequency from existing data regarding pipe failure events is not a straightforward task. In general, pipe failure data for a particular plant/system tend to be very limited, since nuclear piping systems are designed for a very high reliability level. Piping reliability is dependent on many attributes and influenced by many factors [3]. The reliability-related attributes include, but not limited to, diameter and wall thickness, metallurgy, configuration of piping (welds, bends, branch connections, etc.), and method of fabrications. The influencing factors include process medium, water chemistry, flow conditions, stress level, in-service inspection program, and operating procedures. If we categorize the data according to so many attributes and influencing factors, a small data set will be further subdivided into much smaller subsamples. For example, Fleming and Lydell [2] showed that the failure data can be subdivided into 832 subsets, which correspond to four reactor vendors, eight system categories, and 13 types of degradation modes.

Manuscript received October 8, 2008; final manuscript received October 15, 2008; published online June 9, 2009. Review conducted by Dilip R. Ballal. Paper presented at the Sixteenth International Conference on Nuclear Engineering (ICONE16), Orlando, FL, May 12–15, 2008.

The piping failure event can be mathematically modeled as a stochastic process with a time variant intensity function. The reason being that pipe degradation as a function of aging could increase the failure frequency over time.

Several approaches applied to the estimation of piping failure frequencies have been reviewed in detail in this paper. The assumption of homogeneous Poisson process with a constant failure rate is implied in many studies. This paper develops a stochastic point process model to investigate the aging trend in the piping failures. To illustrate the proposed method, the paper analyzes Class 1 piping failure data collected from the U.S. nuclear power plants (NPPs) and summarized in OPDE Database.

2 Literature Review

2.1 General. There are four major approaches that have been used for estimating the piping failure frequency:

- probabilistic fracture mechanics (PFM)
- statistical analysis of service data
- expert elicitation
- synthetic approach that combines the above three approaches

Probabilistic fracture mechanics has been developed to estimate the probability of failure for a specific pipe under given loading conditions. PFM is analytical because the probability of failure is derived using the structural reliability methods [4] based on the loading-resistance interference model in which the probability distributions of the loading and structural resistance are assumed. It is an established method, especially for estimating the reliability in fatigue crack growth in piping important to safety. Moreover, the PFM can usually provide the aging trend of reliability. Therefore, it has been deemed that the PFM approach is suitable for RI-ISI. But the difficulty of applying the PFM is also obvious. Being a microscopic technique, it requires much information that may be hard and costly to obtain. It is also computationally expensive. Moreover, if the physical degradation mechanism is not well known, this method is not applicable. Indeed, according to a recent literature review by Gosselin et al. [5], of more than 7500 open-accessed documents related to structural integrity of passive components of pressurized water reactors (PWRs) and boiling water reactors (BWRs) from 1980 to 2007, only a small fraction was related to the probabilistic structural mechanics calculations. The vast majority of the references addressed various mechanistic aspects of degradation mechanisms and applied deterministic rather

Table 1 Piping rupture frequencies (per hour per foot)

Pipe diameter	90% range	Median
≤3 in.	$3\times10^{-11}\sim3\times10^{-8}$	1×10^{-9}
>3 in.	$3\times10^{-12}\sim3\times10^{-9}$	1×10^{-10}

than probabilistic models.

The most straightforward approach is to obtain statistical estimates of piping failure frequencies from service data. In order to resolve the difficulties (e.g., data scarcity and difficulty of defining population) listed in Sec. 1, it has been proposed to estimate the piping damage frequency first, as its occurrence is more frequent and hence the estimates should be more accurate. Then a conditional probability is used to estimate the piping rupture frequency. The major limitation of the statistical approach is, as Fleming [6] elaborated, "that attempts to segregate the data to isolate the impact of key design parameters and properties of various damage mechanisms that are expected to influence failure rates often leads to subdividing the database into very sparse data sets." That is to say, a relatively small database, after considering the homogeneity of the statistical population, becomes even smaller. This makes the estimation less defensible. Another important drawback of the statistical approach. which is also pointed out by Fleming [6]. is that the service data reflect only the history of the piping and "if changes … are proposed, such changes may render the previous failure rate estimates no longer relevant." Bayesian technique has been used to adapt to the scarce failure data and to the technology change. The issues related to the selection of prior distribution in Bayesian method have been addressed in recent research studies to promote practical applications of this approach.

2.2 Review of Specific Studies. There were two major influential studies in which the piping failure frequencies were estimated using the then most available data. They are the "Reactor Safety Study" (WASH-1400) in 1975 [7] and Thomas' paper in 1981 [8]. Many later studies were carried out to improve the methodologies proposed and the estimates obtained in these two references.

The piping failure rates used in the Reactor Safety Study were derived from handbooks, reports, and nuclear power plant operating experience. Realizing the complexity of the problem, the study maintained that in estimating the failure rates, only order of magnitude accuracy would be generally feasible. The study continued, "these accuracies were sufficient for the risk calculations since only order of magnitude results are required" (WASH-1400, Appendix 3, Sec. 1.3). When presenting the assessment results, the study used the log normal distribution to describe the uncertainty of the failure rates, and the estimated failure rates were summarized by the median values and their lower and upper bounds that cover 90% of range. The estimates of the pipe rupture frequency used in the study are listed in Table 1 (Appendix 3, Table III 4–1). The direct nuclear experience behind these estimates was three ruptures in PWR and nine pipe ruptures in BWR within the 1 year time window from 1972 to 1973. The median value was obtained by applying Eq. (1), i.e., dividing the number of failure 11 by the time 8760 h (1 year) and the total piping length 595,000 ft. An error factor of 30 was further assigned to get the 90% range.

The study also provided estimates for the frequencies of piping rupture failures that initiate a LOCA event, as shown in Table 2 (WASH-1400, Appendix 3, Table III 6–9). Note, however, that in the 150 reactor years of commercial nuclear power plant experience upon which the study was based, there was no catastrophic rupture observed. The estimates in Table 2 were mainly derived from non-nuclear utility experience.

The Reactor Safety Study has a long-standing influence as it was the first authoritative report that studied the nuclear power plant safety in a quantitative fashion. In general, later PSA would commonly use the failure frequencies in WASH-1400 and the validity of the frequencies as such often has been cited solely on the basis of referencing the WASH-1400 without questioning the archival data and approach used in the study. More recently, USNRC published a handbook of parameter estimation for probabilistic risk assessment (NUREG/CR-6823, 2003), in which both Frequentist and Bayesian inference methods are discussed [1].

Table 2 Frequencies of LOCA initiating pipe failures (per plant per year)

	LOCA initiating rupture rates	
Pipe diameter	90% range	Median
1/2–2 in.	1×10^{-4}–1×10^{-2}	1×10^{-3}
2–6 in.	3×10^{-5}–3×10^{-3}	3×10^{-4}
>6 in.	1×10^{-5}–1×10^{-3}	1×10^{-4}

Thomas [8] described a conditional probability approach to estimate the frequency of piping rupture, λ_R, based on piping leakage frequency, λ_L:

$$\lambda_R = \lambda_L \Pr(R|L) \tag{2}$$

in which $\Pr(R|L)$ is the conditional probability of catastrophic rupture given leakage. Several different methods have been proposed to estimate the conditional probability. Based on widespread industrial experience, Thomas [8] gave a rough estimate about 5–10% and this estimate was further refined and tabulated for different failure causes such as fatigue, corrosion, and maloperations. He further suggested the application of fracture mechanics to refine the estimation. Lydell [9] updated the estimation based on SKI-PIPE database and cautioned that application of specific estimates of the conditional probability should include details about the service experience. Beliczey and Schulz [10] recommended the following regression relationship for the conditional probability in the range from DN25 to DN250:

$$\Pr[R|L] = 1/(9.6\mathrm{DN}/2.5 + 0.4\mathrm{DN}^2/25) \tag{3}$$

where DN denotes the nominal diameter of the pipe in millimeter. This correlation was later simplified as [11]

$$\Pr[R|L] = 2.5/\mathrm{DN} \tag{4}$$

Nyman et al. [3] used a Bayesian approach to estimate the conditional probability. In particular, they used a binomial likelihood and the associated noninformative prior and suggested the following:

$$\Pr[R|L] = (2n_r + 1)/(2n_f + 2) \tag{5}$$

where n_r and n_f are the number of ruptures and the number of failures (including cracks, leaks, and rupture), respectively. Lydell [9] compared the Bayesian results with the PFM results for IGSCC-susceptible welds in Barseback-1 reactor coolant pressure boundary piping. Similar work has been done by Choi and Choi [12] for Korean PWRs based on OPDE Database.

For the probability of leakage, Thomas [8] related a plant-specific frequency with the generic frequency through several modification factors. In particular, the relationship is expressed as

$$\lambda_L = \lambda_{L,\mathrm{base}} QFB \tag{6}$$

in which, λ_L denotes the plant-specific frequency; $\lambda_{L,\mathrm{base}}$ denotes the baseline or generic frequency of leakage, suggested to be in the range from 1×10^{-9}/year to 1×10^{-7}/year; Q, F, and B are multiplicative factors accounting for the change in reliability due to piping dimension, plant age, and design learning curve, respectively. The size and shape factor Q was analyzed and discussed in great detail in Thomas paper. Equations were established to consider the different risks to leakage of parent metal and weld zone. For a pipe without welding, this factor is found to be proportional

to mean diameter D and pipe length L but inversely proportional to the square of wall thickness t, i.e.,

$$Q_p = DLt^{-2} \tag{7}$$

For a weld zone, the size and shape factor can be calculated using Eq. (3) if the length L is replaced by $1.75t$. Therefore,

$$Q_w = 1.75Dt^{-1} \tag{8}$$

Quite often, a pipe consists of both parent and weld zone materials. In this case the equivalent size and shape factor equals

$$Q_e = Q_p + 50NQ_w \tag{9}$$

in which N is the number of welds and the factor of 50 was applied to account for the greater vulnerability to leakage than the pipe parent material. In contrast, the estimation of plant age factor F and design learning curve factor B are less accurate. Although the time-related factor was categorized into long-term changes of technology, shorter term design learning curves, and typical bathtub curves, the separation of the time-related facto as age factor and learning factor is arbitrary and statistically unidentifiable.

Nyman et al. [3] argued that realistic parameter estimation based exclusively on fault counts and exposure times is not feasible. Instead, parameter estimation should be based on the thorough understanding of the *why-where-how* of piping failures. Moreover, the selection of an estimation method must reflect the requirements of intended applications. They proposed a five-step framework for estimating failure parameters from service data, incorporating operational service data into Thomas' approach.

In the evaluation of nuclear piping failure frequency using the OPDE Database, Choi and Choi [12] used the information of Korean PWRs in the database to estimate the piping damage frequency and the piping rupture frequency. For a specific diameter pipe in a particular system, they used the following expression to calculate the point estimate of the piping damage frequency, λ:

$$\lambda = \frac{n_f}{\sum_{i=1}^{N_p} N_{c,i} T_i} \tag{10}$$

where n_f is the number of damage events for a specific pipe diameter in the system; N_p and N_c are the number of plant and the number of pipes of the specific diameter, respectively; T_i is the operational year for each plant. Clearly, this method needs the pipe population data, which can be accessed only from the piping isodrawings of each plant involved and they are current not available to us. To evaluate the piping rupture frequency, the authors employed both Bayesian approach and the conditional rupture probability approach. Both approaches are found to give comparable results.

When failure events are even rarer and the modeling of failure is too complicated (e.g., large break LOCA), both the PFM approach and statistical approach are not applicable. In this case, an expert elicitation procedure can be used. In PSA, this procedure was applied in NUREG/CR-1150 for estimating severe accident risks for five nuclear power plants in United States. NUREG-1829 is one of the latest documents that provide the details of the expert elicitation procedure [13].

Time-dependent piping failures are usually modeled by a nonhomogeneous Poisson process (NHPP). The NUREG Handbook of Parameter Estimation discussed parameter estimation and model validation of the NHPP model with log-linear law and power law. The power law NHPP is also known as a Weibull process and it has been extensively used in reliability growth modeling. A log-log plot of number of failure events against cumulative failure times, called Crow-AMSAA plot, or simply Crow plot, can be used for estimating the parameters for the power law model. Sun et al. [14] applied the Crow analysis to predict the NPP equipment performance, while Barringer [15] provided more examples of the application of the Crow plot to failure prediction. The Crow plot is simple and straightforward. But it is applicable only if the failure data come from a single homogeneous system.

Recently, Fleming [6] proposed a Markov model to describe the aging dynamics of piping systems. But the proposed model is of probabilistic nature. The transition rates of the model have yet to be estimated and they are suffered from the same problems as the piping failure frequency.

2.3 Analysis of Aging Effects. Choi et al. [16] presented the first study of aging trend analysis using data from 212 PWRs contained in the OPDE data until 2004. The total sample consisted of 1424 records collected from January 1970 onwards, which is equivalent to 4609 operating years.

In order to assess the aging trend they pooled, the data in three different ways. First, they pooled pipe failure (leak) databased on three reporting intervals: (1) 1970–1984, (2) 1984–1994, and (3) 1994–2004. The leak frequency in each interval was assumed to be constant. The leak frequency exhibited a decreasing trend. It decreases approximately from 0.6 leaks/year for 1984 group to 0.35 leaks/year for 1994 group to 0.3 leaks/year for 2004 group.

In the second method, the plants were categorized according to the operating years. Three groups were formed as (1) young plants with age 0–15 years (28 plants, 284.6 reactor years), (2) intermediate plants of age 15–25 years (119 plants, 2427 reactor years), and (3) old plants of age 25–35 years (63 plants, 1863 reactor years). The leak frequency in older plants (0.4/year) was approximately four times than that in the young plant (0.1/year). The reasons for this were given as lower level of design, construction, and maintenance in old plants as compared with the newer plants.

In the last method, starting dates for all the plants were moved to a common origin: January 1, 1970. The entire data were categorized into six groups at an interval of five calendar years. This analysis showed that the leak frequency typically decreases with plant aging and then it increases slightly for old plants after 20 years of operation.

It should be noted that this method groups data in a heuristic manner and adopts a constant frequency (homogeneous Poisson process) model for each groups of the data. This approach cannot be considered rigorous and statistically consistent. Nevertheless, this study provides motivation for the current model as described in this paper.

3 Data

The piping failure events have been recorded in an international piping failure exchange database, the OPDE Project Database. It is based on an existing database originally developed by the Swedish Nuclear Power Inspectorate (SKI) during 1994–1998. In May 2002, member countries of the Nuclear Energy Agency (NEA) and the OECD decided to establish the OPDE project, based on the SKI-Pipe project [17]. The latest version of the database collects piping failure data from 1970 up to June 2007. The purpose of the project is manifold and a major one is to support statistical analyses to determine pipe leak and rupture frequencies and to support aging trend analysis.

Since the NPPs were built in different years, the data collected within a plant belong to one of the four cases described below and shown in Fig. 1.

- *Case I*. The NPP was built before 1970 and still in operation as of June 30 2007. Failures before 1970 were not recorded.
- *Case II*. The NPP was built before 1970 and permanently shut down before 2007. Failures before 1970 were not recorded.
- *Case III*. The NPP was built after 1970 and still in operation as of June 30 2007. Failures recorded before the first reactor criticality are ignored in the analysis.
- *Case IV*. The NPP was built after 1970 and permanently shut down before 2007.

It should be noted that there are several nuclear plants from which pipe failure data are not available.

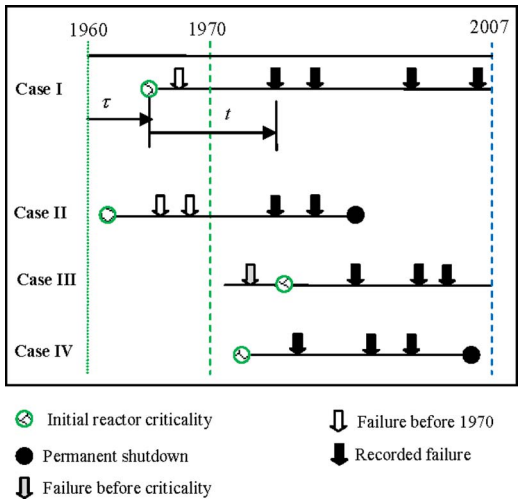

Fig. 1 Four cases of failure records

4 Proposed Model

4.1 General Approach. Although pipe failure is affected by several factors, there are two time scales attached to each failure data. One is the calendar date and the other is plant age. In this paper, we aim at analyzing two global time dependent effects on the failure rate, referred to as (1) aging effect and (2) cohort effect [18].

4.1.1 Cohort Effect on the Failure Rate. Nuclear plants constructed and operated during different time periods employ different levels of technological sophistication. For example, newer plants use more advanced technology, materials, construction methods, and inspection tools than the older plants. For this reason, the newly built plants are expected to have lower failure rates. Thus, depending on the calendar date of construction, nuclear plants can be categorized in different cohorts. This variation in the failure rate across the plants due to difference in the cohort age is referred to as the cohort effect. It encompasses the effects of the advancing technologies in the design, manufacturing, inspection, and maintenances of nuclear power plants.

The cohort effect is quantified by the plant cohort age, denoted by τ, which is the time interval between the date of the first reactor criticality and a reference date of January 1, 1960, as most NPPs were built after 1960 (Fig. 1). Theoretically, a larger cohort age means a newer plant, employing a more advanced technology, design, and materials with less vulnerability to failure.

4.1.2 Aging Effect on the Failure Rate. The other time scale likely to affect the failure rate is the plant age, denoted by t, at the time of a pipe failure. It is simply the time interval between the date of the first reactor criticality and the time of a pipe failure event. In general, it is known that failure events of a system follows a bath-tub pattern [19], which includes burn-in phase, randomly failing or service life and wear-out or aging stage. Depending on the plant age, the failure rate may be decreasing, constant, or increasing. It is referred to as the aging effect on the failure rate.

4.2 Point Process. For a single nuclear power plant, let $0 \leq T_1 < T_2 < \cdots$ denote the failure times (i.e., plant age). It is proposed to consider these failures as a point process and $N(t) = \sum_{k=1}^{\infty} I(T_k < t)$ records the cumulative number of failures generated by the underlying point process. $I(T_k < t)$ is an indicator function, which equals 1 if $T_k < t$ or 0 otherwise. Quite often, a point process can be described uniquely by the so-called intensity function, defined as the instantaneous probability of an event occurring at time t, conditional on the process history, $H(t)$. Formally, the intensity is defined as [20]

$$\lambda(t|H(t)) = \lim_{\Delta t \downarrow 0} \frac{\Pr[\Delta N(t) = 1|H(t)]}{\Delta t} \tag{11}$$

where $\Delta N(t)$ represents the number of failures in the time interval $[t, t+\Delta t)$. When the intensity function is independent of the process history, the point process becomes a Poisson process. If, however, the intensity function is of the form

$$\lambda(t|H(t)) = h(t - t_{N(t-)}) \tag{12}$$

where $t_{N(t-)}$ is the time of the last event prior to t, then the process is a renewal process. Note that for a Poisson process (either homogeneous or non-homogeneous), the intensity function and the rate of occurrence (ROC) function is the same [21].

In this paper, we propose that the piping failures in a nuclear plant follow a NHPP. A power law intensity function is adopted to model the aging effects, i.e., $\lambda(t) \propto t^{\beta-1}$, and the cohort effect is modeled by a term $e^{\gamma\tau}$. Finally, the intensity function takes the form

$$\lambda(t) = \alpha\beta t^{\beta-1} e^{\gamma\tau} \tag{13}$$

If $\beta < 1$, then the piping failure rate is decreasing, suggesting that the NPP is in a burn-in stage. If $\beta = 1$, the piping failures follow a homogeneous Poisson process and the NPP is in the random failing service life, whereas $\beta > 1$ implies that the NPP is aging.

4.3 Statistical Estimation. The proposed NHPP model includes three unknown parameters: α, β, and γ, which can be estimated from the maximum likelihood method. Suppose a sample for a plant consists of n failure times $t_0 \leq t_1 < t_2 < \cdots < t_n < t_e$, where t_0 denotes the starting time of observation, which equals zero or the plant age on January 1, 1970, whichever is less, and t_e denotes the end time of observation, which equals the plant life or the plant age on June 30, 2007, whichever is less. Details about the determination of t_0 and t_e are listed in Table 3.

Table 3 Values of t_0 and t_e

Case	t_0	t_e
I	Plant age on 1/1/1970	Plant age on 6/30/2007
II	Plant age on 1/1/1970	Total service life
III	0	Plant age on 6/30/2007
IV	0	Total service life

For the four scenarios in Fig. 1, the likelihood function is expressed as [20]

$$L = \exp\left\{ - \int_{t_0}^{t_e} \lambda(u)du \right\} \prod_{j=1}^{n} \lambda(t_j) \tag{14}$$

If the plant has undergone no failure during the observed time window from t_0 to t_e, the likelihood function is

$$L = \exp\left\{ - \int_{t_0}^{t_e} \lambda(u)du \right\} \tag{15}$$

Assuming the failure events in one plant are independent of the failures in another plant, then the total log-likelihood function is just the summation of the log-likelihoods for each plant. Therefore, taking the intensity function in the form of Eq. (13), we have for the ith plant, with failure times $t_{i0} \leq t_{i1} < \cdots < t_{ini} < t_{ie}$, the log-likelihood function as

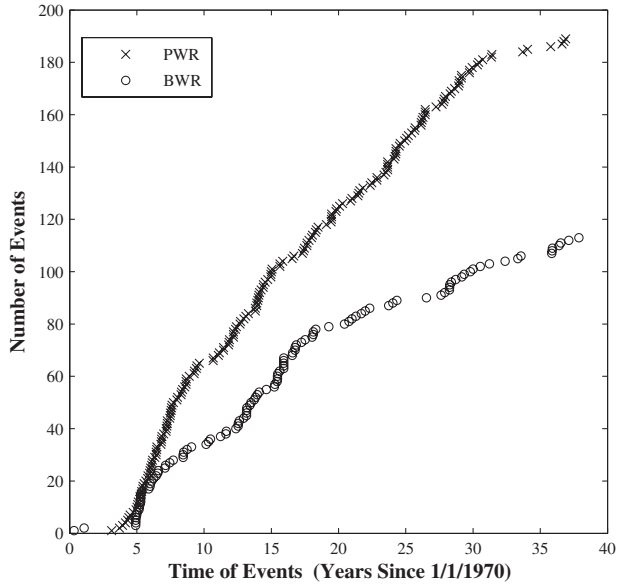

Fig. 2 Number versus time of the failure events

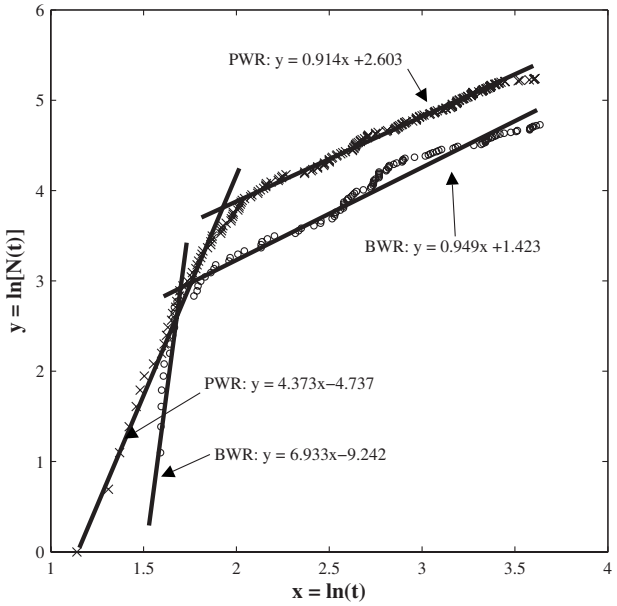

Fig. 3 Crow plot for the leakage events of BWR and PWR in U.S.

$$l_i = n_i(\log\ \alpha + \log\ \beta + \gamma\tau_i) + (\beta - 1)\sum_{j=1}^{n_i} \log\ t_{ij} + \alpha e^{\gamma\tau_i}(t_{i0}^{\beta} - t_{ie}^{\beta}) \tag{16}$$

For the plant without any failure,

$$l_i = \alpha e^{\gamma\tau_i}(t_{i0}^{\beta} - t_{ie}^{\beta}) \tag{17}$$

Further simplifications lead to

$$l = N\ \log\ \alpha + N\ \log\ \beta + \gamma\sum_{i=1}^{m} n_i\tau_i + \beta\sum_{i=1}^{m}\sum_{j=1}^{n_i} \log\ t_{ij} + \alpha\sum_{i=1}^{m} e^{\gamma\tau_i}(t_{i0}^{\beta} - t_{ie}^{\beta}) \tag{18}$$

where $N=\Sigma_{i=1}^{m} n_i$ is the total number of observed failures, and m is the total number of NPPs under observations. Maximization of Eq. (18) gives the maximum likelihood estimates (MLEs) of α, β, and γ.

5 Case Study

5.1 Sample Data. The case study analyzes data concerning leakage in ASME Class 1 pipings of 81 PWRs and 41 BWRs in the U.S. NPPs. The data include leakage event under the time "pinhole leakage," "small leakage," "leakage," and "large leakage." From January 1, 1970 to June 30, 2007, there are 113 leakages recorded in 29 BWRs and 189 leakage events in 52 PWRs. There are 12 BWRs and 29 PWRs that have never reported an event of leakage in Class 1 piping during the collection period.

Initially, we pooled the calendar time of failure times and plotted them in Fig. 2 in which the origin of x-axis represents January

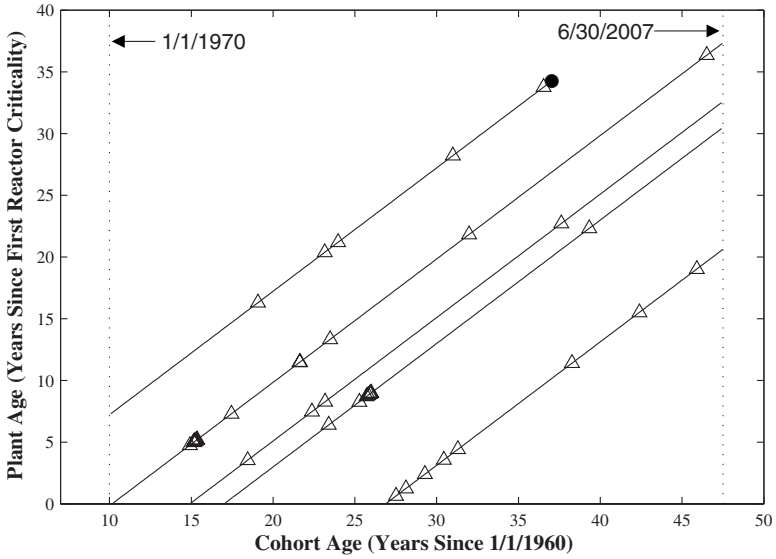

Fig. 4 Lexis diagram for the BWR-Class 1-Leakage data. The triangles denote a leakage event while the solid dot a permanent shutdown of the NPP.

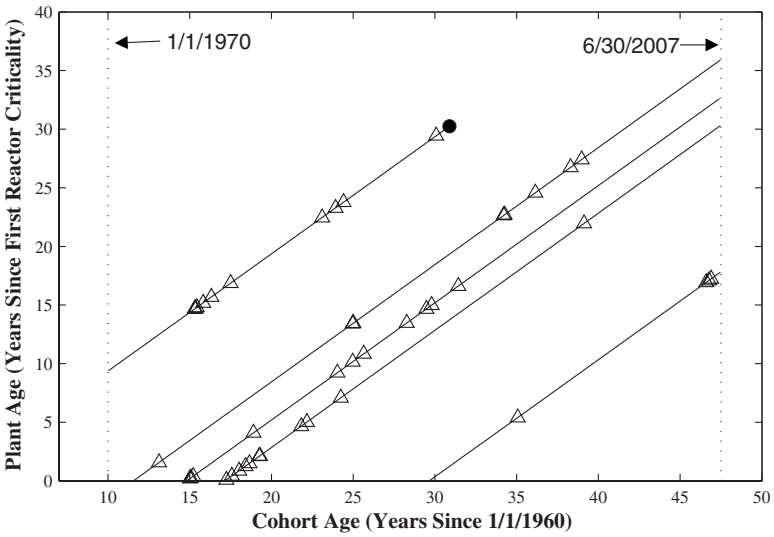

Fig. 5 Lexis diagram of sample data for U.S.-PWR-Class 1-Leakage. The triangles denote a leakage event while the solid dots denote a permanent shutdown of the NPP.

1, 1970. If the pooled data were modeled by a homogeneous Poisson process, then the constant failure rate, or failure frequency, can be estimated as the ratio of the number of failures and the total exposure time. The failure rate is estimated to be 0.096 and 0.104 per plant year for the BWRs and PWRs, respectively. This simple model suggests almost no difference in the leakage frequencies of the two reactor types.

As mentioned in Sec. 2.3, use of the Crow plot of the pooled data to illustrate the aging trend would be misleading. Indeed, the Crow plots of the BWRs and PWRs in Fig. 3 both would show an obvious change in the failure pattern: an increasing failure rate in the early stage followed by a decreasing rate after about 5–7 years of plant operation. But this early increasing failure rate is only an artifact due to the effect of pooling different plants with different failure rates.

Figures 4 and 5 plot the plant age against the cohort age of sample data for the PWR and BWR data, respectively. Such a plot is called *Lexis diagram* in the field of population dynamics [20]. These figures show large variability in the time of occurrence of the failure events. Moreover, the scale variability is different in

Table 4 Maximum likelihood estimates for the NHPP model with standard errors in parentheses

		α	β	γ	Maximized log-likelihood
Without cohort effects	BWR	0.2282(0.0600)	0.7634(0.0723)	0	−130.3
	PWR	0.3037(0.0519)	0.6286(0.0465)	0	−286.5
With cohort effects	BWR	0.5430(0.2053)	0.7208(0.0712)	−0.0459(0.0154)	−125.6
	PWR	0.8380(0.2331)	0.5944(0.0454)	−0.0508(0.0117)	−276.8

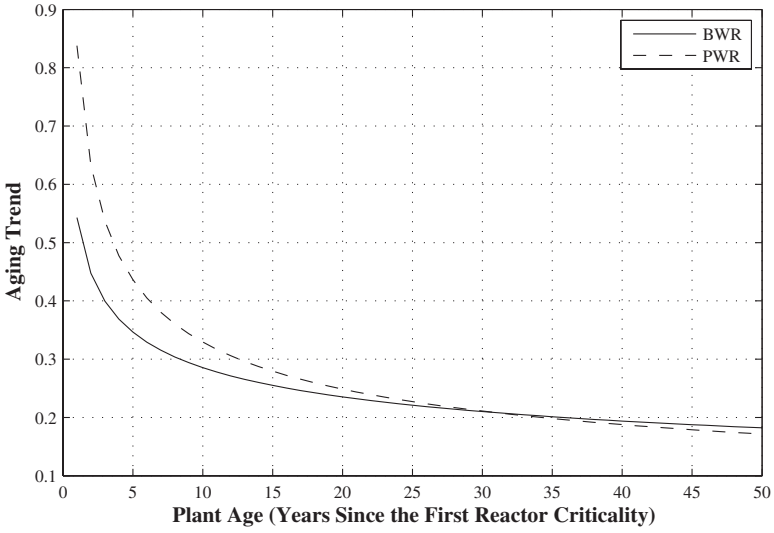

Fig. 6 Aging trend

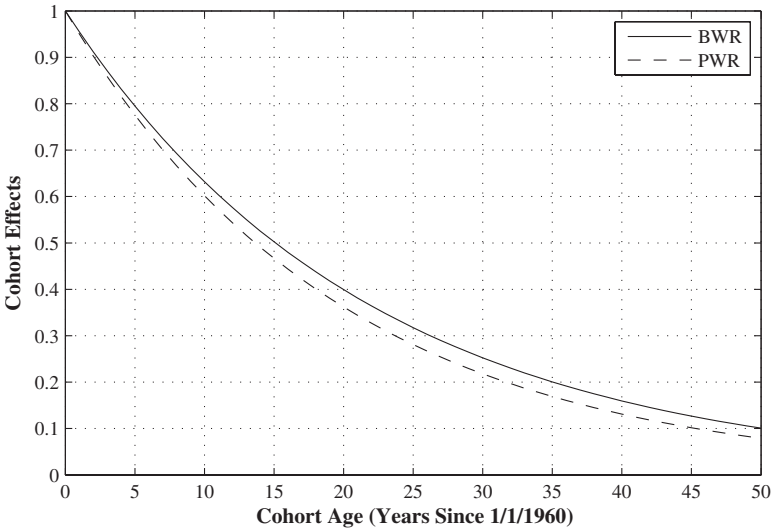

Fig. 7 Cohort effects

different NPPs. Some plants demonstrate a more or less random occurrence while other plants demonstrate a "burn-in" phenomenon. Some plants exhibit aging effect as well.

5.2 Results. Using the proposed likelihood method, we obtain the estimates for both cases with and without considering cohort effects, as summarized in Table 4. It should be emphasized that this approach does not explicitly account for different inspection and mitigation programs employed by different plant operators. In a sense, it is assumed that all degradation management aspects are reflected in the pipe failure rate.

For both the BWR and PWR, the cohort-effect coefficient γ is less than zero as expected. A statistical hypothesis test based on likelihood ratio procedure can be used for testing $\gamma=0$. The likelihood ratio statistics equals $-2(l_1-l_0)$, where l_0 and l_1 are the log-likelihoods under the null and alternative hypotheses, respectively. For BWRs and PWRs, the statistics are greater than 10, which, for a chi-square distribution with one degree of freedom, implies significant statistical evidence against that hypothesis. In other words, the cohort effects present in the data are statistically significant.

The estimated aging trend and cohort effects are plotted in Figs. 6 and 7, respectively. Since neither effect alone could give an absolute value of the failure rate, the figures show only the trend of the effects along time. Figure 6 plots $t^{\beta-1}$ for PWR and BWR plants and it shows that the PWR plants have a relatively higher failure rate in the early life than the BWR plants. Figure 7 plots $e^{\gamma\tau}$ and it shows that the cohort effect is quite strong in the data for both BWR and PWR plants. For example, a plant built in 2005 (cohort age=45 years) would have one-tenth of the failure rate of a plant built in 1960s.

The absolute value of the failure rate for a particular NPP depends on both the plant age and its cohort age, and it can be computed from Eq. (13). Figures 8 and 9 plot the contours of failure rates for BWRs and PWRs, respectively. For a BWR built in 1970 with a cohort age of 10 years, its failure rate at a plant age of 25 years is about 0.1 failure per plant year. But if the BWR is built in 1985, its failure rate at the same plant age becomes only 0.05 failures per plant year. It is clear that the failure rate is very

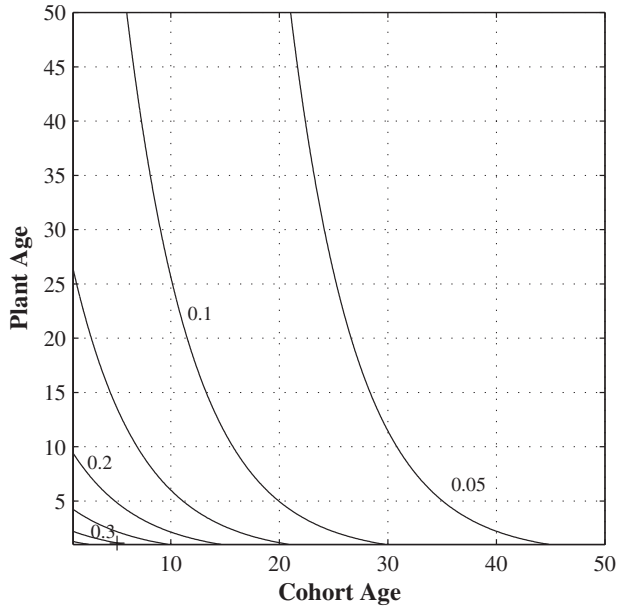

Fig. 8 Contours of failure rate of BWRs (unit: per plant year)

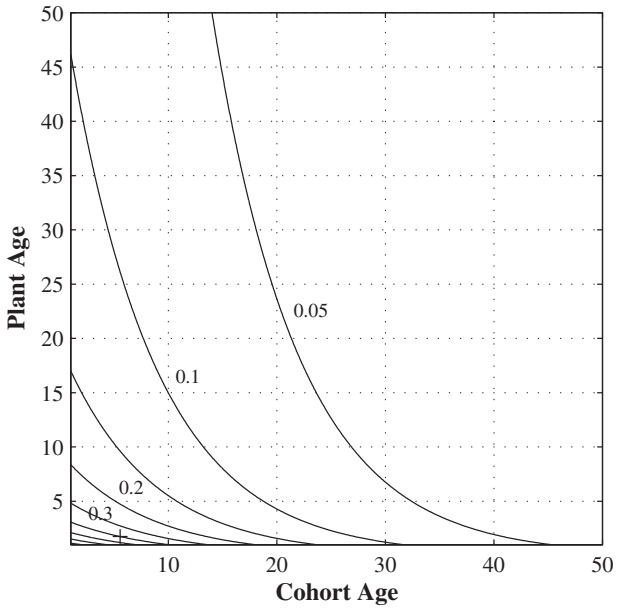

Fig. 9 Contours of failure rate of PWRs (unit: per plant year)

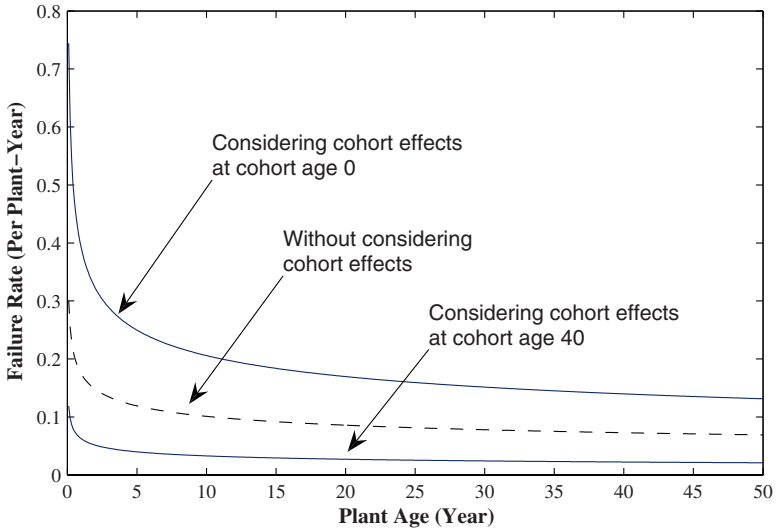

Fig. 10 Comparison of failure rates of BWRs

different from a previous estimate of 0.1 events per plant year obtained by pooling the failure data and assuming a constant failure rate. For a plant (either BWR or PWR) built after 1985, the failure rate is less than 0.1 per plant year. For an older plant however, the failure rate can be higher than 0.1 failure per plant year.

A comparison of the failure rate can be made with and without considering the cohort effect. For the BWRs, the failure rate without the cohort effects ($\gamma=0$) is shown as the broken line in Fig. 10. Two additional curves are shown for cohort ages of $\tau=0$ and $\tau=40$ years. For newer plants ($\tau=40$), ignoring the cohort effect will overestimate the failure rate, whereas the opposite is implied for older plants. Similar trend is seen for PWRs, as shown in Fig. 11.

5.3 Remarks. In the database, the recorded time of a failure event can be uncertain. Some flaws, such as cracks, are found at the time of inspection. Therefore, the occurrence time times are interval censored, i.e., we do not know the exact time, but we know it should lie between two successive inspections. In such cases, the likelihood function must be modified.

The decreasing trend of the failure rate should be interpreted with caution. As pointed out by Thomas [8], the burn-in stage of pressure piping spans about 20 to 30 years. So we need to wait to gain longer operating experience in order to quantify the increasing rate in the wear-out stage. On the other hand, it can be also interpreted as success of maintenance and mitigation programs.

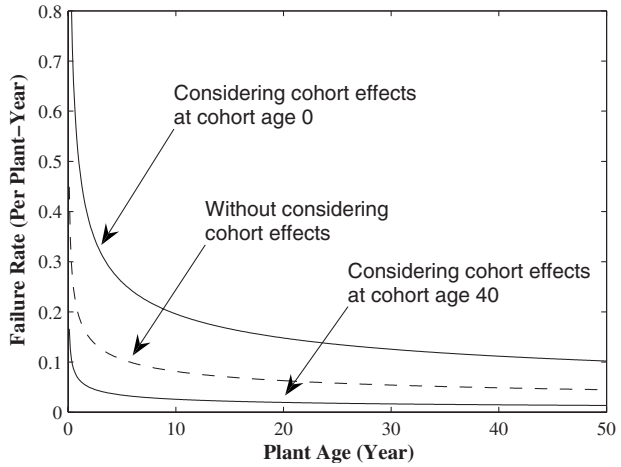

Fig. 11 Comparison of failure rates of PWRs

6 Conclusions

This paper proposes a nonhomogeneous Poisson process model for describing the piping failure events. A novel feature of the model is that it considers the cohort effect in a statistically consistent manner along with the aging effect on the failure rate. The cohort effect is representative of the improvement in plant technology, design, and material. The proposed model is versatile and it can be used to analyze any other stochastic event data. The OPDE data set regarding leakage in Class 1 piping of BWRs and PWRs in the United States are analyzed in detail. This paper shows that statistically significant cohort effect is present in the leak rate. In general, the leak rate exhibits a decreasing trend with the plant age. It implies that the plants are not experiencing increase in leak rates due to aging, or the inspection/maintenance programs are effective in preventing leaks.

Acknowledgment

The authors are grateful to the Canadian Nuclear Safety Commission (CNSC), the National Sciences and Engineering Research Council of Canada (NSERC), and the University Network of Excellence in Nuclear Engineering (UNENE) for providing the financial support for this study.

References

[1] Atwood, C. L., LaChance, J. L., Martz, H. F., Anderson, D. J., Englehardt, M., Whitehead, D., and Wheeler, T., 2003, *Handbook of Parameter Estimation For Probabilistic Risk Assessment*, U. S. Nuclear Regulatory Commission, Washington, DC, NUREG/CR-6823.

[2] Fleming, K. N., and Lydell, B. O. Y., 2004, "Database Development and Uncertainty Treatment for Estimating Pipe Failure Rates and Rupture Frequencies," Reliab. Eng. Syst. Saf., **86**, pp. 227–246.

[3] Nyman, R., Hegedus, D., Tomic, B., and Lydell, B., 1997, "Reliability of Piping System Components: Framework for Estimating Failure Parameters From Service Data," SKI Report No. 97:26.

[4] Melchers, R. E., 1999, *Structural Reliability: Analysis and Prediction*, 2nd ed., Wiley, New York.

[5] Gosselin, S. R., Simonen, F. A., Pilli, S. P., and Lydell, B., 2007, "Probabilities of Failure and Uncertainty Estimate Information For Passive Components—A Literature Review," U.S. Nuclear Regulatory Commission, Washington, DC, NUREG/CR-6936.

[6] Fleming, K. N., 2004, "Markov Models for Evaluating Risk-Informed In-Service Inspection Strategies for Nuclear Power Plant Piping Systems," Reliab. Eng. Syst. Saf., **83**, pp. 27–45.

[7] U.S. Nuclear Regulatory Commission (USNRC), 1975, "Reactor Safety Study-An Assessment of Accident Risks in U.S. Commercial Nuclear Power Plants," WASH-1400, NUREG-75/014, Oct.

[8] Thomas, H. M., 1981, "Pipe and Vessel Failure Probability," Reliab. Eng., **2**, pp. 83–124.
[9] Lydell, B., 1999, "Failure rates in Barseback-1 Reactor Coolant Pressure Boundary Piping: An Application of a Piping Failure Database," SKI Report No. 98:30.
[10] Beliczey, S., and Schulz, H., 1987, "The Probability of Leakage in Piping Systems of Pressurized Water Reactors on the Basis of Fracture Mechanics and Operating Experience," Nucl. Eng. Des., **102**, pp. 431–438.
[11] Beliczey, S., and Schulz, H., 1990, "Comments on Probabilities of Leaks and Breaks of Safety-Related Piping in PWR Plants," Int. J. Pressure Vessels Piping, **43**, pp. 219–227.
[12] Choi, S. Y., and Choi, Y. H., 2005, "Evaluation of Nuclear Piping Failure Frequency in Korean Pressurized Water Reactors," Key Eng. Mater., **297–300**, pp. 1645–1651.
[13] Tregoning, R., Abramson, L., and Scott, P., 2008, "Estimating Loss-of-Coolant Accident (LOCA) Frequencies Through the Elicitation Process," NUREG-1829, Vol. 1, U.S. Nuclear Regulatory Commission, Washington, DC.
[14] Sun, A., Kee, E., Yu, W. et al., 2005, "Application of Crow-AMSAA Analysis to Nuclear Power Plant Equipment Performance," International Conference on Nuclear Engineering ICONE-13, Beijing, China, May 16–20.
[15] Barringer, H. P., 2006, "Use Crow-AMSAA Reliability Growth Plots to Forecast Future System Failures," Second Annual International Maintenance Excellence Conference, Toronto, Nov. 1–3.
[16] Choi, S. Y., Yang, J. E., and Choi, Y. H., 2005, Piping Service Experience Related to Aging in OECD Pipe Failure Data Exchange (OPDE) Database Presentation.
[17] Viglasky, T., Blahoianu, A., Riznic, J., and Lydell, B., 2006, "The OECD Pipe Failure Data Exchange Project—Validation of Canadian Data," International Conference on Nuclear Engineering ICONE-14, Miami, FL, Jul. 17–20.
[18] Simola, K., Pulkkinen, U., Talja, H., Karjalainen-Roikonen, P., and Saarenheimo, A., 2004, "Comparison of Approaches for Estimating Pipe Rupture Frequencies for Risk-Informed In-Service Inspection," Reliab. Eng. Syst. Saf., **84**, pp. 65–74.
[19] Rausand, M., and Høyland, A., 2004, *System Reliability Theory: Models, Statistical Methods, and Applications*, 2nd ed., Wiley, New York.
[20] Cook, R. J., and Lawless, J. F., 2007, *The Statistical Analysis of Recurrent Events*, Springer, New York.
[21] Ascher, H., and Feingold, H., 1984, *Repairable Systems Reliability: Modeling, Inference, Misconceptions and Their Causes*, Dekker, Dordrecht.

Hanno van der Merwe[1]
e-mail: hanno.vdmerwe@pbmr.co.za

Johan Venter

Pebble Bed Modular Reactor (Pty) Ltd.,
1279 Mike Crawford Avenue,
Centurion 0046, South Africa

A Method to Evaluate Fission Gas Release During Irradiation Testing of Spherical Fuel

The evaluation of fission gas release from spherical fuel during irradiation testing is critical to understand expected fuel performance under real reactor conditions. Online measurements of krypton and xenon fission products explain coated particle performance and contributions from graphitic matrix materials used in fuel manufacture and irradiation rig materials. Methods that are being developed to accurately evaluate fission gas release are described here together with examples of evaluations performed on irradiation tests HFR-K5, -K6, and EU1bis. [DOI: 10.1115/1.3097131]

1 Introduction

The activity of gaseous fission product release measured in pile during fuel irradiation testing is a direct indicator of fuel performance and a gauge to predict the release of radiological important fission gas release from a power plant. The key nuclides are ^{88}Kr and ^{131}I for safety analysis during normal operation and following a loss of coolant accident, and ^{85}Kr for long-term waste disposal [1].

The main sources of gaseous release are uranium and thorium contamination in the fuel graphite (matrix contamination) and defective/failed coated particles. The uranium and thorium contamination that is in the outer pyrocarbon layer and the matrix material is from two sources. Trace amounts of uranium are found in all natural materials. Graphite used in the manufacture of matrix material and pyrocarbon layers is no exception, and the fuel element materials are contaminated by this naturally occurring uranium and thorium. The second source is the enriched uranium from the UO_2 kernel that contaminates the subsequent coating layers in the manufacturing facility.

Krypton and xenon have extremely low diffusion coefficients in PyC and all the nuclides considered have relatively short half-lives. Intact particles within the specification limits therefore are not expected to contribute to the release of gaseous fission products under normal operating conditions [2].

A third source that only pertains to irradiation test rigs is the graphite cups in which the test elements are housed in the steel capsules. These graphite cups contain significant uranium and thorium contamination and their contribution to the total fission gas released from an irradiation capsule can be considerable, especially if the test spheres contain a very low fraction of failed particles.

The transport mechanisms of fission gases produced by the finely distributed uranium and thorium contamination of the matrix material are well understood through the irradiation experiments done at the R2 test reactor at Studsvik [2]. The fission gas release behavior from failed particles was studied in detail at the FRJ2 test reactor at Jülich [3]. Fission gas transport data were measured and calculated for each fuel component material. Krypton data are used for all small nuclides (krypton and bromine), and xenon values for the larger nuclides (xenon and iodine). The use of xenon transport data for the radiological important iodine nuclides was validated by several irradiation experiments, which confirmed that at elevated temperatures, the halogen (bromine and iodine) transport behavior is similar to noble gas behavior (krypton and xenon, respectively).

The computer code NOBLEG [4] was developed to simulate the operational conditions of high temperature reactor cores and irradiation experiments. The code is useful in describing fuel behavior in the Jointly Operated Experimental Reactor (Arbeitsgemeinschaft Versuchsreaktor-AVR) and thorium high temperature reactor (THTR) and in the design and safety analysis of the planned high temperature reactor-modular design (HTR-MODUL). It calculates the noble gas and halogen release fractions from the core by solving Booth's "equivalent sphere model" [5].

HTR fuel designs considered here are based on the German fuel sphere design produced for the high temperature reactor 500 (HTR-500) and HTR-MODUL proof tests [6]. Fuel spheres are 60 mm in diameter, manufactured from high quality graphite matrix material, in which low enriched uranium TRISO-coated particles are embedded.

2 Modeling

The fission gas release from spherical fuel elements with coated particles was described in detail previously [2]. The release from matrix contamination and failed particles are described by a multicomponent system. The graphitic matrix material is treated as a three-component system. Component 1 may be attributed to the graphite grains of the raw material and component 2 to the amorphous nongraphitized binder coke between the grains. The open pore system filled with helium constitutes the gaseous component 3. The primary fission products are distributed into the solid components by direct recoil. The gas atoms diffuse from the recoil sites in the grains of the solid components to the open porosity of the fuel sphere.

The steady state fractional release due to this diffusion in each solid component is described by Booth's "equivalent sphere model"

$$R/B = 3\mathrm{U}_c\left(\frac{D_r}{\lambda}\right)^{1/2}\left(\coth\left(\frac{D_r}{\lambda}\right)^{-1/2} - \left(\frac{D_r}{\lambda}\right)^{1/2}\right)$$

where R/B is the release to birth ratio, U_c is the fraction uranium finely distributed in the matrix material. λ is the decay constant of gas nuclide (1/s), and D_r is the reduced diffusion coefficient.

The two solid-state diffusion processes are followed by the pressure and temperature-dependent gas phase transport through the open porosity of the fuel sphere to the coolant. This process is also described by a Booth equation where r equals the radius of

[1]Corresponding author.

Manuscript received October 23, 2008; final manuscript received November 10, 2008; published online June 9, 2009. Review conducted by Dilip R. Ballal. Paper presented at the Fourth International Topical Meeting on High Temperature Reactor Technology (HTR2008), Washington, DC, September 28–October 1, 2008.

the fuel element and D equals the effective diffusion coefficient for the combination of Knudsen and binary gas diffusion given by the Bosanquet equation [7]

$$\frac{1}{D} = \frac{1}{(k_1 v)} + \frac{1}{(k_2 D_{12})}$$

where k_1 and k_2 are the structural parameters of $A3$ matrix material, describing functions of tortuosity, shape, diameter, and volume fraction of the pores; v is the mean thermal velocity of gas atoms (cm/s); and D_{12} is the binary diffusion coefficient of xenon or krypton in helium.

Parameters k_1 and k_2 were measured for unirradiated $A3$ matrix material using a hydrogen permeation method. The binary diffusion constant D_{12} can be calculated with Hirschfelder's relation using the total gas pressure P and real and reference temperatures (T_1 and T_0) [8] as follows:

$$D_{12} = \frac{\text{const}(T_1/T_0)^{3/2}}{P}$$

Failed fuel particles embedded in the matrix are described by a four-component system consisting of kernel "grains," two material components of the buffer layer ("grains" and "amorphous constituents"), and helium-filled open pores in the kernel and in the porous buffer layer. The birth rates of primary fission products in the four components are calculated with the known relations for the recoil stopping ranges in different materials. The noble gas release from the three solid components is treated in the same way as the contamination-induced release. The retention capabilities of the open porosity and the coating defects (e.g., hairline cracks) are neglected.

The release from failed particles is followed by gas phase transport through the open porosity of the fuel sphere. Retention of the fuel sphere pore system is treated in the same way as above for contamination.

In more than six irradiation experiments with R/B values of ^{133}Xe in the range from 10^{-7} up to 10^{-2} covering both contamination and release dominated by failed particles, an approximate 1:1 relation between the ^{133}Xe (half-life: 5.3 days) and ^{131}I (half-life: 8.0 days) R/B values was found. For R/B values below 10^{-5}, the ^{131}I data lie by a factor of about 3 below the ^{133}Xe R/B values. This indicates the effect of adsorption/desorption equilibrium on the surfaces of the open porosity at low iodine partial pressures, which reduces the effective gas phase diffusion constant of iodine. It can thus be concluded that it is conservative to use the same diffusion data for iodine and xenon. The same applies to bromine and krypton.

The diffusion coefficients used by the model combine all possible transport mechanisms of a fission product species within one material zone, depending on temperature according to the Arrhenius relation, where D is the effective diffusion coefficient, E_A is the activation energy, R is the universal gas constant, and T is the absolute temperature;

$$D = D_0 e^{E_A/RT}$$

3 Evaluation Methods

When evaluating fission gas release from fuel spheres in an irradiation rig during an irradiation test, it is important to distinguish between release from contamination of the fuel and irradiation rig materials and the release from defective or failed coated particles. The difference lies in the fact that the fuel inside coated particles is enriched compared with the natural uranium and thorium found in contamination. This means that fission gases formed in the fuel kernels are primarily formed from ^{235}U fissions and fission gases formed in the contamination from ^{233}U and ^{239}Pu (from ^{232}Th and ^{238}U breeding, respectively). The fission yields for each fissionable nuclide differ and, therefore, must be accounted for.

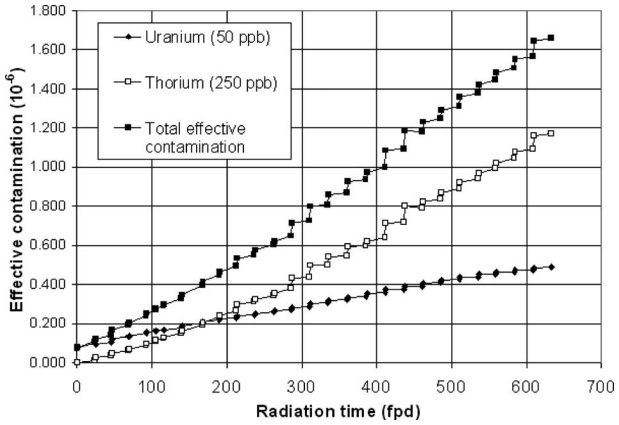

Fig. 1 Effective uranium contamination in the matrix material for test element HFR-K6/1

3.1 Effective Contamination. During irradiation, the fertile ^{238}U and ^{232}Th in the fuel matrix and irradiation rig material contamination capture neutrons to breed fissile $^{239/241}$Pu and ^{233}U. Therefore the effective uranium contamination increases with burn-up, and the release of fission gases from the fuel elements increases as well. The effective uranium contamination is therefore defined as the total fission power of the fissile nuclides ^{233}U, ^{235}U, and $^{239/241}$Pu in the contamination of the fuel sphere divided by the total fission output from the fuel element.

The enrichment factor of natural uranium contamination is 0.72%, which leads to an effective uranium contamination value of 7.2×10^{-8} at the beginning of the irradiation (i.e., 50 ppb U $\times$200 g C$\times$0.72% enrichment/1 g U-235 in kernels=7.2 $\times10^{-8}$). The rate at which the small fraction of ^{235}U is consumed is negligible against that at which ^{233}U and plutonium are bred from the large fraction ^{238}U and also when compared with the relatively large amounts of thorium available in the matrix material. The contribution from thorium is still zero as no ^{233}U breeding from ^{232}Th occurred at the start of irradiation. As an example, the effective uranium contamination for HFR-K6/1 is shown in Fig. 1. During irradiation the uranium contribution to the effective uranium contamination increases to 4.89×10^{-7} at the end of irradiation (633.6 full power days (fpd)). The thorium contribution shows a more remarkably increased contribution to the effective uranium of 1.17×10^{-6} at the end of irradiation. The effective contamination starts off with 7.2×10^{-8} (0.72% ^{235}U in natural uranium) and increases to 1.66×10^{-6} at the end of irradiation (633.6 fpd). The steps in the curve are caused by the radioactive decay of the fission product precursors for ^{233}U (^{233}Pa) and ^{239}Pu (^{239}Np) during the periods that the reactor was shut down between irradiation cycles. The increase in effective contamination explains the general tendency of fission product release to increase over irradiation time, and is therefore not necessarily a function of fuel integrity degradation.

3.2 Contamination Release. When the fuel spheres contain no failed particles, the measured release originates solely from the contamination in fuel and irradiation rig materials.

During irradiation, fission products are formed from the nuclear fission reaction of the fissionable material in the fuel elements: ^{235}U, $^{239/241}$Pu, and ^{233}U. As irradiation progresses, the plutonium and ^{233}U fission fraction increases, but has a different fission yield for each fission product that differs significantly from ^{235}U fission yields. The original calculations to determine the fission product birth rate are based on fission yields for ^{235}U. The measured R/B values must be corrected to include the plutonium and ^{233}U fission

yields by weighing the fission yield ratios (e.g., $^{239}Pu/^{235}U$) with the calculated effective contamination. This was done as follows:

$$\text{Yield ratio} = \frac{(^{235}U_{ef}\ ^{235}U_{fy} + ^{233}U_{ef}\ ^{233}U_{fy} + ^{239}Pu_{ef}\ ^{239}Pu_{fy})}{(^{235}U_{ef} + ^{233}U_{ef} + ^{239}Pu_{ef})}$$

where $^{xxx}A_{ef}$ is the effective contamination of ^{xxx}A, and $^{xxx}A_{fy}$ is the fission yield ratio of ^{xxx}A to ^{235}U. A correction factor for each irradiation period is determined by dividing the measured R/B values by the yield ratios.

From the measurements of $R2$ test rigs, we know that graphite cups contain much more heavy metal contamination than fuel materials and are a significant contributor to measured activity [9]. Previous evaluation of HFR-K5/6 suggested that each cup contributes up to three times the amount of fission gases than the contamination of one fuel sphere [10]. This contamination may be accounted for by increasing the contamination in the fuel materials as the graphite cups can be treated, as a first approximation, as fuel matrix material. Of course, this is not completely satisfactory and it becomes increasingly important to ensure that contaminations in irradiation rig materials are specified in the future.

3.3 Failed Particle Release. The inventory of a single coated particle exceeds the contamination in a fuel sphere by a factor of 35 (considering 14,000 coated particles and 1 g ^{235}U per sphere). The release from a sphere containing one defective or failed particle will therefore dominate the measured activity, and effective contamination corrections become less important. The contributions from contaminations outside the fuel sphere (irradiation rig materials) also become less of an issue, and therefore the evaluations of spheres containing one or more defective particles are much more useful.

4 Results

Three irradiation tests have been evaluated in the past few years at PBMR. All three irradiation tests have been performed at the high flux reactor (HFR) at Petten, The Netherlands. Examples of evaluations are shown and discussed in this section.

The fuel proof test HFR-K6 was originally designed to test the fuel elements for the planned HTR-MODUL, and the proof test HFR-K5 for the validation of fuel for the HTR-500. Before the start of HFR-K5 irradiation it was decided to abandon the HTR-500 project, and HFR-K5 was therefore performed with the same fuel under the same conditions as HFR-K6. The fuel elements were manufactured under similar conditions and standards as the AVR 21–1 reload batch consisting of low enriched uranium (LEU)-TRISO particles at NUKEM/HOBEG. Four 60 mm reference fuel elements with LEU-TRISO-coated particles were selected and inserted into a three-capsule best-rig for irradiation in the HFR at Petten, The Netherlands. Capsule A contained the test element A1K6 (K6/1), capsule B the test elements B1K6 (K6/2) and B2K6 (K6/3), and capsule C test element C1K6 (K6/4). A similar arrangement was applied to the irradiation test HFR-K5.

The irradiation temperature was automatically adjusted by the gas mixture technique (He/Ne). The heat transfer characteristics for neon are lower than for helium, and the temperature of the test elements can be regulated by adjusting the helium/neon gas mixture. In order to simulate the multipass core circulation of the FEs, the central fuel temperatures were planned to be set to ~800°C for one-third of the irradiation time and ~1000°C for the remainder for each HFR cycle. A total of 36 thermocouples, 17 neutron fluence detectors, 9 γ-scanning detectors, and 4 self-powered neutron (SPN) detectors were attached to the fuel elements and capsules to determine the temperature distribution and history with respect to neutron fluence and burn-up. The downstream gas from each capsule was analyzed quantitatively and qualitatively by a 4096 multichannel analyzer with two Ge(Li) detectors. The release of noble gas nuclides $^{85\ m}Kr$, ^{87}Kr, ^{88}Kr, ^{89}Kr, ^{133}Xe, ^{135}Xe, $^{135\ m}Xe$, ^{137}Xe, and ^{138}Xe was measured and reported during irradiation for each capsule [11].

Table 1 HFR-K6 test element /2 and /4 specification and irradiation data

Parameter	Unit	Fuel element designation K6/2	K6/4
	Specification		
Fuel element No.		2953–98	2953–26
Uranium content	g	9.44	9.44
^{235}U enrichment	%	10.6	10.6
CP content		14,600	14,600
Failed CP content	per FE	0	2
	Irradiation data		
Burn-up (FIMA)	%	10.6	9.8
Neutron fluence (>0.1 MeV)	10^{21} cm^{-2}	4.6	2.7
Maximum center temperature	°C	1,130	1,040
Maximum power output	kW/FE	2.51	2.1

The test element specification and irradiation data for two of the test spheres for HFR-K6 are listed in Table 1. All nuclear, temperature, and fission gas release measurement data were reported in a series of progress reports for both HFR-K5 and HFR-K6.

The irradiation experiment HFR-EU1bis was performed by the European Commission's Joint Research Centre-Institute for Energy (JRC-IE) in the HFR Petten to test five spherical HTR fuel pebbles of former German production with TRISO-coated particles for their potential for very high temperature performance and high burn-up [12]. The objective of the HFR-EU1bis test was to irradiate five HTR fuel pebbles at conditions beyond the characteristics of current pebble bed reactor designs, e.g., HTR-Modul, HTR-10, and PBMR.

The central temperature of all pebbles was kept as closely as possible to 1250°C and held constant during the entire irradiation, with the exception of HFR downtime and power transients. This is the expected maximum central fuel temperature of a pebble bed very high temperature reactor (VHTR) with a coolant outlet temperature of 1000°C. Originally a burn-up of 16% FIMA was planned, but only 11% FIMA was realized. The fuel spheres were of the type GLE-4/2 of the AVR batch 21–2. The five pebbles were tested in the "full size HTR fuel element rig" (REFA-170). The irradiation rig is equipped with 24 thermocouples, a gamma scan wire, and 3 fluence detector sets. Central fuel temperatures cannot be directly measured, and therefore the irradiation was conducted by controlling the surface temperature of the pebbles such that the calculated central temperature remained as constant as possible. Nuclear, temperature, and fission gas release data can be found in Refs. [12,13].

4.1 HFR-K5. Unfortunately, the available progress reports from HFR-K5 are incomplete and only a limited evaluation has been possible up to now. The expected calculated release from a single failed particle exceeds the measured release from test elements K5/1, K5/2, and K5/3, significantly, and therefore it can be deduced that no particle failure occurred—either through manufacture or operationally induced. Fission product releases for these test elements therefore are determined by the uranium and thorium contamination of the outer pyrocarbon layers of the coated particles, the graphitic matrix material of the fuel element, and the graphite cups in which the test spheres were housed in the irradiation rig.

Irradiation cycles 12 and 24 R/Bs at temperatures of 897°C and 816°C are plotted in Fig. 2 and Fig. 3, respectively. The effect of corrections for fission yields for especially xenon nuclides are shown by plotting both raw results and corrected values.

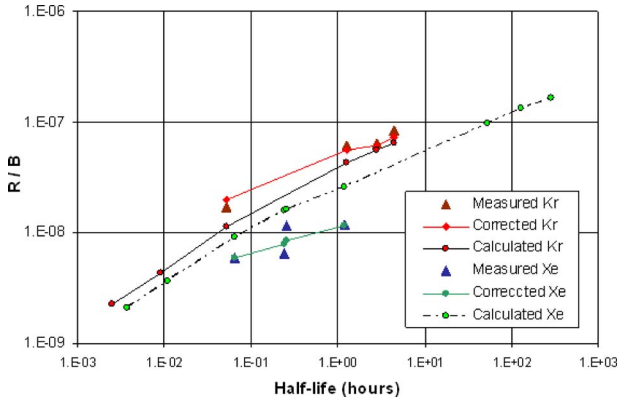

Fig. 2 *R/B* versus half-life graph, HFR-K5/2, cycle 12

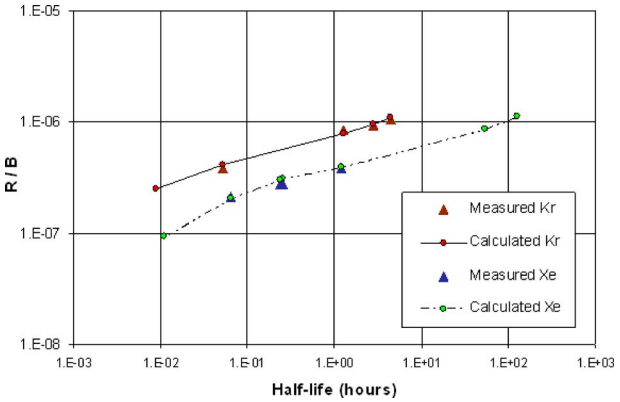

Fig. 5 *R/B* versus half-life graph, HFR-K6/4, cycle 4

4.2 HFR-K6. Almost all the irradiation data for irradiation test HFR-K6 are available and have been evaluated in detail [1]. In the previous evaluation, the noble gas fission product ^{88}Kr was selected to represent the krypton and bromine gas release from spherical fuel elements. The full irradiation experiment's ^{88}Kr release, simulated with NOBLEG for test element K6/2, is presented in Ref. [10]. Test element K6/2 (see Fig. 4) was chosen as its irradiation history had the most consistently available and coherent measurements. There were no failed or defective particles in this test sphere. The NOBLEG simulation matches the measured release with a correlation of 0.94. The largest difference between the measured and calculated values is a factor of 2.0, which is well below the accepted PBMR design factor of 5. The surface fuel temperatures range from 546°C to 820°C, with an average temperature of 702°C. The gradual increase in R/B corresponds to the gradual increase in the effective contamination of Fig. 1.

After investigating the fission gas release during irradiation, it was concluded that test element HFR-K6/4 had failed particles as its release exceeded the contamination based release significantly. Comparisons with releases from compacts that contained known numbers of failed particles suggested that two defective particles existed in the sphere.

Since the R/B values do not significantly increase during irradiation, no particle failure occurred. The releases from this element are thus dominated by defective particle release. Irradiation cycles of 4 R/Bs are plotted at temperatures between 880°C in Fig. 5 and irradiation cycle 24 R/Bs at a temperature of 800°C in Fig. 6.

These two graphs present the fission gas release at both the beginning and the end of the irradiation test. It appears as if there were no systematic changes in the containment properties of the UO_2-buffer-matrix material system, but closer inspection of the R/Bs of all the cycles suggest that some change did occur.

It can be seen in Fig. 7 that the release of the larger xenon atoms over the irradiation time decreases relative to the calculated values. This is also noted to a lesser extent for ^{88}Kr from 300 fpd to 500 fpd. This is possibly due to changes in buffer layer composition during irradiation.

After 500 fpd, the release of ^{88}Kr and ^{138}Xe drastically increases from well below to very close to the calculated values. It is most likely that this rapid increase at the end of the irradiation experiment is caused by swelling of the kernel, so buffer material retention becomes less important. However, the measured fission product release still does not exceed the calculated values.

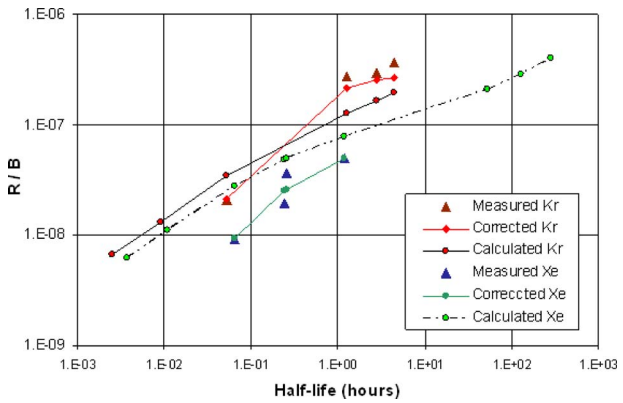

Fig. 3 *R/B* versus half-life graph, HFR-K5/2, cycle 24

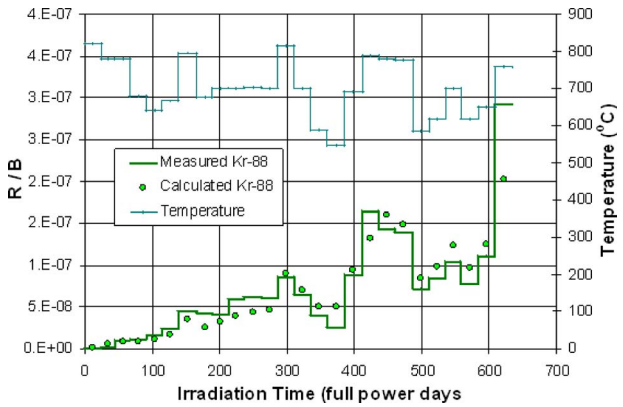

Fig. 4 Measured and calculated ^{88}Kr *R/B* comparison for test element K6/2

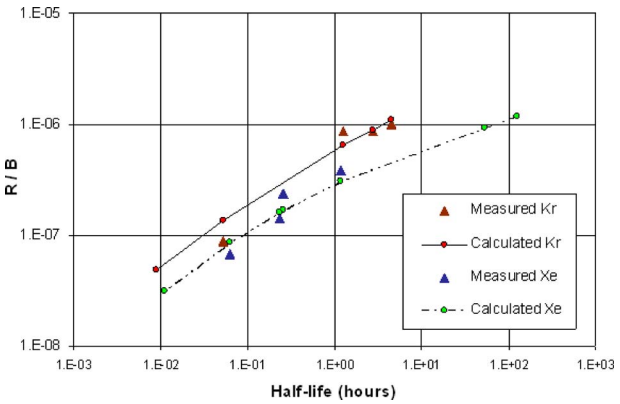

Fig. 6 *R/B* versus half-life graph, HFR-K6/4, cycle 24

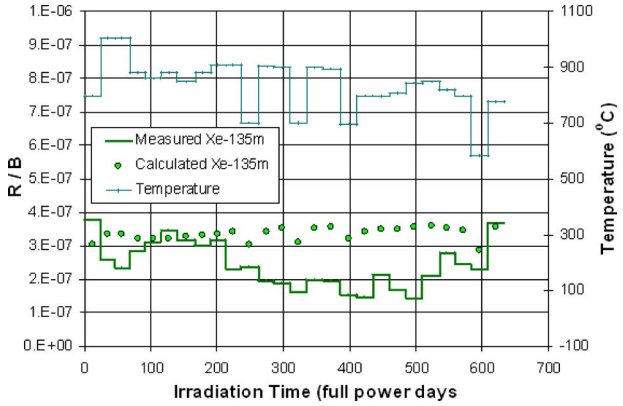

Fig. 7 Measured and calculated $^{135\,m}$Xe *R/B* comparison for test element K6/4

4.3 HFR-EU1bis. A first evaluation of the fission gas release during the HFR-EU1bis was performed. A burn-up calculation to determine the effective contaminations in the fuel materials and graphite cups was done according to the effective contamination evaluation model above and according to available neutronic data [13]. The fission gas R/B values were calculated for HFR-K5 and -K6 with the exception that all five test spheres are in the same purge gas stream, and just one measurement was taken for all five test spheres. All five test spheres are evaluated at the same time with the measured fission gas release data available [12]. It is therefore not possible to determine individual fuel sphere performance directly.

All three krypton isotopes for which R/B values were measured have precursors with very short half-lives compared with measurement times. This has the effect that no corrections need to be made for release from precursors plated out in measurement lines, which simplifies analysis considerably. The general trend of measured R/B values for krypton isotopes is illustrated in Fig. 8 for ^{88}Kr. The center temperature of fuel sphere 4 is shown as reference.

The R/B curve has some distinctive characteristics that need to be taken into account during interpretation.

(1) It starts at a value of about 5×10^{-7}, which is higher than expected for fission gas released from contamination only, but is lower than expected for a single failed coated particle initially present in one of the five fuel spheres. The R/B curve more or less follows center fuel sphere temperatures in this region of the curve.
(2) Apart from a number of distinctive peaks, the R/B curve generally shows an upward trend with increasing irradiation exposure of fuel spheres indicating the important role played by fission gas release from contamination.
(3) There are two distinctive R/B peaks at about 125 efpd and 200 efpd, which correspond to sharp increases in fuel sphere center temperatures as calculated from input fuel sphere surface temperatures and power production in the fuel spheres.
(4) There is a sharp increase in R/B near the end of irradiation that is considerably higher than the previous R/B peak while the temperature increase is similar to the previous temperature peak, which indicates failure of one or more coated particles toward the end of the irradiation test.

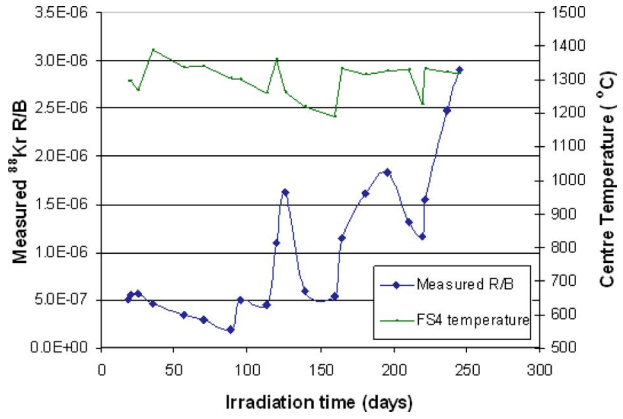

Fig. 8 Measured ^{88}Kr *R/B* and sphere /4 temperatures

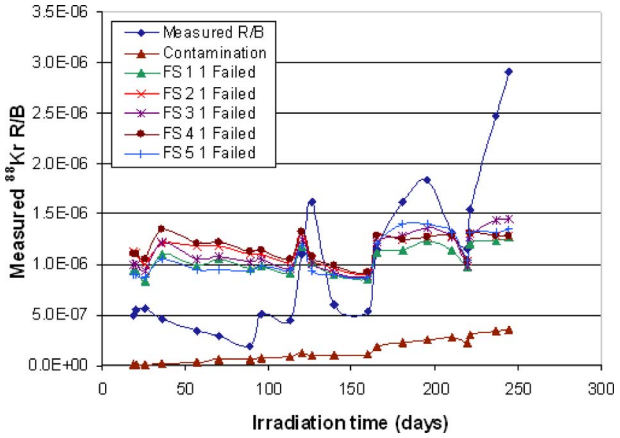

Fig. 9 Measured and calculated ^{88}Kr *R/B* for contamination and one failed particle

Calculated fuel center temperatures are generally higher than 1250°C, which was the target temperature for the HFR-EU1bis irradiation test.

NOBLEG calculations were performed separately for each fuel sphere for two cases. In the first case only contamination was taken into account while for the second case a failed coated particle was initially assumed to be present in each fuel sphere. Results obtained for ^{88}Kr are shown in Fig. 9. As all five fuel spheres were enclosed in the same irradiation container, contamination values for individual fuel spheres were added to obtain a single contamination R/B value per measurement.

It is clear from the graph that contamination R/B values alone, as calculated from fuel sphere and irradiation rig material contamination, could not provide an explanation for the R/B peaks observed in the measured curve. This leads to consideration of the possibility of a failed coated particle being present initially in one of the fuel spheres. The presence of a failed coated particle would explain the R/B peaks that correspond to temperature peaks in the measured R/B curve. However, all the curves for one failed coated particle lie above the measured R/B curve, except for the R/B peaks in the curve.

Interpretation of Fig. 9 suggests the presence of a single failed coated particle from start of irradiation. The initial coating failure appears to extend through all three outer coating layers of a coated particle, and is so small that it restricts release of fission gas at lower temperatures while opening up sufficiently at higher temperatures to allow free release of fission gas. It also appears that an additional coated particle failed at the start of the last temperature peak during irradiation. The results shown in Fig. 10 for ^{88}Kr and in Fig. 11 for $^{85\,m}$Kr were obtained by applying the above assumptions to each of the measured krypton R/B curves.

It was found that the contamination R/B contribution from irradiation rig materials contributed a factor of 0.9 to the fuel material contamination release, while R/B values for a failed coated particle had to be reduced to approximately 40% of expected R/B

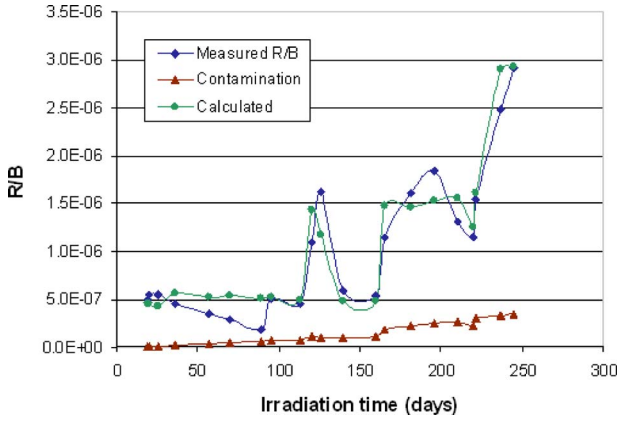

Fig. 10 Measured and calculated ^{88}Kr R/B

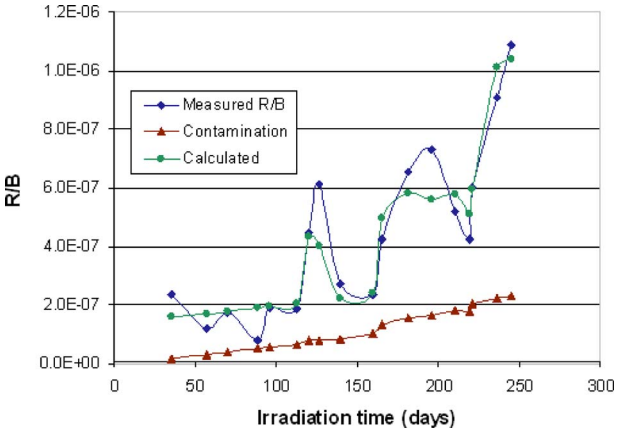

Fig. 12 Measured and calculated ^{135}Xe R/B

values for a totally uncovered kernel at lower temperature in order to produce a good fit to R/B values measured for the three krypton isotopes.

Iodine plates out in the gas lines that remove the purge gas from the irradiation rig. Iodine fission gases ^{133}I and ^{135}I are important gas precursors for ^{133}Xe and ^{135}Xe, respectively. The xenon and krypton fission gases would be disposed of during irradiation through an activated charcoal trap, but iodine would remain in the gas lines. As iodine decays, xenon daughter products are released, adding to the xenon activity. Due to the relative short half-lives of ^{133}I and ^{135}I, the inventory plated out on the cold gas lines come into equilibrium with the release rate from the fuel spheres during irradiation. The activity of iodine nuclides plated out on gas lines can then be calculated and added to the xenon source term. The contribution of ^{133}I to the ^{133}Xe source term amounts to between 47% and 50% of the ^{133}Xe activity released from the fuel spheres. The exact percentage depends on contributions from different fissile materials (i.e., Fig. 1) and the mean fuel temperature. The measured ^{133}Xe activity in the grab sample holder is therefore 47–50% higher than the actual release activity from the fuel spheres. Similarly, the contribution of ^{135}I to the ^{135}Xe activity is between 155% and 170% of the ^{135}Xe activity released from the fuel spheres. This additional activity must be accounted for in the measured R/B values.

The full irradiation experiment's ^{135}Xe release simulated with NOBLEG by including the neutron absorption of ^{135}Xe and contributions from ^{135}I precursor is presented in Fig. 12. Similarly, fuel performance assumptions were used in the same way as for the ^{88}Kr and $^{85\ m}$Kr calculations.

Both the xenon and krypton R/B curves suggest that a coated particle has a single crack through all the three coating layers. At steady temperatures below 1300°C only 40% of the kernel-released fission gas is released through coating failure. During a relative fast temperature transient above 1300°C the crack is forced open by fission gas pressure in the kernel and the coated particle acts as a completely failed particle releasing all available fission gas already released from the kernel. When the temperature drops below 1300°C the crack closes again and only a fraction of the available fission gas is released.

To test this mechanism R/B versus half-life plots were made for cases below and above 1300°C. Cycle 13, which had a relatively low irradiation temperature, is plotted in Fig. 13. The center fuel temperature was below 1300°C and only ~40% of a failed particle's release and contamination was used as a source of fission products. The slopes of the measured krypton and xenon curves are well matched with the calculated slopes.

Cycle 10, which had a relatively high irradiation temperature, is plotted in Fig. 14. The center fuel temperature was above 1300°C and a completely failed particle was used with contamination as sources of fission product release. The slopes of the krypton and xenon curves appear less steep for the measured data compared with the calculated curves, but this could be due to measurement errors and the small number (three and two) fission gases measured for each curve.

5 Conclusion

Evaluations of fission gas release during irradiation tests of spherical fuel elements are important to monitor fuel performance

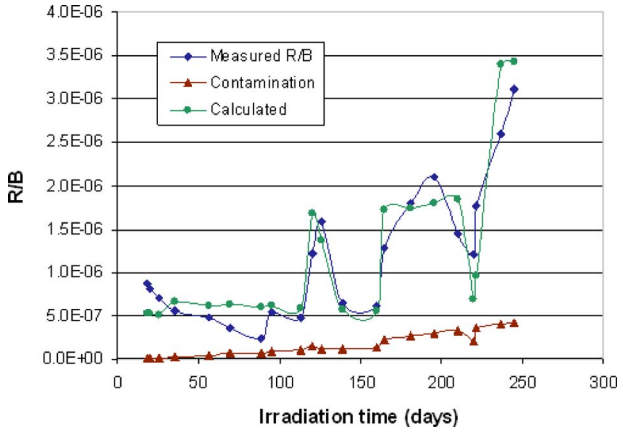

Fig. 11 Measured and calculated $^{85\ m}$Kr R/B

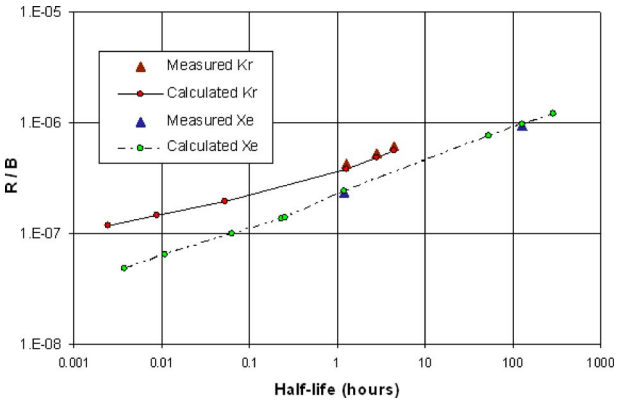

Fig. 13 R/B versus half-life graph for HFR-EU1bis, cycle 13

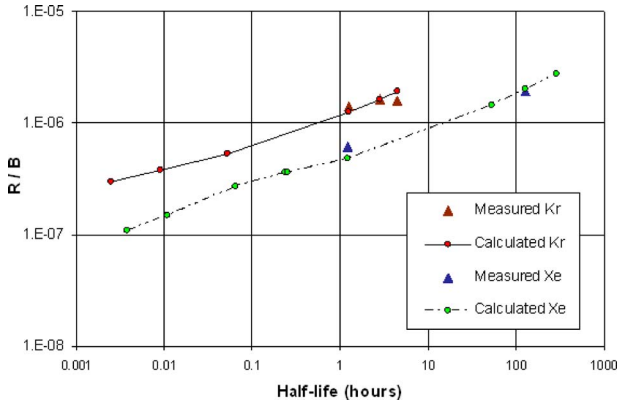

Fig. 14 *R/B* versus half-life graph, HFR-EU1bis, cycle 10

and to evaluate fission gas transport parameters. The steady state release of fission gas from fuel spheres in pile during irradiation testing can be modeled by a modification of "Booth's equivalent sphere" model.

It is important to distinguish between releases from contamination and defective/failed particle sources. If no defective or failed particles exist in a fuel sphere then the release is caused by contamination of the fuel and irradiation rig materials. Burn-up calculations are required to determine the effective contamination in these materials as the majority of fissile contamination is bred during irradiation. Corrections may then be required to ensure that the correct fission yields are used in the production calculation.

If a defective or failed particle exists in a fuel sphere it will be the dominating release source. Water ingress will only significantly affect fuel spheres containing defective or failed particles, and simple relations exist to evaluate the effect of water vapor on fission gas release.

The described model was used to do an in-depth evaluation of the HFR-K6 irradiation test and some irradiation cycles of HFR-K5. Good simulations of both tests were achieved, showing its usefulness in understanding irradiation test results.

A first evaluation of the HFR-EU1bis irradiation test was performed. It was found that for center fuel temperatures below 1300°C, the main contributor to the fission gas release is contamination in fuel and irradiation rig materials and only a fraction of a coated particle's release. For temperatures above 1300°C the fission gas release increases beyond what can be expected from contamination only and a failed particle is the only possible explanation. R/B versus half-life graphs suggest that the high releases at temperatures above 1300°C may be from a failed coated particle that does not release its full kernel-released inventory of fission gases below 1300°C.

It appears that an additional in-pile coated particle failure occurred during the second to the last irradiation test as the fission gas release for all nuclides significantly exceed the release of contamination and one failed particle only. Whether the two (or more) failed particles occurred in the same fuel sphere or different spheres cannot be deduced from the data. Postirradiation examination of the test spheres should be able to explain the observed release rates.

Acknowledgment

The authors wish to thank PBMR for allowing the publication of this work.

Nomenclature

λ = decay constant (s^{-1})
v = mean thermal velocity (cm/s)
D = effective diffusion coefficient (cm^{-2}/s)
D_r = reduced diffusion coefficient (s^{-1})
D_{12} = binary diffusion coefficient (cm^{-2}/s)
E_A = activation energy (kJ/mol)
R = universal gas constant (8.314 J/K mol)
R/B = steady state ratio of fission products released to fission products produced
T = absolute temperature (K)
TRISO = tristructural isotropic

References

[1] Van Der Merwe, J. J., 2004, "Development and Validation of Fission Product Release Models and Software at PBMR," *Proceedings of the Second International Conference on High Temperature Reactors, HTR-2004*, Beijing, China, Sept. 22–24.
[2] Röllig, K., 1977, "Release of Rare Fission Gases From Spherical Elements With Coated Particles," Nucl. Technol., **35**, pp. 516–523.
[3] Röllig, K., 2001, "Release of Noble Gases and Halogens From the PBMR Core," Westinghouse Reaktor, Report No. GBRA 052 336.
[4] Röllig, K., 2001, "Description of the Computer Code NOBLEG," Westinghouse Reaktor, Report No. GBRA 054 350.
[5] Booth, A., 1957, "A Method of Calculating Fission Gas Diffusion From UO_2 Fuel and Its Application to the X-2-F Loop Test," Atomic Energy of Canada Ltd., Report No. CRDC-721.
[6] Lohnert, G. H., Nabielek, H., and Schenk, W., 1988, "The Fuel Element of the HTR-Module, A Prerequisite of an Inherently Safe Reactor," Nucl. Eng. Des., **109**, pp. 257–263.
[7] Schmidt, A., and Röllig, K., 1970, *Proceedings of Reaktortagung Deutches Atomforum*, Berlin.
[8] Hirschfelder, J. O., Curtiss, C. F., and Bird, R. B., 1954, *Molecular Theory of Gases and Liquids*, Elsevier, New York, p. 718.
[9] Christ, A., and Röllig, K., 1983, "The Sensitivity of Core Release Calculations to Transport Parameters," Hahn-Meitner-Institut für Kernforschung, Report No. B372.
[10] Van Der Merwe, J. J., 2004, "Verification and Validation of the PBMT Models and Codes Used to Predict Gaseous Fission Product Releases From Spherical Fuel Elements," MSc thesis, Rand Afrikaans University, Johannesburg, South Africa.
[11] Conrad, R., 1990, "Irradiation of High Temperature Fuel Elements for the HTR Module in the HFR Petten, HFR-K6," HFR Petten Design and Safety, Report No. D138.05.
[12] Fütterer, M. A., Berg, G., Marmier, A., Toscano, E., Freis, D., Bakker, K., and de Groot, S., 2008, "Results of AVR Fuel Pebble Irradiation at Increased Temperature and Burn-Up in the HFR-Petten," Nucl. Eng. Des., **238**(11), pp. 2877–2885.
[13] De Groot, S., Bakker, K., van Heek, A. I., and Fütterer, M. A., 2008, "Modelling of the HFR-EU1bis Experiment and Thermo Mechanical Evaluation," Nucl. Eng. Des., **238**(11), pp. 3114–3120.

Ways to Increase Efficiency of the High-Temperature Gas Reactor Coupled With the Gas-Turbine Power Conversion Unit

V. F. Golovko
e-mail: golovko@okbm.nnov.ru

N. G. Kodochigov

A. V. Vasyaev

OKB Mechanical Engineering,
Burnakovsky Proezd 15,
Nizhny Novgorod 603074, Russia

A. Shenoy
e-mail: arkal.shenoy@gat.com

C. B. Baxi

General Atomics,
P.O. Box 85608,
San Diego, CA 92186-5608

This paper deals with the issue of increasing efficiency of nuclear power plants with the modular high-temperature gas reactor (HTGR) and direct gas-turbine cycle. It should be noted that only this combination can highlight the advantages of the HTGR, namely, the ability to heat helium to about 1000°C, in comparison with other reactor plants for electricity generation. The HTGR has never been used in the direct gas-turbine cycle. At present, several designs of such commercial plants are at the stage of experimental validation of main technical features. In Russia, OKB Mechanical Engineering together with General Atomics (United States) are developing the GT-MHR project with a reactor power of 600 MW, a reactor outlet helium temperature of 850°C, and an efficiency of about 45.2%; the South African Republic is developing the PBMR project with a reactor power of 400 MW, a reactor outlet helium temperature of 900°C, and an efficiency of about 42%; and Japan is developing the GTHTR-300 project with a reactor power of 600 MW, a reactor outlet helium temperature of 850°C, and an efficiency of about 45.6%. As it has been proven by technical and economic estimations, one of the most important factors for successful promotion of reactor designs is their net efficiency, which must not be lower than 47%. A significant advantage of a reactor plant with the HTGR and gas-turbine power conversion unit over the steam cycle is considerable simplification of the power unit layout and reduction in the required equipment and systems (no steam generators, no turbine hall including steam lines, condenser, deaerator, etc.), which makes the gas-turbine power conversion unit more compact and less costly in production, operation, and maintenance. However, in spite of this advantage, it seems that in the projects currently being developed, the potential of the gas-turbine cycle and high-temperature reactor to more efficiently generate electricity is not fully used. For example, in modern reactor plants with highly recuperative steam cycle with supercritical heat parameters, the net efficiency of electricity generation reaches 50–55%. There are three methods of the Brayton cycle carnotization: regeneration, helium cooldown during compression, and heat supply during expansion. These methods can be used both separately and in combination, which gives a total of seven complex heat flow diagrams. Besides, there are ways to increase helium temperature at the reactor inlet and outlet, to reduce hydraulic losses in the helium path, to increase the turbomachine rotation speed in order to improve the turbine and compressor efficiency, to reduce helium leaks in the circulation path, etc. The analysis of GT-MHR, PBMR, and GTHTR-300 development experience allows identification of the main ways of increasing the efficiency by selecting optimal parameters and design solutions for the reactor and power conversion unit. This paper estimates the probability of reaching the maximum electricity generation efficiency in reactor plants with the HTGR and gas-turbine cycle with account of the up-to-date development status of major reactor plant components (reactor, vessels, turbocompressor, generator, heat exchange equipment, and structural materials).
[DOI: 10.1115/1.3097133]

1 Introduction

One of the top-priority goals at the current stage of nuclear power plant construction is high efficiency of electricity generation. The rise in fuel costs and the requirements to environmental parameters bring about the necessity of introducing high effective electricity generation technologies with an efficiency of 50% and above. Most promising in this respect are nuclear power plants based on HTGRs generating electricity in the direct closed Brayton cycle using helium as a coolant. A significant advantage of such nuclear power plants is the potential to achieve efficiency of electricity production as high as 50% combined with the maximum possible safety level, which would allow their arrangement in direct proximity to settlements and industrial sites. Successful implementation of the HTGR technology for electricity generation will encourage their nonelectrical application, including large-scale production of hydrogen and other technological processes. The most effective way to enjoy all the advantages of a HTGR coupled with the gas-turbine cycle is to use them for cogeneration of electricity and waste heat for desalination and district heating purposes.

Advantages of reactor plants with the HTGR and gas-turbine power conversion unit (PCU), as compared with steam cycle plants, include considerable simplification of the power unit diagram and, especially if the integral PCU layout is used (turboma-

Manuscript received October 28, 2008; final manuscript received December 4, 2008; published online June 9, 2009. Review conducted by Dilip R. Ballal.

Table 1 Gas turbine cycle parameters and PCU equipment characteristics

Parameter	Project			
	GT-MHR	GTHTR-300 [3]		PBMR[a] [4]
Net efficiency	46.7 45.2	45.6	47.6	42
Reactor inlet/outlet temperature (°C)	490/850	587/850		536/900
No. of intermediate cooling stages during compression	1	None	1	1
Cycle recuperation effectiveness (%)	95	95	95	96
Cycle compression ratio	2.86	2.0	2.4[a]	2.7
Shaft rotation speed (rpm)				
-high-pressure TC	3000 4400	3000		15,200
-low-pressure TC				14,200
-turbogenerator				3,000
Adiabatic efficiency (%)				
-generator turbine	93.0	93.8	93.5	90
-compressor turbine				89
Adiabatic efficiency LPC/HPC (%)	88.0/87.0	89.5	89.0	89
Relative hydraulic losses in the helium circuit (%)	7.49 8.1	6.4	7.1	~5
Generator efficiency/frequency converter (%)	98.65 97.7/98.5	98.7		98.5

[a]There are no published detailed data on a new PCU.

chine (TM), recuperator, and coolers in one high-pressure vessel), reduction in the number of needed equipment and systems (steam generators, turbine hall, including steam pipelines, condenser, deaerator, etc.). For such nuclear power plants the prime cost of produced electricity, including capital investments in construction, fuel costs, and operation and maintenance costs, is estimated at about 2 ¢/kW h, which allows them to compete with steam cycle nuclear power plants or fossil fuel electric plants. At the same time, for successful promotion of these plants in the world, in accordance with technical and economic evaluations, they must have a net efficiency of not lower than 47–48%. Such level is already achieved by modern steam turbine plants with supercriticial steam parameters: temperature of 540–560°C and pressure of 24–26 MPa [1]. For comparison, application of gas-turbine power plants as extensions to the steam units of existing cogeneration plants, as it is often done in the countries of the Commonwealth of Independent States, makes possible to raise the plant efficiency to 52–60% [2].

Meanwhile HTGRs with the direct gas-turbine cycle have never been used anywhere in the world. At present, designs of such commercial plants are at the stage of experimental validation of main technical solutions. The Russian Federation (OKB Mechanical Engineering) and the USA (General Atomics) are jointly developing the GT-MHR project featuring a modular reactor of 600 MW, a reactor outlet helium temperature of 850°C, and an efficiency of 45.2%. The South African Republic is developing the PBMR design with a reactor of 400 MW, a reactor outlet helium temperature of 900°C, and an efficiency of ~42%. Japan is developing the GTHTR-300 project with a reactor of 600 MW, a reactor outlet helium temperature of 850°C, and an efficiency of ~45.6%.

One of the major factors of successful development of nuclear power plants based on HTGRs coupled with the gas-turbine cycle is optimal selection of cycle thermodynamic parameters and achievement of maximum efficiency of PCU equipment.

2 The Analysis of Ways to Increase Efficiency

This paper analyzes the possibilities of increasing the net efficiency of such nuclear power plants based on the state-of-the-art research and technologies. It seems that the key factors for achieving the competitive level of 48% are as follows:

- carnotization of the Brayton cycle
- reduction in the compression ratio in the cycle
- improvement of the efficiency of turbomachine components (turbine, Eff_t; compressor, Eff_c; and generator, Eff_g)

Besides that, it is necessary to consider the effect of reducing the hydraulic losses in the helium path, as well as other parameters, which together can make quite a noticeable contribution to the plant efficiency.

The analysis was performed on the basis of GT-MHR nuclear power plant (NPP) development experience and with account of the PBMR and GTHTR-300 experience. Table 1 gives comparison of main gas-turbine cycle parameters and PCU equipment characteristics of the above mentioned projects.

Carnotization of the Brayton cycle. At present, the economically acceptable way of Brayton cycle carnotization in order to increase its efficiency is regenerative heating of the helium directed from the compressor to the reactor inlet with the helium leaving the turbine, and intermediate cooling of the gas at the stage of compression in the compressors. These measures require development of respective heat exchange equipment (recuperator and intercoolers) in addition to the precooler.

As per the analysis of recuperation effectiveness on cycle efficiency, it was determined that the recuperator efficiency shall be 95% minimum. This efficiency is accepted in all projects under consideration. Modern processes of compact heat exchanger fabrication afford grounds for development of recuperator of such effectiveness and for arrangement in the most severe conditions of heat exchange equipment and TM integral layout in a single vessel of reduced dimensions (up to 7 m). These fabrication technologies have been mastered in Japan and South Korea. The necessity of intermediate gas cooling in contrast to recuperative heating is not so indisputable. For example, the GT-MHR project applies one intercooler of ~94% efficiency between high-pressure compressor (HPC) and low-pressure compressor (LPC). This intercooler increases efficiency by ~4% (Fig. 1). The presented GT-MHR efficiency is equal to the ratio between TC shaft power and reactor power (without loss for reactor cavity cooling and shutdown reactor cooling system).

The introduction of the second cooling stage increases the efficiency by ~1% more, but the design becomes more complicated and the PCU cost increases. The precooler and intercooler influence the removed heat temperature in the gas-turbine cycle, increasing the plant efficiency by 0.7% for each 5°C of gas temperature decrease at the compressor inlet.

In the GTHTR-300 project, intermediate cooling is eliminated [3] based on economic estimations substantiating the benefit from simplification of the PCU design and layout, decrease in the capital costs component in the electricity costs, and reduction in pipe leak accident probability. NPP efficiency decrease is estimated at 2% (instead of 4%). Lower efficiency decrease is explained by the

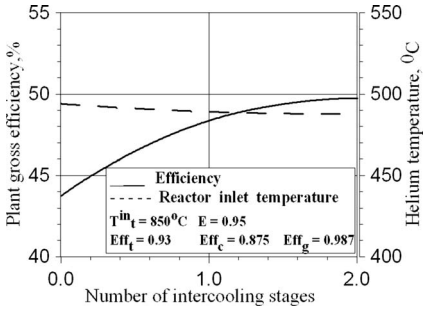

Fig. 1 Efficiency as a function of cooler number with a helium temperature of 850°C at the turbine inlet

decrease in the corresponding parameters and characteristics of cycle components caused by design changes and by the optimal selection of compression ratios for both GTHTR-300 options. Nevertheless, in compliance with the goal to investigate the possibility of maximum NPP efficiency increase, single cooling stage is preferable.

Decrease in compression ratio in the cycle. Position of maximum efficiencies as a function of compression ratio (Figs. 2 and 3) depends on recuperation effectiveness in the cycle and does not depend (for other equal status) on helium temperature at the reactor outlet (turbine inlet). Thus, for a recuperation effectiveness of 0.95 the optimal compression ratio is equal to ~2.25. The maximum temperature of the cycle, which is the temperature at the reactor outlet, influences the cycle efficiency considerably (Fig. 3). The temperature change by each 50°C leads to the corresponding efficiency change of 1.5–2%. Helium temperature at the reactor outlet is limited by the allowable temperature of structural materials of the turbine and hot gas duct and maximum fuel temperature. The value of 850°C accepted in the GT-MHR reflects the current status of high-temperature materials research and gas-cooled reactor operation experience. For a helium temperature of

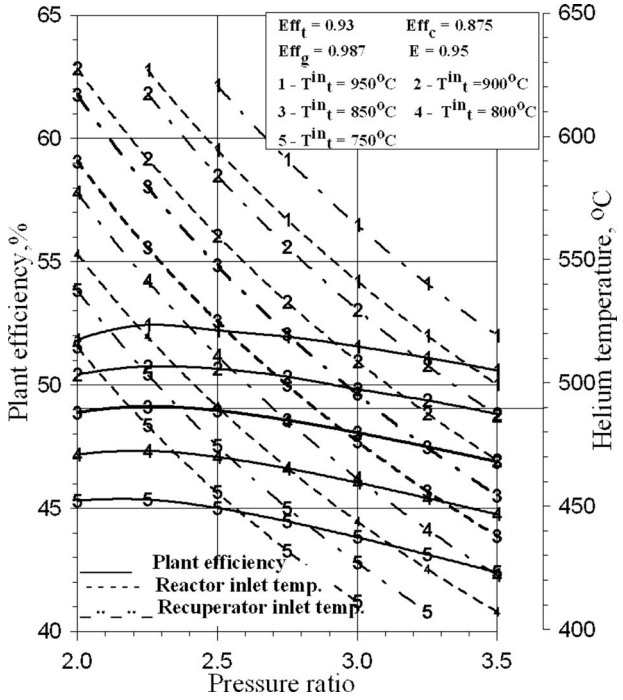

Fig. 2 Influence of helium temperatures of 950°C (1), 900°C (2), 850°C (3), 800°C (4), and 750°C (5) at the reactor outlet (turbine inlet) on the GT-MHR efficiency at a recuperator effectiveness of 0.95

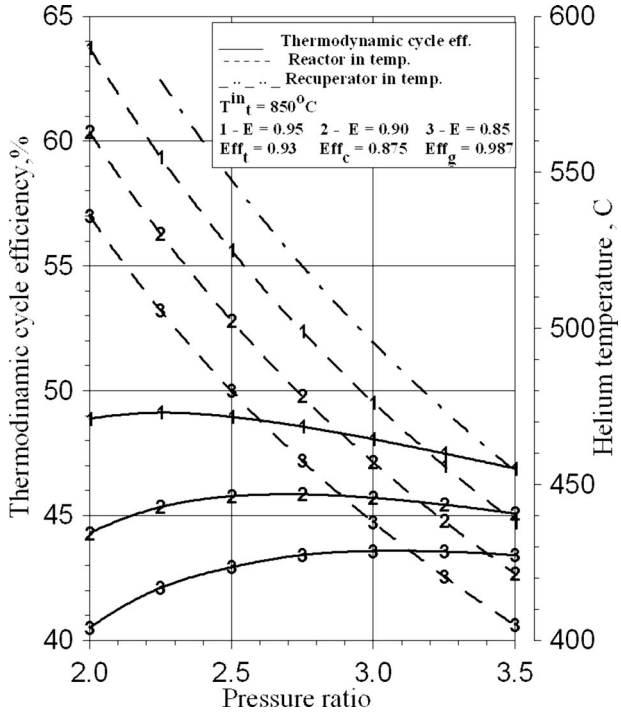

Fig. 3 Influence of compression ratio and recuperator effectiveness of 0.95 (1), 0.9 (2), and 0.85 (3) on the GT-MHR efficiency at a helium inlet turbine temperature of 850°C

850°C and a recuperation effectiveness in the cycle of 0.95 in the range of optimal compression ratios of the cycle, the efficiency is 49%.

The temperature drop and, correspondingly, expansion ratio in the turbine influence the helium temperature at the turbine outlet and reactor inlet and, from the viewpoint of the design, they influence the quantity of turbine stages. For a compression ratio of 2.25 and a reactor outlet temperature of 850°C the helium temperature at the reactor inlet shall be about 550°C. In the GT-MHR project the helium temperature of 490°C at the reactor inlet was determined by the allowable vessel temperature and was obtained by the increase in compression ratio to 2.86 and the corresponding decrease in net efficiency of the cycle to 48.6%.

To increase the GT-MHR NPP net efficiency to the maximum value corresponding to the reactor outlet temperature of 850°C, the structural-design solutions for the reactor and PCU with decreased (to 2.24) compression ratio and increased (to 560°C) temperature at the core inlet with no exceeding of allowable temperature limits for fuel and reactor vessel materials were analyzed and mastered.

3 Possible Improvements

As a result of the performed investigations the following principal technical solutions on PCU (Table 2) are recommended to increase the efficiency of the gas-turbine cycle, repairability of PCU elements, to decrease their technical risk, and to improve their operation conditions.

The performed design analysis confirms that the required reactor vessel temperature of 370°C in normal and emergency modes at the reactor inlet helium temperature up to 562°C can be achieved by optimal heat removal from the vessel to the reactor cavity cooling system. Several technical solutions are proposed, which, if implemented, will allow decreasing the reactor vessel temperature, in particular, arrangement of heat insulation near the reactor support belt and installation of graphite sleeves with low heat conductivity coefficient into coolant channels of the replaceable side reflector.

Table 2 Recommended technical solutions

Technical solutions	Advantages
Decrease in compression ratio in the cycle up to optimal value	Increased NPP (~1%) and TC efficiency, lower the number of TC stages, pressure losses and bearing loads
Analyze possible replacement of the last axial compressor stages with the centrifugal ones	
Analyze possible decrease in mass and size characteristics of the generator, catcher bearings, and electromagnetic bearings at a TC rotation speed of 3000 rpm	
Assign a TC rotation speed of 3000 rpm equal to the frequency of the grid and exclude the frequency converter	Increased NPP (~1,5%) and TM efficiency and improved plant controllability
Change circulation circuit to ensure helium supply from the HPC discharge line directly to the PCU cavity	Decreased temperature and improved reliability of PCU invessel metalwork
Optimize layout of components and pipelines inside the PCU, exclude the complicated recuperator support	Decreased hydraulic losses and improved plant reparability

In accordance with operation conditions of reactor core materials, the allowable helium temperature at the reactor outlet amounts to 850–950°C. This is a potential margin for improving the NPP economy. However, advantages of helium can be considerably reduced or even eliminated at coolant temperature increase when changing over to gas-turbine structures subject to cooling. In a closed cycle, helium supplied from circuit sections with lower temperature to cool disks of the first turbine stages considerably decreases the turbine temperature and increases circuit leaks, thereby decreasing the cycle efficiency. It is assessed that 1% of the coolant used for turbine cooling leads to a 1.5% decrease in plant electric power.

At cooling the turbine, heat removal from working helium stream increases due to high heat transfer properties of helium, in comparison, for example, with air. Increasing the inlet turbine temperature becomes ineffective starting from some value, as shown in Fig. 4. It should be taken into account that turbine components to be cooled can experience high-temperature stresses due to high heat transfer capacity of helium that is a serious design problem [3], which can be solved by using helium with higher temperature and higher flow rate. Cooling shall be selected by taking into account the relative contribution of the organized leak to the overall decrease in cycle efficiency.

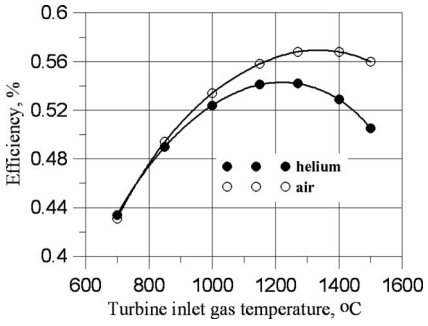

Fig. 4 Cycle efficiency dependence on turbine inlet gas temperature with account of leakage for turbine cooling

Table 3 NPP net efficiency dependence on TM component efficiency

Component	Value (%) GT-MHR	Value (%) Max.	NPP efficiency increase (%)
Turbine (adiabatic)	93	93.5 [3]	0.3
LPC (adiabatic)	88	89 [3,5]	0.25
HPC (adiabatic)	87	89 [3,5]	0.5
Generator	97.7	98.7 [3]	0.49
Frequency converter	98.5	Excluded	0.7

In accordance with estimates, at an inlet helium temperature of 850°C, turbine disk cooling by HPC helium mixed with helium coming from the recuperator on high-pressure side will be the most acceptable and effective method. The estimated total flow rate of gas with a temperature of ~300°C to be used for turbine cooling amounts to 1.7%.

Proposed technical solutions, if implemented, will allow increasing the NPP net efficiency up to 47%. For this purpose it is necessary to prevent the deterioration of other basic cycle parameters and equipment performance. Preliminary developments have confirmed such a possibility. Thus, relative hydraulic losses for the GT-MHR project will amount to 7.5%, and total relative leaks in helium circuit will amount to 0.82.

Improvement of TM component efficiency. Current achievements in this field are of great interest because of NPP net efficiency dependence on TM component efficiency.

With account of actually achieved maximum TM component efficiency (see Table 3), excluding frequency converter and current status of development of NPP main components (reactor, vessels, and heat exchange equipment and materials), it is possible to increase the projected net efficiency of the NPP up to 48%. In particular, at the reactor inlet/outlet helium temperature of 850/560°C, the net efficiency of the GT-MHR NPP can be increased up to 48.5%. It should be noted that the decreased efficiency and increased generator weight in the GT-MHR NPP (as compared with foreign designs, for example, to generators produced by ALSTOM) are conditioned by higher deviation range of electric main frequency, which is applicable in Russia.

4 Conclusion

Thus, the analysis of GT-MHR, PBMR, and GTHTR-300 design experience can serve as the basis for determining ways for improving efficiency of plants with HTGR and gas-turbine cycle by adopting optimal solutions on parameters and main components of the reactor and the power conversion unit. Similar analysis can be a basis of design specification for components and systems guaranteeing high efficiency of NPP as a whole.

Further prospective improvement of electricity generation efficiency up to 50% at plants with HTGR and gas-turbine cycle relates to application of TC ceramic materials capable to withstand long-term operation at the temperature of 1000°C and higher.

Nomenclature

Eff_t = turbine efficiency
Eff_c = compressor efficiency
Eff_g = generator efficiency
E = recuperator effectiveness
P = pressure (Pa)
T = temperature (K)

Subscript/Superscript

in = inlet
t = turbine

References

[1] Dmitriev, A. M., Kavun, O. Y., Khrennikov, N. N., and Piskunova, N. A., 2008, "Evaluation of the Technological Parameters of the High-Temperature Reactor With a Solid Coolant in the Electricity Generation Mode," At. Energy, **104**(4), pp. 268–272.

[2] Romanov, V. V., Raimov, R. I., and Chorniy, G. V., 2008, "Gas Turbine Plants With the Power of 45 and 60 MW and High Effective Power Plants on Their Basis," Gas Turbine Technologies, **62**(1), pp. 3–5.

[3] Yan, X., and Takizuka, T. et al., 2003, "Cost and Performance Design Approach for GTHTR300 Power Conversion System," Nucl. Eng. Des., **226**, pp. 351–373.

[4] Matzner, D., Mulder, E., and Pretorius, P., 2001, "Review of the Pebble Bed Modular Reactor (PBMR) Plant," *Current Status and Future Development of Modular High Temperature Gas Cooled Reactor Technology*, IAEA, Vienna, pp. 19–68.

[5] Takada, S., Takizuka, T. et al., 2003, "The 1/3-Scale Aerodynamics Performance Test of Helium Compressor for GTHTR300 Turbo Machine of JAERI (STEP1)," ICONE11, Tokyo, Japan, Apr. 20–23.

Density Change of an Oxidized Nuclear Graphite by Acoustic Microscopy and Image Processing

Se-Hwan Chi
Nuclear Hydrogen Development and Demonstration Project,
Korea Atomic Energy Research Institute,
1045 Daedeok-daero,
Daejeon, 305-353 South Korea
e-mail: shchi@kaeri.re.kr

Cristian I. Contescu
e-mail: contescuci@ornl.gov

Timothy D. Burchell
e-mail: burchelltd@ornl.gov

Materials Science and Technology Division,
Oak Ridge National Laboratory,
P.O. Box 2008,
Oak Ridge, TN 37831

The strong correlation between the density and the physical and mechanical properties of graphite suggests that the method of nondestructive density evaluation could be developed into a characterization technique of great value for the overall improvement of the safety of graphite moderator reactors. In this study, the oxidation-induced density changes in nuclear graphite for very high temperature reactor were determined by a conventional destructive bulk density measurement method (BM) and by a new nondestructive method based on acoustic microscopy and image processing (AM). The results were compared in order to validate the applicability of the latter method. For a direct comparison of the results from both measurements, two specimens were prepared from a cylindrical graphite sample (1 in. diameter and 1 in. height, oxidized to 10% weight loss at 973 K in air for 5 h). The specimens were used for characterization by BM and AM methods, respectively. The results show that, even with a large standard deviation of the AM, the density changing trend from both methods appeared the same. The present observation may be attributed to the fact that AM images reflect characteristic density changes of the graphite sample through the acoustic impedance changes. This study demonstrates the possibility of using AM as a nondestructive technique for the evaluation of density changes in graphite when a database is prepared through a systematic series of experiments. [DOI: 10.1115/1.3098415]

1 Introduction

Currently, a graphite-moderated very high temperature reactor (VHTR) is being developed as one of six nuclear reactor systems within the Generation IV International Forum (GIF) [1]. Also, as part of the Generation IV program in the United States, the Next Generation Nuclear Plant (NGNP) demonstration project is underway focusing on VHTR technologies. In this reactor, the overall structural safety of the core and the core support structures are supposed to be determined by the structural integrity of graphite components.

Numerous graphite studies are being designed or performed throughout GIV member countries, and most of the studies are related with the design of the graphite component, or with understanding, evaluating, and monitoring the degradation of the graphite components during operation under high temperature and high neutron irradiation environment. The long term oxidation of the nonreplaceable graphite components and the resultant physical and mechanical property changes are among the critical research subjects that should be monitored throughout the reactor lifetime.

A range of evaluation methods and techniques have been developed, or are being developed, for the characterization of the oxidation damage in graphite for VHTR; they have variable merit levels and limits [2–4]. An ASTM graphite oxidation test method is being developed for the characterization of the air oxidation of graphite [2]. The micro-indentation method and the ultrasonic wave method are being developed for the evaluation of stress conditions and the stress and inner porous conditions of the graphite component [3]. A method based on X-ray tomography has also been examined for the evaluation of thermal oxidation of the pile grades A (PGA) graphite through local density measurements [4]. Of these methods, the methods using micro-indentation and X-ray tomography are nondestructive.

Graphite has complicated acoustic properties due to its heterogeneous structure, and because of that, the attempts to characterize this material by conventional nondestructive ultrasound techniques were very scarce [5]. Thus, if a viable nondestructive method applicable for graphite is available, it is believed that the method could be developed into a characterization technique of great value for the overall improvement of the safety of the graphite moderator reactor.

On the other hand, scanning acoustic microscopy (SAM) is a viable technique for the nondestructive evaluation of various materials including graphite [6]. The technique is based on the principle of propagation and reflection of acoustic waves at interfaces where a change in acoustic impedance (AI=density $\times$ velocity) occurs. As a result, it is expected that the intensity images from SAM could be processed for density information of the materials.

In the present study, based on the previous discussion, the oxidation-induced density changes in nuclear graphite for VHTR were determined by a conventional destructive bulk density measurement method and by a new nondestructive method based on acoustic microscopy and image processing. The results from the two methods were compared in order to validate the applicability of the latter method.

2 Experiment

2.1 Materials, Oxidation, Specimen, and Step Machining Bulk Density Measurement. The graphite specimen used for the present study was prepared by machining a specimen with standard size and shape recommended by the draft ASTM method for graphite oxidation test (cylinder, 25.4 mm diameter and 25.4 mm in height, about 22 g weight). The sample was machined from an extruded, pitch coke NBG-10 nuclear graphite block manufac-

Manuscript received November 5, 2008; final manuscript received November 18, 2008; published online June 10, 2009. Review conducted by Dilip R. Ballal. Paper presented at the Fourth International Topical Meeting on High Temperature Reactor Technology (HTR2008), Washington, DC, September 28–October 1, 2008.

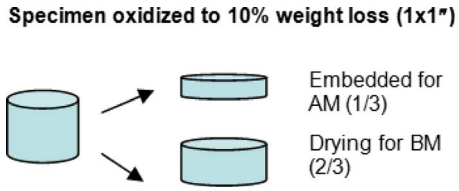

Fig. 1 Schematics of specimen preparation for AM and BM

tured at SGL. The specimen was oxidized at 973 K in air for 5 h (10% burn-off) using a three-zone vertical tube furnace (90 cm long) and an analytical balance (resolution: 0.001 g) with weigh-below port feature. The details of the oxidation procedure are reported elsewhere [2].

After oxidation, the specimen was cut into two portions (H =6 mm and 16 mm) (Fig. 1). The smaller portion (H=6 mm) was embedded by using an epoxy and was polished for density measurement by AM with image processing method; the larger portion (H=16 mm) was dried at 383 K for 2 h for a step machining BM. In BM, by referring to ASTM C 559 [7], the density profile was measured by machining off a thin layer (0.5–1 mm) from the outer surface of the sample (H=16 mm) and by accurately weighing (10^{-3} g) and measuring (10^{-3} mm) the residual core dimension after each machining step. The density of the layer removed was calculated by comparing with the previous measurements as follows. The density of the removed ith layer (d_i) is

$$d_i = \delta_{m_i}/\delta_{v_i} \tag{1}$$

where δ_{mi} is m_{i-1}-m_i, and δ_{vi} is v_{i-1}-v_i.

This operation was repeated until the density of the removed layer d_i reaches the density of the unoxidized sample (~1.81 g/cm^3).

2.2 Scanning Acoustic Microscopy. SAM was performed by using the scanning acoustic microscope available at the High Temperature Materials Laboratory (HTML) at Oak Ridge National Laboratory (ORNL) (Oak Ridge, TN) [8].

Figure 2 shows the schematic of SAM (model: KSI 2000) used in the present study. The KSI SAM 2000 has working frequencies

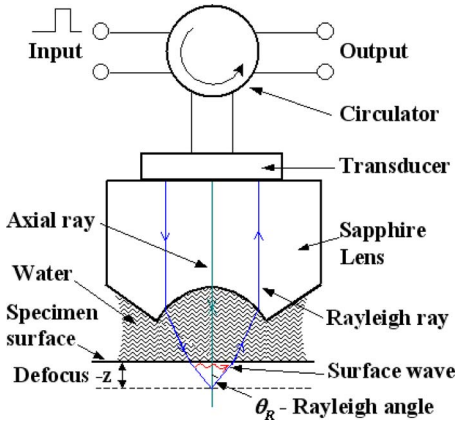

Fig. 2 Schematic of scanning acoustic microscopy. Acoustic waves generated by the transducer pass through the sapphire rod. The curvature at the end of the rod focuses the plane waves to a point on or below the sample surface. Blue ray is incident at Rayleigh angle (θ_R) on the sample. These rays generate Rayleigh waves, which travel along the blue line to the transducer. The axial ray (green) is a normally reflected ray. These two rays together contribute to the impedance information. The AM microstructural image is produced from the interference patterns between normally reflected longitudinal waves and the Rayleigh waves [8].

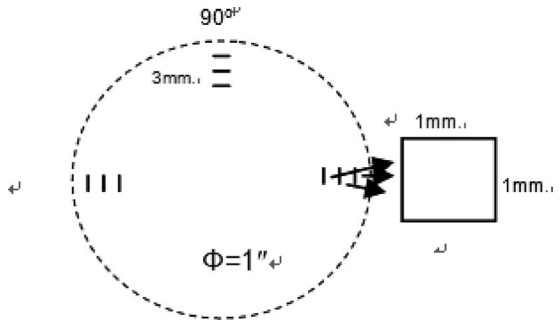

Fig. 3 Schematics of the acoustic microscopy plan on the AM specimen cross section for density estimation

from 100 MHz to 2 GHz. In the present study, based on the prior examination of the image quality due to frequencies and depths of the sample, all the acoustic images (i.e., subsurface defocused images) were obtained at 5 μm in depth at 400 MHz by C-scan. Assuming the velocity of the wave in graphite is at 4260 m/s, the maximum resolution was 2.50 μm.

Prior tests on density profile measurements for a series of oxidized graphite samples showed that most of the density change will occur near the surface within ~10 mm at maximum. Based on this observation, the specimen surface area per image was selected at 1×1 mm^2. This choice was made by considering the distances of interest for the gradient estimation and the specimen volume requirements for the density estimation. In order to acquire reasonable intensity information representing the density changes from the limited area, three images were obtained from the surface inward at three intervals in depth, i.e., 0–1 mm, 1–2 mm, and 2–3 mm, on three radial directions from the specimen surface oriented at 0 deg, 90 deg, and 180 deg angles. Figure 3 shows schematics of the acoustic microscopy plan for density estimation via acoustic intensity images. Before acoustic microscopy, the specimen surface was thoroughly examined by optical microscope to avoid possible unusually larger pores.

2.3 Image Processing. Image processing on the AM images was conducted by using a commercial image processing software IMAGE PRO-PLUS, version 5.0 for Windows [9]. In this study, all the obtained image intensities were converted to gray scale 8 image class. The image had 512 pixels in the X and Y directions with 256 gray level from 0 (=black) to 255 (=white). Intensity calibration was performed using the SAM result, where gray level 0 was set to density 0, and the gray level 255 was set to the density level obtained from the unoxidized center portion of the sample used in

Table 1 Results of density measurements by BM for a NBG-10 specimen oxidized to 10% weight loss at 973 K in air for 5 h (g cm^{-3})

Decrease in radius (mm)	Depth from surface (mm)	Density (g cm^{-3})
12.715	0	
12.515	0.10	1.54
12.220	0.35	1.32
11.970	0.62	1.32
11.735	0.86	1.52
11.505	1.01	1.58
11.005	1.46	1.52
10.505	1.96	1.63
10.005	2.46	1.65
9.005	3.21	1.74
8.005	4.21	1.75
6.005	5.71	1.79
5.005	7.21	1.79

Table 2 Results of density measurements by AM for a NBG-10 specimen oxidized to 10% weight loss at 973 K in air for 5 h (g cm^{-3})

Distance from surface (mm)	AM image obtained positions around the specimen cross section			
	0 deg	90 deg	180 deg	Average
0–1	1.35 ± 0.78	1.24 ± 0.48	1.49 ± 0.80	1.36 ± 0.69
1–2	1.66 ± 0.75	1.77 ± 0.11	1.11 ± 0.10	1.51 ± 0.32
2–3	1.68 ± 0.59	1.79 ± 0.47	1.72 ± 0.67	1.73 ± 0.58
center		1.79[a]		

[a]The density value obtained by BM for the present specimen.

the present study (i.e., 1.79 g cm^{-3}, Table 2). In order to obtain a reliable, reproducible, and reasonable density information as possible from SAM images, the images were processed for three to four times by a combination of routes including histogram analysis and line profile analysis, with some adjustments on the selected area. The objective was to increase the processing area if possible.

3 Results and Discussion

Density values obtained by BM and AM are shown in Tables 1 and 2, respectively, and compared in Fig. 4. Examples of acoustic microscope images used for image processing are shown in Fig. 5. In Fig. 4, the intensity values, i.e., densities, from AM were expressed as a function of distance from the surface to the center of the images: 0.5 mm, 1.5 mm, and 2.5 mm.

First, Fig. 4 shows that, while the data are limited for the AM method, the density changing behavior obtained by two methods are nearly the same. It appears that there are no large differences between the BM and the AM for density determination. These observations may be attributed to the characteristics of AM intensity images, which are determined by density-dependent acoustic impedance changes [10]. Present observation implies that even no direct comparisons are possible due to the lack of data obtained by other methods or techniques of nondestructive graphite density measurements, there is a clear possibility of using AM as a nondestructive technique for the evaluation of density changes in graphite, provided a database is prepared through a systematic series of experiments.

On the other hand, Table 1 and Fig. 4 show that, in case of NBG-10 with 10% weight loss by oxidation in air at 973 K, all the

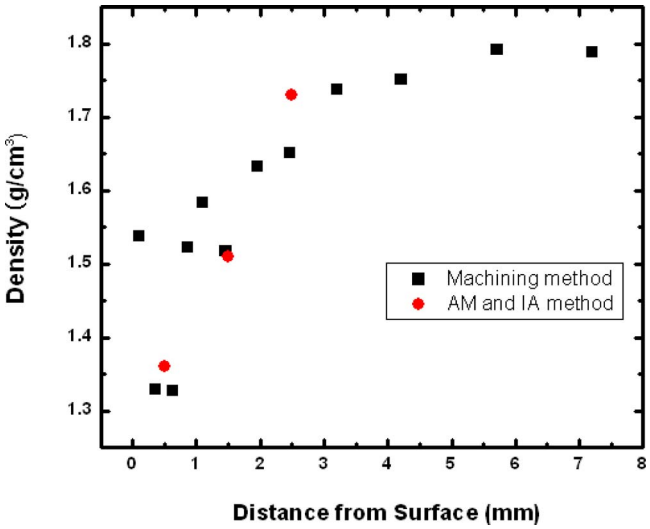

Fig. 4 Density gradient determined by BM and AM machining methods in the 10% burn-off NBG-10 nuclear graphite in air at 973 K

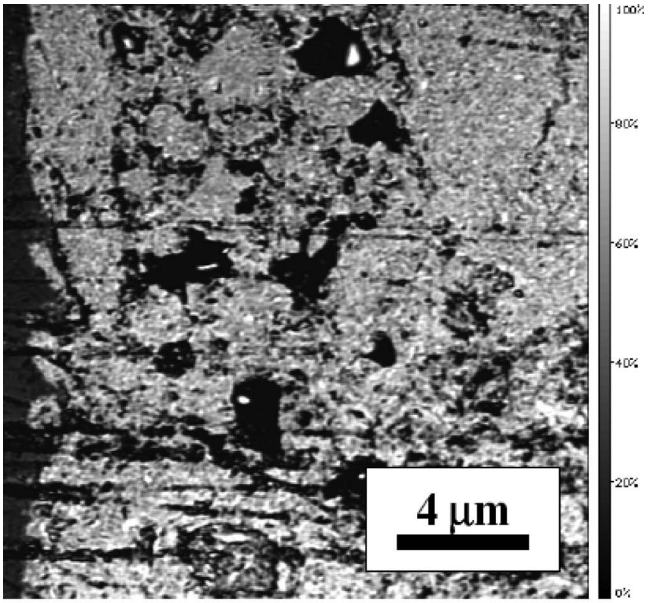

(a)

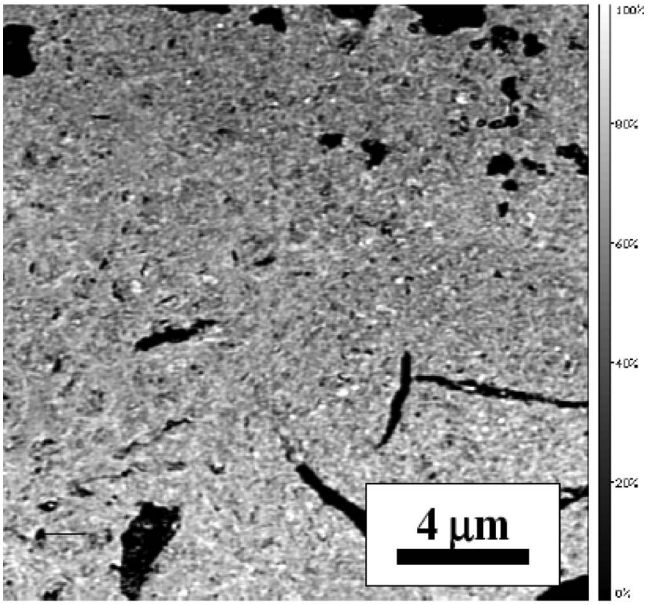

(b)

Fig. 5 (*a*) Acoustic microscope images obtained at 180 deg surface (W0) and (*b*) at the center of specimen in Fig. 3. Differences in the intensity are observed. It is seen that (*b*) of the center is brighter (higher intensity) than (*a*) of the surface.

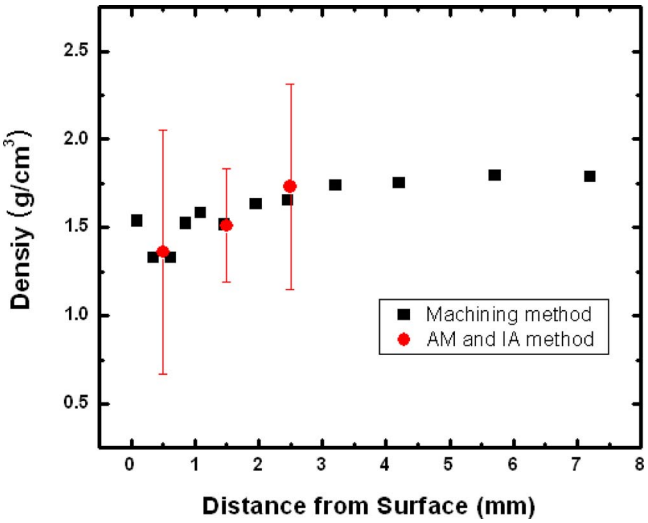

Fig. 6 Reproduced Fig. 1 with a large standard deviation for AM data

oxidation damages occur within 6 mm from the specimen surface. When compared the observation with those of grade R4-650 graphite at 973 K [11], where all the oxidation damages occur within 2.5 mm from surface even at a higher weight loss of 15%, a higher oxidation damage depth may be noted for NBG-10.

Finally, a discussion may be needed regarding the standard deviation of the measurement, especially of the AM with image processing method. Figure 6 is reproduced after Fig. 4 and shows the specified standard deviations of the AM measurements. The observed large standard deviations in the AM method, i.e., 20–50%, may be attributed to the characteristics of the AM method and to the higher heterogeneity of the graphite microstructure. The AM method includes a large degree of freedom during the density determination process. For comparison, the typical standard deviation for the bulk density measurements on 80 NBG-10 specimens is 0.93% [12]. Present observation strongly suggests that a thorough consideration should be given to the reduction in deviation and standardization of procedures in order to develop the AM method into a nondestructive technique for the evaluation of density changes in graphite.

4 Conclusion

Even with a large standard deviation, similarities in the trends in oxidation-induced density changes obtained by the bulk density measurement and the acoustic microscopy with image processing show the possibility that the latter method could be developed into a characterization technique of great value for the overall improvement of the safety of graphite moderator reactors when a database is prepared through a systematic series of experiments. The observed possibility for the use of the latter method for graphite density determination may be attributed to the fact that acoustic images reflect characteristic density changes of the graphite sample through the acoustic impedance changes.

Acknowledgment

The authors wish to acknowledge all the help received from ORNL colleagues throughout the study: Ashli Clark and Denny Wilson for the bulk density measurements, Jun Qu for the acoustic microscopy and for Fig. 2, Jim Kigan for metallography, T. Paul Karnowski for the image analysis demonstration, and Ramsey Sharon for all nontechnical assistance. This work was sponsored in part by the ORNL graphite research and development program for NGNP through the DOE Office of Nuclear Energy.

Nomenclature

d_i = density of the removed ith layer of mass δ_{m_i} and volume δ_{v_i} (g cm^{-3})
m = mass (g)
v = volume (cm^{-3})

Greek

δ_{m_i} = finite mass removed between $i-1$ and ith machining pass (g)
δ_{v_i} = finite volume removed between $i-1$ and ith machining pass (cm^3)

Subscripts

m_i = mass removed per ith pass (g)
v_i = volume removed per ith pass (cm^{-3})

References

[1] http://www.gen-4.org/PDFs/GIF_introduction.pdf.
[2] Contescu, C. I., Baker, F. S., and Burchell, T. D., 2006, "Development of an ASTM Graphite Oxidation Test Method," Extended Abstracts of CARBON '06 International Carbon Conference, Aberdeen, Scotland, p. 193.
[3] Shibata, T., Hanawa, S., Sumita, J., Tada, T., Sawa, K., and Iyoku, T., 2005, "Non-Destructive Evaluation on Mechanical Properties of Nuclear Graphite With Porous Structure," *Proceedings of GLOBAL 2005*, Tsukuba, Japan, Oct. 9–13, Paper No. 360.
[4] Babout, L., Mummery, P. M., Marrow, T. J., Tzelpi, A., and Withers, P. J., 2005, "The Effect of Thermal Oxidation on Polycrystalline Graphite Studied by X-Ray Tomography," Carbon, **43**, pp. 765–774.
[5] El Guerjouma, R., Mouchtachi, A., Jayet, Y., and Baboux, J. C., 1992, "Non Destructive Evaluation of Graphite by Ultrasonic Velocity Measurement Using Cross-Correlation and Hilbert Transform Methods," *IEEE Proceedings of the 1992 Ultrasonics Symposium*, pp. 829–832.
[6] Briggs, A., 1985, *An Introduction to Scanning Acoustic Microscopy*, Oxford University Press, Oxford, UK.
[7] ASTM, 2000, "Standard Test Method for Bulk Density by Physical Measurements of Manufactured Carbon and Graphite Articles," *Annual Book of ASTM Standards*, DO2.FO, Paper No. ASTM C 559-90.
[8] Qu, J., and Blau, P. J., 2006, "Scanning Acoustic Microscopy for Characterization of Coatings and Near-Surface Features of Ceramics," The 30th International Conference & Exposition on Advanced Ceramics & Composites, Cocoa Beach, FL.
[9] IMAGE-PRO PLUS, 2006, Version 5.0 for Windows, Media Cybernetics, Inc.
[10] Prasad, M., 2001, "Mapping Impedance Microstructure in Rocks With Acoustic Microscopy," The Leading Edge, **20**, pp. 172–179.
[11] Contescu, C. I., Azad, S., Miller, D., Lance, M. J., Baker, F. S., and Burchell, T. D., 2008, unpublished.
[12] Contescu, C. I., 2008, private communication.

Results of Tests to Demonstrate a 6-in.-Diameter Coater for Production of TRISO-Coated Particles for Advanced Gas Reactor Experiments

Charles M. Barnes
e-mail: charles.barnes@inl.gov

Douglas W. Marshall
e-mail: douglas.marshall@inl.gov

Idaho National Laboratory,
P.O. Box 1625,
Idaho Falls, ID 83415-3855

Joe T. Keeley
B&W Nuclear Operations Group,
P.O. Box 785,
Lynchburg, VA 24504
e-mail: jtkeely@babcock.com

John D. Hunn
Oak Ridge National Laboratory,
P.O. Box 2008,
Oak Ridge, TN 37831-6093
e-mail: hunnjd@ornl.gov

The next generation nuclear plant (NGNP)/advanced gas reactor (AGR) fuel development and qualification program includes a series of irradiation experiments in Idaho National Laboratory's advanced test reactor. Tristructural isotropic (TRISO)-coated particles for the first AGR experiment, AGR-1, were produced at Oak Ridge National Laboratory (ORNL) in a 2-in.(5-cm)-diameter coater. A requirement of the NGNP/AGR program is to produce coated particles for later experiments in coaters more representative of industrial scale. Toward this end, tests have been performed by Babcock and Wilcox (Lynchburg, VA) in a 6-in.(15-cm)-diameter coater. These tests have led to successful fabrication of particles for the second AGR experiment, AGR-2. While a thorough study of how coating parameters affect particle properties was not the goal of these tests, the test data obtained provide insight into process parameter/coated particle property relationships. Most relationships for the 6-in.-diameter coater followed trends found with the ORNL 2-in. coater, in spite of differences in coater design and bed hydrodynamics. For example, the key coating parameters affecting pyrocarbon anisotropy were coater temperature, coating gas fraction, total gas flow rate, and kernel charge size. Anisotropy of the outer pyrolytic carbon layer also strongly correlates with coater differential pressure. In an effort to reduce the total particle fabrication run time, silicon carbide (SiC) was deposited with methyltrichlorosilane (MTS) concentrations up to 3 mol %. Using only hydrogen as the fluidizing gas, the high concentration MTS tests resulted in particles with lower than desired SiC densities. However, when hydrogen was partially replaced with argon, high SiC densities were achieved with the high MTS gas fraction.
[DOI: 10.1115/1.3098424]

Keywords: TRISO-coatings, nuclear fuel, coater, pyrocarbon, silicon carbide, particle properties

1 Introduction

Production of tristructural isotropic (TRISO) particles using an industrial-scale coater must be demonstrated in order to develop and qualify fuel for the NGNP reactor [1]. High quality TRISO-coated particles for the AGR-1 irradiation experiment were produced by ORNL in a 2-in.(5-cm)-diameter coater. For AGR-2, an existing 6-in.(15-cm)-diameter coater was chosen to demonstrate industrial-scale coated particle production [2]. A separate study evaluated coater crucible and gas distributor designs and recommended initial designs to test [3].

Following modifications to the coating process at the B&W (Lynchburg, VA) facilities [4], 21 partial or full coating tests were performed using 400 μm yttria stabilized zirconia (YSZ) surrogate kernels and then 16 tests using 520 μm YSZ kernels [5]. The larger surrogate kernel was used so that after applying a buffer layer of about 50 μm, hydrodynamic similarity to uranium oxycarbide (UCO) kernels would be achieved for the final three coating layers. In the final phase of testing, natural uranium UCO kernels were coated so that SiC defects in resulting coated particle batches could be determined using the burn-leach method. Twenty-one TRISO-coating runs were made with natural uranium UCO kernels prior to coating low-enriched uranium kernels to obtain particles for the AGR-2 irradiation experiment.

The coater tests had three purposes. The first purpose was to demonstrate a coater design and determine coating conditions that produce particles meeting all AGR-2 fuel specifications. The second purpose was to provide data for selection of variant coating conditions for AGR-2 fuel. Fuel for the AGR-1 experiment includes particles made with the inner pyrolytic carbon (IPyC) layer applied at two temperatures and two coating gas fractions, and the SiC layer applied with and without argon dilution. Plans for the AGR-2 test also include fuel with particles having SiC layers produced with methyltrichlorosilane (MTS) in hydrogen only and, in a separate capsule, fuel with particles having SiC deposited with MTS in an argon-hydrogen mixture. Substituting argon for a portion of the hydrogen during silicon carbide coating has been reported in coating literature to offer advantages of less severe coating conditions without compromising SiC layer properties [6]. The third purpose of the coater tests was to obtain and evaluate pressure fluctuation data as a real-time indicator of coater fluid dynamics and to determine if pressure data could be correlated with particle properties.

Two other papers presented at the HTR2008 conference focused on B&W coater test results that achieved these three pur-

Manuscript received November 14, 2008; final manuscript received November 25, 2008; published online June 10, 2009. Review conducted by Dilip R. Ballal. Paper presented at the Fourth International Topical Meeting on High Temperature Reactor Technology (HTR2008), Washington, DC, September 28–October 1, 2008.

poses and included descriptions of the coater [7,8]. This paper reviews all of the test data and compares coating parameter trends with those from the AGR-1 coater.

2 Experimental

The coater tube used to produce AGR-1 particles was 2 in. in diameter and had a conical gas distributor. The gas inlet was water cooled. Further details of the AGR-1 coater are given in Ref. [9].

The B&W coater has a 6-in.-diameter tube and a multiholed gas distributor. A liquid cooled inlet was used in some early tests but showed no significant benefits and so was not used in later tests. Additional details of the B&W coater are given in Ref. [7]. Total gas flow rates for the B&W coater were approximately 19–20 times the flow rates of the 2-in. coater for the buffer and IPyC layers and 11–13 times the flow rates of the smaller coater for the SiC and outer pyrolytic carbon (OPyC) layers.

For both coaters, coatings were applied without interruption, that is, without stopping at any intermediate point to cool, unload, and sample the partially-coated particles to obtain quality control (QC) measurements. The B&W coater has a hot sampler that can be used to take two 2 cm^3 samples per run. Typically two samples of either buffer-coated or IPyC-coated particles were taken during a coating run.

Layer thicknesses and particle aspect ratios were measured using photographs of ceramographic mounts of coated particles and image analysis software developed by ORNL [10].

Two methods were used to determine densities of the buffer layer. In both methods mercury porosimetry was used to determine the volume or density of a sample of buffer-coated particles. In early tests B&W calculated the buffer density using measurements of buffer particle density, kernel diameter, buffer thickness, and kernel density. For ORNL-produced particles and later buffer density measurements at B&W, the average weight of buffer-coated particles was determined using multiple samples. Using this average weight and the mass of the porosimeter sample, an average number of particles in the buffer-coated sample was calculated. From the sample volume measured by the porosimeter and the number of particles in the sample, the volume per particle was calculated. The same measurements were made on uncoated kernels. The mass per particle and volume per particle of the buffer coating were determined by subtraction, and the buffer density then calculated from these differences.

Pyrocarbon and SiC densities were determined using sink-float density columns. Pyrocarbon anisotropies were measured using an ellipsometry method developed at ORNL [11]. Pyrocarbon surface connected porosities were determined by mercury porosimetry over a pressure range of 250–10,000 psi. The burn-leach method was used to determine SiC defects. SiC inclusions and the missing OPyC layer defect fraction were determined by visual examination of ceramographic mounts and loose particles, respectively.

3 Buffer Layer

Specifications for the buffer layer of AGR-2 particles include a density of 1.05 ± 0.10 g/cm^3 and a thickness of 100 ± 15 μm. For a given coater charge and coating gas, the primary coating parameter that determines the buffer layer density is the partial pressure of coating gas [6,12,13]. The buffer layer was applied to AGR-1 fuel particles using an acetylene to total gas (acetylene plus argon) ratio of 0.6, a coating gas flow rate of 8.5 slpm (standard liters per minute), and a temperature of 1450 °C. These conditions gave an average coating rate of 21 $\mu m/min$ and a buffer density of 1.1 g/cm^3. The laboratory AGR-1 coater had the capability to control the temperature with a cooling jacket during the exothermic reaction of buffer coating.

Similar conditions in the B&W coater gave similar densities. Using the same coating gas fraction (0.6) and a total gas flow rate of typically 162 slpm (corresponding to about the same average coating rate [22–24 $\mu m/min$]), particles with buffer densities of 0.94–1.1 g/cm^3 were obtained. Typically, the bed temperature for the B&W coater increased by about 130 °C during buffer coating, from a temperature of 1370 °C at the start of buffer coating to a temperature near 1500 °C at the end of the coating. Temperature in the B&W coater is controlled by a thermocouple located near the outer surface of the coating tube. The above typical temperature rise during buffer coating corresponds to a control temperature of 1470 °C.

Buffer-coated particle samples were taken for density analysis from 22 B&W coating runs. For these runs the coating gas fraction varied from 0.54 to 0.60, the total gas flow rate from 102 slpm to 186 slpm, the average coating rate from 12 $\mu m/min$ to 25 $\mu m/min$, and the control temperature from 1400 °C to 1520 °C. For three runs in which the buffer layer was applied with low coating rates and low temperatures, the buffer density was found to be 0.88–0.90 g/cm^3. However, at all other conditions, buffer densities were in the range of 0.94–1.16 g/cm^3.

4 Pyrolytic Carbon Layers

AGR fuel specifications for pyrocarbon layers include layer densities (1.90 ± 0.05 g/cm^3), thicknesses (40 ± 4 μm), and anisotropies (mean equivalent $BAF_o \leq 1.045$ for IPyC and ≤ 1.035 for OPyC). The mean equivalent BAF_o, calculated as $1+3$ times the diattenuation, is used in order to compare results to historical German particle anisotropy values. Although not a specification, the surface connected porosity of the pyrocarbon layers is also an important property and was measured for samples from many of the coating tests.

AGR-1 fuel includes particles with IPyC layers deposited at three different coating conditions:

Fuel	Coating temperature	Coating gas fraction
Baseline	1265 °C	0.3
Variant 1	1290 °C	0.3
Variant 2	1265 °C	0.45

Due to the IPyC layer being applied at a higher temperature, variant 1 particles have a lower IPyC density and a lower anisotropy than baseline particles. Increasing the coating gas fraction, as was done for variant 2 particles, is an alternative means of increasing the coating rate and generally results in a lower anisotropy [14]. However, for the AGR-1 particles, the anisotropies of baseline particles and variant 2 particles were nearly equivalent (0.0074 diattenuation for baseline particles compared with 0.0075 for variant 2 particles).

Prior to fabrication of AGR-1 particles, a study was performed in which IPyC coating temperatures and gas fractions were systematically varied [15]. Consistent with previous fuel coating literature in Refs. [6,12,13], pyrocarbon density was found to be primarily dependent on bed temperature. A comparison of the trends of pyrocarbon density versus temperature for the 2-in.- and 6-in.-diameter coaters is shown in Fig. 1.

Interestingly, for the IPyC layer, the trend lines for the two coaters intersect very near to a density of 1.9 g/cm^3, which is the target density for AGR fuel. The trend line for the IPyC density of particles produced in the 6-in.-diameter coater has a lower slope than the IPyC density trend line for the 2-in. coater; hence acceptable IPyC densities can be obtained with the larger coater over a wider temperature range. The same is true for the OPyC layer. These trends likely reflect differences in temperature profiles between the two coaters.

Figure 1 also shows that to achieve the same OPyC density as IPyC density, a higher temperature is required, at least up to a temperature of about 1325 °C. The scatter in the data shown in Fig. 1, such as the range of OPyC densities for the 2-in.-diameter coater at 1300 °C, illustrates the fact that coater temperature measurements have uncertainties. Internal thermocouples, external thermocouples, and pyrometers all have limitations.

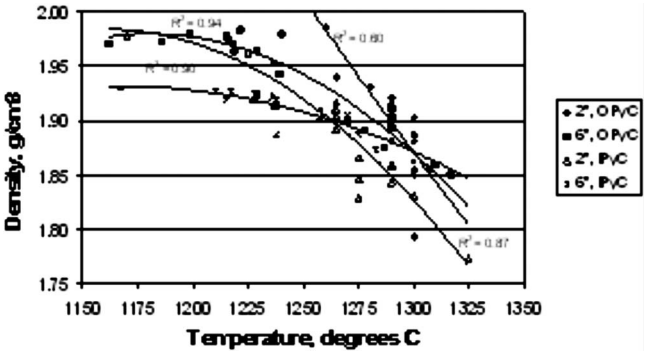

Fig. 1 Comparison of pyrocarbon density versus temperature for 2-in.- and 6-in.-diameter coaters

Figure 2 shows data only for the B&W coater. Densities plotted against bed temperature are the same as shown in Fig. 1. The other two data sets shown in Fig. 2 are densities plotted versus coater control temperatures. Figure 2 shows that to have high confidence in meeting the density specification, a control temperature in the range of 1175–1340°C is needed for the IPyC layer, while the narrower range of 1335–1365°C is needed for the OPyC layer.

Past studies have shown that the anisotropy of pyrocarbon layers decreases with increasing coating temperature and increasing coating rate [12,14,16]. Figure 3 shows trends of equivalent anisotropy versus temperature, coating gas fraction, and average coating rate[1] for the 2-in.-diameter coater used to produce AGR-1 particles. The AGR-1 coating data confirm the trend of decreasing anisotropy with increasing coating temperature, but indicate that for any temperature, there is an optimum coater rate that gives a minimum anisotropy. Furthermore, there is an optimum coating gas fraction that appears to be nearly independent of temperature. For the AGR-1 coater, this optimum coating gas fraction is about 0.35.

Figure 4 shows equivalent anisotropy plotted against temperature. With two exceptions, all data plotted in Fig. 4 are for particles produced with a coating gas fraction in the range of 0.28–0.32.

At all temperatures, the IPyC anisotropy is greater for particles produced in the 6-in. coater than those produced in the 2-in. coater. Increasing the coating gas fraction (to 0.40) or total gas flow rate (by 14%) during IPyC coating increased the layer anisotropy for the large coater. However, these alternative conditions

[1]Coating rate varies with time during any coating. Coating rates plotted in Fig. 3 and later figures have not been adjusted for small variations in layer thicknesses observed in the difference tests.

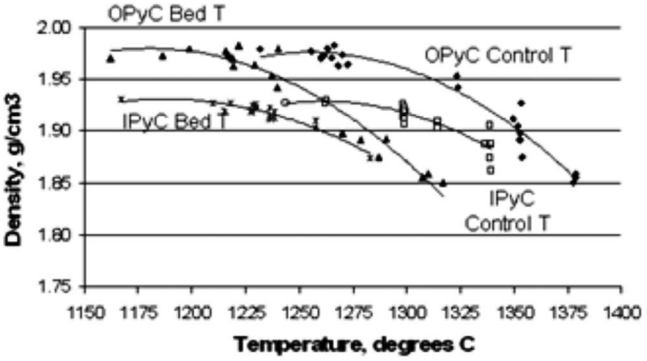

Fig. 2 Pyrocarbon densities versus bed and control temperatures for 6-in. coater

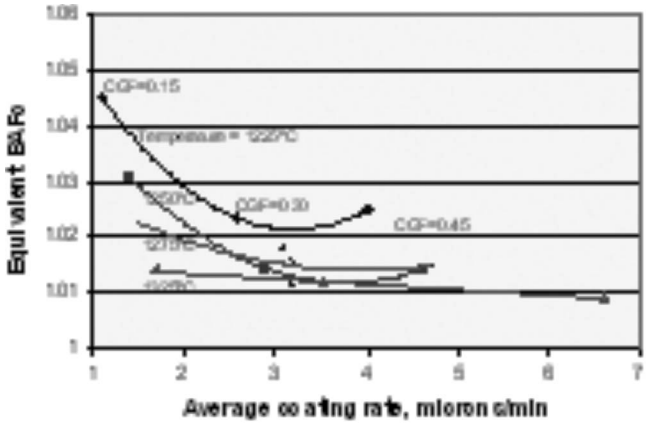

Fig. 3 Pyrocarbon anisotropy versus coating parameters

were tested in only one run each; hence caution is advised in drawing any conclusions from these limited data.

Figure 4 also compares IPyC and OPyC anisotropies for the 6-in. coater. At temperatures lower than about 1250°C, the OPyC anisotropy is clearly lower than that for the IPyC layer. At higher temperatures, there appears to be only a small difference between IPyC and OPyC anisotropy. For AGR fuel, pyrocarbon anisotropy specifications push coating temperatures to the maximum that will still result in acceptable layer densities. Since the upper temperature limit for acceptable density is higher for the OPyC layer than the IPyC layer, the OPyC layer is typically deposited at a higher temperature than the IPyC layer, and anisotropies are thus lower for the OPyC layer than for the IPyC layer. Hunn et al. [17] also reported that IPyC exposure to the higher temperature SiC coating results in an increase in IPyC anisotropy. Contrary to the results for the IPyC layer, an increase in the coating gas fraction for OPyC resulted in a decrease in the layer anisotropy.

While most anisotropy results for the 6-in. coater can be explained based on coating conditions, results for two runs (tests 93046 and 93055) do not fit trends for variation in anisotropy with temperature, coating gas fraction, or coating rate. In an effort to explain these results, the anisotropy data were plotted against additional coating parameters. When plotted versus coater differential pressure (Fig. 5), one of the anomalous points fell in line with much but not all of the remaining data. Plotted versus the coater inlet pressure at the end of the run (Fig. 6), both anomalous data points fit the general trend, although the correlation (r^2) is not as good. These data suggest that coater pressure parameters may affect pyrocarbon anisotropy.

A third important pyrocarbon property is the surface connected porosity. An IPyC surface connected porosity greater than about 1.3 ml/m^2 is desired to ensure a good bond between the IPyC and SiC layer. An OPyC porosity of the same magnitude is desired to minimize OPyC failure during irradiation [18]. AGR-1 coating

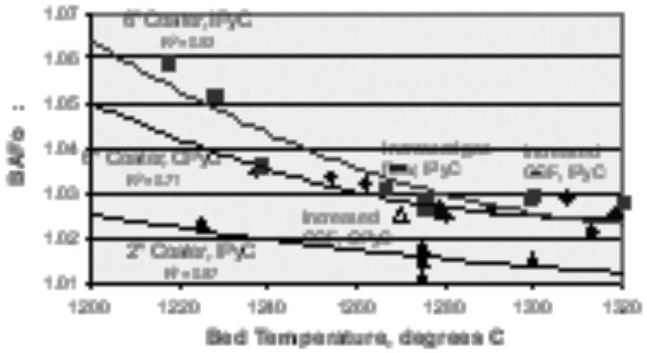

Fig. 4 Pyrocarbon anisotropy versus coating temperatures

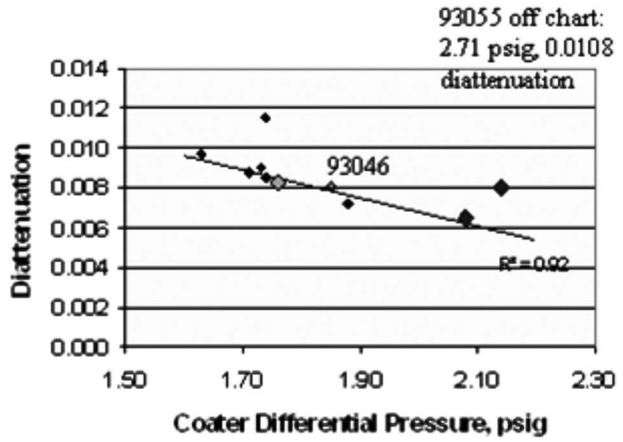

Fig. 5 OPyC diattenuation versus coater differential pressure

tests showed that the IPyC surface connected porosity increased with increasing temperature and increasing coating gas fraction [15]. Figure 7 compares IPyC surface connected porosities versus coating rate for the 2-in. and 6-in. coaters. Trend lines for the two sets of data intersect at a porosity of 1 ml/m^2. The increase in porosity with increasing coating rate is slightly greater for the 6-in. coater than for the 2-in. coater, which will result in a higher IPyC surface connected porosity for AGR-2 particles than for AGR-1 particles. The IPyC porosity of AGR-2 particles is about 2.5 ml/m^2.

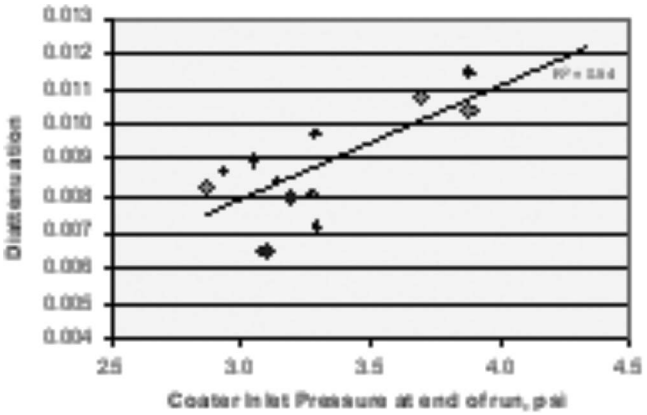

Fig. 6 OPyC diattenuation versus coater inlet pressure

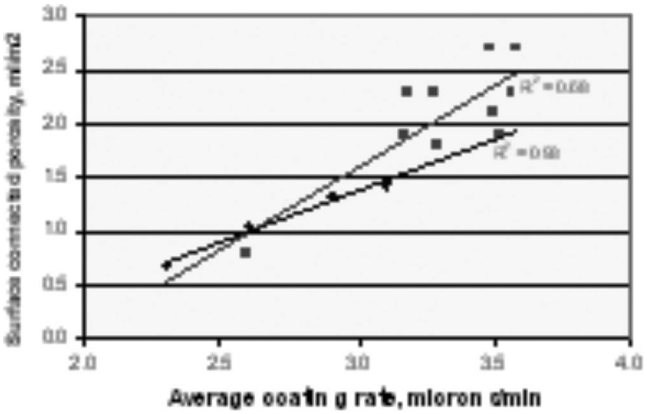

Fig. 7 Comparison of IPyC surface connected porosities for the two coaters

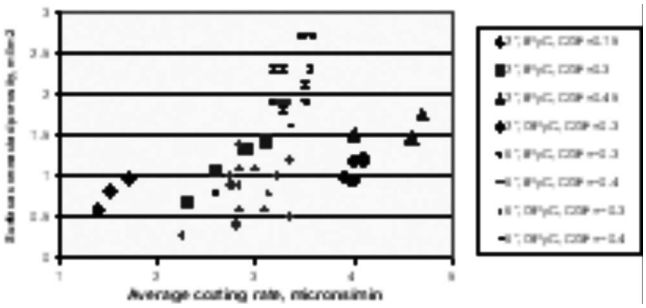

Fig. 8 Pyrocarbon surface connected porosity versus average coating rate

Figure 8 shows surface connected porosity data for both the IPyC and OPyC layers and for both coaters. The effect of coating gas fraction on IPyC porosity can be seen in comparing data for the 2-in. coater at coating gas fractions of 0.15, 0.3, and 0.45. The comparison of OPyC layer surface connected porosity for the two coaters is less straightforward than the comparison for the IPyC layer. An OPyC layer coating rate of about 4.0 $\mu m/min$ was achieved for the 2-in. coater by using a coating gas flow rate of about 170% of that used for the IPyC layer. The coating gas fraction for both pyrocarbon layers was the same (0.30), while the OPyC coating temperature was 25°C higher than that for the IPyC layer. These conditions resulted in porosities of 0.95–1.3 ml/m^3 for each pyrocarbon layer for particles produced in the 2-in. coater.

The OPyC data for particles produced in the larger coater show more scatter, in part reflecting variations in OPyC flow rates, temperatures, and coating gas fractions used in the various tests. However, for both coaters it is clear that at equivalent coating rates, OPyC surface connected porosities are significantly lower than those for the IPyC layer at equivalent coating conditions, and increasing OPyC temperature alone is not sufficient to increase the OPyC porosity to values above 1.3 ml/m^2. In three tests of the 6-in. coater, OPyC samples were taken from the coater bed after OPyC coating but prior to cooling. The hot samples of OPyC particles were analyzed to see if post-coating activities (cooling, unloading, sieving, and tabling) modify the particle surface so as to reduce the OPyC surface connected porosity. In all three cases, the porosity of the hot sample was higher than that of the bulk particle sample. These results are shown in Table 1.

5 Silicon Carbide Layer

Specifications for the silicon carbide layer include the thickness, the density, a maximum defect fraction as measured by the burn-leach method, the SiC-coated particle aspect ratio, the SiC grain size, and the "gold spot" defect fraction. The usual method for gold spot analysis, optical analysis of particles burned back to the SiC layer, was found inadequate to accurately detect these SiC anomalies for particles with small-grained microstructure. So to evaluate particles against this specification, particles were sectioned and examined for soot inclusions in the SiC layer.

Table 1 Comparison of surface connected porosities of hot and bulk OPyC samples

	Porosity (ml/m^2)	
Test	Hot sample	Bulk sample
93063	0.9	0.8
93065	0.7	0.4
93069	0.9	0.6

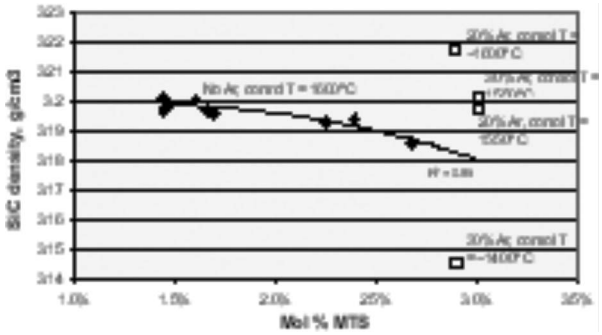

Fig. 9 SiC density versus coating parameters

Figure 9 shows SiC density results for a number of 6-in. coater tests made at different concentrations of MTS, concentrations of argon, and coating temperatures. For tests using hydrogen only as the fluidization and dilution gas, the SiC layer density decreased with increasing MTS concentration. Higher MTS concentrations have the economic advantage of reduced coating times.

High density (>3.19 g/cm^3) SiC was obtained with 3% MTS when a hydrogen-argon mixture was used to fluidize the particle bed and the control temperature was greater than 1550°C. Near theoretical density SiC was obtained using a gas mixture of 20% Ar/80%H_2 containing 3% MTS and a coater control temperature of 1600°C. At a control temperature of 1550°C, particles with SiC densities near 3.2 g/cm^3 were obtained with gas mixtures of 20–30% argon. At this temperature, the SiC density for the test with 30% argon was slightly higher than the test with 20% argon. Lowering the control temperature to 1400°C resulted in particles with SiC densities of only 3.145 g/cm^3. Low density SiC from the test at 1400°C was not analyzed for the presence of free Si or free C. Compared with the traditional method of depositing SiC with hydrogen only, partial substitution with argon both allowed for using higher MTS concentrations and reduced coating temperatures to achieve the desired SiC density.

Figures 10(*a*)–10(*d*) compare the SiC microstructure of particles from both coaters. The largest grains are seen for particles produced in the 2-in. coater at a temperature of 1500°C, a MTS concentration of 1.5%, and hydrogen only as the fluidization gas. Partial replacement of hydrogen with argon resulted in achieving the same desired SiC density at a temperature of 1425°C and a smaller grain size.

For the 6-in. coater, it was found that a slightly lower temperature (~1470°C) than used in the small coater could achieve adequate layer density and a smaller grain size for the hydrogen-only case. The SiC grain size for particles from the two coaters is similar when argon dilution is used.

Lenticular flaws in SiC coatings have been reported in particles from ORNL, General Atomics (San Diego), and Japanese coaters [9,19–21]. Typically observed as gold-colored areas on particles burned back to the SiC layer, examination of cross-sectioned particles shows that these flaws are circumferential inclusions of low density SiC or carbon. Minimizing these flaws in AGR-1 particles involved controlling gas flow rates within a very narrow range. However, while an occasional SiC inclusion has been seen in images of particles coated in the B&W 6-in. coater (Fig. 11), examination of samples of about 12,000 particles from two later runs by cross sectioning showed only 1 particle with an inclusion. It is believed that the design of the B&W coater with a relatively long tube is the primary cause for the significant reduction in SiC flaws for this coater compared with the AGR-1 coater. The longer tubes prevent particles from contact with cooler surfaces where SiC soot is deposited during coating.

SiC defects include radial cracks in the SiC layer, broken particles, missing SiC layers, or other anomalies that compromise the structural integrity of the layer. AGR particle specifications allow

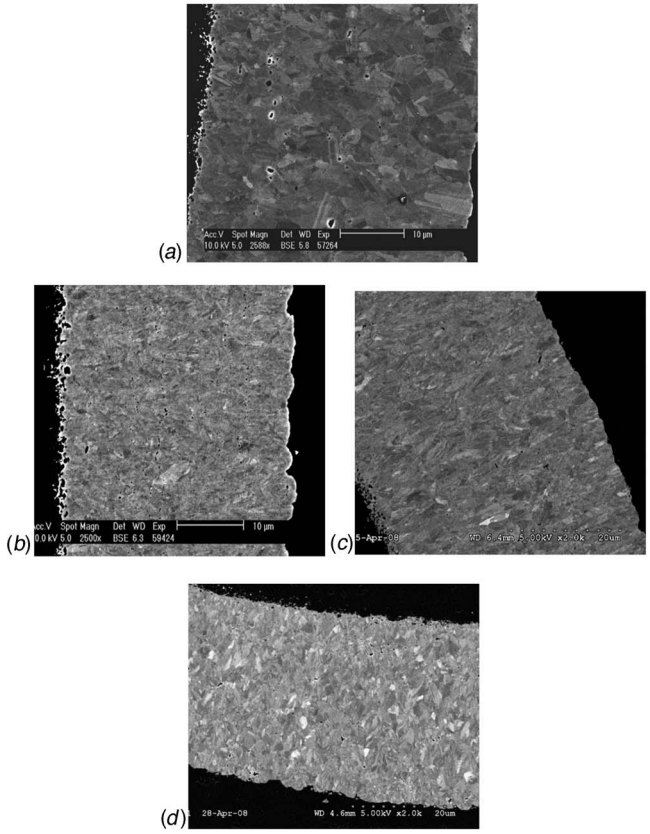

Fig. 10 (*a*) SiC microstructure of particle produced in 2-in. coater with H2 only, 1.5% MTS, and 1500°C bed temperature. (*b*) SiC microstructure of particle produced in 2-in. coater with 50% Ar, 2% MTS, and 1425°C bed temperature. (*c*) SiC microstructure of particle produced in 6-in. coater using H2 only, 1.5% MTS, and 1600°C coater control temperature (~1470°C bed temperature). (*d*) SiC microstructure of particle produced in 6-in. coater using 30% Ar, 3% MTS, and 1550°C coater control temperature (~1425°C bed temperature).

only 1 defective particle in a sample of 50,000 particles, 6 defective particles in a sample of 120,000, or 14 defects in a sample of

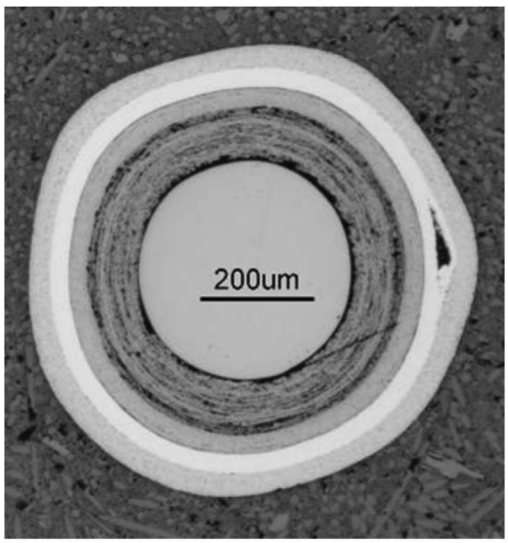

Fig. 11 Example of SiC inclusion in particle from B&W coating run 93019

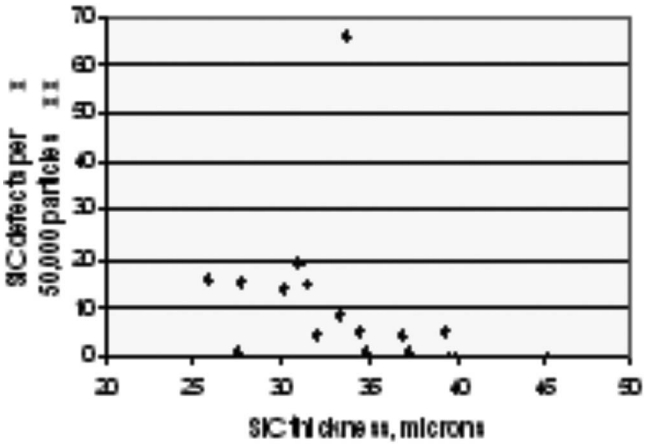

Fig. 12 Correlation of SiC defects with coating thickness

220,000. SiC defects for the AGR-1 particles were very low, with 0 or 1 defect found in samples of 120,000 particles for three of the AGR-1 fuels and 1 defect found in a sample of 50,000 particles for the fourth fuel.

The level of defects in particles from the 6-in. coater has varied widely. The specification for SiC defects has been met for particles from 12 out of 20 runs. The level of SiC defects does not correlate with any coating parameter, but, as shown in Fig. 12, most coating runs resulting in particles with higher levels of SiC defects had thinner SiC layer thicknesses. Low levels of SiC defects were achieved in the final five consecutive coating tests by ensuring that the layer thickness was at least 35 μm and also by careful particle upgrading (sieving and tabling).

A final characteristic of the SiC layer, while not a specification, relates to the bonding of the layer with the IPyC layer. As identified by Petti et al. [22] and Miller et al. [23], interlacing of these two layers is desired in order to achieve a strong bond. Localized debonding can lead to stress intensification during irradiation and possible failure. Figure 13 shows an example of this interface for a particle coated in the 6 in. furnace by B&W. The relatively high IPyC surface porosity results in SiC infiltration during coating, which gives the desired strong interface.

6 Conclusions

Demonstration tests of a 6 in. fluidized bed chemical vapor deposition (CVD) coating furnace have provided data that have been used to prepare for coating particles for AGR-2 fuel. The tests have demonstrated a coater design and coating process parameters needed to meet particle specifications. Most trends of particle property relationships with coating parameters were found to be very similar to those determined for a 2-in. laboratory coater, but a few exceptions were found. Besides determining specific coating parameters for AGR-2 baseline and variant particles, the test data have provided information as to how tightly these parameters must be controlled.

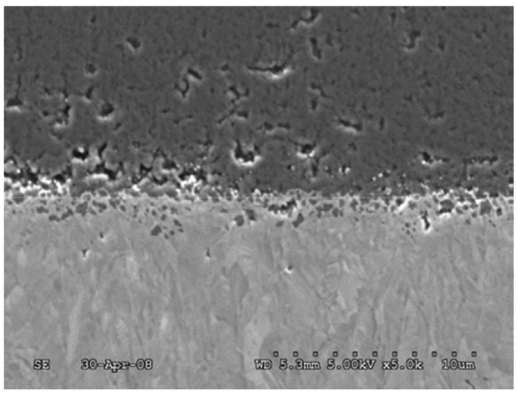

Fig. 13 Example of IPyC-Sic interface showing interlacing of the two layers

Acknowledgment

This paper has been authored by Battelle Energy Alliance, LLC with the U.S. Department of Energy under Contract No. DE-AC07-05ID14517. The authors wish to thank the operators at B&W that performed the coating test and researchers at ORNL that supported particle characterization.

References

[1] Petti, D., Hobbins, R., Kendall, J., and Saurwein, J., 2005, "Technical Program Plan for the Advanced Gas Reactor Fuel Development and Qualification Program," Report No. INL/EXT-05-00465.
[2] Barnes, C. M., and Marshall, D. W., 2006, "Advanced Gas Reactor Coater Scale Up Plan," Report No. PLN-1975.
[3] Marshall, D. W., 2006, "Six-Inch TRISO Fuel Coater Design for AGR-2," Report No. EDF-6666.
[4] Marshall, D. W., and Barnes, C. M., 2007, "AGR Fuel Development-Coater and Control System Upgrade," Report No. INL/EXT-07-12458.
[5] Barnes, C. M., and Marshall, D. W., 2007, "FY 2007 Six-Inch Diameter Coater Test Report," Report No. INL/EXT-07-13090.
[6] Ford, L. H., Hibbert, N. S., and Martin, D. G., 1972, "Recent Developments of Coatings for GCFR and HTGCR Particles and Their Performance," J. Nucl. Mater., **45**, pp. 139–149.
[7] Keeley, J. T., and Tomlin, B. L., 2008, "Development of a Continuous CVD Process for TRISO Coating of AGR Fuel," *Proceedings of the Fourth International Topical Meeting on High Temperature Reactor Technology*, Paper No. HTR2008-58008.
[8] Marshall, D. W., and Barnes, C. M., 2008, "Mining Process and Product Information From Pressure Fluctuations Within a Fuel Particle Coater," *Proceedings of the Fourth International Topical Meeting on High Temperature Reactor Technology*, Paper No. HTR2008-58073.
[9] Lowden, R. A., 2006, "Fabrication of Baseline and Variant Particle Fuel for AGR-1," ORNL Report No. CF-06/02.
[10] Kercher, A. K., Hunn, J. D., Price, J. R., Jellison, G. E., Montgomery, F. C., Morris, R. N., Giaquinto, J. M., and Denton, D. L., 2005, "Advanced Characterization Methods for TRISO Fuels," *Proceedings of the Advanced Reactors With Innovative Fuels Workshop (ARWIF-2005).*
[11] Jellison, G. E., Jr., Hunn, J. D., and Lowden, R. A., 2006, "Optical Characterization of Tristructural Isotropic Fuel Particle Cross-Sections Using Generalized Ellipsometry," J. Nucl. Mater., **352**, pp. 6–12.
[12] Pratt, B., Sease, J. D., Pechin, W. H., and Lotts, A. L., 1969, "Pyrolytic Carbon Coating in an Engineering-Scale System," Nucl. Appl., **6**, pp. 241–255.
[13] Charollais, F., Fonquernie, S., Perrais, C., Perez, M., Dugne, O., Cellier, F., Harbonnier, G., and Vitali, M.-P., 2006, "CEA and AREVA R&D on HTR Fuel Fabrication and Presentation of the CAPRI Experimental Manufacturing Line," Nucl. Eng. Des., **236**, pp. 534–542.
[14] Stinton, D. P., Thiele, B. A., Lackey, W. J., and Morgan, C. S., 1982, "Detection and Control of As-Produced Pyrocarbon Permeability in Biso-Coated HTGCR Fuel Particles," Ceram. Bull., **61**, pp. 245–250.
[15] Lowden, R. A., Hunn, J. D., Nunn, S. D., Kercher, A. K., Price, J. R., Menchhofer, P. A., and Jellison, G. E., Jr., 2005, "Effects of Deposition Conditions on the Properties of Pyrolytic Carbon Deposited in a Fluidized Bed," ORNL Report No. TM-2005/533.
[16] Lackey, W. J., Stinton, D. P., and Sease, J. D., 1977, "Improved Gas Distributor for Coating HTGCR Fuel Particles," Nucl. Technol., **35**, pp. 227–238.
[17] Hunn, J. D., Jellison, G. E., Jr., and Lowden, R. A., 2008, "Increase in Pyrolytic Carbon Optical Anisotropy and Density During Processing of Coated Particle Fuel Due to Heat Treatment," J. Nucl. Mater., **374**, pp. 445–452.
[18] Bullock, R. E., 1993, "Historical Review of Coated-Particle Fuel as Related to the Performance of TRISO-P Particles," CEGA Interoffice Correspondence No. CEGA-M-93–1274.
[19] Scott, C. B., 1971, "Carbon Inclusions in SiC Coatings of FSV Production Fuel Particles," General Atomics Memorandum No. CBS-014-FMB-71.
[20] Saurwein, J., 1992, "Characterization of Gold Spots in NPR Performance Test Fuel SiC Coatings," General Atomics Document No. 910523.
[21] Minato, K., Kikuchi, H., Fukuda, K., Suzuki, N., Tomimoto, H., Kitamura, N., and Kaneko, M., 1994, "Internal Flaws in the Silicon Carbide Coatings of Fuel Particles for High-Temperature Gas-Cooled Reactors," Nucl. Technol., **106**, pp. 342–349.
[22] Petti, D. A., Buongiorno, J., Maki, J. T., Hobbins, R. R., and Miller, G. K., 2003, "Key Differences in the Fabrication, Irradiation and High Temperature Accident Testing of US and German TRISO-Coated Particle Fuel, and Their Implications on Fuel Performance," Nucl. Eng. Des., **222**, pp. 281–297.
[23] Miller, G. K., Petti, D. A., and Maki, J. T., 2004, "Considerations of the Effects of Partial Debonding of the IPyC and Particle Asphericity on TRISO-Coated Fuel Behavior," J. Nucl. Mater., **334**, pp. 79–89.

Autonomous Control Strategies for Very High Temperature Reactor Based Systems for Hydrogen Production

Pavel V. Tsvetkov
e-mail: tsvetkov@tamu.edu

Ayodeji B. Alajo

David E. Ames II

Department of Nuclear Engineering,
Texas A&M University,
129 Zachry Engineering Center,
MS 3133 TAMU,
College Station, TX 77843-3133

This paper is focused on feasible autonomous control strategies for Generation IV very high temperature reactors (VHTRs)-based systems for hydrogen production. Various burnable poison distributions and fuel compositions are considered. In particular, utilization of transuranium nuclides (TRUs) in VHTRs is explored as the core self-stabilization approach. Both direct cycle and indirect cycle energy conversion approaches are discussed. It is assumed that small-scale VHTRs may be considered for international deployment as grid-appropriate variable-scale self-contained systems addressing emerging demands for hydrogen. A Monte Carlo-deterministic analysis methodology has been implemented for coupled design studies of VHTRs with TRUs using the ORNL SCALE 5.1 code system. The developed modeling approach provides an exact-geometry 3D representation of the VHTR core details properly capturing VHTR physics. The discussed studies are being performed within the scope of the U.S. DOE Nuclear Energy Research Initiative project on utilization of higher actinides (TRUs and partitioned minor actinides) as a fuel component for extended-life VHTR configurations.
[DOI: 10.1115/1.3098427]

1 Introduction

This paper is focused on feasible autonomous control strategies for Generation IV very high temperature reactors (VHTRs)-based systems for hydrogen production. Various burnable poison distributions and fuel compositions are considered. In particular, utilization of TRUs in VHTRs is explored as the core self-stabilization approach. The resulting configurations should also have an inherent potential for autonomous operation with minimized maintenance. It is expected that light water reactors (LWRs) will eventually be replaced by Generation IV VHTRs. At that time, sustainable nuclear systems consisting of fast reactors (FRs) and VHTRs will become possible. Both direct cycle and indirect cycle energy conversion approaches are discussed. It is assumed that small-scale VHTRs may be considered for international deployment as grid-appropriate variable-scale self-contained systems addressing emerging demands for hydrogen.

Behavior of the advanced nuclear energy systems such as Generation IV VHTRs is difficult to predict due to inherent safety features resulting in tight coupling between energy production, transport and conversion, and system behavior during normal operation and off-normal situations [14,15]. The systems should have satisfactory performance characteristics in several inherently noncommensurable areas simultaneously [2].

A Monte Carlo-deterministic analysis methodology has been implemented for coupled design studies of VHTRs with TRUs using the ORNL standardized computer analyses for licensing evaluation (SCALE) 5.1 code system [16]. The developed modeling approach provides an exact-geometry 3D representation of the VHTR core details properly capturing VHTR physics. Searches for acceptable performance domains are handled as trade-off optimization problems with multidisciplinary design criteria including output requirements, safety characteristics, system longevity, waste minimization, environmental impacts, economics, and other characteristics.

Evidently, there is no unique system configuration that equally meets all criteria at the same time. Only equally acceptable (preference nondominated) end-configurations can be found. Such configurations form a set of Pareto-optimal solutions representing a compromise between postulated design criteria. Promising multiobjective optimization (MO) strategies can be developed using stochastic search mechanisms of sufficiently robust genetic algorithms (GAs) that allow surveying the entire space of performance characteristics. Existing sensitivities and uncertainties in input parameters and performance characteristics are taken into account.

The discussed studies are being performed within the scope of the U.S. DOE Nuclear Energy Research Initiative (NERI) project on utilization of higher actinides (TRUs and partitioned minor actinides (MAs)) as a fuel component for extended-life VHTR configurations. Based on the initial evaluations of the VHTR with TRUs/MAs, the major thrust is the detailed analysis of configuration variation capabilities to achieve prolonged operation without refueling, maximize burnup, and minimize reactivity swings [5,20,22,23].

The TRU-fueled VHTR systems are developed and analyzed accounting for controllability, dynamics, and safety margins during the entire reactor lifetime. The resulting configurations should have inherent capabilities for utilization of TRUs from spent LWR fuel [5].

2 VHTR Core Model

To create advanced nuclear energy systems it is desirable to have a high fidelity modeling-based design development that relies on simulating features of the entire life cycle of the system before actual physical prototyping—from concept development to detailed design, prototyping, and safety analysis. This approach would provide consistency between neutronics and other performance aspects such as thermal hydraulics, mechanical integrity, plant heat transfer, and conversion balances. It is convenient to consider both requirements and constraints as objectives with special characteristics. The multi-objective optimization process can

Manuscript received November 29, 2008; final manuscript received December 7, 2008; published online June 11, 2009. Review conducted by Dilip R. Ballal. Paper presented at the Fourth International Topical Meeting on High Temperature Reactor Technology (HTR2008), Washington, DC, September 28–October 1, 2008.

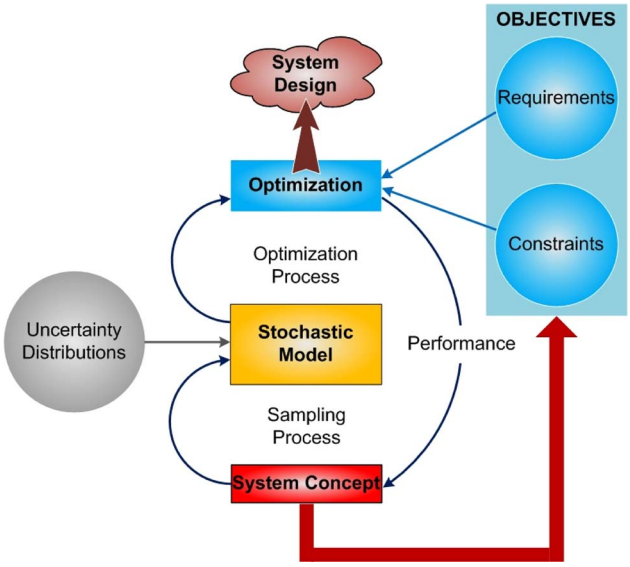

Fig. 1 Design development and optimization

be developed as shown in Fig. 1. The framework requires solving specialized multilevel nonconvex optimization problems with large numbers of variables. These problems involve objectives with certain hierarchical structure imposed by the specifics of postulated constraints [8,12,21].

The design development begins with the inception of a system concept. The system concept helps defining objectives. The representative stochastic model with assumed uncertainty distributions for model parameters initiates the optimization process. Postulated uncertainty distributions at the model parametrization stage lead to the corresponding uncertainties in system performance characteristics. Ultimately, once Pareto optimality criteria are met under the defined set of objectives, the end-system configuration can be finalized. Because solving multi-objective optimization problems is a very difficult task, in addition to Pareto-based techniques, multi-objective evolutionary algorithms can be applied. Some of the vector evaluated genetic algorithms could also facilitate the solution process. There are no universal optimization techniques, the optimization step should be an intelligent combination of several algorithms such as nondominated sorting genetic algorithm, niched-Pareto genetic algorithm, multi-objective genetic algorithm, strength Pareto evolutionary algorithm, Pareto archived evolution strategy, and nondominated sorting genetic algorithm [12].

The suggested integrated/hybrid Monte Carlo-deterministic modeling approach offers the desirable analysis capabilities for the VHTR design studies. The use of Monte Carlo codes creates a potential for explicit 3D whole-core/reactor studies of the VHTR configurations addressing the key reactor physics areas such as the double and multilevel heterogeneities, neutron streaming in the low-density regions, and neutron spectrum transitions at the interfaces [13]. The 3D whole-core exact-geometry VHTR model has been developed for use in calculations with SCALE 5.1 code system. The model takes into account tristructural isotropic (TRISO) microparticles, fuel compacts, fuel assembly blocks, control rod blocks, replaceable reflectors, and a permanent outer reflector. The project uses the actual test results and benchmark problems of the high temperature test reactor (HTTR) program (prismatic core design, reactor experiments) [1,22].

The VHTR model is a nearly explicit representation of the existing HTTR core configuration. The model was created in the SCALE code system utilizing the CSAS6/KENO-VI module. The obtained benchmark results are in agreement with the available HTTR data and confirm applicability of the chosen modeling

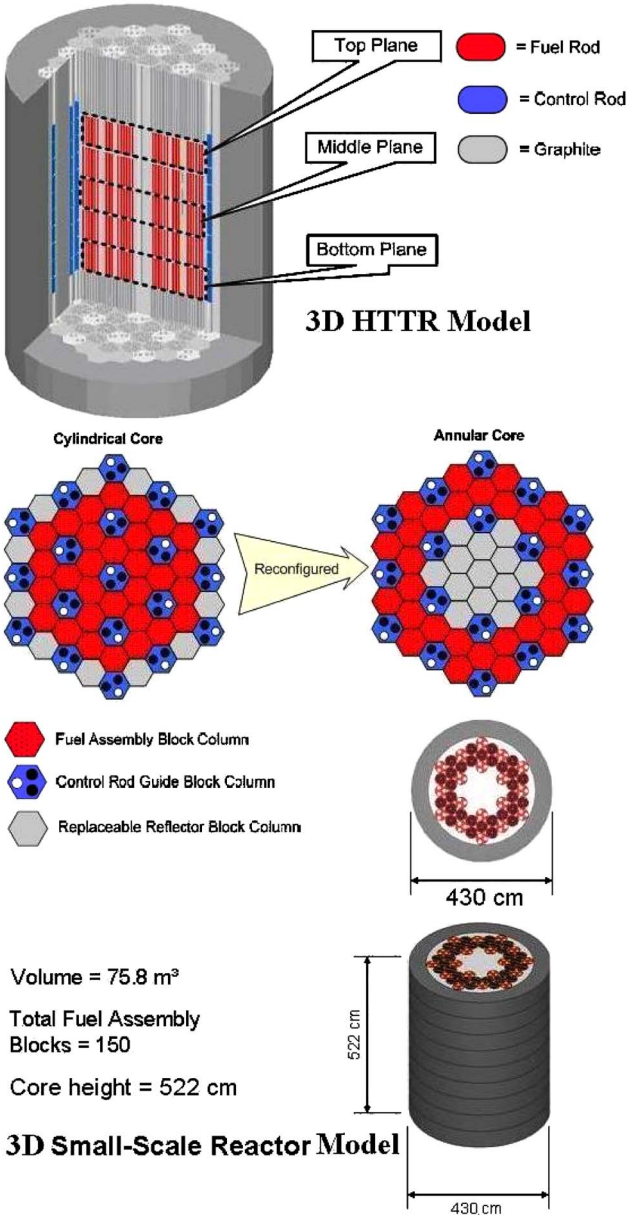

Fig. 2 Small-scale VHTR configuration (HTTR basis)

methodology. Each of the benchmark cases is within 0.25% of the experimental values and fall within experimental error [1].

As shown in Fig. 2, the basis configuration has been developed using the Generation IV VHTR core specifications and the HTTR hexagonal block geometry data [4,6]. The HTTR is currently the only operating VHTR prismatic core design, making it a focal point of VHTR related research [3,4,17].

The prismatic whole-core 3D model was adjusted from the original cylindrical core of the HTTR to that of an annular core. The annular core is one of the promising core types for the future VHTRs because of its high inherent safety characteristics following a loss of coolant accident. The decay heat removal is enhanced by the introduction of the annular core because the heat transfer path will be shortened due to the relatively thin active core region. As a result, the fuel temperature in a loss of coolant accident can be maintained at less than the fuel temperature limit of 1600°C.

The transition from the HTTR basis to the small-scale VHTR configuration included changing the fuel in the core from a mixture of uranium enrichments (12 types) to just one enrichment throughout the entire core (8 wt %). To create the annular core

Table 1 Isothermal temperature coefficients of small-scale VHTR configurations

VHTR configuration	Isothermal temperature coefficient, 10^{-5} (1/°C)
HTTR	-9.626 ± 2.409
Cylindrical core	-6.670 ± 1.415
Annular core	-7.817 ± 1.474

the model was reconfigured by replacing the fuel assembly block columns located in the inner region of the core with the replaceable reflector block columns in the outer region, and vice versa. An exact representation of the configuration adjustment is provided in Fig. 2.

3 Safety and Control of Small-Scale VHTR-H_2

The VHTR systems achieve their safety through their design approach, the materials used, and the fuel form. The key safety features of VHTRs, in addition to the radionuclide retention capability of the TRISO fuel particle, is a small operational excess reactivity, a large negative temperature coefficient, and a passive heat removal capability of the reactor design. The combination of the small excess reactivity and large negative temperature coefficient stops the nuclear fission process with only a moderate temperature increase in the core even if the control and shutdown systems fail.

In addition, the introduction of an annular core allows fuel decay heat to be conducted through the reactor structures to the vessel cavity and then to the atmosphere without outside intervention. This provides the reactor with a high degree of inherent safety, in turn, making the temperature coefficient a major component for safety analysis of VHTRs.

Table 1 shows the calculated values obtained for the isothermal temperature coefficients for the HTTR basis and the corresponding cylindrical and annular configurations of the small-scale VHTR. The isothermal temperature coefficients for each core configuration are within the standard deviation limits of one another.

Table 2 summarizes basic reactor physics characteristics obtained for the fuel loadings in the (a) cylindrical core configuration and in the (b) annular core configuration. The VHTR configurations include conventional fuels like UO_2 as well as advanced fuels with compositions containing UC, mixed oxide fuel (MOX), and/or TRUs.

The corresponding initial excess reactivity values and the isothermal temperature coefficients for each fuel loading are given in Table 3. The coefficients in all cases are negative. Achievability of small initial excess reactivity values suggests potential reduction options for control system requirements assuming that desirable configuration longevities are attainable.

Table 3 Initial excess reactivities and isothermal temperature coefficients of the small-scale VHTR cylindrical and annular core configurations

Fuel	Initial excess reactivity (%)	Isothermal temperature coefficient, 10^{-5} (1/°C)
	Cylindrical core configuration	
UO_2, 8%	9.90	-6.670 ± 1.415
UC, 8%	11.0	-7.699 ± 1.508
TRU	1.40	-7.097 ± 1.148
RGPu	20.5	-3.526 ± 0.978
	Annular core configuration	
UO_2, 8%	7.80	-7.817 ± 1.474
UC, 8%	9.00	-6.445 ± 1.627
TRU	1.50	-5.085 ± 1.228
RGPu	19.6	-3.279 ± 1.080

The VHTR power unit configurations can have sufficiently high energy conversion efficiencies of up to 57% even for simple Brayton cycles that allow for multiple simultaneous applications of produced high temperature heat assuming operating temperatures around 800°C. Consequently, accounting for H_2-production components, control options include flow/temperature (heat removal control), burnable poisons, solid control rods, core configuration, and burnable poison gas ejectors. Each of these options can be designed to function in an autonomous configuration with minimized external actions.

4 Autonomous Control Strategies

The VHTR configurations can be designed with smaller initial excess reactivity values by adjusting graphite content in the system. It is possible to optimize systems varying the carbon-to-heavy metal atom ratio through adjustments in fuel characteristics such as TRISO content per compact.

There is a relative trend for fast fluence to dominate effective multiplication factor as a factor limiting core lifetime. Because of material properties (graphite and SiC) and neutron flux spatial distributions, core lifetime is defined by fast fluence limitations and not as strongly by effective multiplication factor. Changes to ZrC and reductions in power density help increasing core lifetime values by shifting dominance to effective multiplication factor from fast fluence limitations [10]. Flux peaking reductions facilitate this trend. Figure 3 illustrates behavior of the VHTR core lifetime as a function of fast fluence.

Table 2 Basic reactor physics of the small-scale VHTR cylindrical and annular core configurations

Fuel	k_{eff}	Fission-inducing energy (eV)	System mean free path (cm)	Fission neutron yield
		Cylindrical core configuration		
UO_2, 8%	1.099 ± 0.001	0.2504 ± 0.0004	2.6897 ± 0.0006	2.43859 ± 0.00001
UC, 8%	1.110 ± 0.001	0.2639 ± 0.0004	2.6914 ± 0.0006	2.43871 ± 0.00001
TRU	1.014 ± 0.001	9.43 ± 0.05	2.7218 ± 0.0007	2.90387 ± 0.00004
RGPu	1.205 ± 0.001	9.32 ± 0.04	2.7250 ± 0.0008	2.90006 ± 0.00004
		Annular core configuration		
UO_2, 8%	1.078 ± 0.001	0.2409 ± 0.0004	2.6409 ± 0.0004	2.43861 ± 0.00001
UC, 8%	1.090 ± 0.002	0.2530 ± 0.0004	2.6424 ± 0.0005	2.43870 ± 0.00001
TRU	1.015 ± 0.001	7.29 ± 0.04	2.6669 ± 0.0006	2.90356 ± 0.00004
RGPu	1.196 ± 0.001	7.32 ± 0.03	2.6668 ± 0.0006	2.89993 ± 0.00004

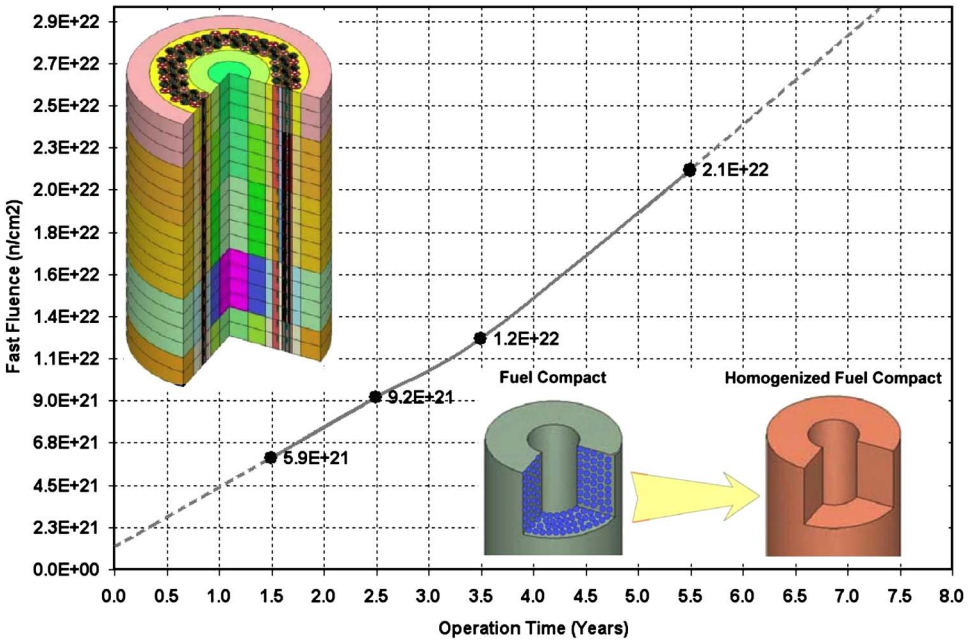

Fig. 3 Longevity analysis of the VHTR design configurations as a function of fast fluence

Fissile fuel inventory requirements are shown in Fig. 4 for various TRU-fueled VHTR configurations relative to the low-enriched uranium (LEU)-fueled VHTR configuration. [9] Trade-offs between loading operations, fuel activity, and other factors will ultimately constrain the VHTR design with respect to its TRU content [7,8,10].

Taking advantage of three burnable poison locations in the HTTR fuel block design, it is possible to reduce initial excess reactivity values in the VHTR configurations. The same three locations also allow controlling reactivity swings during operation. Figure 5 shows the HTTR fuel block model and burnable poison locations as they are used in the present analysis [1,18,19].

The VHTR system response on burnable poison distribution variations is shown in Fig. 6. For one of the considered LEU-fueled VHTR configurations, one, two, and three burnable poison locations (see Fig. 5) have been utilized sequentially to evaluate distribution effects during operation and to identify potential control system needs and requirements [11].

Reactivity swings can passively be controlled and optimized during operation by using burnable poison distributions. In the present analysis, heterogeneous distributions are considered using dedicated absorber locations in the HTTR fuel block design. Figure 7 illustrates observed self-adjustments in the operation char-

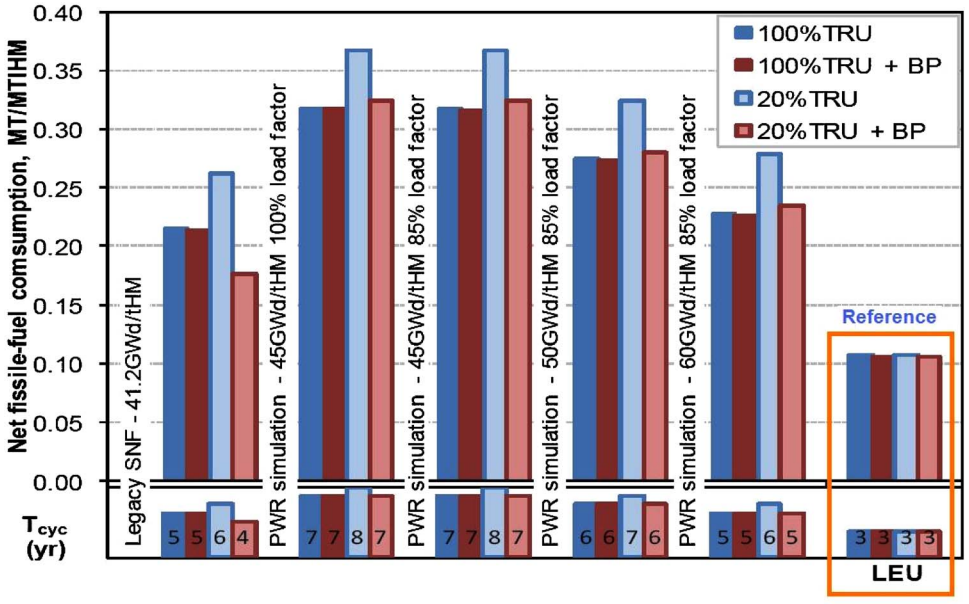

Note:
BP - Burnable Poison

Fig. 4 Fissile content requirements for various TRU-fueled VHTR configurations operating at 600 MW(th) relative to the corresponding LEU-fueled VHTR system

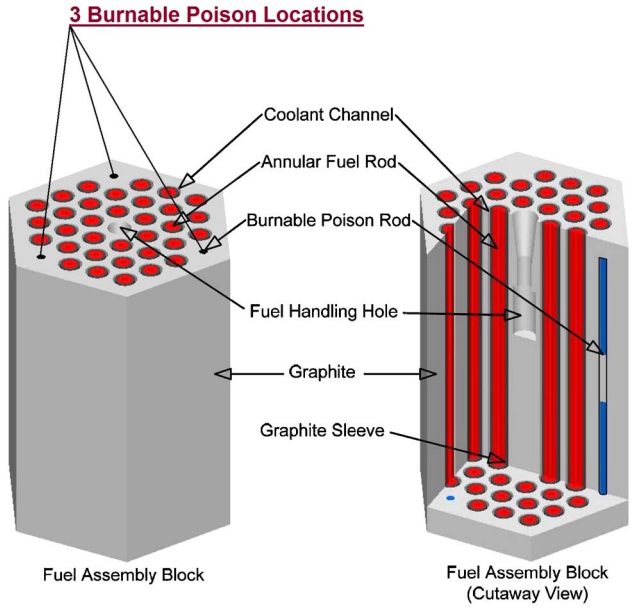

Fig. 5 Burnable poison locations in the HTTR fuel block (KENO3D plot)

acteristics of the LEU- and TRU-fueled VHTR systems as a result of system response variations triggered by different burnable poison distributions.

5 Conclusions

In the present analysis, performance characteristics of various burnable poison distributions and fuel compositions in the VHTR core have been evaluated. The basis configuration is developed using Generation IV VHTR core specifications and the HTTR hexagonal block geometry data. Utilization of TRUs in VHTRs is explored as the core self-stabilization approach. The resulting configurations have an inherent potential for autonomous operation with minimized maintenance. Adjustments of heterogeneous burnable poison distributions in the VHTR core leads to substantial reductions in initial excess reactivity levels and allows to passively control reactivity swings during operation. Both outcomes facilitate studies of potential deployment options for autonomous control in the VHTR systems with LEU and/or TRUs.

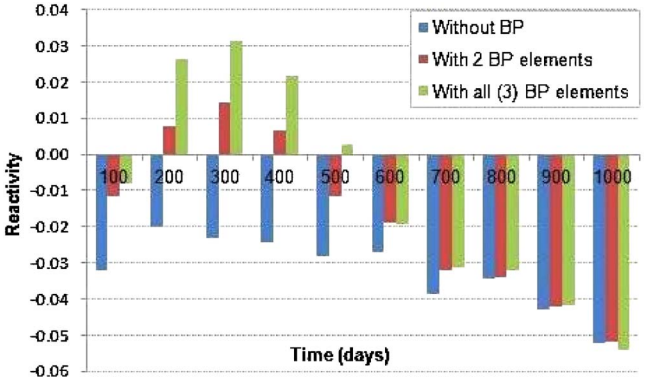

Fig. 6 Reactivity swing in the LEU-fueled VHTR configurations during operation

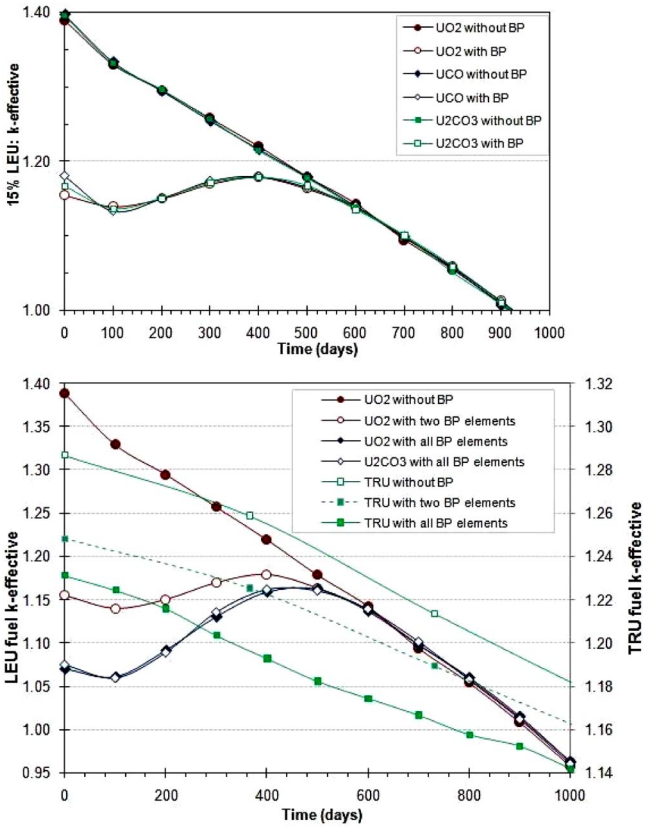

Fig. 7 Passive reactivity swing control using heterogeneous burnable poison distributions in the LEU- and TRU-fueled VHTR configurations

Acknowledgment

This paper is based on the work supported by the U.S. Department of Energy under Award No. DE-FC07-05ID14655 (05-094).

Nomenclature

RGPu = Reactor-grade plutonium

References

[1] Ames, D. E., II, 2006, "Configuration Adjustment Potential of the VHTR Prismatic Cores With Advanced Actinide Fuels," MS thesis, Texas A&M University, College Station, Texas.
[2] Bruna, G. B., Labella, R., Trakas, C., Baxter, A., Rodriguez, C., and Venneri, F., 2004, "Uncertainty Analysis and Optimization Studies on the Deep-Burner-Modular Helium Reactor (DB-MHR) for Actinide Incineration," *Proceedings of the International Conference on Reactor Physics (PHYSOR2004)—The Physics of Fuel Cycle and Advanced Nuclear System: Global Developments*, American Nuclear Society, Lagrange Park, IL, April 25–29.
[3] 2001, "Critical Experiments and Reactor Physics Calculations for Low-Enriched HTGRs," International Atomic Energy Agency, Vienna, Austria, Paper No. IAEA-TECDOC-1249.
[4] 2003, "Evaluation of High Temperature Gas-cooled Reactor Performance: Benchmark Analysis Related to Initial Testing of the HTTR and HTR-10," International Atomic Energy Agency, Vienna, Austria, Paper No. IAEA-TECDOC-1382.
[5] U.S. DOE, 2002, "Final Environmental Impact Statement for a Geologic Repository for the Disposal of Spent Nuclear Fuel and High-Level Radioactive Waste at Yucca Mountain, Nye County, Nevada," Vol. 2, U.S. DOE Paper No. DOE/EIS-0250.
[6] Office of Advanced Nuclear Research, 2005, "Generation IV Nuclear Energy Systems: Ten Year Program Plan," U.S. DOE Office of Nuclear Energy, Science, and Technology.
[7] Kim, T., Taiwo, T., Hill, R., Yang, W., and Venneri, F., 2005, "A Feasibility Study of Reactor-Based Deep-Burn Concepts," Argonne National Laboratory, Report No. ANL-AFCI-155.
[8] Kunitomi, K., 1995, "Development of New Type of HTGR," *Proceedings of the 73rd JSME Fall Annual Meeting*, JSME, Japan.
[9] Lewis, T., III, Ames, D., II, and Tsvetkov, P., 2007, "Analysis of TRU-Fueled

VHTR Prismatic Core Performance Domains," Trans. Am. Nucl. Soc., **97**, pp. 859–861.
[10] Minato, K., Ogawa, T., Sawa, K., Ishikawa, A., Tomita, T., Iida, S., and Sekino, H., 2000, "Irradiation Experiment on ZrC-Coated Fuel Particles for High Temperature Gas-Cooled Reactors," Nucl. Technol., **130**, pp. 272–280.
[11] Minato, K., Sawa, K., Koya, T., Tomita, T., and Ishikawa, A., 2000, "Fission Product Release Behavior of Individual Coated Fuel Particles for High Temperature Gas-Cooled Reactors," Nucl. Technol., **131**, pp. 36–46.
[12] Pereira, C. M. N. A., 2004, "Evolutionary Multicriteria Optimization in Core Design: Basic Investigations and Case Study," Ann. Nucl. Energy, **31**, pp. 1251–1264.
[13] Plukiene, R., and Ridikas, D., 2003, "Modeling of HTRs With Monte Carlo: From a Homogeneous to an Exact Heterogeneous Core With Microparticles," Ann. Nucl. Energy, **30**, pp. 1573–1585.
[14] U.S. DOE, 2003, "Report to Congress on Advanced Fuel Cycle Initiative: The Future Path for Advanced Spent Fuel Treatment and Transmutation Research," Office of Nuclear Energy, Science, and Technology, U.S. DOE Report No. 03-GA50439-06.
[15] Rodriguez, C., Baxter, A., McEachern, D., Fikani, M., and Venneri, F., 2003, "Deep-Burn: Making Nuclear Waste Transmutation Practical," Nucl. Eng. Des., **222**(2), pp. 299–317.
[16] Oak Ridge National Laboratory, 2006, "SCALE: A Modular Code System for Performing Standardized Computer Analyses for Licensing Evaluation," Ver. 5.1, Oak Ridge National Laboratory, TN, Paper No. ORNL/TM-2005/39.
[17] Taiwo, T. A., Kim, T. K., Yang, W. S., and Khalil, H. S., 2005, "Evaluation of High Temperature Gas-Cooled Reactor Physics Experiments as VHTR Benchmark Problems," Argonne National Laboratory, Report No. ANL-GenIV-059.
[18] Talamo, A., 2006, "Managing the Reactivity Excess of the Gas Turbine-Modular Helium Reactor by Burnable Poison and Control Rods," Ann. Nucl. Energy, **33**(1), pp. 84–98.
[19] Talamo, A., 2008, "Conceptual Design of QUADRISO Particles for High Temperature Reactors," Trans. Am. Nucl. Soc., **98**, pp. 727–728.
[20] Tsvetkov, P., Alajo, A., Ames, D., II, and Pritchard, M., 2006, "Spectrum Shifting as a Mechanism to Improve Performance of VHTRs With Advanced Actinide Fuels," *Proceedings of the 14th International Conference on Nuclear Engineering (ICONE 14)*, ASME, Miami, FL, Jul. 17–20.
[21] Tran, H. N., and Kato, Y., 2008, "An Optimal Loading Principle of Burnable Poisons for an OTTO Refueling Scheme in Pebble Bed HTGR Cores," *Proceedings of the 2008 International Congress on Advances in Nuclear Power Plants, Embedded Topical Meeting*, Anaheim, CA, Jun. 8–12, pp. 289–297.
[22] Tsvetkov, P. V., Ames, D. E., II, Pritchard, M. L., Alajo, A. B., and Lewis, T. G., III, 2007, "TRU-Fueled VHTRs: Design, Performance, and Applications," *Proceedings of GLOBAL2007: Advanced Fuel Cycles and Systems*, Boise, ID, Sept. 9–13, pp. 852–855.
[23] Tsvetkov, P. V., Lewis, T. G., III, and Alajo, A. B., 2008, "TRU-Fueled VHTRs for Applications Requiring an Extended Operation With Minimized Control and No Refueling," *Proceedings of the 16th International Conference on Nuclear Engineering (ICONE 16)*, ASME, Orlando, FL, May 11–15.

TRU-Fueled Very High Temperature Reactors for Applications Requiring an Extended Operation With Minimized Control and No Refueling

Pavel V. Tsvetkov
Tom G. Lewis III
Ayodeji B. Alajo

Department of Nuclear Engineering,
Texas A&M University,
129 Zachry Engineering Center,
MS 3133 TAMU,
College Station, TX 77843-3133
e-mail: tsvetkov@tamu.edu

This paper presents an analysis of transuranium nuclide (TRU)-fueled very high temperature reactor (VHTR) systems focusing on applications requiring an extended operation with minimized control and no refueling (single-batch mode). As an example of such applications, international deployment opportunities for grid-appropriate VHTR systems could be mentioned addressing demands for electricity, industrial heat, and cogeneration in those regions where minimized servicing is desirable for various reasons. The study is performed for the hexagonal block core concept within the framework of the ongoing U.S. DOE Nuclear Energy Research Initiative project on utilization of higher actinides (TRUs and partitioned minor actinides (MAs)) as a fuel component for extended-life VHTRs. The up-to-date analysis has shown reasonable reactivity swings, core life limits with respect to fast fluences, and criticality. [DOI: 10.1115/1.3098428]

Keywords: transuranics, VHTR, refueling, extended operation

1 Introduction

New approaches to nuclear waste management are being developed. They involve recovery and re-use of TRUs in thermal and fast reactors to reduce the amount of wastes requiring permanent geological disposal options and to facilitate nuclear energy sustainability [1]. Multiple studies explore TRU-bearing fuels for use in next generation nuclear systems [2]. In this context, it is viable to consider pressurized water reactor (PWR) spent fuel vectors as being reprocessed and recycled for further utilization as transmutation fuel (TF) feeds of VHTRs [3]. As generation III+ reactors phase out, the TRU-fueled VHTRs would become a dominant thermal reactor transmutation option taking advantage of the unique characteristics of TRUs [4].

The study is performed for the hexagonal block core concept within the framework of the ongoing U.S. DOE Nuclear Energy Research Initiative (NERI) project on utilization of higher actinides (TRUs and partitioned MAs) as a fuel component for extended-life VHTRs [5]. Researchers analyze TRU-fueled VHTR configurations and their capabilities to approach the extended operation with minimized reactivity swing and no refueling. The TRU-fueled systems are compared with the VHTR cases with low enriched uranium (LEU). The up-to-date analysis has shown reasonable reactivity swings, core life limits with respect to fast fluences, and criticality.

To assure comprehensive and realistic assessment of the VHTR design parameters and performance characteristics targeting safety confirmation, the adequacy of the applied computational methods and models is justified through validation and verification (V&V) comparison series with experimental data covering appropriate ranges of conditions [6,7]. The use of Monte Carlo codes creates a potential for explicit 3D whole-core/reactor studies [8].

Depending on the neutron spectra, neptunium, americium, and curium may contribute to small reactivity swings (self-stabilization) over prolonged irradiation periods. As a result, under certain spectral conditions TRUs would be able to contribute to the VHTR core neutron balance compensating for fuel depletion effects through their chain transformations. Self-stabilization features of advanced actinide fuels should facilitate capabilities of VHTRs to sustain a single-batch mode operation. The resulting configurations should also have an inherent potential for autonomous operation with minimized maintenance. Their implementation will allow worldwide deployment including developing countries and remote areas.

Flexibility of VHTRs with respect to their fuel cycle choices is one of the well-known features of high temperature gas-cooled reactors (HTGRs). Tolerance to potential variations of fuel loading vectors is especially important for binary systems with significantly varying characteristics of their constituents such as PWRs and VHTRs. As envisioned in the present analysis, Fig. 1 shows a symbiotic quasisustainable system consisting of PWRs and TRU-fueled VHTRs that takes advantage of this feature. Because of fissile feeds (like LEU (fresh) in Fig. 1), only quasisustainability can be claimed for asymptotic configurations where external LEU-feeds of PWRs approach zero $N_{\mathrm{LEU}}^{(0)} \rightarrow 0$ as internal transmutation fuel feeds of VHTRs (while PWRs phase out) move toward equilibrium $N_{\mathrm{TF}}^{(0,0)} \rightarrow \cdots \rightarrow N_{\mathrm{TF}}^{(0,i)} \rightarrow N_{\mathrm{TF}}^{(0,\infty)}$.

In the present analysis, potential PWR spent fuel vectors $N_{\mathrm{SNF}}^{(0)}$ were determined using the IAEA's nuclear fuel cycle simulation system (VISTA code system). To evaluate potential perturbations in $N_{\mathrm{SNF}}^{(0)}$ and their influence on the TRU-fueled VHTR performance characteristics, fuel burnup and load factor values for PWRs were perturbed. The reference $N_{\mathrm{SNF}}^{(0)}$ was determined from the analysis of legacy spent fuel vectors of PWRs [9].

Manuscript received November 30, 2008; final manuscript received December 7, 2008; published online June 11, 2009. Review conducted by Dilip R Ballal. Paper presented at the 16th International Conference on Nuclear Engineering (ICONE16), Orlando, FL, May 12–15, 2008.

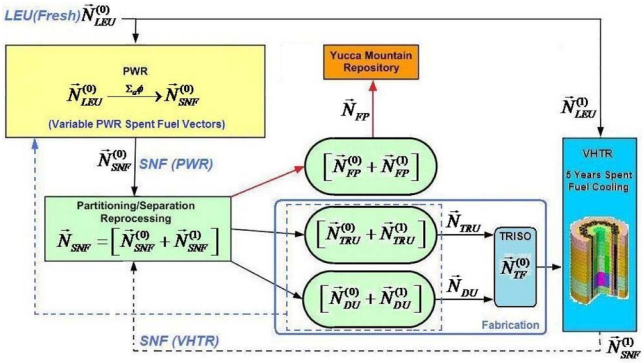

Fig. 1 Symbiotic quasisustainable PWR-VHTR system

2 High Fidelity Modeling Approach

To create advanced nuclear energy systems it is desirable to have a high fidelity modeling-based design development that relies on simulating features of the entire life cycle of the system before actual physical prototyping—from concept development to detailed design, prototyping, and safety analysis. This approach would provide consistency between neutronics and other performance aspects such as thermal hydraulics, mechanical integrity, plant heat transfer, and conversion balances. The suggested integrated/hybrid Monte Carlo-deterministic modeling approach offers the desirable analysis capabilities for the VHTR design studies. The use of Monte Carlo codes creates a potential for explicit 3D whole-core/reactor studies of the VHTR configurations addressing the key reactor physics areas such as the double and multilevel heterogeneities, neutron streaming in the low-density regions, and neutron spectrum transitions at the interfaces.

The 3D whole-core exact-geometry VHTR model has been developed for use in calculations with SCALE 5.1 code system [10]. As shown in Fig. 2, the model takes into account tristructural isotropic (TRISO) microparticles, fuel compacts, fuel assembly blocks, control rod blocks, replaceable reflectors, and a permanent outer reflector. The fuel assembly blocks are based on the high temperature test reactor (HTTR) fuel block configuration. The SCALE 5.1 double-heterogeneity treatment supports quasi-explicit representation of TRISO microparticles within a compact fuel region.

The adequacy of the applied computational methods and models used to evaluate performance has been assessed and confirmed by comparisons with experimental data covering appropriate ranges of conditions. Validation data are available from research reactors and zero-power critical assemblies. The project uses the actual test results and benchmark problems of the HTTR program (prismatic core design, reactor experiments). Observed differences are taken into account at the implementation and interpretation stages of the present analysis. The modeling results are obtained using general material properties and standard SCALE cross section libraries without any special tailoring to specific systems.

3 Neutron Spectra in VHTR Configurations

Figure 3 illustrates 3D spectral effects in VHTRs due to fuel vector variations. In all cases, there are noticeable neutron leakage effects at the core ends contributing to decreasing thermal and fast flux peak magnitudes. To produce a distinct thermal neutron peak in TRU-fueled VHTR configurations, much larger carbon-to-heavy metal (C/HM) ratios should be chosen. For comparable C/HM ratios in the critical LEU- and TRU-fueled configurations, the VHTR system with TRUs does not have a distinct thermal peak.

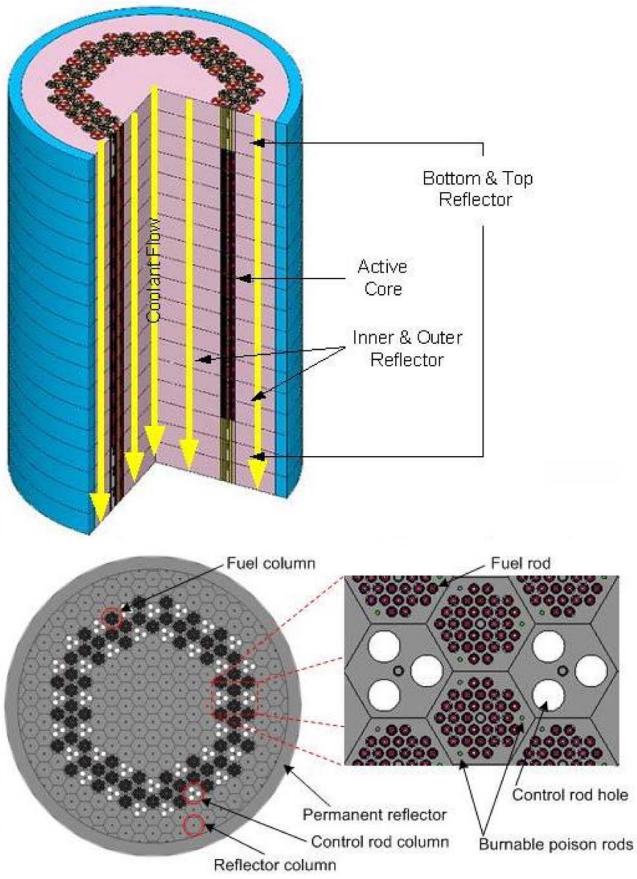

Fig. 2 3D whole-core exact-geometry VHTR model

4 VHTR Configurations in a Single-Batch Mode

The use of coated microparticles gives flexibility in fuel selection, management, core performance, and adaptability. The VHTR multiheterogeneity features allow material separation by using different types of microparticles and graphite blocks. The degree of heterogeneity and the moderator-to-fuel ratio (C/HM atom ratio) can be adjusted to achieve desirable spectrum shifting.

Several TRU-fueled VHTR configurations have been analyzed to determine the effect of the C/HM atom ratio on the single-batch core lifetime. Figure 4 illustrates the TRU-fueled VHTR operation in a single-batch mode as a function of the C/HM atom ratio per compact.

In these studies, all considered TRU-fueled VHTR configurations were analyzed assuming their operation at 103 MW/MTHM. As shown in Fig. 4, the core lifetimes of up to 9 years are possible if attained fast fluence levels can be tolerated by TRISO particles. Furthermore, by simply adjusting the C/HM atom ratio inside a compact, the corresponding compact adjustment can extend core lifetime from less than 3 years to 9 years. Figure 5 shows the fast fluence levels attained by TRISO particles in the LEU- and TRU-fueled VHTR configurations with the longest lifetimes with respect to criticality. According to Fig. 5, the highest fast fluence level is approximately 7×10^{22} n/cm^2. Therefore, expected fast fluences in the longest-operating VHTR configurations approach and may potentially exceed the traditional TRISO fast fluence limitations of about 10^{26} n/m^2 [2,7,12]. These results clearly indicate the need for radiation-tolerant materials to facilitate a single-batch mode extended operation without refueling. Advanced coating configurations and materials such as ZrC offer promising performance characteristics including reductions in coating failure probabilities yielding fission product (FP) releases

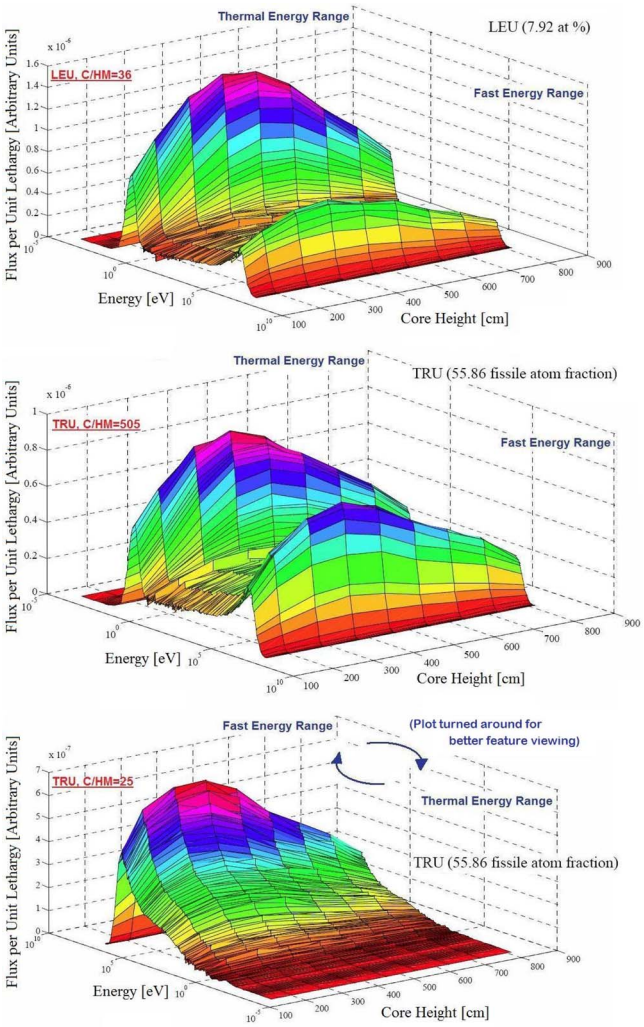

Fig. 3 Fuel effects in VHTRs–spectral variations (fluxes in the innermost fuel ring of the three-ring VHTR)

[11,12]. Consequently, higher fast fluence limits, and hence longer core lifetimes, may become acceptable approaching criticality core lifetime limitations [5].

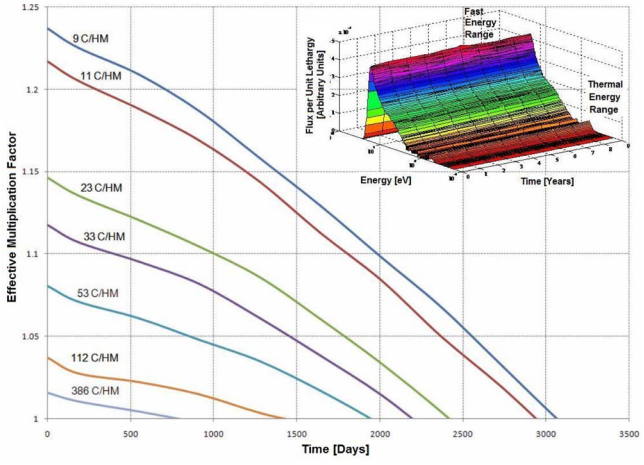

Fig. 4 TRU-fueled VHTR lifetime as a function of C/HM

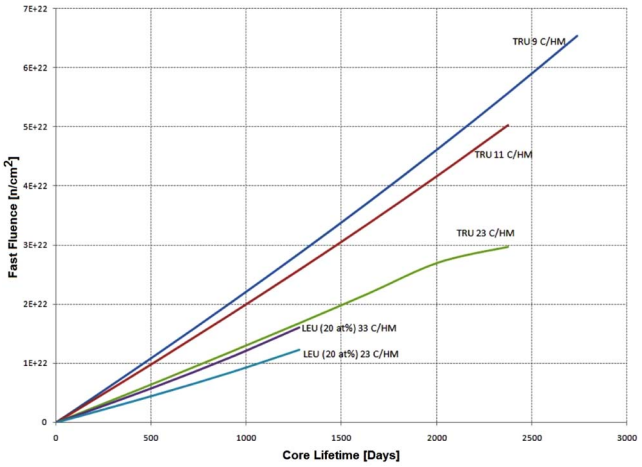

Fig. 5 Fast fluence levels in the longest-operating VHTRs

5 Potential Variations of TRU Vectors

Figure 6 illustrates potential variations of TRU vectors due to some anticipated variations of the PWR performance characteristics. These variations will ultimately affect the TRU-fueled VHTR performance characteristics.

The corresponding equilibrium neutron balance is shown in Fig. 7. The neutron balance calculations for systems with thermal and fast neutrons indicated excess neutrons for all considered TRU vectors. The thermal neutron balance shows increasing values with increasing scalar flux. In the fast spectrum, the TRU vectors showed a small variation in neutron balance as scalar flux increases.

6 Conclusions

As presented in this paper, the studies of TRU-fueled VHTR configurations indicate promising performance characteristics. The symbiotic quasisustainable PWR-VHTR system has been established. Its feasibility and performance characteristics will be explored further in future studies.

The up-to-date results have been analyzed and compared taking into account the existing systems and the Generation IV VHTR concepts with estimated characteristics. Substantial differences between the traditional LEU- and advanced TRU-fueled VHTR configurations have been observed.

Evidently, the use of TRU vectors in VHTRs leads to prolonged single-loading lifetimes. Nine year core lifetimes were found to be possible for single-batch TRU-fueled VHTR configurations with-

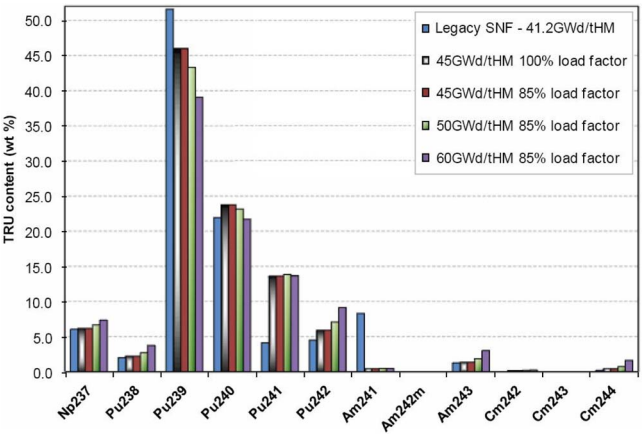

Fig. 6 Variations of TRU vectors due to PWR data

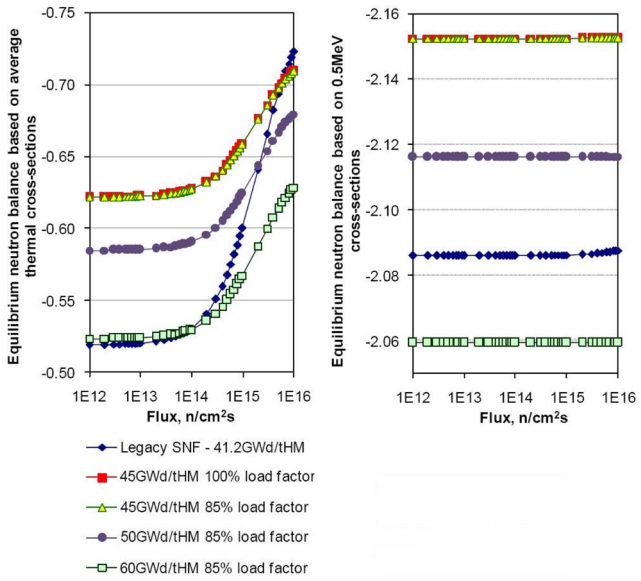

Fig. 7 Equilibrium neutron balance in the TRU-systems

out intermediate refueling. Four year core lifetimes were found to be possible for single-batch LEU-fueled VHTR configurations without intermediate refueling. The attained fast fluence levels represent a significant challenge and a strong indication of the need for radiation-tolerant materials to facilitate a single-batch mode extended operation without refueling.

Acknowledgment

This paper is based on the work supported by the U.S. Department of Energy under Award No. DE-FC07-05ID14655 (05-094).

Nomenclature

SNF = Spent Nuclear Fuel

References

[1] U.S. DOE, 2003, "Report to Congress on Advanced Fuel Cycle Initiative: The Future Path for Advanced Spent Fuel Treatment and Transmutation Research," Office of Nuclear Energy, Science, and Technology, U.S. DOE Report No. 03-GA50439-06.

[2] Rodriguez, C., Baxter, A., McEachern, D., Fikani, M., and Venneri, F., 2003, "Deep-Burn: Making Nuclear Waste Transmutation Practical," Nucl. Eng. Des., **2805**, pp. 1–19.

[3] Kim, T., Taiwo, T., Hill, R., Yang, W., and Venneri, F., 2005, "A Feasibility Study of Reactor-Based Deep-Burn Concepts," Argonne National Laboratory, Report No. ANL-AFCI-155.

[4] Office of Advanced Nuclear Research, 2005, "Generation IV Nuclear Energy Systems: Ten Year Program Plan," DOE Office of Nuclear Energy, Science, and Technology.

[5] Lewis, T., III, Ames, D., II, and Tsvetkov, P., 2007, "Analysis of TRU-Fueled VHTR Prismatic Core Performance Domains," Trans. Am. Nucl. Soc., **97**, pp. 859–861.

[6] IAEA, 2003, "Evaluation of High Temperature Gas-cooled Reactor Performance: Benchmark Analysis Related to Initial Testing of the HTTR and HTR-10," International Atomic Energy Agency, Paper No. IAEA-TECDOC-1382.

[7] IAEA, 2001, "Critical Experiments and Reactor Physics Calculations for Low-Enriched HTGRs," International Atomic Energy Agency, Paper No. IAEA-TECDOC-1249.

[8] Plukiene, R., and Ridikas, D., 2003, "Modeling of HTRs With Monte Carlo: From a Homogeneous to an Exact Heterogeneous Core With Microparticles," Ann. Nucl. Energy, **30**, pp. 1573–1585.

[9] U.S. DOE, 2002, "Final Environmental Impact Statement for a Geologic Repository for the Disposal of Spent Nuclear Fuel and High-Level Radioactive Waste at Yucca Mountain, Nye County, Nevada," Vol. 2, U.S. DOE Paper No. DOE/EIS-0250.

[10] Oak Ridge National Laboratory, 2006, "SCALE: A Modular Code System for Performing Standardized Computer Analyses for Licensing Evaluation," Ver. 5.1, Oak Ridge, TN, Paper No. ORNL/TM-2005/39.

[11] Minato, K., Ogawa, T., Sawa, K., Ishikawa, A., Tomita, T., Iida, S., and Sekino, H., 2000, "Irradiation Experiment on ZrC-Coated Fuel Particles for High Temperature Gas-Cooled Reactors," Nucl. Technol., **130**, pp. 272–280.

[12] Minato, K., Sawa, K., Koya, T., Tomita, T., and Ishikawa, A., 2000, "Fission Product Release Behavior of Individual Coated Fuel Particles for High Temperature Gas-Cooled Reactors," Nucl. Technol., **131**, pp. 36–46.

Thermodynamic Analysis and Comparison on Oxy-Fuel Power Generation Process

Shimin Deng

Rory Hynes

Hatch Energy,
1235 North Service Road West,
Oakville, ON, L6M 2W2, Canada

In this paper, pressurized oxy-fuel combustion power generation processes are modeled and analyzed based on a 350 MW subcritical reheat boiler associated with a condensing steam turbine. The performance results are obtained. Furthermore, the influences of slurry concentration and coal properties on power plant performance are investigated. An oxy-fuel configuration operating at ambient pressure is studied to compare the performance with pressurized oxy-fuel configuration. Thermodynamic analysis reveals the true potentials of the pressurized oxy-fuel process. Based on the system integration, an improved configuration is proposed in which plant efficiency of pressurized oxy-fuel process is increased by 1.36%. [DOI: 10.1115/1.3078204]

1 Introduction

Oxy-fuel combustion is one of three main approaches (postcombustion, oxy-fuel combustion, and precombustion) to capture CO_2 to address the global warming issue, for power plant applications. Oxy-fuel combustion uses oxygen instead of air for combustion, producing a flue gas that is mainly H_2O and CO_2 and which is readily captured [1,2]. In terms of thermal efficiency, it is typically acknowledged that precombustion is the most efficient approach and postcombustion is the least efficient [3]. Precombustion capture typically features fuel gasification associated with a combined cycle, which is most favorable to efficiency. Oxy-fuel combustion, by burning with pure oxygen, eliminates additional energy consumption by physical or chemical CO_2 absorption processes, thus has higher efficiency than the postcombustion CO_2 capture process.

There is an assortment of techniques, which takes advantage of the exothermic nature of the reaction, resulting in a variety of power cycles with substitution of oxygen, yielding a similar variety of oxy-fuel systems. Generally it can be distinguished into two main categories: direct and indirect heating. Direct heating requires that the working fluid be in direct contact with the fuel. Direct heating is usually associated with a gas turbine and a combined cycle is employed, and thus it results in higher thermal efficiency. But direct heating methods need to develop new gas turbines suitable to oxy-fuel combustion. Indirect heating via oxy-fuel involves heat transfer across a surface from the combustion chamber to the working fluid used in process heating or power generation. Typically, the indirect heating process is based on the Rankine cycle resulting in lower efficiency, but it is close to conventional combustion with less technical difficulties [4].

For indirect heating oxy-fuel processes, there are two different configurations: ambient combustion and pressurized combustion. An ambient combustion system has been studied extensively. Laboratory researches and pilot-scale testing have been conducted and well documented in various publications, and demonstration-scale projects are currently under development [5–10].

The pressurized oxy-fuel combustion process was proposed only recently [11–13]. The advantage of a pressurized process is to improve the energy potential of the fuel by condensing out the water vapor in the flue gas and recovering the latent heat, making the water vapor in the flue gas a useful heat source. As a result, the heat of condensation can be used to reduce the requirements for the extraction of steam from the turbine used for the boiler feedwater heating system requirements, and the thermal efficiency of the boiler is significantly improved. It is indicated that a pressurized oxy-fuel process is slightly more efficient than IGCC with CO_2 capture [11].

In addition, the pressurized oxy-fuel process enables collection of particulates, acid gases, and mercury into a condensed phase that is an order of magnitude smaller than the volume of gas treated by conventional atmospheric pressure flue gas clean-up systems. The energy consumption and capital cost of pollutant treatment could be less than the atmospheric pressure combustion system that requires particulate collection, desulfurizers, de-NO_x, and mercury abatement equipment [11].

The existing pressurized oxy-fuel process uses slurry as fuel feed. The high operating pressure, typically 80 bars, is achieved by using a slurry pump. Slurry concentration is defined as the ratio of dry solids of coal to total slurry in this study [12].

Two coals, Wyoming PRB subbituminous and Illinois No. 6 bituminous, are selected for this study. Wyoming PRB coal has very high moisture content, making its heating value small compared with most other coals. Illinois No. 6 coal is a typical bituminous coal with high volatile.

In order to carry out a comprehensive study, an oxy-fuel configuration operating at ambient pressure is compared. Based on the simulation results, quantitative analysis is performed to look at thermal performance, and it reveals the true potentials of the pressurized oxy-fuel process. In addition, influencing factors such as slurry concentration and coal properties are investigated.

A new configuration is proposed based on process integration to optimize utilization of condensation heat from flue gas. The simulation is carried out to identify the effect of the improvement.

This study is based on process modeling using ASPEN PLUS™ (for boiler) and GATECYCLE™ (for steam turbine and auxiliary systems) software tools. Detailed models are set up for the whole power plant including boiler, steam turbine and flue gas recycling, condensing heat exchanger (CHE), etc. Five cases in total are modeled and investigated; they are as follows:

- Case 1: base case, pressurized process, PRB coal, slurry concentration of 55%
- Case 2: pressurized process, Illinois No. 6 coal, slurry concentration of 55%
- Case 3: pressurized process, Illinois No. 6 coal, slurry concentration of 66.5%
- Case 4: ambient process, PRB coal, dry-fed
- Case 5: improved case, pressurized process, PRB coal, slurry concentration of 55%

Manuscript received July 30, 2008; final manuscript received November 11, 2008; published online May 28, 2009. Review conducted by Kalyan Annamalai.

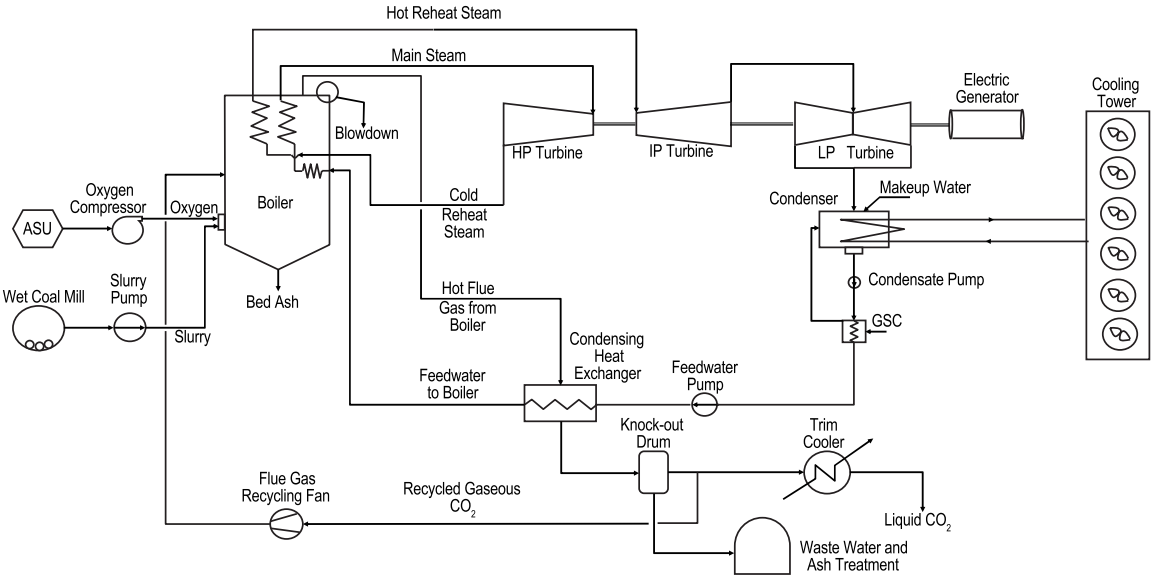

Fig. 1 Pressurized oxy-fuel combustion power plant schematic

2 Pressurized Oxy-Fuel Process

2.1 Process Description. Figure 1 shows a flow schematic of a typical coal-fired pressurized oxy-fuel power generation process [11,12]. The general arrangement is similar to conventional power plants with the following differences.

- The boiler is fired by coal slurry with pure oxygen.
- A large quantity of flue gas is recycled to control furnace outlet temperature.
- A cryogenic air separation unit (ASU) produces pure oxygen.
- A slurry preparation system replaces solid coal pulverization.
- No regenerative feedwater heat exchangers.
- No extraction steam from the steam turbine resulting in the same flow rate for all three turbine cylinders.
- Feedwater is heated up by a CHE.
- Liquid CO_2 is recovered while pollutants are removed through a dedicated process.

Oxygen from a cryogenic ASU is compressed by a three-stage compressor with intercoolers. Water is added to coal mills to produce slurry at a specific concentration. The furnace, operating at high pressure, is fired by coal slurry with pure oxygen. The steam produced inside the boiler drives high pressure (HP), intermediate pressure (IP), and low pressure (LP) steam turbines in sequence generating electricity. The exhaust steam from the LP turbine is cooled by a surface condenser that is further cooled by a mechanical draft cooling tower. The flue gas coming out of the boiler is cooled by feedwater through a dedicated CHE to low temperature at which almost all moisture is condensed out. The moisture of the flue gas condensed in the CHE is knocked out in a drum, which is sent to a waste water and ash treatment facility. The majority of the cooled dry flue gas is recycled to keep the furnace outlet temperature below fuel ash fusion temperature, and the balance is further cooled down close to ambient temperature and all CO_2 becomes liquid.

2.2 Process Modeling. The gross output of the power plant is 350 MW, which is based on burning Wyoming PRB subbituminous coal in a boiler at subcritical parameters with reheat. The base case uses a slurry concentration of 55% solids by weight [12]. A sensitivity review of slurry concentration is also presented. Ambient conditions are 1.013 bars, dry bulb temperature is 25°C, and relative humidity is at 60%. The specific power consumption of oxygen is selected as 0.23 kWh/kg [12]. The major assumed parameters are listed in Table 1. Property data of PRB and Illinois No. 6 coals are listed in Table 2.

The boiler including oxygen compression, flue gas cooling, and recycling processes is simulated with the ASPEN PLUS™ software. The steam turbine and cooling system are simulated using GATECYCLE™. The auxiliary loads of power plant include the following three main groups:

Table 1 Main assumptions for pressurized oxy-fuel process

Furnace pressure (gas side) (bar)	80
Slurry concentration (%)	55
Excess oxygen (%)	3
Oxygen purity (vol %)	99.5
Oxygen compressor efficiency (%)	85
Main steam pressure (bar)	180
Main steam temperature (°C)	540
Hot reheat steam pressure (bar)	32
Hot reheat steam temperature (°C)	540
Feed water temperature (°C)	242
Condenser pressure (kPa)	6.9

Table 2 Properties of coals

Proximate analysis (wt %)	PRB	Illinois No. 6
Moisture	31.63	12.00
Fixed carbon	34.08	39.00
Volatile matter	29.73	33.00
Ash	4.56	16.00
Ultimate analysis (wt %) DAF	**PRB**	**Illinois No. 6**
Carbon	73.03	76.98
Hydrogen	5.30	5.56
Nitrogen	0.97	1.50
Sulfur	0.58	5.56
Oxygen	20.13	10.39
Heating value, kJ/kg	**PRB**	**Illinois No. 6**
HHV	18,955	23,492
LHV	17,443	22,326
Ash softening temperature (°C)	1,135	1,182

Table 3 Performance data of oxy-fuel power plant cases

Case	1	2	3	4	5
Process type	Pressurized	Pressurized	Pressurized	Ambient	Pressurized
Fuel	PRB	Illinois No. 6	Illinois No. 6	PRB	PRB
Slurry concentration (%)	55	55	66.5		55
Plant gross output (MW)	350.0	350.0	350.0	350.0	350.0
Plant net output (MW)	235.8	233.6	233.9	221.7	238.6
Auxiliary load of CO_2 capture (MW)	88.0	89.2	89.0	95.8	84.8
Auxiliary load of slurry pump (kW)	462	480	396		442
Total auxiliary load (MW)	114.2	116.4	116.1	128.3	111.4
Fuel heat input, HHV (MWth)	856.2	855.2	853.3	904.2	825.5
Steam cycle efficiency (%)	41.34	41.34	41.35	45.86	43.00
Net plant efficiency (with CO_2 capture), HHV (%)	27.54	27.31	27.41	24.52	28.90
Boiler efficiency, HHV (%)	98.88	98.97	99.2	84.41	98.61
Furnace outlet temperature (°C)	1135.8	1166.0	1166.0	1141.0	1135.6
Recycle rate (%)	70.9	70.3	73.9	75.1	73.9
Coal feed rate (kg/s)	45.2	36.4	36.3	47.7	43.6
Slurry water flow rate (kg/s)	11.0	21.8	11.7		10.6
Slurry feed rate (kg/s)	56.1	58.3	48.1		54.1
Oxygen flow rate (kg/s)	64.9	65.8	65.6	69.1	62.6
CHX duty (MWth)	197.5	197.5	197.5	119.0	92.9
Duty of recycled gas and slurry preheater (MWth)					91.2
Final flue gas (entering PRT[a]) property					
Flow rate (kg/s)	80.0	78.8	78.7	96.6	77.2
Temperature (°C)	52.0	52.0	52.0	37.8	52.0
Composition					
CO_2 (mol %)	94.93	93.29	93.26	76.46	94.91
H_2O (mol %)	0.39	0.40	0.40	6.72	0.39
O_2 (mol %)	3.28	2.50	2.50	6.05	3.27
N_2 (mol %)	0.54	0.78	0.78	9.98	0.54
SO_2 (mol %)	0.27	2.41	2.44	0.23	0.27
Ar (mol %)	0.60	0.61	0.61	0.56	0.62
CO_2 recovery rate (%)	99.7	99.7	99.7	99.8	99.7

[a]PRT—the process to recover CO_2 from final flue gas.

- CO_2 capture (ASU, oxygen compression, slurry pump, and flue gas recycling fan)
- boiler (fuel delivery, fans, ash handling, etc.)
- steam turbine (feed water pump, cooling tower fans, etc.)

The performance results of the pressurized oxy-fuel firing power plant are summarized in Case 1 of Table 3.

The results indicate that the plant net efficiency of the pressurized oxy-fuel process of Case 1 is 27.54%, which is much lower than conventional power plant. This is mainly due to energy consumption by CO_2 capture, which leads to an auxiliary load rate of about 33%. Boiler efficiency reaches as high as about 99% due to the utilization of latent heat of flue gas. The duty of CHE is very big, 197.5 MWth, equivalent to 23% of fuel heat input to boiler. It indicates that almost all generated CO_2 can be recovered at purity of about 95%.

It is noted that the pressurized oxy-fuel process removes all feedwater heaters and does not have a deaerator. The water quality needs to be managed by a deaeration facility for a practical power generation system. This issue will be addressed by an improved configuration in Sec. 4 of the paper.

2.3 Impact of Slurry Concentration. The pressurized oxy-fuel power plant firing with PRB slurry of different concentrations is modeled with the same methodology as described above. The slurry concentrations considered range from a low of 40% solids by weight to an equivalent fuel feed using raw as-received coal only with no slurry system. The results are presented in Fig. 2.

It shows that power plant efficiency decreases from 27.63% to 26.57% as concentration of slurry water increases. The reason is that more water is added to the boiler for lower slurry concentration. To evaporate additional water, more fuel needs to be burned. Although the latent heat is recovered in the downstream CHE, the energy gains cannot compensate for the efficiency penalty because the recovered latent heat is utilized at a lower grade use (heating feedwater) but the consumed fuel is a higher grade source (heating steam inside boiler).

When the slurry concentration reduces, moisture content of the flue gas will be increased. The pinch point of the CHE will shift to a higher temperature. When the concentration is lower than 55%, it will result in a higher exit temperature of flue gas of CHE, in order to maintain the minimum temperature difference at the

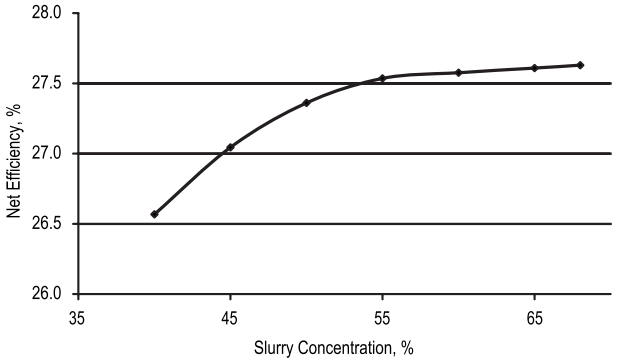

Fig. 2 Power plant net efficiency versus slurry concentration

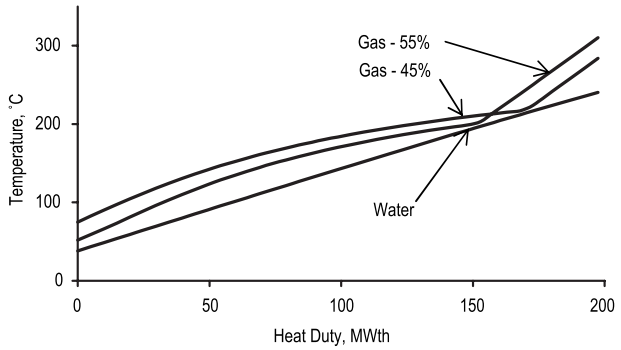

Fig. 3 T-Q diagram of CHE for two different slurry concentration cases

pinch point. Figure 3 compares the heat transfer profiles of CHE for two different slurry concentration cases (45% versus 55%). It shows that the exit temperature of flue gas is higher for lower slurry concentrations. As a result, the trend of efficiency drop is accelerated at low slurry concentrations. This explains the efficiency variation in the curve in Fig. 2.

2.4 Impact of Coal Property. A pressurized oxy-fuel process burning Illinois No. 6 coal is simulated to investigate the influence of coal property on the thermal performance of a power plant. As discussed earlier, slurry concentration will influence the whole power plant performance. Two cases, Cases 2 and 3, with slurry concentration of 55% (same as Case 1) and 66.5% (typical value for Illinois No. 6 [14]), respectively, are studied. The plant performance data are listed in Table 3.

In comparison, between Cases 2 and 1 in Table 3, the plant net efficiency of Case 2 is lower than Case 1 by 0.23%. The water content of Illinois No. 6 is significantly lower than PRB (12% versus 31.63%). Slurry concentration is defined as the ratio of dry solids of coal to total slurry. Therefore, to reach the same slurry concentration (55%), more water needs to be added into Illinois No. 6 than PRB. The slurry water quantity of Case 2 is almost double than of Case 1 (21.8 kg/s versus 11.0 kg/s). This is the main reason why Case 2 is less efficient than Case 1.

Case 3 has a typical slurry concentration for Illinois No. 6. The net efficiency is higher and close to Case 1. The reason why Case 3 is still slightly less efficient than Case 1 is due to the difference in coal properties. PRB has less ash content (resulting in less heat loss) but has more oxygen content (resulting in less oxygen consumption) than Illinois No. 6. Both noted factors will make the PRB case more efficient than the Illinois No. 6 case.

The efficiency difference between Cases 1 and 3 is small. It demonstrates that there is no significant performance difference for pressurized oxy-fuel process between two coals.

3 Comparison With Ambient Oxy-Fuel Process

Ambient oxy-fuel process has been well studied and is viewed as a simple and elegant method to solve the CO_2 emission problem for power plants. Furthermore, the key technology components in ambient oxy-fuel combustion are mostly "off the shelf" technologies that have been widely used for a long period of time. The study will simulate the ambient oxy-fuel process and compare the performance with the pressurized case, so that the true potential of the pressurized oxy-fuel process can be explored.

3.1 Simulation of Ambient Oxy-Fuel Process. The ambient oxy-fuel process is similar to the pressurized process in terms of boiler firing with pure oxygen and flue gas recycling.

However it is different in the following aspects.

- The boiler operates at ambient pressure (gas side).
- Pulverized coal is directly fed to boiler.
- Air heater heats up the recycled flue gas before entering the furnace.
- Steam turbine has extraction steam with regenerative heat exchangers, similar to conventional power plant.
- More complex product recovery train (PRT) is used to recover CO_2.

Figure 4 shows a flow schematic of a typical coal-fired ambient

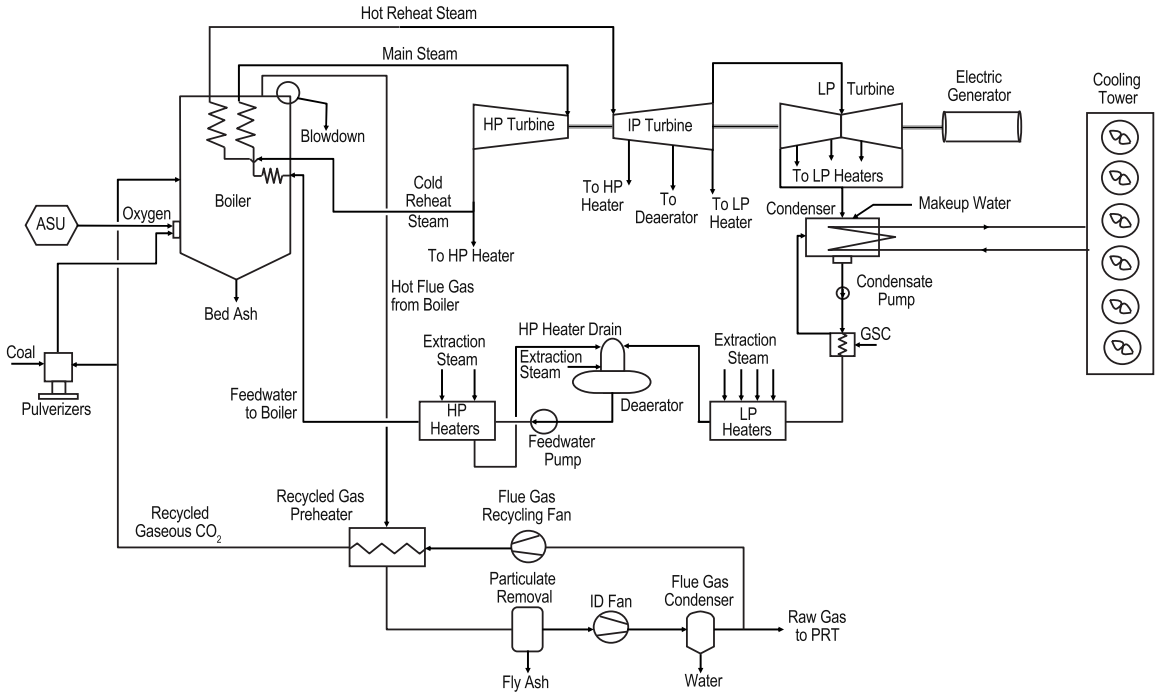

Fig. 4 Ambient oxy-fuel combustion power plant schematic

Table 4 Performance parameters of Cases 1 and 4

	Case 1	Case 4						
η_b	98.88%	84.41%	$\Delta\eta_b$	14.47%	k_b	0.286	$k_b\Delta\eta_b$	4.14%
η_{st}	41.34%	45.86%	$\Delta\eta_{st}$	−4.52%	k_{st}	0.603	$k_{st}\Delta\eta_{st}$	−2.73%
R_a	32.64%	36.67%	ΔR_a	−4.03%	k_a	−0.400	$k_a\Delta R_a$	1.61%
η_{net}	27.54%	24.52%					$\Delta\eta_{net}$	3.02%

oxy-fuel power generation process [12].

The dry recycle configuration, in which the flue gas coming out of the recycled gas preheater is cooled to a selected temperature (typically close to the ambient temperature), is selected for the ambient oxy-fuel case study. The flue gas water vapor is condensed and the dry flue gas is split into recycle gas and raw product gas for the PRT process.

In this ambient oxy-fuel process study, the latent heat of vapor condensation from flue gas is typically not used, as it is recognized as low grade heat [12]. It is assumed that the infiltration air is 3% and is distributed in both the furnace and the backend system.

The steam turbine has seven uncontrolled extraction ports to provide feedwater heating steam. There are six feed water heaters and one deaerator. The steam parameters are the same as for the base case.

Based on the simulation, the performance of the ambient oxy-fuel process is outlined in Case 4 of Table 3.

The net efficiency of Case 4 is 24.52%. In comparison with base Case 1, it indicates that the efficiency of the pressurized oxy-fuel process is higher than the ambient oxy-fuel process by 3.02%.

3.2 Thermodynamic Analysis. To identify the performance difference between the ambient and pressurized processes, it is necessary to introduce the following parameters.

Boiler efficiency can be defined as

$$\eta_b = \frac{Q_{st}}{m_f H_u} \tag{1}$$

Steam cycle (Rankine cycle) efficiency can be defined as

$$\eta_{st} = \frac{Pg}{Q_{st}} \tag{2}$$

Auxiliary load rate is defined as

$$R_a = \frac{P_{aux}}{P_g} \tag{3}$$

As a result, power plant net efficiency will be

$$\eta_{net} = \eta_b \eta_{st}(1 - R_a) \tag{4}$$

Based on mathematic deduction, the difference of net efficiency can be described as

$$\Delta\eta_{net} = k_b\Delta\eta_b + k_{st}\Delta\eta_{st} + k_a\Delta R_a \tag{5}$$

The above parameters for both Cases 1 and 4 are calculated and listed in Table 4.

According to Table 4, the net efficiency increase in pressurized oxy-fuel process of 3.02% is attributed to three major items: 4.14% from boiler efficiency increase, −2.73% from steam cycle efficiency decrease, and 1.61% from auxiliary load decrease.

Although boiler efficiency increases significantly (14.47%) for the pressurized oxy-fuel process due to latent heat utilization, the contribution to plant efficiency is only 4.14% because of its small influencing coefficient (k_b=0.286). The reason is that the steam energy output of the boiler needs to be converted into mechanical power through the steam cycle and the value of η_{st} is relatively small.

In order to utilize the latent heat of the flue gas, the pressurized oxy-fuel process removes all regenerative heat exchangers, which are displaced by preheated condensate directly entering the boiler (at the CHE). This results in a reduction in boiler feedwater temperature from 242°C to 50°C. The impact of the reduction in feedwater temperature is a significant decrease in the steam cycle efficiency due to the elimination of the regenerative feedwater heaters. Without regenerative feedwater heating, the change in steam cycle efficiency $\Delta\eta_{st}$ is −4.52%. The influencing coefficient of the steam cycle efficiency is relatively high (k_{st}=0.603). Therefore, the contribution to net efficiency reduction reaches 2.73%. This is the main drawback of pressurized oxy-fuel process.

Because the pressurized oxy-fuel process does not need a dedicated flue gas cleanup process (to remove SO_x, particulates, etc.) and a complicated PRT, the auxiliary load is reduced. As a result, it contributes to a net efficiency increase of 1.61%.

4 Improvement on Pressurized Oxy-Fuel Process

Based on the above discussion, the major drawback of the pressurized oxy-fuel process is a lower steam cycle efficiency due to removing all regenerative feedwater heaters. The authors propose to utilize the latent heat of the flue gas by heating up recycled flue gas and slurry. The flow schematic of the improved pressurized oxy-fuel power generation process is shown in Fig. 5.

In the case presented, the quantity of heat duty of the flue gas cooling (mainly from latent heat) is larger than the duty of heating up recycled flue gas and slurry. To solve the problem, the heat of flue gas cooling is first utilized to heat up the recycled flue gas and slurry, and then the balance is utilized to heat up condensate from the condenser.

For the improved configuration, there will be two HP heaters and one deaerator in which feedwater will be heated by the extraction of steam from the steam turbine before entering the boiler. Similar to Case 1, the steam cycle will have reheat and the condenser cooling system will be the same.

The components with dotted lines are additional to the existing pressurized oxy-fuel process. The heat duty of flue gas cooling will be distributed in both the recycle gas and slurry preheater and the CHE.

With PRB coal and a slurry concentration of 55%, the improved case (Case 5) is simulated (all assumptions are the same as for Case 1). The performance data are outlined in Table 3.

It indicates that the net plant efficiency of the improved case increases by 1.36% (from 27.54% of Case 1 to 28.90% of Case 5). The boiler efficiency is almost same because of the same exit temperature at CHE, but the steam cycle efficiency increases from 41.34% to 43.00%. The reason for the steam cycle efficiency increase is that three feedwater heaters are added resulting in higher boiler feedwater temperature.

In addition, the improved case has a dedicated deaerator that will provide a better measure to manage water quality resulting in higher operational reliability of power plant.

The above study to improve the existing pressurized oxy-fuel process is preliminary. It would be expected that the potential to further improve the plant performance still exists. It will be presented in forthcoming papers.

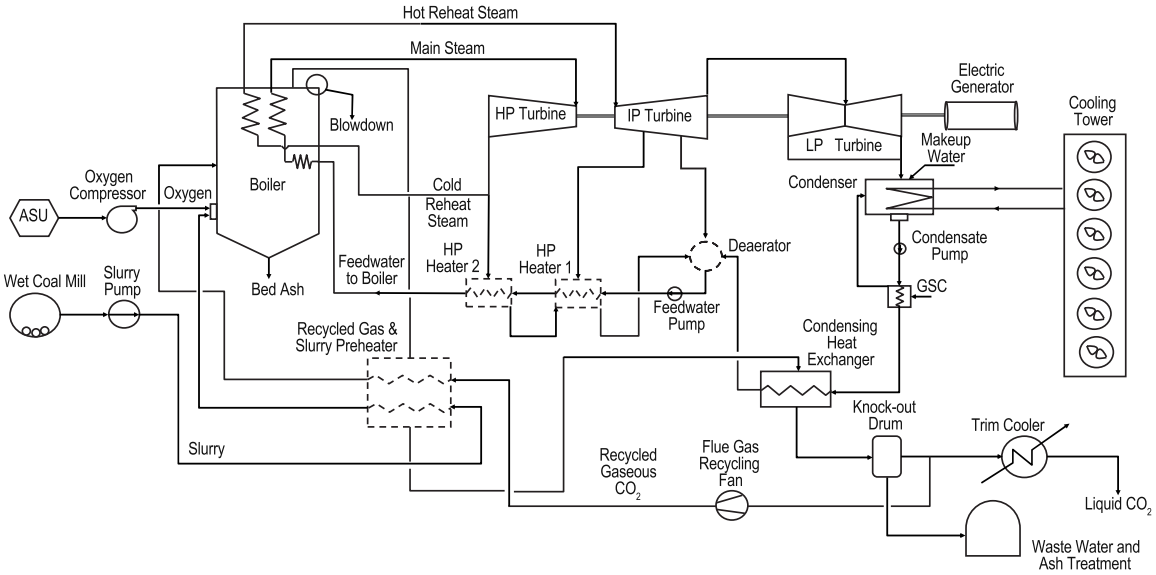

Fig. 5 Improved pressurized oxy-fuel combustion power plant schematic

Table 5 Equipment cost comparison between two processes

Major equipment	Ambient process	Pressurized process	Notes
Pulverizer versus slurry preparation	−	+	Pressurized process needs to prepare slurry and pump to very high pressure
Boiler	−	++	Pressurized process boiler operates at very high pressure
ASU	+	−	Ambient process consumes more oxygen due to lower efficiency
Recycling gas fans	−	++	Recycling gas fans of pressurized process operates at very high pressure
Flue gas treatment	+	−	Ambient process has more complicated pollutant treatment system
Flue gas ducts	−	+	Ducts of pressurized process operate at very high pressure
O_2 versus CO_2 compressor	+	−	Ambient process needs to compress CO_2; pressurized process compresses O_2
Steam turbine		+	Pressurized process features nonconventional steam turbine
Deaerator	++	−	Pressurized process does not have a deaerator
Water quality control	−	+	Without a deaerator, pressurized process needs additional equipment to control water quality
Condenser and cooling tower	−	+	Pressurized process has more turbine exhaust steam
HP/LP heaters versus CHE	+	−	For similar heat duty, condensing heat exchanger could be less expensive

5 Discussion

The pressurized oxy-fuel combustion process is more efficient than the ambient oxy-fuel combustion process. In order to investigate the technologies more comprehensively, a comparison in capital cost between the two processes needs to be carried out. Table 5 presents an indicative comparison in equipment cost between the two processes.

According to the above table, the pressurized oxy-fuel combustion process could have higher equipment cost than ambient combustion process, which mainly results from the very high operational pressure of the boiler. More detailed economic analysis will be carried out at the next stage of the study.

6 Conclusions

This study is based on system modeling and thermodynamic analysis for various cases of oxy-fuel combustion power generation processes. It indicates that the efficiency of a 350 MW pressurized oxy-fuel power plant with a reheat and subcritical boiler firing PRB coal can reach 27.54% (higher heating value (HHV)).

The findings indicate that the efficiency difference between ambient and pressurized cases is 3%. Thermodynamic analysis reveals the root causes of the performance difference between the two configurations. It is pointed out that the steam cycle efficiency decrease due to removing all feedwater heaters is the major drawback of the pressurized oxy-fuel process.

The assessment indicates that a higher slurry concentration will benefit plant efficiency and coal properties will not have significant influence on plant efficiency.

Based on the analysis, an improved configuration is proposed in which the plant efficiency of the pressurized oxy-fuel process is increased by 1.36%. Further study is expected to optimize the existing configuration to improve power plant efficiency and examine capital and operating costs.

Nomenclature

H_u = HHV of fuel, MJ/kg
k_b = influencing coefficient of boiler thermal efficiency

k_{st} = influencing coefficient of steam cycle efficiency
k_a = influencing coefficient of auxiliary load rate
m_f = fuel feed rate, kg/s
Q_{st} = absorbed heat of steam cycle, MW
P_{aux} = total auxiliary load of power plant, MW
P_g = gross output of power plant, MW
R_a = auxiliary load rate of power plant
η_b = boiler thermal efficiency
η_{st} = steam cycle efficiency
η_{net} = power plant net efficiency (HHV basis)
Δ = difference of parameter values

References

[1] Kutz, M., 2006, *Mechanical Engineers' Handbook—Energy and Power*, Wiley, Hoboken, NJ.
[2] IEA Clean Coal Centre, 2005, http://www.iea-coal.co.uk/site/ieaccc/home.
[3] Strakey, J. P., 2007, "The New Clean Coal Technologies," Presentation of National Energy Technology Laboratory, http://www.wvdo.org/community/120407Presentations/8Strakey.pps.
[4] IPCC, 2005, *IPCC Special Report on Carbon Dioxide Capture and Storage*, Cambridge University Press, New York.
[5] Wall, T., Gupta, R., Buhre, B., Khare, S., 2005, "Oxy-fuel (O_2/CO_2, O_2/RFG) Technology for Sequestration-Ready CO_2 and Emission Compliance," The Clearwater Coal Conference: The 30th International Technical Conference on Coal Utilization & Fuel Systems, Coal Technology: Yesterday—Today—Tomorrow, Clearwater, April 17–21.
[6] Kimura, K., Omata, K., Kiga, T., Takano, S., and Shikisima, S., 1995, "Characteristics of Pulverized Coal Combustion in O_2/CO_2 Mixtures for CO_2 Recovery," Energy Convers. Manage., **36**, pp. 805–808.
[7] Tan, Y., Douglas, M. A., and Thambimuthu, K. V., 2002, "CO_2 Capture Using Oxygen Enhanced Combustion Strategies for Natural Gas Power Plants," Fuel, **81**, pp. 1007–1016.
[8] Buhre, B. J. P., Elliott, L. K., Sheng, C. D., Gupta, R. P., and Wall, T. F., 2005, "Oxy-Fuel Combustion Technology for Coal-Fired Power Generation," Prog. Energy Combust. Sci., **31**, pp. 283–307.
[9] Spero, C., 2007, "Callide Oxyfuel Project," CLET Seminar: Deployment of CCS in Queensland, July 12.
[10] Singh, D. J., Croiset, E., Douglas, P. L., and Douglas, M. A., "CO_2 Capture Options for an Existing Coal Fired Power Plant: O_2/CO_2 Recycle Combustion vs. Amine Scrubbing," www.netl.doe.gov/publications/proceedings/01/carbon_seq/p6.pdf.
[11] Fassbender, A., "Pressurized Oxy-Fuel Combustion for Multi-Pollutant Capture," ThermoEnergy Power Systems, LLC, www.thermoenergy.com.
[12] Zheng, L., Pomalis, R., and Clements, B., 2007, "Technical and Economic Feasibility Study of a Pressurized Oxy-Fuel Approach to Carbon Capture: Part 1," Combustion Optimization Group: CANMET Energy Research Centre: Natural Resources Canada.
[13] Fassbender, A. G., 2001, "Power System With Enhanced Thermodynamic Efficiency and Pollution Control," Patent No. 6,196,000.
[14] Process Engineering Division, 1998, "Texaco Gasifier IGCC Base Cases, PED-IGCC-98-001," DOE Report, www.netl.doe.gov/technologies/coalpower/turbines/refshelf/igcc-h2-sygas/texac3y.pdf.

Improving Performance of Refrigerant Cooled Steam Power Plant by Using Cooling Thermal Storage

A. S. Hegazy[1]
Department of Mechanical Engineering,
Menoufia University,
Shebin Al Kom 11911, Egypt
e-mail: ahegazy7@yahoo.com

It is proposed in the current paper to combine the steam plant with two refrigeration cycles and a cooling storage container. Throughout the time of a day, the steam plant is made to work at full power, where the excess power generated over the electric power demand is used to drive the compressors of the refrigeration cycles. The stored cooling is used for dissipating the heat absorbed by the cooling refrigerant in the steam condenser during the period of peak-loads, while the two refrigeration machines are stopped. In this way, the energy used for driving the refrigeration machine is saved so that the whole power generated by the steam plant is exported to the grid. Energy analyses of the proposed combined system has led to inferring that the net power of the steam plant during the period of exclusive direct cooling of the steam condenser (only the first refrigeration machine is running) is about 70–86% of the whole power generated by the steam plant when the coefficient of performance of the first refrigeration cycle lies in the range of 4–10. Also, it has been found that relatively small coefficients of performance of the first and second cycles, less than 6 and 1.5, respectively, result in low net power of the steam plant over the period of charging the cooling storage container (both refrigeration machines run in unison). In this case, the net plant power amounts to less than 26% of the total generated plant power when the time of storing the cooling is lower than double the time of the peak-loads. This necessitates increasing the storing time to assure reasonable available power to be exported to the grid. Economical analyses of the proposed system have showed that both the capital cost and energy charges are less for the proposed system than that of the steam plant without cooling storage for practically possible operating conditions. [DOI: 10.1115/1.3078385]

Keywords: steam power plant, steam cycle, refrigeration cycle, refrigerant cooled condenser, cooling thermal storage, combined system

1 Introduction

Steam power plants represent the largest segment of the world electricity production. These plants rely on a fuel source (fossil or nuclear) to heat water to steam that is used to drive a turbine generator. Steam exhausted from the turbine is condensed and recycled to the steam generator or boiler. The steam condensation occurs in a steam condenser. Cooling water mass flow rates of greater than 25 times the steam mass flow rate are necessary depending on the allowable temperature rise of the cooling water—typically 8–14 °C. There are basically two types of cooling water system designs: once-through (open loop) and recirculating (closed loop). Plants equipped with once-through cooling water systems have relatively high water use in the range of 3 m^3/min for each MWe, and they cause detrimental impact on aquatic ecosystem [1].

The most common type of recirculating system uses wet cooling towers to dissipate the heat from the cooling water to the atmosphere. This type requires a supply water make-up rate of about 5% [2]. In addition, cooling water is the major source of wastewater generated by most thermal power plants. For each MWe of a facility about 7.5 m^3 per day of waste water are generated, with about 70% of this wastewater coming from cooling tower blow-down [3].

Due to enhanced concern about water supplies and water use priorities, dry cooling systems for thermal power plants are receiving increased consideration, even though electric power from dry-cooled power plants currently costs 10–15% more than power from wet-cooled plants [4]. There is little current research and development work being reported in literature on dry cooling systems for power plants. A few important exceptions include improved heat exchanger geometries for finned tube bundles in air-cooled condensers [5,6]; enhancement of air-cooled condenser performance with the use of limited water [7,8]; the use of evaporative condenser [9]; optimization techniques [10]; and using double wet and dry condenser, where the heat of the wet condenser is dissipated into a cooling storage container [11].

The concept of ammonia dry cooling system is reported in Ref. [12]. The system is an indirect type, in which the usual circulating water loop is replaced by a phase-change ammonia loop, where ammonia is evaporated in the tubes of the steam condenser and condensed in an air-cooled condenser. This concept was tested and well documented [12–15], with the participation of several major equipment vendors (Baltimore Air Coil (Baltimore, MD), The Trane Co. (Piscataway, NJ), Curtiss-Wright (Cleveland, OH), CB&I (Denver, CO), and Union Carbide (Danbury, CT)). To date, the concept has not been pursued commercially but may bear reexamination in light of increasing interest in economical dry cooling.

Considering the approach proposed in Ref. [12], it should be noticed that, in a conventional steam plant, nearly double the rate of net power generation is rejected as waste heat through the

[1]Present address: P.O. Box 26240, Riyadh 11486, Kingdom of Saudi Arabia.

Manuscript received May 19, 2008; final manuscript received January 11, 2009; published online June 4, 2009. Review conducted by Ashok Rao.

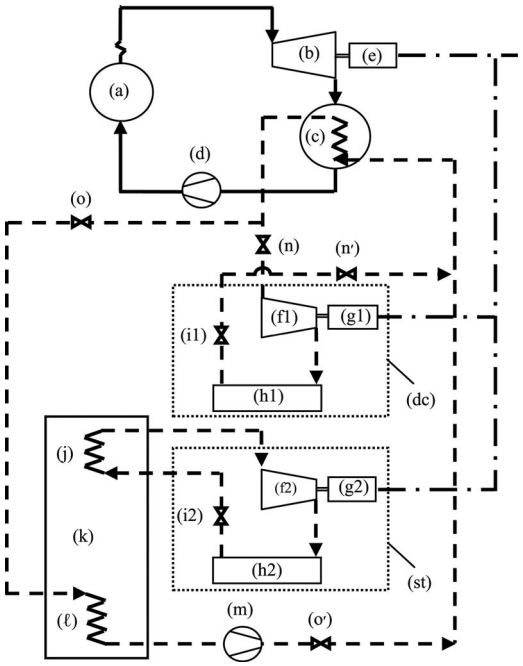

Fig. 1 Schematic of the proposed combined system: (a) boiler, (b) steam turbine, (c) steam condenser, (d) boiler feed water pump, (e) generator, (f) refrigerant compressor, (g) motor, (h) refrigerant condenser, (i) throttling valve, (j) evaporator, (k) cooling storage container, (⌿) heat exchanger, (m) refrigerant circulating pump, (n), (n′), (o), and (o′) valves, —— water/steam, – – refrigerant, and – • – electricity

steam condenser [16]. Accordingly, most of the generated power during peak-loads (highest ambient temperature) is used for driving the refrigerant compressor. This results in a great deficiency in the net generated power available to be fed to the grid so that the demanding load would not be covered during this period. For overcoming this problem, it is proposed in the present paper to use a cooling thermal storage system with the combined steam plant and refrigerating cycle described in Ref. [12]. This proposal allows utilizing the discounted rates for energy during off peak loads to produce cooling that is stored in the cooling storage container. Over the period of the peak-loads (standard energy rate), the refrigeration machine is stopped and the cooling refrigerant dissipates the heat absorbed from the steam condenser into the cooling storage system. This allows the whole power generated by the steam plant to be exported to the grid.

2 Description of the Proposed Combined System

The configuration of the proposed combined system is shown schematically in Fig. 1. This system consists of three cycles and a cooling storage container. The three cycles are a steam power plant cycle and two vapor compression refrigeration cycles. The steam cycle can comprise the components of which a modern steam power plant is composed. Of these components only the boiler (a), steam turbine (b), refrigerant cooled condenser (c), feed water pump (d), and generator (e) are shown in Fig. 1. The first refrigeration cycle is referred to as (dc). It is made up of a compressor (f1), driven by an electric motor (g1), a refrigerant condenser (h1), a throttling valve (i1), and an evaporator (c), which acts at the same time as the condenser of the steam plant. In this cycle, the low pressure refrigerant vapor is compressed by the compressor (f1) and transferred to the refrigerant condenser (h1). The heat absorbed from the condensing steam and the heat of compression are removed by the air-cooled refrigerant condenser (h1), where the high pressure vapor refrigerant is condensed. The condensed refrigerant liquid is transferred to the refrigerant expansion valve (i1). This valve has the function to reduce the pressure of the liquid refrigerant, and in turn, the boiling point of the refrigerant is lowered. The low pressure liquid refrigerant flows through the tubes of the evaporator condenser (c), absorbing heat, changing into vapor, in turn condensing the steam. The water condensate and low pressure vapor refrigerant leaving the evaporator condenser (c) complete the steam and the first refrigeration cycles, respectively.

The second refrigeration cycle is designated by (st). It consists of a compressor (f2), operated by an electric motor (g2), a refrigerant condenser (h2), a throttling valve (i2), and an evaporator (j). This cycle functions quite similar to the first refrigeration cycle except that the low pressure liquid refrigerant leaving the throttle valve (i2) evaporates as it flows through the evaporator (j) by absorbing heat from the cooling storage container (k), where the cooling is stored.

The two refrigeration cycles have three different operating periods along the time of a day: the period of exclusive direct cooling of the steam condenser, the period of charging, and the period of discharging the cooling storage container. The first period occurs at part-loads when the steam plant can generate excess power over the electric power to be exported to the grid (it is referred hereafter to as power demand), which is adequate or larger than that needed for running the refrigerant compressor of the first refrigeration cycle but less than the power required to operate the compressors of both refrigeration cycles. The second period takes place at part-loads (charging the cooling storage container) when the excess power of the steam plant suffices to drive the compressors of both refrigeration cycles. The cooling produced by the first cycle serves to directly condense the exhaust steam of the turbine (b) at this period, while the cooling produced by the second cycle is stored in the cooling storage container (k). During this period the valves (o) and (o′) are closed, whereas the valves (n) and (n′) are opened. The refrigerant vapors coming out of the evaporator condenser (c) and evaporator (j) are compressed in the compressors (f1) and (f2), respectively, and complete the refrigeration cycles.

The third period comes about throughout the peak-loads. During this period, the refrigeration compressors (f1) and (f2) are set out of operation, and the valves (n) and (n′) are closed, while the valves (o) and (o′) are opened. The cooling refrigerant of the steam condenser changes its loop, in which it no longer flows through the first refrigeration cycle. Rather, the refrigerant vapor exiting the evaporator condenser (c) flows through the heat exchanger (⌿), where it rejects the heat absorbed from the condensing steam to the cooling storage container (k) and is condensed. It is then repumped by the circulating pump (m) to the evaporator condenser (c) for condensing the exhaust steam of turbine (b). The refrigerant is vaporized in the evaporator condenser (c) and repeats this cooling loop until the power demand gets low enough so that the first refrigeration cycle is reactivated.

Fixation of the lengths of the second and third periods depends mainly on the amount of the plant energy to be exported to the grid and electricity price during each of the two periods. The plant is caused to work according to the second period only when the cost of the total energy consumed to drive the compressor of the refrigeration cycle (st) during the second period is less than the cost of the excess energy added to the grid by the plant during the third period as a result of using the cooling storage container.

Optimal operation of the steam plant is achieved when the turbine exhaust steam is cooled to its design point, which is in the range of 15–30°C. Accordingly, the temperature of the steam condenser cooling refrigerant can be in the range of 10–25°C. As a result, the evaporator temperature of the first refrigeration cycle (used for direct cooling of the steam condenser) is high enough to effect large coefficient of performance for direct cooling.

As to the second refrigeration cycle (st), which serves to charge the cooling storage container, it is worth mentioning that cooling is stored as ice, chilled water, or some other materials. As a tre-

mendous amount of heat must be removed from the steam condenser, ice storing is preferred in this case to limit the volume of the storing container. Production of ice forces the second refrigerating machine to operate at inevitably low evaporator temperature and cause low coefficient of performance. Fortunately, the storing process takes place when the power demand is minimum, which occurs at night hours and early morning, where the ambient temperature has its lowest value. This makes the temperature of the condenser of the refrigerating machine relatively low that partially compensates for the low temperature of the evaporator by fairly improving the coefficient of performance. As the condensers of the both refrigeration cycles (dc) and (st) are air cooled, their coefficients of performances are 77–85% lower than those of the refrigeration cycles with water cooled condensers [17]. Accordingly and concerning the performance of the large industrial cooling refrigeration cycles given in Ref. [18], it is expected for the coefficient of performance of the refrigeration cycle (dc) to be greater than 4 and for the coefficient of performance for the refrigeration cycle (st) to lie in the range of 1.5–3.

3 Energy Analyses

The aim of the energy analyses presented in this section is to predict the energy output of the proposed combined system at the different operating periods. It is to be mentioned here that the studied steam plant is illustrated in Fig. 1 by a simple steam Rankine cycle. However, the overall and thermal efficiencies of this cycle are modified in the following analyses to take into account the complexity of the actual modern cycle. Also, it is assumed that the steam condenser temperature remains constant for the three operating periods. This is brought about by the refrigeration cycles and the cooling storage container. Since the steam plant in continuously running at full power and according to the above mentioned assumption, it follows that the maximum power P_p generated by the steam plant is constant for the three operating periods explained in Sec. 2. The steam plant with maximum generated power P_p is referred hereafter to as basic plant.

In order to be able to calculate the power of the refrigeration machine (dc) during the first period (exclusive direct cooling of the steam condenser), it is first necessary to determine the rate of heat it removes from the steam condenser. The overall efficiency η_o of the steam plant and the thermal efficiency of the steam cycle are defined as

$$\eta_o = \frac{P_p}{Q_b} \tag{1}$$

$$\eta_{\text{th}} = \frac{Q_b - Q_c}{Q_b} \tag{2}$$

Solving Eqs. (1) and (2) to get Q_c results in

$$Q_c = \frac{P_p}{\eta_o}(1 - \eta_{\text{th}}) \tag{3}$$

Given the coefficient of cooling loss ξ_{dc} for direct cooling, the rate of heat $Q_{\text{ev,dc}}$ to be removed by the evaporator (steam condenser) of the refrigeration machine (dc) during this period may be given in combination with Eq. (3) by

$$Q_{\text{ev},1} = Q_{\text{ev,dc}} = \frac{P_p}{\eta_o}(1 - \eta_{\text{th}})(1 + \xi_{\text{dc}}) \tag{4}$$

As only the refrigerant compressor (f1) of the first refrigeration cycle (dc) is operating during this period, the total power Pr_1 of the refrigerant compression is equal to the power $Pr_{\text{dc},1}$ of the refrigerant compressor (f1). Accordingly, the average coefficient of performance $\text{COP}_{\text{dc},1}$ of the refrigeration machine (dc) during this period is defined as

$$\text{COP}_{\text{dc},1} = \frac{Q_{\text{ev,dc}}}{Pr_{\text{dc},1}} = \frac{Q_{\text{ev},1}}{Pr_1} \tag{5}$$

Combination of Eqs. (5) and (4) results in

$$\frac{Pr_1}{P_p} = \frac{Pr_{\text{dc},1}}{P_p} = \frac{(1 - \eta_{\text{th}})(1 + \xi_{\text{dc}})}{\text{COP}_{\text{dc},1}\,\eta_o} \tag{6}$$

The net power $P_{n,1}$ generated by the power plant and is available for feeding the grid during the first period is given by

$$P_{n,1} = P_p - Pr_1 \tag{7}$$

Dividing both sides of Eq. (7) by P_p and combining the resulted equation with Eq. (6), the following equation can be derived:

$$\frac{P_{n,1}}{P_p} = 1 - \frac{(1 - \eta_{\text{th}})(1 + \xi_{\text{dc}})}{\text{COP}_{\text{dc},1}\,\eta_o} \tag{8}$$

Concerning the third period (discharging the cooling storage container), it is worth mentioning that no energy is consumed for driving the refrigerant compressors. As a result, the net power output of the steam plant $P_{n,3}$ for this period is equal to the maximum power P_p. Therefore, the reciprocal of $P_{n,1}/P_p$ gives the power ratio $P_{n,3}/P_{n,3'}$. Hence, it follows that

$$\frac{P_{n,3}}{P_{n,3'}} = \frac{\text{COP}_{\text{dc},3}\,\eta_o}{\text{COP}_{\text{dc},3}\,\eta_o - (1 - \eta_{\text{th}})(1 + \xi_{\text{dc}})} \tag{9}$$

where $P_{n,3'}$ is the net power output of the steam plant without cooling storage during the third period, and $\text{COP}_{\text{dc},3}$ is the coefficient of performance of the refrigeration cycle (dc) over the third period.

During the second period (charging the cooling storage container), both refrigeration machines (dc) and (st) are working in unison. The cooling generated by the refrigeration machine (dc) serves to cool the steam condenser directly, whereas the cooling produced by the refrigeration machine (st) is stored in the storing container to be used during the third period. Accordingly, the total heat rate $Q_{\text{ev},2}$ removed by the evaporators of the refrigeration machines (dc) and (st) and the total power Pr_2 of their refrigeration compressors are given by

$$Q_{\text{ev},2} = Q_{\text{ev,dc}} + Q_{\text{ev,st}} \tag{10}$$

$$Pr_2 = Pr_{\text{dc},2} + Pr_{\text{st},2} \tag{11}$$

where $Q_{\text{ev,dc}}$ is given by Eq. (4) and $P_{\text{dc},2}$ is expressed by analogy to Eq. (6) as

$$\frac{Pr_{\text{dc},2}}{P_p} = \frac{(1 - \eta_{\text{th}})(1 + \xi_{\text{dc}})}{\text{COP}_{\text{dc},2}\,\eta_o} \tag{12}$$

The average coefficient of performance COP_{st} of the refrigeration machine (st) during the second period is given as

$$\text{COP}_{\text{st}} = \frac{Q_{\text{ev,st}}}{Pr_{\text{st},2}} \tag{13}$$

Given that the duration time of the second period is Δt_2, the total thermal energy $E_{\text{ev,st}}$ to be removed by the evaporator of the refrigeration cycle (st) during this period can be expressed in combination with Eq. (13) as

$$E_{\text{ev,st}} = Q_{\text{ev,st}}\Delta t_2 = \text{COP}_{\text{st}} Pr_{\text{st},2}\Delta t_2 \tag{14}$$

$E_{\text{ev,st}}$ equals the sum of the thermal energy to be removed from the steam condenser through the third period and the heat transferred from the surroundings to the cooling refrigerant and the cooling storage container. Given that the duration time of the third period is Δt_3, $E_{\text{ev,st}}$ is calculated similar to Eq. (4) by

$$E_{\text{ev,st}} = \frac{P_p}{\eta_o}(1 - \eta_{\text{th}})(1 + \xi_{\text{st}})\Delta t_3 \tag{15}$$

where ξ_{st} is the cooling loss coefficient during storing the cooling and conveying it to the steam condenser.

Equating the right hand sides of Eqs. (14) and (15) and solving for $Pr_{\text{st},2}/P_p$, the following equation is obtained:

$$\frac{Pr_{st,2}}{P_p} = \frac{(1-\eta_{th})(1+\xi_{st})}{COP_{st}\eta_o}\frac{\Delta t_3}{\Delta t_2} \tag{16}$$

Insertion of Eqs. (12) and (16) into Eq. (11), it follows that

$$\frac{Pr_2}{P_p} = \left[\frac{1-\eta_{th}}{\eta_o}\right]\left[\frac{1+\xi_{dc}}{COP_{dc,2}} + \frac{\Delta t_3}{\Delta t_2}\left(\frac{1+\xi_{st}}{COP_{st}}\right)\right] \tag{17}$$

The net power $P_{n,2}$ of the steam plant during the second period is given by

$$P_{n,2} = P_p - Pr_2 \tag{18}$$

Dividing both sides of Eq. (18) by P_p and substituting Eq. (17) into the resulted equation leads to obtaining the following equation:

$$\frac{P_{n,2}}{P_p} = 1 - \left[\frac{1-\eta_{th}}{\eta_o}\right]\left[\frac{1+\xi_{dc}}{COP_{dc,2}} + \frac{\Delta t_3}{\Delta t_2}\left(\frac{1+\xi_{st}}{COP_{st}}\right)\right] \tag{19}$$

4 Economical Analyses

The analyses presented in Sec. 3 have shown that the net power output of refrigerant cooled steam plant with cooling storage container at peak-loads is always equal to the maximum generated power P_p of the basic plant. This comes from stopping both refrigeration machines (dc) and (st), while using the stored cooling to condense the steam in the plant condenser rather than the refrigeration cycle (dc). In this case, the cost of the steam plant with cooling storage container exceeds the cost of the plant without cooling storage container. The additional cost comprises the capital cost of the cooling storage container with its refrigeration machine and the charges of energy used for producing the cooling to be stored. In the following analyses, the steam plant with cooling storage container is referred to as plant A.

For the steam plant without cooling storage container, to give the same net power output P_p at peak-loads, it should be modified so as to generate the power P_p beside the power required to drive the compressor of the direct cooling refrigeration cycle (dc) at peak-loads. Hence, the maximal rating of the modified plant $P_{p''}$ becomes higher than P_p and it can be expressed by a similar derivation of Eq. (8) as

$$\frac{P_{p''}}{P_p} = \frac{COP_{dc,3}\eta_o}{COP_{dc,3}\eta_o - (1-\eta_{th})(1+\xi_{dc})} \tag{20}$$

Also, the compressor power $Pr_{dc''}$ of the refrigeration cycle (dc) gets greater. It can be determined by analogy to Eq. (6) and in combination with Eq. (20) by

$$\frac{Pr_{dc''}}{P_p} = \frac{(1-\eta_{th})(1+\xi_{dc})}{COP_{dc,3}\eta_o - (1-\eta_{th})(1+\xi_{dc})} \tag{21}$$

The steam plant without cooling storage container, which develops a net power output equals to the maximum power P_p of the basic plant, is designated in the following analyses as plant B.

Both plants A and B are composed of the same components of the basic steam plant cycle without cooling storage container. But, they differ in the supplemental components, which enable each plant accomplishing its function. Hence, it is clear that the costs of the two plants vary only in the additional costs of the supplementary components. To be able to evaluate the economy of using the cooling storage container with refrigerant cooled steam plant, a comparison between the additional costs of plants A and B is to be made. Consequently, the additional costs are adopted as the objective function for economical evaluation of plants A and B. It is composed of the capital cost of the supplementary equipment and energy charges of utilities. The operation and maintenance costs are not considered explicitly since they are small as compared with the energy charges and they are assumed to be included in the capital costs.

Table 1 Basic design data of the studied combined system

Steam plant overall efficiency	η_o	–	0.35
Average thermal efficiency of the steam cycle	η_{th}	–	0.5
Cooling loss coefficient for direct cooling	ξ_{dc}	–	0.025
Cooling loss coefficient for cooling through the cooling storage container	ξ_{st}	–	0.05
Steam condenser temperature	T_c	°C	20

The capital cost C_A and daily energy charge EC_A of the supplemental equipment of plant A can be estimated by

$$C_A = \rho_{sc}E_{ev,st} + \rho_r Pr_{st,2} \tag{22}$$

$$EC_A = \rho_{de}\Delta t_2 Pr_{st,2} \tag{23}$$

$E_{ev,st}$ and $P_{st,2}$ are determined by aid of Eqs. (15) and (16), respectively.

For plant B, the additional capital cost C_B and daily energy charge EC_B can be expressed as

$$C_B = \rho_p(P_{p''} - P_p) + \rho_r(Pr_{dc''} - Pr_{dc,1} \quad \text{or} \quad Pr_{dc,2} \quad \text{whichever is greater}) \tag{24}$$

$$EC_B = \rho_{se}\Delta t_3(P_{p''} - P_p) \tag{25}$$

where $Pr_{dc,1}$, $Pr_{dc,2}$, $P_{p''}$, and $Pr_{dc''}$ are given by Eqs. (6), (12), (20), and (21), respectively.

Concerning Eq. (24), it is to be mentioned that the first operating period of the refrigeration machines takes often place at higher atmospheric temperature than the second period does. As a result, the power $Pr_{dc,1}$ is frequently greater than $Pr_{dc,2}$. Hence, $Pr_{dc,1}$ is considered in Eq. (24) for the calculation carried out in Sec. 5.

5 Results and Discussion

The energy analyses developed in Sec. 4 have been used for predicting the energy output of the proposed combined system and energy required for operating the refrigerating compressors for the three operating periods. The data of the proposed combined system required for carrying out the computations are given in Table 1. The results presented hereafter are based on these data. It is to be noticed that the values of η_o and η_{th} given in Table 1 are approximately close to those of a real modern steam plant. Also, the value ξ_{st} in Table 1 is valid for ice storage container used for inlet air cooling of gas turbines [18]. ξ_{dc} is assumed to be half the value of ξ_{st} since heat transferred from the surroundings to the cooling refrigerant during direct cooling is considerably less than that when the cooling is stored. Condensation temperature T_c of the steam in the plant condenser is assumed to be 20°C. The values of η_o, η_{th}, ξ_{dc}, ξ_{st}, and T_c were kept unchanged as listed in Table 1 for the whole calculations carried out in this study.

The power ratio Pr_1/P_p determined by aid of Eq. (6) is plotted against the coefficient of performance $COP_{dc,1}$ of the first refrigeration cycle in Fig. 2. Pr_1 is the power required for driving the refrigerant compressor of the direct cooling refrigeration cycle to generate cooling for direct use in the steam condenser. Figure 2 shows obviously that Pr_1/P_p is greatly dependent on the coefficient of performance $COP_{dc,1}$. It is decreased sharply with growing $COP_{dc,1}$. The rate of decrease in Pr_1/P_p with $COP_{dc,1}$ declines gradually as $COP_{dc,1}$ grows up. Pr_1/P_p amounts to 0.366, 0.244, 0.183, and 0.146 at $COP_{dc,1}$ of 4, 6, 8, and 10, respectively. Accordingly, the net power ratio $P_{n,1}/P_p$ calculated by aid of Eq. (8) reaches 0.634, 0.756, 0.817, and 0.854 for $COP_{dc,1}$ of 4, 6, 8, and 10, respectively. This indicates the significance of having the highest possible $COP_{dc,1}$ for this period.

In Fig. 3, the power ratio $P_{n,3}/P_{n,3'}$ determined by using Eq. (9) is plotted versus the coefficient of performance $COP_{dc,3}$. Figure 3 reveals that the effect of using cooling thermal storage on the power ratio $P_{n,3}/P_{n,3'}$ is very remarkable when $COP_{dc,3}$ is less

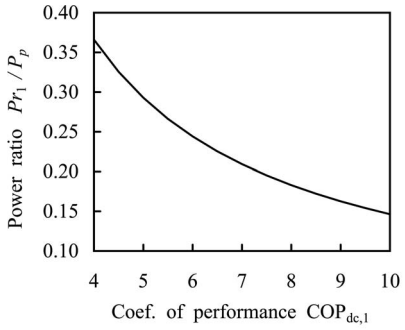

Fig. 2 Direct cooling refrigeration power during the first period

than 7. $P_{n,3}/P_{n,3'}$ amounts to 1.58, 1.42, 1.32, and 1.26 at $COP_{dc,3}$ of 4, 5, 6, and 7, respectively. Mostly, the peak-load period is characterized by high ambient temperatures, and in turn, $COP_{dc,3}$ has medium values in a range less than 7. As a result, the power ratio $P_{n,3}/P_{n,3'}$ would be great. This enhances the role of cooling thermal storage during peak-loads; i.e., the third period (discharging the cooling storage container).

During the second period (charging the cooling storage container), both refrigerant compressors (f1) and (f2), see Fig. 1, are brought in unison into operation to produce cooling for both direct cooling of the steam condenser and charging the cooling storage container. This entails consumption of a considerable portion of the power generated by the steam plant for driving the refrigerant compressors. In Fig. 4, the power ratios Pr_2/P_p is plotted versus the time ratio $\Delta t_2/\Delta t_3$ for coefficient of performance $COP_{dc,2}$ of 4, 6, 8, and 10. The curves in Fig. 4 represent coefficient of performance COP_{st} of 1.5, 2.0, 2.5, and 3. It is seen from Fig. 4 that, in some cases, the power of the refrigerant compressors is greater than the whole power generated by the steam plant. This occurs at low values of $COP_{dc,2}$, COP_{st}, and $\Delta t_2/\Delta t_3$; e.g., Pr_2/P_p is greater than 1.0 for $COP_{dc,2}$ of 4 and COP_{st} of 1.5 and 2.0 when $\Delta t_2/\Delta t_3$ is less than 1.45 and 1.3, respectively. For $COP_{dc,2}$ equal to 6, Pr_2/P_p exceeds 1.0 as COP_{st} and $\Delta t_2/\Delta t_3$ are less than 1.5 and 1.27, respectively. Pr_2/P_p decreases with rising $COP_{dc,2}$, COP_{st}, and $\Delta t_2/\Delta t_3$ and thus $P_{n,2}/P_p$ grows up. For $\Delta t_2/\Delta t_3$ of 2.0 and $COP_{dc,2}$ equal to 4.0, $P_{n,2}/P_p$ is estimated by aid of Eq. (19) to be 0.14, 0.26, 0.34, and 0.39 at COP_{st} of 1.5, 2.0, 2.5, and 3.0, respectively. As $COP_{dc,2}$ is increased to 10.0 for the same $\Delta t_2/\Delta t_3$ of 2.0, $P_{n,2}/P_p$ becomes 0.36, 0.48, 0.56, and 0.61 at COP_{st} of 1.5, 2.0, 2.5, and 3.0, respectively. The values of $COP_{dc,2}$ and COP_{st} are imposed by the environmental conditions and temperature of the steam condenser. In the cases of having unfavorable values of $COP_{dc,2}$ and COP_{st}, which cause high values of Pr_2/P_p and low values of $P_{n,2}/P_p$, it is recommended to increase the time ratio $\Delta t_2/\Delta t_3$ to a reasonably high value that can effect the availability

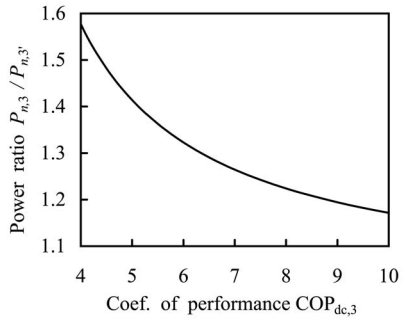

Fig. 3 Net power of the steam plant during peak-loads (third period)

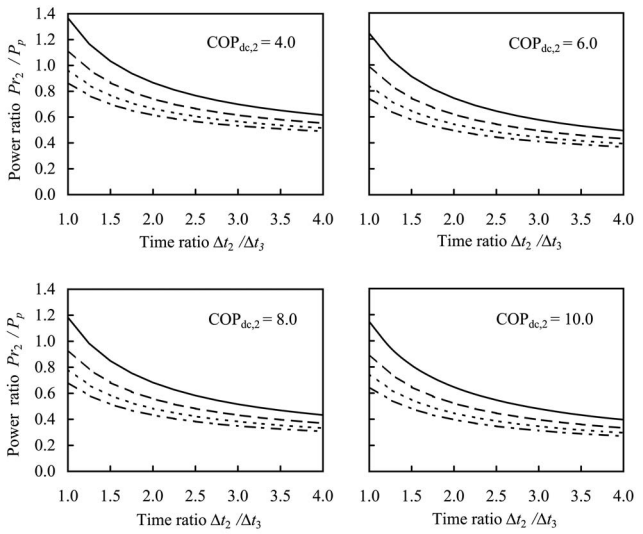

Fig. 4 Effect of storing time interval on the refrigeration machines' power during the cooling storage period: ——— COP_{st}=1.5, — — — COP_{st}=2.0, …….. COP_{st}=2.5, and — • — COP_{st}=3.0

of enough power for covering the power demand. Accordingly, $\Delta t_2/\Delta t_3$ is fixed by the power demand and coefficients of performance $COP_{dc,2}$ and COP_{st}. In general, $\Delta t_2/\Delta t_3$ less than 2.0 leads to relatively great compressors' power and low net power output of the steam plant. As a result, $\Delta t_2/\Delta t_3$ should be selected larger than 2.0 to assure the availability of enough power covering the power demand.

The economical analyses presented in Sec. 5 are used to evaluate the economical utilization of cooling storage container with refrigerant cooled steam plant. The unit capital costs of the supplemental equipment and electrical energy charges of utilities, needed for conducting this evaluation, have been cited from Ref. [19] as given in Table 2. The cost of the steam turbine generator has been taken as the same as that of the gas turbine generator as both costs are very close to each other. The energy charges illustrated in Table 2 are valid for Osaka in Japan [19].

Investigating Eq. (21), it can be inferred that the power $Pr_{dc''}$ of the direct cooling compressor for plant *B* during the third period depends on only the coefficient of performance $COP_{dc,3}$. For better understanding the results presented hereafter, $Pr_{dc''}$ is plotted in Fig. 5 versus $COP_{dc,3}$. Figure 5 shows that $Pr_{dc''}$ is strongly affected by the value of $COP_{dc,3}$. It decreases steeply with increasing $COP_{dc,3}$, especially at low $COP_{dc,3}$.

Figure 6 illustrates the additional capital cost C_A/P_p per kilowattt of the maximum power of the basic steam plant for plant *A* versus the duration time Δt_3 and for time ratio $\Delta t_2/\Delta t_3$ of 1.0, 2.0, and 3.0. The curve parameter COP_{st} has the values of 1.5, 2.0, 2.5, and 3.0. C_A grows up with increasing Δt_3 as a result of growing

Table 2 Unit capital costs of supplemental equipment and energy charges of utilities

Equipment/utility		Unit cost
Steam turbine generator ρ_p		1850 \$/kW
Electric compression refrig ρ_r		280 \$/kW
Ice storage container ρ_{sc}		16\$/kW h
	Standard rate ρ_{se}	10¢/kW h
Electricity charge		
	Discounted rate ρ_{de}	4¢/kW h

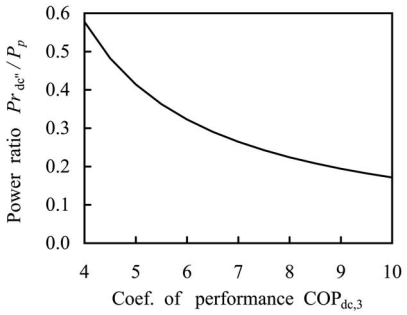

Fig. 5 Power of the direct cooling compressor during peak-loads (third period)

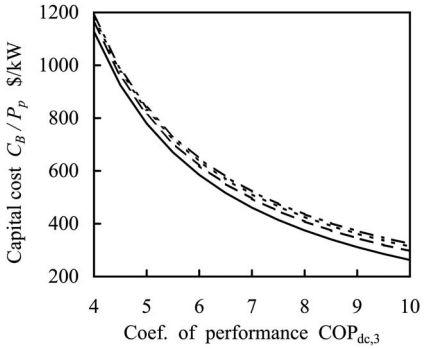

Fig. 7 Additional capital cost of plant *B* per kilowatt of the basic steam plant maximum power: ——— $COP_{dc,1}=4.0$, — — — $COP_{dc,1}=6.0$, …….. $COP_{dc,1}=8.0$, and — • —$COP_{dc,1}=10.0$

capacity of the cooling storage container, as indicated by Eq. (15). Also, C_A is raised as Δt_2 and COP_{st} decline due to the rising value of $P_{st,2}$, as suggested by Eq. (16).

Examining Eq. (24) along with Eqs. (6) and (21), it can be inferred that C_B is dependent on only $COP_{dc,1}$ and $COP_{dc,3}$. Figure 7 shows C_B/P_p against $COP_{dc,3}$ for $COP_{dc,1}$ of 1.5, 2.0, 2.5, and 3.0. Figure 7 reveals that C_B recedes steeply as $COP_{dc,3}$ rises due to the excessive drop in $Pr_{dc''}$, and in turn, in $P_{p''}$. A comparison between Figs. 6 and 7 leads to deducing that for the studied ranges of Δt_2, Δt_3, $COP_{dc,1}$, $COP_{dc,3}$, and COP_{st}, C_A is far less than C_B except for high values of $COP_{dc,3}$ (greater than 8) and low values of $\Delta t_2/\Delta t_3$ in the range of 1.0. Mostly, peak-loads take place at high ambient temperatures, which lead to low values of $COP_{dc,3}$. Besides, $\Delta t_2/\Delta t_3$ has to be quite greater than 1.0 so that $Pr_{st,2}$ is small enough to allow sufficient net power of the steam plant available to cover the power demand. So, high values of $COP_{dc,3}$ (greater than 8) and low time ratios $\Delta t_2/\Delta t_3$ (in the range of 1.0) are improbable to occur.

A test of Eq. (23) together with Eq. (16) leads to conclude that the value of EC_A is affected by the duration time Δt_3 as well as the coefficient of performance COP_{st}. Equations (21) and (25) suggest clearly that EC_B depends only on Δt_3 and $COP_{dc,3}$. EC_A/P_p and EC_B/P_p are plotted in Figs. 8(*a*) and 8(*b*), respectively, versus Δt_3. The curves in Fig. 8(*a*) are drawn for COP_{st} of 1.5, 2.0, 2.5, and 3, while the curves in Fig. 8(*b*) represent $COP_{dc,3}$ of 4, 6, 8, and 10, respectively. It is seen from Fig. 8 that EC_A is less than EC_B when COP_{st} is greater than 2 and $COP_{dc,3}$ is lower than 6. As the cooling storage process (the second period) is conducted at night and early morning hours, where the ambient temperature is relatively low, COP_{st} is expected to exceed 2. Furthermore, the third period (peak-loads) is characterized by relatively high ambient temperature, which results in a low $COP_{dc,3}$; it is anticipated in most cases to be less than 6. These make plant *A* more attractive concerning energy charges than plant *B* for the range of COP_{st} greater than 2 and $COP_{dc,3}$ less than 6. Out of this range, the comparison depends on the values of Δt_3, COP_{st}, and $COP_{dc,3}$; e.g., if $\Delta t_3=3$ h and $COP_{dc,3}=8$, EC_{Ae} is greater than EC_B when COP_{st} is less than 2.5 and vice versa when COP_{st} is larger than 2.5.

6 Conclusions

It is proposed in the present work to combine steam power plant using refrigerant cooled condenser with two vapor compression refrigeration cycles and a cooling thermal storage container. Energy analyses have been developed for predicting the energy consumed by the refrigeration machines and net energy output of the steam plant. Besides, economical analyses have been conducted to economically evaluate the use of cooling storage with refrigerant cooled steam plants. The results of this study led to drawing the following conclusions.

1. During the period of exclusive direct cooling of the steam condenser, the power of the first refrigeration machine depends essentially on its coefficient of performance. It amounts to 35–14.6% of the total power generated by the steam plant for average coefficient of performance 4–10.
2. The power generated by the steam plant over the period of discharging the cooling storage container (peak-loads of the steam plant) is greater when the steam condenser is cooled through the cooling storage container than that if a refrigeration machine is used directly for this purpose. The increase in steam plant power is adversely proportional to the average coefficient of performance of the direct cooling refrigeration cycle during this period. It comes up to 17–58% for coefficient of performance 10–4.
3. To minimize the average power needed for driving both the refrigeration machines during charging the cooling storage

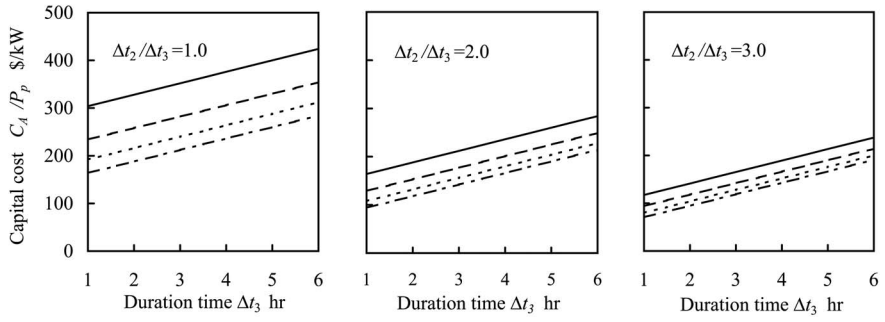

Fig. 6 Additional capital cost of plant *A* per kilowatt of the maximum power of the basic steam plant: ——— $COP_{st}=1.5$, — — — $COP_{st}=2.0$, ……. $COP_{st}=2.5$, and — • — $COP_{st}=3.0$

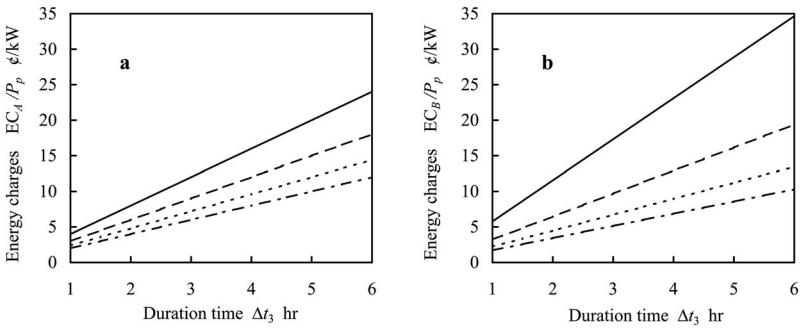

Fig. 8 Additional energy charges per kilowatt of the basic steam plant maximum power: (*a*) plant *A*: ——— $COP_{st}=1.5$, — — — $COP_{st}=2.0$, ……. $COP_{st}=2.5$ — • —, and $COP_{st}=3.0$ and (*b*) plant *B*: —— $COP_{dc,3}=4.0$, — — — $COP_{dc,3}=6.0$, ……. $COP_{dc,3}=8.0$, and — • — $COP_{dc,3}=10.0$

container, the time interval of this process is fixed in accordance with the values of the refrigerating machines' coefficient of performance during this process. In general, the time interval of charging the cooling storage container should be greater than twice the time of discharging the container. This would assure relatively low power of the refrigeration compressors' power and thus high enough power would be available for covering the electric power demand of the grid.

4. Both the capital cost and energy charges of the steam plant with cooling storage are always less than that of the steam plant without cooling storage for practically possible operating conditions.

Nomenclature

C = capital cost ($)
COP = refrigeration cycle average coefficient of performance
E = energy (kJ)
EC = daily energy charge (¢/kW day)
P = power generated by the steam plant (kW)
Pr = power of the refrigerant compressor (kW)
Q = heat rate (kW)
T = temperature (°C)

Greek Letters

Δt = time period (s)
η_o = power plant overall efficiency
η_t = steam turbine internal efficiency
η_{th} = steam cycle thermal efficiency
ξ = cooling loss coefficient
ρ = unit capital cost ($/kW) and energy rate of the utility (¢/kW h)

Subscripts

A, B = plant designation
b = boiler
c = condenser
dc = direct cooling of the steam condenser
de = discounted energy rate
ev = evaporator
n = net power of the steam plant
p = maximum power of the basic steam plant
r = refrigeration machine
sc = cooling storage container
se = standard energy rate
st = cooling thermal storage
1, 2, 3 = refrigeration machines operating periods
′ = basic steam plant without cooling storage
″ = steam power plant without cooling and its net output equals to the maximum power of the basic plant

References

[1] Maulbetsch, J., and Zammit, K., 2003, "Cooling System Retrofit Costs," EPA Workshop on Cooling Water Intake Technologies, Arlington, VA, May 6.
[2] Feeley, T. J., Green, L., Murphy, J. T., Hoffmann, J., and Carney, B. A., 2005, "Department of Energy/Office of Fossil Energy's Power Plant Water Management R&D Program," http://www.netl.gov/technologies/IEP_Power_Plant_R&D_Fina_1.pdf.
[3] Maulbetsch, J., 2002, "Comparison of Alternate Cooling Technologies for California Power Plants: Economic, Environment and Other Tradeoffs, Public Energy Research Program," CEC/EPRI, Final Report No. 500-02-079F.
[4] Johnson, B. M., Allemann, R. T., Faletti, D. W., Fryer, B. C., and Zaloudek, F. R., 1976, "Dry Cooling of Power Generating Station: A Summary of the Economic Evaluation of Several Advanced Concepts via a Design and Cost Estimate," Battelle Pacific Northwest Labs, Technical Report No. BNWL-21120.
[5] Bonger, R., and Chandron, R., 1995, "New Developments in Air-Cooled Steam Condensing," EPRI Paper No. 18.
[6] Kroeger, D. G., 1998, *Air-Cooled Heat Exchangers and Cooling Towers*, Begell House, New York.
[7] Balogh, A., and Takacs, Z., 1998, "Developing Indirect Dry Cooling Systems for Modern Power Plants," http://www.nemesis.at/publication/gpi_98_2/articles/33.html.
[8] Maulbetsch, J. S., and Di Filippo, M. N., 2001, "Spray Cooling Enhacement of Air-Cooled Condensers," *Proceedings of the XIIth International Conference on Cooling Towers*, Sydney, Australia, International Association of Hydraulic Research.
[9] Hutton, D., 1999, "Improved Power Plant Performance With Evaporative Steam Condensing," Technical Paper No. TP99-08, CTI Bulletin PRM No. 103 (08).
[10] Conradie, A. E., Buys, J. D., and Kröger, D. G., 1998, "Performance Optimization of Dry-Cooling Systems for Power Plants Through SQP Methods," Appl. Therm. Eng., **18**(1–2), pp. 25–45.
[11] Hegazy, A. S., 2008, "Use of Cooling Thermal Storage as a Heat Sink for Steam Power Plant," JSME J. of Thermal Science and Technology, **3**(2), pp. 330–341.
[12] Allemann, R. T., Johnson, B. M., and Werry, E. V., 1987, "Wet-Dry Cooling Demonstration: A Transfer of Technology," Electric Power Research Institute, Report No. CS-5016.
[13] Allemann, R. T., Faletti, D. W., Fryer, B. C., and Zaloudek, F. R., 1986, "Wet-Dry Cooling Demonstration: Test Results," Electric Power Research Institute, Report No. CS-4321.
[14] Allemann, R. T., 1981, "Advanced Concepts Test (ACT) Facility Summary Safety Report," Electric Power Research Institute, Report No. CS-1915.
[15] Allemann, R. T., 1981, "Development of an Advanced Concept of Dry/Wet Cooling of Power Generating Plants," Electric Power Research Institute, Report No. CS-1668.
[16] Lees, M., 1995, "The Economics of Wet Versus Dry Cooling for Combined Cycle," Proc. Inst. Mech. Eng., Part B, **209**, pp. 37–44.
[17] Wilbert, F., 1988, *Industrial Refrigeration Handbook*, 1st ed., McGraw-Hill, New York.
[18] Hosoz, M., and Kilicarslan, A., 2004, "Performance Evaluations of Refrigeration Systems With Air-Cooled, Water-Cooled and Evaporative Condensers," Int. J. Energy Res., **28**(8), pp. 683–696.
[19] Yokoyama, R., and Ito, K., 2004, "Effect of Inlet Air Cooling by Ice Storage on Unit Sizing of a Gas Turbine Cogeneration Plant," ASME J. Eng. Gas Turbines Power, **126**, pp. 351–357.

Improved Discharge Measurement Using the Pressure-Time Method in a Hydropower Plant Curved Penstock

Adam Adamkowski
e-mail: aadam@imp.gda.pl

Zbigniew Krzemianowski

Waldemar Janicki

Department of Hydraulic Machinery,
The Szewalski Institute of Fluid-Flow Machinery,
Polish Academy of Sciences,
Fiszera 14,
PL 80-952 Gdansk, Poland

One of the basic flow rate measurement methods applied in hydropower plants and recommended by the International Standard IEC 60041–1999 and American National Standard ASME PTC 18–2002 is the pressure-time method, generally known as Gibson method. The method consists in determining the flow rate (discharge) by integration of the recorded time course of pressure difference variations between two cross sections of the hydropower plant penstock. The accuracy of measurement depends on numerous factors and, according to the International Standard, generally is confined within the range 1.5–2.3%. Following the classical approach, the pressure-time method applicability is limited to straight cylindrical pipelines with constant diameters. However, the International Standard does not exclude application of this method to more complex geometries, i.e., curved pipeline (with elbows). It is obvious that a curved pipeline causes deformation of the uniform velocity field in pipeline cross sections, which subsequently causes aggravation of the accuracy of the pressure-time method flow rate measurement results. The influence of a curved penstock application on flow rate measurements by means of the considered method is discussed in this paper. The special calculation procedure for the problem solution has been developed. The procedure is based on the FLUENT computational fluid dynamic solver. Computations have been carried out in order to find the so-called equivalent value of the geometric pipe factor F required when using the pressure-time method. An example of application of this method to a complex geometry (two elbows in a penstock) is presented. The systematic uncertainty caused by neglecting the effect of the elbows on velocity field deformation has been estimated.
[DOI: 10.1115/1.3078794]

Keywords: hydraulic machines, flow rate measurements, efficiency measurements, pressure-time method, Gibson method

1 Introduction

The current-meter (velocity-area), pressure-time (Gibson), and tracer techniques belong to the primary methods of discharge measurement through hydraulic machinery [1,2]. The ultrasonic method, as a no primary method according to Ref. [1], is recently the subject of numerous researches focusing on its progress and accuracy. Mainly, because of its capability for continuous flow rate monitoring, nowadays the ultrasonic method is ever more frequently applied in hydraulic flow systems. However, the basic flow measurement methods in efficiency tests of large hydraulic machines (especially in guarantee tests) are still the current-meter and pressure-time methods. Moreover, the current-meter method, very frequently applied in hydropower plants, has been lately substituted by the pressure-time method in powerplants of medium and high heads. This is mainly the result of a number of advantages over the current-meter method, for instance, lower costs of using the pressure-time method, which is related to the development of computer techniques that simplify the process of data acquisition and processing and are more likely to provide higher accuracy. The increased accuracy of the devices used for pressure measurements and the use of computer techniques for collecting recorded data and their numerical processing make this method more attractive than the outdated versions, which employed optical techniques to record pressure variations combined with manual graphics.

The classical approach to the pressure-time method application is limited to straight pipelines with constant diameters. However, Ref. [1] did not exclude application of this method to more complex geometries, i.e., curved pipeline (with elbows). It is obvious that a curved pipeline causes deformation of the velocity field in pipeline cross sections, which subsequently aggravates the accuracy of the pressure-time method flow rate measurement results.

In this paper a special numerical procedure is proposed for considering the influence of a penstock elbow (or elbows) on the pressure-time method results. The procedure is based on the computational fluid dynamic (CFD) simulation using a commercial software. Its application may enable improvement of flow measurement results achieved from the pressure-time method. As an example, the measurements of the flow rate through a 180 MW hydraulic turbine are described including a discussion of the particular conditions of a penstock containing two pipeline elbows.

2 Theoretical Principles of the Pressure-Time Method

The pressure-time method utilizes the effect of hydraulic transients (water hammer phenomenon) in a pipeline [1–5]. The method requires recording of static pressure difference, which occurs between two cross sections of a pipeline as a result of the

Manuscript received September 18, 2008; final manuscript received January 12, 2009; published online June 9, 2009. Review conducted by Dilip R. Ballal.

change in momentum. This situation takes place when the liquid flow in a pipeline is stopped using a cut-off device, for instance, turbine wicket gates. The flow rate is determined by integrating, within a proper time interval, the measured pressure difference time-variation caused by the water hammer phenomenon.

According to the theoretical principle of the pressure-time method, the volumetric flow rate Q_0 under initial conditions (before the water flow stoppage was initiated) can be calculated from the following well-known integral formula:

$$Q_0 = \frac{1}{\rho F}\int_{t_0}^{t_k} (\Delta p(t) + \Delta p_d(t) + \Delta P_f(t))dt + q_k \tag{1}$$

where q_k is the flow rate in the final conditions, t is the actual time, $[t_0, t_k]$ is the time interval in which the flow conditions change from initial to the final ones, Δp is the static pressure difference between pipeline sections 2–2 and 1–1, Δp_d is the dynamic pressure difference between pipeline sections 2–2 and 1–1, ΔP_f is the pressure drop caused by friction losses between sections 1–1 and 2–2, ρ is liquid density, and, finally, F is the geometrical factor of the examined pipeline segment between pipeline sections 2–2 and 1–1 of length L and defined by the following formula:

$$F = \int_0^L \frac{dx}{A(x)} \tag{2}$$

The flow rate in the final conditions (q_k), if different from zero due to leakage in the closing device, has to be measured or assessed using a separate method.

It is worthwhile to state that the pressure-time method can be used in cases in which the liquid density change and the pipeline wall deformation resulting from the pressure increase caused by stopping the stream of liquid are negligibly small. On the one hand, the objects of interest are rather nonelastic pipes, for instance, steel or concrete pipelines (penstocks), and incompressible liquids, such as water, for instance. On the other hand, pressure rises caused by the stopped stream of liquid in a pipeline should be relatively small—smaller than the possible maximum values, which are observed in the conditions of a so-called "simple water hammer" caused by a very fast closure of cut-off devices, i.e., in the time shorter than that of the pressure wave passage from one pipeline end to the other one and backward. In other words, when this method is used, the closure duration for the devices cutting off the flow should be at least several times longer than the wave passage time [6].

The integral formula (1) reveals that in order to determine the flow rate Q_0, the pressure drop ΔP_f caused by hydraulic loss in the examined pipeline segment and the dynamic pressure difference Δp_d in the hydrometric sections of the pipeline should be extracted from the measured static pressure difference Δp between these sections. The values of Δp_d and ΔP_f can be calculated using their dependencies on the flow rate square. The need for calculating these quantities unfavorably affects the measurement accuracy. However, since the nature of water flow in large-dimension penstocks is strongly turbulent, the use of these dependencies (functions) returns good results, especially for steady-state and for unsteady, slowly changing flows. Moreover, Refs. [7,8] showed that dissipation of mechanical energy during flow deceleration (taking place when the pressure-time method is applied) is slightly less than that obtained from the quasisteady hypothesis, which is in opposite to accelerating flow where energy dissipation is much larger. Some of unsteady friction loss models in the closed conduits use these features [9]. These models have been confirmed experimentally—there is a high conformity between experimental and numerical results of water hammer course [10,11].

Besides the simplifications discussed above, other main sources of inaccuracy of the considered flow measurement method include the inaccuracy of the measuring devices used [12], the numerical calculations applied, and the determination of the F factor. The problem of determining the F factor (Eq. (4)) in case of the pressure-time method applied to a curved pipeline measuring segment is the main topic of this paper.

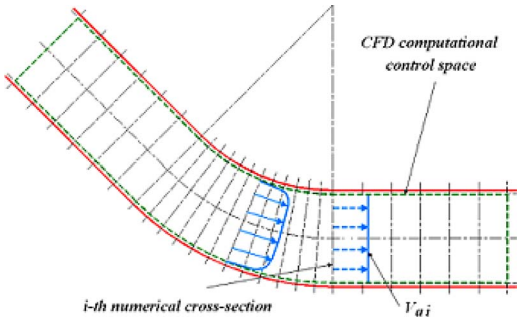

Fig. 1 A pipeline elbow with marked computational space

3 Proposal for the Problem Solution

The geometrical factor F (Eq. (2)) for a pipeline segment of length L, consisting of K subsegments with different dimensions, can be calculated using the following formula:

$$F = \int_0^L \frac{dx}{A(x)} = \sum_{k=1}^{k=K} \frac{l_k}{A_k} \quad \text{with} \quad \sum_{k=1}^{i=K} l_k = L \tag{3}$$

with l_k and A_k denoting the length and internal cross-sectional area of the kth subsegment, respectively.

The value of the geometrical factor F, as determined from Eq. (3), is generally correct for a straight pipeline segment with no irregularities. It does not account for changing the velocity profiles in a curved pipe flow element. Therefore, in order to take into account the influence of the irregular shape of a considered flow element on the Gibson method results, the authors of this paper propose the following procedure of calculation (see Fig. 1):

Step 1. Determine the boundary conditions (geometry of the considered pipeline flow system, discharge Q_j, etc.) and assume the computational control space.

Step 2. Divide the computational control flow space in n numerical segments using cross sections normal to the axis of the considered ith ($i=1,2,\ldots,n$) pipe segment.

Step 3. Simulate velocity distributions (velocity field $V(x,y,z)$) in the flow elements of the considered pipeline within the frame of the computational control space by means of a relevant computer software (for instance, FLUENT™).

Step 4. Compute average values of flow velocity V_{ai} for each ith numerical cross section from the previously derived CFD results (Step 3) and the assumption of equal kinetic energy resulting from the simulated and the uniform flow velocity distribution

$$\dot{e}_{k\mathrm{CFD}i} = \dot{e}_{kai}, \quad \rho = \text{const} \tag{4}$$

$$\dot{e}_{k\mathrm{CFD}i} = \int_{A_i}\int \frac{1}{2}V_i^2[\rho V_i dA] = \frac{1}{2}\rho\int_{A_i}\int V_i^3 dA \tag{5}$$

$$\dot{e}_{kai} = \tfrac{1}{2}\dot{m}V_{ai}^2 = \tfrac{1}{2}\rho A_i V_{ai}^3, \quad \dot{m} = \rho V_{ai}A_i \tag{6}$$

⇓

$$V_{ai} = \left(\frac{\int_{A_i} \int V_i^3 dA}{A_i} \right)^{1/3} \tag{7}$$

where V_i denotes the flow velocity axial component (perpendicular to the ith cross section).

Step 5. Basing on the continuity equation $Q_j = V_{ai} A_{ei} = \text{const}$, compute the equivalent value of cross-sectional area A_{ei} for each numerical cross section $(i = 1, 2, \ldots, n)$

$$A_{ei} = \frac{Q_j}{V_{ai}}, \quad i = 1, 2, \ldots, n \tag{8}$$

Step 6. Compute coordinates of flow velocity centers in all chosen ith numerical cross sections $i = 1, 2, \ldots, n$

$$x_{Ci} = \frac{\int_{A_i} \int xV(x,y,z)dA}{V_{ai} A_{ei}}$$

$$y_{Ci} = \frac{\int_{A_i} \int yV(x,y,z)dA}{V_{ai} A_{ei}}$$

$$z_{Ci} = \frac{\int_{A_i} \int zV(x,y,z)dA}{V_{ai} A_{ei}} \tag{9}$$

Step 7. For the considered flow rate Q_j through the analyzed pipe element, compute the equivalent value of the factor F_{eQj} from the following formula:

$$F_{eQj} = \sum_{i=1}^{n-1} \frac{l_{i \to i+1}}{0.5(A_{ei} + A_{ei+1})} \tag{10}$$

where $l_{i \to i+1}$ is the distance between the resultant velocity centers for computational sections i and $i+1$, and A_{ei} and $A_{e\,i+1}$ are equivalent areas of computational cross sections i and $i+1$, respectively.

The above computation should be conducted for several discharge values $(Q_j,\ j = 1, 2, \ldots, m)$ from the whole scope of its variation $(0 < Q_j \leq Q_{\max})$. The average value of equivalent F factor, calculated as follows:

$$F_e = \frac{1}{m} \sum_{j=1}^{m} F_{eQj} \tag{11}$$

is recommended to be used in the pressure-time method.

In the calculation procedure presented above, it has been assumed that the changes in the velocity profiles are the same during steady and unsteady (transient) flow conditions. This assumption is close to reality for not very fast closure of turbine wicket gates during Gibson method tests. Practically, such conditions occur in all hydraulic turbines, because it is necessary to protect turbine flow systems from the water hammer destructive effect.

Taking the equivalent value of F_e instead of the value F calculated directly from the pipeline segment geometry, it is possible to increase the pressure-time method accuracy in cases when pipelines are curved.

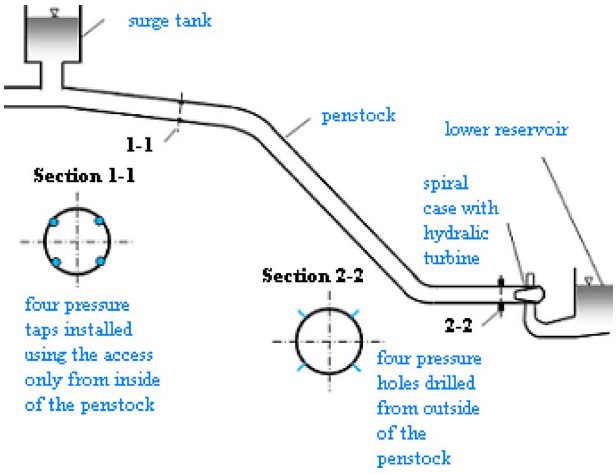

Fig. 2 A schematic of the tested turbine flow system

4 Example

Flow measurement conditions. Figure 2 shows an example of flow rate measurements using the pressure-time method in the hydraulic turbine penstock with two elbows. The flow rate was measured using the pressure-time method in the version based on separate pressure measurements in two hydrometric sections. In each of these sections, four pressure taps were installed and connected by impulse tubes to the manifold and a pressure transducer. A typical manifold was used in the lower penstock section 2–2. The whole system of pressure collection and measurement in this section used the access from the outside of the penstock.

Since there was no access from outside to the upper section 1–1 (the penstock was buried in a rock mass and surrounded by concrete), a special instrumentation for pressure reception and measurement was installed inside the penstock, using a manhole for access [13–16].

The length of penstock subsegments between cross sections 1–1 and 2–2 was determined by direct measurement. The penstock diameters were read from the technical drawings and experimentally verified. The resulting penstock geometry data are presented in Table 1. These data enable determining the F geometrical factor, needed in the Gibson method application, without taking into account the velocity profile changes caused by two elbows in the analyzed penstock segment.

Flow simulation. The flow simulation was conducted using the FLUENT™ 6.3 commercial software (solver). This software employs

Table 1 Geometrical data of the penstock segment measured between cross sections 1–1 and 2–2

Segment name	Segment length, L (m)	Diameter, D (m)	Cross-sectional area, A (m^2)	F factor, $F = L/A$
Cylinder No. 1	14.390	6.5	33.18315	0.433654
Elbow No. 1 (R=23,894 mm)	16.681	6.5	33.18315	0.502700
Cylinder No. 2	68.940	6.5	33.18315	2.077560
Elbow No. 2 (R=25,800 mm)	20.263	6.5	33.18315	0.610649
Cylinder No. 3	19.440	6.5	33.18315	0.585839
Total	139.714			4.210402

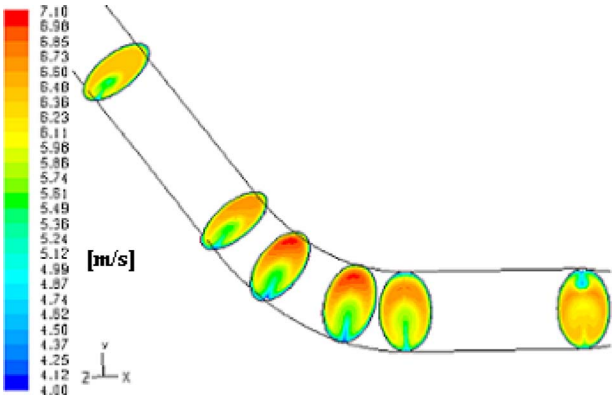

Fig. 3 The velocity magnitude distributions in the penstock cross sections within the elbow no. 2 for mass flow of 200,000 kg/s ($Q = \sim 200\ m^3/s$)

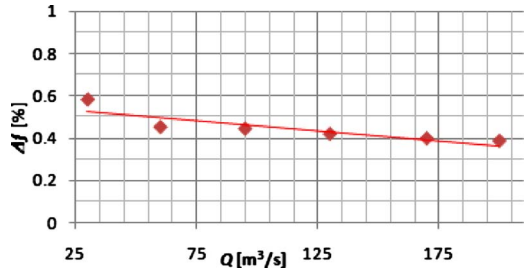

Fig. 4 The values of Δf deviation factor determined for the assumed flow rate values

a cell-centered finite-volume method [17]. The flow was simulated by solving the steady-state Reynolds Averaged Navier–Stokes equations in the full three-dimensional coordinate system.

The geometry of the considered penstock segment was taken from Table 1 and the available design drawings. A computational grid, representing the penstock geometry, was created using the GAMBIT™ 2.4 commercial software. The flow boundary conditions were assumed from the operating parameters of the tested hydraulic turbine.

The k-ω shear stress transport (SST) turbulence model was chosen for computation of the analyzed cases. This turbulence model is very suitable for nonoblique (parallel) flows and also for flow without stagnation regions and strong acceleration. Otherwise, it produces too large turbulence.

Six values of mass flow (or discharge) from the entire range of the flow rate variation (up to 200,000 kg/s to $\sim 200\ m^3/s$) were taken for computations.

The numerical grids with about 1.8×10^6 of hexahedral elements were generated. Basing on the preliminary analysis it was stated that the density of the created grids was satisfactory for the chosen turbulence model and for the analyzed flow cases.

The F factor was calculated between the 1–1 and 2–2 cross sections (Fig. 2). In order to determine the velocity profile with boundary layer at the 1–1 cross section the virtual inflow segment was created. The virtual outflow segment was also created downstream the 2–2 cross section for reducing the effect of outlet section on the simulated back field flow. The flow boundary conditions at the inlet section were assumed in the form of uniform velocity and pressure distributions (with no boundary layer) and the flow boundary conditions at the outlet section were determined by the given turbulence intensity and static pressure.

To obtain the equivalent value of F factor, the penstock segment between 1–1 and 2–2 cross sections was divided numerically into subsegments for which the average velocities were calculated. It is worthwhile to stress that each elbow was divided with higher density than the straight penstock part.

In Fig. 3, the simulation results obtained can be generally characterized as follows. The inflow to the first elbow (Elbow No. 1) is uniform. Elbow No. 1 introduces nonuniformity (disturbance) in the flow pattern, which propagates along the straight penstock segment with decreasing intensity to the second elbow (Elbow No. 2) introducing some additional disturbance to the flow field.

The numerical results so obtained were used to calculate the equivalent factor F_e (according to Steps 4–7 in the procedure presented above). In order to present the results, a deviation factor Δf was introduced. This represents a relative difference between the equivalent factor F_e and the geometrical factor F, calculated as follows:

$$\Delta f = \frac{F_e - F}{F} \tag{12}$$

The quantity Δf, determined as a function of discharge, is presented in Fig. 4. The average value of Δf is about 0.45%. The value $\Delta f = 0.45\%$ was taken to correct the flow rate values following from the preliminary calculation, in the efficiency tests of the considered hydraulic turbine. It is worthwhile to notice that the values of Δf deviation factor are positive and do not change substantially versus flow rate.

It can be concluded that disregarding this correction may result in overestimation of the discharge value by $\sim 0.45\%$ and consequently too small value of the measured hydraulic turbine efficiency.

Experimental results. The experiment, described below, was conducted at several power values ranging between 80 MW and 190 MW.

After setting the electric power value, constant guide vane opening was kept for about 240 s in order to stabilize the flow conditions in the entire hydraulic system. After this time period, the hydraulic turbine parameters were recorded for at least 180 s. Then the flow rate measurement was performed using the Gibson method. For this purpose the flow was cut off using the turbine guide vanes. The speed of the closure was close to that applied in emergency turbine stoppage cases. Following the Gibson method requirements, the generator was not disconnected from the electric grid even after the guide vanes were in closed position for a time period of about 60 s required for stabilization. It caused absorption of small power from the electric grid. After this procedure the turbine guide vanes were reopened and measurement at another test point was performed.

In order to measure the pressure at cross sections 1–1 and 2–2, semiconductor pressure transducers with technical data as described below were applied:

(1) measurement range: upper cross section 1–1 (0–1100 kPa) absolute, and lower cross section 2–2 (0–1600 kPa) relative
(2) accuracy class (basic error): 0.1%
(3) linear error: 0.04%

Flow rate values were computed using the GIB-ADAM code [18]. The input data consisted in the recorded time-variations of pressure difference between 1–1 and 2–2 penstock cross sections and factor F, calculated basing on the geometry measurement and the numerical simulation.

Figure 5 shows the time-histories of (1) the recorded wicket gate closure, (2) the static pressures measured in sections 1–1 and 2–2, (3) the static pressure difference resulting from (2), and (4) the flow rate calculated using the GIB-ADAM code. The quantities were recorded with sampling frequency of 500 Hz. The input data files to calculations using GIB-ADAM code were prepared in the ASCII format, applying the sampling frequency of 100 Hz.

The leakage through the closed guide vanes was calculated from the rate of water level fall in the cylindrical penstock seg-

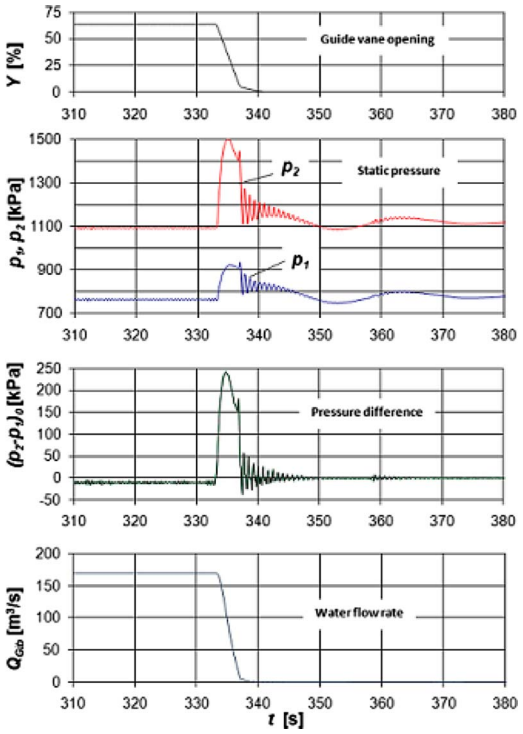

Fig. 5 Pressure changes measured in the turbine penstock measuring sections and the flow rate determined on this basis

ment (with the inlet valve open). The leakage (at low head) was recalculated to the values corresponding to the flow cut-off process (as described above).

Basing on the results following from the executed tests, the efficiency characteristics were derived. For instance, two efficiency curves are presented in Fig. 6. The first curve represents efficiency calculated using the geometrical factor F without correction. The second one represents efficiency calculated using the equivalent value of factor $F=F_e$ obtained according to the above proposed procedure. The correction shows that the F factor increases by 0.45%, which means a decrease in the flow rate and an increase in the hydraulic turbine efficiency.

5 Conclusions

The special, innovative numerical procedure has been developed for evaluating the influence of a penstock elbow (or elbows) on discharge values measured by means of the pressure-time method (Gibson method). The procedure is based on the CFD simulation. It allows calculation of the equivalent value of the geometry factor F for a measuring penstock segment with an elbow (or elbows). The value can improve the discharge measurement results of the standard pressure-time method.

Basing on the developed procedure, for the example of using the pressure-time method for a 180 MW rated power hydraulic turbine fed by penstock with two elbows, it was stated that correction of F factor reduced the discharge results of about 0.45% and, consequently, increased the turbine efficiency of the same value.

The proposed procedure of a flow rate measurement improvement using correction of F factor in the pressure-time method is recommended for cases of penstocks with elbows.

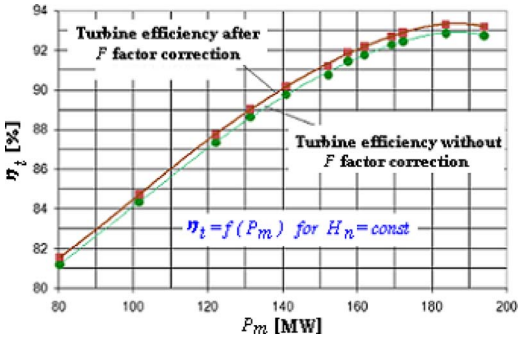

Fig. 6 Turbine efficiency versus mechanical power determined for the *F* factor calculated directly from the penstock geometry and for the *F* factor corrected by the developed procedure

Acknowledgment

Some results of research work published in this paper were presented on the Seventh International Conference on Hydraulic Efficiency Measurements, IGHEM 2008, Milan, Italy, Sept. 3–6, 2008.

Nomenclature

A = area (m^2)
D = internal diameter of a pipeline (m)
$\dot{e}_k$ = kinetic energy (J)
F = geometrical factor of pipeline element (m^{-1})
L, l = pipe length (m)
$\dot{m}$ = mass flow rate (kg/s)
n = total number of numerical cross sections in a pipeline
K = total number of subsegments with different dimensions in a considered pipeline segment
p = pressure (Pa)
Q, q = volumetric flow rate (m^3/s)
t = time (s)
V = flow velocity in a pipe (m/s)
x = distance along pipe axis (m)
x, y, z = linear measures (coordinates) (m)
Y = turbine guide vane opening
z = vertical coordinate of pipe cross-section location (m)
Δf = relative deviation factor of F factor (%)
η = efficiency coefficient (%)
ρ = liquid density (kg/m^3)

Indices

a = average value
d = dynamic pressure value
e = equivalent value
f = friction losses
Gib = discharge determined according the pressure-time method
i = number of a numerical cross section in the pipe
k = final value
max = maximum value
n = rated value
t = water turbine
0 = initial value

References

[1] 1999, IEC 60041: International Standard: Field Acceptance Tests to Determine the Hydraulic Performance of Hydraulic Turbines, Storage Pumps and Pump-Turbines, European Equivalent: EN 60041.
[2] ASME PTC 18–2002, American National Standard: Hydraulic Turbines and Pump–Turbine, Performance Test Codes (Consolidation of ASME PTC 18–1992 and ASME PTC 18.1–1978).
[3] Gibson, N. R., 1923, "The Gibson Method and Apparatus for Measuring the Flow of Water in Closed Conduits," Trans. ASME, **45**, pp. 343–392.
[4] Gibson, N. R., 1959, "Experience in the Use of the Gibson Method of Water

Measurement for Efficiency Tests of Hydraulic Turbines," ASME J. Basic Eng., **81**, pp. 455–487.
[5] Troskolański, A., 1960, *Hydrometry*, Pergamon, New York.
[6] Adamkowski, A., 2001, "Flow Rate Measurement in Operation Conditions of Hydraulic Turbines," Scientific-Technical Monthly Journal POMIARY AUTOMATYKA KONTROLA, pp. 10–13.
[7] Brunone, B., Golia, U. M., and Greco, M., 1991, "Some Remarks on the Momentum Equations for Fast Transients," *International Meeting on Hydraulic Transients With Column Separation, Ninth Round Table*, IAHR, Valencia, Spain, pp. 201–209.
[8] Bughazem, M. B., and Anderson, A., 2000, "Investigation of Unsteady Fiction Model for Waterhammer and Column Separation," *Proceedings of the Eighth International Conference on Pressure Surges*, Hague, The Netherlands, Professional Engineering Publishing Limited, Bury St. Edmonds and London, UK, pp. 483–498.
[9] Brunone, B., Golia, U. M., and Greco, M., "Modelling of Fast Transients by Numerical Methods," *International Meeting on Hydraulic Transients With Water Column Separation, Ninth Round Table*, IAHR, Valencia, Spain, pp. 273–280.
[10] Bergant, A., and Simpson, A., 1994, "Estimating Unsteady Friction in Transient Cavitating Pipe Flow," *Proceedings of the Second International Conference on Water Pipeline Systems*, Edinburgh, Scotland, pp. 3–16.
[11] Adamkowski, A., and Lewandowski, M., 2006, "Experimental Examination of Unsteady Friction Models for Transients Pipe Flow Simulation," ASME J. Fluids Eng., **128**, pp. 1351–1363.
[12] Adamkowski, A., and Janicki W., 2007, "Influence of Some Components of Pressure-Time Method Instrumentation on Flow Rate Measurement Results," International Conference of HYDRO2007, Granada, Spain, Oct. 15–17.
[13] Adamkowski, A., Janicki, W., Kubiak, J., Urquiza, B. G., Sierra, E. F., and Fernandez, D. J. M., 2006, "Water Turbine Efficiency Measurements Using the Gibson Method Based on Special Instrumentation Installed Inside Penstocks," *Proceedings of the Sixth International Conference on Innovation in Hydraulic Efficiency Measurements*, Portland, OR, Jul. 30–Aug. 1, pp. 1–12.
[14] Kubiak, J., Urquiza, B. G., Adamkowski, A., Sierra, E. F., Janicki, W., and Rangel, R., 2005, "Special Instrumentation and Hydraulic Turbine Flow Measurements Using a Pressure-Time Method," *Proceedings of the 2005 ASME Fluids Engineering Division Summer Meeting and Exhibition*, Houston, TX, Jun. 19–23, Paper No. FEDSM2005–77394.
[15] Adamkowski, A., Janicki W., Urquiza B. G., Kubiak J., Basurto M., 2007, "Water Turbine Tests Using the Classical Pressure-Time Method With Measuring Instrumentation Installed Inside a Penstock," International Conference of HYDRO2007, Granada, Spain, Oct. 15–17.
[16] Urquiza, G., Adamkowski, A., Kubiak, J., Janicki, W., and Fernandez, J. M., 2007, "Medicion del flujo de una turbina hidraulica de 170 MW utilizando en metodo Gibson," Ingenieria Hidraulica en Mexico, **XXII**(3), pp. 125–137.
[17] 2006, FLUENT 6.2 Documentation.
[18] Adamkowski, A., and Waberska, G., 2005, "Updating of the GIB-ADAM Software to Determine the Flow Rate From the Time Variations of Pressure Difference Between Two Hydrometric Sections of a Closed Conduit," IMP PAN No. 5114/05, Gdansk (unpublished).

Combustion Oscillations in Bluff Body Stabilized Diffusion Flames With Variable Length Inlet

M. Madanmohan

S. Pandey

A. Kushari

Department of Aerospace Engineering,
Indian Institute of Technology Kanpur,
Kanpur UP 208016, India

K. Ramamurthi
Department of Mechanical Engineering,
Indian Institute of Technology Madras,
Chennai 600 036, India

This paper describes the results of an experimental study to understand the influence of inlet flow disturbances on the dynamics of combustion process in bluff body stabilized diffusion flames of liquid petroleum gas and air. The results show the influence of weak disturbances created by the change in incoming pipe length on the amplitude of pressure oscillations and the phase angle between pressure and heat release. It is seen that the phase delay increases as the entry length increases. The rms value of pressure, however, generally falls with the increase in length. The phase angle is seen to be in the second quadrant, showing that the heat release oscillations damp the pressure oscillations. Therefore, the decrease in the phase angle results in the reduction in damping and hence an increase in pressure fluctuations. The dominant frequencies of combustion oscillations are found to be the low frequency oscillations, and the frequency of oscillations increases with a decrease in the inlet pipe length and an increase in the flow Reynolds number. It is suggested that such low frequency oscillations are driven by vortex shedding at the wake of the bluff body, which energizes the diffusion and mixing process.
[DOI: 10.1115/1.3078387]

Keywords: combustion instability, bluff body stabilization, diffusion flames

1 Introduction

Combustion instabilities are characterized by large amplitude pressure oscillations driven by heat release oscillations that can occur in a wide range of combustion systems. Combustion instabilities are particularly hazardous when they crop up in high performance propulsion systems [1,2] and perturb the normal operation and in extreme cases may lead to devastating effects [3]. A general feedback loop leading to the combustion instability was described by Zinn and Lieuwen [4]. Yu et al. [5] studied low frequency pressure oscillations in a model ramjet combustor driven by periodic vortex shedding at the instability frequency. Pressure and heat release oscillations showed the Rayleigh criterion [6] to be satisfied to drive the instability. Poinsot et al. [7] investigated vortex driven acoustically coupled combustion instabilities and studied the vortex shedding, growth, interaction, and burning and showed that the heat release rate is closely related to the vortex history and the instability follows Rayleigh's criteria. The review paper on combustion instability by Schadow and Gutmark [8] summarized the vortex shedding and vortex-combustion interactions driving the combustion instability. They showed that the vortex shedding in the cold flow is magnified by acoustic modes or the external forcing, and in view of the reduced acoustic emission from nonreacting vortices, a closed feedback loop was not possible. However, the periodic heat release due to the vortex shedding in reacting flows closed the loop. Bakrozis et al. [9] studied the turbulent structure of reacting diffusion flame over bluff bodies and showed that the combustion affects the vortex formation and shedding by directly interfering with the process of shear layer interaction initiating double vortex sheet instability.

In the present study, an attempt was made to create weak disturbances in the incoming flow in a bluff body stabilized diffusion flame of air and liquid petroleum gas (LPG) to understand the effect of these disturbances on combustion oscillations. The results reported in this paper suggest a strong influence of the vortex shedding from the edge of the conical flame holder on combustion oscillations. The results obtained in this study would provide inputs for designing an active feedback loop to suppress combustion instabilities through the incoming flow perturbation, which can be readily implemented in practical combustion systems.

2 Experimental Details

The experimental setup used in this study is shown in Fig. 1. Air was supplied to the cylindrical settling chamber from a compressor. A 21 mm diameter feed line is connected to the settling chamber, which delivers the air into the inlet pipe with a 57 mm diameter and a 460 mm length. The length of the inlet pipe can be varied between 140 mm and 300 mm by moving the feed line inside the inlet pipe using a traverse arrangement, operated by a screw, on which the settling chamber and feed line are mounted. The inlet pipe is attached to the combustion chamber inlet that has a rectangular cross section of 10×40 mm^2. This area is gradually tapered to the combustion chamber, which is of a rectangular cross section of 34×51 mm^2 with a length of 191 mm. A quartz window is provided on the combustor for optical access to the flame. Fuel (LPG) is passed into the combustor through the conical flame holder placed inside the combustor to stabilize the flame.

The air and the fuel flow rates were measured using calibrated rotameters of appropriate ranges. The combustor pressure was measured using a strain gauge based water-cooled pressure sensor. A National Instruments (Texas) SC 2043 SG eight-channel strain gauge signal conditioner having an inbuilt low pass filter with a cutoff frequency of 1600 Hz was used to condition the signal from the sensor. The heat release rate was estimated using CH chemiluminescence. The light emitted from the flame was passed through an optical filter of 431 nm and then focused onto a photodiode through a biconvex lens. Calibration of the heat release rate was not carried out, and only the relative values of the heat release rates were used in this study. The signals from the sensors were acquired to a personal computer using a PCI 6036E National Instruments® 16 bit data acquisition card. The data were acquired using LABVIEW 7.0® at a rate of 2^{13} samples/s for 4 s. The phase angle between pressure fluctuations and heat release fluctuation was determined from their cross correlation function.

The mixture of fuel and air was ignited using a spark plug. For a given air and fuel flow rate, the inlet pipe length was varied from 300 mm to 140 mm at a step of 20 mm, and the combustion chamber pressure and heat release rates were measured. The air flow rate was varied from 80 lpm (liters/min) to 150 lpm, which correspond to Reynolds numbers (Re) between 4.8×10^3 and 9.2×10^3, respectively. The Reynolds number was defined for the height of the effective annular passage of air between the combustor walls and the flame holder, which was equal to 36 mm. The fuel flow rate was held constant at 0.077 g/s, so that the overall

Manuscript received June 7, 2008; final manuscript received October 15, 2008; published online May 22, 2009. Review conducted by Nader Rizk.

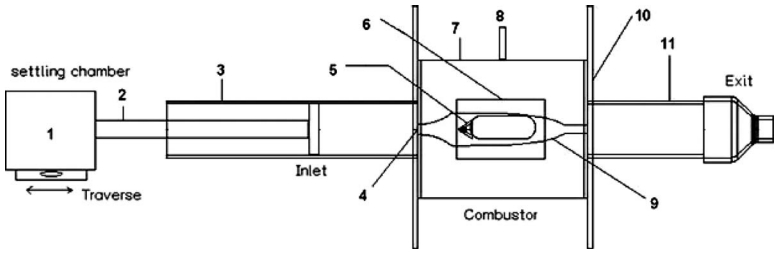

Fig. 1 Diagram of experimental setup: (1) settling chamber, (2) inlet pipe with ram, (3) cylindrical pipe housing the inlet pipe for air supply, (4) combustor inlet, (5) bluff body, (6) quartz window opening, (7) combustor, (8) location of pressure sensor, (9) combustion chamber, (10) supporting plates, and (11) exhaust section

heat addition in the process is constant. The global equivalence ratio corresponding to different air flow rates therefore varied from 0.35 to 0.18.

3 Results and Discussion

The experiments were conducted for the variations in the inlet length and Reynolds number over the range mentioned in Sec. 2. Figure 2 shows the variation in the pressure fluctuations with the change in inlet pipe length. It can be seen in Fig. 2 that the magnitude of the oscillations is much higher for a shorter inlet length than for a longer inlet length, even though the equivalence ratio and the flow Reynolds number are the same. To find the reason for the observed changes with the inlet length, the phase angles between pressure and heat release oscillations with the change in entry length were estimated and are also shown in Fig. 2. It is seen that the phase delay increases as the entry length increases. Furthermore, the phase angle (θ) is seen to be in the second quadrant ($90\ \text{deg} < \theta < 180\ \text{deg}$) showing that the heat release oscillations damp the pressure oscillations. Therefore, the decrease in the phase angle results in the reduction in damping and hence an increase in pressure fluctuations according to Rayleigh's criterion [6].

In order to estimate the frequency of the oscillations seen in the pressure and the heat release rates, the time series data were converted into frequency domain using fast Fourier transform (FFT), and the representative results are shown in Fig. 3. The data presented in Fig. 3 show that for the given conditions, the most dominant frequencies of oscillation in both the sound pressure level and the heat release exactly coincide at a value of 29 Hz. The dominance of such low frequency oscillations suggests that the combustion oscillations in such diffusion flames are not controlled by the standing wave modes (which are of the order of 1 kHz for the present system) present in premixed flames, as reported by Logan et al. [10]. Such low frequency oscillations in jet diffusion flames have been reported by Grant and Jones [11]. Later, Eickhoff and Winandy [12] showed that the low frequency oscillations are governed by the vortex formation, and the subsequent effect of diffusion on the vortex dynamics is responsible for such low frequency oscillations. Similar low frequency oscillations were reported by Uhm and Achraya [13] and Chatterjee et al. [14] in a liquid fueled combustor and a Rijke tube, respectively, leading to amplitude modulation of the pressure spectrum, which they attributed to the bulk mode. The bulk mode oscillations in tubes are primarily governed by the fluid mechanics, and only highly energetic oscillations can lead to the dominance of standing wave modes.

The dominance of low frequency oscillations in the data reported in this paper reveals that the disturbances are fluidic or convective in nature, affecting the diffusion and mixing process, which can be related to the vortex shedding at the edges of the flame holder. In order to further elucidate this feature, the effect of variation in the inlet length on the dominant low frequency oscillation for different Reynolds numbers is presented in Fig. 4. The data in Fig. 4 show that for a given Re the low frequency oscillations remain invariant with a reduction in the pipe length for a while, and then, below a certain length, it starts to increase with a decrease in the inlet pipe length. This may be due to the increase in the frequency of vortex shedding behind the flame holder. A conjecture for the increase in the vortex shedding frequency is given as follows: The tube connecting the settling chamber and the inlet of the combustor has a diameter of 2.1 cm, and the

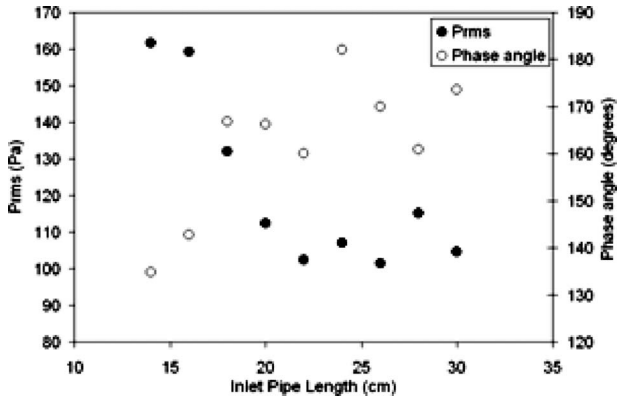

Fig. 2 Variation in the rms pressure and the phase angle between the heat release oscillations and the pressure oscillations with inlet length for $Re = 4.8 \times 10^3$ and an equivalence ratio of 0.35

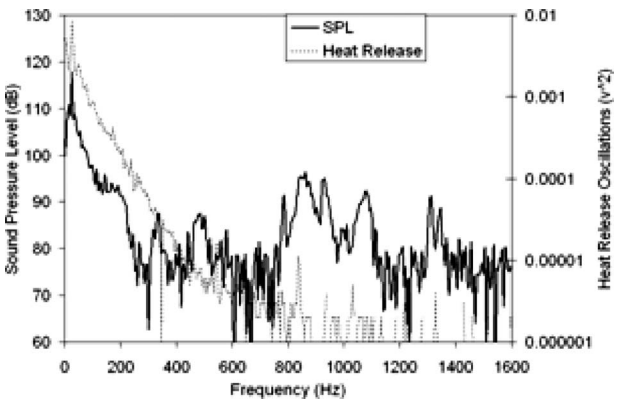

Fig. 3 Frequency domain representation of pressure and heat release oscillations for an inlet length of 14 cm and the flow Reynolds number of 4.8×10^3 (equivalence ratio of 0.35)

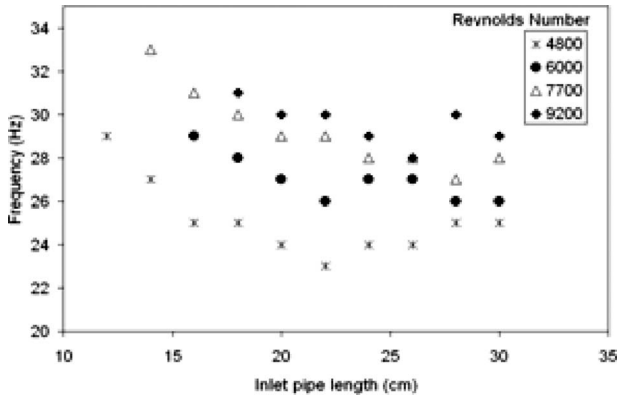

Fig. 4 Dependence of low frequency oscillations on the inlet pipe length for different Reynolds numbers

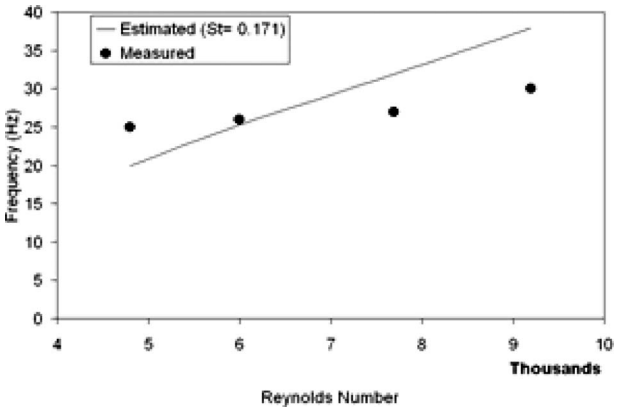

Fig. 5 Comparison of measured and estimated dominant frequency variations for 28 cm pipe length

diameter of the inlet is 1.156 cm. There is an abrupt expansion in the junction, which creates a flow separation region. At the junction between the inlet and the combustor, there is a sudden contraction as the area changes from a circle of diameter of 1.16 cm to a rectangle of area of 4×1 cm^2. Thus, a vena contracta will be formed at the combustor entry plane. The flow at the combustor entry plane will be uniform only when the separated flow at the entry of the inlet reattaches inside the inlet pipe. However, the reattachment length corresponding to the pipe diameter is 16.8 cm [15]. If the inlet length is less than 16.8 cm, the flow will not reattach, the velocity of the flow entering the combustor will not be uniform, and the local variation in the velocity will be high. In other words, the momentum distribution from the central jet to the surrounding air inside the inlet will be less and the core jet will have higher momentum when the length of the inlet is decreased. This results in higher velocity regions at the entry of the combustor for the smaller inlet length. Calvert [16] studied the effect of incoming flow velocity on the vortex shedding frequency for a 60 deg inverted cone immersed in a uniform flow stream and reported a constant Strouhal number ($\mathrm{St}=f_s^* D/V$) of 0.171, where f_s is the frequency of vortex shedding, V is the average flow velocity, and D is the cone diameter. According to the definition of St, the vortex shedding frequency would be proportional to the inlet velocity. Hence, the vortex shedding frequency will be higher for lower inlet lengths and lower for higher inlet lengths.

The data presented in Fig. 4 further show that for a given inlet length, an increase in the incoming flow Re causes an increase in the dominant frequency, which is exactly in accordance to the discussion in the previous paragraph regarding the increase in vortex shedding frequency and its effect on the combustion oscillation frequency. However, the increase in the dominant frequency with Re is not linear, as should have been the case according to the definition of St, as shown in Fig. 5. This confirms the observation made by Grant and Jones [11] that the boundary layer instability is not enough to explain the behavior of low frequency oscillations unless one considers the effect of diffusion and mixing. The reacting flow results reported in this paper are bound to be different from that reported by Calvert [16], which was for cold flow studies. The increase in the flow Re is accompanied by a decrease in the equivalence ratio as the fuel flow rate was kept constant. This leads to a decrease in the flame temperature. The increase in flow velocity results in an increase in mass diffusion. The increased mass diffusion rate improves mixing and hence leads to faster combustion, causing an increase in the combustion frequency. However, the decreasing temperature leads to a decrease in the rate of thermal diffusion, resulting in a delay in combustion. Furthermore, the chemical reaction is also delayed due to the drop in temperature. These cumulative and opposing effects introduce the nonlinearity in the variation in combustion frequency, as seen in Fig. 5.

4 Conclusions

The experimental results presented in this paper show the influence of weak disturbances created by changing the incoming pipe length on the amplitude of pressure oscillations and the phase angle between pressure and heat release. It is seen that the phase delay increases as the entry length increases. The rms value of pressure, however, generally falls with the increase in length. Furthermore, the phase angle is seen to be at the second quadrant ($90 \text{ deg} < \theta < 180 \text{ deg}$) showing that the heat release oscillations damp the pressure oscillations. Therefore, the decrease in the phase angle results in a reduction in damping and hence an increase in pressure fluctuations. The dominant frequencies of combustion oscillations are found to be the low frequency oscillations (order of 30 Hz). The frequency of oscillations increases with an increase in flow Reynolds number. It was seen that the frequency of such oscillations is quite close to the frequency of vortex shedding from a conical body immersed in a nonreacting turbulent flow, as reported in the literature [16]. Therefore, it is suggested that such low frequency oscillations in bluff body stabilized diffusion flames are driven by vortex shedding from the bluff body, which energizes the diffusion and mixing process.

Acknowledgment

This project is sponsored by the ISRO-IIT Kanpur Space Technology Cell. Mr. N. K. Gupta of LPSC is the focal scientist at ISRO.

References

[1] Candel, S., 1992, "Combustion Instabilities Coupled by Pressure Waves and Their Active Control," Proc. Combust. Inst., **20**, pp. 1277–1296.
[2] Putnam, A. A., 1971, *Combustion Driven Oscillations in Industry*, Elsevier, New York.
[3] Lieuwen, T., and McManus, K., 2003, "Introduction: Combustion Dynamics in Lean-Premixed Prevaporized (LPP) Gas Turbines," J. Propul. Power, **19**(5), p. 721.
[4] Zinn, B. T., and Lieuwen, T. C., 2006, "Combustion Instabilities: Basic Concepts," *Combustion Instabilities in Gas Turbine Engines: Operational Experience, Fundamental Mechanisms and Modeling* (Progress in Aeronautics and Astronautics Vol. 210), T. C. Lieuwen and V. Yang, eds., AIAA, Reston, VA, pp. 3–28.
[5] Yu, K. H., Trouve, A., and Daily, J. W., 1991, "Low Frequency Pressure Oscillations in a Model Ramjet Combustor," J. Fluid Mech., **232**, pp. 47–72.
[6] Rayleigh, J. W. S., 1945, *The Theory of Sound*, Dover, New York.
[7] Poinsot, T. J., Trouve, A. C., Veynante, D. P., Candel, S. M., and Esposito, E. J., 1987, "Vortex-Driven Acoustically Coupled Combustion Instabilities," J. Fluid Mech., **177**, pp. 265–292.
[8] Schadow, K. C., and Gutmark, E., 1992, "Combustion Instability Related to Vortex Shedding in Dump Combustors and Their Passive Control," Prog. En-

ergy Combust. Sci., **18**, pp. 117–132.
[9] Bakrozis, A. G., Papailiou, D. D., and Koutmos, P., 1999, "A Study of the Turbulent Structure of a Two-Dimensional Diffusion Flame Formed Behind a Slender Bluff-Body," Combust. Flame, **119**(3), pp. 291–306.
[10] Logan, P., Lee, J. W., Lee, L. M., and Karagozian, A. R., 1991, "Acoustics of a Low-Speed Dump Combustor," Combust. Flame, **84**, pp. 93–109.
[11] Grant, A. J., and Jones, J. M., 1975, "Low-Frequency Diffusion Flame Oscillations," Combust. Flame, **25**, pp. 153–160.
[12] Eickhoff, H., and Winandy, A., 1985, "Visualization of Vortex Formation in Jet Diffusion Flames," Combust. Flame, **60**(1), pp. 99–101.
[13] Uhm, J. H., and Acharya, S., 2004, "Control of Combustion Instability With a High-Momentum Air-Jet," Combust. Flame, **139**(1–2), pp. 106–125.
[14] Chatterjee, P., Vandsburger, U., Saunders, W. R., Khanna, V. K., and Baumann, W. T., 2005, "On the Spectral Characteristics of a Self-Excited Rijke Tube Combustor—Numerical Simulation and Experimental Measurements," J. Sound Vib., **283**, pp. 573–588.
[15] Drewry, J. E., 1978, "Fluid Dynamic Characterization of Sudden-Expansion Ramjet Combustor Flow Fields," AIAA J., **16**(4), pp. 313–319.
[16] Calvert, J. R., 1967, "Experiments on the Low-Speed Flow Past Cones," J. Fluid Mech., **27**(2), pp. 273–279.

Optimization of Controllers for Gas Turbine Based on Probabilistic Robustness

Chuanfeng Wang

Donghai Li

Zheng Li

Xuezhi Jiang

Institute of Simulation and Control for Thermal Power Engineering,
Department of Thermal Engineering;
Key Laboratory for Thermal Science and Power Engineering of Ministry of Education,
Tsinghua University,
Beijing, 100084, China

An optimization method for controller parameters of a gas turbine based on probabilistic robustness was described in this paper. As is well known, gas turbines, like many other plants, are stochastic. The parameters of a plant model are often of some uncertainties because of errors in measurements, manufacturing tolerances and so on. According to model uncertainties, the probability of satisfaction for dynamic performance requirements was computed as the objective function of a genetic algorithm, which was used to optimize the parameters of controllers. A Monte Carlo experiment was applied to test the control system robustness. The advantage of the method is that the entire uncertainty parameter space can be considered for the controller design; the systems could satisfy the design requirements in maximal probability. Simulation results showed the effectiveness of the presented method in improving the robustness of the control systems for gas turbines.
[DOI: 10.1115/1.2981174]

Keywords: gas turbine, probabilistic robustness, Monte Carlo experiment, genetic algorithm

1 Introduction

Gas turbines are now extensively used in aerospace, marine, and industrial applications. With this increasing use in a diverse range of applications, designing controllers for an optimal performance is an important consideration. However, most controllers were designed based on the nominal condition [1–4]. All parts of a gas turbine were considered as ideal systems, and the designed controllers provided a single point consideration of the system response or behavior. In reality, engineering systems are stochastic because of the disturbances and errors in system modeling and identification or due to manufacturing tolerances, so the parameters of models are often of some uncertainties. Without considering the entire uncertainty parameter space, the design method based on nominal conditions can hardly satisfy the requirements when parameters vary. Confronted with this problem, some researchers attempted to design H_∞ based controllers for gas turbines to improve the system's robustness [5,6], which means achieving excellent performance under a wide range of operating conditions. However, such determined design method based on the worst condition encountered some difficulties hardly conquered with the development of robust control technologies. For example, parameter bounds can usually be obtained from physical considerations, while it is often difficult to define meaningful bounds; the underlying assumption is in agreement with conventional modeling and manufacturing practices that consider uncertainties as unstructured, with all directions equally likely, and make small perturbations more likely than large perturbations. This leads to great conservatism. In addition, it is often necessary to transform the real analysis and design problems to fit the design framework in deterministic worst-case approaches. This transformation is always not easy. Some analysis and designing methods are NP hard.

To overcome these deficiencies, such as NP hard complexity and the conservatism associated with the deterministic worst-case framework of robust control, probabilistic robustness gets increasing attention, whose heart is the idea of sacrificing the extreme instances of uncertainty. It is in sharp contrast to the deterministic robust control, which approaches the issue of uncertainty with a "worst-case" philosophy.

References [7,8] showed that the proportion of the systems guaranteeing the robustness requirements can be close to 1 even if the radii of uncertainty set are much larger than the worst-case deterministic robustness margin. Reference [9] qualified the risk worst-case analysis takes and probabilistic analysis takes, and the result illustrated that the deterministic worst-case analysis is not necessarily more reliable than the probabilistic analysis. It is not uncommon for a probabilistic controller (which guarantees only most instances of the uncertainty bounding set assumed in the design) to be significantly less risky than a deterministic worst-case controller. Reference [10] applied the adaptive importance sampling method to the probabilistic robustness analysis problem of an uncertain control system in order to overcome the difficulty that the standard Monte Carlo simulation method cannot efficiently deal with rare events. Probabilistic robustness analysis and design have been applied to the search of a robust AFL controller for a system with uncertainties [8,11–14] and to linear-quadratic-Gaussian regulators [8,12], control of a high-performance aircraft [13], and control of an integrated vehicle [14].

In this paper, probabilistic robustness analysis was applied to optimize controllers for a gas turbine to improve the robustness, maximizing the probability of the system to satisfy requirements under some certain control configuration when the model of gas turbines varies. Simulation examples for two automotive gas turbine models were carried out to show the effectiveness of the proposed method.

The organization of the paper is as follows. Section 2 introduces the optimizing method for controllers based on probabilistic robustness. Two simulation examples for automotive gas turbines are given in Sec. 3. Finally, some concluding remarks are presented in Sec. 4.

2 Optimization Method for Controllers Based on Probabilistic Robustness

Denote a plant structure as $H(q)$, where q is a random vector of parameter uncertainties in the parameter space Q. The probability density function of q is denoted as $pr(q)$. The probabilistic robustness characterize a controller, $C(d)$, with $d \in R^s$ as the design parameters of the controller, with the probability that the closed loop system will have acceptable stability and performance in the presence of possible parameter variations. When all uncertain parameters and adjustable controller parameters are defined, the performance of the controller can be evaluated by examining whether or not it satisfies design requirements. For design requirements on stability and performance, define a corresponding binary indicator function I. The value of I is determined as follows:

$$I = \begin{cases} 1 & \text{design requirements are satisfied} \\ 0 & \text{design requirements are not satisfied} \end{cases} \quad (1)$$

The dependency of I on q and d is represented functionally as

Manuscript received January 28, 2008; final manuscript received May 11, 2008; published online June 4, 2009. Review conducted by Allan Volponi

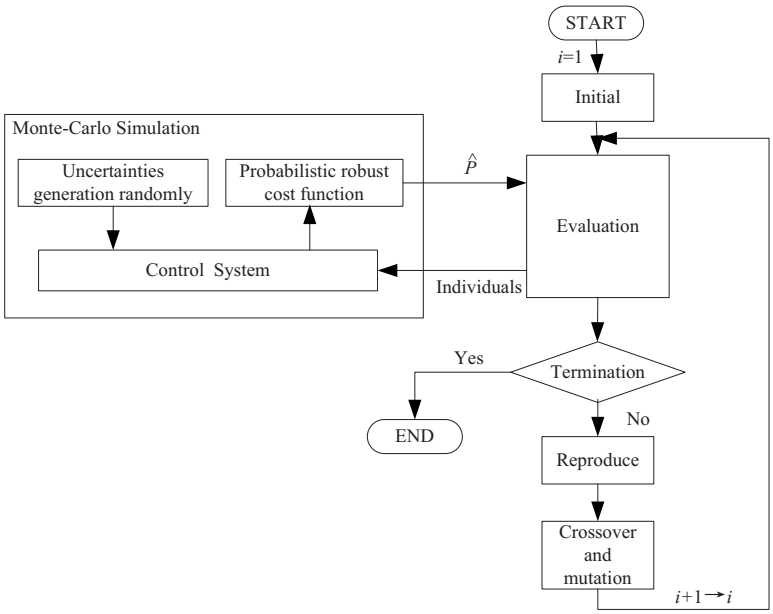

Fig. 1 Probabilistic optimization based on the genetic algorithm

$I=I[H(q),C(d)]$. The probability P that the controller satisfies design requirements can be defined as the integral of the binary indicator function over the parameter space,

$$P(d)=\int_Q I[H(q),C(d)]pr(q)dq \tag{2}$$

Many different aspects of performance can be examined using this probabilistic framework.

The goal of the design is to find the optimal controller parameters d^* that maximizes the satisfaction probability $P(d^*)$. The final design will provide a direct answer on how likely it is that design requirements will be satisfied.

However, in most cases, Eq. (2) cannot be integrated analytically. The Monte Carlo simulation is a practical and efficient way to estimate the satisfaction probability P. The estimate of the probability based on N samples is

$$\hat{P}(q)=\frac{1}{N}\sum_{k=1}^{N} I[H(q),C(d)] \tag{3}$$

The estimated $\hat{P}(q)$ approaches the actual P in the limit as $N \to \infty$.

However, a finite N brings an estimation error while simulating. A minimal N that guarantees a certain confidence level to a risk parameter could be calculated by Massart inequality.

2.1 Massart Inequality. For given risk parameter ε and confidence level $1-\delta$, the sample size is chosen as [15,16]

$$N>\frac{2\left(1-\varepsilon+\frac{\alpha\varepsilon}{3}\right)\left(1-\frac{\alpha}{3}\right)\ln\frac{2}{\delta}}{\alpha^2\varepsilon}$$

with $\alpha\in(0,1)$. Such a sample size ensures $P_r\{|P_x-K/N|<\alpha\varepsilon\}>1-\delta$, where P_x is the probability of the system to satisfy the design requirements, K/N is the estimated value, and K is the number of the design requirements satisfaction in N simulations. The confidence interval is $[K/N-\alpha\varepsilon \quad K/N+\alpha\varepsilon]$.

There are two fundamental difficulties in the optimization of the satisfaction probability in Eq. (3): the evaluation of the probability by Monte Carlo simulations is not deterministic, and the satisfaction probability is nonconvex, with the possibility of multiple minima and large plateau areas [12,13]. Therefore, conventional gradient-based randomized algorithms are not effective in minimizing such a nonconvex satisfaction probability as Eq. (3). In this paper, a genetic algorithms [9,14] is adopted to optimize the controller parameters. The genetic algorithm does not use gradient or Hessian information. In additon, as addressed in Ref. [14], genetic algorithms are less likely to become trapped in a local minimum and are more likely to have probabilistic convergence. The structure of the probabilistic optimization based on genetic algorithm is show in Fig. 1.

3 Application to Gas Turbine Plants

A gas turbine consists of an axial compressor, a combustion system, and a turbine. The air sucked into the engine is compressed by the compressor. Then in the combustion chamber, the compressed air mixed with fuel, which is injected continuously into the chamber, is ignited. The hot gas is expanded through the turbine where energy is extracted. In controlling a gas turbine in their steady state, stabilizing the turbine rotor speed and exhaust temperature to a rated value is very important. The rotor speed is directly related to the quality of the generated power, and the well-controlled exhaust temperature contributes to the energy efficiency of a connected steam turbine. In this paper, we take automotive gas turbines for example. As far as automotive gas turbine power plants are concerned, to improve fuel efficiency at less than full load, they have variable geometry power turbine nozzles. So automotive gas turbine power plants have manipulatable in-

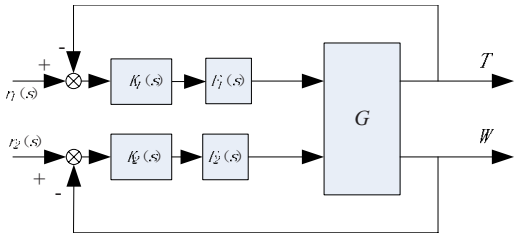

Fig. 2 Control structure for the model in Ref. [1]

Table 1 Parameters and satisfaction probability for the plant in Ref. [1]

Method	K_{p1}	K_{i1}	K_{p2}	K_{i2}	p
Ref. [1]	0.232	5.8	56,700	56,700	0.271
Proposed	0.34751	2.0465	58,367	36,209	0.846

puts, which comprise the power turbine nozzle area and the fuel flow rate to the combustion chamber. The outputs to be regulated are the gas temperature at the nozzle exit and the gas generator speed. Considering the uncertainties presented in Sec. 1, an optimization method based on probabilistic robustness was adopted to optimize the controller parameters to improve the robustness. In the following examples, a scatter of 5% independently around the nominal parameter by uniform distributions was specified for all the elements of the transfer function matrix.

The genetic algorithm used in this paper is developed based on the basic frame of genetic algorithm optimization toolbox (GAOT) [17], and is implemented in MATLAB6.5 environment. Each optimized controller is obtained by choosing the best result out of three independent GA runs. An elitist strategy is also introduced, which means that the optimum individual in the ith generation will enter the $(i+1)$th generation directly and will replace the worst one of it. It has been proven that a genetic algorithm with an elitist strategy has global convergence [18,19]. During the process of optimization, each candidate control law is evaluated by 500 Monte Carlo simulations; the initial population contains 500 chromosomes. After 20 generations, the genetic algorithm produces control parameters.

While estimating the value of P, the estimated value is fully close to the real value only if N is big enough. In order to improve the calculation efficiency, a small N was adopted in the genetic algorithm. After optimized parameters were obtained, an N big enough determined by the Massart inequality according to risk parameter ε and confidence level $1-\delta$ was used to test the probability that the system satisfies the design requirements. We choose risk parameter $\varepsilon=0.01$, confidence level $1-\delta=0.99$, and $\alpha=0.2$. By the Massart inequality, the minimum number of Monte Carlo simulations needed was obtained as $N=24{,}495$ to describe the performance of the controller more exactly.

3.1 Example 1. Reference [1] has designed a control system for a presented model of gas turbine, which is described as follows:

$$\begin{bmatrix} y_1 \\ y_2 \end{bmatrix} = G \begin{bmatrix} u_1 \\ u_2 \end{bmatrix}$$

where u_1 and u_2 are the fuel mass flow and turbine nozzle area, respectively, and the outputs y_1 and y_2 are the turbine inlet temperature and gas generator speed, respectively.

The plant transfer function is

$$G(s) = \begin{bmatrix} \dfrac{1.3\times10^6 s + 3.36\times10^8}{s^2+392s+13{,}900} & \dfrac{-(5.6s^2+246s+744)}{s^2+28.9s+24.6} \\ \dfrac{9.04\times10^6 s + 2.84\times10^8}{s^3+233s^2+8610s+11{,}900} & \dfrac{83.4s+6300}{s^2+115s+195} \end{bmatrix}$$

The control structure is shown in Fig. 2, where

$$F_1(s) = \frac{1}{s+400}$$

$$F_2(s) = \frac{1}{(s+50)(s+600)}$$

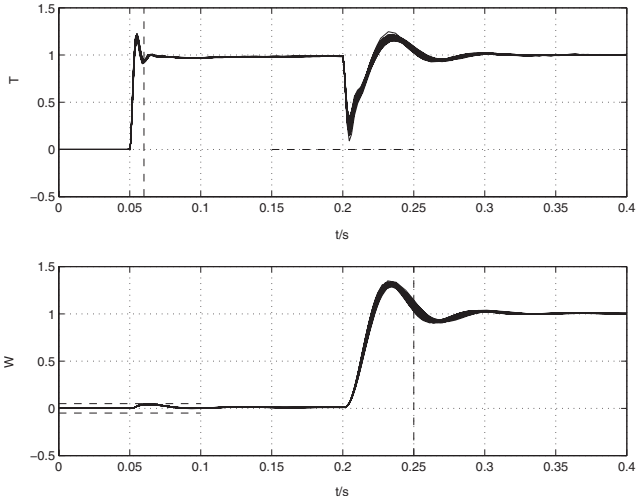

Fig. 3 Response of the controller by the method proposed in this paper

$$K_1(s) = \frac{K_{p1}s + K_{i1}}{s}$$

$$K_2(s) = \frac{K_{p2}s + K_{i2}}{s}$$

The control system is supposed to take into account the following specifications:

(1) response time to a step change in turbine temperature demand less than 0.01 s
(2) response time to a step change in gas generator speed demand less than 0.05 s
(3) maximum excursion in the gas generator speed of magnitude 0.05 in response to a unit step change in turbine temperature demand
(4) maximum excursion in the turbine temperature of magnitude 1 in response to a unit step change in gas generator speed demand

The adjustable parameters of the controller are listed in Table 1. By using the optimization method proposed in this paper, another set of parameters is acquired. The comparison of the correspond-

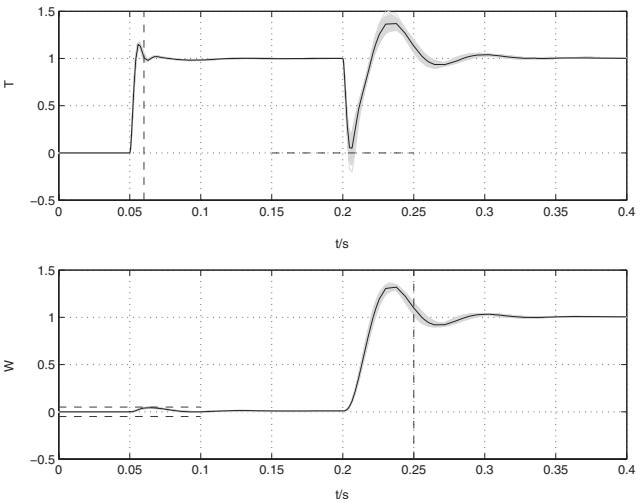

Fig. 4 Response of the controller proposed in Ref. [1]

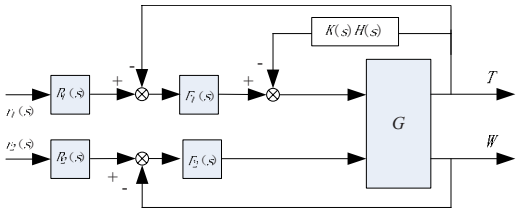

Fig. 5 Control structure for the model in Ref. [2]

ing satisfaction probabilities P between them is in Table 1 as well.

A step change in temperature $r_1(s)$ of magnitude 1 is applied at $t=0.05$; a step change in gas generator speed $r_2(s)$ of magnitude 1 is applied at $t=0.2$. The responses of the turbine temperature (T) and the gas generator speed (W) are given in Figs. 3 and 4.

Table 2 Parameters and satisfaction probability for the plant in Ref. [2]

Method	K_1	K_2	K_3	K_4	p
Ref. [2]	2.8757	1	0.04	0.06666	0.783
Proposed	5.1372	1.5107	0.0693	0.0707	0.978

3.2 Example 2. Reference [2] has designed a control system for another model of gas turbine, which is described as follows:

$$\begin{bmatrix} y_1 \\ y_2 \end{bmatrix} = G \begin{bmatrix} u_1 \\ u_2 \end{bmatrix}$$

where u_1 and u_2 are the fuel mass flow and turbine nozzle area, respectively, and the outputs y_1 and y_2 are the turbine inlet temperature and gas generator speed, respectively.

The plant transfer function is

$$G_1(s) = \begin{bmatrix} \dfrac{1.3 \times 10^6 (s+258.46)}{(s+39.4241)(s+352.5758)} & \dfrac{-5.6(s+3.2674)(s+40.6617)}{(s+28.001)(s+0.95)} \\ \dfrac{9.04 \times 10^6 (s+31.412)}{(s+187.3925)(s+44.1697)^2} & \dfrac{83.4(s+75.5395)}{(s+113.2745)(s+1.7214)} \end{bmatrix}$$

The control structure is shown in Fig. 5, where

$$R_1(s) = 1.3592$$

$$R_2(s) = 1$$

$$F_1(s) = \frac{K_3}{0.0002s^2 + 0.05s + 1}$$

$$F_2(s) = \frac{K_4(s+500)}{(s+50)}$$

$$K(s) = \frac{K_2(s+40)}{(s+400)}$$

$$H(s) = \frac{K_1(s+0.95)}{(s+1.55)(s+187.4)}$$

The control system is supposed to take into account the following specifications:

(1) response time to a step change in turbine temperature demand less than 0.05 s
(2) response time to a step change in gas generator speed demand less than 0.08 s
(3) maximum excursion in the gas generator speed of magnitude 0.1 in response to a unit step change in turbine temperature demand
(4) maximum excursion in the turbine temperature of magnitude 0.5 in response to a unit step change in gas generator speed demand

The adjustable parameters of the controller are listed in Table 2. By using the optimization method proposed in this paper, another set of parameters is acquired. The comparison of corresponding satisfaction probabilities P between them is in Table 2 as well.

A step change in temperature $r_1(s)$ of magnitude 1 is applied at $t=0.005$; a step change in gas generator speed $r_2(s)$ of magnitude 1 is applied at $t=0.1$. The responses of the turbine temperature (T) and the gas generator speed (W) are shown in Figs. 6 and 7.

From Tables 1 and 2 we can find that the value of the satisfaction probability by the method presented in this paper is much larger than that in the reference. It could be found by the simulation results that considering the entire uncertainty parameter space as a whole, the proposed method could optimize the controller parameters to enable the system to satisfy the design requirements in a maximal probability when parameter uncertainties exist. When plant parameters vary, the step response curves are more concentrative, which indicates better robustness.

4 Conclusion

Facing the uncertainties of gas turbines, this paper proposed an optimization method for controllers to maximize the probability

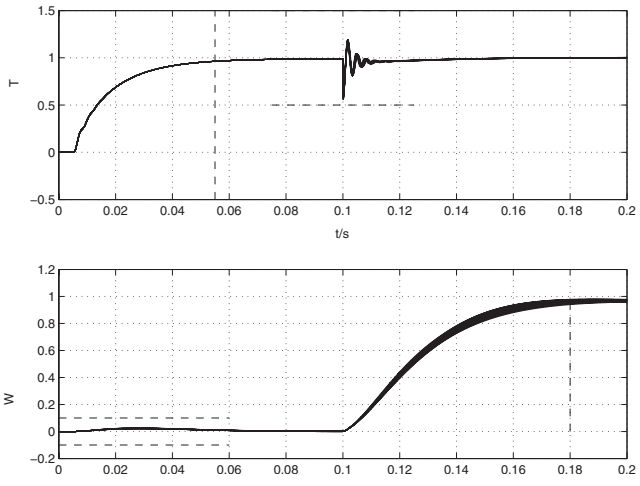

Fig. 6 Response of the controller by the method in this paper

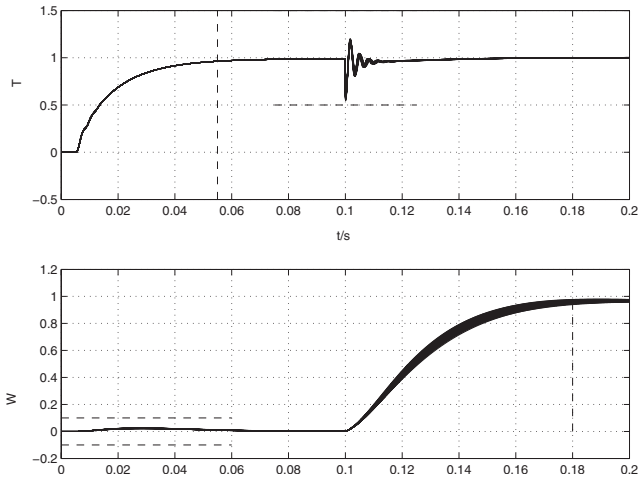

Fig. 7 Response of the controller proposed in Ref. [2]

that the systems satisfy the design requirements. By taking probability distribution and probability density into account, this method has overcome the deficiencies of controllers based on the nominal condition that the parameter uncertainties were not fully considered and global robustness could not be assured and deficiencies such as NP hard complexity and the conservatism associated with the deterministic worst-case framework of robust control. Giving attention to every condition in the uncertainty parameter space, this method has better robustness. Simulation results have shown the effectiveness of the proposed method in improving the robustness in the presence of parameter uncertainties.

References

[1] Leithead, W. E., and O'Reilly, J., 1991, "Multivariable Control by Individual Channel Design an Automotive Gas Turbine Case Study," *Proceedings of the International Conference on Control*, Edinburgh, UK, Mar. 25–28, Vol. 2, pp. 1261–1266.

[2] Whalley, R., and Ebrahimi, M., 2004, "Automotive Gas Turbine Regulation," IEEE Trans. Control Syst. Technol., **12**(3), pp. 465–473.

[3] Kim, J.-W., and Kim, S. W., 2003, "Design of Incremental Fuzzy PI Controllers for a Gas-Turbine Plant," IEEE/ASME Trans. Mechatron., **8**(3), pp. 410–414.

[4] Tavakoli, S., Griffin, I., and Fleming, P. J., 2006, "Tuning of Decentralised PI (PID) Controllers for TITO Processes," Control Eng. Pract., **14**(9), pp. 1069–1080.

[5] Gomma, H. W., and Owens, D. H., 1999, "Robust Control of Gas Generator in a 1.5 MW Gas Turbine Engine," *Proceedings of the 1999 IEEE International Conference on Control Applications*, Kohala Coast, HI, Aug. 22–29, pp. 634–639.

[6] Korson, S., and Helmicki, A. J., 1995, "An H∞ Based Controller for a Gas Turbine Clearance Control System," *Proceedings of the Fourth IEEE Conference on Control Applications*, Dearborn, MI, Sept. 28 and 29, pp. 1154–1159.

[7] Barmish, B. R., 2000, "A Probabilistic Robustness Result for a Multilinearly Parameterized H∞ Norm[C]," *Proceedings of the American Control Conference*, Chicago, June, pp. 1–6.

[8] Calafiore, G. C., Dabbene, F., and Tempo, R., 2000, "Randomized Algorithms for Probabilistic Robustness With Real and Complex Structured Uncertainty [c]," IEEE Trans. Autom. Control, **45**(12), pp. 2218–2235.

[9] Chen, X., Aravena, J. L., and Zhou, K., 2005, "Risk Analysis in Robust Control: Making the Case for Probabilistic Robust Control [c]," *Proceedings of the American Control Conference*, June 8–10, AIAA, Portland, OR, pp. 1533–1538.

[10] Huai-ning, W., and Kai-yuan, C., 2004, "Probabilistic Robust Analysis of Uncertain Control Systems Using Adaptive Importance Sampling," Control Theory & Applications, **21**(5), pp. 812–816 (in Chinese).

[11] Wang, Q., and Stengel, R. F., 2002, "Robust Control of Nonlinear Systems With Parametric Uncertainty," Automatica, **38**(9), pp. 1591–1599.

[12] Tempo, R., Calafiore, G., and Dabbene, F., 2004, *Randomized Algorithms for Analysis and Control of Uncertain Systems*, Springer-Verlag, New York.

[13] Wang, Q., and Stengel, R. F., 2005, "Robust Nonlinear Flight Control of a High-Performance Aircraft," IEEE Trans. Control Syst. Technol., **13**(1), pp. 15–26.

[14] Nohtomi, S., Okada, K., and Horiuchi, S., 2004, "Application of Analytic Hierachy Process to Stochastic Robustness Synthesis of Integrated Vehicle Controllers," Veh. Syst. Dyn., **42**(1–2), pp. 3–21.

[15] Massart, P., 1990, "The Tight Constant in the Dvoretzky-Kiefer-Wolfowitz Inequality," Ann. Probab., **18**, pp. 1269–1283.

[16] Chen, X., Zhou, K., and Aravena, J. L., 2003, "Fast Universal Algorithms for Robustness Analysis," *Proceedings of the 42nd IEEE Conference on Decision and Control*, Maui, HI, Dec., pp. 1926–1931.

[17] Houck, C., Joines, J., and Kay, M., 1995, "A Genetic Algorithm for Function Optimization: A Matlab Implementation," North Carolina State University, Technical Report No. NCSU-IE TR 95-09.

[18] He, J., and Yu, X., 2001, "Conditions for the Convergence of Evolutionary Algorithms," Journal of System Architecture, **47**, pp. 601–612.

[19] Mitchell, M., 1999, *An Introduction to Genetic Algorithms*, MIT, Cambridge, MA.

A Computational Model of the Mark-IV Electrorefiner: Phase I—Fuel Basket/Salt Interface

Robert Hoover

Supathorn Phongikaroon[1]
e-mail: supathor@uidaho.edu

Department of Chemical Engineering,
Nuclear Engineering Program,
University of Idaho-Idaho Falls,
1776 Science Center Drive, Idaho Falls, ID 83402

Shelly Li

Michael Simpson

Tae-Sic Yoo

Pyroprocessing Technology Department,
Idaho National Laboratory,
P. O. Box 1625, Idaho Falls, ID 83415

Spent driver fuel from the Experimental Breeder Reactor-II is currently being treated in the Mark-IV electrorefiner in the Fuel Conditioning Facility at Idaho National Laboratory. The modeling approach to be presented here has been developed to help understand the effect of different parameters on the dynamics of this system. The first phase of this new modeling approach focuses on the fuel basket/salt interface involving the transport of various species found in the driver fuels (e.g., uranium and zirconium). This approach minimizes the guessed parameters to only one, the exchange current density (i_0). U^{3+} and Zr^{4+} were the only species used for the current study. The result reveals that most of the total cell current is used for the oxidation of uranium, with little being used by zirconium. The dimensionless approach shows that the total potential is a strong function of i_0 and a weak function of wt % of uranium in the salt system for initiation processes.
[DOI: 10.1115/1.3078776]

1 Introduction

The Experimental Breeder Reactor-II (EBR-II) is a sodium cooled fast breeder reactor developed at Argonne National Laboratory (ANL) that first went critical in 1965 [1,2]. The spent driver fuel from EBR-II is currently being treated in the Mark-IV (Mk-IV) electrorefiner (ER) in the Fuel Conditioning Facility (FCF) at Idaho National Laboratory (INL) [3]. The Mark-IV ER is a stainless steel vessel with an inside diameter of 100 cm. At the bottom of the ER lies a roughly 10 cm thick layer of molten cadmium (Cd) with 32 cm of a molten LiCl–KCl eutectic containing approximately 10% UCl_3 above the Cd layer [4].

The spent driver fuel containing primarily uranium, zirconium, sodium, and fission products is chopped and placed in stainless steel fuel dissolution baskets (FDBs), which become the anode.

Within this ER the spent fuel is separated into four different streams:

1. pure uranium on the solid stainless steel cathode
2. group actinides (U/TRU) (uranium/transuranic elements) in the liquid Cd pool
3. metallic high-level metal waste form containing the cladding and noble metal fission products from what was remaining in the anode basket
4. ceramic high-level waste forms containing sodium and active metal fission products from the molten salt

The Mk-IV ER is currently used for low throughput systems designed to treat the relatively small amount of spent EBR-II fuel. In order to optimize the design of future systems, an accurate model of electrorefining based on chemical kinetics, chemical thermodynamics, and transport phenomena is needed.

The electrochemical device simulated is comprised of a number of different regions (e.g., fuel baskets, cathode, walls, and electrolyte salt) and interfaces (e.g., basket/salt, pool/salt, wall/salt, and salt/cathode). Each region contains a mixture of chemical species and is separated from other regions by an interface at which a number of different mass transport processes take place. It can be described by a set of parameters, such as species, mole number, size, density, viscosity, etc, as a function of time. The interface reactions between the regions can be driven by mass transport processes under concentration gradients or by electrochemical reactions under electrical potential differences.

The focus area of this study is the initiation at the interface between the fuel basket/anode and the eutectic salt mixture (see Fig. 1).

The fundamental theory is applied and the new implemented mathematical routine is developed to increase the robustness of the initiation and to reduce the complication of several unknown parameters.

2 Fundamental Theory

The equilibrium potential of the half-cell reaction relative to a reference electrode (as shown in Fig. 1) can be given by the approximation of the equilibrium potential, E_i^0, plus concentration overpotentials at the fuel basket/salt interface [5]

$$E_i = E_i^0 + \frac{RT}{n_i F}\ln(\gamma_{i,s}X_{i,s}) \tag{1}$$

where R is the ideal gas constant (8.314 J/mol K), T is the ER operating temperature (K), n_i is the number of electrons of species i in the half-reaction, F is Faraday's constant (96,480 C/eq), γ_i is the activity coefficient of species i, and $X_{i,s}$ is the mole fraction of species i in the salt next to the fuel basket.

From Eq. (1), it is possible to solve for $X_{i,s}$, which is then used to solve for the concentration of species i at the basket/salt interface

$$C_{i,s} = C_{\text{salt}}X_{i,s} \tag{2}$$

where C_{salt} is the sum of the concentration of all the species within the bulk salt (mol/m^3).

The molar mass transfer of species i, N_i (mol/s), can then be determined given the total surface area of the fuel basket/salt interface, A_t.

$$N_i = k_i A_t(C_{i,s} - C_{i,\text{salt}}) \tag{3}$$

where k_i (m/s) is the mass transfer coefficient of species i at the interface and $C_{i,\text{salt}}$ is the bulk concentration of species i in the salt. If $N_i > 0$, mass is transported from the basket to the salt, while if $N_i < 0$, mass transfer occurs in the opposite direction [6].

The current arising due to species i, I_i (A), can then be calculated.

[1]Corresponding author.

Manuscript received August 5, 2008; final manuscript received August 11, 2008; published online June 5, 2009. Review conducted by Dilip R. Ballal. Paper presented at the 16th International Conference on Nuclear Engineering (ICONE16), Orlando, FL, May 12–15, 2008.

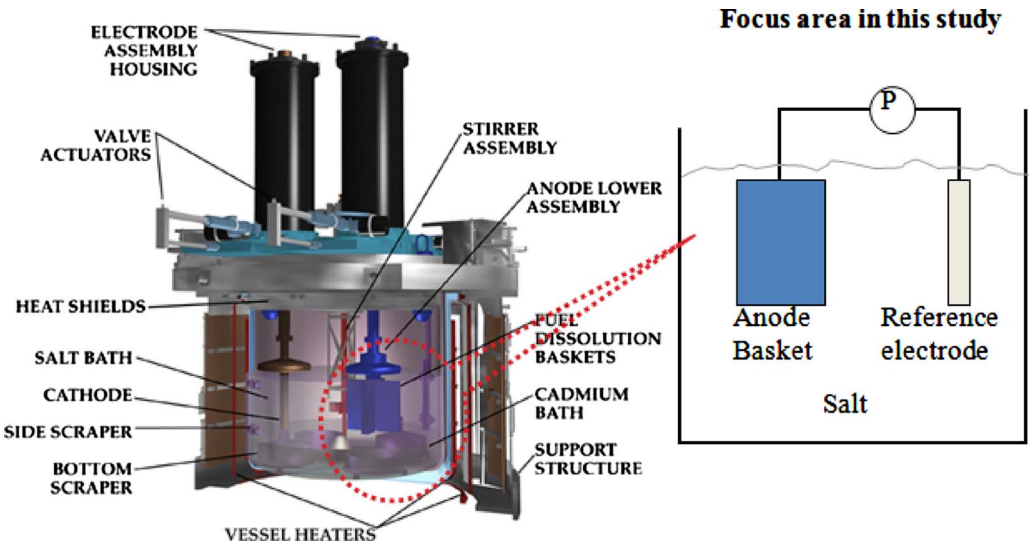

Fig. 1 Focus area of this study

$$I_i = n_i F N_i \tag{4}$$

This current should be equal to that which passes through the interface due to the surface overpotentials, as calculated using the Butler–Volmer equation [7]:

$$I_i = i_0 A_t \left(e^{n_i \alpha F \eta_{i,s}/RT} - e^{-n_i(1-\alpha)F\eta_{i,s}/RT}\right) \tag{5}$$

where i_0 is the exchange current density (A/m^2), α is the anodic transfer coefficient, and $\eta_{i,s}$ is the surface overpotential of species i at the anode surface.

In the end, the sum of the currents arising due to each species must equal the total ionic current at the electrode, or in this case the overall cell current, I_{cell}, that is,

$$\sum_i I_i = I_{\text{cell}} \tag{6}$$

3 Mathematical Methods

The new approach is to focus on the different variables in all proposed theoretical equations and all possible constraints, as shown in Fig. 2. Here, we determine the guessing variables and variables that can be obtained from thermodynamics data and/or operating conditions. From this aspect, there will be two more constraints aside from Eq. (6), which are

$$I_i(E_i) = I_i(\eta_{i,s}) \tag{7}$$

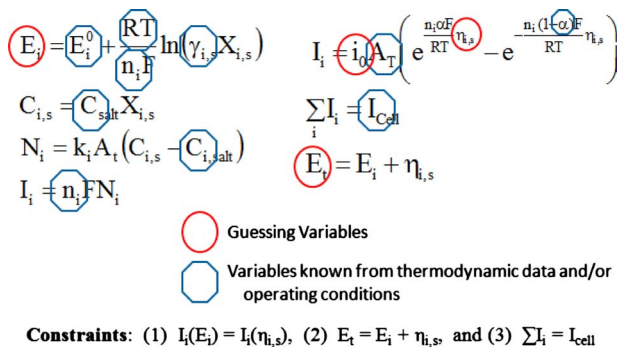

Fig. 2 New modeling approach organization

$$E_t = E_i + \eta_{i,s} \tag{8}$$

where I_i is the current arising due to salt species, E_i is the equilibrium potential drop of the fuel half-cell reaction relative to some reference electrode just outside of the electrode, and E_t is the total anode potential.

For N species, the three constraints will have N, N, and 1 equations, respectively. Therefore, the zero of the system of $2N+1$ equations and $2N+1$ unknowns is simply

$$F(E_1, \ldots, E_N, \eta_{1,s}, \ldots, \eta_{N,s}, E_T) = 0 \tag{9}$$

This system of equations can be solved using the Gauss–Newton optimization method. This new method minimizes the guessed variables down to one, the exchange current density, i_0. This allows the user to alter other variables (e.g., initial wt % of species in salt, mass transfer coefficient, and surface area of the anode basket/salt interface) without affecting the overall solving scheme.

Different case studies can be investigated for each separate interface, while not affecting the solving scheme for the other interfaces and allowing the solution to converge without propagating errors throughout the full simulation.

4 Computational Procedures

The numerical scheme was executed using MATLAB. Results were generated for the following values of i_0 (1 A/m^2, 2.5 A/m^2, 5 A/m^2, 10 A/m^2, 50 A/m^2, 100 A/m^2, 500 A/m^2, 1000 A/m^2, and 5000 A/m^2) and wt % of uranium initially in the salt phase (0, 2, 4, 6, 8, 10, 12, 14, 16, 18, and 20). Here, I_{cell} is fixed at 100 A and other known parameters were obtained from the experimental condition at 450°C with Ag/AgCl reference electrode [4,5,8–11]. U^{3+} and Zr^{4+} were the only species used for the current study because they were the most prevalent species in the system [12]. Thus, in this study, N is 2 and the system has five equations and five unknowns. The general parameters at 450°C are listed in Table 1.

5 Results and Discussion

The current plots of U^{3+} and Zr^{4+} are shown in Fig. 3 as a function of wt % of uranium. They show that at high i_0, wt % of uranium has negligible effect on the current of each species. Figure 3 also shows that I_U is dominant over I_{Zr} in the system. The surface overpotential for U^{3+} ($\eta_{U,s}$) ranges from 0.0022 V to 0.32 V, while Zr^{4+} surface overpotential ($\eta_{Zr,s}$) ranges from 0 to 0.13 V.

Table 1 Important parameters for calculation at 450°C

Variables	Formula/values
V_{mix}	0.251 m^3
C_{salt}	$(mol_U+mol_{salt})/V_{mix}$
α	0.4
γ_U, γ_{Zr}	0.000647, 0.00308
E^0_U, E^0_{Zr}	−1.287 V, −1.088 V
k	1.9×10^{-5} m/s
$C_{U,salt}$	mol_U/V_{mix}
$C_{Zr,salt}$	0 mol/m^3
n_U, n_{Zr}	3, 4
A_t	0.193 m^2

The dimensionless analysis is employed to determine the similarity of the system and to determine the trend and effect of each parameter on the dynamics of this system. Figure 4 shows the plot of dimensionless surface overpotential ($\eta_{U,s}n_U\alpha F/RT$) versus dimensionless current exchange density (i_0A_t/I_{cell}) of U^{3+}. The numerical result shows that wt % of uranium has no effect on surface overpotential. This behavior suggests that the surface overpotential value is fixed at any uranium concentration in the salt and is mainly a function of i_0.

Figure 5 shows the dimensionless current (I_i/I_{cell}) plots. It appears that as the initial wt % of uranium in salt increases, its control of the species' partial currents decreases. It is interesting to note that as i_0 increases more current is carried by the uranium. The figure shows that at $i_0A_t/I_{cell}>0.1$ ($i_0>50$ A/m^2) the partial currents reach the limit of all the current oxidizing uranium. It can be seen that if uranium is of primary interest to be dissolved from the anode basket, it is better to operate at higher i_0.

Figure 6 illustrates the total anode potential plot (E_t). It can be seen that all curves are almost lying on top of each other, indicating that E_t is a strong function of i_0, and a weak function of the initial wt % of uranium in salt.

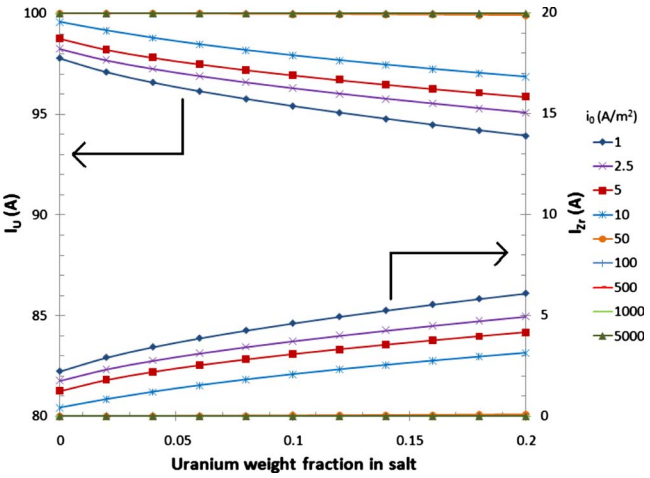

Fig. 3 U^{3+} and Zr^{4+} current plots

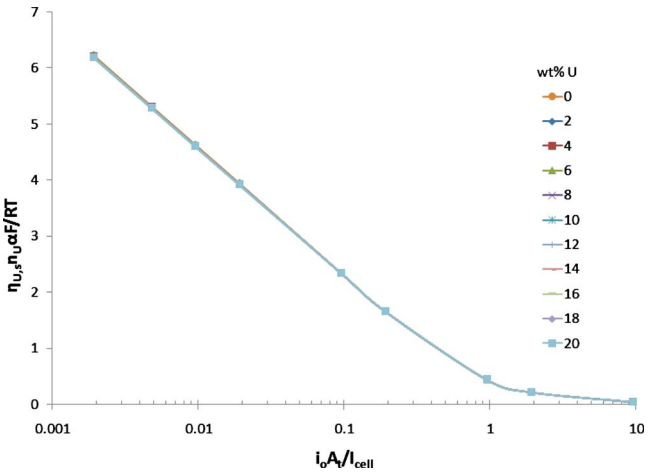

Fig. 4 Dimensionless surface overpotential of U^{3+}

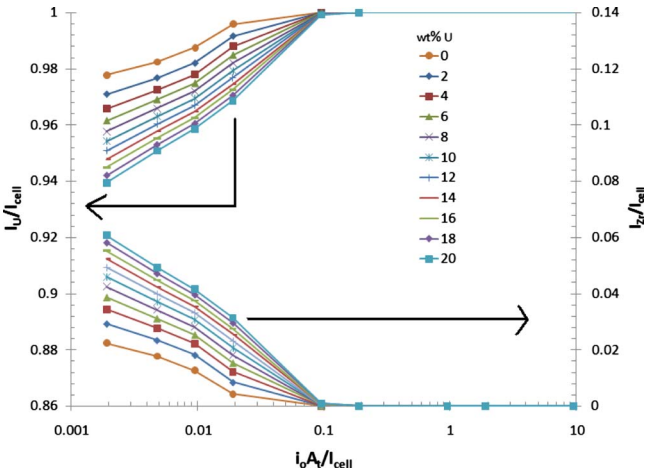

Fig. 5 Dimensionless U^{3+} and Zr^{4+} current plots

6 Conclusions and Recommendations

A new optimization routine has been developed that helps in reducing the global guess parameters. All unknowns have now been based on the value of i_0. Another parameter, wt % of uranium, was used as an additional adjusting variable to show its significant effect in the system. The simulation reveals that (1) I_U is dominant over I_{Zr} in the system, which is the goal of the ER process, (2) E_i is a function of wt % U in salt, and (3) E_t is a strong function of i_0 and a weak function of wt % U in salt. For the future work, other nodes of the ER (e.g., Cd pool/salt interface, vessel walls/salt interface, etc.) will be examined, the number of species will be increased, a time dimension will be added, and an attempt will be made to measure i_0 experimentally in order to validate the computational work.

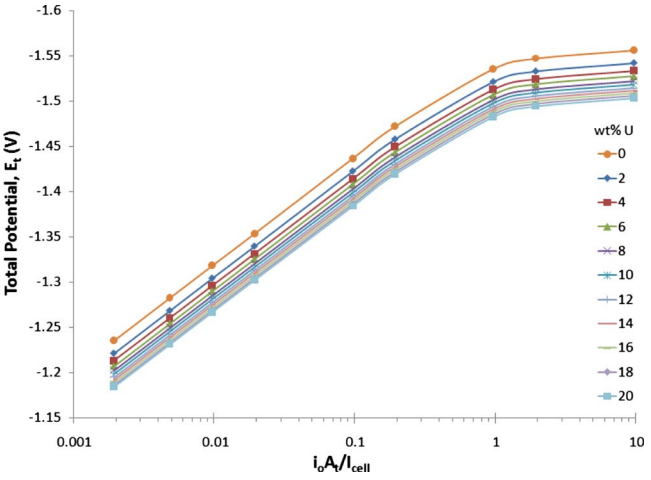

Fig. 6 Total anode potential plot

Acknowledgment

This work was performed for the United States Department of Energy and administered by the Pyroprocessing Technology Department through the Idaho National Laboratory.

Nomenclature

A_t = total surface area of the fuel basket/salt interface
$C_{i,s}$ = concentration of species i at salt/electrode interface
$C_{i,\text{salt}}$ = concentration of species i in the salt phase
C_{salt} = sum of the concentration of all salt species in the bulk
E_i = potential of species i
E_t = total cell potential
E_i^0 = standard potential of species i
F = Faraday's constant
I_i = current arising due to salt species i
I_{cell} = cell current
i_0 = exchange current density
k_i = mass transfer coefficient of species i
n_i = electron number of species i
N_i = molar mass transfer of species i
R = universal gas constant
T = absolute operating temperature
$X_{i,s}$ = mole fraction of species i at the salt/electrode interface
α = anodic transfer coefficient
$\gamma_{i,s}$ = activity coefficient of species i
$\eta_{i,s}$ = surface overpotential of species i

References

[1] Chang, Y. I., 1989, "The Integral Fast Reactor," Nucl. Technol., **88**, pp. 129–138.
[2] Tomczuk, Z., Ackerman, J. P., Wolson, R. D., and Miller, W. E., 1992,"Uranium Transport to Solid Electrodes in Pyrochemical Reprocessing of Nuclear Fuel," J. Electrochem. Soc., **139**, (12), pp. 3523–3528.
[3] Benedict, R. W., and McFarlane, H. F., 1998, "EBR-II Spent Fuel Treatment Demonstration Project Status," Radwaste Magazine, **5**, pp. 23–27.
[4] Li, S. X., and Simpson, M. F., 2005, "Anodic Process of Electrorefining Spent Driver Fuel in Molten LiCl-KCl-UCl_3/Cd System," Miner. & Metall. Proc., **22**(4), pp. 192–198.
[5] Ahluwalia, R. K., and Hua, T. Q., 2002, "Electrotransport of Uranium From a Liquid Cadmium Anode to a Solid Cathode," Nucl. Technol., **140**(1), pp. 41–50.
[6] Middleman, S., 1998, *An Introduction to Mass and Heat Transfer*, Wiley, New York.
[7] Bard, A. J., and Faulkner, L. R., 2001, *Electrochemical Methods: Fundamentals and Applications*, Wiley, New York.
[8] Ahluwalia, R. K., Hua, T. Q., and DeeEarl, V., 2004, "Uranium Transport in a High-Throughput Electrorefiner for EBR-II Blanket Fuel," Nucl. Technol., **145**(1), 67–81.
[9] Bard, A. J., 1976, *Encyclopedia of Electrochemistry of the Elements: Fused Salt Systems*, Vol. X, Marcel Dekker, New York.
[10] Roy, J. J., Grantham, L. F., Grimmett, D. L., Fusselman, S. P., Krueger, C. L., Storvick, T. S., Inoue, T., Sakamura, Y., and Takahashi, N., 1996, "Thermodynamic Properties of U, Np, Pu, and Am in Molten LiCl–KCl Eutectic and Liquid Cadmium," J. Electrochem. Soc., **143**(8), pp. 2487–2492.
[11] Masset, P., Bottomley, D., Konings, R., Malmbeck, R., Rodrigues, A., Serp, J., and Glatz, J. P., 2005, "Electrochemistry of Uranium in Molten LiCl–KCl Eutectic," J. Electrochem. Soc., **152**(6), pp. A1109–A1115.
[12] Iizuka, M., Kinoshita, K., and Koyama, T., 2005, "Modeling of Anodic Dissolution of U–Pu–Zr Ternary Alloy in the Molten LiCl–KCl Electrolyte," J. Phys. Chem. Solids, **66**, pp. 427–432.

Gas Turbine Aero-Engine First Stage Turbine Blade Failure Investigation

Alaaeldin H. Mustafa
Mechanical Services Shops Department,
Saudi Aramco,
P.O. Box 6092,
Dhahran 31311, Saudi Arabia

Hameed H. Badairy

Sudhir Mehta

Research and Development Center,
Saudi Aramco,
P.O. Box 6092,
Dhahran 31311, Saudi Arabia

Plugging material in some of the film cooling channels of a failed aero-gas turbine engine first stage turbine blade is analyzed using the energy dispersive X-ray spectroscopy in an environmental scanning electron microscope. The objective of the analysis was to identify the nature and source of the plugging material that appears to have caused overheating and eventual failure of some of the blades. The results of the analysis indicate that the plugging material, which occurs as a dense aggregate of 0.1 m diameter fibers, is mainly composed of Zr, Y, and O. In addition, the material shows presence of micron size particles dispersed between the fibers. The analysis of the particles indicates they are fluoride-rich compounds, possibly of yttrium or calcium. Small or trace amounts of Ca, Na, and Mg are also observed in the plugging material. The analysis of the areas surrounding the plugged cooling channels shows presence of Cr–Co–Ni–aluminide bond coat and a discontinuous platinum coat over the bond coat. In contrast, the areas surrounding the fractured surface and melted edge show significant presence of calcium fluoride and Mg–Al–silicate. The analysis of melted edge shows presence of all the elements representing various coating layers as well as the impurities; however, Zr and Y were not detected in the melted areas.
[DOI: 10.1115/1.3078782]

Keywords: aero-engines, turbine blade, cooling channels

1 Introduction

It is a recognized fact that contaminations and suspended particles in the environment affect aero-gas turbine engine performance and the engine internal parts adversely. Aero-gas turbine engines have always experienced some amount of environmental contamination in certain areas of the world. The main areas affected are North Africa, China, and the Middle East. The dust, dirt, and sand in the air stream can enter the inner liners of the combustors after passing through the compressor stages and accumulate in the internal parts such as high pressure compressor (HPC) rear stages and high pressure turbine (HPT) blade cooling cavities. The supply of air from the compressor for blade film cooling is thus blocked by the accumulated material, which in turn can cause failure of thermal barrier coatings (TBCs) followed by overheating, thermal stresses, and eventual failure of the blade. Moreover, it is also widely believed that plugging of cooling cavities in the blades adversely impacts combustion chamber, which can lead to cracks, holes, burns, and overheating of fuel nozzles.

Thus, it is essential that for internal cooling and film cooling to be effective, the cooling channels need to be kept clean and clear of any obstacles that might block the flow of air. Failure to keep the cooling air flow channels clear will lead to cooling air starvation at the blades, which in turn can result in catastrophic failure of the blades and turbine.

Few research studies could be found in public domain regarding investigations of the hot gas path components of aero-engines and, in particular, turbine blades. Some of the reported studies include fracture characteristics of the blades, effects of flow rate on the blade cooling system [1,2], Auger microprobe study of the distribution of the microstructure/composition in Co–Cr–Al–Y coatings and a modified Rene'80 substrate of gas turbine blades [3], and the current and future applications of the TBCs in IGTs [4]. It is generally accepted that the TBC can act as thermal insulator reducing the heat transmitted to the component, and the temperature gradient across the coating to allow for higher operating temperature without degradation or distortion of the base metal [5].

The turbine blade under study was from a twin-spool aero-gas turbine engine. The main parts of the engine include one low pressure compressor, four booster stages and nine high pressure compressor stages, one annular combustion chamber, one high pressure turbine stage, and four low pressure turbine stages with a 24,200 lb (107.6 KN) International Standard Atmosphere Sea Level Standard (ISA SLS) maximum take-off thrust. The turbine section of the engine has one stage high pressure turbine stage, which contains 80 blades. In contrast, the low pressure turbine consists of four stages, the first stage with 162 blades, the second and third stages with 150 blades, and the fourth stage with 134 blades. The engines first high pressure turbine blades are air cooled internally in addition to the film cooling technique. The protection of the blade material is further augmented with TBC.

During a routine borescope inspection of an aero-gas turbine engine, material loss in one of the first stage HPT blades was detected. Upon further borescope inspections more damaged blades were found. The engine manufacturer and other operators of the same engine type confirmed that this is a common problem shared by many users. Upon each subsequent borescope inspection it was noted that the problem was spreading all over the fleet. The objective of this study was to determine the identity of the plugging material found in some of the cooling channels of a failed aero-gas turbine engine first stage turbine blade to identify the source of this material.

The analysis was conducted in an environmental scanning electron microscope (ESEM) using backscattered electron imaging and energy dispersive X-ray spectroscopy (EDS). The results on the nature of the plugging material, its possible source, and recommendations to minimize plugging of cooling channels are presented in this paper.

2 Background

Data collected from the operational history record of the concerned fleet showed that there were higher than normal rates (>50%) of unplanned engine removal from service with the midlife inspection (i.e., hot section inspection, HIS) at 7000 $\pm$ 500 cycles and the full-life inspection at 14,000 $\pm$ 500 cycles as the target operational life. In addition, about 89% of the unplanned removals were due to missing HPT blade material, and among the failures that occurred due to the blade cooling cavity plugging—100% occurred above the 2000 cycle mark, and 37% occurred above the 4000 cycle mark with none of the engines reaching the target life cycles on-wing.

Contributed by the International Gas Turbine Institute ASME for publication in the JOURNAL OF ENGINEERING FOR GAS TURBINES AND POWER. Manuscript received August 6, 2008; final manuscript received September 2, 2008; published online June 5, 2009. Review conducted by Dilip R. Ballal.

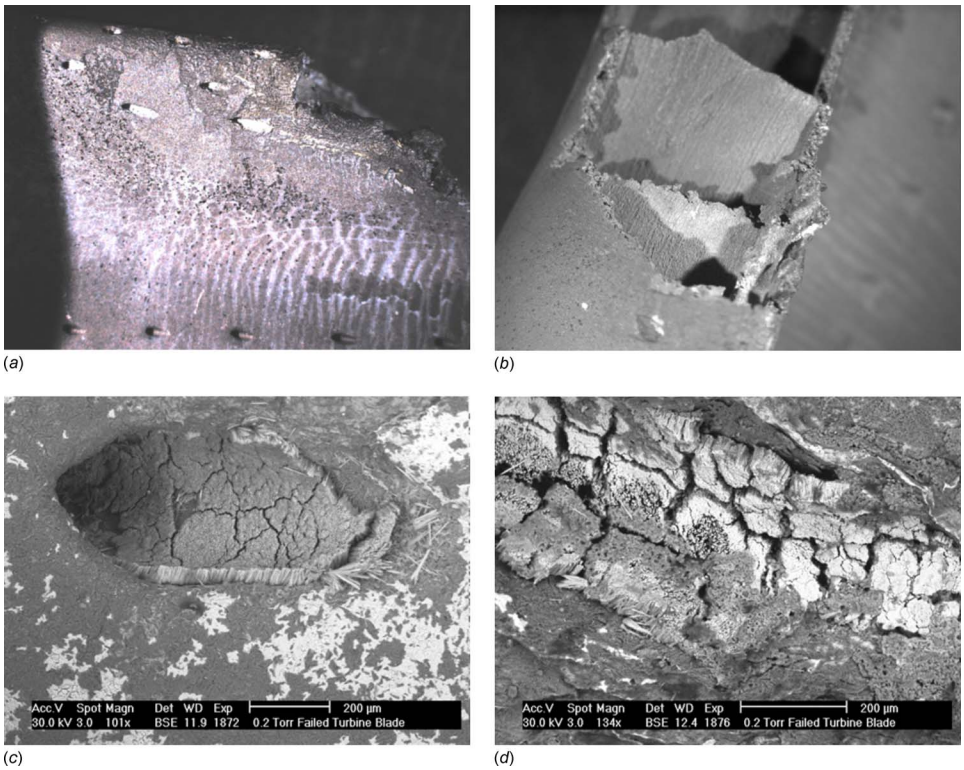

Fig. 1 (*a*) Photo micrograph showing whitish material plugging the cooling channels (red circle), (*b*) photo micrograph of the fractured surface of the failed turbine blade, (*c*) ESEM/BSE image of a plugging material in a cooling channel showing thick growth and fibrous fence surrounding the channel 101×, and (*d*) ESEM/BSE image of another plugged cooling channel. Notice the bright Pt-rich surface and polygonal cracks in the plugging material 134×.

3 Experimental

A failed blade was first photographed to record the location and the nature of the plugged cooling channels, fractures, and melted areas. The blade was then examined in the "as received condition" in an ESEM without any conductive coating. The ESEM was operated in the low vacuum mode at 30 kV acceleration potential and 30 Pa (0.23 torr) chamber pressure. In the ESEM backscattered electrons (BSE) and EDS were used to acquire images and elemental compositions of the plugging material and the coating layers.

The failed areas of the blade were also examined in cross section. Backscattered electron images, EDS X-ray spectra, and elemental X-ray maps were acquired from polished sections to determine the nature and origin of cracks and characteristics of the coating layers.

4 Results and Discussion

The photomicrographs, backscattered electron images, and EDS X-ray spectra of the failed blade are shown in the following figures. Figure 1(*a*) shows whitish material plugging some but not all the cooling channels. Moreover, near the blocked channels the blade shows hot spots, fractures, and melted edges (Fig. 1(*b*)).

Figures 1(*c*) and 1(*d*) show backscattered electron images of the plugging material in the blocked cooling channels. The material appears to have accumulated or grown in the channel as a thick deposit and its surface appears smooth and in some instances seems to be coated with platinum. Also, the material shows numerous polygonal and/or perpendicular cracks but has not disintegrated. This suggests the material is well bonded on the underside with the surface of the cooling channels. The higher magnification images of the plugging material shown in Figs. 2(*a*)–2(*c*) indicate that the material occurs as an aggregate of 50 $\times 0.1$ μm^2 diameter fibers that appear to have grown (accumulated?) vertically inside the channels. The images also show 1 μm size particles that are interdispersed between the fibers (Fig. 2(*c*)).

The EDS X-ray spectra shown in Figs. 2(*b*)–2(*d*) indicate that the fibers are mainly composed of Zr and Y. The EDS spectra also indicate that the micron size particles between the fibers seem to be fluoride-rich and are probably yttrium and/or calcium fluoride. Beside, Zr and Y, the EDS X-ray spectra also show small or trace amounts of Ca, Na, and Mg as impurity in the plugging material.

Figures 3(*a*) and 3(*b*) shows backscattered electron images and EDS X-ray spectra of the areas surrounding the plugged channels. The spectra indicate that these areas have the composition of a Cr–Co–Ni–aluminide bond coat with a top layer of platinum. In contrast, areas surrounding the fractured surface and the melted edges show significant presence of calcium fluoride and Mg–Al–silicate (Figs. 3(*c*) and 3(*d*). In addition, the analysis of the melted edge shows presence of all the elements representing various coating layers as well as the impurities; however, Zr and Y were not detected in the melted areas.

The ESEM-EDS results from the cross-sectional sample analyses are shown in Fig. 4. The results indicate that the integrity of the thermal barrier coating layer was damaged to the extent that it completely failed over most of the blade surface. Also, cracks extending to the base metal were observed. However, in some parts of the blades the coating is still intact as shown in Fig. 4(*c*).

5 Conclusions and Recommendations

It is widely believed that the problem of blade film cooling channels plugging in aero-gas turbine engines and its adverse effects on the engine parts, components, and performance are due to environmental contaminants deposited inside the engine parts. However, the failure investigation of a first stage failed blade conducted in this study indicates that the above assumption is not

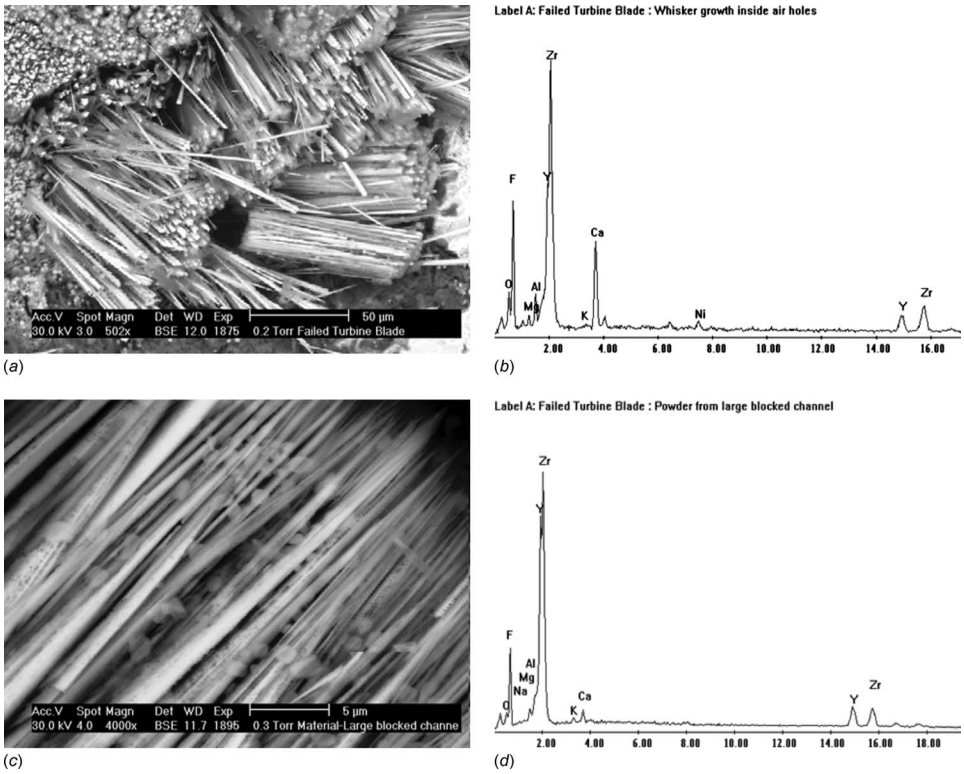

(*a*) (*b*) (*c*) (*d*)

Fig. 2 (*a*) BSE image of the plugging material showing aggregate of fibers underneath the smooth surface 502×; 2B EDS X-ray spectrum of fibers in (*a*) indicating they are mainly compounds of Zr and Y. The Ca and F peaks indicate the presence of Ca–F and/or Y–F compounds with the fibers. (*c*) BSE image of fibers and micron size particles in the plugging material 4000×; (*d*) EDS X-ray spectrum of fibers in (*c*) indicating the presence of Zr and Y. Notice the presence of strong fluorine peak probably originating from small particles with fibers.

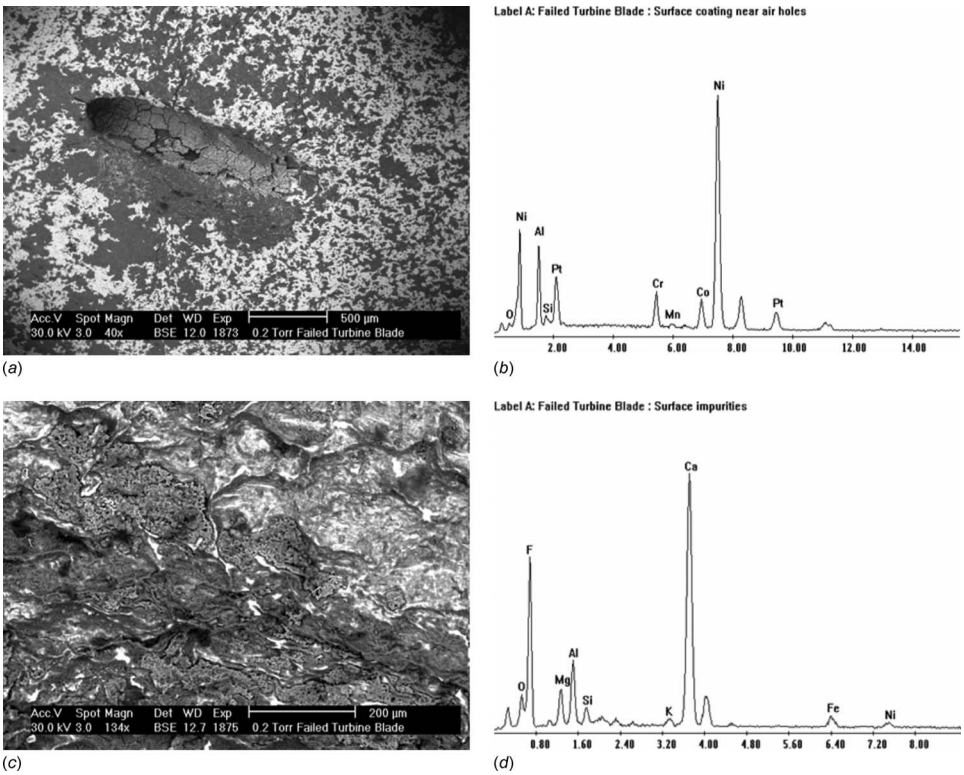

(*a*) (*b*) (*c*) (*d*)

Fig. 3 (*a*) BSE image of a plugged cooling channel surrounded by bright particles on a gray matrix 40×, (*b*) EDS X-ray spectrum of the gray matrix in (*a*) indicating it is Cr–Co–Ni–aluminide bond coat on the blade. The bright areas are platinum on top of the bond coat. (*c*) ESEM image of an area near the melted edge of the blade showing accumulation of dark material 134×; (*d*) EDS X-ray spectrum of the dark material near the melted edge of the blade indicating it is most likely calcium fluoride with minor amounts of Mg–Al–silicate.

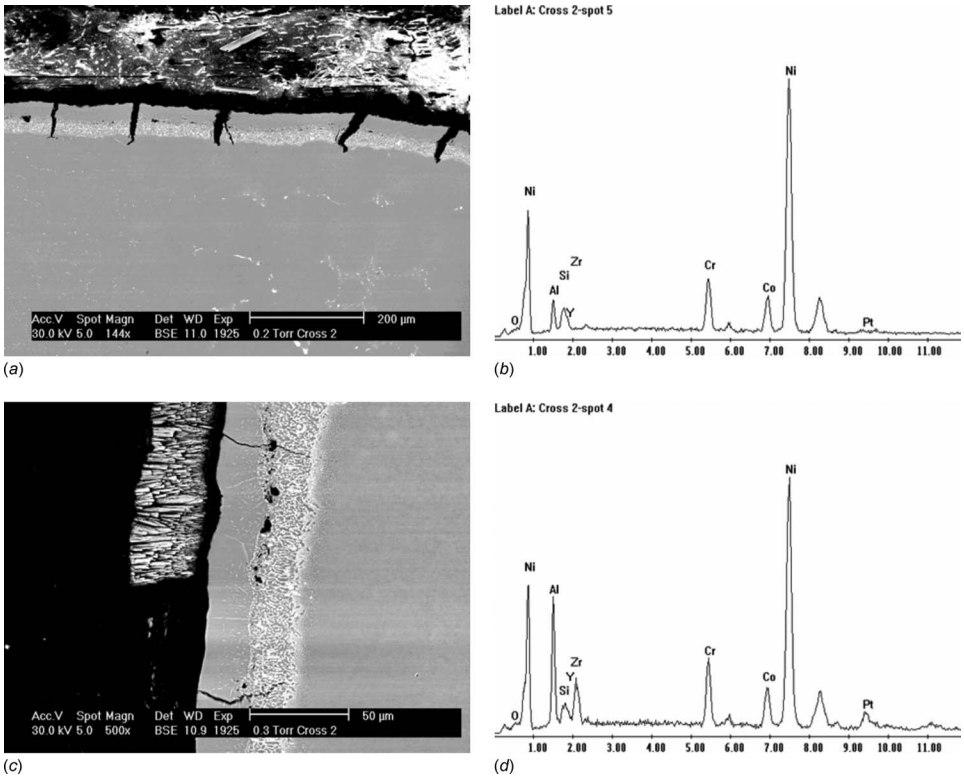

Fig. 4 (*a*) BSE image of a failed blade cross section showing formation of cracks through the Al–Pt–Ni rich layer 144×, (*b*) EDS X-ray spectrum of the base metal in the cross-sectional image shown in (a), (*c*) BSE image of the cross-sectional sample showing partial removal of the TBC from the surface 500×, (*d*) EDS X-ray spectrum of the Ni–Al–Pt rich layer shown as bright band in the cross-sectional image in (*c*)

true, at least in this case. The results of the ESEM/EDS X-ray analysis showed that the failure occurred due to hot spots and melting, which apparently resulted from insufficient cooling of the blade. The cause of insufficient cooling was mainly from plugging of some of the cooling channels with material that has composition and morphology similar to that of yttria stabilized zirconia in TBC. Thus, it appears that the source of the plugging material is most likely the failed TBC on the blade and not any environmental contaminants.

In order to minimize the effects of the film cooling channel plugging, the following recommendations are made.

1. Even though the borescope inspections are conducted as per the intervals guidelines given in the aircraft maintenance manual (AMM) and in line with the industry practices, the frequency of inspections needs to be increased and the time intervals reduced to closely monitor changes in the TBC on turbine blades.
2. The TBC process procedure needs to be reviewed to tighten up the quality assurance process.
3. Rear HPC stages core compressor washing procedures need to be adopted. Also, for fan washing approved detergent rather than water only (as mentioned in standard procedure) should be used. In addition the time intervals for fan washing need to be reviewed.
4. The monitoring of data system to capture any changes in the turbine behavior and performance parameters as indicators of internal engine condition need to be optimized.

References

[1] Bazhenov, V. A., Gulyar, A. I., and Piskunov, S. O., 2006, "Life Assessment for a Gas Turbine Blade Under Creep Conditions Based on Continuum Fracture Mechanics," Strength Mater., **38**(4), pp. 392–397.

[2] Khomenok, L. A., Zolotogorov, M. S., Nikolaev, A. G., Egorov, I. N., Lebedev, A. S., Krivonosova, V. V., and Sundukov, Yu. M., 2008, "Experimental-Calculation Investigations of the Cooled Blades of the GTE-65 Gas-Turbine Unit," Therm. Eng., **55**(1), pp. 50–53.

[3] Kameda, J., Bloomer, T. E., and Sakurai, S., 1999, "Oxidation/Carbonization/Nitridation and In-Service Mechanical Property Degradation of CoCrAlY Coatings in Land-Based Gas Turbine Blades," J. Therm. Spray Technol., **8**(3), pp. 440–446.

[4] Mutasim, Z., and Brentnall, W., 1997, "Thermal Barrier Coatings for Industrial Gas Turbine Applications: An Industrial Note," J. Therm. Spray Technol., **6**(1), pp. 105–108.

[5] Bounazef, M., Guessasma, S., and Bedia, A. A., 2007, "Blade Protection and Efficiency Preservation of a Turbine by a Sacrificial Material Coating," Adv. Power Technol., **18**(2), pp. 123–133.

Design and Experiment of Oil Lubricated Five-Leaf Foil Bearing Test-Bed

H.-J. Xu[1]
e-mail: xuhuaijin@tom.com

Z.-S. Liu

G.-H. Zhang

Y.-L. Wang

Department of Energy Science and Engineering,
Harbin Institute of Technology,
Harbin, 150001, P.R. China

Multileaf foil bearing has various advantages including long-life, high-speed, low power loss, etc. Oil lubricated multileaf foil bearing compared with gas lubricated foil bearing is more favorable to greatly decrease foil performance requirements, foil surface coating technology, and foil processing. The special oil lubricated five-leaf foil bearing test-bed is designed and established, and a speed of 30,000 rpm is achieved primarily. The experiments including the influence of different radial clearances on rotor dynamical characteristics, speed run-up and coastdown, etc., are implemented on the test-bed. The experimental results indicate that oil lubricated multileaf foil bearing can offer high-speed, long-life, and lower friction loss. Radial clearance plays an important role to rotor dynamical characteristics. Moreover, oil lubricated multileaf foil bearing represents strong adaptive capacity of speed run-up and coastdown, and the capacity of withstanding impact and vibration. [DOI: 10.1115/1.3078703]

Keywords: oil lubrication, five-leaf foil bearing, test-bed design, radial clearance, experiment

1 Introduction

Gas foil bearing is a compliant, self-acting, elastic foil hydrodynamic gas bearing. It has many advantages including long-life, high-speed, low energy loss, well hydrodynamic characteristics [1], etc. Multileaf foil bearing was developed by Allied Signal Aerospace Co. (ASAC) under the support of U.S. Air Force and NASA between 1960s and 1970s in the 20th century. The structure of the multileaf foil bearing is shown in Fig. 1(*o*), which includes journal, bearing sleeve, and multileaf foils. The inner surface of the bearing is comprised of leaf foil or foil unit. One end of a leaf foil is rigidly fixed or articulated at the longitudinal groove; the other end freely overlaps on the adjacent foil surface.

For multileaf foil bearing, up to now, the lubricant was mainly focused on gas. Multileaf foil gas bearing was successfully applied to air refrigeration system in the turbo expander of the DC-10, commercial aircraft 727/757/767, air force F-4/15/18, and even A200B, A-7E [1], etc. Between 1971 and 1976, multileaf foil bearing had been installed into small aeronautic gas turbines. In theory and experiment, Sudheer Kumar Reddy et al. [2] established a foil deformation theoretical analysis model, coupled the elastic deformation equation and Reynolds equation, and discussed stiffness and damping coefficients. Radil et al. [3] analyzed the influence of radial clearance of load capacity by experiment and indicated that the optimal radial clearance resulted in the maximal load coefficient. Gu [4] finished the multileaf foil bearing turbopump test with liquid oxygen lubrication in NASA Marshall Space Flight Center (MSFC) and pointed out that multileaf foil bearing had high durability, high reliability, and good stability.

Material, coating, and processing are the key technologies and difficulties for gas foil bearing development [5,6]. However, oil lubricated foil bearing compared with gas foil bearing is favorable to decrease foil material performance requirements, foil surface coating, and foil processing. There was no relevant report about the research of oil lubricated multileaf foil bearing.

The special oil lubricated multileaf foil bearing test-bed is designed and established, and the speed is more than 30,000 rpm.

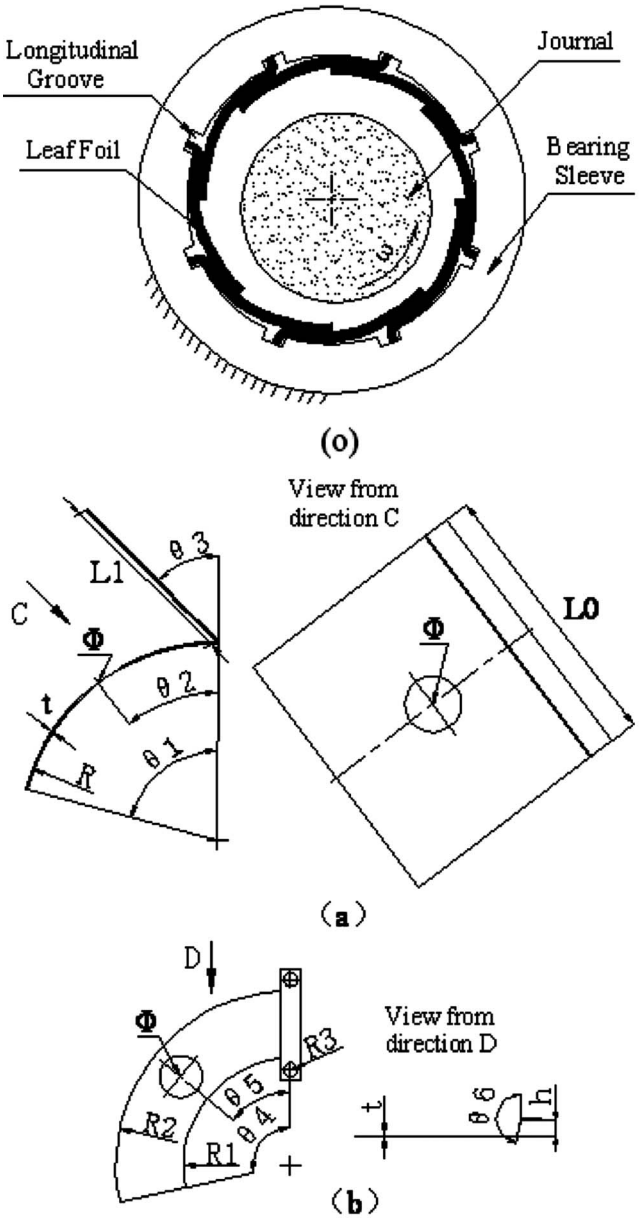

Fig. 1 Multileaf foil bearing configuration (*o*), journal foil (*a*), and thrust foil (*b*) design

[1]Corresponding author.

Manuscript received August 25, 2008; final manuscript received September 8, 2008; published online June 9, 2009. Review conducted by Dilip R. Ballal.

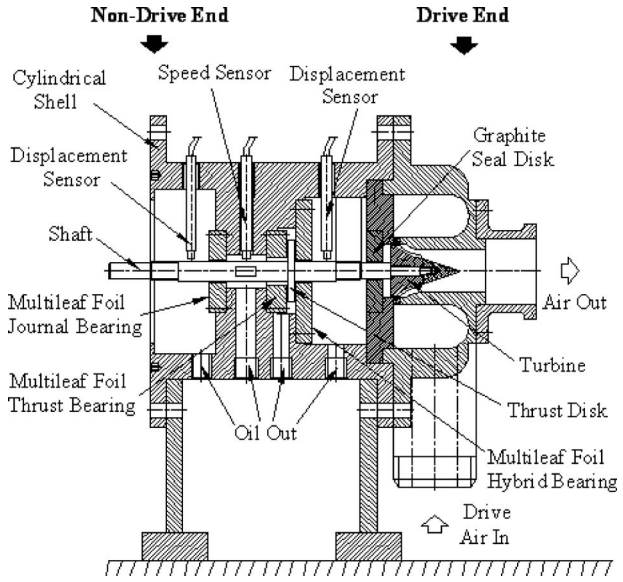

Fig. 2 Structure of five-leaf foil bearing test-bed

Experiments including the influence of different radial clearance on rotor dynamical characteristics, speed run-up and coastdown, etc., have been done on the test-bed. The experimental results show that radial clearance is an important factor to influence rotor dynamical characteristics. Oil lubricated multileaf foil bearing can offer high-speed, long-life, and low friction loss and also represents strong adaptive capacity of speed run-up and coastdown, and the capacity of withstanding impact and vibration.

Table 1 Structural parameters of the test-bed

Parameter	Magnitude
Diameter of cylindrical shell, *Dc*	106 mm
Length of cylindrical shell, *L*	119 mm
Diameter of shaft, *Ds*	10 mm
Thickness of thrust disk, *Td*	3 mm
Diameter of thrust disk, *Dd*	30 mm
Shaft length, *Ls*	160 mm
Diameter of turbine moving blade, *Db*	35 mm
Radial clearance of foil journal bearing, *Cj*	0.10 mm
Maximum axial clearance, *Cs*	0.20 mm
Radial clearance of graphite seal disk, *Cd*	0.20 mm

Table 2 Design parameters of the journal and thrust foils

Parameter	Magnitude
Length of journal foil, *L*0	10 mm
Length of journal foil fixed end, *L*1	4 mm
Radius of journal foil, *R*	7 mm
Angle of journal foil, $\theta 1$	75 deg
Angle of oil hole of journal foil, $\theta 2$	37.5 deg
Angle of fixed end of journal foil, $\theta 3$	45 deg
Diameter of oil hole, $\varnothing$	2 mm
Inner radius of thrust foil, *R*1	7.5 mm
Outer radius of thrust foil, *R*2	12.5 mm
Fixed hole radius of thrust foil, *R*3	0.5 mm
Angle of thrust foil, $\theta 4$	102 deg
Angle of oil hole of thrust foil, $\theta 5$	51 deg
Angle of thrust foil bending, $\theta 6$	170 deg
Height of thrust foil bending, *h*	1.2 mm
Foil thickness, *t*	0.10 mm
Foil Young's modulus, *E*	1.34×10^7 N m^2

2 Test-Bed and Five-Leaf Foil Design

2.1 Test-Bed Design. The structure of five-leaf foil bearing test-bed is designed in Fig. 2. The maximum axial vibration amplitude is given by axial clearance between thrust bearing surface and thrust disk of shaft. The graphite seal disk is applied to seal the leakage air coming from the turbine. Structural parameters of the test-bed are listed in Table 1.

2.2 Journal and Thrust Five-Leaf Foil Design. All bearings are designed as oil lubricated five-leaf foil bearings. The common beryllium bronze is used for foil material. Journal and thrust foils are designed in Figs. 1(*a*) and 1(*b*). Each foil has an oil inlet hole at the foil geometrical center. All design parameters of the journal and thrust foils are given in Table 2.

3 Results and Discussion

At both nondrive and drive ends, displacement sensors are applied to measure the vertical and horizontal vibrations of the rotor. Speed sensor is installed for measuring the rotating speed. Figure 3 depicts Bode diagrams in vertical motion at nondrive (*c*) and drive (*d*) ends with a speed of 20,069 rpm. It shows that the fundamental frequency vibration is the main mode, the maximum

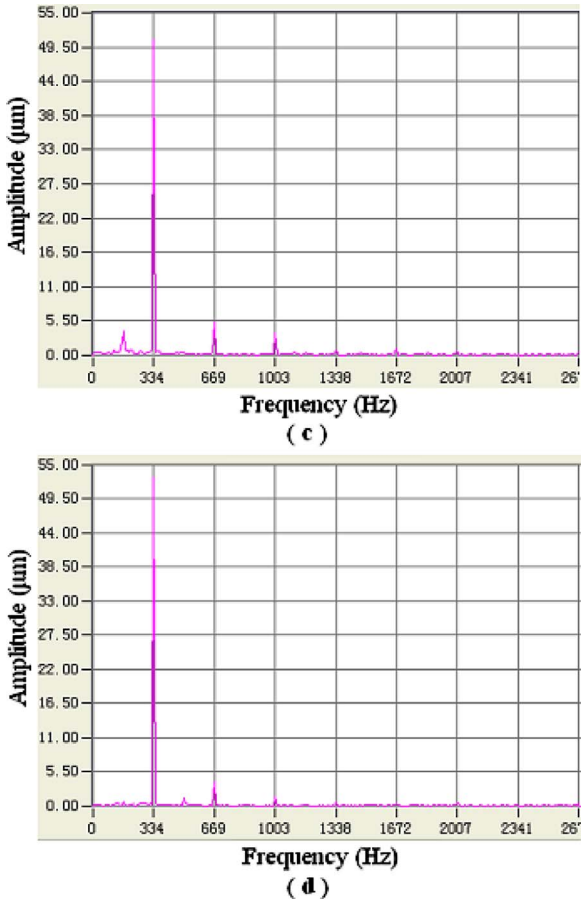

Fig. 3 Bode diagrams in vertical motions at the nondrive (*c*) and drive (*d*) ends with a speed of 20,069 rpm

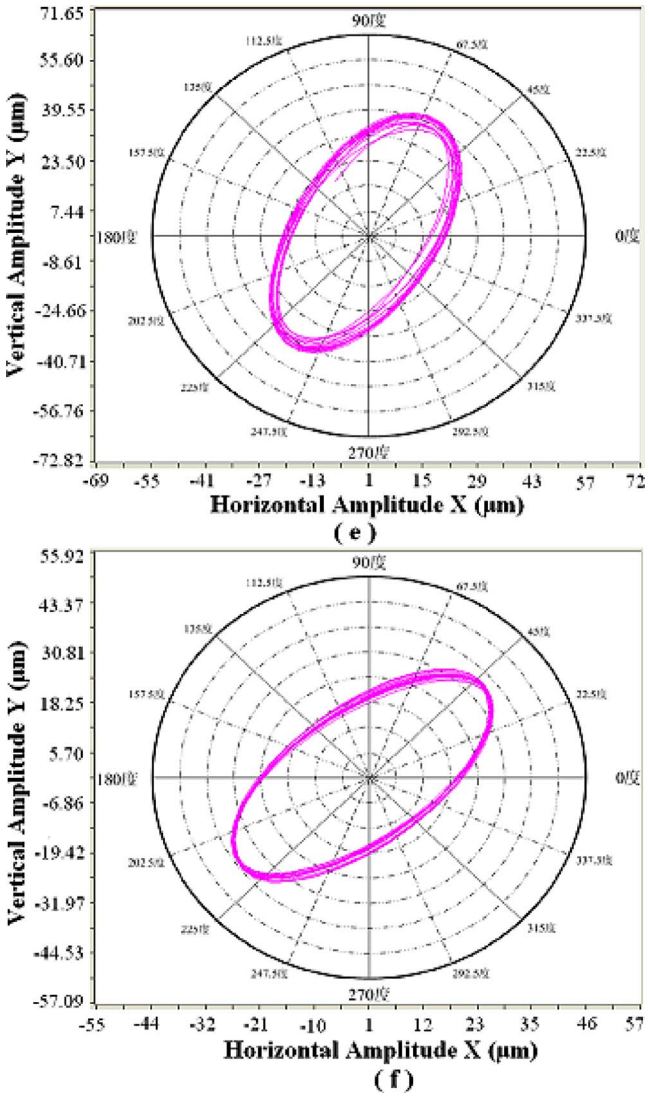

Fig. 4 Axis orbits at the drive end with speeds of 20,069 rpm (*e*) and 27,224 rpm (*f*)

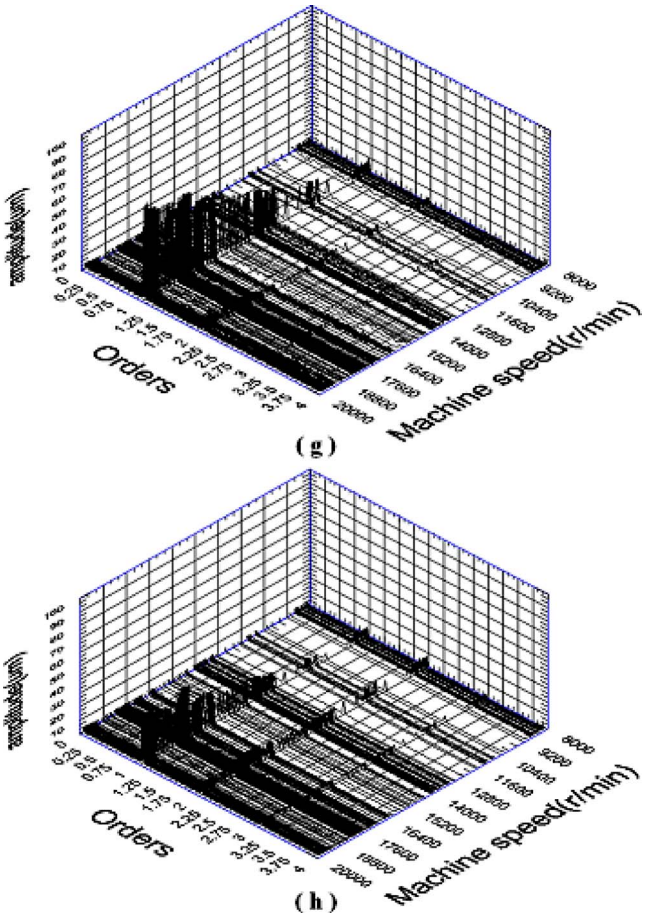

Fig. 5 Waterfalls in vertical motion from 8000 rpm to 20,000 rpm (*g*) and from 21,000 rpm to 8000rpm (*h*) at the drive end

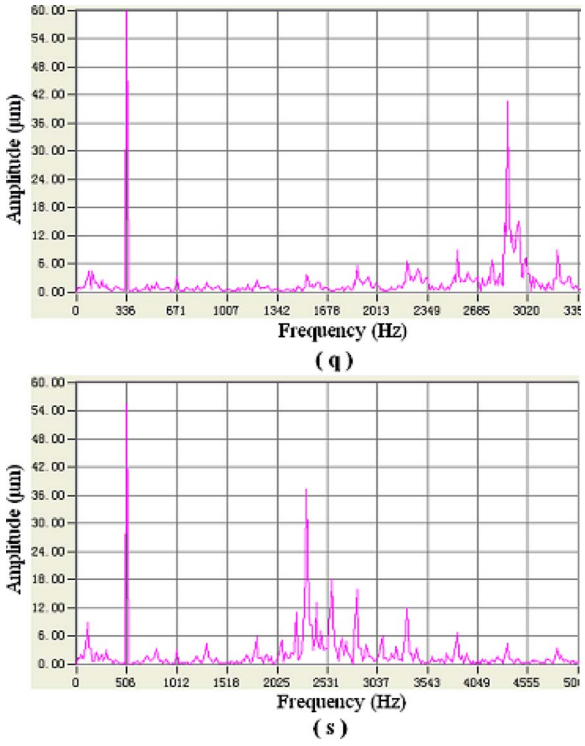

Fig. 6 Bode diagrams at the drive end with speeds of 20,134 rpm (*q*) and 30,368 rpm (*s*); radial clearance of 20 μm

amplitude of the fundamental frequency vibration is not more than 52 μm, and meanwhile there exists small half-frequency whirl, frequency doubling, and frequency tripling at the nondrive end, and small frequency doubling at the drive end, whose amplitudes are under 5.5 μm. In general, the half-frequency whirl is nearly related to the oil film itself and foil design, and high frequency vibrations may be excited by compressed air acting on the drive turbine. In Fig. 4, orbits at both 20,069 rpm and 27,224 rpm remain clear and regular, and fine periodic rotor motion remains stable.

Figure 5 displays waterfall plots in vertical motion from 8000 rpm to 20,000 rpm (*g*) and from 21,000 rpm to 8000 rpm (*h*) at the drive end. Besides the main fundamental frequency vibration, both waterfall plots have frequency doubling and tripling, and high frequency vibrations during speed up are more obvious than that during speed coastdown. It indicates that compressed air excitation greatly influences the rotor dynamic response. Furthermore, foil friction acting on the thrust disk or rotor surface may be one of the reasons to excite the high frequency vibration.

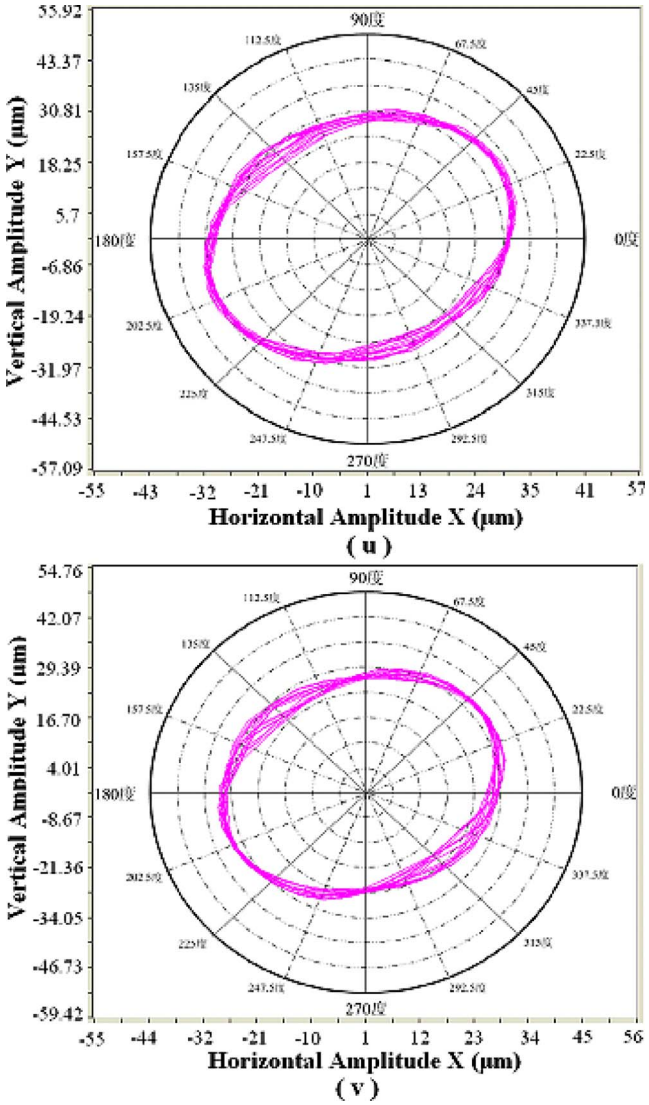

Fig. 7 Axis orbits at the drive end with speeds of 20,134 rpm (*u*) and 30,368 rpm (*v*); radial clearance of 20 μm

By comparing the foil working surface with the initial foil surface, some slight abrasion appears on both journal and thrust foil surfaces, and foil elasticity almost keeps unchanged. It proves that the oil lubricated multileaf foil bearing is favorable to decrease the foil abrasion and to improve the foil cooling because of higher viscosity of oil than air. Besides, the oil lubricated multileaf foil bearing represents the strong adaptive capacity of speed run-up and coastdown, and the capacity of withstanding impact and vibration.

Different radial clearances can be implemented by the change in the inner diameter of the bearing sleeve. Herein, the radial clearance is designed as 20 μm, and foils are the same ones as before. As shown in Fig. 6, many high and low frequency vibrations emerge simultaneously under the speeds of 20,134 rpm and 30,368 rpm; the rotor response is quite complicated. In Fig. 7, axis orbits are confusing. Comparing Figs. 3 and 4 with Figs. 6 and 7, it indicates that the radial clearance greatly influences the dynamic characteristics of the rotor-multileaf foil bearing system. For oil lubricated multileaf foil bearing, there were not any design rules and computing equations to decide the best radial clearance. Therefore, experiment is more important and necessary.

4 Conclusions

This paper designs and establishes the oil lubricated multileaf foil bearing test-bed and implements the experiments including different radial clearances, speed run-up and coastdown, etc. The experimental results indicate that the oil lubricated multileaf foil bearing can offer high-speed, long-life, and low friction loss. Also, this oil lubricated bearing represents strong adaptive capacity of speed up and down, and the capacity of withstanding impact and vibration. Moreover, different radial clearances greatly influence the rotor dynamic characteristics, and radial clearance is one of the most important tasks in oil lubricated multileaf foil bearing design.

References

[1] Agrawral, G. L., 1997, "Foil Air/Gas Bearing Technology—An Overview," ASME Paper No. GT-347.

[2] Sudheer Kumar Reddy, D., Swarnamani, S., and Prabhu, B. S., 1997, "Analysis of Aerodynamic Multileaf Foil Journal Bearings," Wear, **209**, pp. 115–122.

[3] Radil, K., Howard, S., and Dykas, B., 2002, "The Role of Radial Clearance on the Performance of Foil Air Bearings," NASA Report No. TM-211705.

[4] Gu, A., 1993, "Foil Bearing Turbopumps," AIAA Space Programs and Technologies Conference and Exhibit, Huntsville, AL, Sept. 21–23.

[5] Dellacorte, C., Zaldana, A. R., and Radil, K. C., 2004, "A Systems Approach to the Solid Lubrication of Foil Air Bearings for Oil-Free Turbomachinery," ASME J. Tribol., **126**, pp. 200–207.

[6] Walton, J. F., II, Heshmat, H., Tomaszewski, M. J., 2008, "Testing of a Small Turbocharger/Turbojet Sized Simulator Rotor Supported on Foil Bearings," ASME J. Eng. Gas Turbines Power, **130**, p. 035001.

Air-Standard Aerothermodynamic Analysis of Gas Turbine Engines With Wave Rotor Combustion

M. R. Nalim[1]
Associate Professor
Department of Mechanical Engineering,
Indiana University-Purdue University Indianapolis,
Indianapolis, IN 46202-5132

H. Li
Graduate Student
Department of Mechanical Engineering,
Purdue University,
West Lafayette, IN 47907

P. Akbari
Research Associate
Department of Mechanical Engineering,
Indiana University-Purdue University Indianapolis,
Indianapolis, IN 46202-5132

The wave rotor combustor can significantly improve gas turbine engine performance by implementing constant-volume combustion. The periodically open and closed combustor complicates thermodynamic analysis. Key cycle parameters depend on complex gas dynamics. In this study, a consistent air-standard aerothermodynamic model with variable specific heat is established. An algebraic model of the dominant gas dynamics estimates fill fraction and internal wave compression for typical port designs, using a relevant flow Mach number to represent wave amplitudes. Nonlinear equations for thermodynamic state variables are solved numerically by Newton–Raphson iteration. Performance measures and key operating conditions are predicted, and a quasi-one-dimensional computational model is used to evaluate the usefulness of the algebraic model. [DOI: 10.1115/1.3078790]

1 Introduction

Significant efficiency improvement is theoretically possible using pressure-gain combustors for gas turbines and jet engines [1]. Pressure gain can be achieved by confining the combustion mixture or by promoting detonation, with examples in pulse combustors [1], wave rotor combustors [2], and pulse detonation engines (PDEs) [3]. While the PDE relies on the inherent properties of a detonation wave, constant-volume combustion in wave rotor combustors relies mainly on mechanical confinement [4]. Deflagrative pulsed combustion was employed in the earliest known gas turbine [5] and the V-1 "buzz bomb." An inherent challenge of pulsed combustion is integration with nozzles, inlets, and turbines that prefer steady flow [3].

The wave rotor combustor integrates relatively well with turbomachinery and benefits from internal compression, as explained below. First developed as a pressure-exchange device, the wave rotor has been demonstrated [6] as a combustion device. Computational fluid dynamics (CFD) models [7] can determine varying gas properties on the inlet and outlet planes and integrate them over a cycle to estimate pressure gain. At a simpler level, purely thermodynamic analyses provide quick assessment of engine performance, but ignore gasdynamic constraints. Previous analytical models [8,9] have considered thermodynamic or particular gasdynamic cycles of pressure-exchange wave rotors, rather than "on-rotor" combustion. CFD models are necessarily specific in geometric and physiochemical features, and not as broadly applicable. It is desirable to establish an analytic aerothermodynamic model with the gasdynamic and energetic characteristics of the wave rotor combustor, providing realistic performance and thermal data for engine configuration design and operation.

This study establishes a consistent air-standard aerothermodynamic model evolved from previous models [10]. It specifically includes the dominant gas dynamics of the wave rotor combustor, with complex fluid losses represented by wave process efficiencies. Real gas caloric behavior is represented by a polynomially temperature-dependent specific heat, $c_p(T)$. Important engine performance parameters, temperature, and pressure data are evaluated as functions of an independent gasdynamic parameter that represents the primary wave amplitude in the rotor. CFD predictions are presented for some wave rotor cycles and combustion modes in a limited range of parameters to complement the predictions of the analytic model.

2 Wave Rotor Combustor

Although pressure-exchange wave rotors were commercialized decades ago [11], wave rotor combustors have been investigated only in recent years. Predicted potential for gas turbines and stand-alone engines led to experiments by General Electric (GE) in the early 1960s [2], and a successful demonstration by Asea Brown Boveri (ABB) in Switzerland in the early 1990s [6]. Both efforts highlighted needed improvements, mainly in mechanical design. A recent rig design by Rolls Royce awaits testing [12].

2.1 Wave Rotor Geometry and Working Principle. A wave rotor combustor consists of several combustion channels on a drum that rotates between two stationary end plates [2]. By rotation, each channel is periodically charged and discharged as it rotates past properly sized and timed inlet and outlet ports. When recharged with combustible mixture and closed, combustion is initiated and completed within the channel. Mechanical confinement of combustion gas in a fixed channel volume allows relatively even pressure rise by deflagrative combustion, but detonative or intermediate modes of combustion are also possible [4]. The flows in the manifolds (ducts) connected to the inlet/outlet ports are nearly steady, while rotor channel flow and combustion are inherently nonsteady—a key advantage of the wave rotor configuration [2].

The general model of gasdynamic processes inside the rotor channels used here is illustrated in Fig. 1, a simple schematic wave diagram of the typical outflow-inflow-combustion cycle in the wave rotor, with the common gas turbine and compressor shown schematically. Indispensable for cycle depiction, the wave diagram represents the time history of wave processes in each rotor channel as it rotates. Simplified pictorial depictions of three selected channels are shown at key reference states during the cycle of operation, and the trajectories of important waves are shown as various lines. Details of the combustion process are not shown; it is assumed to be completed under fixed volume. The focus is on the inflow-outflow gas dynamics that significantly influences the overall thermodynamic outcome. Unlike many other pulse combustion systems and PDEs, the wave rotor combustor operation is characterized by internal wave compression and expansion processes due to exit valving.

Atmospheric air (State 1) is compressed conventionally and enters the wave rotor (State 2) with fuel. Discharged burned gas (State 3) is expanded in a turbine to ambient pressure (State 4). Each channel undergoes filling, initiation and completion of combustion, and blowdown of the pressurized gas to the turbine. Following combustion, high-pressure gas is expelled when the right

[1]Corresponding author.

Manuscript received August 28, 2008; final manuscript received November 22, 2008; published online June 9, 2009. Review conducted by Dilip R. Ballal.

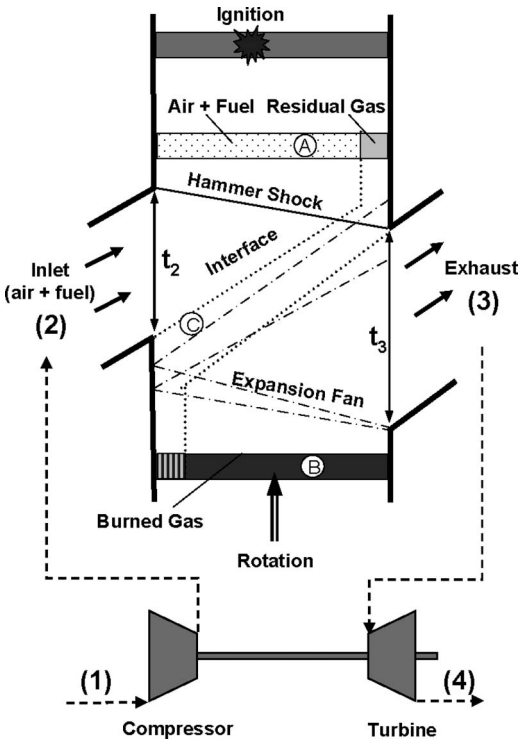

Fig. 1 Wave pattern in a developed view of the wave rotor combustor

end of the channel opens to the exhaust port, creating an expansion wave that travels to the left. As pressure falls, the left end of the channel opens to the inlet port, admitting combustible mixture. While filling continues, the scavenging of burned gas through the exit port is stopped by closing the exhaust port, generating a compressive wave or "hammer shock." The residual gas and fresh air-fuel mixture (State *A*) trapped in the channel are favorably compressed by this shock wave, which propagates toward the inlet end wall. With both ends of the channel closed, the mixture is ignited. Confined combustion increases the pressure and temperature in the channel to State *B*, with any residual gas moderating the pressure gain. Every channel undergoes exactly the same cycle in phase with its angular location, providing relatively steady flow at any port location.

A variety of cyclic flow and wave patterns are possible, depending on port timing, fuel distribution, and combustion modes [2]. In particular, flammability limits dictate nonuniform fuel distribution resulting in stratified combustion and leaves either hot burned residual gas or cold unburned gas within the channels. This work presents an algebraic model for the case of burned residual gas, providing periodic solutions for a wide range of wave amplitudes and residual gas fraction, down to the limit of zero fill with no pressure gain.

3 Aerothermodynamic Cycle Analysis

Air-standard cycles often assume either a homogeneous control-mass closed system (e.g., Otto cycle), or steady-flow control-volume component open systems (e.g., Brayton cycle). Oddly, the wave rotor combustor is characterized by nonsteady wave processes in nonhomogeneous fluid and by periodically open and closed phases. Nalim [10] provided a generalized *thermodynamic* model for pressure-gain combustors, considering internal losses and the buffering effect of residual gas. Their model's independent parameters—fill fraction and wave compression—are linked in the present *aerothermodynamic* model to a single independent variable, using the theory of characteristics and shock waves.

3.1 Assumptions. The conventional combustor in an unrecuperated gas turbine is replaced by the wave rotor, while the compressor and turbine are retained, with fixed adiabatic efficiencies. Wave rotor internal compression and expansion are also assigned adiabatic efficiencies to account for internal friction, shock losses, gradual opening/closing losses, and nonuniform port-mixing losses, by associating inflow with compression and outflow with expansion. Heat and leakage losses are neglected, consistent with adiabatic treatment of the turbomachinery. Combustion is treated as an external heat addition, and the working fluid is standard air [13] with $c_p(T)=0.9703+6.790\times10^{-5}T+1.658\times10^{-7}T^2-6.786\times10^{-11}T^3$ kJ/kg/K, T in kelvin. While the thermodynamic cycle is constructed on a calorically-true air-standard basis using this formulation consistently, the *gasdynamic* model assumes locally linear caloric behavior.

3.2 Analytical Procedures. The compressor inlet state is assumed as atmospheric (stagnation temperature T_{1t} and stagnation pressure P_{1t}), and its adiabatic efficiency η_c and pressure ratio $\Pi_c=P_{2t}/P_{1t}$ are prescribed. The compressor discharge stagnation temperature T_{2t} is determined [14] using Newton–Raphson iteration [15] to solve nonlinear polynomial equations.

The wave rotor cyclic wave pattern and ideal pressure gain depend on port timings and boundary conditions, and on mixture composition and combustion characteristics. This study, condensed here from a more detailed report [16], considers a simple wave pattern amenable to algebraic modeling, characterized by a single independent gasdynamic variable (outflow Mach number) that controls fill fraction, μ, and wave amplitudes of compression and expansion. It uses a simplified representation of the exhaust-port wave dynamics, leaving more complex cycles to be analyzed with CFD modeling.

Assuming thorough mixing of channel gases during combustion for conservative performance estimation [10], any residual gas will originate from mixed burned gas at postcombustion State *B*. We assume further that residual gas expands isentropically from State *B* to *rA* (assigning equivalently any irreversibility to the exiting gas expansion process). Thus, the mass conservation of ideal gases (gas constant, *R*) during combustion in a fixed volume requires

$$\mu T_A + (1-\mu)T_{rA} = T_B\frac{P_A}{P_B} = T_B\left[\exp\left(-\int_{T_{rA}}^{T_B}\frac{c_p(T)}{RT}dT\right)\right] \quad (1)$$

Conservation of energy requires heat addition evaluated for the trapped channel mass to equal that over the entire combustor as an open system

$$\mu\int_{T_A}^{T_B}c_v(T)dT + (1-\mu)\int_{T_{rA}}^{T_B}c_v(T)dT = \mu\int_{T_{2t}}^{T_{3t}}c_p(T)dT \quad (2)$$

For chosen combustor inlet and exit total temperatures T_{2t} and T_{3t}, these mass and energy equations involve four unknowns, T_A, T_{rA}, T_B, and μ. To close the analysis, we seek additional relationships below to obtain estimates of μ and T_B based on the gas dynamics of the exhaust and filling processes.

The initial rotor exit Mach number (M_3) is selected as an independent parameter, and distinguished from a port average M_{3avg}. Note that a low value of M_3 corresponds to a weak outflow expansion wave, and thus both a weak hammer shock and a low fill fraction, tending to Brayton-cycle constant-pressure combustion in the limit, as $M_3\rightarrow0$. Assuming constant port static pressure and entropy, static temperature T_3 is calculated iteratively from T_{3t} and M_{3avg}.

M_{3avg}, μ, and T_B are estimated based on a model of gas dynamics and port timing greatly simplified by iteratively estimating a mean specific heat ratio, γ, for the expansion process only, with-

out contradicting the fidelity of the overall thermodynamic analysis to air-standard caloric relations. Sound speed, a, and velocity, u, across an isentropic expansion wave are related by a Reimann invariant equation of one-dimensional unsteady gas flow [8]

$$u_B + \frac{2a_B}{\gamma - 1} = u_3 + \frac{2a_3}{\gamma - 1} \Rightarrow T_B = T_3 \left[\frac{\gamma - 1}{2} \mathrm{M}_3 + 1 \right]^2 \tag{3}$$

Although determined by approximate gas dynamics, this estimate of T_B anchors a particular thermodynamic cycle that will be constructed on a calorically-true air-standard basis. Other properties at State B are derived from calorically-true air-standard relations to States 3 and $3t$. The expansion wave fan has wave speed a_B at its leading edge, and initially $a_3 - u_3$ at its trailing edge. Upon reflection after traversing the channel length, L, the wave speed of the reflected leading edge changes as it passes through the wave fan from a_B initially to $a_3 + u_3$. Using a linear average for the variable speed region, the intersection location, x, of the reflected leading edge with the initial trailing edge, and arrival time of the reflected leading edge, t_{lead}, are, respectively

$$x = \frac{L(a_B - a_3 + u_3)(a_B + a_3 + u_3)}{a_B(a_B + 3a_3 - u_3)}$$

$$t_{\mathrm{lead}} = \frac{L}{a_B} + \frac{x}{(a_B + a_3 + u_3)/2} + \frac{L - x}{a_3 + u_3} \tag{4}$$

For $\mathrm{M}_3 < 0.9$, this estimate of t_{lead} is found to be within 1% of an exact analytical calculation reported in Ref. [8]. A similar assumption is made to estimate the time of arrival of the reflected trailing edge of the fan as

$$t_{\mathrm{trail}} = \frac{L - x}{a_3 - u_3} + \frac{x}{(a_C + a_3 - u_3)/2} + \frac{L}{a_C} \quad \text{with}$$

$$a_C = a_3 \left[1 - \frac{\gamma - 1}{2} \mathrm{M}_3 \right] \tag{5}$$

being the speed of sound in the simple wave region C behind the reflected expansion, estimated using the appropriate Reimann invariant. The exit port is assumed to close when the exit velocity reaches zero at t_3, taken to be the simple average of t_{lead} and t_{trail}. Furthermore, we assume a linear exit velocity profile between u_3 at t_{lead} and zero at t_3 to define $\mathrm{M}_{3\mathrm{avg}}$ such that it predicts mass flow equivalently in the exit port.

The computed $\mathrm{M}_{3\mathrm{avg}}$ is compared with the nominal value specified as a parameter, and the calculation is iterated to improve the estimates of T_B and $\mathrm{M}_{3\mathrm{avg}}$. The fill fraction is the ratio of outflow mass to channel mass

$$\mu = \frac{\rho_3 \mathrm{M}_{3\mathrm{avg}} a_3 t_3}{\rho_B L} = \frac{P_3}{P_B} \frac{T_B}{T_3} \frac{(t_{\mathrm{trail}} + t_{\mathrm{lead}}) a_3}{2L} \mathrm{M}_3 \frac{t_{\mathrm{lead}} + (t_{\mathrm{trail}} - t_{\mathrm{lead}})/4}{t_{\mathrm{lead}} + (t_{\mathrm{trail}} - t_{\mathrm{lead}})/2} \tag{6}$$

The remaining unknowns T_A and T_{rA} are determined by two-dimensional Newton–Raphson iteration of mass and energy conservation, with evaluation of the Jacobian matrix of the functions. The pressure ratios for adiabatic internal compression and expansion are obtained by applying isentropic efficiencies η_{WC} and η_{WE} to the internal compression and expansion processes, respectively, and the combustor pressure gain P_{3t}/P_{2t} is determined. Turbine specific work is calculated, applying a given turbine efficiency, η_t, and the cycle performance is determined.

4 Application

For illustration, the above methodology is applied to a wave rotor combustor retrofit of a commercial small gas turbine: the Capstone C-60 microturbine engine, with manufacturer-estimated $\Pi_c = 4.8$, $T_{3t} = 1227$ K, $\eta_c = 83\%$, $\eta_t = 85\%$, with $T_{1t} = 300$ K, and assumed wave rotor internal efficiencies.

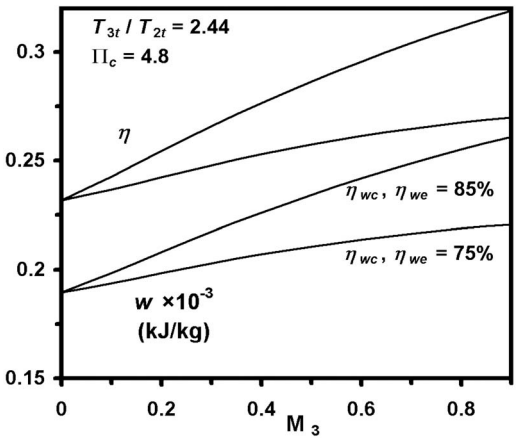

Fig. 2 Efficiency, η, and specific work, w, as functions of wave rotor combustor exit Mach number for different wave rotor internal efficiencies

4.1 Wave Rotor Combustion Effect on Existing Engine. Design of a wave rotor combustor for this engine assumes fixed P_{2t}, T_{2t}, and T_{3t}, and a resized turbine for flow matching. As design parameter M_3 increases from zero (no filling) to near unity (choked condition), a stronger expansion fan with larger pressure drop (P_B/P_{3t}) and larger positive flow work generates correspondingly higher wave compression pressure ratio $\Pi_{\mathrm{WC}} = P_A/P_{2t}$ and larger inlet flow work due to the stronger hammer shock. Fixed heat addition at higher temperature and larger fill fraction, causes higher overall pressure ratio, $\Pi = P_{3t}/P_{2t}$. Conversely, as $\mathrm{M}_3 \to 0$, all wave amplitudes die out, $\mu \to 0$, and the cycle degenerates to the Brayton cycle.

The effect of μ and Π_{WC} predicted by simpler thermodynamic models [10] is confirmed, but the aerothermodynamic model illustrates how these two parameters tend to work together, rather than independently. An effective gasdynamic cycle design must provide both strong wave action and high fill fraction. Overall cycle performance metrics are shown in Fig. 2, for internal efficiencies $\eta_{\mathrm{WC}} = \eta_{\mathrm{WE}} = 0.85$ or 0.75, for each calculation. Compression and expansion efficiencies have significant impact on overall performance, highlighting the need for better understanding of wave rotor loss mechanisms using detailed CFD modeling and experiments.

4.2 Effect of Combustor Heat Addition Temperature Ratio. The combustor fuel burn and consequent temperature increase will vary for off-design operating conditions and for other engines. Performance metrics are shown in Fig. 3, as the combustor temperature ratio varies between 2.0 and 3.5, for fixed compressor outlet conditions with internal efficiencies assumed at 80% and M_3 set to 0.6. The fuel-air mass ratio is varied to match an average fuel heating value. Unlike in the ideal Brayton cycle, where cycle efficiency is a direct function of compressor pressure ratio, the wave rotor combustor increases gains with more heat input, due to its pressure gain. Different combustor designs should be evaluated for a given combustor temperature ratio.

5 Computational Model

Using the results of the algebraic model as a guide, CFD is used to investigate more complex and realistic gasdynamic and combustion features, and to provide quantitative predictions for specific rotor and port geometry. CFD models should be selected judiciously, depending on knowledge of grid-scale physics. Detailed model features cannot be validated until equally detailed experimental observations are available. Measurements of the unsteady gas dynamics in a pressure-exchange wave rotor have been recently used [17] to validate a quasi-one-dimensional unsteady

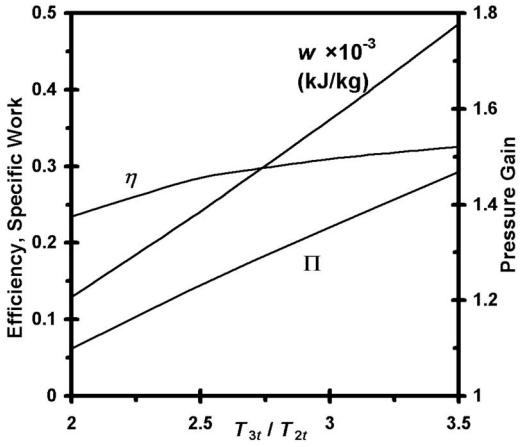

Fig. 3 Cycle efficiency, specific work, and pressure gain as functions of temperature ratio with $M_3=0.6$, $\eta_{WE}=\eta_{WC}=0.8$

flow code (NASA-Q1D) with comprehensive loss modeling [7,18] and a simple combustion model. This simplified CFD model differs from the presented algebraic model in the following aspects.

(a) The port timing and boundary conditions can be set arbitrarily without simplistic wave patterns or uniform flow assumptions, but require significant judgment, experience, and creativity, for example, allowing the designer to optimize port opening and closing to maximize wave compression and fill fraction.

(b) Different timing and combustion models are used, and there is no large-scale mixing of postcombustion gases affecting residual gas density and fill fraction.

(c) The algebraic model is indifferent to combustion rate and assumes uniform overlean combustible mixture. In the CFD model, a minimally flammable mixture with an equivalence ratio of 0.7 is required, and thus requires the channel mixture to include "dilution" air (apart from residual gas). The resulting thermal stratification strongly influences wave speeds, port timing optimization, mixing losses, and pressure gain. The flame speed depends principally on turbulent eddy diffusivity, assigned to be 1000 times the molecular diffusivity.

(d) The CFD model explicitly includes wall friction drag, shock losses, and port-mixing losses, while other losses modeled in the code were not activated. Loss effects are case dependent, unlike the assumed η_{WC} and η_{WE} of the algebraic model.

(e) Specific heat ratio is constant at $\gamma=1.3$, and the hydraulic diameter is set at $0.083L$ for estimating friction losses.

An example CFD simulation is presented in Fig. 4 as computed contour plots or "wave diagrams" of nondimensional pressure, temperature, and fuel concentration as a function of time (vertical axis) for one cycle period. A plot of inflow and outflow velocity is also presented, leftmost. The temperature, pressure, and velocity are nondimensionalized by the combustor inlet stagnation state properties, T_{2t}, P_{2t}, and a_{2t}, respectively, while the fuel concentra-

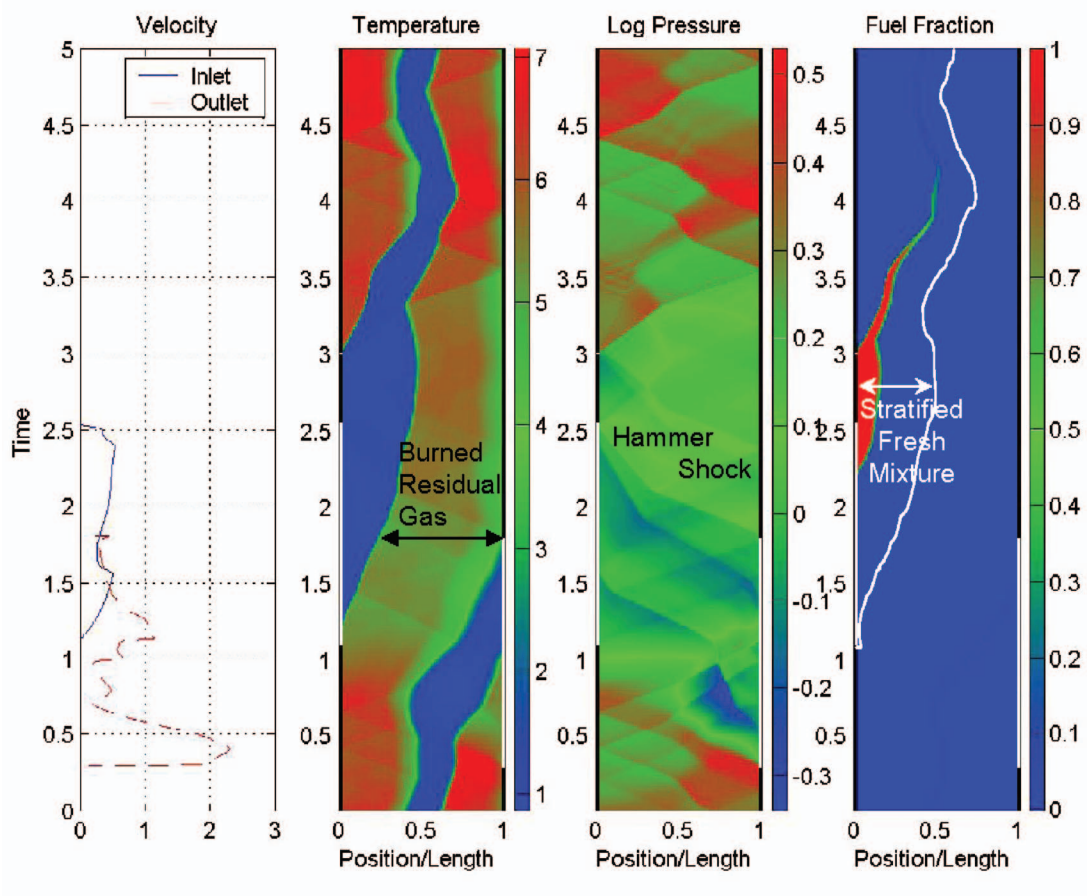

Fig. 4 CFD simulation of wave rotor combustor cycle with burned residual gas ($\mu=0.76$) and forward propagating deflagration in stratified fuel-air mixture

tion is referenced to an equivalence ratio of 0.70. Axial distance is nondimensionalized by channel length, L, and time by L/a_{2t}. A color scale bar is provided to the immediate right of each contour plot. The port and wall durations are indicated, respectively, by white and black vertical lines sidelining each contour plot.

Following prior combustion the exit port opens with its static pressure set at 60% of inlet stagnation pressure, and generates an expansion wave that travels to the left, causing high speed outflow. As pressure falls at the inlet wall, the inlet port opens, and subsequently, the exit port closes, generating the hammer shock. The inlet port closes exactly when the hammer shock arrives, having supplied a stratified mixture that places fuel in flammable mixture near the inlet end wall and unfueled air in the remainder of the channel. Unlike in the algebraic model, neither outflow nor inflow is uniform (see velocity plot), and neither precombustion nor postcombustion gases are uniform. When the exit port closes, the right side of the channel is occupied by residual hot gas, consisting of almost all the hot gas from stratified combustion in the previous cycle, much hotter than the equivalent burned residual of the algebraic model where the combustion gases mix fully in the channel. Hot residual gas degrades performance [11], and the highly nonuniform exit velocity and enthalpy flux profiles suggest a large mixing loss. The flame propagates "forward" from the igniter placed on the inlet-side end wall. The hot and cold gases are expelled when the exit opens again, and are assumed to fully mix in the exhaust duct to reach the required State $3t$ conditions.

5.1 Summary of CFD Studies and Comparison With the Algebraic Model. Diverse cycle features [2] are possible with additional ports, nonuniform fuel-air mixtures, or different combustion modes and ignition methods. The computational study included cycles in which residual gas is unburned and relatively cold, obtained by limiting combustion to a downstream part of the channel. Although the main thermodynamic parameters of algebraic and CFD models are similar, the CFD model makes fewer simplifying assumptions and retains more detailed features, including significant kinetic energy and pressure imbalance in the gas at all times. Furthermore, the states identified as A and B in the algebraic model generally cannot be identified unambiguously in the CFD models, as the flow does not completely equilibrate in pressure nor at all in temperature. Wave compression pressure ratio, Π_{WC}, is estimated from mass and energy conservation. However, equivalent compression and expansion efficiencies cannot be determined, except for the cases of $\mu \approx 1$.

With these caveats in mind, the data from ten CFD solutions for combustion with burned residual gas (six cases) and unburned residual gas (four cases) were examined. They all involve stratified fresh mixture, in contrast to the uniform mixture assumed in the algebraic model. The overall temperature ratio is maintained at $T_{3t}/T_{2t}=2.44\pm0.02$, and a range of exit static pressure and port timings are used to obtain varying μ.

Π_{WC} and μ were independent parameters in earlier purely thermodynamic models [10], but gas dynamics drives both up at higher flow Mach numbers. For burned residual gas, their correlations were positive but different for CFD and algebraic methods. Stratified burned and cold gas layers in the CFD model multiply and delay the wave reflections, and dictate different port timings, as exit velocity gradually decreases and weakens the hammer shock.

The algebraic model was exercised for constant $\gamma=1.3$ and $\eta_{WC}=0.73$ and $\eta_{WE}=0.86$ efficiencies derived from a fully purged CFD case with the same combustion direction as the burned-gas residual CFD cases. Comparison of the algebraic and CFD calculations of performance must consider the combined influence of cycle parameters. A useful linear extension of the dependence of Π on parameters Π_{WC} and μ can be extracted from the algebraic model by approximating the algebraic solution with a linear multivariate regression fit. Such a correlation is potentially useful for design guidance, and can be tested for validity using CFD prediction for similar cases.

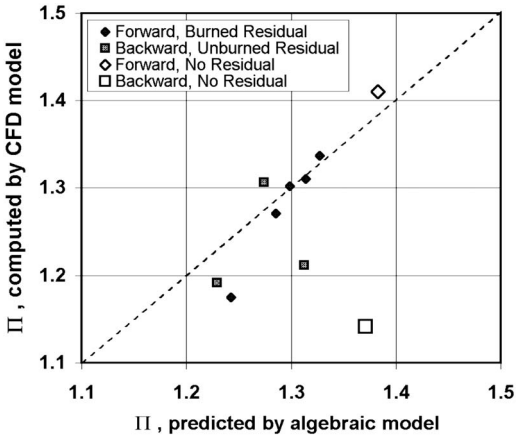

Fig. 5 Pressure-gain comparison of CFD and linear approximation to algebraic model

The algebraically predicted pressure gain was analyzed using standard statistical regression techniques available in a spreadsheet software program and found to be approximated well (correlation coefficient 0.999642) by a linear fit $\Pi=0.815+0.287\mu+0.166\Pi_{WC}$. The limited number of CFD cases with burned residual gas and forward combustion propagation are tested against this prediction in Fig. 5 (small diamond markers). Although they lie in a different region of the μ-Π_{WC} space, the computed pressure gain of the burned residual CFD cases are reasonably well matched with the predictions of the linearly-extended algebraic model. This correlation allows the predictions of the algebraic model to be extended to wider gasdynamic regimes, if the residual gas density is comparable to algebraic model assumptions. Much of the deviation from fit to the CFD model may be due to variations in wave compression and expansion efficiency that are difficult to estimate.

Also shown in Fig. 5 are the same comparison for the CFD cases of unburned gas residual (backward flame propagation) and no residual (both forward and backward propagations). It is unsurprising that the correlation is poor for unburned residual gas, as this contradicts an important assumption of the present algebraic model. A separate model for unburned residual gas cycles may allow a parallel correlation to be established.

6 Conclusions

A consistent air-standard aerothermodynamic algebraic analysis is applied to the wave rotor combustor, using the theory of characteristics and shock waves and variable specific heat. As wave amplitudes, fill fraction, and degree of combustion confinement vary with an independent design parameter, the model evaluates the combustor pressure gain and cycle performance. Furthermore, an existing wave rotor combustor CFD model is exercised to evaluate algebraic model applicability. Although the linkage between wave compression and fill fraction in the CFD model is different from the algebraic model, the general performance trends, as a function of these variables, are similar.

Analytic predictions that a fully purged wave rotor combustor could provide a nominal 60 kW microturbine with nearly 40% pressure gain and 30% fuel savings are consistent with CFD analysis allowing shock, friction, gradual opening, and port-mixing losses, but additional losses must be considered.

Nomenclature

a = speed of sound (m/s)

c_p and c_v = constant-pressure and constant-volume specific heats (kJ/kg/K)
L = channel length (m)
M = Mach number
P = pressure (Pa)
R = gas constant (kJ/kg K)
T = temperature (K)
t = port open time (s)
w = specific work (kJ/kg-air)
u = velocity (m/s)
μ = fill fraction
Π = pressure ratio
η = efficiency
γ = specific heat ratio

Subscripts

A = state before combustion
B = state after combustion
C = state after reflected expansion wave
c = compressor
r = residual gas
t = stagnation state total property
WC = wave compression
WE = wave expansion

References

[1] Kentfield, J. A. C., and O'Blenes, M., 1988, "Methods for Achieving a Combustion-Driven Pressure Gain in Gas Turbines," ASME J. Eng. Gas Turbines Power, **110**(4), pp. 704–711.
[2] Akbari, P., and Nalim, M. R., 2009, "Recent Developments in Wave Rotor Combustion Technology and Future Perspectives: A Progress Review," J. Propul. Power, in press.
[3] Roy, G. D., Frolov, S. M., Borisov, A. A., and Netzar, D. W., 2004, "Pulse Detonation Propulsion: Challenges, Current Status, and Future Perspective," Prog. Energy Combust. Sci., **30**(6), pp. 545–672.
[4] Nalim, M. R., 1999, "Assessment of Combustion Modes for Internal Combustion Wave Rotors," ASME J. Eng. Gas Turbines Power, **121**(2), pp. 265–271.
[5] Stodola, A., 1927, *Steam and Gas Turbines*, Vol. 2, McGraw-Hill, New York,.
[6] Walraven, F., 1994, "Operational Behavior of a Pressure Wave Machine With Constant Volume Combustion," ABB Technical Report No. CHCRC 94-10.
[7] Nalim, M. R., 2000, "Longitudinally Stratified Combustion in Wave Rotors," J. Propul. Power, **16**(6), pp. 1060–1068.
[8] Resler, E. L., Moscari, J. C., and Nalim, M. R., 1994, "Analytic Design Methods for Wave Cycles," J. Propul. Power, **10**(5), pp. 683–689.
[9] Akbari, P., Müller, N., and Nalim, M. R., 2006, "Performance Enhancement of Microturbine Engines Topped With Wave Rotors," ASME J. Eng. Gas Turbines Power, **128**(1), pp. 190–202.
[10] Nalim, M. R., 2002, "Thermodynamic Limits of Work and Pressure Gain in Combustion and Evaporation Processes," J. Propul. Power, **18**(6), pp. 1176–1182.
[11] Akbari, P., Nalim, M. R., and Müller, N., 2006, "A Review of Wave Rotor Technology and Its Applications," ASME J. Eng. Gas Turbines Power, **128**(4), pp. 717–735.
[12] Matsutomi, Y., Hein, C., Lian, C., Meyer, S., and Heister, S., 2007, "Facility Development for Testing of Wave Rotor Combustion Rig," AIAA Paper No. 2007-5052.
[13] Cengel, Y. A., and Boles, M. A., 2005, *Thermodynamics: An Engineering Approach*, 5th ed., McGraw-Hill, New York.
[14] Sarabchi, K., 2004, "Performance Evaluation of Reheat Gas Turbine Cycles," Proc. Inst. Mech. Eng., Part A, **218**(7), pp. 529–539.
[15] Chapra, S. C., and Canale, R. P., 2001, *Numerical Methods for Engineers: With Software and Programming Application*, 4th ed., McGraw-Hill, New York.
[16] Nalim, M. R., Li, H., and Akbari, P., 2009, "Air-Standard Aerodynamic Analysis of Gas Turbine Engines With Wave Rotor Combustion," ASME Paper No. GT2009-60055.
[17] Wilson, J., Welch, G. E., and Paxson, D. E., 2007, "Experimental Results of Performance Tests on a Four-Port Wave Rotor," AIAA Paper No. 2007-1250.
[18] Paxson, D. E., 1997, "A Numerical Investigation of the Startup Transient in a Wave Rotor," ASME J. Eng. Gas Turbines Power, **119**(3), pp. 676–682.